Electromagnetic Wave Scattering by Aerial and Ground Radar Objects

EDITED BY

Oleg I. Sukharevsky

CRC Press
Taylor & Francis Group

Electromagnetic Wave Scattering by Aerial and Ground Radar Objects

Electromagnetic Wave Scattering by Aerial and Ground Radar Objects

EDITED BY
Oleg I. Sukharevsky
Kharkov University of Air Forces, Kharkov, Ukraine

CRC Press
Taylor & Francis Group
Boca Raton London New York

CRC Press is an imprint of the
Taylor & Francis Group, an **informa** business

CRC Press
Taylor & Francis Group
6000 Broken Sound Parkway NW, Suite 300
Boca Raton, FL 33487-2742

First issued in hardback 2019

ISBN-13: 978-1-4665-7678-0 (hbk)

Library of Congress Cataloging-in-Publication Data

Electromagnetic wave scattering by aerial and ground radar objects / editor, Oleg I. Sukharevsky.
pages cm
Includes bibliographical references and index.
ISBN 978-1-4665-7678-0 (hardback)
1. Radar--Data processing. 2. Electromagnetic waves--Scattering. 3. Radar cross sections. 4. Radar targets. I. Sukharevsky, Oleg I., editor of compilation.

TK6578.E43 2014
621.3848--dc23 2014004209

Visit the Taylor & Francis Web site at
http://www.taylorandfrancis.com

and the CRC Press Web site at
http://www.crcpress.com

In cherished memory
of our teacher, Professor
Il'ya Vladimirovich Sukharevsky

Contents

Preface

This book is intended for scientists and engineers working in the field of radar and computational electrodynamics.

The contents of the book is the result of the compilation of works by group of authors who represent the scientific school of applied electrodynamics established in the 1960s by Professor I.V. Sukharevsky within the Govorov Military Radiotechnical Academy. Representatives of this school studied electromagnetic wave scattering from objects of various natures in the Kharkiv Military University, United Scientific Research Institute of Ukrainian Armed Forces, and Kharkiv Ivan Kozhedub University of Air Force.

An important place that the study of radar scattering from airborne and ground objects occupies in the whole radar field predetermined the book's main content. In the first place, it was the number of generalizations of the key postulates of classical electrodynamics theory that needed to be introduced in order to provide grounds for the methods of radar object scattering computation developed later on. The basic results regarding development of both the electrodynamics theory and numerical computation methods are original and are presented in the first two chapters of the book.

Chapter 3, intended as a reference, is for consumers who are engineers pursuing the design of radar detection and identification algorithms with regard to airborne and ground objects. The chapter contains a great deal of reference material obtained by computation: circular diagrams of radar backscattering; mean and median RCS values of various objects; probability distributions of echo signal amplitude given various parameters of illumination and various kinds of underlying surface (for ground objects); and impulse responses of various airborne and ground objects given their illumination with wideband signals.

The book can be useful to a wide audience: scientists concerned with the development of electromagnetic wave scattering theory, computational electrodynamics specialists, as well as to radio physics engineers pursuing development of radar detection and identification algorithms of radar objects.

The authors' contributions to the book have been as follows: Chapter 1 has been written by Oleg I. Sukharevsky; Sections 2.1 through 2.3 and 2.5 are the combined work of Vitaly A. Vasilets and Oleg I. Sukharevsky; Section 2.4 has been written by Sergey V. Nechitaylo and Oleg I. Sukharevsky (except for Section 2.4.2, which has been written by Vitaly A. Vasilets and Oleg I. Sukharevsky); Chapter 3 has been written by the mutual effort of Vitaly A. Vasilets, Sergey V. Nechitaylo, Oleg I. Sukharevsky, and Valery M. Orlenko.

Acknowledgment

The authors express their sincere gratitude to professors Sergey Aleksandrovich Masalov, Yuri Konstantinovich Sirenko, and Sergey Petrovich Leshchenko. Their advice and valuable observations facilitated improvement of the contents of the book.

Editor

Professor Oleg I. Sukharevsky has worked in the field of applied mathematics and computational electrodynamics since 1972 when he received a diploma degree in computational mathematics from Kharkov Gorky State University and joined the Kharkov Govorov Military Academy of Air Defense as an engineer. Since 1977 Dr. Sukharevsky has studied and developed numerical computation methods that were based on solving the two-dimensional integral equations to obtain scattering characteristics of nonclosed screen and antenna under frame radome. In 1983, Dr. Sukharevsky earned the candidate of technical science degree (PhD analog) from the All Union Research Institute of Radiotechniques, by that time he was raised to the position of a senior researcher. Since then, he has carried on studying the scattering phenomenon and started the development of scattering theory and technique for computing radar cross section of complex objects, special emphasis being put on the objects that had surface fractures (sharp edges) and were covered (partly) with radar absorbing materials. In 1993, he earned a doctor of science degree in radar technology from Kharkov Govorov Military Academy of Air Defense.

Since the fall of the Soviet Union in 1991, Dr. Sukharevsky has held various academic and faculty positions. He taught applied mathematics and computational electrodynamics at the Govorov Academy, which had been reorganized in 1993 into Kharkov Military University, and later, in 2004, into Kharkov Kozhedub University of Air Forces. He was also employed as principal researcher by the Usikov Institute of Radio Physics and Electronics of the National Academy of Sciences of Ukraine from 1996 to 2001 and from 2004 to 2008. During the turbulent time that ensued after the fall of the Soviet Union, he founded a scientific school that was instrumental in shaping many prominent Ukrainian engineers and scientists. Around that time there was a burst in the development of computer power that introduced a whole new capability for implementing theoretical electrodynamics methods in operational software. The introduction of personal computers facilitated the development of computer models of scattering from a number of aerial, ground, and subsurface objects. Dr. Sukharevsky along with alumni of his academic school had acquired wide experience of scattering simulation from real radar objects sounded by not only narrowband but also wideband and ultrawideband probing signals. He authored and coauthored five books and more than 150 papers in both Russian and in English. Oleg Sukharevsky is a Senior Member of the IEEE (The Institute of Electrical and Electronics Engineers) and a Honored Science Worker of Ukraine.

Currently, Dr. Sukharevsky is a leading scientific researcher and a professor in the Air Force Research Center at Kharkov Kozhedub University of Air Forces. His main areas of interests include, but are not limited by, mathematical theory of diffraction and scattering characteristics of radar targets.

Contributors

Sergey V. Nechitaylo earned a diploma in radioelectronic devices and systems from Kharkov Military University in 1996 and a PhD in radar in 2004.

Currently, Dr. Nechitaylo is a leading scientific researcher within the Air Force Research Center at Kharkiv Kozhedub University of Air Forces and a senior scientist. His scientific interests include antenna theory and the study of radar observability of various objects.

Valery M. Orlenko earned a diploma in radio engineering from Zhitomir Higher Military School of Radio Electronics of Air Defense in 1992 and a PhD in radar in 1998.

Currently, Dr. Orlenko is a leading scientific researcher within the Air Force Research Center at Kharkiv Kozhedub University of Air Forces and a senior scientist. His scientific interests include the study of the methods for processing wideband radar signals.

Oleg I. Sukharevsky earned a diploma in computational mathematics from Kharkiv Gorky State University in 1972, a PhD in 1983, and a doctor of science in radar in 1993.

Currently, Dr. Sukharevsky is a leading scientific researcher within the Air Force Research Center at Kharkiv Kozhedub University of Air Forces, and a professor. His main areas of interest are mathematical theory of diffraction and scattering characteristics of radar targets. He is a senior member of the IEEE.

Vitaly A. Vasilets earned a diploma in radio engineering from Zhitomir Higher Military School of Radio Electronics of Air Defense in 1991, a PhD in 1994, and a doctor of science in radar in 2006.

Currently, Dr. Vasilets is a leading scientific researcher and a senior scientist in the Air Force Research Center at Kharkiv Kozhedub University of Air Forces. His scientific interests include the study of scattering characteristics of radar targets.

Abbreviations

ADC	Analog-to-digit converter
AFR	Amplitude–frequency response
ALCM	Air launch cruise missile
AnC	Anechoic chamber
AS	Antenna system
DFT	Discrete Fourier transform
ED	Envelope detector
EM	Electro-magnetic
FFT	Fast Fourier transform
GDT	Geometrical diffraction theory
GO	Geometrical optics
HFA	High-frequency amplifier
HRRP	High-range resolution profile
IR	Impulse responses
LFA	Low-frequency amplifier
LFM	Linear frequency modulation
PDT	Physical diffraction theory
PO	Physical optics
RA	Reflector antenna
RAM	Radar absorbent material
RCS	Radar cross section
RecA	Receive antenna
RV	Radar visibility
TPG	Timing pulse generator
TrA	Transmit antenna
TSG	Transmit signal generator

Introduction

Analysis of existing and future weapon systems, of available scientific publications, of research programs (stealth program for instance), as well as of the local war experiences shows the special place that scattering (secondary radiation) characteristics of different air assault means (aircraft, cruise missiles, etc.) and of ground military objects (tanks, armored personnel carriers, etc.) take in the process of armaments and military equipment development. Sometimes the term radar visibility is used with regard to these objects [1]. It is worth mentioning that for military radar aimed at detecting aerial objects, information on scattering characteristics of not only air assault means but also of civilian aircraft is vital.

One of the mainstreams of up-to-date assault means and military equipment design is the creation of cruise missiles, aircraft, ground objects (armored vehicles) with low radar cross section (RCS).

Lowering of the radar visibility of air and ground objects is usually achieved by streamlining them in special ways and applying radar absorbing materials (RAM) to those local parts of their surfaces that provide the most intense scattering, the latter being caused by geometry-optical specular reflections and scattering at the surface fractures. Measures taken to lower radar visibility not only reduce the power of scattered signals but also lead to significant changes in other scattering characteristics, polarization ones in particular, which make it harder to predict the detection and recognition performance by radar. An important theoretical and applied problem is also to find and account for scattering peculiarities introduced by use of a separate transmitter and receiver placed at some distance from one another (bistatic or multistatic radar), which provides for some benefits when solving the target identification tasks [2].

Therefore, to solve the target detection and identification tasks, modern radar requires a priori information to be obtained about the target scattering characteristics that would take into account a complex of complicating factors such as irregularities of the target surfaces, presence of RAM, and multistatic radar configuration.

Since satisfactorily accurate and statistically consistent experiments on the scattering characteristics are hard to organize and are very expensive, development of methods for the theoretical prediction of scattering characteristics of air vehicles and for their computer simulation taking into account the complicating factors mentioned above becomes vital.

Let us also note that mathematical simulation of the signals scattered from complex radar objects that account for multistatic transmission and reception and other complications is very helpful when analyzing target identification performance in future radar systems. Such simulation allows one to determine the optimal placement of radar sites over the area of interest together with the requirements of the characteristics of the radars themselves.

The well-known short-wave diffraction methods that have long since become classical—geometrical optics (GO), geometrical diffraction theory (GDT), physical optics (PO), and physical diffraction theory (PDT)—cannot be used directly without significant correction and generalization to solve the radar scattering problems in this complicated formulation.

Development of improved methods adapted to specifics of radar scattering problems formulated here is the main aim of this book. Development of such methods and performance of a considerable amount of research based on these methods, in its turn, required further development of the radar scattering electrodynamics theory for different kinds of scattering object structures.

Chapter 1 contains generalizations of such basic electrodynamics statements as the Lorentz reciprocity theorem and the image principle with regard to the fields corresponding, respectively, to different material fillings of the same space area, and to a space containing different type irregularities—dielectric, conductor, or magnetic. These generalizations allow obtaining integral

field representations, based on which one can study the influence of underlying surface, radar absorbing and heat-insulating materials, as well as other layered structures on electromagnetic fields scattered from radar targets.

Among other general theoretical results presented in the chapter, there is the generalization on the case of nonflat region (and corresponding stationary phase points of not only the elliptical but also the hyperbolic kind) of the well-known formula by M.I. Kontorovich in the two-dimensional stationary phase method. Combined with its nonstationary analog, this result allows significant improvement to the physical optics method when applied to computing secondary radiation from radar targets for both monostatic and multistatic radar. When doing so, we provide regularization of solutions obtained, the latter being based on elimination of "terminator discontinuities" appearing due to inadequate description, in physical optics approximation, of the surface current density in the vicinity of the "light-shadow" border.

Computation of such an important parameter as RCS of radar object is related, in general, to considerable theoretical and computational difficulties. In this book, RCS computation is described consequently in two- and three-dimensional formulations within bounds of strict theory and approximations of physical optics. Besides, for some classes of objects, there are practical useful RCS estimates, which are expressed for the three-dimensional problem through the values of RCS per unit length in the corresponding two-dimensional problem for the two orthogonal polarizations of incident wave [3].

An important theoretical issue considered in Chapter 1 is whether the reciprocity principle [4] holds for the case of approximating fields, in particular, of those appearing in physical optics approximation. It is shown that in this case the reciprocity principle holds for monostatic radar, yet in the case of multistatic radar the reciprocity principle does not hold in general, which should be accounted for in practical calculation.

Chapter 1 also contains the original method for computing impulse responses (IR) or smoothed out IRs of smooth objects in the general case of multistatic radar using the physical optics approach. It is worth mentioning that the physical optics approximation of IR in the known work [5] is received for the very narrow limits, which include the following: (1) only monostatic radar configuration is considered; and (2) the terminator (shadow boundary) is assumed to be a flat curve with its plane being perpendicular to the direction of incidence. However, it is easy to bring forward simple examples of smooth closed (even convex) surfaces that would have a nonflat terminator. Moreover, in the case of scattering from ellipsoid, illumination from any direction $\vec{R}^0$ by electromagnetic wave creates the flat terminator curve (ellipse), and this terminator plane is perpendicular to $\vec{R}^0$ only if the incidence direction $\vec{R}^0$ is parallel to one of the ellipsoid's semi axes.

In the work [6] (assuming the same conditions as in clauses (1), and (2) above), the sum members are singled out that are brought into the high-frequency asymptotic of the IR Fourier image by the break in surface current density at terminator in physical optics approximation. Let us note that the research methods in the works cited above are essentially based on the conditions (1), and (2) and these methods cannot be used when either one is violated.

The method proposed in this book for the bistatic radar case is applicable for arbitrary orientation of the terminator's plane relative to the incident wave direction (in principle, the same method works in the case of a nonflat terminator too). We also consider a characteristic example of scattering from a smooth convex object and we study the specifics of its IR structure in the bistatic case. We single out and eliminate from the IR solution the major sum members of asymptotic contribution from the surface current density break at the terminator. The latter makes the IR solution regularized and, as a result, increases significantly the accuracy of physical optics approximation over the time span up to arrival of the diffraction "creeping" wave that goes over the shadow area.

In Chapter 2, methods are developed for computing the scattering from the radar objects with surface fractures and those covered with RAM.

We propose in this chapter the asymptotic method for solving the scattering problem for perfectly conducting objects with toroidal RAM covering the surface fractures in the case of the arbitrary

multistatic radar configuration. The method is based on integral representations by Stratton-Chu and their asymptotic expression for the far-field zone. The solution to the simulative problem of oblique incidence of a plane electromagnetic wave on a perfectly conducting wedge with a radar absorbing cylinder at its edge is used to facilitate the method. Such an approach, unlike the edge wave method [7,8], turns out to be well adjusted to the presence of nonperfectly conducting scatterers of resonant dimensions and to the general case of the multistatic radar configuration.

To elaborate the estimate of the contribution from the perfectly conducting vicinity of a "specular" point of elliptical type to the total scattered field in the case of the multistatic radar configuration, we obtained two sum members of the ray asymptotic for this field and estimated the contribution of such a local scatterer to the total field also in the case when it contains the RAM coating.

Verification of the methods developed for computing the scattering characteristics is also done here using objects of simple shapes such as a cylinder, a cone, and so on. Our computation results have been compared here to those obtained using the "FEKO" software package [9] as well as to the measurement results obtained in an anechoic chamber for a finite-length cylinder.

Verification of the computational methods developed here is finalized by comparing the cruise missile model RCS's computation results to the experimental measurement data.

The electromagnetic-wave-scattering computation method for airborne objects is spread over ground radar objects. While doing this, we took into account the "four-ray" propagation of incident and scattered waves in integral field representations the method is based upon. The latter four-ray representation appears because of onefold reflections between the object and the homogeneous half-space boundary.

Bearing in mind that the contribution from reflector antennas to the total field scattered from aircraft is usually significant, we have dedicated Section 2.4 to developing methods for computing scattering from reflector antenna systems (including those under pointed-nose radomes).

As a result, based on the method developed in the chapter for computing the scattering from complex objects with surface fractures and RAM coatings, we further developed a method for computing the scattering characteristics of electrically large reflector-type antennas with toroidal RAM coating at their edges.

We have also provided an approximate (engineering) approach to computation of the field scattered from a three-dimensional model of the reflector (parabolic) antenna under the pointed (cone-shaped) radome. The method is based on geometrical and physical optics approximations and takes into account the current density over the reflector induced by an electromagnetic wave that has just passed through the radome wall and by the wave that has been reflected once from the radome inner surface.

Chapter 2 concludes with the introduction of a definition for the smoothed impulse response approximation of a radar object (i.e., a nonstationary response to the probing signal with a rectangular amplitude spectrum) along with some examples of this transient scattering characteristic computed for simple shape objects such as a cylinder and a cone.

Chapter 3 can be used as a reference. It contains all-round RCS diagrams (including smoothed or noncoherent ones) for a wide assortment of airborne objects (military and civil aircraft, cruise missiles) and for three specimens of ground armored machines. The diagrams are given for different oblique incidence angles and polarizations. These all-round RCS diagrams of the ground specimens also take into account different types of underlying surfaces.

When designing radar-target-detection and -identification algorithms, there appears the need to know the target's RCS probability distribution in various sectors of their aspect angles. In this regard, this chapter contains corresponding data on various target RCS probability distributions, their mean and median values.

There are also examples of smoothed impulse responses (IR) of aerial and ground objects for a variety of illumination conditions. The importance of IR in radar is conditioned by the fact that it reveals the changes in target reflectivity index along the radar line-of-sight, which bears additional

information on targets of interest and provides a basis for their radar imaging and recognition. Such IRs are also known among the radar community as high-range resolution profiles (HRRPs).

So, as a whole, this book puts together theoretical grounds, original computation methods, and a great deal of computational results on the scattering characteristics of aerial and ground radar targets.

1 Elaboration of Scattering Electrodynamics Theory
Studying Secondary Radiation from Radar Targets

Oleg I. Sukharevsky

CONTENTS

Mathematical simulation of radar scattering (secondary radiation) from aerial and ground objects requires development and elaboration of some principles and methods of applied electrodynamics. The latter would allow obtaining the instrument for studying the electromagnetic wave scattering problems given such complicating factors as radar absorbent material (RAM) coatings coupled with bistatic radar configuration, pulsed, and, particularly, ultrawideband target probing, presence of underlying surface, and so on.

This chapter contains generalizations of such basic issues of electrodynamics as Lorentz reciprocity theorem and image principle aimed at expanding them over to the presence of irregularities

in space of various kinds, or to the electromagnetic fields corresponding to different material fillings of space of interest. Based on these generalizations, which are interesting scientifically for their own sake, it is possible to receive special integral equations allowing study of influence of the RAM coatings or other layered structures (including underlying surface) onto the radar target scattering.

Another set of issues considered in this chapter provides further development of the stationary phase method and of physical optics with practical aim at radar problems with transient target illumination and bistatic configurations.

Besides, some new results are obtained regarding RCS in three-dimensional problems expressed via two-dimensional models of various objects, which makes them much easier to compute.

1.1 GENERALIZATION OF LORENTZ RECIPROCITY THEOREM ONTO THE CASE OF FIELDS CORRESPONDING TO DIFFERENT MATERIAL FILLING OF A REGION IN SPACE

Integral representations are efficient means for studying and solving numerically a number of practical problems in applied electrodynamics and radar. The basic and auxiliary electromagnetic fields in these representations may correspond to different and, in general, nonhomogeneous filling of some regions in space. The latter facilitates the use of properly generalized Lorentz reciprocity theorem to form such a representation.

In this chapter, we give such a generalization of the Lorentz reciprocity theorem [10], using which, for instance, one can form and study integral field representations that provide corrections due to dielectrics and radar absorbent irregularities into the total diffraction field at a system of metallic scatterers (Section 1.2).

Let us take the region V in space filled with isotropic but nonhomogeneous, in general, medium with permittivity $\varepsilon_1(\vec{x})$, and permeability $\mu_1(\vec{x})$ and let this region contain extraneous currents with density $\vec{J}_1^e(\vec{x})$, then electromagnetic field $\vec{E}_1(\vec{x}), \vec{H}_1(\vec{x})$ appears in this region. However, another field $\vec{E}_2(\vec{x}), \vec{H}_2(\vec{x})$ corresponds (another boundary conditions are possible) to permittivity $\varepsilon_2(\vec{x})$, permeability $\mu_2(\vec{x})$, and extraneous current density $\vec{J}_2^e(\vec{x})$. Thus, for the region V we have

$$\begin{aligned} \operatorname{rot} \vec{E}_\alpha &= j\omega\mu_\alpha \vec{H}_\alpha,^{*} \\ \operatorname{rot} \vec{H}_\alpha &= -j\omega\varepsilon_\alpha \vec{E}_\alpha + \vec{J}_\alpha^e, \quad \alpha = 1,2. \end{aligned} \tag{1.1}$$

Given usual assumptions on the smoothness of functions in Equations 1.1 over the region V up to its boundary surface L, we have equality following from Equation 1.1:

$$\begin{aligned} \operatorname{div}[-(\vec{E}_1 \times \mu_2\vec{H}_2) + (\vec{E}_2 \times \mu_1\vec{H}_1)] &= j\omega(\varepsilon_1\mu_1 - \varepsilon_2\mu_2)\vec{E}_1 \cdot \vec{E}_2 \\ &+ [\mu_2\vec{J}_2^e + (\vec{\nabla}\mu_2 \times \vec{H}_2)] \cdot \vec{E}_1 - [\mu_1\vec{J}_1^e + (\vec{\nabla}\mu_1 \times \vec{H}_1)] \cdot \vec{E}_2. \end{aligned} \tag{1.2}$$

Using the Ostrogradsky–Gauss theorem [10], we receive the following:

$$\begin{aligned} \int_L \left[\mu_2\vec{E}_1^T \cdot \vec{H}_2^\perp - \mu_1\vec{E}_2^T \cdot \vec{H}_1^\perp\right] \mathrm{d}S &= j\omega \int_V (\varepsilon_1\mu_1 - \varepsilon_2\mu_2)\vec{E}_1 \cdot \vec{E}_2 \, \mathrm{d}V \\ &+ \int_V \left\{ [\mu_2\vec{J}_2^e + (\vec{\nabla}\mu_2 \times \vec{H}_2)] \cdot \vec{E}_1 - \left[\mu_1\vec{J}_1^e + (\vec{\nabla}\mu_1 \times \vec{H}_1)\right] \cdot \vec{E}_2 \right\} \mathrm{d}V. \end{aligned} \tag{1.3}$$

* Time dependence of the fields throughout the book is assumed to have the form of $\exp(-j\omega t)$.

The symbols $\vec{A}^T$, $\vec{B}^\perp$ here have the following meaning:

$$\vec{A}^T = \vec{A} - \vec{n}(\vec{n}\cdot\vec{A}), \quad \vec{B}^\perp = \vec{n}\times\vec{B}. \tag{1.4}$$

where $\vec{n}$ is the unit vector of external normal to V.

Let us mention here that expression (1.3) becomes the usual Lorentz integral representation given $\varepsilon_2 = \varepsilon_1 = \text{const}, \mu_2 = \mu_1 = \text{const}$.

Using the following substitution in Equation 1.3

$$\vec{E}_\alpha \leftrightarrow \vec{H}_\alpha, \quad \vec{J}^e_\alpha \leftrightarrow -\vec{J}^m_\alpha, \quad \varepsilon_\alpha \leftrightarrow -\mu_\alpha \quad (\alpha = 1,2),$$

we derive the equality expressing the fields excited by magnetic currents

$$\int_L [\varepsilon_2 \vec{E}_2^T \cdot \vec{H}_1^\perp - \varepsilon_1 \vec{E}_1^T \cdot \vec{H}_2^\perp]\,\mathrm{d}S = j\omega \int_V (\varepsilon_1\mu_1 - \varepsilon_2\mu_2)\vec{H}_1\cdot\vec{H}_2\,\mathrm{d}V$$
$$+ \int_V \left\{ [\varepsilon_2 \vec{J}_2^m - (\vec{\nabla}\varepsilon_2 \times \vec{E}_2)]\cdot\vec{H}_1 - [\varepsilon_1\vec{J}_1^m - (\vec{\nabla}\varepsilon_1\times\vec{E}_1)]\cdot\vec{H}_2 \right\}\mathrm{d}V. \tag{1.3′}$$

Formulas of Equation 1.3 type are generalization of the Lorentz reciprocity theorem [4,11] onto the case of nonhomogeneous media and the fields corresponding to two different material filling inside the region of interest V.

If the region V is infinite, then (as in usual Lorentz reciprocity theorem) to ensure the validity of expressions (1.3), (1.3′) one must put a requirement upon extraneous currents to be concentrated in some limited area and upon the fields to satisfy the radiation conditions [4,11].

Another form of generalization for the Lorentz reciprocity theorem was obtained in later works [12,13].

1.2 APPLICATION OF GENERALIZED LORENTZ RECIPROCITY THEOREM TO OBTAINING INTEGRAL REPRESENTATIONS OF SCATTERED FIELD DISTURBANCES INTRODUCED BY RADIO TRANSPARENT AND RADAR ABSORBENT LAYERED STRUCTURES

Let us assume that L be a set of boundary surfaces cutting out the perfectly conducting scatterers $V_1^+, V_2^+, \ldots, V_M^+$ from the rest of space; and in the external region V, characterized by permittivity $\varepsilon(\vec{x})$ and permeability $\mu(\vec{x})$, there be extraneous currents with known density $\vec{J}^e(\vec{x})$ or equivalent to them magnetic currents with density $\vec{J}^m(\vec{x})$. Total resulted field $\vec{E}, \vec{H}$ satisfies the condition

$$\vec{E}^T|_L = 0. \tag{1.5}$$

Our goal is to find such integral representations of the field $\vec{E}, \vec{H}$, which would allow to single out and estimate the contributions from individual scatterers or the influence of physical parameters of the medium filling the region V onto this field. To achieve this, we compare the field $\vec{E}, \vec{H}$ with some additional auxiliary ("standard") fields using the generalized Lorentz reciprocity theorem (1.3).

We introduce the auxiliary field (of "electric kind") $\vec{\mathcal{E}}^e(\vec{x}|\vec{x}_0, \vec{p})$, $\vec{\mathcal{H}}^e(\vec{x}|\vec{x}_0, \vec{p})$ into region V, the latter satisfying the following equations within V:

$$\begin{aligned} \mathrm{rot}\,\vec{\mathcal{E}}^e &= j\omega\mu_0\,\vec{\mathcal{H}}^e, \\ \mathrm{rot}\,\vec{\mathcal{H}}^e &= -j\omega\varepsilon_0\,\vec{\mathcal{E}}^e - j\omega\vec{p}\,\delta(\vec{x}-\vec{x}_0), \end{aligned} \tag{1.6}$$

(ε_0, μ_0 are the permittivity and permeability of free space, and $\vec{x}_0 \in V$) and the other boundary conditions at L (formulated specifically for every problem at hand). Similarly, one can introduce the field of "magnetic kind."

We consider here the case where material media (homogeneous or piecewise homogeneous) are only distributed over some part T of the whole region V, and its complementary to the whole region $V^- = V \backslash T$ being the free space. The homogeneous parts of the medium are separated from one another and from the V^- by smooth surfaces $S_1, S_2, \ldots, S_N$*, and in this manner they form a layered structure. Moreover, we consider distribution of extraneous sources only within region V^-, where $\mu(\vec{x}) \equiv \mu_0, \varepsilon(\vec{x}) \equiv \varepsilon_0$. Now, in the region V we apply the generalized Lorentz reciprocity theorem to the field $\vec{E}_1 = \vec{E}(\vec{x}), \vec{H}_1 = \vec{H}(\vec{x})$, for which $\varepsilon_1 = \varepsilon(\vec{x}), \mu_1 = \mu(\vec{x}), \vec{J}_1^e = \vec{J}^e(\vec{x})$; and to the field $\vec{E}_2 = \vec{\mathcal{E}}^e(\vec{x}|\vec{x}_0, \vec{p}), \vec{H}_2 = \vec{\mathcal{H}}^e(\vec{x}|\vec{x}_0, \vec{p})$, for which $\varepsilon_2 = \varepsilon_0, \mu_2 = \mu_0, \vec{J}_2^e = -j\omega\vec{p}\,\delta(\vec{x} - \vec{x}_0)$ (given arbitrary orientation of $\vec{p}$). While doing so, we use the superposition principle and the fact that in the vicinity of S_i we have

$$\begin{aligned} \vec{\nabla}\mu &= \vec{n}\frac{\partial \mu}{\partial n} = \vec{n}(\mu_i^+ - \mu_i^-)\delta(n) = \vec{n}\,\Delta\mu_i\delta(n), \\ \vec{\nabla}\varepsilon &= \vec{n}\frac{\partial \varepsilon}{\partial n} = \vec{n}\,(\varepsilon_i^+ - \varepsilon_i^-)\delta(n) = \vec{n}\,\Delta\varepsilon_i\delta(n). \end{aligned} \tag{1.7}$$

Here, $\vec{n}$ is the unit normal vector to S_i; n is the coordinate along the normal, $n = 0$ at S_i, $n > 0$ in the direction of $\vec{n}, \delta(n)$ is the delta-function; μ_i^+, μ_i^- are the marginal values of $\mu(\vec{x})$ on S_i respectively at positive and negative ends of n.

Then, from Equation 1.3, we receive the following expression:

$$\begin{aligned} j\omega\mu_0\,\vec{p}\cdot[\vec{E}(\vec{x}_0) - \vec{\mathcal{E}}(\vec{x}_0)] &= \int_L \mu(\vec{x})\vec{\mathcal{E}}^{eT}(\vec{x}\,|\vec{x}_0, \vec{p})\cdot\vec{H}^{\perp}(\vec{x})\,\mathrm{d}S \\ &+ j\omega\int_T [\varepsilon(\vec{x})\mu(\vec{x}) - \varepsilon_0\mu_0]\vec{E}(\vec{x})\cdot\vec{\mathcal{E}}^e(\vec{x}|\vec{x}_0, \vec{p})\,\mathrm{d}V - \sum_{i=1}^{N}\Delta\mu_i\int_{S_i}\vec{\mathcal{E}}^{eT}(\vec{x}|\vec{x}_0, \vec{p})\cdot\vec{H}^{\perp}(\vec{x})\,\mathrm{d}S. \end{aligned} \tag{1.8}$$

Similar integral representation of magnetic field intensity $\vec{H}$ is received from Equation 1.3′:

$$\begin{aligned} j\omega\varepsilon_0\,\vec{q}\cdot[\vec{H}(\vec{x}_0) - \vec{\mathcal{H}}(\vec{x}_0)] &= j\omega\int_T [\varepsilon(\vec{x})\mu(\vec{x}) - \varepsilon_0\mu_0]\,\vec{H}(\vec{x})\cdot\vec{\mathcal{H}}^m(\vec{x}|\vec{x}_0, \vec{q})\,\mathrm{d}V \\ &- \varepsilon_0\int_L \vec{\mathcal{E}}^{mT}(\vec{x}|\vec{x}_0, \vec{q})\cdot\vec{H}^{\perp}(\vec{x})\mathrm{d}S + \sum_{i=1}^{N}\Delta\varepsilon_i\int_{S_i}\vec{\mathcal{H}}^{mT}(\vec{x}|x_0, \vec{q})\cdot\vec{E}^{\perp}(\vec{x})\,\mathrm{d}S. \end{aligned} \tag{1.8′}$$

Here, $\vec{\mathcal{E}}(\vec{x}_0), \vec{\mathcal{H}}(\vec{x}_0)$ are the vectors of electric and magnetic field intensities for the standard field excited in the space region V by the same extraneous sources that in real medium filling V excite the field $\vec{E}(\vec{x}_0), \vec{H}(\vec{x}_0)$, although given different boundary conditions at L the latter being determined by the structure and boundary properties of the chosen auxiliary field of a point source. For example, $\vec{\mathcal{E}}(\vec{x}_0)$ is set according to formula

$$-j\omega\vec{p}\cdot\vec{\mathcal{E}}(\vec{x}_0) = \int_{V^-}\vec{J}^e(\vec{x})\cdot\vec{\mathcal{E}}^e(\vec{x}|\vec{x}_0, \vec{p})\,\mathrm{d}V.$$

* S_i are the closed surfaces, those coming into infinity or those with an end (boundary line) belonging to the boundary L of region V.

If, we assume now $\vec{x}_0 = |\vec{x}_0|\vec{r}^0$ and put $|\vec{x}_0| \to \infty$ in representation (1.8), we receive integral representation for complex vector directivity diagram $\vec{E}(\vec{r}^0)$:

$$j\omega\mu_0\vec{p}\cdot[\vec{E}(\vec{r}^0)-\vec{\mathcal{E}}(\vec{r}^0)] = \int_L \mu(\vec{x})\vec{\mathcal{E}}^{eT}(\vec{x}|\vec{r}^0,\vec{p})\cdot\vec{H}^{\perp}(\vec{x})\,\mathrm{d}S$$
$$+ j\omega\int_T [\varepsilon(\vec{x})\mu(\vec{x})-\varepsilon_0\mu_0]\vec{E}(\vec{x})\cdot\vec{\mathcal{E}}^{e}(\vec{x}|\vec{r}^0,\vec{p})\,\mathrm{d}V - \sum_{i=1}^{N}\Delta\mu_i\int_{S_i}\vec{\mathcal{E}}^{eT}(\vec{x}|\vec{r}^0,\vec{p})\cdot\vec{H}^{\perp}(\vec{x})\,\mathrm{d}S. \quad (1.9)$$

The field $\vec{\mathcal{E}}^{e}(\vec{x}|\vec{r}^0,\vec{p}), \vec{\mathcal{H}}^{e}(\vec{x}|\vec{r}^0,\vec{p})$ in representation (1.9) is excited by plane wave:

$$\begin{aligned}\vec{\mathcal{E}}_0^{e}(\vec{x}|\vec{r}^0,\vec{p}) &= k_0^2\omega\sqrt{\frac{\mu_0}{\varepsilon_0}}[\vec{p}-\vec{r}^0(\vec{p}\cdot\vec{r}^0)]\exp(-jk_0(\vec{r}^0\cdot\vec{x})),\\ \vec{\mathcal{H}}_0^{e}(\vec{x}|\vec{r}^0,\vec{p}) &= -k_0^2\omega\,(\vec{r}^0\times\vec{p})\exp(-jk_0(\vec{r}^0\cdot\vec{x})),\end{aligned} \quad (1.10)$$

where $k_0 = \omega\sqrt{\varepsilon_0\mu_0}$.

If, as an auxiliary field in Equation 1.9, we choose the solution of Equations 1.6 that, given $\vec{x}_0 \in V$, satisfies the boundary condition

$$\vec{\mathcal{E}}^{eT}(\vec{x}|\vec{x}_0,\vec{p})|_{x\in L} = 0, \quad (1.11)$$

or, in other words, as an auxiliary field we choose that of a point source placed at the point $\vec{x}_0$ and having the vector-moment $\vec{p}$ in the presence of perfectly conducting scatterers with shape described by surface L, then representation (1.9) takes the following form:

$$j\omega\mu_0\vec{p}\cdot[\vec{E}(\vec{r}^0)-\vec{\mathcal{E}}(\vec{r}^0)] = j\omega\int_T[\varepsilon(\vec{x})\mu(\vec{x})-\varepsilon_0\mu_0]\vec{E}(\vec{x})\cdot\vec{\mathcal{E}}^{e}(\vec{x}|\vec{r}^0,\vec{p})\,\mathrm{d}V$$
$$-\sum_{i=1}^{N}\Delta\mu_i\int_{S_i}\vec{\mathcal{E}}^{eT}(\vec{x}|\vec{r}^0,\vec{p})\cdot\vec{H}^{\perp}(\vec{x})\,\mathrm{d}S. \quad (1.12)$$

In this manner, $\vec{\mathcal{E}}(\vec{x}_0)$ and $\vec{\mathcal{H}}(\vec{x}_0)$ describe the field excited by these sources when any material media are absent, and representation (1.12) expresses the far-field correction due to material medium T.

In the simplest case where $\mu \equiv \mu_0, \varepsilon(x) \equiv \varepsilon = const$, representation (1.9) takes especially simple form given arbitrary $\vec{p}$ and $\vec{x}_0 \in V$:

$$\vec{p}\cdot[\vec{E}(\vec{x}_0)-\vec{\mathcal{E}}(\vec{x}_0)] = (\varepsilon-\varepsilon_0)\int_T\vec{E}(\vec{x})\cdot\vec{\mathcal{E}}^{e}(\vec{x}|\vec{x}_0,\vec{p})\,\mathrm{d}V. \quad (1.13)$$

From Equation 1.13, we obtain corrections to the complex directivity diagram:

$$\vec{p}\cdot[\vec{E}(\vec{r}^0)-\vec{\mathcal{E}}(\vec{r}^0)] = (\varepsilon-\varepsilon_0)\int_T\vec{E}(\vec{x})\cdot\vec{\mathcal{E}}^{e}(\vec{x}|\vec{r}^0,\vec{p})\,\mathrm{d}V. \quad (1.14)$$

If the fields $\vec{\mathcal{E}}(\vec{x}_0)$ and $\vec{\mathcal{E}}(\vec{x}|\vec{x}_0,\vec{p})$ are known, then, given $\vec{x}_0 \in T$ equality (1.13) becomes the integral equation with respect to the field excited in medium T.

So, when the variety of T is a set of thin dielectric layers (their thickness δ being small), asymptotic formulas can be obtained from Equation 1.13, the latter being the more accurate the lesser the

value of dimensionless parameter $\bar{\delta} = \delta/\lambda_0$. Given small $\bar{\delta}$, integral term in Equation 1.13, as it follows from physical considerations, must become small. It can be shown that this integral, as any other integral of the form

$$I(\vec{x}_0) = \int_T \vec{F}(\vec{x}) \cdot \vec{\mathcal{E}}^e(\vec{x}|\vec{x}_0, \vec{p})\,\mathrm{d}V$$

with smooth over region T (up to its boundary) vector function $\vec{F}(\vec{x})$, allows existence of the following estimate given $\vec{x}_0 \in T$:

$$|I(\vec{x}_0)| \le \text{const}\,\bar{\delta}.^{*} \tag{1.15}$$

From equality (1.13) and estimate of Equation 1.15 type, it follows that given $\vec{x} \in T$

$$\vec{E}(\vec{x}) = \vec{\mathcal{E}}(\vec{x}) + O(\bar{\delta}),$$

therefore, we obtain from Equation 1.14 that

$$\vec{p} \cdot [\vec{E}(\vec{r}^{\,0}) - \vec{\mathcal{E}}(\vec{r}^{\,0})] = (\varepsilon - \varepsilon_0)\int_T \vec{\mathcal{E}}(\vec{x}) \cdot \vec{\mathcal{E}}^e(\vec{x}|\vec{r}^{\,0}, \vec{p})\,\mathrm{d}V + o(\bar{\delta}). \tag{1.16}$$

Equalities of Equation 1.16 type can serve as computation formulas along with the estimate of computation error $o(\bar{\delta})$.

Below, we consider another application of generalized Lorentz theorem. Let some perfectly conducting surface L be covered with layer T of RAM (Figure 1.1) with permittivity ε_1 and permeability μ_1.

Let us further assume that the field $(\vec{\mathcal{E}}_2, \vec{\mathcal{H}}_2)$ excited by electric dipole $\vec{J}_2^{\,e} = -j\omega\vec{p}\delta(\vec{x} - \vec{x}_0)^{\dagger}$ is known in presence of the scattering surface specified above, however with the permittivity and permeability ε_2, μ_2 of the layer T. We need to find the field $\vec{E}_1$ excited by extraneous sources (with the current density $\vec{J}_1^{\,e}$) situated in the region V^- in the presence of radar absorbent layer T over metallic base L. It is additionally known that value of ε_1 is close to ε_2 and value of μ_1 is close to μ_2.

Let the observation point satisfy the condition $\vec{x}_0 \in V^-$. We apply generalized Lorentz reciprocity theorem (1.3) to the fields $(\vec{E}_1, \vec{H}_1)$ and $(\vec{\mathcal{E}}_2, \vec{\mathcal{H}}_2)$ in the region $V = V^-$ with boundary $\partial V = S$. As a result, we get the following expression:

$$-j\omega\vec{p} \cdot [\vec{E}_1(\vec{x}_0) - \vec{E}_2(\vec{x}_0)] = \int_S (\vec{E}_1^T \cdot \vec{\mathcal{H}}_2^{\perp} - \vec{\mathcal{E}}_2^T \cdot \vec{H}_1^{\perp})\,\mathrm{d}S. \tag{1.17}$$

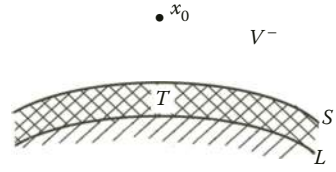

FIGURE 1.1 Perfectly conducting surface covered with the layer of RAM.

---

* Estimate (1.15) is nontrivial since it is based on eventual computation of singular integrals of the $\int_T \Phi(x)(-\vec{p} + 3(\vec{p} \cdot \vec{R}^0)\vec{R}^0)/R^3\,\mathrm{d}V$ kind, where $\vec{R} = \vec{x} - \vec{x}_0$, $R = |\vec{R}|$, $\vec{R}^0 = \vec{R}/R$.

† It is worth mentioning that using the superposition principle, the field $\vec{E}_2$ excited by a preset extraneous current distribution $\vec{J}_1^{\,e}$ can be expressed as: $-j\omega\vec{p}\vec{E}_2(\vec{x}_0) = \int_V \vec{J}_1^{\,e} \cdot \vec{\mathcal{E}}_2(\vec{x}|\vec{x}_0, \vec{p})\,\mathrm{d}V$, where V contains all the extraneous sources of radiation.

Let, further, region $V = T$ and its boundary be $\partial V = S \bigcup L$. Application of theorem (1.3) to the same fields in this case gives us the following:

$$\int_S \{\mu_2 \vec{E}_1^T \cdot \vec{\mathcal{H}}_2^\perp - \mu_1 \vec{\mathcal{E}}_2^T \cdot \vec{H}_1^\perp\} \mathrm{d}S = j\omega(\varepsilon_1\mu_1 - \varepsilon_2\mu_2) \int_T \vec{E}_1 \cdot \vec{\mathcal{E}}_2 \, \mathrm{d}V. \tag{1.18}$$

Multiplying Equation 1.17 by μ_1 and subtracting the equality thus received from Equation 1.18, we arrive at the following expression:

$$j\omega\mu_1 \vec{p}[\vec{E}_1(\vec{x}_0) - \vec{E}_2(\vec{x}_0)] = (\mu_2 - \mu_1) \int_S \vec{E}_1^T \cdot \vec{\mathcal{H}}_2^\perp \mathrm{d}S - j\omega(\varepsilon_1\mu_1 - \varepsilon_2\mu_2) \int_T \vec{E}_1 \cdot \vec{\mathcal{E}}_2 \, \mathrm{d}V. \tag{1.19}$$

Having done similar transformations for the case of $\vec{x}_0 \in T$, we receive integral equation for the field $\vec{E}_1$ inside layer T:

$$-j\omega\vec{p}\{\mu_2\vec{E}_1(\vec{x}_0) - \mu_1\vec{E}_2(\vec{x}_0)\} = (\mu_2 - \mu_1) \int_S \vec{E}_1^T \cdot \vec{\mathcal{H}}_2^\perp \mathrm{d}S - j\omega(\varepsilon_1\mu_1 - \varepsilon_2\mu_2) \int_T \vec{E}_1 \cdot \vec{\mathcal{E}}_2 \, \mathrm{d}V. \tag{1.20}$$

Having accounted for the smallness of values $|\mu_1 - \mu_2|$ and $|\varepsilon_1 - \varepsilon_2|$, one can obtain from Equation 1.20 the asymptotic representation of field $\vec{E}_1(\vec{x}_0)$ given $\vec{x}_0 \in T$. The major term of this asymptotic has evidently the following form:

$$\vec{E}_1(\vec{x}_0) \sim \frac{\mu_1}{\mu_2} \vec{E}_2(\vec{x}_0). \tag{1.21}$$

Having integrated once Equation 1.20 while substituting expression (1.21) into the right-hand side integrand of Equation 1.20, one obtains an elaborated asymptotic representation of the field $\vec{E}_1(\vec{x}_0)$ inside layer T:

$$\begin{aligned} -j\omega\vec{p} \cdot \vec{E}_1(\vec{x}_0) \sim & -j\omega\vec{p} \cdot \vec{E}_2(\vec{x}_0) \cdot \frac{\mu_1}{\mu_2} \\ & + \left(1 - \frac{\mu_1}{\mu_2}\right) \frac{\mu_1}{\mu_2} \int_S \vec{E}_2^T \cdot \vec{\mathcal{H}}_2^\perp \mathrm{d}S - j\omega \left(\varepsilon_1 \frac{\mu_1}{\mu_2} - \varepsilon_2\right) \frac{\mu_1}{\mu_2} \int_T \vec{E}_2 \cdot \vec{\mathcal{E}}_2 \, \mathrm{d}V. \end{aligned} \tag{1.22}$$

Having used expression (1.22) on the right-hand side of Equation 1.19, we come to the expression of field $\vec{E}_1(\vec{x}_0)$ given $\vec{x}_0 \in V^-$, which, in its turn, allows expressing the field $\vec{E}_1$ in the region external to the scattering surface via fields $\vec{E}_2$, $\vec{\mathcal{E}}_2$, $\vec{\mathcal{H}}_2$ obtained given another material filling of the region T.

Finally, let us note that practical applications of generalized Lorentz reciprocity theorem is not by any means limited by examples presented above in Section 1.1. The generalization can be applied to quite a number of practical tasks. For instance, integral representation (1.8) can be applied not only to the scattering structures consisting of perfectly conducting scatterers and radar absorbent media, but also to evaluating the influence of radomes onto the propagation and scattering of electromagnetic waves.

1.3 GENERALIZED IMAGE PRINCIPLE AND ITS APPLICATION TO SOLVING SOME ELECTROMAGNETIC WAVE SCATTERING PROBLEMS

Major content of this section is the description of rigorous and physically interpretable mathematical models for the EM wave scattering from different types of scatterers (perfect conductors, perfect

magnetics, perfectly absorbing objects) placed over underlying surface, as well as of mathematical model of antenna aperture under radio transparent covering (fairing, radar dome, and so on). It is with regard to this later problem that we give generalization of the equivalent currents method interpretation by Ya.N. Pheld [14], which is of fundamental importance when computing the field excited by antenna aperture radiating into the half-space that contains scatterers—dielectrics, conductors, magnetic, and so on. In this context, it turned necessary to generalize also the classical image principle.

1.3.1 Generalized Image Principle

Let us denote a half-space $\Omega^+(x_3 > 0)$ and its reflection (image) $\Omega^-(x_3 < 0)$. Region Ω^+ contains:

a. Perfectly conducting scatterers with a set of boundary surfaces denoted as S_E, so that

$$\vec{E}^T\Big|_{S_E} = 0; \tag{1.23}$$

b. Scatterers that are perfect magnetics, at the boundary surface (S_H) of which we have

$$\vec{H}^T\Big|_{S_H} = 0; \tag{1.24}$$

at the same time, the part Ω_1^+ of half-space Ω^+, boundary of which consists of plane $S(x_3 = 0)$, S_E, and S_H, is filled with isotropic and, generally, nonhomogeneous medium with complex permittivity $\varepsilon(\vec{x})$ and permeability $\mu(\vec{x})$ that may have also the discontinuity surfaces (interfaces).

Let us denote also the image Ω_1^- of the region Ω_1^+ in plane S and consider the "symmetrized" region $\Omega_1 = \Omega_1^+ \bigcup S \bigcup \Omega_1^-$ with symmetrical, by geometry and physical properties, scatterers and the filling medium, in which

$$\begin{cases} \varepsilon(x_1, x_2, -x_3) \equiv \varepsilon(x_1, x_2, x_3) \\ \mu(x_1, x_2, -x_3) \equiv \mu(x_1, x_2, x_3). \end{cases} \tag{1.25}$$

Let us introduce the necessary symbols: if $\vec{A} = \{A_1, A_2, A_3\}$ is any vector field, then $\vec{A}' = \{A_1, A_2, -A_3\}$; particularly, if the radius-vector of the point $\vec{x} = (x_1, x_2, x_3)$, then $\vec{x}' = (x_1, x_2, -x_3)$. Thus, the following statement holds true (generalized image principle).

Let $\vec{\mathcal{E}}_0(\vec{x}|\vec{x}_0, \vec{p}), \vec{\mathcal{H}}_0(\vec{x}|\vec{x}_0, \vec{p})$ be the field excited in the symmetrized region Ω_1 by the electrical dipole with the moment $\vec{p}$ placed at point $\vec{x}_0 \in \Omega_1$. Then, for every point $\vec{x} \in \Omega_1$ the following equalities hold true:

$$\vec{\mathcal{E}}_0(\vec{x}|\vec{x}_0', \vec{p}') = \vec{\mathcal{E}}_0'(\vec{x}'|\vec{x}_0, \vec{p}), \tag{1.26}$$

$$\vec{\mathcal{H}}_0(\vec{x}|\vec{x}_0', \vec{p}') = -\vec{\mathcal{H}}_0'(\vec{x}'|\vec{x}_0, \vec{p}), \tag{1.27}$$

that express the generalized image principle.

Rigorous derivation of these equalities (quite evident from the standpoint of physical intuition) can be based upon the following expression that can be easily verified:

$$\operatorname{rot}\vec{A}'(\vec{x}') = -(\operatorname{rot}\vec{A}(\vec{x}))'|_{\vec{x}\Rightarrow\vec{x}'} \tag{1.28}$$

(the symbol $\vec{x} \Rightarrow \vec{x}'$ means that having computed the vector $-(\mathrm{rot}\,\vec{A}(\vec{x}))'$, one must replace vector $\vec{x}$ by vector $\vec{x}'$). Let us introduce the abbreviated symbols:

$$\vec{\mathcal{E}}_0(\vec{x}) = \vec{\mathcal{E}}_0(\vec{x}|\vec{x}_0, \vec{p}); \quad \vec{\mathcal{H}}_0(\vec{x}) = \vec{\mathcal{H}}_0(\vec{x}|\vec{x}_0, \vec{p}),$$

$$\vec{\mathcal{E}}_0^{(1)}(\vec{x}) = \vec{\mathcal{E}}_0'(\vec{x}'|\vec{x}_0, \vec{p}); \quad \vec{\mathcal{H}}_0^{(1)}(\vec{x}) = -\vec{\mathcal{H}}_0'(\vec{x}'|\vec{x}_0, \vec{p}).$$

Then, from Maxwell's equations we have

$$\mathrm{rot}\,\vec{\mathcal{E}}_0(\vec{x}) = j\omega\mu(\vec{x})\vec{\mathcal{H}}_0(\vec{x}),$$

$$\mathrm{rot}\,\vec{\mathcal{H}}_0(\vec{x}) = -j\omega\varepsilon(\vec{x})\vec{\mathcal{E}}_0(\vec{x}) - j\omega\vec{p}\,\delta(\vec{x} - \vec{x}_0).$$

Using expressions (1.25), (1.28), we obtain

$$\mathrm{rot}\,\vec{\mathcal{E}}_0^{(1)}(\vec{x}) = \mathrm{rot}\,\vec{\mathcal{E}}_0'(\vec{x}') = (\mathrm{rot}\,\vec{\mathcal{E}}_0(\vec{x}))'|_{\vec{x}\Rightarrow\vec{x}'} = -j\omega\mu(\vec{x}')\vec{\mathcal{H}}_0'(\vec{x}') = j\omega\mu(\vec{x})\vec{\mathcal{H}}_0^{(1)}(\vec{x}). \quad (1.29)$$

In the same manner, we obtain that

$$\mathrm{rot}\,\vec{\mathcal{H}}_0^{(1)}(\vec{x}) = -j\omega\varepsilon(\vec{x})\vec{\mathcal{E}}_0^{(1)}(\vec{x}) - j\omega\vec{p}'\delta(\vec{x} - \vec{x}_0'). \quad (1.30)$$

Thus, the field $\vec{\mathcal{E}}_0^{(1)}(\vec{x}), \vec{\mathcal{H}}_0^{(1)}(\vec{x})$ is the one excited by the current $\vec{J}_0(\vec{x}) = -j\omega\vec{p}'\delta(\vec{x} - \vec{x}_0')$. Next, we can directly verify that boundary conditions at S_E, S_H and at their images are satisfied.

For instance, since $\vec{\mathcal{E}}_0(\vec{x}) = \vec{n}\mathcal{E}_{0n}(\vec{x})$ (where $\vec{n}$ is the unit normal vector) at S_E, then $\vec{\mathcal{E}}_0'(\vec{x}) = \vec{n}'\mathcal{E}_{0n}(\vec{x}')$, from where we get $\vec{\mathcal{E}}_0^{(1)}(\vec{x})|_{S_E} = \vec{\mathcal{E}}_0'(\vec{x}') = \vec{n}\mathcal{E}_{0n}(\vec{x})$ and, accordingly, $\vec{\mathcal{E}}_0^{(1)T}|_{S_E} = 0$.

Finally, the field $\vec{\mathcal{E}}_0^{(1)}(\vec{x}), \vec{\mathcal{H}}_0^{(1)}(\vec{x})$ evidently satisfies the radiation condition (in case of unlimited region Ω_1).

Because of uniqueness of the boundary problem considered here, from Equations 1.29, 1.30 and boundary conditions at S_E, S_H and at their images (as well as from radiation condition, if Ω_1 is unlimited), we get that the field $\vec{\mathcal{E}}_0^{(1)}(\vec{x})$, $\vec{\mathcal{H}}_0^{(1)}(\vec{x})$ coincides with the field $\vec{\mathcal{E}}_0(\vec{x}|\vec{x}_0', \vec{p}')$, $\vec{\mathcal{H}}_0(\vec{x}|\vec{x}_0', \vec{p}')$ that proves the statement formulated above.

We need to make some remarks regarding the latter statement. First, the same statement holds true for the fields excited by magnetic dipoles too.

Second, using the superposition principle and integral representation of the following kind:

$$\vec{J}(\vec{x}) = \int_{\Omega_1} \vec{J}(\vec{x}_0)\delta(\vec{x} - \vec{x}_0)\,\mathrm{d}V_{x_0},$$

one can extend the image principle of the form presented above (and used in [15–17]) onto the fields excited by arbitrary extraneous currents.

1.3.2 On the Influence of Underlying Surface onto the Scattering Properties of a Target

Let the plane Σ (we assume it perfectly conducting) to be bounding a half-space containing the scattering object outlined by the boundary surface S (perfect conductor or perfect magnetic).

Standard method of obtaining an integral equation for the surface currents excited by known set of extraneous sources situated in the half-space under consideration (the one based on the Stratton–Chu integral equations [11]) leads to equations containing not only integral over the scatterer's surface S, but also over unlimited plane Σ that complicates dramatically numerical computation of its solution. Use of generalized image principle, in this context, allows obtaining the integral equation with regard to currents that involves integration only over S, which can be used as basis for stable and efficient computation algorithms. Below, we give the corresponding considerations.

Let us denote as Ω_1^+ the region in space bounded by surfaces S and Σ. Region Ω_1^+ may contain both nonhomogeneities and other scatterers.

Let us introduce the following symbols:

$\vec{E}^i(\vec{x}), \vec{H}^i(\vec{x})$ is the incident wave;
$\vec{E}_1(\vec{x}), \vec{H}_1(\vec{x})$ is the scattered field;
$\vec{E}(\vec{x}), \vec{H}(\vec{x})$ is the total field;
$\vec{\mathcal{E}}^e(\vec{x}|\vec{x}_0, \vec{p}), \vec{\mathcal{H}}^e(\vec{x}|\vec{x}_0, \vec{p})$ is the field of point electric dipole in the half-space bounded by plane Σ given the object S is absent;
$\vec{\mathcal{E}}^m(\vec{x}|\vec{x}_0, \vec{q}), \vec{\mathcal{H}}^m(\vec{x}|\vec{x}_0, \vec{q})$ is similar field of the point magnetic dipole.

It is worth mentioning that using the field $\vec{\mathcal{E}}_0, \vec{\mathcal{H}}_0$ introduced in Section 1.3.1 (the one excited in the symmetrized region Ω_1 in the absence of object S), one can express the field $\vec{\mathcal{E}}^e$, $\vec{\mathcal{H}}^e$ as follows:

$$\vec{\mathcal{E}}^e = \vec{\mathcal{E}}_0(\vec{x}|\vec{x}_0, \vec{p}) - \vec{\mathcal{E}}_0(\vec{x}|\vec{x}_0', \vec{p}'), \tag{1.31}$$

$$\vec{\mathcal{H}}^e = \vec{\mathcal{H}}_0(\vec{x}|\vec{x}_0, \vec{p}) - \vec{\mathcal{H}}_0(\vec{x}|\vec{x}_0', \vec{p}'). \tag{1.32}$$

The latter is a consequence of the fact that according to Equations 1.31 and 1.26,

$$\vec{\mathcal{E}}^e = \vec{\mathcal{E}}_0(\vec{x}|\vec{x}_0, \vec{p}) - \vec{\mathcal{E}}_0'(\vec{x}'|\vec{x}_0, \vec{p});$$

from where, given $\vec{x} \in \Sigma$, we obtain

$$\vec{\mathcal{E}}^{eT}\Big|_\Sigma = 0.$$

Having applied the Lorentz reciprocity theorem to the fields $(\vec{E}_1, \vec{H}_1)$ and $(\vec{\mathcal{E}}^e, \vec{\mathcal{H}}^e)$ as well to the fields $(\vec{E}_1, \vec{H}_1)$, and $(\vec{\mathcal{E}}^m, \vec{\mathcal{H}}^m)$, and having accounted for the fact that field $(\vec{\mathcal{E}}^e, \vec{\mathcal{H}}^e)$ is created by the current $\vec{J}^e = -j\omega\vec{p}\,\delta(\vec{x} - \vec{x}_0)$ and the field $(\vec{\mathcal{E}}^m, \vec{\mathcal{H}}^m)$ is created by current $\vec{J}^m = -j\omega\vec{q}\,\delta(\vec{x} - \vec{x}_0)$ (in the former case $\vec{J}^m = 0$ and in the latter case $\vec{J}^e = 0$), we arrive at the expressions:

$$j\omega\vec{p} \cdot \vec{E}_1(\vec{x}_0) = \int_{S+\Sigma} [(\vec{E}_1\, \vec{\mathcal{H}}^e\, \vec{n}) - (\vec{\mathcal{E}}^e\, \vec{H}_1 \vec{n})]\, \mathrm{d}S,^* \tag{1.33}$$

$$-j\omega\vec{q} \cdot \vec{H}_1(\vec{x}_0) = \int_{S+\Sigma} [(\vec{E}_1 \vec{\mathcal{H}}^m \vec{n}) - (\vec{\mathcal{E}}^m\, \vec{H}_1 \vec{n})]\, \mathrm{d}S. \tag{1.34}$$

* Here and further on the symbol $(\vec{a}\vec{b}\vec{c})$ means the mixed vector product.

Having applied the Lorentz reciprocity theorem to the fields $(\vec{E}^i, \vec{H}^i)$ and $(\vec{\mathcal{E}}^e, \vec{\mathcal{H}}^e)$,as well to the fields $(\vec{E}^i, \vec{H}^i)$ and $(\vec{\mathcal{E}}^m, \vec{\mathcal{H}}^m)$, we obtain the following:

$$\int\limits_{S+\Sigma} [(\vec{E}^i \ \vec{\mathcal{H}}^{(e,m)} \vec{n}) - (\vec{\mathcal{E}}^{(e,m)} \ \vec{H}^i \vec{n})] \mathrm{d}S = 0. \tag{1.35}$$

Having combined expressions (1.33), (1.34) with (1.35), we get the total field representation:

$$j\omega \vec{p} \cdot [\vec{E}(\vec{x}0_0) - \vec{E}^i(\vec{x}_0)] = \int\limits_{S+\Sigma} [(\vec{E}\, \vec{\mathcal{H}}^e \vec{n}) - (\vec{\mathcal{E}}^e \vec{H} \vec{n})] \mathrm{d}S, \tag{1.36}$$

$$-j\omega \vec{q} \cdot [\vec{H}(\vec{x}_0) - \vec{H}^i(\vec{x}_0)] = \int\limits_{S+\Sigma} [(\vec{E}\, \vec{\mathcal{H}}^m \vec{n}) - (\vec{\mathcal{E}}^m \vec{H} \vec{n})] \mathrm{d}S. \tag{1.37}$$

We consider two options here:

A. S is the perfectly conducting surface and then $\vec{E}^T\Big|_\Sigma = 0$, $\vec{E}^T\Big|_S = 0$;
B. S is the perfect magnetic surface and then $\vec{H}^T\Big|_S = 0, \vec{E}^T\Big|_\Sigma = 0$.

If option A is the case, the expressions (1.36) and (1.37) take the following form given $\vec{x}_0 \in \Omega_1^+$:

$$j\omega \vec{p} \cdot [\vec{E}(\vec{x}_0) - \vec{E}^i(\vec{x}_0)] = -\int\limits_S (\vec{\mathcal{E}}^e \vec{H} \vec{n}) \mathrm{d}S, \tag{1.38}$$

$$-j\omega \vec{q} \cdot [\vec{H}(\vec{x}_0) - \vec{H}^i(\vec{x}_0)] = -\int\limits_S (\vec{\mathcal{E}}^m \vec{H} \vec{n}) \mathrm{d}S. \tag{1.39}$$

If option B is the case, then:

$$j\omega \vec{p} \cdot [\vec{E}(\vec{x}_0) - \vec{E}^i(\vec{x}_0)] = \int\limits_S (\vec{E}\, \vec{\mathcal{H}}^e \vec{n}) \mathrm{d}S, \tag{1.40}$$

$$-j\omega \vec{q} \cdot [\vec{H}(\vec{x}_0) - \vec{H}^i(\vec{x}_0)] = \int\limits_S (\vec{E}\, \vec{\mathcal{H}}^m \vec{n}) \mathrm{d}S. \tag{1.41}$$

The fields $(\vec{\mathcal{E}}^e, \vec{\mathcal{H}}^e)$,$(\vec{\mathcal{E}}^m, \vec{\mathcal{H}}^m)$ contain, as an additive component, the field of electric (magnetic) dipole in free space. So, for instance,

$$\vec{\mathcal{H}}^e = \vec{H}_0^e + \vec{H}^{scat},$$

where $\vec{H}^{scat}$ is the regular field and

$$\vec{H}_0^e = j\omega (\vec{p} \times \vec{\nabla} g),$$

$$g = \frac{\exp(j k_0 |\vec{x} - \vec{x}_0|)}{4\pi |\vec{x} - \vec{x}_0|}.$$

Then,

$$(\vec{E}\,\vec{H}_0^e\,\vec{n}) = -j\omega\vec{E}\left(\vec{p}\,\frac{\partial g}{\partial n} - (\vec{p}\cdot\vec{n})\vec{\nabla}\,g\right)$$

and, if we present the operator $\vec{\nabla}$ in the following form:

$$\vec{\nabla} = \vec{n}\,\frac{\partial}{\partial n} + \vec{D},$$

where $\vec{D}$ is tangential differential operator, then

$$(\vec{E}\,\vec{H}_0^e\,\vec{n}) = -j\,\omega\,\vec{E}\cdot\left(\vec{p}^{\,T}\,\frac{\partial\, g}{\partial\, n} - (\vec{p}\cdot\vec{n})\,\vec{D}\,g\right).$$

Let us note that function $\partial g/\partial n$ is the kernel of the double-layer potential.

If we use now the fact that at the surface S $H_n\big|_S = 0$ for the option A; and $E_n\big|_S = 0$ for the option B (these follow from Maxwell equations and boundary conditions at the boundary surface S); and use the boundary property of the double-layer potential while letting the point $\vec{x}_0$ to tend to the surface S, then from Equations 1.39 and 1.40 we can obtain integral equations:

$$-\frac{1}{2}\,j\omega\vec{q}\cdot\vec{H}^{\,T}(\vec{x}_0) + j\omega\vec{q}\cdot\vec{H}^{\,i}(\vec{x}_0) = -\int_S(\vec{E}^m\,\vec{H}^{\,T}\,\vec{n})\,\mathrm{d}\,S\,, \tag{1.42}$$

$$\frac{1}{2}\,j\omega\vec{p}\cdot\vec{E}^{\,T}(\vec{x}_0) - j\omega\vec{p}\cdot\vec{E}^{\,i}(\vec{x}_0) = \int_S(\vec{E}^{\,T}\,\vec{\mathcal{H}}^e\,\vec{n})\,\mathrm{d}\,S. \tag{1.43}$$

Equations 1.42 and 1.43 contain only integration over limited surface S and they, therefore, are Fredholm integral equations of second kind, which can be reduced effectively to the well-defined systems of linear algebraic equations.

Having solved integral Equation 1.42, we find $\vec{H}^T(\vec{x}_0)$ and, having substituted it into the right-hand side of Equations 1.38 and 1.39, we find the field $\vec{E}^A(\vec{x}_0), \vec{H}^A(\vec{x}_0)$ for any $\vec{x}_0 \in \Omega_1^+$ in case where S is the surface of perfect conductor. In the same way, using integral Equation 1.43 and representations (1.40) and (1.41), we find the field $\vec{E}^B(\vec{x}_0), \vec{H}^B(\vec{x}_0)$ in case where S is the surface of perfect magnetic.

Next, applying the Macdonald model [18] of perfect "black" body, one can obtain the field scattered by the object under consideration (with underlying surface present) given the assumption that its surface S possesses the properties of perfect "black" body. This field

$$\vec{E}^C = \frac{1}{2}(\vec{E}^A + \vec{E}^B), \quad \vec{H}^C = \frac{1}{2}(\vec{H}^A + \vec{H}^B) \tag{1.44}$$

appears as result of illumination by primary incident wave $\vec{E}^i, \vec{H}^i$ of perfectly absorbing (according to Macdonald) object in presence of underlying surface and the medium nonhomogeneities.

1.3.3 Calculation of Field Excited by Radiating Aperture in Presence of Arbitrary System of Scatterers

Let an aperture S_0 to be placed in the plane $S(x_3 = 0)$ and let it radiate into the half-space Ω^+ $(x_3 > 0)$ the field $\vec{E}(\vec{x}), \vec{H}(\vec{x})$ excited by extraneous sources situated in the half-space Ω^- $(x_3 < 0)$. The region Ω^+ contains the following:

a. Perfectly conducting scatterers, a set of boundary surfaces, which we denote as S_E so that

$$\vec{E}^T|_{S_E} = 0; \tag{1.45}$$

b. Scatterers being perfect magnetics, at the boundary surface (S_H) of which

$$\vec{H}^T|_{S_H} = 0; \tag{1.46}$$

In this case, the part Ω_1^+ of the half-space Ω^+, boundary of which consists of S, S_E, and S_H is filled with isotropic but, in general, nonhomogeneous medium with complex permittivity $\varepsilon(\vec{x})$ and permeability $\mu(\vec{x})$ that may have the discontinuity surfaces (interfaces). Particularly, one may relate this to the presence in Ω^+ of radio transparent antenna radome G^+ of some design (Figure 1.2).

Our goal here is to derive and interpret physically rigorous and approximated computation formulas expressing the radiated field via distributions over aperture of tangential components of vectors $\vec{E}$ and $\vec{H}$ (or, that is equivalent, via densities of equivalent surface currents—magnetic and electric) under following different assumptions on physical properties of the surface $\Sigma = S \backslash S_0$, the symbol $S \backslash S_0$ meaning complementation of region S_0 to the total region S:

A. Σ is the surface of perfect conductor, $\vec{E}^T\Big|_\Sigma = 0$;

B. Σ is the surface of perfect magnetic, $\vec{H}^T\Big|_\Sigma = 0$.

Extraneous sources and all the boundary conditions for the options A and B above are the same except the conditions at the surface Σ adjoining the region Ω^+ (the latter being as stated above).

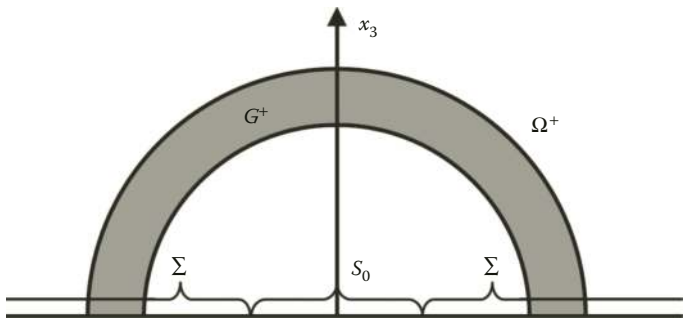

FIGURE 1.2 Radio transparent antenna radome.

Here, we denote by $(\vec{E}^A, \vec{H}^A)$ and $(\vec{E}^B, \vec{H}^B)$ the fields excited in the region Ω_1^+ by the extraneous sources at hand for the options A and B, respectively. Along with these fields, we consider their half-sums

$$\vec{E}^C = \frac{1}{2}(\vec{E}^A + \vec{E}^B), \quad \vec{H}^C = \frac{1}{2}(\vec{H}^A + \vec{H}^B), \tag{1.47}$$

which provide for some "averaging" of fields radiated by aperture S_0 in situations where Σ is the surface of perfect conductor (option A); and it is the surface of perfect magnetic (option B). The field averaged by means of Equation 1.47 can be considered as the one formally corresponding to Macdonald's model of perfect black surface Σ.

Now, we apply the Lorentz reciprocity theorem to the field of our concern $\vec{E}, \vec{H}$ (for both options A and B), as well as to the field $\vec{\mathcal{E}}(\vec{x}|\vec{x}_0, \vec{p}), \vec{\mathcal{H}}(\vec{x}|\vec{x}_0, \vec{p})$ excited in the region Ω_1^+ by an electric dipole with the moment $\vec{p}$ placed at point $\vec{x} \in \Omega_1^+$ in case where all the surface $S(x_3 = 0)$ is one of the material interface surfaces of region Ω_1^+, with one of the following conditions being satisfied:

$$\vec{\mathcal{E}}^T|_S = 0 \quad \text{(for option A)}, \tag{1.48}$$

$$\vec{\mathcal{H}}^T|_S = 0 \quad \text{(for option B)}. \tag{1.49}$$

Since all the extraneous currents that excite the field $\vec{\mathcal{E}}, \vec{\mathcal{H}}$ are distributed over Ω^-, and the density of current exciting the field $\vec{\mathcal{E}}, \vec{\mathcal{H}}$ is

$$\vec{J}_0 = -j\omega\vec{p}\,\delta(\vec{x} - \vec{x}_0), \tag{1.50}$$

then

$$j\omega\vec{p} \cdot \vec{E}(\vec{x}_0) = \int_S + \int_{S_E} + \int_{S_H} ((\vec{E} \times \vec{\mathcal{H}}) - (\vec{\mathcal{E}} \times \vec{H})) \cdot \mathrm{d}\vec{S}. \tag{1.51}$$

According to boundary conditions of the (1.45), (1.46) kind, we have

$$\vec{E}^T\Big|_{S_E} = \vec{\mathcal{E}}^T\Big|_{S_E} = 0, \quad \vec{H}^T\Big|_{S_H} = \vec{\mathcal{H}}^T\Big|_{S_H} = 0.$$

Therefore, integrals over S_E, S_H, and $\Sigma = S \backslash S_0$ in Equation 1.51 are equal to zero. For the options A and B, we have, respectively:

$$j\omega\vec{p} \cdot \vec{E}^A(\vec{x}_0) = \int_{S_0} (\vec{E}^A \times \vec{\mathcal{H}}^A) \cdot \vec{\mathrm{d}}S, \tag{1.52}$$

$$j\omega\vec{p} \cdot \vec{E}^B(\vec{x}_0) = -\int_{S_0} (\vec{\mathcal{E}}^B \times \vec{H}^B) \cdot \mathrm{d}\vec{S}. \tag{1.53}$$

Having computed the half-sums of right- and left-hand sides of equalities (1.52) and (1.53) and having used the notation of Equation 1.47, we get the following:

$$j\omega\vec{p}\cdot\vec{E}^{C}(\vec{x}_0)=\frac{1}{2}\int\limits_{S_0}((\vec{E}^{A}\times\vec{\mathcal{H}}^{A})-(\vec{\mathcal{E}}^{B}\times\vec{H}^{B}))\cdot\mathrm{d}\vec{S}. \tag{1.54}$$

Equality (1.54) obtained in this way expresses the "averaged" (in sense of Equation 1.47) field radiated by aperture S_0 at any point $\vec{x}\in\Omega_1^+$ via distribution over S_0 of tangential components of vectors $\vec{E}^{A},\vec{H}^{B}$, and the fields of point source (electric dipole) $\vec{\mathcal{E}}^{A},\vec{\mathcal{H}}^{B}$ that are excited in region Ω_1^+ with perfect (in sense of Equations 1.48 or 1.49) interface plane S.

Further considerations are aimed at some transformation and interpretation of formula (1.54).

First of all, we substitute the vector fields $\vec{\mathcal{E}}_0(\vec{x}|\vec{x}_0,\vec{p}),\vec{\mathcal{H}}_0(\vec{x}|\vec{x}_0,\vec{p})$ introduced in Section 1.3.1 for the fields $\vec{\mathcal{E}}^{B}(\vec{x}|\vec{x}_0,\vec{p}),\vec{\mathcal{H}}^{A}(\vec{x}|\vec{x}_0,\vec{p})$ in Equation 1.54. Let $\vec{x},\vec{x}_0\in\Omega_1^+$, then electromagnetic field $\vec{\mathcal{E}},\vec{\mathcal{H}}$, where

$$\vec{\mathcal{E}}=\vec{\mathcal{E}}_0(\vec{x}|\vec{x}_0,\vec{p})+\vec{\mathcal{E}}_0(\vec{x}|\vec{x}_0',\vec{p}'), \tag{1.55}$$

$$\vec{\mathcal{H}}=\vec{\mathcal{H}}_0(\vec{x}|\vec{x}_0,\vec{p})+\vec{\mathcal{H}}_0(\vec{x}|\vec{x}_0',\vec{p}') \tag{1.56}$$

is the field $\vec{\mathcal{E}}^{B}(\vec{x}|\vec{x}_0,\vec{p}),\vec{\mathcal{H}}^{B}(\vec{x}|\vec{x}_0,\vec{p})$. To make it sure for oneself, one should just check the condition (1.49) to be satisfied. According to Equations 1.56 and 1.27

$$\vec{\mathcal{H}}=\vec{\mathcal{H}}_0(\vec{x}|\vec{x}_0,\vec{p})-\vec{\mathcal{H}}_0'(\vec{x}'|\vec{x}_0,\vec{p}),$$

from where, given $\vec{x}\in S$, we have

$$\vec{\mathcal{H}}^{T}\Big|_{S}=0. \tag{1.57}$$

In this manner, the field (1.55), (1.56) is indeed the field of the point source corresponding to option B above. Therefore, accounting for Equation 1.26 we have $\vec{\mathcal{E}}^{B}=\vec{\mathcal{E}}_0(\vec{x}|\vec{x}_0,\vec{p})+\vec{\mathcal{E}}_0'(\vec{x}'|\vec{x}_0,\vec{p})$ from where, given $\vec{x}\in S$, we receive at once the following:

$$\vec{\mathcal{E}}^{B^T}\Big|_{S}=2\vec{\mathcal{E}}_0^{T}(\vec{x}|\vec{x}_0,\vec{p})\Big|_{\vec{x}\in S}. \tag{1.58}$$

In the same way, we find that

$$\vec{\mathcal{H}}^{A}=\vec{\mathcal{H}}_0(\vec{x}|\vec{x}_0,\vec{p})-\vec{\mathcal{H}}_0(\vec{x}|\vec{x}_0',\vec{p}')=\vec{\mathcal{H}}_0(\vec{x}\mid\vec{x}_0,\vec{p})+\vec{\mathcal{H}}_0'(\vec{x}'|\vec{x}_0,\vec{p}),$$

due to which we have

$$\vec{\mathcal{H}}^{A^T}\Big|_{S}=2\vec{\mathcal{H}}_0^{T}(\vec{x}|\vec{x}_0,\vec{p})\Big|_{\vec{x}\in S}. \tag{1.59}$$

Combining results of Equations 1.54, 1.58, and 1.59 together, we find that for any point $\vec{x}_0 \in \Omega_1^+$ and any vector-moment $\vec{p}$ there is exact equality

$$j\omega\vec{p}\cdot\vec{E}^C(\vec{x}_0) = \int_{S_0}((\vec{E}^A(\vec{x})\times\vec{\mathcal{H}}_0(\vec{x}|\vec{x}_0,\vec{p})) - (\vec{H}^B(\vec{x})\times\vec{\mathcal{E}}_0(\vec{x}|\vec{x}_0,\vec{p})))\cdot \mathrm{d}\vec{S}, \tag{1.60}$$

where $d\vec{S} = \vec{n}\,dS$, $\vec{n}$ is the unit normal vector to S pointed toward Ω^-.

So, the averaged field radiated by aperture S_0 into the half-space Ω^+ filled with nonhomogeneous medium and different scattering objects (containing, for instance, a radome) is expressed by formula (1.60) via distribution over aperture of tangential components of vector fields $\vec{\mathcal{E}}^A(\vec{x}), \vec{\mathcal{H}}^B(\vec{x})$ excited by sources spread over Ω^- if Σ is the surface of perfect conductor or perfect magnetic, respectively; the field $\vec{\mathcal{E}}^0, \vec{\mathcal{H}}^0$ in this expression is the field excited in the symmetrized region Ω_1 by point source (electric dipole) given that any material screens in the plane $x_3 = 0$ are absent.

If, for instance, there is some dielectric radome G^+ present in region Ω^+ (Figure 1.2), then $\vec{\mathcal{E}}_0$, $\vec{\mathcal{H}}_0$ is the field excited by point source in space occupied only by closed dielectric envelope (Figure 1.3) symmetrical (by geometry and physical properties) with respect to plane $x_3 = 0$.

Finally, to conclude our consideration, we transform the exact formula (1.60) into approximate one corresponding to physical optics approximation where edge effects (fringe radiation) of the aperture are relatively small so that one may assume (as it is usually done in theoretical and practical antenna calculations) that for S_0 the following approximate equalities hold true

$$\vec{E}^A(\vec{x}) \approx \vec{E}^B(\vec{x}), \quad \vec{H}^A(\vec{x}) \approx \vec{H}^B(\vec{x}).$$

Then, having omitted the indices A and B (while retaining the exact equality sign instead of approximate one in Equation 1.54), we arrive at the following:

$$j\omega\vec{p}\cdot\vec{E}^C(\vec{x}_0) = \int_{S_0}((\vec{E}(\vec{x})\times\vec{\mathcal{H}}_0(\vec{x}|\vec{x}_0,\vec{p})) - (\vec{H}(\vec{x})\times\vec{\mathcal{E}}_0(\vec{x}|\vec{x}_0,\vec{p})))\cdot \mathrm{d}\vec{S}. \tag{1.61}$$

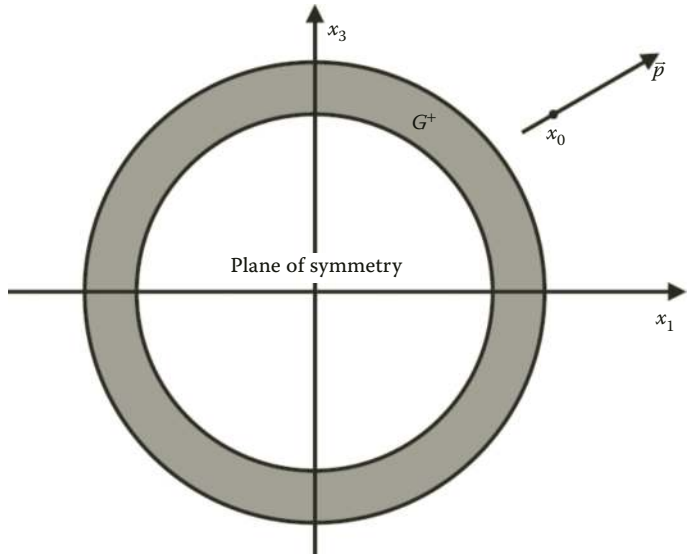

FIGURE 1.3 Closed dielectric envelope.

The right-hand side of integral in Equation 1.61 expresses the field of radiating aperture by means of equivalent currents method via distributions of $\vec{E}^T$, $\vec{H}^T$ over aperture that can be set directly. This formulation differs from the usual problem of the free space radiation by an aperture (antenna aperture particularly) in the way that the field $\vec{\mathcal{E}}_0, \vec{\mathcal{H}}_0$ in formula (1.61) is the field diffracted at aligned system of scatterers (instead of explicit expression of the field by electric dipole in unlimited free space). Equality (1.61) itself means that, given the presence of nonhomogeneous medium and arbitrary set of scatterers, the field computed using the equivalent current (or aperture) method coincides (within accuracy of physical optics) with the averaged field corresponding formally to Macdonald's model, the latter meaning that result by Ya.N. Pheld [14] can be extended onto the more general case being considered here.

In case where all nonhomogeneities of the propagation medium and all the scatterers of Ω^+ are situated within limited distance from S_0, one can derive from Equations 1.60 and 1.61 the formulas expressing complex directivity diagram of the radiating system under consideration, $\vec{E}(\vec{R}^0)$, where $\vec{R}^0$ is the unit vector showing direction to the observation point in far-field (Fraunhofer) zone:

$$\vec{p} \cdot \vec{E}(\vec{R}^0) = \int_{S_0} ((\vec{E}^A(\vec{x}) \times \vec{\mathcal{H}}_0(\vec{x}, \vec{R}^0, \vec{p})) - (\vec{H}^B(\vec{x}) \times \vec{\mathcal{E}}_0(\vec{x}, \vec{R}^0, \vec{p}))) \cdot \mathrm{d}\vec{S}, \tag{1.62}$$

(exact formula);

$$\vec{p} \cdot \vec{E}(\vec{R}^0) = \int_{S_0} ((\vec{E}^T(\vec{x}) \times \vec{\mathcal{H}}_0(\vec{x}, \vec{R}^0, \vec{p})) - (\vec{H}^T(\vec{x}) \times \vec{\mathcal{E}}_0(\vec{x}, \vec{R}^0, \vec{p}))) \cdot \mathrm{d}\vec{S}, \tag{1.63}$$

(approximate formula; $\vec{E}^T, \vec{H}^T$ are the distributions over aperture of tangential components of field vectors in Kirchhoff's approximation).

In formulas (1.62) and (1.63), $\vec{\mathcal{E}}_0(\vec{x}, \vec{R}^0, \vec{p})$, $\vec{\mathcal{H}}_0(\vec{x}, \vec{R}^0, \vec{p})$ is the diffracted field of aligned system of scatterers excited by the propagating in direction $(-\vec{R}^0)$ plane wave

$$\vec{E}_0 = (\vec{R}^0 \times (\vec{p} \times \vec{R}^0)) \exp(-jk_0(\vec{R}^0 \cdot \vec{x})),$$

$$\vec{H}_0 = (\vec{p} \times \vec{R}^0) \sqrt{\varepsilon_0 / \mu_0} \exp(-jk_0(\vec{R}^0 \cdot \vec{x})),$$

where ε_0, μ_0 are the permittivity and permeability of free space, and k_0 is the wave number of free space.

It is worth mentioning that formulas (1.38) through (1.44) and (1.60) through (1.63) are of not only practical computation interest but they are also of instructional value: calculations presented above along with physical interpretations allow estimating their applicability limits in every specific class of computational task at hand. It is out of any doubt that use of formula (1.63) for calculating directivity diagrams of antenna systems with radomes is more preferable than the use of such coarse computing methods as, for instance, the one of remote apertures ("false aperture method" [19]).

1.4 REGULARIZATION OF SOLUTIONS TO NONSTATIONARY SCATTERING PROBLEMS IN CASE OF PHYSICAL OPTICS APPROXIMATION IN BISTATIC RADAR

If one applies the physical optics method to compute fields scattered from smooth perfectly conducting bodies, the errors occur due to inadequate description of surface currents in the vicinity of terminator (the "light-shadow" boundary). In the work [6], these "terminator discontinuities" have

been eliminated for a handful of very special cases of stationary scattering (monostatic radar, two-dimensional problems, or three-dimensional problems but given terminator being a flat curve and its plane being perpendicular to the incidence direction). In [6], the summands have been singled out that are responsible for these false discontinuities, these summands being then subtracted from physical optics integral, which improved the result significantly. It should be noted that the computation method in [6] is based essentially on the limited assumptions listed above and it cannot be used if any of the assumptions do not apply.

However, it is easy to give examples of smooth closed convex surfaces with nonflat terminator.

One such example of smooth closed convex surfaces with nonflat terminator is an egg-shaped surface (Figure 1.4) defined by the equation:

$$F(x, y, z) = 0,$$

where

$$F = y^2 + z^2 - u(x),$$

$$u(x) = \frac{1}{4}(x + 3)^2(1 - x^2), \quad |x| \le 1.$$

Let this surface be illuminated by plane wave with the wave vector $\vec{k} = (-1;0;1)$; then the terminator curve equations

$$\begin{cases} F(x, y, z) = 0, \\ \vec{k} \cdot \operatorname{grad} F(x, y, z) = 0 \end{cases}$$

can be presented in the following form:

$$(T): \begin{cases} y = \pm\sqrt{u(x) - v^2(x)}, \\ z = v(x), \end{cases}$$

where $v(x) = (1/4)(x + 3)(2x^2 + 3x - 1)$.

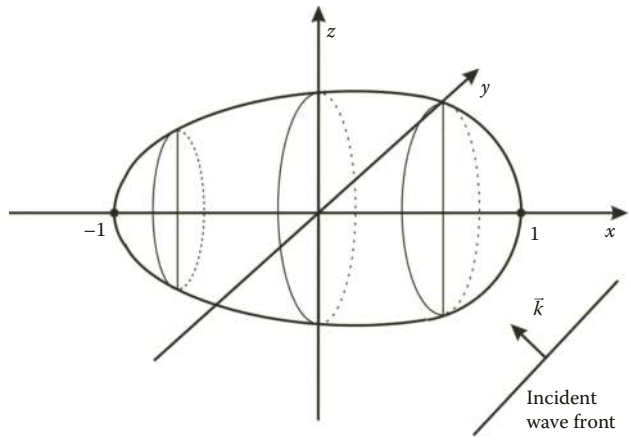

FIGURE 1.4 The egg-shaped surface.

Assume that line (T) belongs to some plane

$$Ay + Bz + Dx + C = 0,$$
$$(A^2 + B^2 + D^2 \neq 0).$$

Then, we have an identity:

$$A^2 (u - v^2) \equiv (C + Bv + D)^2.$$

Since

$$u(x) = -\frac{1}{4}x^4 + \cdots, \quad v(x) = -\frac{1}{2}x^3 + \cdots,$$

then, it follows from this identity that: $(1/4)(A^2 + B^2)x^6 + \cdots = 0$, from where $A = B = 0$ and we have $x \equiv const$ at the terminator, which contradicts the terminator equations (T).

The contradiction thus received lets us to draw a conclusion that terminator curve (T) is nonflat.

Besides, even the ellipsoid illuminated from arbitrary direction $\vec{R}^0$ forms the terminator, which is a flat curve (ellipse) with its plane being perpendicular to $\vec{R}^0$ only in case where $\vec{R}^0$ is parallel to one of the ellipsoid's principal axes.

In this section, we develop the method for finding the summands introduced by terminator discontinuity of surface current density due to physical optics approximation into the object's impulse response asymptotic and into its Fourier image* for the case of bistatic radar, and in case where this flat terminator being arbitrarily oriented with respect to incidence direction, or even being nonflat.

To move further, we need the well-known formula by M.I. Kontorovich [20,21], which gives us the contribution from a boundary contour in two-dimensional stationary phase method, to be generalized in such way that it would include nonflat region and nonsingular stationary phase point of any type (and not only elliptical).

In this manner, asymptotic method that we are about to obtain would give us the edge asymptotic for practically important case of amplitude function with singularity at the contour.

1.4.1 Surface Integral Asymptotic Given Arbitrary Type of Nonsingular Stationary Phase Point and Singular, at the Edge Contour, Amplitude Function

Integral representations of high-frequency electromagnetic fields contain the surface integrals of the following form:

$$I = \iint_S \exp(jk\Phi(x_1, x_2, x_3)) F(x_1, x_2, x_3) \, \mathrm{d}S, \tag{1.64}$$

given $k \gg 1$.

If the surface S is not closed (wave diffraction at finite screen or aperture antenna radiation, for instance), then asymptotic of the integral I consists of contributions brought in by surface (two-dimensional) stationary phase points and the edge contour L. The case, where surface S is a part of plane, functions Φ and F being smooth enough, has been considered in [20,21]. The method used

* We deal here with high-frequency asymptotic of the impulse response Fourier transform (Fourier image) asymptotic and the corresponding asymptotic representation of the object impulse response in the vicinity of wave front.

here relies on the vector analysis theorems. It allowed us to single out the scattering contribution from the stationary phase point of elliptical type only.

Below, we consider the

a. Integral over nonflat (in general) surface S given smooth phase Φ and amplitude F functions; the asymptotic representation of integral (1.64) in form of sum of contributions from L as well as from isolated stationary phase point of any type [22];
b. Contribution from edge contour L of flat region S given the amplitude function (as is the case in practically important classes of diffraction theory and radiating system theory problems)

$$F = \frac{F_0(x_1, x_2)}{d^p(x_1, x_2)}, \quad 0 < p < 1. \tag{1.65}$$

Here, function F_0 is continuous over $S \bigcup L$, and $d(x_1, x_2)$ is the distance from point $M(x_1, x_2) \in S$ to the contour L. It is worth mentioning that the method used in [21] cannot be applied in this case;

c. Asymptotic formulas for some nonstationary fields, which can be used in the vicinity of wave fronts, obtained by recovering original functions from operational representations of the short wave asymptotic received.

Asymptotic of integral (1.64) given absent surface stationary points and edge singularities. Let $f(x_1, x_2, x_3) = 0$ be the surface S equation, the surface having relatively smooth edge contour L. We consider functions f, Φ, F as being smooth enough at the surface S and in its vicinity. Let us introduce the normal unit vector

$$\vec{n} = \vec{n}\,(x) = \vec{n}\,(x_1, x_2, x_3) = \vec{\nabla} f \Big/ \left|\vec{\nabla} f\right| \tag{1.66}$$

and tangential differential operators $\vec{D} = \vec{\nabla} - \vec{n}\,(\partial/\partial\, n)$, $\vec{D}^{\perp} = \vec{n} \times \vec{D}$.

The assumption of stationary points absence at the surface means that $|\vec{D}\,\Phi| = |\vec{D}^{\perp}\,\Phi| \neq 0$ all over $S \bigcup L$.

Let us introduce the vector function

$$\vec{u} = \frac{\vec{D}^{\perp}\Phi}{\left|\vec{D}^{\perp}\Phi\right|^2} = \frac{\vec{D}^{\perp}\Phi}{\left|\vec{D}\Phi\right|^2}. \tag{1.67}$$

Then, $\vec{n} \cdot \mathrm{rot}(\exp(jk\Phi)\, F\vec{u}) = jk \exp(jk\Phi) F\, (\vec{D}^{\perp}\Phi\, \vec{u}) + \exp(jk\Phi)\, \vec{D}^{\perp}(F\vec{u})$, and, accounting for (1.67),

$$jk \exp(jk\Phi) F = \vec{n} \cdot \mathrm{rot}\left(\exp(jk\Phi) F \frac{\vec{D}^{\perp}\Phi}{\left|\vec{D}\Phi\right|^2}\right) - \exp(jk\Phi)\, \vec{D}^{\perp}\left(F \frac{\vec{D}^{\perp}\Phi}{\left|\vec{D}\Phi\right|^2}\right). \tag{1.68}$$

From where, according to Stokes integral theorem,

$$jk \iint\limits_S \exp(jk\Phi) F\, dS = \oint\limits_L \exp(jk\Phi)\, F \frac{\vec{\tau} \cdot \vec{D}^{\perp}\Phi}{\left|\vec{D}\Phi\right|^2} \mathrm{d}\, l - \iint\limits_S \exp(jk\Phi)\, \vec{D}^{\perp}\left(F \frac{\vec{D}^{\perp}\Phi}{\left|\vec{D}\,\Phi\right|^2}\right) \mathrm{d}\, S, \tag{1.69}$$

where $\vec{\tau}$ is the unit vector of a tangent to L (direction of circulation about edge contour L is coordinated with the unit normal vector to surface S defined according to Equation 1.66). Let us note (to use it later on) that

$$\vec{\tau} \cdot \vec{D}^{\perp}\Phi = \frac{\partial \Phi}{\partial \nu},$$

where $\vec{\nu} = (\vec{\tau} \times \vec{n})$ is the unit normal vector to L that lies in the plane tangent to S. Expression (1.69), therefore, can be put in the following form:

$$I_0 = \frac{1}{jk} K_0 - \frac{1}{jk} I_1. \tag{1.70}$$

Here,

$$I_0 = \iint_S \exp(jk\Phi) F \, \mathrm{d}S; \quad I_1 = \iint_S \exp(jk\Phi)\, T\, F \, \mathrm{d}S$$

$$K_0 = \oint_L \exp(jk\Phi)\, F \left[\left(\frac{\partial \Phi}{\partial \nu} \right) / \left| \vec{D}\Phi \right|^2 \right] \mathrm{d}l,$$

and $TF = \vec{D}^{\perp}(F(\vec{D}^{\perp}\Phi / |\vec{D}\Phi|^2))$ is the operator acting on function F.

Having applied several times transform (1.70), we obtain for any m that

$$I_0 = \sum_{s=0}^{m-1} \frac{(-1)^s}{(jk)^{s+1}} K_s + \frac{(-1)^m}{(jk)^m} I_m, \tag{1.71}$$

where K_s, I_m are the results of replacing in K_0, I_0 the function F by $T^s F$, $T^m F$, respectively. From Equation 1.71 follows asymptotic formula for the surface integral (1.70) given the assumptions made above:

$$\iint_S \exp(jk\Phi) F \, \mathrm{d}S = \oint_L \exp(jk\Phi) \left[\left(\frac{\partial \Phi}{\partial \nu} \right) \Big/ \left| \vec{D}\Phi \right|^2 \right] F_m \, \mathrm{d}l + o\left(\frac{1}{k^m} \right), \tag{1.72}$$

where

$$F_m = F_m(x_1, x_2, x_3, k) = \sum_{s=0}^{m-1} \frac{(-1)^s}{(jk)^{s+1}} T^s F. \tag{1.73}$$

Contour integral in Equation 1.72, if necessary, can be replaced by a sum of squares of contributions from the contour stationary phase points known to be existing in advance. If at some simple closed contour encircled by edge contour L the condition $0 \le l \le l_{\max}$ holds, then $\Phi_{l=l_{\max}} = \Phi_{l=0}$, and, therefore, the interval $0 < l < l_{\max}$ contains points with $\mathrm{d}\Phi/\mathrm{d}l = 0$.

Let, for instance, these points be $l_1, l_2, \ldots, l_N$ and $\Phi''(l_i) \neq 0$, $(i = 1, \ldots, N)$ (the latter condition can be replaced by a more general assumption). Then, integral in the right-hand part of Equation 1.72 can be represented as

$$\sum_{i=1}^{N} \sqrt{\frac{2\pi}{k\left|\Phi''(l_i)\right|}} \cdot F_m(l_i) \left(\frac{\partial\Phi/\partial\nu}{\left|\vec{D}\Phi\right|^2} \right)_{l=l_i} \cdot \exp\left(jk\Phi(l_i) + \frac{j\pi}{4} \operatorname{sgn}\Phi''(l_i) \right).$$

Method of "neutralizers," localization of asymptotic contributions. Let us assume that surface S and its edge contour L are infinitely smooth, and functions f, F, and Φ are infinitely differentiable at the surface S and in its vicinity, the condition $\vec{\nabla} f \neq 0$ being held true all over $S \cup L$, and the condition $\vec{D}\Phi = 0$ being held true at the only point $M_0(x_0) = M_0(x_1^0, x_2^0, x_3^0)$ situated at surface S at distance $R > 0$ from the edge contour L.

Having transformed coordinates back into Cartesian system (ξ_1, ξ_2, ξ_3) with origin at $M_0(x_0)$ and axis $M_0\xi_3$ coinciding with the direction of the unit normal vector $\vec{n}(x_0)$, we get the following:

$$f(x_1, x_2, x_3) = \hat{f}(\xi_1, \xi_2, \xi_3), \quad F(x_1, x_2, x_3) = \hat{F}(\xi_1, \xi_2, \xi_3), \quad \Phi(x_1, x_2, x_3) = \hat{\Phi}(\xi_1, \xi_2, \xi_3).$$

Surface S, according to [23] (given $\rho = \sqrt{\sum_{i=1}^{3} \xi_i^2} < R_0$, where R_0 is relatively small, and $R_0 < R$), is described by equation of the form $\xi_3 = g(\xi_1, \xi_2)$. At point M_0, we have that $g = 0$, $g_{\xi 1} = g_{\xi 2} = 0$. Now, we introduce the function $\gamma(\rho)$, the so-called "neutralizer," which is infinitely smooth all over the semiaxis $0 \leq \rho < +\infty$, and

$$\gamma(\rho) = \begin{cases} 1, 0 \leq \rho \leq \varepsilon_0 \\ 0, \rho \geq \varepsilon_1 \end{cases},$$

where $0 < \varepsilon_0 < \varepsilon_1 < R_0$.

Let us "split the unit" as $1 = \gamma(\rho) + [1 - \gamma(\rho)]$ in the integral I

$$I = \iint_S \exp(jk\Phi)\, F\, \mathrm{d}S = J_1 + J_0. \tag{1.74}$$

Here, $J_1 = \iint_{S_1} \exp(jk\Phi)\, F_1\, \mathrm{d}S$, $S_1 = S \cap \{|\vec{x} - \vec{x}_0| \leq \varepsilon_1\}$, $F_1 = F\gamma$, $J_0 = \iint_{S_0} \exp(jk\Phi) F_0\, \mathrm{d}S$, $S_0 = S \cap \{|\vec{x} - \vec{x}_0| \geq \varepsilon_0\}$, $F_0 = F(1 - \gamma)$.

The edge contour of surface S_0 consists of line L and the intersection line L_0 of sphere $|\vec{x} - \vec{x}_0| = \varepsilon_0$ and S. Function F_0 and all its derivatives are equal to zero at line L_0, and at line L they coincide with corresponding values of function F and its derivatives. Besides, at $S_0 \cup L \cup L_0$, there are no surface stationary phase points, therefore, according to results obtained above we have

$$J_0 = \oint_L \exp(jk\Phi) \left[\left(\frac{\partial\Phi}{\partial\nu} \right) \Big/ \left|\vec{D}\Phi\right|^2 \right] F_m\, \mathrm{d}l + o\left(\frac{1}{k^m} \right), \tag{1.75}$$

where F_m is represented by Equation 1.73.

We proceed now with the integral J_1 asymptotic. Since $\varepsilon_1 < R_0$, then surface S_1 is described by equation $\xi_3 = g(\xi_1, \xi_2)$, and its edge contour L_1 is the intersection of surface S and sphere $|\vec{x} - \vec{x}_0| = \varepsilon_1$. Let us denote the contour and surface projection onto the coordinate plane (ξ_1, ξ_2) as L_1' and S_1', respectively. Then,

$$J_1 = \iint_{S_1'} \exp(jk\overline{\Phi})\overline{F}_1 \, \mathrm{d}S_1', \tag{1.76}$$

where $\overline{\Phi}(\xi_1, \xi_2) = \hat{\Phi}(\xi_1, \xi_2, g(\xi_1, \xi_2))$, $\overline{F}_1(\xi_1, \xi_2) = \gamma(\overline{\rho})\hat{F}(\xi_1, \xi_2, g(\xi_1, \xi_2))\sqrt{1 + g_{\xi_1}^2 + g_{\xi_2}^2}$, $\overline{\rho} = \sqrt{\xi_1^2 + \xi_2^2 + g^2(\xi_1, \xi_2)}$.

Multiplier $\gamma(\overline{\rho})$ at contour L_1' makes the function $\overline{F}_1$ and all its partial derivatives of any order to vanish given $\overline{\rho} = \varepsilon_1$. Under these conditions and given nonsingular stationary phase point M_0, double integral in Equation 1.76 allows [24,25] asymptotic representation of the form

$$J_1 \sim k^{-1} \exp\left[jk\Phi(M_0)\right] \sum_{m=0}^{+\infty} a_m k^{-m}. \tag{1.77}$$

The major value approximation of integral is

$$J_1 = \frac{2\pi}{k} \exp(jk\Phi(M_0)) \left[\frac{\exp((j\pi/4)\operatorname{sgn}\overline{\Phi})}{\sqrt{|\det\overline{\Phi}|}} F(M_0) + O\left(\frac{1}{k}\right) \right], \tag{1.78}$$

where $\overline{\Phi} = \begin{bmatrix} \overline{\Phi}_{\xi_1^2} & \overline{\Phi}_{\xi_1\xi_2} \\ \overline{\Phi}_{\xi_1\xi_2} & \overline{\Phi}_{\xi_2^2} \end{bmatrix}$ given $\xi_1 = \xi_2 = 0$, and $\operatorname{sgn}\overline{\Phi} = \mu^+ - \mu^-$ is the difference between the numbers of positive and negative eigenvalues λ_1, λ_2 of matrix $\overline{\Phi}$. In elliptical case $((\lambda_1\lambda_2 > 0)$, $\operatorname{sgn}\overline{\Phi} = \pm 2$, and in hyperbolic case $\lambda_1\lambda_2 < 0$, $\operatorname{sgn}\overline{\Phi} = 0$.

Elements of matrix $\overline{\Phi}$ can be expressed (as it can be shown) via derivatives of functions $\hat{\Phi}$ and $\hat{f}$ depending on ξ_1, ξ_2, ξ_3 at the point M_0 (0, 0, 0) given $l, m = 1,2$ as follows:

$$(\overline{\Phi}_{\xi_l\xi_m})_{\xi_1=\xi_2=0} = \hat{f}_{\xi_3}^{-1} \left[\overline{\Phi}_{\xi_l\xi_m} \hat{f}_{\xi_3} - \hat{f}_{\xi_l\xi_m} \overline{\Phi}_{\xi_3} \right]_{M_0} \tag{1.79}$$

In this manner, there is no necessity to solve the equation $\hat{f}(\xi_1, \xi_2, \xi_3) = 0$ with respect to ξ_3 and to find the explicit expression of function $g(\xi_1, \xi_2)$ in order to represent integral J_1 according to Equation 1.78.

So, the asymptotic of integral I has been localized in form of contributions from the edge L of surface S (1.75), and from stationary phase point M_0 (1.77), (1.78). This result can be spread onto the case of several surface phase points. Besides, the method of "neutralizers" used above allows us, relying upon results presented in [24–26], to receive also asymptotic contributions from isolated stationary phase points in various cases of their singularity. For example, if, after proper rotation of coordinate system in $\hat{f}(\xi_1, \xi_2, \xi_3) = 0$ about axis $M_0\xi_3$, the phase function can be expanded (in the vicinity of point M_0) as

$$\overline{\Phi}(\xi_1, \xi_2) = \Phi(M_0) + \lambda_1\xi_1^2 + \sum_{\substack{p+q\geq 3 \\ p,q\geq 0}} \lambda_{pq}\xi_1^p\xi_2^q,$$

and if $\lambda_1 \neq 0$, $\lambda_{03} \neq 0$, then [26]

$$J_1 \sim \frac{1}{\sqrt{3}} \exp\left(jk\Phi(M_0)\right) F(M_0) \frac{\sqrt{\pi}\,\Gamma(1/3)\exp\left((j\pi/4)\operatorname{sgn}\lambda_1\right)}{\sqrt{|\lambda_1|}\ \sqrt[3]{|\lambda_{03}|}\ k^{5/6}}. \tag{1.80}$$

If, now, one considers integral I as a spectral image, then its original will be the integral

$$\bar{I} = \iint_S \delta\left(t - \Phi(\vec{x})\right) F(\vec{x})\, \mathrm{d}S.$$

Taking inverse Fourier transform of the right-hand part of Equation 1.74 (taking into consideration (1.75) and (1.77)), we get the ray expansion for $\bar{I}$, the latter being the more accurate the closer value $\left|t - \Phi(\vec{x})\right|$ is to zero. Principle member of this expansion has the form:

$$\bar{I} = \iint_S \delta(t-\Phi(\vec{x}))F(\vec{x})\mathrm{d}S \sim -j2\pi\exp\left(j\frac{\pi}{4}\operatorname{sgn}\bar{\Phi}\right)\frac{F(M_0)}{\sqrt{\left|\det\bar{\Phi}\right|}}\chi(t-\Phi(\vec{x}))$$
$$-\oint_L \chi(t-\Phi(\vec{x}))\left[\left(\frac{\partial\Phi}{\partial\nu}\right)\Big/\left|\vec{D}\Phi\right|^2\right]F(\vec{x})\,\mathrm{d}l. \tag{1.81}$$

Here, M_0 is the stationary phase point (the one, in which $\vec{D}\,\Phi = 0$) at the surface S; $\delta(t)$ is the Dirac delta-function; $\chi(t)$ is the Heaviside step function. So, formula (1.81) can be considered as transient analog to the generalization of the M.I. Kontorovich formula [21] considered above in this chapter.

Asymptotic of integrals with edge singularity. Integrals with the edge singularity appear in some electrodynamics problems such as the following:

1. The total diffracted field $\vec{H}(\vec{x})$ is sought from the primary wave $\vec{H}_0(\vec{x})$ incident on flat perfectly conducting infinitely thin screen S bounded by contour L. In this case, Green's formula [27] gives integral representation of the magnetic field strength vector at any point $\vec{x}_0$ outside the screen:

$$\vec{H}(\vec{x}_0) = \vec{H}_0(\vec{x}_0) + \iint_S (\vec{\nabla}g \times \vec{J}(\vec{x}))\,\mathrm{d}S. \tag{1.82}$$

   Here, $\vec{J}(\vec{x})$ is the surface current density; $g = g(\vec{x}_0, \vec{x}) = \exp(jkr)/(4\pi r)$; $r = \left|\vec{x}_0 - \vec{x}\right|$; and the scattered field has the form

$$\vec{H}(\vec{x}_0) - \vec{H}_0(\vec{x}_0) = \iint_S \exp(jk\Phi)\,\vec{F}(\vec{x}_0, \vec{x})\,\mathrm{d}S,^{*} \tag{1.83}^{*}$$

   given phase function $\Phi = \Phi(\vec{x}_0, \vec{x}) = r$.
2. Integrals of the same kind as in Equation 1.83 and with the same phase function are obtained for the radiation of aperture antenna in rigorous mathematical model [16,17].

---

* Without restricting generality, hereinafter we assume F to be a component of vector $\vec{F}$, as well as we assume k to be dimensionless parameter equal to wave number k_0 times characteristic screen size.

In each of the examples given earlier, the physically necessary condition at the edge is applied in order to ensure the energy to be finite in the vicinity of the surface fracture [27]. Because of this, the amplitude function F may have singularity at infinitely thin edge i.e. $F = F_0/\sqrt{d}$, where F_0 is continuous in the vicinity of edge contour, and $d = d(x_1, x_2)$ is the distance from a point in region S to the edge contour.

In a more general case of fractures with interior angles $\theta \in [0, \pi]$, we have $F = F_0/d^p$ and $p = (\pi - \theta)/2\pi \in [0, 1/2]$.

Method for obtaining the short wave asymptotic given edge singularities is presented below as applied to integral P over flat and strictly convex region S with relatively smooth edge contour L and function F_0:

$$P = \iint_S \exp(jkr) \frac{F_0(\vec{x})}{\sqrt{d(\vec{x})}} \mathrm{d}S, \tag{1.84}$$

where $r = \sqrt{(x_1^0 - x_1)^2 + (x_2^0 - x_2)^2 + h^2}$, $(h = x_3^0 \neq 0)$.

Point $M_0(x_1^0, x_2^0, 0) \in S$ is separated from the edge contour L by distance $R_1 > 0$. Then, complex directivity diagram is as follows:

$$Q = \iint_S \exp\left(-jk(\vec{R}^0 \cdot \vec{x})\right) \frac{F_0(\vec{x})}{\sqrt{d(\vec{x})}} \mathrm{d}S, \tag{1.85}$$

where $\vec{R}^0 = (0, -\cos\psi, \sin\psi)$.

Integral P is convenient to be analyzed if we set the edge contour L by an equation in polar coordinates (ρ, θ) with the center at point M_0:

$$\rho = \omega(\theta), \quad 0 \leq \theta \leq 2\pi. \tag{1.86}$$

In this case (as it can be shown), the amplitude function in integral P can be represented as a ratio $F_1(\rho, \theta)/\sqrt{\omega(\theta) - \rho}$ with numerator, having no singularities. We thus obtain

$$P = \int_0^{2\pi} \mathrm{d}\theta \int_0^{\omega(\theta)} \exp\left(jk\sqrt{\rho^2 + h^2}\right) \frac{F_1(\rho, \theta)\, \rho\, \mathrm{d}\rho}{\sqrt{\omega(\theta) - \rho}}. \tag{1.87}$$

Let us substitute new variable $r = \sqrt{\rho^2 + h^2}$ into integral P:

$$P = \int_0^{2\pi} \mathrm{d}\theta \int_h^{\Omega} \exp(jkr)(\Omega - r)^{-1/2} G\, r\, \mathrm{d}r, \tag{1.88}$$

where $\Omega = \Omega(\theta) = \sqrt{\omega^2(\theta) + h^2}$, $G = G(r, \theta) = F_1\left(\sqrt{r^2 - h^2}, \theta\right)[(\omega(\theta) + \sqrt{r^2 - h^2})/(\Omega(\theta) + r)]^{1/2}$.

Given $h \leq r \leq \Omega(\theta)$, we introduce infinitely differentiable by r (given every fixed value of θ) neutralizers $\gamma_0(r, \theta)$ and $\gamma_1(r, \theta)$, such that $\gamma_1 = 1 - \gamma_0$, $\gamma_0(r, \theta) = \begin{cases} 1, h \leq r \leq \varepsilon_1 \\ 0, \varepsilon_0 \leq r \leq \Omega(\theta) \end{cases}$ $\left(h < \varepsilon_1 < \varepsilon_0 < \min\limits_{0 \leq \theta \leq 2\pi} \Omega(\theta)\right)$. Given the condition that $1 = \gamma_0(r, \theta) + \gamma_1(r, \theta)$, we obtain $P = P_0 + P_1$.

Let us consider the asymptotic of integral P. The stationary phase point $\rho = 0$ ($r = h$) contribution is as follows:

$$P_0 = \int_0^{2\pi} d\theta \int_h^{\varepsilon_0} \exp(jk\,r)(\Omega - r)^{-1/2} G\,\gamma_0\,r\,dr. \tag{1.89}$$

Since function $G_0(r, \theta) = (\Omega - r)^{-1/2}\,G\gamma_0 r$, given every fixed value of θ, is continuous by $r \in [h, \varepsilon_0]$ along with all its derivatives (they equal to zero given $r = \varepsilon_0$), then integrating by parts gives us the following expression:

$$P_0 = \sum_{m=1}^{N} \frac{(-1)^m \exp(jkh)}{(jk)^m} \int_0^{2\pi} \frac{\partial^{m-1} G_0(h,\,\theta)}{\partial r^{m-1}} d\theta + O\left(\frac{1}{k^{N+1}}\right). \tag{1.90}$$

In principle value approximation, we have

$$P_0 = -\frac{h \exp(jkh)}{jk} F_1(M_0) \int_0^{2\pi} \frac{d\theta}{\sqrt{\omega(\theta)}} + O\left(\frac{1}{k^2}\right). \tag{1.91}$$

Given asymptotic expansion of integral

$$P_1 = \int_0^{2\pi} d\,\theta \int_{\varepsilon_1}^{\Omega} \exp(jkr)(\Omega - r)^{-1/2} G\,\gamma_1\,r\,dr, \tag{1.92}$$

our goal is achieved by integrating the inner integral by parts. However, due to singularity of function $(\Omega - r)^{-1/2}$ at point $r = \Omega$, it cannot be differentiated under the integral sign. So, instead of e^{jkr}/jk and $e^{jkr}/(jk)^2$, one must use the sequence of special kind of antiderivatives to the product $e^{jkr}(\Omega - r)^{-1/2} = U_0(r, \theta)$ or, in other words, one must use the sequence of functions

$$U_m(r, \theta) = \frac{(-1)^m}{(m-1)!} \int_r^{+j\infty} (t - r)^{m-1} \exp(jkt)(\Omega - t)^{-1/2}\,dt, \quad (m = 1,2,\ldots), \tag{1.93}$$

that possess the following properties:

1. $\dfrac{\partial U_m(r, \theta)}{\partial r} = U_{m-1}(r, \theta)$, $(m = 1,2,\ldots)$,
2. $U_m(\Omega, \Omega) = \dfrac{(-1)^m}{(m-1)!} \exp(\pi j(m + 1/2)/2)\,\dfrac{\Gamma(m - 1/2)}{k^{m-1/2}} \exp(jk\Omega)$,
3. $\left|U_m(r, \Omega)\right| \le \dfrac{1}{(m-1)!}\,\dfrac{\Gamma(m - 1/2)}{k^{m-1/2}}$, $(h \le r \le \Omega)$.

The following asymptotic representation stems from these properties:

$$P_1 = \sum_{m=1}^{N} \frac{(-1)^{m-1} \exp(-j\pi(m - 1/2)/2)\,\Gamma(m - 1/2)}{k^{m-1/2}} \int_0^{2\pi} \exp(jk\Omega)\,\Psi_{m-1}(\theta)\,d\theta + O\left(\frac{1}{k^{N+1/2}}\right), \tag{1.94}$$

where

$$\Psi_{m-1}(\theta) = \left.\frac{\partial^{m-1}[G(r,\theta)\,r]}{\partial r^{m-1}}\right|_{r=\Omega(\theta)}.$$

In the principle value approximation

$$P_1 = \frac{\exp(-j\pi/4)\sqrt{\pi}}{\sqrt{k}}\int_0^{2\pi}\exp(jk\Omega)\,F_1(\omega,\theta)\sqrt{\omega\Omega}\,\mathrm{d}\theta + O\left(\frac{1}{k^{3/2}}\right).$$

Now, we are ready to consider asymptotic representation of integral Q (1.85). We restrict ourselves with the case of edge contour L being symmetrical with respect to one of coordinate axes, as well as by obtaining only two major members of asymptotic representation.

Let L in coordinates (x, y) be set by equations $x = \pm w(y)$ $(a \le y \le b)$ and, in the vicinity of points a, b w (y), to have the following asymptotic:

$$w(y) \sim \begin{cases} p(y)\sqrt{y-a}, & (y \to a+0) \\ q(y)\sqrt{b-y}, & (y \to b-0) \end{cases}.$$

In this case, $p(y)$, $q(y)$, $w^2(y)$ are smooth enough within $[a, a+\varepsilon)$, $[b-\varepsilon, b)$, and $[a, b]$, respectively (given $\varepsilon < (b-a)/2$).

Amplitude function in Equation 1.85 can be represented as the ratio $f(x,y)\big/\sqrt{w^2(y)-x^2}$, in which $f(x, y)$ does not have any singularities. Let us assume that this function is satisfactorily smooth over $S \bigcup L$. After some math, we obtain the following:

$$Q = \int_a^b \exp(j\bar{k}y)\,U(y)\mathrm{d}y, \quad (\bar{k} = k\cos\psi), \tag{1.95}$$

$$U(y) = \int_{-1}^{1} f(\xi w(y), y)\frac{\mathrm{d}\xi}{\sqrt{1-\xi^2}}, \tag{1.96}$$

$$U'(y) = \int_{-1}^{1}\frac{\partial f(\xi w(y),y)}{\partial y}\frac{\mathrm{d}\xi}{\sqrt{1-\xi^2}} + \frac{1}{2}\frac{\partial w^2(y)}{\partial y}\int_{-1}^{1}\frac{\partial^2 f(\theta\,\xi w(y),y)}{\partial x^2}\frac{\xi^2\,\mathrm{d}\xi}{\sqrt{1-\xi^2}} (0<\theta<1). \tag{1.97}$$

From Equations 1.96 and 1.97, it follows that

$$U(a) = f(0,a)\pi, \quad U(b) = f(0,b)\pi,$$

$$U'(a) = \left(\frac{\partial f(0,a)}{\partial y} + \frac{1}{4}\frac{\partial^2 f(0,a)}{\partial x^2}A\right)\pi, \tag{1.98}$$

$$U'(b) = \left(\frac{\partial f(0,b)}{\partial y} + \frac{1}{4}\frac{\partial^2 f(0,b)}{\partial x^2}B\right)\pi,$$

where

$$A = \lim_{y \to a+0} \left[\frac{w(y)}{\sqrt{y-a}} \right]^2, \quad B = \lim_{y \to b-0} \left[\frac{w(y)}{\sqrt{b-y}} \right]^2.$$

Integrating by parts twice into Equation 1.95, we obtain the following asymptotic formula:

$$Q = \pi \exp(j\bar{k}b) \left[\frac{1}{j\bar{k}} f(0,b) - \frac{1}{(j\bar{k})^2} \left(\frac{\partial f(0,b)}{\partial y} + \frac{1}{4} \frac{\partial^2 f(0,b)}{\partial x^2} B \right) \right]$$
$$- \pi \exp(j\bar{k}a) \left[\frac{1}{j\bar{k}} f(0,a) - \frac{1}{(j\bar{k})^2} \left(\frac{\partial f(0,a)}{\partial y} + \frac{1}{4} \frac{\partial^2 f(0,a)}{\partial x^2} A \right) \right] + O\left(\frac{1}{\bar{k}^3} \right). \quad (1.99)$$

In this manner, the asymptotic representation of integral Q obtained above is of discrete nature and it consists of contributions from vicinities of points (0, a) and (0, b) of edge contour. Such phenomenon is known well in the short wave diffraction theory and it is related with the "specular point" concept in radar.

Methods used above to compute integrals P and Q allow us to obtain asymptotic representation of integrals with other phase functions and other types of edge singularities.

Let us apply Kontorovich's formula generalization (1.81) obtained above to solve the problem of electromagnetic wave diffraction at perfectly conducting convex body (in physical optics approximation).

1.4.2 Impulse Response of Perfectly Conducting Smooth Convex Body in Bistatic Radar (Physical Optics Method). Elimination of Terminator Discontinuities

Using asymptotic expression (1.81), one can obtain impulse response of perfectly conducting smooth convex body in general case of bistatic radar.

Let the object with surface S be illuminated with plane monochromatic electromagnetic wave

$$\vec{E}^0 = \vec{p} \exp(jk_0(a + \vec{R}^0 \cdot \vec{x})),$$

$$\vec{H}^0 = \sqrt{\frac{\varepsilon_0}{\mu_0}} (\vec{R}^0 \times \vec{p}) \exp(jk_0(a + \vec{R}^0 \cdot \vec{x})). \quad (1.100)$$

Here, a is the distance from the zero phase plane to the coordinate origin, $\vec{p}$ is the polarization unit vector, $\vec{R}^0$ is the wave unit vector of incident wave.

Operational original for the field (1.100) is the pulsed plane wave

$$\vec{\mathcal{E}}^0(t, \vec{x}|\vec{R}^0) = \vec{p}\,\delta(t - a - \vec{R}^0 \cdot \vec{x}),$$

$$\vec{\mathcal{H}}^0(t, \vec{x}|\vec{R}^0) = \sqrt{\frac{\varepsilon_0}{\mu_0}} (\vec{R}^0 \times \vec{p})\delta(t - a - \vec{R}^0 \cdot \vec{x}). \quad (1.101)$$

Field scattered from the body in the direction of unit vector $\vec{r}^{\,0}$, when the body is illuminated with wave (1.100), can be presented in the form:

$$\vec{H}^{scat}(r\vec{r}^{\,0}) \approx \frac{\exp(jk_0 r)}{4\pi r} jk_0 \iint_S (\vec{H}^{\perp} \times \vec{r}^{\,0}) \exp(-jk_0(\vec{r}^{\,0} \cdot \vec{x}))\, \mathrm{d}S,$$

where $\vec{H}$ is total field at the surface S. Physical optics approximation gives us the following expression for the scattered field:

$$\vec{H}^{scat}(r\vec{r}^{\,0}) \approx jk_0 \iint_{S_{illum}} \exp(jk_0\Phi)\vec{A}\, \mathrm{d}S, \tag{1.102}$$

where S_{illum} is the object surface part that illuminated with the wave (1.100),

$$\vec{A} = \frac{1}{2\pi r}\sqrt{\frac{\varepsilon_0}{\mu_0}} \left(\vec{n} \times \left(\vec{R}^0 \times \vec{p}\right)\right) \times \vec{r}^{\,0}, \quad \Phi = a + r + \left(\vec{R}^0 - \vec{r}^{\,0}\right) \cdot \vec{x}.$$

Impulse response of the object, in its turn, is the original, spectral image of which in high-frequency approximation is represented by expression (1.102):

$$\vec{\mathcal{H}}^{scat}(t, \vec{x}|\vec{r}^{\,0}) \approx -\frac{\partial}{\partial t} \iint_{S_{illum}} \delta(t - \Phi(\vec{x}))\vec{A}\, \mathrm{d}S. \tag{1.103}$$

In this manner, expression for the impulse response can be obtained using formula (1.81) simply by differentiating it by t.

By the way, we are going to get a representation for the solution estimate to stationary diffraction problem described by expression (1.102).

To achieve this, we evaluate, first, the contribution from stationary phase point. The stationary phase point M_0 is determined by the following equality at point M_0:

$$\vec{D}\Phi = \left(\vec{R}^0 - \vec{r}^{\,0}\right)^T = \vec{R}^{0T} - \vec{r}^{\,0T} = 0$$

or

$$\vec{R}^0 \cdot \vec{n} = -\vec{r}^{\,0} \cdot \vec{n},$$

where $\vec{n}$ is the normal to S_{illum} at the stationary phase point M_0.

In the vicinity of point M_0, we introduce local coordinate system ξ_1, ξ_2, ζ described above in Section 1.4.1 (here, $\zeta = \xi_3$). In the vicinity of point M_0 at S_{illum}

$$\zeta = -\left(\frac{a_{11}}{2}\xi_1^2 + a_{12}\xi_1\xi_2 + \frac{a_{22}}{2}\xi_2^2\right) + o\left(\xi_1^2 + \xi_2^2\right),$$

or, within accuracy of the higher-order infinitesimal,

$$\zeta = -\frac{1}{2}\vec{\xi}' A\vec{\xi}, \quad A = \begin{pmatrix} a_{11} & a_{12} \\ a_{21} & a_{22} \end{pmatrix}.$$

In this case, in the vicinity of M_0 we have

$$\bar{\Phi}(\xi_1,\xi_2) = a + r + l_1^0 \xi_1 + l_2^0 \xi_2 - \frac{1}{2}\left(\vec{l}^{\,0} \cdot \vec{n}_{M_0}\right)\left(\vec{\xi}' A\vec{\xi}\right),$$

where $\vec{l}^{\,0} = \vec{R}^0 - \vec{r}^{\,0}$, so that

$$\left(\frac{\partial^2 \bar{\Phi}}{\partial\xi_i\, \partial\xi_k}\right)_{M_0} = -\frac{1}{2}\left(\vec{l}^{\,0} \cdot \vec{n}_{M_0}\right) a_{ik},$$

$$\bar{\Phi}_{M_0} = -\frac{1}{2}\left(\vec{l}^{\,0} \cdot \vec{n}_{M_0}\right) A.$$

Taking into account that

$$\left(\vec{l}^{\,0} \cdot \vec{n}_{M_0}\right) = 2\left(\vec{R}^0 \cdot \vec{n}_{M_0}\right) = -2\left(\vec{r}^{\,0} \cdot \vec{n}_{M_0}\right),$$

we get

$$\bar{\Phi}_{M_0} = \left(\vec{r}^{\,0} \cdot \vec{n}_{M_0}\right) A.$$

Since $\vec{n}_{M_0}$ is the unit vector of external normal to S_{illum}, then, evidently, $\left(\vec{r}^{\,0} \cdot \vec{n}_{M_0}\right) > 0$.
Let λ_1, λ_2 be the eigenvalues of matrix A. Then,

$$\operatorname{sgn} \bar{\Phi}_{M_0} = \operatorname{sgn} A,$$

$$\left|\det \bar{\Phi}_{M_0}\right| = \left(\vec{r}^{\,0} \cdot \vec{n}_{M_0}\right)^2 \left|\det A\right| = \left(\vec{r}^{\,0} \cdot \vec{n}_{M_0}\right)^2 \left|\lambda_1\, \lambda_2\right|.$$

Next, given proper rotation of coordinate system about axis ζ, we get equation for S_{illum} in the vicinity of M_0

$$\zeta = -\frac{1}{2}\left(\lambda_1 \eta_1^2 + \lambda_2 \eta_2^2\right) + \cdots,$$

from which it follows that λ_1, λ_2 are the principal curvatures of S_{illum} at point M_0:

$$\lambda_1 = æ_1, \quad \lambda_2 = æ_2;$$

$$\left|\det \bar{\Phi}_{M_0}\right| = \cos^2\left(\vec{r}^{\,0}, \vec{n}_{M_0}\right) \cdot \left|æ_1\, æ_2\right|.$$

To move on further, we need to assume that $æ_1 æ_2 \neq 0$. Particularly, if surface S around point M_0 is strictly convex, then $æ_1 > 0, æ_2 > 0$ and

$$\left| \det \bar{\Phi}_{M_0} \right| = æ_1 æ_2 \cos^2\left(\vec{r}^{\,0}, \vec{n}_{M_0}\right),$$

$$\operatorname{sgn} \bar{\Phi}_{M_0} = 2.$$

If, in its turn, M_0 is the saddle point, then $æ_1 æ_2 < 0, \operatorname{sgn} \bar{\Phi}_{M_0} = 0$. For definiteness, we give all the considerations below for the case of $æ_1 > 0$, $æ_2 > 0$. Using expression (1.78), we get contribution from the stationary phase point into the scattered field:

$$\vec{H}^{scat}(r\vec{r}^{\,0})\Big|_{st.ph.} \sim -\sqrt{\frac{\varepsilon_0}{\mu_0}} \frac{[\vec{n}_{M_0} \times (\vec{R}^0 \times \vec{p})] \times \vec{r}^{\,0}}{r\sqrt{æ_1 æ_2}\left|\cos(\vec{r}^{\,0}, \vec{n}_{M_0})\right|} \cdot \exp(jk_0(a + r + \vec{l}^{\,0} \cdot \vec{x}_{M_0})). \tag{1.104}$$

Boundary of the surface S_{illum} is terminator L, which determines the "light-shadow" border line. We estimate its contribution into the scattered field asymptotic using (1.75):

$$(\vec{H}^{scat}(r\vec{r}^{\,0}))_{cont.L} \sim \int_L e^{jk_0\Phi} \vec{A} \frac{\partial\Phi/\partial\nu}{\left|\vec{D}\Phi\right|^2} \mathrm{d}l. \tag{1.105}$$

Here,

$$\frac{\partial\Phi}{\partial\nu} = \vec{l}^{\,0} \cdot \vec{\nu} = \vec{l}^{\,0} \cdot (\vec{\tau} \times \vec{n}),$$

$$\left|\vec{D}\Phi\right|^2 = \left|\vec{l}^{\,0^T}\right|^2 = \left|\vec{l}^{\,0}\right|^2 - \left(\vec{l}^{\,0} \cdot \vec{n}\right)^2.$$

Let us assume that contour L is defined parametrically:

$$\vec{x} = \vec{x}(t).$$

Then, contour points of stationary phase can be found from equation

$$\vec{l}^{\,0} \cdot \vec{x}'(t) = 0,$$

and let these points be M_i $(i = 1, \ldots, N)$. Then, integral in Equation 1.105 can be computed asymptotically:

$$(\vec{H}^{scat}(r\vec{r}^{\,0}))_{cont.L} \sim \sum_{m=1}^{N} \sqrt{\frac{2}{k_0\left|\vec{l}^{\,0} \cdot \left(\frac{\mathrm{d}\vec{\tau}}{\mathrm{d}l}\right)_{M_m}\right|}} \left(\vec{A}\right)_{M_m} \frac{(\vec{l}^{\,0}\vec{\tau}\vec{n})_{M_m}}{\left|\vec{l}^{\,0}\right|^2 - (\vec{l}^{\,0} \cdot \vec{n}_{M_m})^2}$$
$$\cdot \exp\left(jk_0\left(a + r + \vec{l}^{\,0} \cdot \vec{x}_{M_m}\right) + \frac{j\pi}{4} \operatorname{sgn}\left(\vec{l}^{\,0} \cdot \frac{\mathrm{d}\vec{\tau}}{\mathrm{d}l}\right)_{M_m}\right). \tag{1.106}$$

It is taken into account here that

$$\left(\Phi''(l)\right)_{M_m} = \vec{l}^{\,0} \cdot \left(\frac{\mathrm{d}\vec{\tau}}{\mathrm{d}\,l}\right)_{M_m},$$

where

$$\vec{\tau}(t) = \frac{\vec{x}'(t)}{\left|\vec{x}'(t)\right|}, \quad \frac{\mathrm{d}\,\vec{\tau}}{\mathrm{d}\,l} = \vec{\tau}'(t)\frac{\mathrm{d}\,t}{\mathrm{d}\,l} = \frac{\vec{\tau}'(t)}{\left|\vec{x}'(t)\right|}.$$

So, having combined formulas (1.104) and (1.105), we get the following:

$$\vec{H}^{scat}(r\vec{r}^{\,0}) \sim -\sqrt{\frac{\varepsilon_0}{\mu_0}}\frac{[\vec{n}_{M_0} \times (\vec{R}^0 \times \vec{p})] \times \vec{r}^{\,0}}{r \cdot \sqrt{\left|æ_1 æ_2\right|}(\vec{r}^{\,0} \cdot \vec{n}_{M_0})} \times \exp(jk_0(a + r + \vec{l}^{\,0} \cdot \vec{x}_{M_0})) + \oint_L e^{jk_0\Phi}\vec{A}\left(\frac{\partial\Phi}{\partial\nu}\Big/\left|\vec{D}\Phi\right|^2\right)\mathrm{d}l. \tag{1.107}$$

Formula (1.107) gives solution to the stationary diffraction problem, where perfectly conducting smooth convex body is illuminated by plane wave (1.100).

Expression of the impulse response, in its turn, for the object under consideration (scattered field in case of transient pulsed illumination of the object by the field (1.101)) can be considered as the original, spectral image of which is given by formula (1.107):

$$\vec{\mathcal{H}}^{scat}(t, \vec{x}|\vec{r}^{\,0}) \sim -\sqrt{\frac{\varepsilon_0}{\mu_0}}\frac{[\vec{n}_{M_0} \times (\vec{R}^0 \times \vec{p})] \times \vec{r}^{\,0}}{r \cdot \sqrt{\left|æ_1\, æ_2\right|}\,(\vec{r}^{\,0} \cdot \vec{n}_{M_0})}\,\delta(t - a - r - \vec{l}^{\,0} \cdot \vec{x}_{M_0}) + \oint_L \delta(t - a - r - \vec{l}^{\,0} \cdot \vec{x})\vec{A}\left(\frac{\partial\Phi}{\partial\nu}\Big/\left|\vec{D}\Phi\right|^2\right)\mathrm{d}l. \tag{1.108}$$

So, in the physical optics approximation of impulse response, we have singled out the members responsible for terminator discontinuities appearing due to inadequate description of surface current density in the vicinity of "light-shadow" boundary in physical optics approximation. Solution obtained above for the stationary diffraction problem can be improved, like that of [6], by subtracting the major members of terminator asymptotic described by (1.106) from physical optics solution obtained above.

Impulse response (1.108) can be smoothed out by subtracting the operational original, which corresponds to the operational image $(\vec{H}^{scat}(r\,\vec{r}^{\,0}))_{cont.L}$:

$$\vec{\mathcal{H}}^{scat}(t, \vec{x}|\vec{r}^{\,0})\Big|_{cont.L} \sim \sum_{m=1}^{N}\sqrt{\frac{2}{\left|\vec{l}^{\,0} \cdot \left(\frac{\mathrm{d}\,\vec{\tau}}{\mathrm{d}\,l}\right)_{M_m}\right|}}(\vec{A})_{M_m}\frac{(\vec{l}^{\,0}\vec{\tau}\vec{n})_{M_m}}{\left|\vec{l}^{\,0}\right|^2 - (\vec{l}^{\,0} \cdot \vec{n}_{M_m})^2} \cdot \exp\left(j\frac{\pi}{4}\left(\mathrm{sgn}\left(\vec{l}^{\,0} \cdot \frac{\mathrm{d}\,\vec{\tau}}{\mathrm{d}\,l}\right)_{M_m} - 1\right)\right)\frac{\chi(t - a - r - \vec{l}^{\,0} \cdot \vec{x}_{M_m})}{\sqrt{t - a - r - \vec{l}^{\,0} \cdot \vec{x}_{M_m}}}, \tag{1.109}$$

from the right-hand part of Equation 1.108.

Representation of the impulse response obtained in such way does not have spurious peaks, absent in reality, and which appear due to discontinuous character of surface current density adopted in physical optics approximation.

Let us mention also a special case, where terminator L belongs to the plane with normal vector $\vec{l}^{\,0}$. In this case

$$\Phi(\vec{x})|_L = \text{const}$$

and, consequently,

$$\vec{l}^{\,0} \cdot \vec{x} = c \text{ at } L,$$

where c is some constant.

It follows from here that

$$(\vec{\mathcal{H}}^{scat}(r\vec{r}^{\,0}))_{cont.L} \sim \exp(jk_0(a+r+c)) \oint_L \vec{A}\left(\frac{\partial\Phi}{\partial\nu}\Big/\left|\vec{D}\Phi\right|^2\right) \mathrm{d}l,$$

$$(\vec{\mathcal{H}}^{scat}(t,\vec{x}|\vec{r}^{\,0}))_{cont.L} \sim \delta(t-a-r-c) \oint_L \vec{A}\left(\frac{\partial\Phi}{\partial\nu}\Big/\left|\vec{D}\Phi\right|^2\right) \mathrm{d}l.$$

It can be seen that intense spurious "terminator" peak appears in this case in impulse response, which is needed to be eliminated.

In some cases, slightly different approach can turn out to be more preferable for estimating impulse responses of complex scatterers in bistatic radar. Such approach (also developed by the authors of this book) uses the physical optics approximation too, but it passes by the need of estimating scattering contributions from stationary phase points [28–30].

Therefore, in this chapter, we presented the method for computing impulse responses of perfectly conducting smooth objects in bistatic radar case.

In the asymptotic representation obtained below, we also singled out the summands responsible for appearance of spurious peaks that were expressed by contour integral. The major members of this integral asymptotic have been obtained, which are needed to be eliminated from the impulse response representation in order to smooth it out. The latter allowed us to increase the computation accuracy over time period up to arrival moment of creeping wave traversing the shadow zone.

All these results rely upon the generalization of M.I. Kontorovich formula obtained above, which gave us the scattering contribution from edge contour in two-dimensional method of stationary phase in case of nonflat region and nonsingular stationary phase points of any type.

1.5 REMARKS ON RECIPROCITY PRINCIPLE FOR THE SCATTERED FIELDS IN PHYSICAL OPTICS APPROXIMATION

As it is known, the reciprocity principle holds true with respect to the fields satisfying the Maxwell equations and, in general, any boundary conditions at the surface of a scatterer. However, when we deal with the fields approximating real ones (such as high-frequency asymptotic solutions to the

Maxwell equations), it turns out that reciprocity principle may not hold true. We consider this issue in more detail with respect to physical optics method used in Section 1.4.

Let the perfectly conducting scatterer V to be bounded by closed surface S and let the Cartesian coordinate system origin to be placed inside the region V.

We consider the object V as being illuminated by electric dipole, with vector-moment $\vec{p}$ that is localized at the point with radius-vector $\vec{a} = -a\vec{R}^0$. Primary field $\vec{E}(\vec{x}|\vec{a},\vec{p}), \vec{H}(\vec{x}|\vec{a},\vec{p})$ excited by the dipole has the following asymptotic representation given fixed unit vector $\vec{R}^0$ and $a \to +\infty$:

$$\begin{pmatrix} \vec{E}(\vec{x}|\vec{a},\vec{p}) \\ \vec{H}(\vec{x}|\vec{a},\vec{p}) \end{pmatrix} = \frac{k_0^2}{\varepsilon_0}\frac{\exp(jk_0 a)}{4\pi a}\begin{pmatrix} \vec{E}^0(\vec{x}|\vec{R}^0,\vec{p}) \\ \vec{H}^0(\vec{x}|\vec{R}^0,\vec{p}) \end{pmatrix}, \tag{1.110}$$

where

$$\begin{pmatrix} \vec{E}^0(\vec{x}|\vec{R}^0,\vec{p}) \\ \vec{H}^0(\vec{x}|\vec{R}^0,\vec{p}) \end{pmatrix} = \begin{pmatrix} (\vec{p} - \vec{R}^0(\vec{p}\cdot\vec{R}^0))\exp(jk_0(\vec{R}^0\cdot\vec{x})) \\ \sqrt{\frac{\varepsilon_0}{\mu_0}}(\vec{R}^0\times\vec{p})\exp(jk_0(\vec{R}^0\cdot\vec{x})) \end{pmatrix}, \tag{1.111}$$

which is the plane wave field.

It follows from vector integral equations of Green's kind for electromagnetic fields [11] and formula (1.110) that the field scattered from object V in far-field zone at a point with radius-vector $\vec{r} = r\cdot\vec{r}^0$ has the asymptotic representation (given $a \to +\infty$, $r \to +\infty$):

$$\begin{pmatrix} \vec{E}^{scat}(\vec{r}|\vec{a},\vec{p}) \\ \vec{H}^{scat}(\vec{r}|\vec{a},\vec{p}) \end{pmatrix} = \frac{k_0^2}{\varepsilon_0}\frac{\exp(jk_0(a+r))}{(4\pi)^2 a r}\begin{pmatrix} \vec{\mathcal{E}}^{scat}(\vec{r}^0|\vec{R}^0,\vec{p}) \\ \vec{\mathcal{H}}^{scat}(\vec{r}^0|\vec{R}^0,\vec{p}) \end{pmatrix}, \tag{1.112}$$

in which vectors $\vec{\mathcal{E}}^{scat}$, $\vec{\mathcal{H}}^{scat}$ constitute the complex scattering diagram that is the field scattered in direction $\vec{r}^0$ (in far-field zone) given incidence of plane wave (1.110) onto V. In this case,

$$\begin{aligned} \vec{\mathcal{E}}^{scat}(\vec{r}^0|\vec{R}^0,\vec{p}) &= -jk_0\sqrt{\frac{\mu_0}{\varepsilon_0}}\int_S (\vec{K} - \vec{r}^0(\vec{r}^0\cdot\vec{K}))\exp(-jk_0(\vec{r}^0\cdot\vec{x}))\,\mathrm{d}S, \\ \vec{\mathcal{H}}^{scat}(\vec{r}^0|\vec{R}^0,\vec{p}) &= -jk_0\int_S (\vec{r}^0\times\vec{K})\exp(-jk_0(\vec{r}^0\cdot\vec{x}))\,\mathrm{d}S, \end{aligned} \tag{1.113}$$

where $\vec{K} = \vec{n}\times\vec{H}^{total}$ and $\vec{H}^{total}$ is the total field excited by plane wave (1.110).

From the reciprocity principle in its usual formulation

$$\vec{q}\cdot\vec{\mathcal{E}}^{scat}(\vec{r}|\vec{a},\vec{p}) = \vec{p}\cdot\vec{\mathcal{E}}^{scat}(\vec{a}|\vec{r},\vec{q}), \tag{1.114}$$

as well as from asymptotic formula (1.112), and the following expressions:

$$\vec{r} = r\cdot\vec{r}^0, \quad \vec{a} = -a\cdot\vec{R}^0$$

follows the reciprocity principle for the complex scattering diagrams:

$$\vec{q} \cdot \vec{\mathcal{E}}^{scat}(\vec{r}^{\,0}|\vec{R}^0, \vec{p}) = \vec{p} \cdot \vec{\mathcal{E}}^{scat}(-\vec{R}^0| - \vec{r}^{\,0}, \vec{q}). \tag{1.115}$$

Equalities (1.114) and (1.115) are strict, which rigorously follows from Maxwell's equations. Let us study the satisfiability of equality (1.115) in case of scattered fields computed in physical optics approximation given Kirchhoff's approximation in formulas (1.113) of equivalent surface current density

$$\vec{K}(\vec{x}) \approx 2\vec{n} \times \vec{H}^0(\vec{x}|\vec{R}^0, \vec{p})$$

over that part of $S'(\vec{R}^0) \subset S$ where $\vec{n} \cdot \vec{R}^0 > 0$ ($\vec{n}$ is the unit vector of inner normal), and $\vec{K}(\vec{x}) \approx 0$ over complementary part $S \backslash S'(\vec{R}^0)$. Under this approximation, we have

$$\begin{aligned}\vec{\mathcal{E}}^{scat}(\vec{r}^{\,0}|\vec{R}^0, \vec{p}) = -2jk_0 \int\limits_{S'(\vec{R}^0)} [(\vec{R}^0 - \vec{r}^{\,0}(\vec{r}^{\,0} \cdot \vec{R}^0))(\vec{n} \cdot \vec{p}) \\ -(\vec{p} - \vec{r}^{\,0}(\vec{r}^{\,0} \cdot \vec{p})(\vec{R}^0 \cdot \vec{n}))]\exp(jk_0(\vec{R}^0 - \vec{r}^{\,0}) \cdot \vec{x})\mathrm{d}S,\end{aligned} \tag{1.116}$$

$$\begin{aligned}\vec{\mathcal{E}}^{scat}(-\vec{R}^0| - \vec{r}^{\,0}, \vec{q}) = -2jk_0 \int\limits_{S'(-\vec{r}^{\,0})} [-(\vec{r}^{\,0} - \vec{R}^0(\vec{R}^0 \cdot \vec{r}^{\,0}))(\vec{n} \cdot \vec{q}) + \\ +(\vec{q} - \vec{R}^0(\vec{R}^0 \cdot \vec{q})(\vec{r}^{\,0} \cdot \vec{n}))]\exp(jk_0(\vec{R}^0 - \vec{r}^{\,0}) \cdot \vec{x})\mathrm{d}S.\end{aligned} \tag{1.117}$$

For the monostatic radar, where $-\vec{r}^{\,0} = \vec{R}^0$, the surfaces $S'(\vec{R}^0)$ and $S'(-\vec{r}^{\,0})$ coincide, and $\vec{R}^0 - \vec{r}^{\,0}(\vec{r}^{\,0} \cdot \vec{R}^0) = \vec{r}^{\,0} - \vec{R}^0(\vec{R}^0 \cdot \vec{r}^{\,0}) = 0$, so that

$$\vec{\mathcal{E}}^{scat}(\vec{r}^{\,0}|\vec{R}^0, \vec{p}) = 2jk_0(\vec{p} - \vec{r}^{\,0}(\vec{r}^{\,0} \cdot \vec{p})) \cdot I, \tag{1.118}$$

$$\vec{\mathcal{E}}^{scat}(-\vec{R}^0| - \vec{r}^{\,0}, \vec{q}) = 2jk_0(\vec{q} - \vec{r}^{\,0}(\vec{r}^{\,0} \cdot \vec{q})) \cdot I, \tag{1.119}$$

where

$$I = \int\limits_{S'(\vec{R}^0)} (\vec{R}^0 \cdot \vec{n})\exp(2jk_0(\vec{R}^0 \cdot \vec{x}))\mathrm{d}S. \tag{1.120}$$

From Equations 1.118 and 1.119 follow the equalities (for the case $-\vec{r}^{\,0} = \vec{R}^0$

$$\vec{q} \cdot \vec{\mathcal{E}}^{scat}(\vec{r}^{\,0}|\vec{R}^0, \vec{p}) = \vec{p} \cdot \vec{\mathcal{E}}^{scat}(-\vec{R}^0| - \vec{r}^{\,0}, \vec{q}) = 2jk_0[(\vec{p} \cdot \vec{q}) - (\vec{r}^{\,0} \cdot \vec{q})(\vec{r}^{\,0} \cdot \vec{p})] \cdot I.$$

So, in the monostatic radar case, equality (1.115) holds true also for the scattered fields computed in physical optics approximation.

Yet in case of bistatic radar ($-\vec{r}^{\,0} \neq \vec{R}^0$), integration in Equations 1.116 and 1.117 is done over different noncoinciding varieties (the scalar products of integrands with $\vec{q}$ and $\vec{p}$ respectively do not coincide in this case either).

So, the reciprocity principle in bistatic radar case (given physical optics approximation) does not hold in general.

This conclusion is of even more practical value since bistatic radar is an important part of modern radar; and physical optics approximation together with reciprocity principle is the common approach used in electrodynamics, sometimes without thorough grounding.

1.6 RCS OF THREE-DIMENSIONAL OBJECTS AND ITS RELATION TO THE RCS OF TWO-DIMENSIONAL OBJECTS

Let the finite size object bounded by surface S be illuminated with plane wave (from radar)

$$\vec{E}^0(\vec{x}) = \vec{p}\exp(-jk_0(\vec{R}^0 \cdot \vec{x})),$$
$$\vec{H}^0(\vec{x}) = (\vec{p} \times \vec{R}^0)\sqrt{\frac{\varepsilon_0}{\mu_0}}\exp(-jk_0(\vec{R}^0 \cdot \vec{x})),$$

where $-\vec{R}^0$ is the unit vector of ray from radar to a target, and $\vec{p} = p \cdot \vec{p}^0$ is the unit vector of polarization, $\vec{p}^0 \perp \vec{R}^0$.

The RCS is determined as [31]

$$\sigma = \lim_{R\to\infty} 4\pi R^2 \frac{\left|\vec{p}^{rec} \cdot \vec{E}^{scat}\right|^2}{\left|\vec{p}^0 \cdot \vec{E}^0\right|^2}, \tag{1.121}$$

where R is the distance from scatterer to the receiving antenna, $\vec{p}^{rec}$ is the unit vector determining polarization of receiving antenna, $\vec{E}^{scat}$ is the field scattered by the object toward the receiving antenna.

So, computation of the scatterer RCS reduces to finding scattered field $\vec{E}^{scat}$ at the reception point.

If $\vec{E}(\vec{x})$, $\vec{H}(\vec{x})$ is the total field, then scattered field $\vec{E}^{scat}(\vec{x}) = \vec{E}(\vec{x}) - \vec{E}^0(\vec{x})$, as it follows from the Lorentz reciprocity theorem, can be expressed as

$$j\omega\vec{q} \cdot \vec{E}^{scat}(\vec{x}_0) = \int_S (\vec{H}^{\perp}(\vec{x}) \cdot \vec{\mathcal{E}}_0^{eT}(\vec{x}|\vec{x}_0, \vec{q}) - \vec{E}^T(\vec{x}) \cdot \vec{\mathcal{H}}_0^{e\perp}(\vec{x}|\vec{x}_0, \vec{q}))\,\mathrm{d}S, \tag{1.122}$$

where $\vec{\mathcal{E}}_0^e(\vec{x}|\vec{x}_0, \vec{q})$, $\vec{\mathcal{H}}_0^e(\vec{x}|\vec{x}_0, \vec{q})$ is the field of point electric dipole with vector-moment $\vec{q}$ placed at point $\vec{x}_0$, the point being situated anywhere outside S and $\vec{q}$ having arbitrary amplitude and direction.

We assume that $\vec{q} = \vec{p}$ and let the radius-vector of observation point be $\vec{x}^0 = R\vec{R}^0$.

We substitute in Equation 1.122 asymptotic expressions, given $R \to \infty$, for vector-functions $\vec{\mathcal{E}}_0^e(\vec{x}|\vec{x}_0, \vec{p})$, $\vec{\mathcal{H}}_0^e(\vec{x}|\vec{x}_0, \vec{p})$

$$\vec{\mathcal{E}}_0^e(\vec{x}|\vec{x}_0, \vec{p}) \sim \Omega(k_0 R)\vec{\mathcal{E}}_0^e(\vec{x}|\vec{R}^0, \vec{p}),$$
$$\vec{\mathcal{H}}_0^e(\vec{x}|\vec{x}_0, \vec{p}) \sim \Omega(k_0 R)\vec{\mathcal{H}}_0^e(\vec{x}|\vec{R}^0, \vec{p}),$$

where

$$\Omega(k_0R) = \frac{\exp(jk_0R)}{4\pi k_0R},$$
$$\vec{\mathcal{E}}_0^{\,e}(\vec{x}|\vec{R}^0,\vec{p}) = k_0^2\omega\sqrt{\frac{\mu_0}{\varepsilon_0}}\,\vec{p}^{\,T}\exp(-jk_0(\vec{R}^0\cdot\vec{x})), \tag{1.123}$$

$$\vec{\mathcal{H}}_0^{\,e}(\vec{x}|\vec{R}^0,\vec{p}) = -k_0^2\,\omega\vec{p}^{\,\perp}\exp(-jk_0(\vec{R}^0\cdot\vec{x})),$$
$$\vec{p}^{\,T} = \vec{p} - \vec{R}^0(\vec{R}^0\cdot\vec{p}), \quad \vec{p}^{\,\perp} = \vec{R}^0\times\vec{p}. \tag{1.124}$$

Formulas (1.123) and (1.124) represent the field of linearly polarized plane wave with wave vector $(-\vec{R}^0)$ that is arriving from infinite distance. These asymptotic representations hold true given $x \in S$ and $R \gg D$, where D is the diameter of the object being illuminated by radar (i.e., its largest linear measure).

Now, scattered field $\vec{E}^{scat}(x)$ in far-field zone has the following form:

$$j\omega\,\vec{p}\cdot\vec{E}^{scat}(R\vec{R}^0) \sim \Omega(k_0R)k_0^2\omega\int_S \exp(-jk_0(\vec{R}^0\cdot\vec{x}))$$
$$\cdot[\vec{p}\cdot\vec{H}^{\perp}(\vec{x})\sqrt{\frac{\mu_0}{\varepsilon_0}} - (\vec{R}^0\times\vec{p})\cdot\vec{E}^{\perp}(\vec{x})]\mathrm{d}S, \tag{1.125}$$

where $\vec{H}^{\perp} = \vec{n}\times\vec{H}$, $\vec{E}^{\perp} = \vec{n}\times\vec{E}$, and $\vec{n}$ is the unit normal vector to S.

Once we assume dealing with perfectly conducting objects, i.e., $\vec{E}^T|_S = 0$ then equality (1.125) reduces to the following:

$$j\omega\vec{p}\cdot\vec{E}^{scat}(R\vec{R}^0) \sim \Omega(k_0R)k_0^2\omega\int_S \exp(-jk_0(\vec{R}^0\cdot\vec{x}))(\vec{p}\cdot\vec{H}^{\perp}(\vec{x}))\sqrt{\frac{\mu_0}{\varepsilon_0}}\,\mathrm{d}\,S. \tag{1.126}$$

Nonetheless, it is worth mentioning that representation similar to expression (1.126) follows from Equation 1.125 also for a wider class of scatterers, boundary conditions for which can be (with satisfactory accuracy) expressed by an impedance type condition:

$$\vec{E}^T = \sqrt{\frac{\mu_0}{\varepsilon_0}}Z\,\vec{H}^{\perp} \quad \text{at } S. \tag{1.127}$$

Indeed, given boundary condition of the kind (1.127) (satisfied, for instance, at the surface of a body with great but finite conductivity, or at the surface of some kinds of RAMs used for camouflage, etc.), representation of vector $\vec{E}^{scat}(R\,\vec{R}^0)$ can be obtained by replacing vector $\vec{p}$ by vector $\vec{p}_Z = \vec{p} + (\vec{R}^0\times\vec{p})Z$ in scalar product $\vec{p}\cdot\vec{H}^{\perp}(\vec{x})$ of formula (1.126).

From formula (1.126) follows rigorous expression for RCS of perfectly conducting object. Since $\left|\vec{p}\cdot\vec{E}^0(\vec{x})\right| = p$, then, given $R/D \gg 1$, the following asymptotic equality takes place:

$$4\pi R^2\frac{\left|\vec{p}\cdot\vec{E}^{scat}(R\vec{R}^0)\right|^2}{\left|\vec{p}\cdot\vec{E}^0\right|^2} \sim \frac{\pi}{\lambda^2}\left|\int_S \exp(-jk_0(\vec{R}^0\cdot\vec{x}))\frac{1}{p}(\vec{p}\cdot\vec{H}^{\perp}(\vec{x}))\sqrt{\frac{\mu_0}{\varepsilon_0}}\,\mathrm{d}\,S\right|^2,$$

from where we derive the strict expression for RCS:

$$\sigma_S^{III} \sim \frac{\pi}{\lambda^2}\left|\int_S \exp(-jk_0(\vec{R}^0\cdot\vec{x}))\frac{1}{p}(\vec{p}\cdot\vec{H}^{\perp}(\vec{x}))\sqrt{\frac{\mu_0}{\varepsilon_0}}\,\mathrm{d}S\right|^2. \tag{1.128}$$

The use of exact formula (1.128) requires the surface current density $\vec{H}^{\perp}$ over S to be found in advance by means of any rigorous method (eigenfunction method, integral equation, etc.).

In practical RCS computations for the objects of large dimensions, far beyond resonant scattering, it is common to express the surface current density $\vec{H}^{\perp}$ according to physical optics approximation, which leads to replacement of formula (1.128) by the widely known computational expression [7,8]:

$$\sigma_S^{III} \sim \frac{4\pi}{\lambda^2}\left|\int_{S_{illum}} \exp(-2jk_0(\vec{R}^0\cdot\vec{x}))(\vec{n}\cdot\vec{R}^0)\,\mathrm{d}S\right|^2, \tag{1.129}$$

where S_{illum} is the part of the surface S illuminated by incident plane wave.

In the same way, in case of two-dimensional model of cylindrical body with the directrix l that is not restricted along generating lines and that is illuminated by plane wave, front of which being parallel to generatrix, the RCS value per unit length of generatrix is as follows:

$$\sigma_l^{II} = \lim_{R\to\infty} 2\pi R\frac{\left|\vec{p}^0\cdot\vec{E}^{scat}(R\vec{R}^0)\right|^2}{\left|\vec{p}^0\cdot\vec{E}^0\right|^2}. \tag{1.130}$$

This value, as it will be shown duly in rigorous theory, is expressed differently for E- and H-polarizations.

We introduce Cartesian coordinate system $Ox_1x_2x_3$ with axes tied to the cylindrical scatterer in such manner that unit vector $\vec{e}_3$ be parallel to generatrix, and unit vector $\vec{e}_1 = \vec{R}^0$ (which is the unit vector of ray coming from target to radar). We assume for E-polarization that $\vec{p}^0 = \vec{e}_3$, and $\vec{p}^0 = -\vec{e}_2$ for H-polarization. Let us note that given $R \to \infty$ and $\vec{p}^0 \perp \vec{R}^0$,

$$\begin{aligned}\int_{-\infty}^{\infty}\vec{\mathcal{E}}_0^e(\vec{x}|R\vec{R}^0,\vec{p})\,\mathrm{d}x_3 &\sim \vec{p}\int_{-\infty}^{\infty}\frac{k_0^2}{\varepsilon_0}\Omega(k_0R)\,\mathrm{d}x_3\\ &= -\vec{p}\frac{k_0^2}{4j\varepsilon_0}H_0^{(1)}(k_0R)\underset{R\to\infty}{\sim}\vec{p}\Omega^{II}(k_0R)k_0\omega\sqrt{\frac{\mu_0}{\varepsilon_0}}\exp(-jk_0(\vec{R}^0\cdot\vec{x})),\end{aligned} \tag{1.131}$$

where

$$\Omega^{II}(k_0R) = -\frac{1}{4j}\sqrt{\frac{2}{\pi k_0R}}\exp\left(jk_0R - \frac{\pi j}{4}\right).$$

From Equations 1.122 and 1.131, it follows that

$$\vec{p}^0\cdot\vec{E}^{scat}(R\vec{R}^0) \sim \Omega^{II}(k_0R)k_0\int_l(\vec{p}^0\cdot\vec{H}^{\perp})\sqrt{\frac{\mu_0}{\varepsilon_0}}\exp(-jk_0(\vec{R}^0\cdot\vec{x}))\,\mathrm{d}l, \tag{1.132}$$

where, given E-polarization

$$\vec{p}^0 = \vec{e}_3, \quad \vec{E} = \vec{e}_3 u,$$
$$(\vec{p}^0 \cdot \vec{H}^\perp) = -\frac{1}{j\omega\mu_0}\frac{\partial u}{\partial n}, \tag{1.133}$$

and given H-polarization

$$\vec{p}^0 = -\vec{e}_2, \quad \vec{H} = \vec{e}_3 v,$$
$$(\vec{p}^0 \cdot \vec{H}^\perp) = (\vec{n} \cdot \vec{R}^0)v. \tag{1.134}$$

So, according to Equations 1.130 and 1.132

$$\sigma_l^{II} = \frac{\pi}{2\lambda}\left|\int_l (\vec{p}^0 \cdot \vec{H}^\perp)\sqrt{\frac{\mu_0}{\varepsilon_0}}\exp(-jk_0(\vec{R}^0 \cdot \vec{x}))\,\mathrm{d}\,l\right|^2, \tag{1.135}$$

where $(\vec{p}^0 \cdot \vec{H}^\perp)$ are determined by expressions (1.133) or (1.134), depending on polarization (parallel or perpendicular).

In physical optics approximation, at the illuminated surface of object we have

$$\vec{p}^0 \cdot \vec{H}^\perp \approx 2\vec{p}^0 \cdot \vec{H}^{0\perp} = 2(\vec{n} \cdot \vec{R}^0)\sqrt{\frac{\varepsilon_0}{\mu_0}}\exp(-jk_0(\vec{R}^0 \cdot \vec{x})),$$

and formula (1.135) reduces to

$$\sigma_l^{II} \approx \frac{2\pi}{\lambda}\left|\int_{l_{illum}} (\vec{n} \cdot \vec{R}^0)\exp(-2jk_0(\vec{R}^0 \cdot \vec{x}))\,\mathrm{d}\,l\right|^2. \tag{1.136}$$

If the scatterer is the infinitely thin perfectly conducting screen, then one may integrate over S^+ and S^- (over l^+ and l^- respectively) in exact formulas (1.128), (1.135) given fixed direction of the normal. As a result, these formulas will include $\vec{K} = (\vec{H}^\perp)^+ - (\vec{H}^\perp)$ instead of $\vec{H}^\perp$:

$$\sigma_S^{III} \approx \frac{\pi}{\lambda^2}\left|\int_S \exp(-jk_0(\vec{R}^0 \cdot \vec{x}))(\vec{p}^0 \cdot \vec{K})\sqrt{\frac{\mu_0}{\varepsilon_0}}\,\mathrm{d}\,S\right|^2, \tag{1.137}$$

$$\sigma_l^{II} \approx \frac{\pi}{2\lambda}\left|\int_l \exp(-jk_0(\vec{R}^0 \cdot \vec{x}))(\vec{p}^0 \cdot \vec{K})\sqrt{\frac{\mu_0}{\varepsilon_0}}\,\mathrm{d}\,l\right|^2. \tag{1.138}$$

In their turn, formulas (1.129) and (1.136) evidently stay unchanged.

RCS computation of infinite (by generating lines) cylindrical bodies, both approximate and exact, requires much less computation power than that of real three-dimensional objects and, at the

same time, provides qualitatively accurate scattering characteristics of different objects, as well as their RCS dependencies on frequency and other parameters.

At the same time, as it will be shown below, the quantitatively accurate estimates of real object RCS can also be obtained under specific conditions by their two-dimensional values. We demonstrate such possibility, first, by analyzing expressions for RCS of perfectly conducting cylindrical screen S with arbitrary (open) directing line l. Let us assume that l is placed in plane x_1Ox_2, and that at S holds the condition $-d/2 \le x_3 \le d/2$, and the unit vector $\vec{R}^0 = \sum_{i=1}^{3} \vec{e}_i \cos\theta_i$.

Now, we introduce another two unit vectors such that

$$\vec{R}_1^0 = \frac{1}{\sin\theta_3}(\vec{e}_1 \cos\theta_1 + \vec{e}_2 \cos\theta_2), \quad \vec{R}_2^0 = \vec{e}_3 \cos\theta_3 + \vec{e}_2 \sin\theta_3.$$

Then, according to physical optics approximation

$$\begin{aligned}
\sigma_S^{III} &\approx \frac{4\pi}{\lambda^2}\left|\int_S \exp(-2jk_0(\vec{R}^0 \cdot \vec{x}))(\vec{R}^0 \cdot \vec{n})\,\mathrm{d}S\right|^2 \\
&= \frac{4\pi}{\lambda^2}\left|\int_l \exp(-2jk_0 \sin\theta_3(\vec{R}_1^0 \cdot \vec{x}))(\vec{R}_1^0 \cdot \vec{n})\,\mathrm{d}l\right|^2 \cdot \left|\int_{-d/2}^{d/2} \exp(-2jk_0 x_3 \cos\theta_3)\sin\theta_3\,\mathrm{d}x_3\right|^2 \\
&= \frac{1}{\pi\sin\theta_3}\frac{2\pi}{\lambda_1}\left|\int_l \exp(-2jk_1(\vec{R}_1^0 \cdot \vec{x}))(\vec{R}_1^0 \cdot \vec{n})\,\mathrm{d}l\right|^2 \cdot \frac{2\pi}{\lambda}\left|\int_{-d/2}^{d/2} \exp(-2jk_0(\vec{R}_2^0 \cdot \vec{e}_3)\vec{x}_3)(\vec{R}_2^0 \cdot \vec{e}_2)\,\mathrm{d}x_3\right|^2,
\end{aligned}$$

where $k_1 = k_0 \sin\theta_3$, $\lambda_1 = \lambda/\sin\theta_3$ and, therefore,

$$\sigma_S^{III} = \frac{1}{\pi\sin\theta_3}\sigma_1^{II}(\vec{R}_1^0, \lambda_1) \cdot \sigma_2^{II}(\vec{R}_2^0, \lambda). \tag{1.139}$$

Here, $\sigma_1^{II}(\vec{R}_1^0, \lambda_1)$ is the RCS of infinitely long cylindrical surface, its directrix l and generating lines being parallel to Ox_3, that is illuminated by radar at the wavelength $\lambda_1 = \lambda/\sin\theta_3$ in the direction $-\vec{R}_1^0$ (Figure 1.5).

In this case,

$$\cos\varphi = \frac{\cos\theta_1}{\sin\theta_3}, \quad \sin\varphi = \frac{\cos\theta_2}{\sin\theta_3}.$$

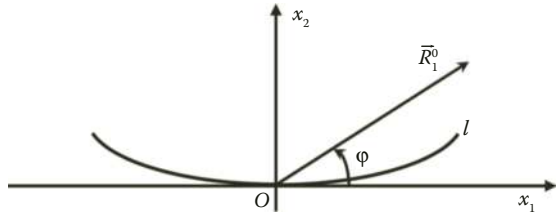

FIGURE 1.5 Illumination geometry of infinite cylindrical surface.

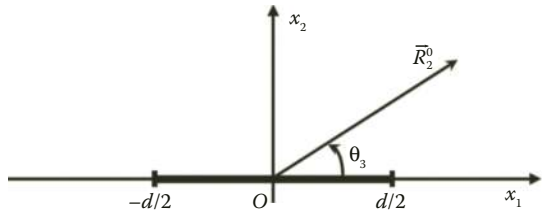

FIGURE 1.6 Illumination geometry of infinite strip.

In its turn, value $\sigma_2^{II}(\vec{R}_2^0, \lambda)$ is the RCS of a strip ($x_2 = 0$, $-d/2 \le x_3 \le d/2$, $-\infty < x_1 < +\infty$) illuminated by radar in direction $-\vec{R}_2^0$ at the wavelength λ (Figure 1.6).

Practically, expression (1.139) is useful given rather large values of angle θ_3. Assume, for instance, that $\pi/6 \le \theta_3 \le \pi/2$, then $(1/\pi \sin \theta_3) \in (1/\pi, 2/\pi)$. When the object S is illuminated by wave, front of which is parallel to the cylinder generatrix, we have $\theta_3 = \pi/2$ and, therefore,

$$\begin{aligned} \lambda_1 &= \lambda, \quad \vec{R}_1^0 = \vec{R}^0, \quad \vec{R}_2^0 = \vec{e}_2, \\ \sigma_S^{III} &= \frac{1}{\pi}\sigma_1^{II}(\vec{R}^0, \lambda) \cdot \sigma_2^{II}(\vec{e}_2, \lambda). \end{aligned} \tag{1.140}$$

It is important to note that an equation similar to Equation 1.129 derived, given physical optics approximation still holds true even if other, more accurate methods than physical optics one, are used to express the surface current density $\vec{K}(\vec{x})$.

We consider here that only parameter $k_0 d$ is large (linear dimensions characterizing l must not be necessarily large), and we assume that, given $-d/2 \le x_3 \le d/2$, the function $\vec{K}(\vec{x})$ at surface S coincides with the surface current density $\vec{K}^{II}(x_1, x_2)$ that is excited at corresponding infinite cylindrical surface. We assume also that $\theta_3 = (\pi/2)$, the unit vector $\vec{R}^0$ being oriented arbitrarily in plane $x_1 O x_2$; and vector $\vec{p}$, in its turn being, oriented arbitrarily in the plane normal to $\vec{R}^0$.

Then, using exact expression (1.137) we get

$$\begin{aligned} \sigma_S^{III} &= \frac{\pi}{\lambda^2}\left|\int_l \exp(-jk_0(\vec{R}^0 \cdot \vec{x}))(\vec{p}^0 \cdot \vec{K}^{II})\sqrt{\frac{\mu_0}{\varepsilon_0}}\,\mathrm{d}\,l \int_{-d/2}^{d/2} \mathrm{d}\,x_3\right|^2 \\ &= \frac{1}{\pi}\frac{\pi}{2\lambda}\left|\int_l \exp(-jk_0(\vec{R}^0 \cdot \vec{x}))(\vec{p}^0 \cdot \vec{K}^{II})\sqrt{\frac{\mu_0}{\varepsilon_0}}\,\mathrm{d}\,l\right|^2 \cdot \frac{2\pi}{\lambda} d^2. \end{aligned}$$

The latter means that according to the approximation considered here

$$\sigma_S^{III} = \frac{1}{\pi}\sigma_1^{II}(\vec{R}^0, \lambda, \vec{p}^0) \cdot \sigma_2^{II}(\vec{e}_2, \lambda), \tag{1.141}$$

but, unlike Equation 1.139, σ_1^{II} here is the exact value of two-dimensional RCS, and σ_2^{II} is the same as in Equation 1.139 approximate RCS value of flat strip given its normal illumination. It is essential to note that in formula (1.141) the value σ_1^{II} and, therefore, the RCS value σ_S^{III} of real object appearing in left-hand part depends on polarization unit vector $\vec{p}^0$, which, as it was shown, can be chosen arbitrarily (provided that condition $\vec{p}^0 \perp \vec{R}^0$ is satisfied).

Therefore, having computed exact RCS value σ_1^{II} of two-dimensional model (having solved for this purpose corresponding integral equation with respect to induced surface current density $\vec{K}^{II}(\vec{x})$), we find then, by formula (1.141), a more accurate and more informative (particularly with respect to the incident wave polarization dependence) expression for the real object RCS.

In the same manner as we have derived expression (1.140), we can receive another expression of the same structure, in the left-hand part of which appears exact value of σ_S^{III} computed by formula (1.137) given true distribution of $\vec{K}(\vec{x})$; and the two-dimensional model RCS σ_1^{II} being computed by exact formula (1.138) yet using approximate expression for the current density $\vec{K}^{II}(x_1, x_2)$ obtained by averaging $\vec{K}(\vec{x})$ over coordinate x_3:

$$\vec{K}^{II}(x_1, x_2) = \frac{1}{d}\int_{-d/2}^{d/2} \vec{K}(\vec{x})dx_3. \tag{1.142}$$

The latter remark has rather theoretical than practical sense: equality (1.141) turns to be exact if the surface current density in two-dimensional model is replaced by its integral average (1.142). Practically, however, the more important approximate equality (1.141) takes precedence in its original formulation described above.

Finally, we note that in all the considerations related to formula (1.141), the line l may not only be single one but it may represent a set of arcs and, in its turn, the surface S may represent a set of cylindrical surfaces with their generating lines parallel to axis Ox_3. For instance, using (1.141), we can compute the RCS of a double reflector antenna given its illumination from the outside: having solved the system of integral equations with respect to currents over the system of reflectors l_1, l_2, and having computed current densities $\vec{K}_1^{II}$, $\vec{K}_2^{II}$ while accounting for all the interactions and resonances inside the system, we get the antenna system RCS σ_S^{III} by formula (1.141).

In case of scatterers, which are the "double curvature surfaces" and which posses such characteristic that none of their principal curvatures is identical to zero (unlike cylindrical surfaces), the resonant effects of RCS dependence on frequency cannot be computed using two-dimensional models.

The difficulties appearing in such computational problems and some approaches to their resolution are considered below using simple example of computing RCS of infinitely thin perfectly conducting paraboloid of revolution in case of its illumination along the axis.

Axial illumination of paraboloid S, defined by equation $2qx_3 = x_1^2 + x_2^2$, where $x_1^2 + x_2^2 \le a^2$ and $k_0 a \gg 1$, leads (in approximation of physical optics) to RCS:

$$\sigma_S^{III} = 2\pi q^2(1 - \cos 2k_0 d), \tag{1.143}$$

where $d = a^2/2q$ is the elevation of edge points of the screen (paraboloid) under consideration over plane $x_1 Ox_2$.

Yet in corresponding two-dimensional problem given illumination along the axis of parabolic cylinder with directrix l, defined by equation $2qx_3 = x_1^2$, we get (under the same physical optics approximation) specific RCS value with respect to the unit length of generatrix

$$\sigma_l^{II} = 4q\left|\int_0^{\sqrt{2kd}} e^{jt^2}\,\mathrm{d}\,t\right|^2 = 4\pi q[C^2(\sqrt{2k_0 d}) + S^2(\sqrt{2k_0 d})], \tag{1.144}$$

where $C(x)$, $S(x)$ are the Fresnel integrals [32].

---

* We omit simple calculations leading to expression (1.143) and expression (1.144) presented below for the two-dimensional RCS model.

As functions of frequency (or wave number $k_0 = \omega\sqrt{\varepsilon_0\mu_0}$), the values (1.143) and (1.144) are of fast oscillating nature, the amplitude of oscillations in two-dimensional case (formula (1.144)) damping as the frequency increases and, given $k_0 d \geq 10$, they settle down at value $\sigma_l^{II} \approx \pi q$.

Yet, in case of three-dimensional object, these RCS oscillations described by equality (1.143) do not dump even in high-frequency zone, small changes in frequency being able to change significantly the value of σ_S^{III}; resonant effects taking place here given $k_0 a \gg 1$ are due to the second parameter, $k_0 d$, and, given $k_0 d \to 0$, they disappear.

However, instead of such unstable characteristic as σ_S^{III}, which is subject to random fluctuations, one can introduce the value averaged over certain frequency interval

$$\bar{\sigma}_S^{III}(k_1,k_2) = 2\pi q^2 \frac{1}{k_2 - k_1}\int_{k_1}^{k_2}\left(1 - \cos(2k_0 d)\right)\mathrm{d}\,k_0 = 2\pi q^2\left(1 - \frac{\sin(2k_2 d) - \sin(2k_1 d)}{2(k_2 - k_1)d}\right),$$

which, given significantly large values of parameter $2(k_2 - k_1)d$, is quite close to the constant:

$$\bar{\sigma}_S^{III}(k_1,k_2) \approx 2\pi q^2. \tag{1.145}$$

In the same manner, we have also the averaged value of

$$\bar{\sigma}_l^{II}(k_1,k_2) \approx \pi q, \tag{1.146}$$

so that the following expression takes place:

$$\bar{\sigma}_S^{III}(k_1,k_2) \approx \frac{2}{\pi}[\bar{\sigma}_l^{II}(k_1,k_2)]^2. \tag{1.147}$$

Equalities (1.139)*, (1.140), (1.141), (1.147) expressing RCS of different objects, which have been obtained using different methods, share the same structure and follow similar quantitative pattern: RCS of three-dimensional object (fixed frequency one if the case is nonresonant, and frequency averaged one if the resonance is present) can be expressed as the product of corresponding† "two-dimensional" RCS (or frequency averaged ones) multiplied by a dimensionless parameter of the order of few tenths, which depends, in general, on the scattering object configuration, illumination direction, and radar signal polarization.

This quantitative pattern can be shown to hold for a large number of RCS examples computed using both physical optics approximation and more accurate approximations of surface currents (particularly, using the edge wave method [7,8]).

For example, in physical optics approximation, the RCS of plane body S (of arbitrary shape) given its illumination along the normal is

$$\sigma_S^{III} = \frac{4\pi}{\lambda^2}\left|\iint_S \mathrm{d}\,S\right|^2 = \frac{4\pi}{\lambda^2}S^2 = \frac{4\pi}{\lambda^2}\gamma^2 d_1^2 d_2^2,$$

* Given large enough values of θ_3; for instance, $\theta_3 \geq \pi/6$.

† We mean here the RCS per unit length of two cylindrical surfaces, the generating lines of which are perpendicular to each other, and their directing lines being determined by geometry of the object of interest.

where d_1, d_2 are the measures of any rectangular enveloping the object S, and parameter γ being the ratio of the S area to $d_1 d_2$, so that $0 < \gamma \leq 1$. However, two-dimensional RCSs of strips ("bands") of the widths d_1 and d_2, which are tangent to S, are

$$\sigma_1^{II} = \frac{2\pi}{\lambda} d_1, \quad \sigma_2^{II} = \frac{2\pi}{\lambda} d_2,$$

and, therefore,

$$\sigma_S^{III} = \frac{\gamma^2}{\pi} \sigma_1^{II} \sigma_2^{II}. \tag{1.148}$$

In special case of circular or elliptical disk, this dimensionless parameter is $\gamma^2/\pi = \pi/16$.

Finally, it must be emphasized that quantitative dependence formulated with respect to three-dimensional RCS, which relates it to that of two-dimensional model, is rigorously proved only for a limited number of scatterers illuminated under exactly specified conditions as to illumination direction and the surface current density approximation method. In other situations that are beyond the rigorous considerations presented here, this quantitative dependence can be considered as a heuristic approach to computation of the RCS rough estimates.

2 Methods for Computing Scattering Characteristics of Complex-Shaped Objects

Vitaly A. Vasilets, Oleg I. Sukharevsky, and Sergey V. Nechitaylo

CONTENTS

Radar information gathering on numerous objects of interest by means of full-scale and physical experiments involves considerable amount of expense in the form of materials, time, and management. Therefore, one can consider mathematical simulation as one of the most affordable ways of getting scattering characteristics data. Classical asymptotic methods of high-frequency diffraction do not allow, unless proper improvements and generalizations are introduced, to compute scattering characteristics given such complicating factors as the object shape, presence of various radar absorbing materials on the object's surface (including fractures), influence of underlying surface, and multistatic radar configuration. Accordingly, the need to obtain scattering characteristics on a variety of real airborne and ground objects requires electromagnetic scattering theory to be elaborated, and generalized methods for computing scattering characteristics to be developed for the complex-shaped objects with nonperfectly reflecting surface.

This chapter presents the method developed by the authors for computing scattering characteristics of airborne objects having complex shape and nonperfectly reflecting surface [33,34]. The method is based on separate evaluation of contributions that smooth surface part and edges (fractures) brought into total scattered field. In this case, total field over smooth parts of the object's surface is computed by Kirchhoff's method or by its generalization onto the case of present radar absorbing materials. The field scattered by edges (fractures) is computed using a solution to the simulative problem of plane monochromatic wave diffraction at perfectly conducting wedge with radar absorbing cylinder placed over its edge in case of oblique wave incidence. The method proposed here allows computing RCS of ideally conducting airborne object completely or partially covered with RAM (Figure 2.1). The object itself may have surface irregularities in the form of fractures that may be covered with RAM too. The object RCS can be computed for both monostatic and bistatic radar configuration.

It should be mentioned that the method presented here allows computing RCS of the objects completely made of dielectrics or composites.

In case of ground objects (Figure 2.2), we propose here the computation method that accounts for the presence of underlying surface with known electromagnetic characteristics [35–39]. Presence of the "air–ground" interface leads to the appearance of two mutually overlapping illuminated regions at the object's surface. The first one is due to direct incident wave from radar; the second one is due to the wave reflected from the ground.

Integral representations obtained here allow us to single out four basic paths of electromagnetic wave propagation through the system under consideration as follows: "transmitter–object–receiver," "transmitter–object–ground–receiver," "transmitter–ground–object–receiver," "transmitter–ground–object–ground–receiver." As applied to ground objects, this method provides computation of scattering characteristics also in case of radar absorbing materials presence at the object's surface.

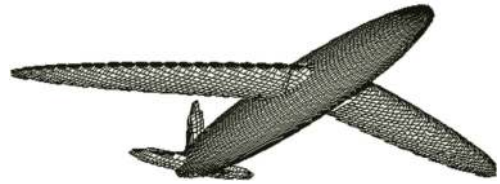

FIGURE 2.1 The airborne object model.

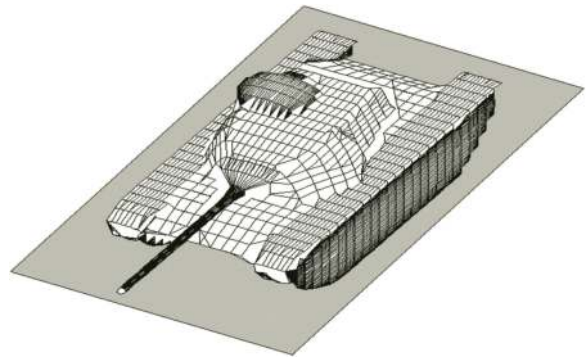

FIGURE 2.2 The ground object model.

In this chapter, we also consider the method for approximating the smoothed impulse response (IR) of the object given definite spectrum range of illumination signal. The method is applicable for computing impulse responses (high-resolution range profiles) for various radar objects.

2.1 SURFACE GEOMETRY MODELING FOR THE COMPLEX-SHAPED OBJECTS

Vitaly A. Vasilets and Oleg I. Sukharevsky

Scattering characteristics computation for a complex-shaped object requires its surface to be mathematically described [40]. Besides, the information on electromagnetic properties of materials, which the objects consist of, must be available too.

As the methods for computing scattering characteristics progressed and computation means steadily improved, various methods were used for the object surface description that involved less manual labor. However, even today, mathematical description of the complex radar object's surface involves a great deal of manual work.

The following methods for such object surface description are still the basic ones [41–45]:

1. *Bodies of revolution method*. It is useful, for instance, for the aircraft or missile body description since its shape can usually be approximated with a body of revolution.
2. *Method of analytical surface description*. It can be applied to the simple shape bodies, surface of which is described, for instance, by the equations of second order (sphere, cylinder, ellipsoid).
3. *The simplest component method*. It is applicable to the electrically large objects, for which holds the inequality $L \gg \lambda$, where L is characteristic object size, and λ is the illumination signal wavelength. The whole object gets split into separate parts, each being described by the mostly fit part of the simple shape object (disk, cylinder, cone, etc.) with the well-known value of RCS. In this manner, the whole surface of the object under consideration can be represented by a set of the simple shape body parts. Disadvantage of the latter approach is its high manual labor input and insufficient surface description accuracy (especially at junctions between the simple shape bodies).

4. *Wire models*. The method is based on representing the object surface by a set of thin wires. It is widely used for computing scattering characteristics of complex objects in resonant and Rayleigh scattering regions.
5. Method of direct surface description by a set of elementary flat regions (triangular or rectangular plates), the so-called facet model. Basic advantages of the method are the following: any limitation on the surface geometry is absent; elaborate evaluation of phase relations in radar scattering characteristics is possible. It is facet method that is now the most popular in the object's surface geometry description. Among the basic drawbacks of the method are the following: surface of the object of interest has to be digitized; algorithms for determining illuminated and shadowed parts of the object are complex and not cost-effective; and very large number of facets is needed to describe the surface. For example, for the model of perfectly conducting ellipsoid with semiaxes of 1, 2, and 3 m, one would need the number of facets ranging from 60,000 through 80,000 to compute the scattered field using Kirchhoff's integral (by preset current density over the surface) within accuracy of 2–4% given the object illumination in centimeter wave band. For the models of real flying vehicles, such number can reach the value of several hundred thousands. Therefore, such computation itself is a high burden.

In this chapter, scattering simulation method is proposed that accounts for the presence of surface fractures. Right from the beginning, the method presumes splitting of all scattering surfaces and elements of the object into several groups: smooth surface part, local scatterers of the edge kind, forward-looking antenna system under the nose radome (if present at the object under consideration). Let us consider the simulation of these scatterer groups one by one.

Smooth part of the surface is approximated by parts of three-axial ellipsoids. The number of ellipsoids used in every specific case is determined individually depending on the surface complexity and the level of its elaboration, which, in its turn, is determined by the radar signal wavelength implied for mathematical simulation of the object's scattering characteristics.

Every ellipsoid is described by the following parameters (Figure 2.3):

1. Ellipsoid's semi axes: a,b,c.
2. Rotation angles of the local coordinate system $O'x'y'z'$ tied to ellipsoid with respect to that tied to the object, $Oxyz$: $\alpha_X,\alpha_Y,\alpha_Z$.
3. Coordinates of the ellipsoid center $O'(x_0, y_0, z_0)$ in the coordinate system $Oxyz$.
4. Electromagnetic properties of the object's surface element described by the depth of RAM δ and its RAM relative permittivity and permeability ε', μ'. If the surface element is considered to be perfectly conducting, then depth of its RAM is assumed to be zero. If the object's surface element is made completely of composite material, then negative value of δ for the ellipsoid is used to indicate this fact.

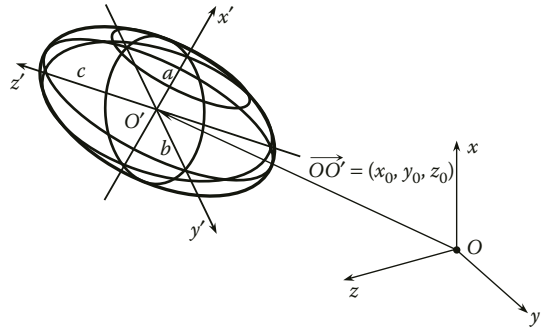

FIGURE 2.3 Geometric parameters of ellipsoid.

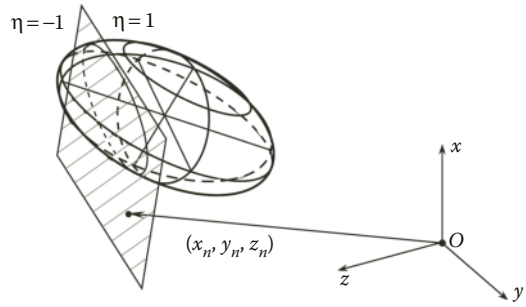

FIGURE 2.4 To determination of the cutting plane.

5. Part of ellipsoid to be used for modeling part of the object's surface is singled out by means of cutting planes. Every such plane is set by the coordinates (x_n, y_n, z_n) of the vector normal to its surface and by parameter η (Figure 2.4). Parameter η determines the choice of the ellipsoid fragment cut out by the plane. Cutting plane divides the space into two half-spaces. If $\eta = 1$, then the half-space containing the coordinate origin is taken, and otherwise if $\eta = -1$. Proper part of ellipsoid is taken together with the proper half-space. Intersection of half-spaces obtained in this manner with ellipsoid determines the ellipsoid's part that is to be used for modeling fragment of the object's smooth surface. The number of cutting planes for every ellipsoid is not limited.

The use of three-axial ellipsoid as the surface approximating element allows modeling a wide range of the object surfaces with considerable accuracy.

Local edge parts of the object's surface are modeled by means of mathematical description of the fracture line. We assume the fracture line to be a fragment of plane curve. In this case, curved fracture edge is approximated with a part of ellipse, and the straight fracture edge is approximated with a line segment.

Every straight fracture edge of the surface is described by the following parameters (Figure 2.5):

1. Coordinates (x_1, y_1, z_1) of the fracture edge beginning in the coordinate system *Oxyz* tied to the object.
2. Coordinates (x_2, y_2, z_2) of the fracture edge end.
3. Coordinates of vector $\vec{g}$, which is the unit-vector orthogonal to one of the fracture faces.
4. Angle ϕπ, which is external angle of the wedge introduced in such way that it is to be tangent to the fracture.

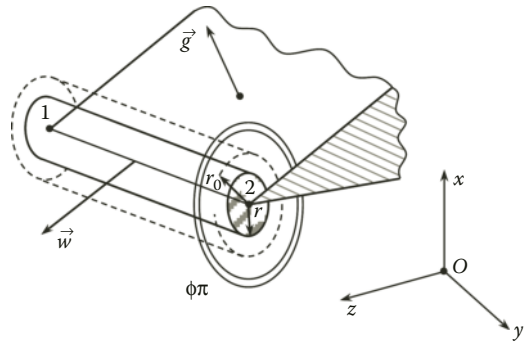

FIGURE 2.5 Straight fracture edge modeling.

5. Unit-vector $\vec{w}$ that is orthogonal to both vector $\vec{g}$ and the fracture edge, the vector $\vec{w}$ being directed toward the free space and away from the fracture.
6. Parameters of the edge RAM toroidal coating, which include its radius r along with its relative permittivity and permeability ε', μ'.
7. Radius of the integrating surface r_0 enclosing the fracture edge. The value of r_0 is determined in such a manner that condition $r \le r_0 < \lambda$ would be satisfied (λ is the wavelength of incident monochromatic wave).

Every curved fracture edge of the surface is described by the following parameters (Figure 2.6):

1. Coordinates (x_0, y_0, z_0) of the center of ellipse approximating the fracture edge in coordinate system $Oxyz$ tied to the object.
2. Coordinates of unit-vector $\vec{g}$ orthogonal to the edge plane.
3. Semiaxes a, b of ellipse approximating the fracture.
4. Unit-vector $\vec{w}$ being orthogonal to the fracture edge line and parallel to one of the ellipse's semiaxes (Figure 2.6).
5. Angle θ between the edge (ellipse) plane and inner face of fracture, the angle lying in the plane containing vectors $\vec{g}$ and $\vec{w}$.
6. Angle $\phi\pi$, which is the external angle of wedge introduced so as to be tangent to the edge.
7. Radius r of toroidal RAM coating, its relative permittivity and permeability ε', μ', as well as the radius r_0 of integrating surface enclosing the fracture edge that is determined in the same way as for the straight fracture edge (Figure 2.5).
8. Part of the ellipse used for modeling the curved surface fracture is singled out by means of cutting planes in the same way as for the smooth parts of object's surface (Figure 2.4). The number of cutting planes is limited, however usually it takes one or two planes to cut the proper ellipse part out.

It is worth noting that the most important parameters of the edge fragments are their angle measures and vector $\vec{g}$ that determine the fracture edge orientation with respect to incident wave direction. Character of the field scattered by fractures has been thoroughly studied in Ref. [7]. In Refs. [29,46], there are also dependencies of scattered field intensity versus the fracture aspect for different values of external wedge angle, as well as different values of radius, permittivity, and permeability of its toroidal RAM coating.

Forward-looking antenna system under the dielectric radome (nose fairing) is described by the following parameters (Figure 2.7):

1. Coordinates of the radome cone base center (x_0, y_0, z_0) in the coordinate system $Oxyz$ tied to the object.

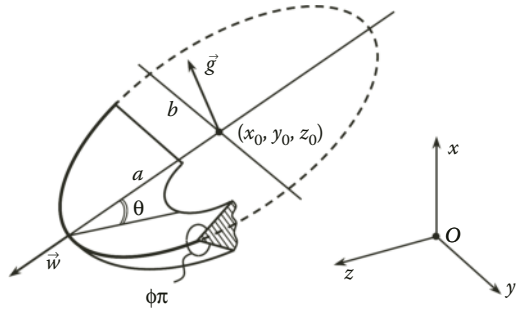

FIGURE 2.6 Curved fracture edge modeling.

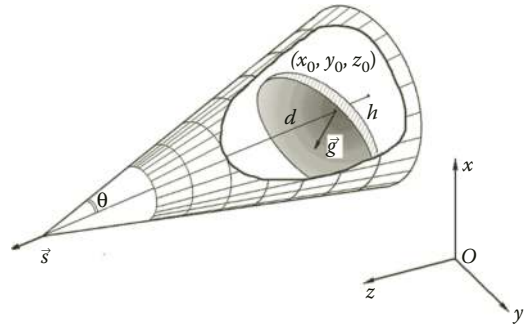

FIGURE 2.7 Model of antenna system under the dielectric cone radome.

2. Vector $\vec{s}$ that determines inclination of the radome axis in the coordinate system $Oxyz$ tied to the object.
3. Radome cone half-angle θ.
4. Radome cone height h and the distance d from the cone's tip to the top of antenna reflector.
5. Radome wall thickness δ along with relative permittivity of its material ε′.
6. Antenna reflector aperture radius r along with its focal parameter p, the antenna being shaped as finite (along the axis) paraboloid of revolution.
7. Unit-vector $\vec{g}$ directed along the antenna axis and determining its orientation.

Modeling of scattering elements of the complex object's surface described above is done manually so far, since automation of this procedure is hindered by scatterer variety and surface complexity.

When actual computation of scattering characteristics is carried out, the smooth fractions of the complex-shaped object surface are split into triangular facets in order to implement the computation method proposed in this chapter. The "lighted" part of the object's surface is found using modified method based on ray tracing [47]. In this case, every jth facet is checked for its being "lighted" in two steps:

1. The jth facet is checked for its belonging to that part of lth ellipsoid used for the complex object surface approximation, in other words it is checked for its belonging to the "working" part of ellipsoid. At the same time, the jth facet is checked for its being on the "lighted" part of lth ellipsoid given that other ellipsoids are absent.
2. The jth facet is checked for its shadowing by other parts of the whole object. We draw the straight line M through the center of jth facet in the direction of unit-vector $\vec{R}^0$, this line connecting the facet with the source of electromagnetic illumination (reception). Every ellipsoid used for approximating the object's surface is checked for whether this line crosses it or not (Figure 2.8). Unlike the ray tracing method [47], the visibility check for jth facet is carried out not with regard to every other facet of kth "obscuring" ellipsoid but with regard to the whole kth ellipsoid. To achieve this we transform linearly the coordinate system in such a manner that corresponding kth ellipsoid becomes the sphere of unity radius with center at the coordinate system origin. Now, if the distance from the line M in the new coordinate space to the origin is less than unity then we conclude that kth ellipsoid can obscure (shadow) the jth facet. In this case, we compute the coordinates of crossing point between line M and kth ellipsoid. Further on, the coordinates of crossing points are checked for their getting into the "working" part of kth ellipsoid. If they do get into the "working" part of the ellipsoid being checked, then we conclude that jth facet is obstructed and we remove it from computation of scattered field. The procedure

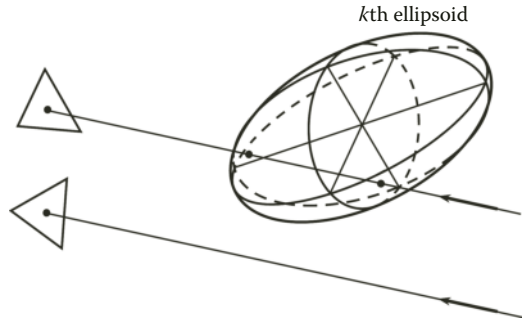

FIGURE 2.8 Visibility check for the facets.

described above is carried out with regard to every ellipsoid we used for approximating the object's surface. Such approach provides much less computation burden while finding the "illuminated" part of the object's surface compared to classical ray tracing method.

In a similar manner, every edge local scatterer is checked for its "visibility" from the electromagnetic illumination point. In this case, we also consider smooth parts of the object's surface as those obscuring the edge scatterers.

When designing mathematical model of scattering from edges, one should consider the implied wavelength band of illumination signal. The latter can be explained by a simple example. The contribution from local edge scatterer of 0.01–0.03 m size given the 3 cm illumination signal wavelength into the field scattered by the whole object would be quite small (for the T-90 tank, it would account for less than 0.1% of the total field). However, it is these edge elements of size comparable to the signal wavelength in millimeter and centimeter wave band that dominate in the design of modern ground objects (brackets, bolts, technological hatches, etc.). Accounting for such elements in the object's surface model significantly increases computational burden but with no significant improvement in the scattered field computation accuracy. So, the small surface fractures and small elements at the external object's surface were not taken into account in the current computer model. If, on the contrary, one needs the maximum possible accuracy of scattering characteristics computation, then all the surface elements with scattering contributions comparable to the needed accuracy level must be accounted for.

Inaccuracy of the object's surface description may lead to errors in the resulted scattered field computation. These errors can manifest themselves as shifted and altered peaks of the scattering intensity diagram. Therefore, surface description of radar objects must be done with all possible thoroughness.

In order to check the feasibility of the surface description method for the complex-shaped objects, we provided scattering simulation for some types of military vehicles. Figure 2.9 shows surface description of the MiG-29 aircraft, consisting of 29 surface fragments of three-axial ellipsoids, 42 wedge fragments, and antenna system under the nose dielectric radome. Figure 2.10 shows the surface description of the T-90 tank consisting of 89 surface fragments of three-axial ellipsoids and 34 wedge fragments.

The method described in this chapter allows representing in mathematical form the surfaces of different radar objects. Accuracy of surface description can be improved by means of increasing the number of ellipsoids and wedges used for mathematical representation of the surface. The method introduced here blends in advantages of the simplest component method while finding illuminated part of the surface and of the facet method while describing the surface mathematically and computing the scattering characteristics.

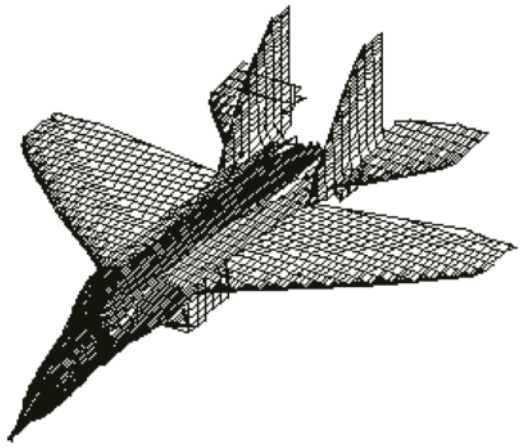

FIGURE 2.9 Surface description example of MiG-29 aircraft.

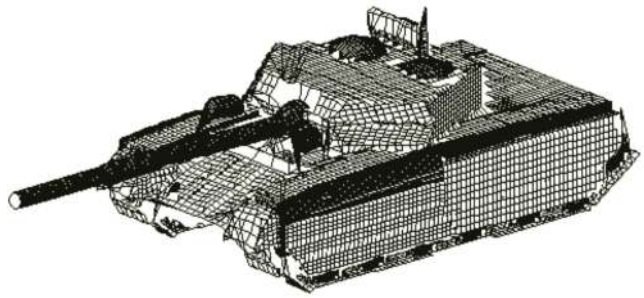

FIGURE 2.10 Surface description example of T-90 tank.

2.2 METHOD FOR COMPUTING SCATTERING CHARACTERISTICS OF AERIAL OBJECTS WITH IMPERFECTLY REFLECTING SURFACE

Vitaly A. Vasilets and Oleg I. Sukharevsky

Computation method introduced here allows computing the scattering characteristics of standalone objects with imperfectly reflecting surface. Object's surface can be smooth or it can have surface fractures in the form of sharp edges covered with RAM. Particularly, the surface of such kind (combination of smooth surfaces intermeshed with RAM-coated edges) pertains to the objects made by "Stealth" technology [48]. Therefore, aerial objects with imperfectly reflecting surface scatter electromagnetic waves by their smooth parts and edge fractures (Figure 2.11).

It is well known [11] that having computed tangential components of total electromagnetic field at any closed surface encompassing the scatterer, one can, using integration, obtain the value of the field scattered by the object at any point outside this closed surface. The method for computing scattering characteristic of the objects with surface fractures is based on splitting a surface encompassing the whole object into some neighborhoods of fractures (lateral dimensions of which correspond to resonant scattering region) and into the smooth parts of the object surface (outside of these neighborhoods). Field scattered by the object is computed by Kirchhoff's kind integral equations. In this case, the surface of integration in those equations that encompasses the whole scatterer is chosen to be coinciding with the object's surface anywhere except some neighborhood of fractures.

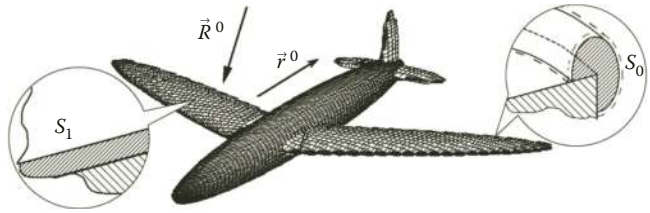

FIGURE 2.11 Example of the standalone object's surface description.

Let us consider plane monochromatic electromagnetic wave of unit amplitude with the polarization unit-vector $\vec{p}^0$ that propagates in the direction of unit-vector $\vec{R}^0$.

$$\begin{aligned}\vec{E}^0(\vec{x}) &= \vec{p}^0 \exp(\, jk_0(\vec{R}^0 \cdot \vec{x})),\\ \vec{H}^0(\vec{x}) &= \sqrt{\frac{\varepsilon_0}{\mu_0}}(\vec{R}^0 \times \vec{p}^0)\ \exp(jk_0(\vec{R}^0 \cdot \vec{x})).\end{aligned} \tag{2.1}$$

This wave is being incident on the surface of the object in free space (Figure 2.11). Here, k_0 is the wave number for free space ($k_0 = 2\pi/\lambda$, λ is the wavelength of incident monochromatic wave), ε_0, μ_0 are the permittivity and permeability of vacuum, $\vec{x}$ is the radius vector of a point in space. The field scattered by the object in the direction $\vec{r}^0$ in far-field zone (projection onto direction $\vec{P}$) can be represented by means of Lorentz reciprocity theorem in the following form [29]:

$$\vec{p} \cdot \vec{E}_S = -jk_0 \frac{\exp(jk_0 R)}{4\pi R} \int_S \left(\sqrt{\frac{\mu_0}{\varepsilon_0}} (\vec{p} \cdot \vec{H}^\perp) + (\vec{p} \times \vec{r}^0) \cdot \vec{E}^\perp \right) \exp(-jk_0(\vec{r}^0 \cdot \vec{x}))\, \mathrm{d}S, \tag{2.2}$$

where R is the distance from the object to an observation point; $\vec{E}^\perp = \vec{n} \times \vec{E}$; $\vec{H}^\perp = \vec{n} \times \vec{H}$; $(\vec{E}, \vec{H})$ is the total field; and $\vec{n}$ is the unit-vector of the external normal to the integration surface S that encompasses the object under consideration. Let us choose S in such a manner that it coincides with the object surface everywhere but in the fracture neighborhoods, where it passes over toroidal surface of circular cross section "pulled over" the fracture (Figure 2.11). Toroidal surface then envelopes both the edge and the RAM covering it. Radius of torus tube is set in such a way that the field at the points, where toroid meets the wedge faces, to contain practically no contributions from the edge, so it could be computed using physical optics approximation as if we were dealing with smooth surface. In this case, surface S can be represented as a sum $S = S_1 + S_0$, where S_1 coincides with smooth (nonperfectly reflecting, in general) parts of the surface, and S_0 is a set of toroidal neighborhoods of the edges. Finally, the integral in Equation 2.2 is a sum of integrals over surfaces S_1 and S_0.

2.2.1 Radar Scattering at Smooth Parts of the Object's Surface

The field scattered from smooth surface can be computed by means of integration given that the tangential components of total field $(\vec{E}^T, \vec{H}^T)$ are known over the object's surface [11]. Taking into account that characteristic size of the smooth surface parts in radar case is large compared to the wavelength (high-frequency scattering), it is only logical to compute the values of $\vec{E}^T$, $\vec{H}^T$, approximately. For instance, for smoothly curved parts of perfectly conducting surface coated with a layer of RAM, the vectors $\vec{E}^T$, $\vec{H}^T$ are assumed to be equal to those at the surface of plain layer of the same RAM on top of perfectly conducting plate substituted for the curved surface part at any

definite point. Field scattered from the smooth part S_1 of the object's surface in the direction $\vec{r}^0$ can be represented using part of expression (2.2)

$$\vec{p}\cdot\vec{E}_{S_1} = -jk_0\frac{\exp(jk_0R)}{4\pi R}\int\limits_{S_1}\left(\sqrt{\frac{\mu_0}{\varepsilon_0}}(\vec{p}\cdot\vec{H}^{\perp}) + (\vec{p}\times\vec{r}^0)\cdot\vec{E}^{\perp}\right)\exp(-jk_0(\vec{r}^0\cdot\vec{x}))\mathrm{d}S. \tag{2.3}$$

In common radar cases, smooth parts of the object's surface are electrically large and has small curvatures. In physical optics approximation [29], tangential field components $\vec{E}^{\perp}(\vec{x})$, $\vec{H}^{\perp}(\vec{x})$ in Equation 2.3 shifted by 90° with respect to each other in the plane tangent to the surface can be replaced by corresponding values $\tilde{\vec{E}}^{\perp}(\vec{x})$, $\tilde{\vec{H}}^{\perp}(\vec{x})$ at the plane tangent to surface S_1 at point $\vec{x}$. If the surface part of interest consists of RAM coating on top of perfectly conducting base, then this tangent plane consists of uniform layer of RAM over perfectly conducting plate too. If a part of the object is made of composite material completely, then, at points $\vec{x}$ of the surface enveloping these parts of the object, the tangent plane is replaced by a half-space with electrodynamic properties corresponding to the composite. The latter is justified by the fact that electromagnetic wave entering deep enough region filled with composite material fades away almost completely. For example, the leading edge of the B-2 bomber aircraft consists of multiple layer RAM of more than 200 mm thickness covering the metallic honeycomb structure, the cells of which being filled with radar absorbing material of density smoothly increasing from the cell's front to its bottom [49]. This results in significant wave absorption starting from the front RAM layer and cells' filling and ending at final wave absorption due to multiple reflections from the cell walls. The aircraft wings are made of composites. Therefore, in order to compute the field scattered from the smooth part of the object's surface in physical optics approximation, we need to solve two typical (simulative) problems. They are as follows: (1) problem of the plane monochromatic wave (2.1) scattering at perfectly conducting plane covered with uniform layer of radar absorbing material (Figure 2.12a); and (2) problem of the same wave scattering at half-space made of composite material (Figure 2.12b).

Standard approach to solving such problems [50] is reduced to finding scattered field for two mutually orthogonal polarizations of incident wave related to vector $\vec{R}^0$ and the unit-vector of axis Ox_2. This makes it more difficult to receive solutions that would be uniformly applicable for arbitrary angles of incidence and polarizations of illuminating wave. For instance, for the wave incidence close to normal, the field decomposition in two orthogonal components leads to ambiguities. But, it is this close-to-normal wave incidence onto the object surface that causes the strongest contributions into total field scattered by the object. In this regard, we need to have a solution that could be used given a wide range of angles of incidence (the uniformly applicable solution), including those approaching normal incidence.

We now consider the solution to the problem of plane monochromatic wave scattering at plain uniform absorbing layer backed by perfectly conducting plate (Figure 2.12a). The problem solution will be sought in the following form [33]:

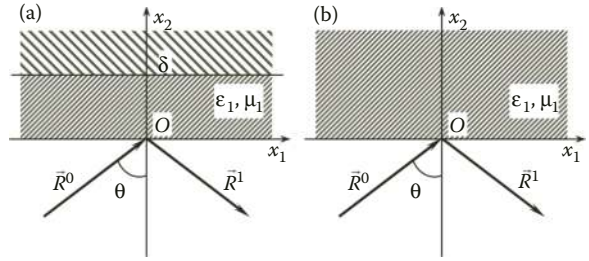

FIGURE 2.12 Wave scattering at nonperfectly reflecting surface.

$$\begin{pmatrix} \tilde{\vec{E}}(\vec{x}) \\ \tilde{\vec{H}}(\vec{x}) \end{pmatrix} = \begin{cases} \begin{pmatrix} \vec{p}^0 \\ (\vec{R}^0 \times \vec{p}^0)\sqrt{\dfrac{\varepsilon_0}{\mu_0}} \end{pmatrix} \exp(jk_0(\vec{R}^0 \cdot \vec{x})) + \begin{pmatrix} \vec{p}^1 \\ (\vec{R}^1 \times \vec{p}^1)\sqrt{\dfrac{\varepsilon_0}{\mu_0}} \end{pmatrix} \exp(jk_0(\vec{R}^1 \cdot \vec{x})), & x_2 < 0, \\ \begin{pmatrix} \vec{\mathcal{E}}(x_2) \\ \vec{\mathcal{H}}(x_2) \end{pmatrix} \exp(jk_0(\vec{R}^{0T} \cdot \vec{x})), & 0 < x_2 < \delta, \end{cases} \tag{2.4}$$

where $\vec{R}^1 = \vec{R}^0 - 2\vec{n}(\vec{R}^0 \cdot \vec{n})$, $\vec{R}^{0T} = \vec{R}^0 - \vec{n}(\vec{R}^0 \cdot \vec{n})$.

It is essential for the solution of this problem to find only scattered back field, therefore solution reduces to finding complex vector $\vec{p}^1$.

Having substituted the expression for the total field inside the layer into the Helmholtz wave equation, we obtain standard differential equations for tangential components of vectors $\vec{\mathcal{E}}(x_2)$ and $\vec{\mathcal{H}}(x_2)$:

$$\left.\begin{aligned} \frac{d^2\vec{\mathcal{E}}^T}{dx_2^2} + k_1^2 \cos^2\theta_1 \ \vec{\mathcal{E}}^T &= 0, \\ \frac{d^2\vec{\mathcal{H}}^T}{dx_2^2} + k_1^2 \cos^2\theta_1 \ \vec{\mathcal{H}}^T &= 0. \end{aligned}\right\} \tag{2.5}$$

Here, $\cos^2\theta_1 = (1 - (\sin^2\theta/\varepsilon'_1\mu'_1))$; $k_1 = k_0\sqrt{\varepsilon'_1\mu'_1}$; ε'_1 , μ'_1 are the relative permittivity and permeability of absorbing material; θ is the angle of wave incidence upon the layer.

Let us write down the boundary conditions for tangential components of field vectors $(\vec{\mathcal{E}}(x_2), \vec{\mathcal{H}}(x_2))$ at perfectly conducting surface $(x_2 = \delta)$:

$$\vec{\mathcal{E}}^T(\delta) = 0, \quad \frac{d\vec{\mathcal{H}}^T(\delta)}{dx_2} = 0. \tag{2.6}$$

Using boundary conditions (2.6), from expression (2.5), we can obtain the following:

$$\left.\begin{aligned} \vec{\mathcal{E}}^T(x_2) &= \vec{U}^T \sin(k_1 \cos\theta_1 \ (\delta - x_2)), \\ \vec{\mathcal{H}}^T(x_2) &= \vec{V}^T \cos(k_1 \cos\theta_1 \ (\delta - x_2)), \end{aligned}\right\} \tag{2.7}$$

where vectors $\vec{U}^T$, $\vec{V}^T$ are to be found. It follows from Maxwell's equations that vectors $\vec{U}^T$ and $\vec{V}^\perp$ are linearly related:

$$\sqrt{\frac{\mu_1}{\varepsilon_1}} \ j\cos\theta_1 \vec{V}^\perp = \vec{U}^T - \frac{\vec{R}^{0\perp}(\vec{R}^{0\perp} \cdot \vec{U}^T)}{\varepsilon'_1 \ \mu'_1}, \tag{2.8}$$

where $\vec{R}^{0\perp} = (\vec{n} \times \vec{R}^0)$, $\vec{V}^\perp = (\vec{n} \times \vec{V}^T)$.

Let us write down the boundary conditions for the surface of absorbing layer $(x_2 = 0)$:

$$\left.\begin{aligned} \vec{p}^{0T} + \vec{p}^{1T} &= \vec{U}^T \sin(k_1 \cos\theta_1 \delta), \\ \sqrt{\frac{\varepsilon_0}{\mu_0}}\vec{n} \times [(\vec{R}^0 \times \vec{p}^0) + (\vec{R}^1 \times \vec{p}^1)] &= \vec{V}^\perp \cos(k_1 \cos\theta_1 \delta). \end{aligned}\right\} \tag{2.9}$$

Then, from Equation 2.8 and boundary conditions (2.9), we receive the equation with respect to $\vec{p}^{1T}$

$$jc\left[(\vec{p}^{1T}-\vec{p}^{0T})\cos\theta+\frac{1}{\cos\theta}\vec{R}^{0T}\cdot((\vec{p}^{1T}-\vec{p}^{0T})\cdot\vec{R}^{0T})\right]$$
$$=(\vec{p}^{1T}+\vec{p}^{0T})-\frac{1}{\varepsilon_1'\mu_1'}\vec{R}^{0\perp}\cdot((\vec{p}^{1T}+\vec{p}^{0T})\cdot\vec{R}^{0\perp}), \tag{2.10}$$

where $c=\sqrt{\frac{\mu_1'}{\varepsilon_1'}}\cos\theta_1\ tg(k_1\ \delta\cos\theta_1)$.

Having solved Equation 2.10, we finally obtain

$$\vec{p}^{1T}=\frac{jc\cos\theta+1}{jc\cos\theta-1}\vec{p}^{0T}-\frac{2jc}{jc\cos\theta-1}\left[\vec{R}^{0T}\frac{(\vec{R}^{0T}\cdot\vec{p}^{0})}{jc-\cos\theta}+\vec{R}^{0\perp}\frac{(\vec{R}^{0\perp}\cdot\vec{p}^{0})}{\varepsilon_1'\mu_1'\left(jc-\frac{\cos^2\theta_1}{\cos\theta}\right)}\right]. \tag{2.11}$$

Accounting for relationship between tangential and normal components of the vector $\vec{p}$, we get the following:

$$\vec{p}^{1}=\vec{p}^{1T}-\vec{n}\frac{(\vec{p}^{1T}\cdot\vec{R}^{0})}{\cos\theta}. \tag{2.12}$$

Let us note that a similar procedure can be followed when solving the simulative problem of the plane monochromatic wave scattering at a half-space made of composites (Figure 2.12b). In this case, we should assume the absorbing layer thickness to be tending to infinity, or $\delta\to\infty$. Such assumption leaves all the expressions unchanged except for expression (2.11) for $\vec{p}^{1T}$, which would take the following form:

$$\vec{p}^{1T}=\frac{c\cos\theta-1}{c\cos\theta+1}\vec{p}^{0T}+\frac{2c}{c\cos\theta+1}\left[\vec{R}^{0T}\frac{(\vec{R}^{0T}\cdot\vec{p}^{0})}{c+\cos\theta}+\vec{R}^{0\perp}\frac{(\vec{R}^{0\perp}\cdot\vec{p}^{0})}{\varepsilon_1'\mu_1'\left(c+\frac{\cos^2\theta_1}{\cos\theta}\right)}\right], \tag{2.13}$$

where $c=\sqrt{\frac{\mu_1'}{\varepsilon_1'}}\cos\theta_1$.

Expressions (2.11) through (2.13) are now applicable to computing scattered field according to Equation 2.4 given any polarization of incident wave and any incidence direction (except those approaching tangent ones). Particularly, for angles θ close to zero, expression (2.10) for the complex (in general) reflection coefficient $\vec{p}^{1}$ does not contain any ambiguity and, given $\theta=0$, expressions (2.11) through (2.13) become the well-known ones [50] for the normal incidence. Finding the vectors $\vec{E}$ and $\vec{H}$ is not a prerequisite to finding the field at the radar absorbing layer surface ($x_2=0$), therefore we will not consider computing $\vec{E}$ and $\vec{H}$ below.

According to physical optics approximation, the field over "unlit" part of the object's surface is identical to zero. Therefore, having replaced the whole surface S_1 by its illuminated part S_1' and

having substituted the expressions for $\tilde{\tilde{E}}(\vec{x}), \tilde{\tilde{H}}(\vec{x})$ derived above into Equation 2.3, we arrive at the following approximate expression for the scattered field:

$$\vec{p} \cdot \vec{E}(R\,\vec{r}^{\,0}) \approx -jk_0 \frac{\exp(jk_0 R)}{4\pi R} \int_{S_1'} f(\vec{x}) \exp(ik_0 \Omega(\vec{x}))\, \mathrm{d}S, \tag{2.14}$$

where $f(\vec{x}) = \vec{h}(\vec{x}) \cdot \vec{p} + \vec{e}(\vec{x}) \cdot (\vec{p} \times \vec{r}^{\,0})$, $\Omega(\vec{x}) = (\vec{R}^0 - \vec{r}^{\,0}) \cdot \vec{x}$, $\vec{h}(\vec{x}) = \vec{n} \times [(\vec{R}^0 \times \vec{p}^{\,0}) + (\vec{R}^1 \times \vec{p}^{\,1})]$, $\vec{e}(\vec{x}) = \vec{n} \times (\vec{p}^{\,0} + \vec{p}^{\,1})$.

Computation of the integral entering into Equation 2.14 necessitates application of special cubature formulas since its integrand is a fast oscillating function. In Ref. [51], the cubature formulas were obtained for similar integrals that were based on linear approximations of functions $f(\vec{x})$ and $\Omega(\vec{x})$.

2.2.2 Cubature Formula for Computing Surface Integrals of Fast Oscillating Functions

Let us define a compact set of points $A_i (i = 1,2,\ldots,n)$ at the surface S_1'. The points themselves may be spread irregularly over the set, which is sometimes helpful and sometimes necessary condition for approximation of smooth parts of real objects. The values of functions $f(\vec{x})$ and $\Omega(\vec{x})$ are known in advance for these points. Given all the aforementioned, one can provide "triangulation" or, in other words, cover the region S_1' with a system of triangles $(\Delta_1),\ldots,(\Delta_m)$ that would have vertices at points $\{A_i\}$. Having done this, one can approximately replace the integral M in Equation 2.14 by a sum of integrals over $\{\Delta_i\}$:

$$M = \int_{S_1'} f(\vec{x}) \exp(jk_0 \Omega(\vec{x}))\, \mathrm{d}S \approx \sum_{i=1}^{m} \int_{(\Delta_i)} f(\vec{x}) \exp(jk_0 \Omega(\vec{x}))\, \mathrm{d}S. \tag{2.15}$$

Accuracy of approximation (2.15) is conditioned by two major factors: replacement of S_1' by flat triangles given that the surface itself is not plain, and approximation errors occurring due to replacement of S_1' by a system of triangles $\{\Delta_i\}$ in the vicinity of the S_1' boundary, the latter being caused, for instance, by the object's surface irregularity (Figure 2.13).

Let us consider integral M_Δ over flat triangle Δ with vertices A_0, A_1, A_2, radius-vectors of the latter being $\vec{a}_0, \vec{a}_1, \vec{a}_2$. We describe, at first, an arbitrary point position $\vec{x} \in \Delta$ by means of its "barycentric" coordinates:

$$\vec{x} = W_0 \vec{a}_0 + W_1 \vec{a}_1 + W_2 \vec{a}_2, \tag{2.16}$$

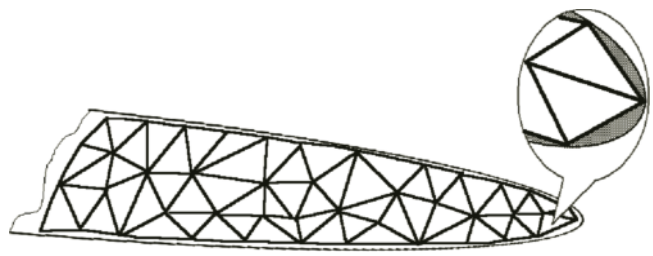

FIGURE 2.13 To the accuracy of smooth surface approximation by a set of triangles.

where W_0, W_1, W_2 are nonnegative parameters such that $W_0 + W_1 + W_2 = 1$. Expression (2.16) can be rewritten in the following form:

$$\vec{x} = W_1(\vec{a}_1 - \vec{a}_0) + W_2(\vec{a}_2 - \vec{a}_0) + \vec{a}_0. \tag{2.17}$$

In the integral under consideration

$$M_\Delta = \int\limits_{(\Delta)} f(\vec{x})\exp(jk_0\Omega(\vec{x}))\,\mathrm{d}S, \tag{2.18}$$

we can use expression (2.17) in order to transform it into barycentric coordinates W_1, W_2:

$$M_\Delta = \left|\frac{\partial \vec{x}}{\partial W_1} \times \frac{\partial \vec{x}}{\partial W_2}\right| \iint\limits_{\Sigma} f[W_1, W_2]\exp(jk_0\Omega[W_1, W_2])\,\mathrm{d}W_1\,\mathrm{d}W_2, \tag{2.19}$$

where

$$f[W_1, W_2] = f(W_1(\vec{a}_1 - \vec{a}_0) + W_2(\vec{a}_2 - \vec{a}_0) + \vec{a}_0), \tag{2.20}$$

$$\Omega[W_1, W_2] = \Omega(W_1(\vec{a}_1 - \vec{a}_0) + W_2(\vec{a}_2 - \vec{a}_0) + \vec{a}_0), \tag{2.21}$$

Σ is the unit triangle shown in Figure 2.14.

Multiplier of the integral in Equation 2.19 equals to the double area of triangle Δ

$$\left|\frac{\partial \vec{x}}{\partial W_1} \times \frac{\partial \vec{x}}{\partial W_2}\right| = 2S_\Delta. \tag{2.22}$$

Cubature formula for the integral M_Δ can be obtained by way of approximating surfaces $f[W_1,W_2]$, $\Omega[W_1,W_2]$ by planes passing through three points: (1, 0, f[1,0]), (0, 1, f[0,1]), (0, 0, f[0,0]), and (1, 0, Ω[1,0]), (0, 1, Ω[0,1]), (0, 0, Ω[0,0]), respectively. In this case, we have

$$f[W_1, W_2] \approx (f[1,0] - f[0,0])W_1 + (f[1,0] - f[0,0])W_2 + f[0,0], \tag{2.23}$$

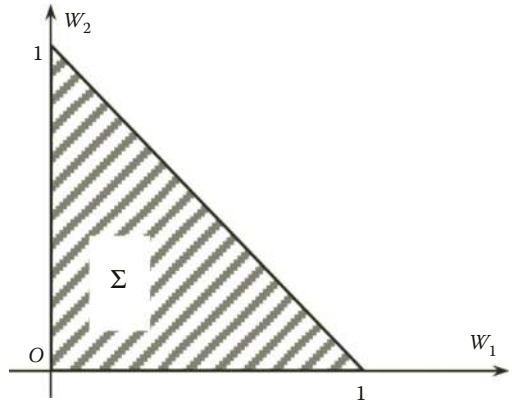

FIGURE 2.14 Unit triangle in barycentric coordinates.

$$k_0\Omega[W_1, W_2] \approx pW_1 + qW_2 + k_0\Omega[0,0], \tag{2.24}$$

where $p = k_0\,(\Omega[1,0] - \Omega[0,0])$ and $q = k_0\,(\Omega[0,1] - \Omega[0,0])$.

The integral M_Δ, in its turn, can be expressed as follows:

$$M_\Delta \approx 2S_\Delta\ \exp(jk_0\,\Omega[0,0])\,((f[1,0] - f[0,0])I_{10} + (f[0,1] - f[0,0])I_{01} + f[0,0]I_{00}), \tag{2.25}$$

where the values I_{00}, I_{01}, I_{10} can be computed by means of the following integrals:

$$\begin{aligned} I_{00} &= \int_0^1 \mathrm{d}W_1 \int_0^{1-W_1} \exp(j(pW_1 + qW_2))\,\mathrm{d}W_2, \\ I_{10} &= \int_0^1 W_1\mathrm{d}W_1 \int_0^{1-W_1} \exp(j(pW_1 + qW_2))\,\mathrm{d}W_2, \\ I_{01} &= \int_0^1 W_2\mathrm{d}W_2 \int_0^{1-W_2} \exp(j(pW_1 + qW_2))\,\mathrm{d}W_1. \end{aligned} \tag{2.26}$$

Having computed these integrals and assuming $\varphi(x) = -j(\exp(jx) - 1)/x$, we receive the following expressions:

$$\left.\begin{aligned} I_{00} &= -j(\varphi(p) - \varphi(q))/(p - q), \\ I_{10} &= -(\varphi(q) - \varphi(p) - (q - p)\varphi'(p))/(q - p)^2, \\ I_{01} &= -(\varphi(p) - \varphi(q) - (p - q)\varphi'(q))/(p - q)^2, \end{aligned}\right\} \tag{2.27}$$

which, taken together with expression (2.25), represent the integral M_Δ by means of cubature formulas.

Next, using representation (2.14) and formulas (2.15), (2.25), and (2.27), one can compute the field scattered from smooth part S_1 of the object's surface. Approximate density of triangular facets can be evaluated as shown in Ref. [52].

In high-frequency domain considered here, the field scattered from smooth part of the object's surface is a fast oscillating function versus frequency, which is due to considerable change of Fresnel zones distribution over the object surface given even the smallest changes in the illumination signal frequency. So, in order to receive robust values of the scattered field amplitude (used later on for the RCS computation), one should provide averaging of this value over some frequency range. Also, it is worth mentioning that besides definite advantages of the cubature formula, there is an expected drawback related with the necessity of increasing the facet density at the surface of integration when the illumination signal wavelength decreases. The problem is that for the very large (electrically) object (such as aircraft, for instance) it is quite difficult to introduce the fine enough mesh of facets. Therefore, we have to content ourselves with the frequency averaged values of scattered field amplitudes and RCS. According to our calculations for the simple shape bodies (sphere, ellipsoid), we can arbitrarily put some fixed mesh of facets over surface and then it is possible to select the frequency range (with preset central frequency) for the RCS value to be averaged over in such a manner that the average RCS would be close enough to the true mean RCS of real surface.

2.2.3 Asymptotic Method for Computing Radar Scattering from Smooth Parts of the Object in Bistatic Radar Case

The method presented in Sections 2.2.1 and 2.2.2 for numerical computation of radar scattering from smooth parts of the object was based on special cubature formulas designed for calculating integrals from fast oscillating functions. The method is a variation of "current" method.

In this section, we consider an alternative computation method based on "ray" asymptotic of corresponding integrals for general bistatic radar configuration.

From Equation 2.3 (Section 2.2.1), one can get the following expression for the field scattered from the smooth part S_1 of the object's surface in far-field zone:

$$\vec{E}_{S_1} = -jk_0\sqrt{\frac{\mu_0}{\varepsilon_0}}\,\frac{\exp(jk_0R)}{4\pi R}\,\vec{I}(\vec{r}_0), \tag{2.28}$$

where

$$\vec{I}(\vec{r}_0) = \int_{S_1}\left[\vec{H}^{\perp} - \sqrt{\frac{\varepsilon_0}{\mu_0}}(\vec{E}^{\perp}\times\vec{r}^{\,0})\right]\exp(-jk_0(\vec{r}^{\,0}\cdot\vec{x}))\,\mathrm{d}S. \tag{2.28′}$$

Therefore, contribution from the "smooth" parts of the object's surface into total scattered field can be evaluated by computing integral $\vec{I}(\vec{r}^{\,0})$. Since all the geometrical parameters (linear dimensions, curvature radii) of "smooth" object parts are large compared to the incident field wavelength, and boundary contours lying closest to the edges are outside of that neighborhood, in which irregular component of surface current density is significant, then it is possible to account for contribution of such object's parts by means of any asymptotic method of short wave diffraction.

In this section, we consider the surface of a scatterer containing, in bistatic radar case, elliptical stationary phase points of both perfectly conducting and RAM-coated kinds.

Let us consider, first, the case of smooth convex perfectly conducting surface part containing elliptical point of stationary phase in case of bistatic radar and let us evaluate its contribution into total scattered field. For the perfectly conducting surface part S_1, expression (2.28′) transforms into the following:

$$\vec{I}(\vec{r}^{\,0}) = \int_{S_1}\exp(-jk_0(\vec{r}^{\,0}\cdot\vec{x}))\vec{v}(\vec{x},k_0)\,\mathrm{d}S, \tag{2.29}$$

where $\vec{v}(\vec{x},k_0) = [\vec{n}_x\times\vec{H}]$.

For the sake of simplicity, we choose the coordinate origin to coincide with the stationary phase point at S_1 (point $\vec{x}=0$). Iterative method for finding solution to the magnetic field integral equation of V.A. Fock [53] in the region S_1 enables us to present $\vec{v}(\vec{x},k_0)$ in form of asymptotic (for great k_0) formula:

$$\vec{v}(\vec{x},k_0) \sim 2\left(\vec{v}^{\,0}(\vec{x},k_0) + \int_{S_1}\left[\frac{\partial g(\vec{x},\vec{\xi})}{\partial n_x}\vec{v}^{\,0}(\vec{\xi},k_0) - \vec{\nabla}_x g(\vec{x},\vec{\xi})(\vec{n}_x\cdot\vec{v}^{\,0}(\vec{\xi},k_0))\right]\mathrm{d}S_\xi\right), \tag{2.30}$$

where $g(\vec{x},\vec{\xi}) = \dfrac{1}{4\pi}\cdot\dfrac{\exp jk_0(|\vec{x}-\vec{\xi}|)}{|\vec{x}-\vec{\xi}|}$.

By means of iterating the equation of V.A. Fock, we can get, one by one, the summands of ray asymptotic for the surface current density. Following this as a guideline, below we present computation of the first two summands of asymptotic $\vec{v}(\vec{x},k_0)$ introduced by stationary phase point of elliptical type.

Taking into account that

$$\vec{v}^0(\vec{x},k_0) = (\vec{n}_x \times \vec{p}^0)\exp(jk_0(\vec{R}^0 \cdot (\vec{a}+\vec{x}))),$$

where $\vec{p}^0 = \sqrt{\frac{\varepsilon_0}{\mu_0}}(\vec{R}^0 \times \vec{p})$, and $\vec{a}$ is the radius-vector of stationary phase point in coordinate system tied to the illumination source, it is easy to conclude from Equation 2.30 that

$$\vec{V}(\vec{x},k_0) = \exp(jk_0\vec{R}^0 \cdot (\vec{a}+\vec{x}))\vec{v}(\vec{x},k_0), \tag{2.31}$$

besides

$$\vec{V}(\vec{x},k_0) \sim 2(\vec{n}_x \times \vec{p}^0) + \frac{1}{\pi}\int_{S_1}\vec{Z}(\vec{\xi},\vec{x})\left(jk_0 - \frac{1}{|\vec{\xi}-\vec{x}|}\right)\exp(jk_0(|\vec{\xi}-\vec{x}| + \vec{R}^0 \cdot (\vec{\xi}-\vec{x})))\,\mathrm{d}S_\xi, \tag{2.32}$$

where

$$\vec{Z}(\vec{\xi},\vec{x}) = \frac{\partial \ln|\vec{\xi}-\vec{x}|}{\partial n_x}(\vec{n}_\xi \times \vec{p}^0) - \frac{\vec{\xi}-\vec{x}}{|\vec{\xi}-\vec{x}|}((\vec{n}_x \times \vec{n}_\xi)\cdot \vec{p}^0). \tag{2.33}$$

It follows from here that

$$\vec{V}(\vec{x},k_0) \sim \vec{V}_0(\vec{x}) + \frac{1}{jk_0}\vec{V}_1(\vec{x}),$$

where

$$\vec{V}_0(\vec{x}) \sim 2(\vec{n}_x \times \vec{p}^0),$$

and $\vec{V}_1(\vec{x})/jk_0$ is the basic member of the integral asymptotic in Equation 2.32.

From Equations 2.29, 2.31, and 2.33, it follows that given great k_0 the following asymptotic representation takes place:

$$\vec{I}(\vec{r}^0)\times\vec{r}^0 \sim \exp(jk_0|\vec{a}|)\int_{S_1}\exp(jk_0((\vec{R}^0-\vec{r}^0)\cdot\vec{x}))\left[\vec{W}_0(\vec{x}) + \frac{1}{jk_0}\vec{W}_1(\vec{x})\right]\mathrm{d}S, \tag{2.34}$$

in which

$$\begin{aligned}\vec{W}_0(\vec{x}) &= 2(\vec{n}_x \times \vec{p}^0)\times\vec{r}^0,\\ \vec{W}_1(\vec{x}) &= \vec{V}_1(\vec{x})\times r^0.\end{aligned} \tag{2.35}$$

Let us introduce cylindrical coordinates (ρ, φ, ζ): $\xi_1 = \rho \cos\varphi$, $\xi_2 = \rho \sin\varphi$. Then, the surface S_1 in the vicinity of $\vec{x} = 0$ becomes represented by the following equation:

$$\zeta = \zeta(\rho, \varphi) = \sum_{m=2}^{4} \frac{g_m(\varphi)}{m!} \rho^m + o(\rho^4), \tag{2.36}$$

where, for instance

$$g_2(\varphi) = æ_1 \cos^2\varphi + æ_2 \sin^2\varphi$$

($æ_1$ and $æ_2$ are the principal curvatures of S_1 at $\vec{x} = 0$). Since $\vec{x} = (\xi_1, \xi_2, \zeta)$, then

$$(\vec{R}^0 - \vec{r}^0) \cdot \vec{x} = 2\cos\theta\zeta(\rho, \varphi), \quad (\vec{x} \cdot \vec{n}_0) = \zeta(\rho, \varphi), \tag{2.37}$$

where θ is the half-angle of spacing between receiver and transmitter, and $\vec{n}_0$ is the inner normal to the surface S_1 at point $\vec{x} = 0$.

Further on

$$dS = \sqrt{1 + \left(\frac{\partial\zeta}{\partial\xi_1}\right)^2 + \left(\frac{\partial\zeta}{\partial\xi_2}\right)^2}\, \rho\, d\rho\, d\varphi = \left(1 + \frac{1}{2} h_2(\varphi)\rho^2 + o(\rho^2)\right) \rho d\rho d\varphi, \tag{2.38}$$

where

$$h_2(\varphi) = æ_1 \cos^2\varphi + æ_2 \sin^2\varphi.$$

Additionally, in the vicinity of point $\vec{x} = 0$

$$\vec{W}_0(\vec{x}) = \vec{W}_0(0) + \rho\vec{W}_{01}(\varphi) + \rho^2\vec{W}_{02}(\varphi) + o(\rho^2), \tag{2.39}$$

$$\vec{W}_1(\vec{x}) = \vec{W}_1(0) + O(\rho), \tag{2.40}$$

where

$$\begin{aligned} \vec{W}_0(0) &= 2(\vec{n}_0 \times \vec{p}^0) \times \vec{r}^0 = 2\cos\theta(-\vec{p}^0 + 2(\vec{p}^0 \cdot \vec{n}_0)\vec{n}_0) = -2\cos\theta\, \vec{p}^0_{ref}, \\ \rho\vec{W}_{01}(\varphi) &= \left(\frac{\partial\vec{W}_0}{\partial\xi_1}\right)_0 \rho\cos\varphi + \left(\frac{\partial\vec{W}_0}{\partial\xi_2}\right)_0 \rho\sin\varphi. \end{aligned} \tag{2.41}$$

Using the Frenet formula, we finally obtain from Equation 2.39 that

$$\vec{W}_{01}(\varphi) = 2\left[æ_1(\vec{\tau}_1 \times \vec{p}^0) \times \vec{r}^0 \cos\varphi + æ_2(\vec{\tau}_2 \times \vec{p}^0) \times \vec{r}^0 \sin\varphi\right], \tag{2.42}$$

$$\vec{W}_{02}(\varphi) = h_2(\varphi)\vec{p}^0_{ref} \cos\theta. \tag{2.43}$$

Here, $\vec{\tau}_1, \vec{\tau}_2$ are the unit-vectors of basic directions at point $\vec{x} = 0$, the vector triplet $(\vec{\tau}_1, \vec{\tau}_2, \vec{n}_0)$ forming the right-hand triad. Vector $\vec{W}_1(0)$ shall be computed below. In our case, we have $æ_1, æ_2 > 0$. Then, accounting for expressions (2.36) through (2.43), we apply the stationary phase point method to evaluate asymptotically the integral (2.34) multiplied by jk_0

$$jk_0\vec{I}(\vec{r}^{\,0}) \times \vec{r}^{\,0} \sim jk_0 \exp(jk_0|\vec{a}|)\int_{S_1} \exp(jk_0 2\cos\theta\zeta(\rho,\varphi)) \times$$
$$\times\left[\vec{W}_0(0) + \rho\,\vec{W}_{01}(\varphi) + \frac{1}{j\,k_0}\vec{W}_1(0)\right]\left(1 + \frac{1}{2}\rho^2 h_2(\varphi) + \cdots\right)\rho\,d\rho\,d\varphi. \tag{2.44}$$

Having introduced some asymptotic estimates and transformation in Equation 2.44, we obtain

$$jk_0\vec{I}(\vec{r}^{\,0}) \times \vec{r}^{\,0} \sim \exp(jk_0|\vec{a}|)\left(\frac{2\pi}{\sqrt{æ_1 æ_2}}\,\vec{p}^{\,0}_{ref} + \frac{1}{jk_0}\vec{T}(\vec{r}^{\,0})\right), \tag{2.45}$$

where

$$\vec{T}(\vec{r}^{\,0}) = -\int_0^{2\pi}\left\{\vec{W}_1(0) - \vec{W}_0(0)\frac{h_2(\varphi)}{2g_2(\varphi)\cos\theta} + \frac{2}{g_2^2(\varphi)\cos\theta}\left(\vec{W}_0(0)\frac{g_4(\varphi)}{12} + \vec{W}_{01}(\varphi)\frac{g_3(\varphi)}{3}\right)\right\}\frac{d\varphi}{2g_2(\varphi)\cos\theta}.$$

If the surface ζ can be represented by the second-order polynomial, that is, $g_3 = g_4 = 0$, then

$$\vec{T}(\vec{r}^{\,0}) = -\frac{\vec{W}_1(0)}{2\cos\theta}\int_0^{2\pi}\frac{d\varphi}{g_2(\varphi)} + \frac{\vec{W}_0(0)}{4\cos^2\theta}\int_0^{2\pi}\frac{h_2(\varphi)}{g_2^2(\varphi)}d\varphi. \tag{2.46}$$

Integrals in Equation 2.46 can be computed explicitly and then

$$\vec{T}(\vec{r}^{\,0}) = \left\{-\vec{W}_1(0) - \frac{\vec{p}^{\,0}_{ref}}{2}(æ_1 + æ_2)\right\}\frac{\pi}{\cos\theta\sqrt{æ_1 æ_2}}. \tag{2.47}$$

Expression (2.47) contains vector $\vec{W}_1(0)$, explicit value of which has not yet been found.

Since

$$\vec{W}_1(0) = \vec{V}_1(0) \times \vec{r}^{\,0},$$

then we need to find the principal asymptotic member $\vec{V}_1(0)/jk_0$ of integral $\vec{J}$ in Equation 2.32 at point $\vec{x} = 0$. This integral can be evaluated asymptotically as

$$\vec{J} \sim \frac{1}{\pi}\int_0^{2\pi} d\varphi \int_0 \vec{Z}(\vec{\xi},0)\left(jk_0 - \frac{1}{\rho}\right)\exp(jk_0\rho(1 + c_0(\varphi)))\rho\,d\rho, \tag{2.48}$$

where $c_0(\varphi) = \sin\theta\cos(\varphi - \alpha)$, and α is the measure of angle formed by the projection of unit-vector $\vec{R}^0$ onto plane $\xi_1 O\xi_2$ and the axis $O\xi_1$. Next, having made a replacement

$$\vec{Z}(\vec{\xi},0) = \vec{Z}(\rho,\varphi),$$

and having carried out all the necessary transformations, we obtain

$$\lim_{\rho\to 0}\vec{Z}(\vec{\xi},0)=\vec{Z}_0(\varphi)=\frac{1}{2}\vec{\tau}_1[p_2^0(æ_2\sin^2\varphi-æ_1\cos^2\varphi)+p_1^0æ_2\sin 2\varphi]$$
$$+\frac{1}{2}\vec{\tau}_2[p_1^0(æ_1\cos^2\varphi-æ_2\sin^2\varphi)-p_2^0æ_1\sin 2\varphi],\quad p_l^0=\vec{\tau}_l\cdot\vec{p}^0.$$

Therefore

$$\vec{J}\sim\frac{1}{j\pi k_0}\int_0^{2\pi}\vec{Z}_0(\varphi)\frac{2+c_0(\varphi)}{(1+c_0(\varphi))^2}\,d\varphi$$

and, consequently,

$$\vec{V}_1(0)=\frac{1}{\pi}\int_0^{2\pi}\frac{2+c_0(\varphi)}{(1+c_0(\varphi))^2}\vec{Z}_0(\varphi)\,d\varphi. \tag{2.49}$$

Having computed integral in Equation 2.49 explicitly, we obtain

$$\vec{V}_1(0)=\vec{\tau}_1\vec{V}_{11}(\theta)+\vec{\tau}_2\vec{V}_{12}(\theta), \tag{2.50}$$

where

$$V_{11}(\theta)=\Phi_0(\theta)\left[\frac{p_1^0æ_2}{2}\sin 2\alpha-\frac{p_2^0(æ_1+æ_2)}{4}\cos 2\alpha\right]+\frac{p_2^0}{4}(æ_2-æ_1)\Phi_1(\theta), \tag{2.51}$$

$$V_{12}(\theta)=\Phi_0(\theta)\left[-\frac{p_2^0æ_1}{2}\sin 2\alpha-\frac{p_1^0(æ_1+æ_2)}{4}\cos 2\alpha\right]+\frac{p_1^0}{4}(æ_2-æ_1)\Phi_1(\theta), \tag{2.52}$$

$$\Phi_0(\theta)=2\left[\frac{tg^2(\theta/2)}{\cos\theta}+\frac{1}{\sin^2\theta}\left(2+\frac{3\sin^2\theta-2}{\cos^3\theta}\right)\right],$$
$$\Phi_0(0)=0,\quad \Phi_1(\theta)=2\frac{1+\cos^2\theta}{\cos^3\theta}.$$

Accounting for expressions (2.50) through (2.52), we obtain the following:

$$\vec{W}_1(0)=-\vec{\tau}_1\cos\theta\,V_{12}(\theta)+\vec{\tau}_2\cos\theta\,V_{11}(\theta)+\vec{n}_0\sin\theta(\sin\alpha\,V_{11}(\theta)-\cos\alpha\,V_{12}(\theta)). \tag{2.53}$$

So, expressions (2.45), (2.47), and (2.50) through (2.53) represent the sought for value of the integral (2.29).

Let us assume, next, that radius-vector of the stationary phase point in some coordinate system related to the target is $\vec{y}^0$, and $|\vec{a}|=d_1$, $R=d_2$. Then, using expression (2.28), we obtain the contribution of surface S_1 into total scattered field:

$$\vec{E}_{S_1} \sim -\sqrt{\frac{\mu_0}{\varepsilon_0}}\frac{\exp(jk_0(d_1+d_2+(\vec{R}^0-\vec{r}^0)\cdot\vec{y}^0))}{2d_2\sqrt{æ_1 æ_2}}$$
$$\times\left[\vec{p}^0_{ref}+\frac{1}{jk_0}\frac{1}{2\cos\theta}\Big((\tau_1\cos\theta V_{12}(\theta)-\tau_2\cos\theta V_{11}(\theta))\right.$$
$$\left.-\vec{n}_0(\sin\alpha V_{11}(\theta)-\cos\alpha V_{12}(\theta))\sin\theta-\frac{\vec{p}^0_{ref}}{2}(æ_1+æ_2)\Big)\right]. \tag{2.54}$$

Let, now, the surface S_1 (either all or some part of it that contains the stationary phase point) to be covered with thin uniform layer of RAM coating. In this case, the surface S_1 itself is not perfectly reflecting anymore (at least in the vicinity of the stationary phase point), and $\vec{E}^{\perp}\neq 0$ in the integral (2.28′). The issue of the integral (2.28′) evaluation, in its turn, depends in the first place on finding the values of vectors $\vec{E}^{\perp}$, $\vec{H}^{\perp}$ entering the integrand. Let, further, the radius-vector $\vec{X}$ of a point at the scatterer surface's vicinity of stationary phase point (i.e., such point that $(\vec{R}^0\cdot\vec{n})=-(\vec{r}^0\cdot\vec{n})$) to be presented as vector sum

$$\vec{X}=\vec{y}^0+\vec{x}, \tag{2.55}$$

where $\vec{y}^0$ is the radius-vector of stationary phase point in some coordinate system related to the target. Then, the primary incident field (2.1) can be presented as

$$\begin{pmatrix}\vec{E}^0(\vec{X})\\ \vec{H}^0(\vec{X})\end{pmatrix}=\exp(jk_0(\vec{R}^0\cdot\vec{y}^0))\begin{pmatrix}\vec{p}^0\exp(jk_0(\vec{R}^0\cdot\vec{x}))\\ \sqrt{\frac{\varepsilon_0}{\mu_0}}(\vec{R}^0\times\vec{p}^0)\exp(jk_0(\vec{R}^0\cdot\vec{x}))\end{pmatrix}. \tag{2.56}$$

Due to linearity of the problem, the equivalent current densities around specular reflection point can be presented in similar form:

$$\begin{pmatrix}\vec{E}^{\perp}(\vec{X})\\ \vec{H}^{\perp}(\vec{X})\end{pmatrix}=\exp(jk_0(\vec{R}^0\cdot\vec{y}^0))\begin{pmatrix}\vec{E}^{\perp}(\vec{x})\\ \vec{H}^{\perp}(\vec{x})\end{pmatrix}. \tag{2.57}$$

The values $\vec{E}^{\perp}(\vec{x})$, $\vec{H}^{\perp}(\vec{x})$ can be approximately (asymptotically) determined as corresponding field components at the surface of tangent (at stationary phase point) plane uniform layer of covering material backed by metal plate [54,55]. The corresponding expressions have the following form:

$$\vec{E}^{\perp}(\vec{x})=(\vec{n}\times\vec{p}^0)\exp(jk_0(\vec{R}^0\cdot\vec{x}))+(\vec{n}\times\vec{p}^1)\exp(jk_0(\vec{R}^1\cdot\vec{x})), \tag{2.58}$$

$$\vec{H}^{\perp}(\vec{x})=\sqrt{\frac{\varepsilon_0}{\mu_0}}[[\vec{n}\times(\vec{R}^0\times\vec{p}^0)]\exp(jk_0(\vec{R}^0\cdot\vec{x}))+[\vec{n}\times(\vec{R}^1\times\vec{p}^1)]\exp(jk_0(\vec{R}^1\cdot\vec{x}))]. \tag{2.59}$$

Here, $\vec{n}$ is the unit-vector of external normal to the surface S_1 at specular reflection point:

$$\vec{R}^1=\vec{R}^0-2\vec{n}(\vec{R}^0\cdot\vec{n});$$
$$\vec{p}^1=\vec{p}^{1T}-\vec{n}\frac{(\vec{p}^{1T}\cdot\vec{R}^0)}{\cos\theta}, \tag{2.60}$$

where

$$\vec{p}^{1T} = \frac{jc\cos\theta + 1}{jc\cos\theta - 1}\vec{p}^{0T} - \frac{2jc}{jc\cos\theta - 1}\left[\vec{R}^{0T}\frac{(\vec{R}^{0T}\cdot\vec{p}^{0})}{jc - \cos\theta} + \vec{R}^{0\perp}\frac{(\vec{R}^{0\perp}\cdot\vec{p}^{0})}{\varepsilon_1'\mu_1'\left(jc - \dfrac{\cos^2\theta_1}{\cos\theta}\right)}\right]; \tag{2.61}$$

$$c = \sqrt{\frac{\mu_1'}{\varepsilon_1'}}\cos\theta_1 \cdot tg\left[k_0\sqrt{\varepsilon_1'\mu_1'}\,\delta\cos\theta_1\right]; \quad \cos\theta_1 = \sqrt{1 - \frac{\sin^2\theta_1}{\varepsilon_1'\mu_1'}};$$

δ is the absorbent layer depth, and ε_1', μ_1' are the relative permittivity and permeability of absorbing material.

Let us note that in the vicinity of specular reflection point the following condition holds:

$$(\vec{R}^0\cdot\vec{x}) \approx (\vec{R}^{0T}\cdot\vec{x}) = (\vec{R}^1\cdot\vec{x}). \tag{2.62}$$

Using expression (2.62), we can rewrite Equations 2.58 and 2.59 in the next form:

$$\begin{pmatrix}\vec{E}^{\perp}(\vec{x})\\ \vec{H}^{\perp}(\vec{x})\end{pmatrix} \approx \begin{pmatrix}\vec{n}\times(\vec{p}^0 + \vec{p}^1)\\ \sqrt{\dfrac{\varepsilon_0}{\mu_0}}[\vec{n}\times((\vec{R}^0\times\vec{p}^0) + (\vec{R}^1\times\vec{p}^1))]\end{pmatrix}\exp(jk_0(\vec{R}^0\cdot\vec{x})). \tag{2.63}$$

Since the major contribution into the integral (2.28′) is from the stationary phase point vicinity, then substituting consequently expression (2.63) into expression (2.57) and then into expression (2.28′), we can reduce this integral to the following form:

$$\vec{I}(\vec{r}^0) \approx \sqrt{\frac{\varepsilon_0}{\mu_0}}\exp(jk_0((\vec{R}^0 - \vec{r}^0)\cdot\vec{y}_0))\int_{S_1}\vec{A}\exp(jk_0((\vec{R}^0 - \vec{r}^0)\cdot\vec{x}))\,dS, \tag{2.64}$$

where

$$\vec{A} = \vec{R}^0(\vec{p}^0\cdot\vec{n}) - 2\vec{p}^1\cos\theta + \vec{R}^1(\vec{p}^1\cdot\vec{n}) + \vec{n}(\vec{p}^0\cdot\vec{R}^1), \quad \cos\theta = -(\vec{R}^0\cdot\vec{n}).$$

Amplitude multiplier $\vec{A}$ in the integrand is the slow oscillating function versus point position at the scatterer's surface, so it can be replaced, within acceptable accuracy margin, by its value at the stationary point itself and be placed outside the integral. It is evident that in this case $\vec{R}^1 = \vec{r}^0$ and, therefore, we have

$$\vec{I}(\vec{r}^0) \approx \sqrt{\frac{\varepsilon_0}{\mu_0}}\exp(jk_0(\vec{R}^0 - \vec{r}^0)\cdot\vec{y}_0)\vec{A}_{st}\int_{S_1}\exp(jk_0(\vec{R}^0 - \vec{r}^0)\cdot\vec{x})\,dS. \tag{2.65}$$

Having computed asymptotically the integral in the right-hand part of Equation 2.65 (by means of stationary phase point) and having done corresponding transformations for the expression of vector $\vec{A}$ at the stationary phase point ($\vec{A}_{st}$), we finally receive

$$\vec{I}(\vec{r}^0) = -\sqrt{\frac{\varepsilon_0}{\mu_0}}\exp(jk_0(\vec{R}^0 - \vec{r}^0)\cdot\vec{y}_0)\frac{2\pi}{jk_0\sqrt{æ_1æ_2}}\cdot\vec{p}^1, \tag{2.66}$$

where $æ_1$ and $æ_2$ are the principal curvatures of the surface at its specular reflection point. Next, using expressions (2.28) and (2.66), we can evaluate the contribution from elliptical local scattering center covered with absorbent into total scattered field.

2.2.4 Radar Scattering at the Local Edge Fractures Covered with Absorbent

Scattering characteristic computation for the object surface singularities such as fractures is connected with solving diffraction problems. Getting an exact solution to the problem of electromagnetic wave diffraction at a fracture is a very complicated (both mathematically and computationally) task. Therefore, the practical way to solve such problems is to use the high-frequency asymptotic diffraction methods [56,57].

The problems of high-frequency diffraction at the objects with ribs are solved using, in the first place, the edge wave diffraction method (physical diffraction theory by P. Ya. Ufimtsev [7,8]). Using this method, we can find the field produced by the irregular part of the current excited on geometrical singularities of the object surface such as edges and fractures. This field, which is the correction to Kirchhoff's approximation, is found directly for the far-field zone. The latter necessitates all the considerations to be carried out in every geometrical optics sector and, mostly challenging, in every boundary region between them. All the aforementioned factors condition the necessity of getting solution to the key problem of diffraction at the wedge in far-field zone. Consequently, the conditions listed above complicate the use of edge wave diffraction method given such real-world configurations as multistatic radar and nonperfectly reflecting surfaces (those covered with absorbent). Thus, the edge wave diffraction method needs modification, which is the change of principle (simulative) problem.

We now present the computation method that is to be used for evaluating the contribution from edge local scatterers covered with RAM into secondary radiation of the object [34,55]. While doing this, we rely on the solution of the simulative problem of arbitrary incidence of plane electromagnetic wave onto perfectly conducting wedge with cylindrically shaped absorbent coating of its edge [46].

In case of multistatic radar, this problem (of oblique incidence of plane wave onto the wedge with cylindrically shaped RAM coating of its edge) cannot be reduced to superposition of two independent two-dimensional problems as it was the case in Ref. [7]. It should be noted that the solution to simulative problem has been obtained for the wedge's rib vicinity, which allowed us to use representations uniformly applicable in all angular sectors. The latter has also conditioned the absence of splitting the surface current density into regular and irregular constituents. This is the basic methodological difference of the method proposed from the edge wave diffraction method.

Expression for the field scattered from the edge local scatterers can be presented in the following form:

$$\begin{aligned} \vec{p}\cdot\vec{E}_{S_0} &= -jk_0\sqrt{\frac{\mu_0}{\varepsilon_0}}\,\frac{\exp(jk_0R)}{4\pi R}(\vec{p}\cdot\vec{F}(\vec{r}^{\,0})), \\ \vec{F}(\vec{r}^{\,0}) &= \int\limits_{S_0}\left[\vec{H}^{\perp}-\sqrt{\frac{\varepsilon_0}{\mu_0}}(\vec{E}^{\perp}\times\vec{r}^{\,0})\right]\exp(-jk_0(\vec{r}^{\,0}\cdot\vec{x}))\,\mathrm{d}S. \end{aligned} \tag{2.67}$$

Let us choose toroidal surface "pulled upon" the edge as the surface of integration S_0. As it is shown in Figure 2.15, integration surface, in cross section orthogonal to the edge, is the part of circumference with radius z_0 and center at O that encompasses the absorbent covering the edge.

In all our further considerations, we assume that absorbent is bounded, in this same cross section, by a part of circumference of radius $z \le z_0$, its center being at point O. The values of z and z_0 are conditioned by the inequality $z \le z_0 < \lambda$ (λ is the wavelength of incident monochromatic wave).

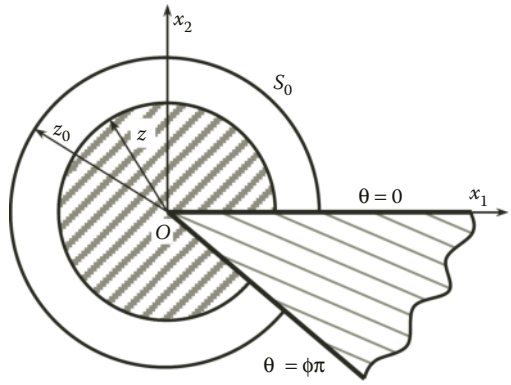

FIGURE 2.15 Cross section of the integration surface S_0 in the vicinity of fracture.

In order to find the value of $\vec{F}(\vec{r}^{\,0})$ in Equation 2.67, we need to know the tangential component distribution of total field ($\vec{E}^{\perp} = \vec{n} \times \vec{E}$, $\vec{H}^{\perp} = \vec{n} \times \vec{H}$) over surface S_0. Let us introduce Cartesian coordinate system $Ox_1x_2x_3$ tied to the edge (Figure 2.15) so that

$$\vec{X} = \vec{x}(\upsilon) + \vec{\tau}(z_0,\theta), \tag{2.68}$$

where $\vec{x}(\upsilon)$ is the radius-vector of a point at the edge Y with the arc coordinate υ, and $\vec{\tau}(z_0,\theta)$ is the vector orthogonal to the edge at this point, this vector having constant norm z_0 and direction determined by angle θ ($0 \le \theta \le \phi\pi$). Here, $\phi\pi$ is the aperture angle of wedge placed to be tangential to the edge at the point with corresponding arc coordinate υ.

Let the object be illuminated with plane wave (2.1). Due to the problem of nonlinearity, the values $\vec{H}^{\perp}, \vec{E}^{\perp}$ over S_0 at point $(\upsilon,\vec{\tau})$ can be presented in the following form:

$$\begin{pmatrix} \vec{E}^{\perp}(\vec{X}) \\ \vec{H}^{\perp}(\vec{X}) \end{pmatrix} = \begin{pmatrix} \tilde{\vec{E}}^{\perp}(\vec{\tau}) \\ \tilde{\vec{H}}^{\perp}(\vec{\tau}) \end{pmatrix} \exp(jk_0(\vec{R}^0 \cdot \vec{x}(\upsilon))), \tag{2.69}$$

where $\tilde{\vec{H}}(\vec{\tau}), \tilde{\vec{E}}(\vec{\tau})$ are the intensity vectors of field excited at surface S_0 by plane wave

$$\begin{aligned} \tilde{\vec{E}}^0(\vec{\tau}) &= \vec{p}^{\,0} \exp(jk_0(\vec{R}^0 \cdot \vec{\tau})), \\ \tilde{\vec{H}}^0(\vec{\tau}) &= \sqrt{\frac{\varepsilon_0}{\mu_0}}(\vec{R}^0 \times \vec{p}^{\,0}) \exp(jk_0(\vec{R}^0 \cdot \vec{\tau})). \end{aligned} \tag{2.70}$$

Now, accounting for Equation 2.69, the integral $\vec{F}(\vec{r}^{\,0})$ can be presented as

$$\vec{F}(\vec{r}^{\,0}) = \int_Y \exp[jk_0((\vec{R}^0 - \vec{r}^{\,0}) \cdot \vec{x}(\upsilon))]\vec{D}(\upsilon,\vec{r}^{\,0})\,\mathrm{d}\upsilon, \tag{2.71}$$

where

$$\vec{D}(\upsilon,\vec{r}^{\,0}) = \int_{S_0'} \exp[-jk_0(\vec{r}^{\,0} \cdot \vec{\tau})]\vec{B}(\vec{\tau})\,\mathrm{d}c, \tag{2.72}$$

S_0' is the line (part of circumference) at the surface S_0 that lies in plane orthogonal to Y, and $dc = z_0\, d\theta$ is the element of S_0' arc length

$$\vec{B}(\vec{\tau}) = \tilde{\tilde{H}}^{\perp}(\vec{\tau}) - \sqrt{\frac{\varepsilon_0}{\mu_0}}\left[\tilde{\tilde{E}}^{\perp}(\vec{\tau}) \times \vec{r}^{\,0}\right]. \tag{2.73}$$

Having evaluated the integral (2.71) by means of stationary phase method, we can show that at least for the edge, which is convex closed plane curve, there should always be two stationary phase points (except for the "singular case," which shall be discussed later). Such edges (fractures) are usually present at the surface of revolution bodies. In general, equation for finding the stationary phase points υ_0 looks as follows:

$$y'(\upsilon_0) = (\vec{R}^0 - \vec{r}^{\,0}) \cdot \vec{q}(\upsilon_0) = 0, \tag{2.74}$$

where $\vec{q}(\upsilon_0)$ is the unit-vector of the tangent to Y at point υ_0. Let us note that at point υ_0 we have

$$y''(\upsilon_0) = æ(\upsilon_0)[(\vec{R}^0 - \vec{r}^{\,0}) \cdot \vec{\nu}(\upsilon_0)], \tag{2.75}$$

where $æ(\upsilon_0)$ is the curvature of Y at point υ_0, and $\vec{\nu}(\upsilon_0)$ is the unit-vector of principal normal to the Y at point υ_0. Further on, we assume for definiteness that $æ(\upsilon_0) > 0$. So, the "singular case," where the stationary phase point cannot be applied, occurs when the following condition holds:

$$(\vec{R}^0 - \vec{r}^{\,0}) \cdot \vec{\nu}(\upsilon_0) \ll 1 \tag{2.76}$$

(for instance, given the body of revolution with edges, this corresponds to the wave incidence along the axis and monostatic radar configuration). In this case, the value of $\vec{F}(\vec{r}^{\,0})$ can be computed using numerical integration, which is not hard if one accounts for condition that z_0/λ is less than unit. Having found the stationary phase points using (2.74), we need to check them for their "visibility" from the direction of plane wave incidence determined by wave parameter $\vec{R}^0$ and from the direction of scattered wave reception $(-\vec{r}^{\,0})$. To achieve this, we find the terminator (the light-shadow boundary line) and, consequently, the illuminated surface regions for both incident and scattered waves, and then we check the stationary phase points one by one for getting into both illuminated regions. If the point does not get into one of these illuminated regions, then contribution from it into the scattered field is not computed and not accounted for. Such analysis is given for every edge (fracture). Having applied the stationary phase method to the integral (2.71), we receive the final computation formula:

$$\vec{F}(\vec{r}^{\,0}) \approx \sum_{(\upsilon_0)} \exp\left[jk_0((\vec{R}^0 - \vec{r}^{\,0}) \cdot \vec{x}(\upsilon_0)) + \delta j\frac{\pi}{4}\right]\vec{D}(\upsilon_0, \vec{r}^{\,0})\sqrt{\frac{2\pi}{k_0 æ(\upsilon_0)|(\vec{R}^0 - \vec{r}^{\,0}) \cdot \vec{\nu}(\upsilon_0)|}}, \tag{2.77}$$

where $\delta = \mathrm{sgn}[(\vec{R}^0 - \vec{r}^{\,0}) \cdot \vec{\nu}(\upsilon_0)]$, and symbol (υ_0) meaning that summation is done over all the "visible" stationary phase points. Since the integrand of Equation 2.72 is respectively slow oscillating function, the value of $\vec{D}(\upsilon_0, \vec{r}^{\,0})$ can be found by means of one-dimensional numerical integration. Taking into account that the objects we consider are electrically large and curvatures of their surfaces are small, we can assume the values $\tilde{\tilde{H}}^{\perp}(\vec{\tau})$, $\tilde{\tilde{E}}^{\perp}(\vec{\tau})$ at the surface S_0' to be approximately equal to corresponding values at the surface of cylindrically shaped absorbent covering the rib of perfectly conducting wedge $(z = z_0)$ placed so as to be tangent to the edge at point υ_0. So, finally the

simulative problem that needs to be solved for evaluating the contribution from edge local scatterers into total scattered field is the problem of oblique incidence of plane electromagnetic wave onto perfectly conducting wedge with cylindrically shaped radar absorbent at its rib.

This problem is three-dimensional in principle. Its solution cannot be represented as a superposition of two independent two-dimensional problems as in case of the problem of oblique incidence of plane wave onto perfectly conducting wedge, or in case of the problem of normal (with respect to the edge) incidence of plane wave onto the structure under consideration. However, it can be shown that this problem can be reduced to a system of two two-dimensional problems, solutions of which being related through boundary conditions (by means of some matrix differential operator) [29,46].

If $E_3 = u(x_1, x_2)\exp(jk_0 x_3 R_3^0)$, $H_3 = v(x_1, x_2)\exp(jk_0 x_3 R_3^0)$, and $\vec{w} = \begin{pmatrix} u \\ v \end{pmatrix}$, then vector $\vec{w}$ can be developed into the Fourier–Bessel series with (2×2) matrix coefficients. For instance, for the region outside the absorbent cylinder we have

$$\vec{w} = \sum_{m=0}^{\infty} [A_m J_{\gamma_m}(\eta_0 r) + C_m H_{\gamma_m}^{(1)}(\eta_0 r)]\vec{f}_m(\theta), \tag{2.78}$$

where J_{γ_m} is the Bessel function, $H_{\gamma_m}^{(1)}$ is the Hankel function,

$$\vec{f}_m(\varphi) = \begin{pmatrix} \sin(\gamma_m \theta) \\ \cos(\gamma_m \theta) \end{pmatrix}, \quad \eta_0 = k_0\sqrt{1 - (R_3^0)^2}, \quad \gamma_m = m/\phi,$$

$\phi\pi$ is the wedge aperture angle ($0 \le \theta \le \phi\pi$). The matrix coefficients A_m, C_m are derived from boundary conditions for functions u, v, and their derivatives at the surface of absorbent cylinder. The series of Equation 2.78 type converge well given small values of r ($z \le r \le z_0$) [46].

It is worth mentioning that expression (2.77) cannot be used for straight edges since the curvature $æ(\upsilon_0)$ of fracture line becomes zero. Let us write parametric equation for the straight edge (Figure 2.16):

$$\vec{x}(\upsilon) = \begin{cases} a_0 + \upsilon_1^0 t, \\ b_0 + \upsilon_2^0 t, \\ c_0 + \upsilon_3^0 t, \end{cases} \tag{2.79}$$

where $\alpha \le t \le \beta$, and α, β are the endmost points of straight edge.

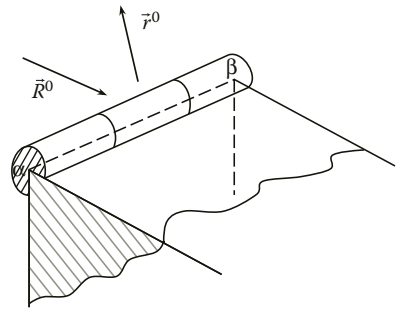

FIGURE 2.16 Straight edge covered with RAM cylinder.

If we assume that such straight edge is at least few wavelengths long and we can neglect the influence of the ends, then the value of function $D(\upsilon,\vec{r}^{\,0})$ can be assumed approximately constant along all the edge Y and this value can be computed using solution to the simulative problem of plane monochromatic wave scattering given its oblique incidence onto perfectly conducting wedge with cylindrically shaped absorbent at its rib [46]. In this regard, expression (2.71) can be presented as follows:

$$\vec{F}(\vec{r}^{\,0}) = \vec{D}_0 \int_Y \exp[jk_0((\vec{R}^0 - \vec{r}^{\,0}) \cdot \vec{x}(\upsilon))]\,d\upsilon. \tag{2.80}$$

If we express the vector difference $\vec{R}^0 - \vec{r}^{\,0}$ as $\vec{R}^0 - \vec{r}^{\,0} = (r_1, r_2, r_3)$ and then account for Equation 2.79, the integral (2.80) takes the following form:

$$\vec{F}(\vec{r}^{\,0}) = \vec{D}_0 \int_Y \exp[jk_0(l + qt)]\,d\upsilon, \tag{2.81}$$

where $l = r_1a_0 + r_2b_0 + r_3c_0$, $q = r_1\upsilon_1^0 + r_2\upsilon_2^0 + r_3\upsilon_3^0$, and $d\upsilon = \sqrt{\upsilon_1^{0^2} + \upsilon_2^{0^2} + \upsilon_3^{0^2}}\,dt = dt$. So, computation of expression (2.81) reduces to evaluating one-dimensional integral:

$$\begin{aligned}\vec{F}(\vec{r}^{\,0}) &= \vec{D}_0 \exp(jk_0l) \int_\alpha^\beta \exp(jk_0qt)\,dt \\ &= \vec{D}_0 \exp(jk_0l)\frac{\exp(jk_0q\alpha)}{jk_0q}(\exp(jk_0q(\beta - \alpha)) - 1).\end{aligned} \tag{2.82}$$

Expression (2.82) allows computing integral $\vec{F}(\vec{r}^{\,0})$ and, later on, it allows us to compute, using Equation 2.67, the field scattered from local scatterers in the form of straight edge covered with RAM for the general case of bistatic radar configuration.

2.2.5 Verification of Methods for Computing Scattering Characteristics of Simple Shape Objects

2.2.5.1 Comparison of RCS Computation Results with the Data Observed in an Anechoic Chamber

The correspondence of results obtained using the computation methods developed here to those observed in real-life scattering of plane electromagnetic wave with respect to simple shape objects has been checked by means of comparing our results with experimental data obtained using radar measurement system based on an anechoic chamber (AnC).

The radar measurement system consisted of anechoic chamber, target modeling, and measurement subsystems.

The anechoic chamber in the system was to represent the free space. It was the chamber with curved "pillow"-shaped walls. Its walls were covered with the spiky wide frequency range radar-absorbent material. Besides, the level of wall reflections in the chamber was below −45 dB, so the anechoic chamber could be used for precise measurements of the most parameters of antennas, radio electronic systems, and most of the target scattering characteristics.

The target modeling subsystem included the low reflecting support (foam plastic) upon the rotator with index dial providing the azimuth aspect reading of the object under study.

The distance to the object was set according to the following considerations: first, the object must be in the anechoic zone of the chamber; second, the distance must be larger than $(2L^2/\lambda)$ [58–60],

where L is the maximum lateral dimension of the object or transmitting antenna and λ the wavelength of wave incident onto the object.

Structural diagram of the measurement system is shown in Figure 2.17. It consisted of the transmit signal generator (TSG), high-frequency amplifier (HFA) of transmitter, transmit, and receive antennas (TrA, RecA), receiver's HFA, squared envelope detector (ED), low-frequency amplifier (LFA), analog-to-digit converter (ADC), timing pulse generator (TPG), and computer.

TSG generated periodic sequence of LFM pulses with the frequency starting at 9.25 GHz and stopping at 9.45 GHz. After amplification in HFA, the signal was transmitted into the chamber's space by means of transmit horn antenna. The echo signal from target was received by the receive horn antenna. At the same time, the signal leaked from transmit antenna to the receive antenna input was used as a heterodyne voltage. Received signal, after amplification in corresponding HFA, came to ED, which extracted the differential signal component between the return and leaked signals.

Next, after its amplification in the LFA, the signal was converted into digital form via ADC and came to the computer. Here, it was processed with discrete Fourier transform (DFT), which was used to compute the received signal's power spectrum density. The latter spectrum density provided us with the value of frequency difference (proportional to the object range); we also retrieved the value of power spectrum density reading at this frequency difference value.

Power of echo signal was measured in relative units. In order to calibrate the radar measurement system and provide actual measurement of RCS, we computed in advance the RCS of simple scatterers (spheres and triangular corner reflectors) to be used as standards. Relative power levels of echoes from these standards provided us with the RCS measurement units and the RCS calibration curve (echo signal power in relative units versus scatterer's RCS in square meters). For every aspect position of the object we took 150 echo power measurements, which, after averaging, were put into table and transformed into the RCS values via the calibration curve. As an object of study, we used the cylinder of 0.1 m diameter and 0.32 m length. The backscattering RCS diagrams corresponding to the experiment and to the computation by method presented above are shown in Figure 2.18. The computation and measurement were done for the signal wavelength $\lambda = 0.032$ m.

Figure 2.18 shows the backscattering RCS diagrams, i.e. RCS σ of the cylinder versus its aspect angle θ counted off the cylinder's axis. Incident field polarization vector was perpendicular to the plane formed by the cylinder axis and the wave incidence direction. The bold line is for experimental RCS values, the thin line is for the RCS by computation.

As can be seen from the figure, RCS computation coincides quite well with experimental data.

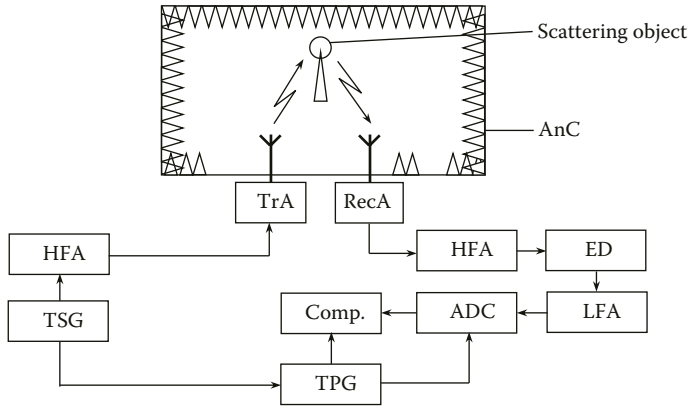

FIGURE 2.17 Structural diagram of measurement system.

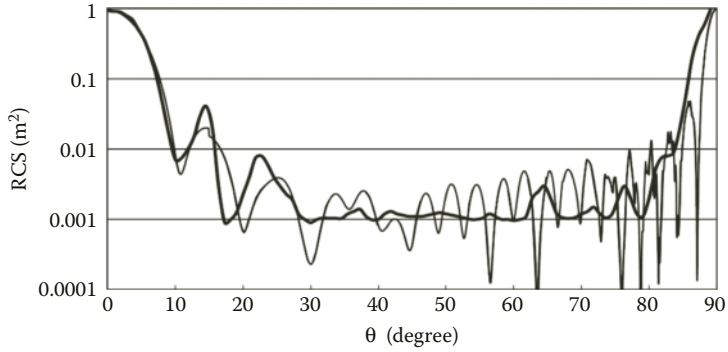

FIGURE 2.18 Backscattering RCS diagram of cylinder.

The mismatch between the two curves is due to the following: first, imperfect alignment in vertical plane of the cylinder axis with the reception direction; second, aspect angle θ increment in measurement was 2.5°, therefore some notches of backscattering diagram could be missed; and third, the LFM signal was used for RCS measurement that smoothed out the backscattering diagram to some degree.

2.2.5.2 RCS Computation Results for the Cylinder Obtained Using Different Computation Methods

The cylinder RCS was evaluated by the following methods:

- Proposed in the book combination of the physical optics method with the method for scattering computation from local edge object parts
- Methods of moments applied in the "FEKO" software [9]

As the first object taken for comparison, we chose the cylinder of 0.66 m radius and 0.28 m height. Illumination signal wavelength was 1 GHz (30 cm wavelength).

Figure 2.19 shows the cylinder RCS versus azimuth aspect of illumination. Bold line is for the dependence obtained by means of the proposed method presented above (computation time ~10 min given azimuth aspect increment of 0.5°). Thin line is for the dependence obtained by means of the "FEKO" software (computation time is more than 9 h given azimuth aspect increment of 1°).

Analysis of dependence in Figure 2.19 shows that computation results for both methods coincide quite well for a wide range of aspect angles.

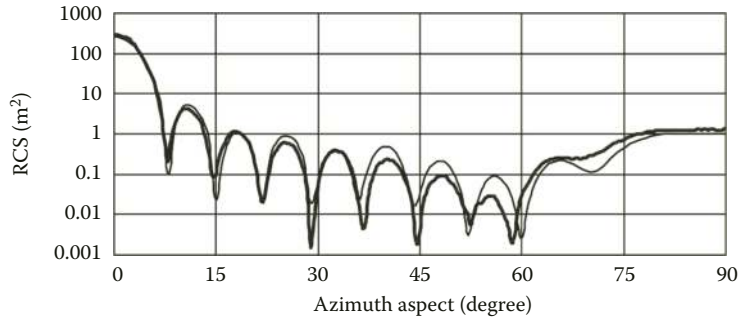

FIGURE 2.19 Cylinder RCS versus azimuth aspect angle.

2.2.5.3 RCS Computation Results for the Cone–Sphere Object Obtained Using Different Computation Methods

RCS of the cone–sphere object was evaluated by the following methods:

- Proposed in the book combination of the physical optics method with the method for scattering computation from local edge object parts
- Methods of moments applied in the "FEKO" software

The cone–sphere object for RCS comparison was chosen in the form of truncated cone terminated with part of the sphere, the sphere radius being 0.16 m, truncated cone height being 1.8 m, and the cone bases being 0.16 m and 0.35 m, respectively. Illumination signal wavelength was 1 GHz (30 cm wavelength).

Figure 2.20 shows the cone–sphere RCS versus its azimuth aspect angle. The bold line is for the computation method proposed in the book for the cone–sphere objects (computation time ~10 min given azimuth aspect increment of 1°). The thin line is for the computation by means of "FEKO" software (computation time is about 14 h given azimuth aspect increment of 1°).

Analysis of dependence in Figure 2.20 shows that computation results for both methods coincide quite well for the whole range of aspect angles.

Verification of the proposed method provided in this manner shows that our method is operational and precise. Small deviations seen in Figures 2.19 and 2.20 are due to the different approaches to the current density estimation over the object surface.

2.2.6 RCS Computation for the Cruise Missile Model

First, we would like to clear up the radar system that we bear in mind when studying scattering by different objects. Schematic of radar configuration assumed in book is shown in Figure 2.21.

We assume the Cartesian coordinate system $Ox_1x_2x_3$ to be tied to the object, its axis Ox_3 coinciding with the object's axis, axis Ox_1 being perpendicular to the wing plane, and the unit-vector of axis Ox_2 complementing the system to the right-hand triad. In this coordinate system, the illumination direction denoted by vector $\vec{R}^0$ is determined by its elevation angle φ (the angle between this vector and plane Ox_2x_3) and by its azimuth θ (the angle between axis Ox_3 and projection of vector $-\vec{R}^0$ onto the plane Ox_2x_3). In this case, this vector has the following components: $\vec{R}^0 = \{-\sin\varphi, -\cos\varphi\sin\theta, -\cos\varphi\cos\theta\}$ Vector that characterizes the receiving direction $\vec{r}^0$ is determined by its elevation angle φ_1 and the bistatic angle β of spacing between projections of $-\vec{R}^0$ and $\vec{r}^0$ onto the plane Ox_2x_3, so $\vec{r}^0 = \{\sin(\varphi_1), \cos(\varphi_1)\sin(\theta+\beta), \cos(\varphi_1)\cos(\theta+\beta)\}$. Horizontal polarization vector of illumination signal $\vec{p}_h$ is parallel to the plane Ox_2x_3, and the vertical polarization vector of illumination signal $\vec{p}_v$ complements the vectors $(\vec{p}_v, \vec{p}_h, \vec{R}^0)$ to the right-hand triad.

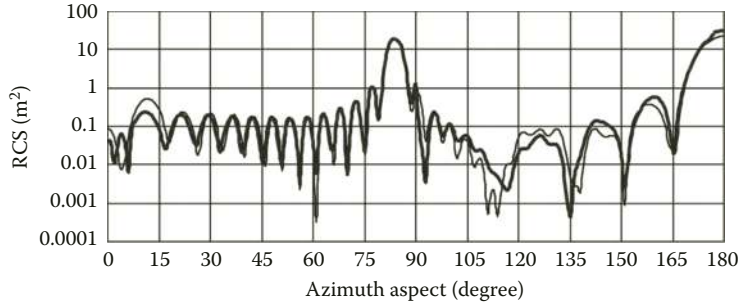

FIGURE 2.20 The cone–sphere RCS versus azimuth aspect.

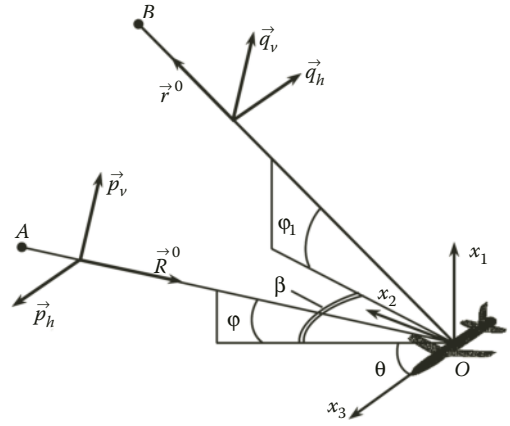

FIGURE 2.21 Radar system configuration assumed for studying scattering objects.

In the same way, we define the horizontal and vertical polarizations for the reception direction $\vec{r}^{\,0}$ (Figure 2.21).

We now show some RCS computation results for the model of cruise missile presented in Figure 2.22 versus illumination and reception aspect in case of monostatic radar, and versus bistatic angle in case of bistatic radar.

RCS was computed for both the model with perfectly conducting surface and the model covered with RAM. The smooth parts of the latter model were assumed to be covered with thin (1.3 mm) RAM layer, its relative permittivity and permeability being $\varepsilon_1' = 20 + j0.1$ and $\mu_1' = 1.35 + j0.8$. The edges of the model's wings were assumed to be covered with the same RAM of toroidal shape, its radius being 1 mm. The model was assumed to be illuminated with the signal at $\lambda = 3$ cm wavelength (frequency $f = 10$ GHz). The missile model length along its longitudinal axis was 6300 mm, the wingspan was 3400 mm.

Figure 2.23 shows RCS dependencies versus azimuth aspect given monostatic radar configuration. Elevation angle is $\varphi = 0°$. Both model illumination and signal reception were done at vertical polarization (purple line) and horizontal one (blue line). The model RCS is small at nose-on aspects ($\theta \approx 0°$) and gradually increases to the maximum when the angle approaches side-on aspects ($\theta \approx 90°$). As can be seen from the Figure 2.23, the RCS values for two polarizations coincide for almost all aspects. The only exception is the azimuth aspects, at which local edge scatterers

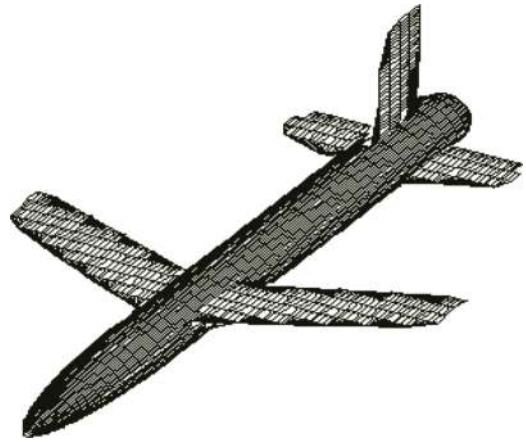

FIGURE 2.22 Cruise missile model.

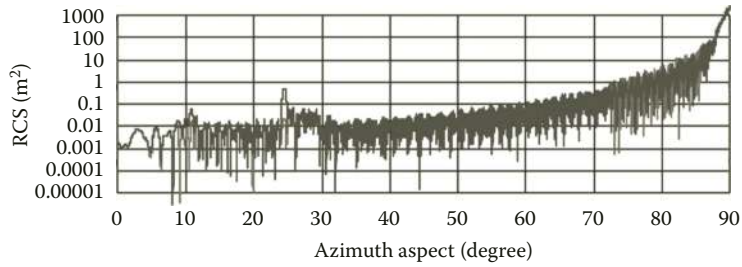

FIGURE 2.23 **(See color insert.)** RCS of the cruise missile model versus azimuth aspect given its illumination in the plane of wings.

contribute significantly to the model RCS. For instance, given aspect angles $\theta \approx 10°$ and $\theta \approx 24°$, the RCS at horizontal polarization is higher than that at vertical one. The latter is due to intense echoes from horizontal edges of wings and tail planes. Given the aspect angles greater than 75°, the RCS values at vertical polarization can go above those at horizontal one, which is due to echoes from the edges of vertical stabilizer.

In the high-frequency domain under consideration, the object's RCS and its scattered field are fast oscillating functions versus frequency (Figure 2.24). This is due to the frequency dependence of phase differences between fields scattered from different parts of the model as well as by significant change in the Fresnel zone pattern over the object's surface given even the slightest changes in the illumination signal frequency. Therefore, obtaining reliable RCS estimates necessitates averaging over frequency range that is several times wider than the oscillation period of RCS frequency dependence (Figure 2.24).

Figure 2.25 shows averaged RCS dependencies similar to those shown in Figure 2.23. Averaging was carried out by RCS values at 50 fixed frequencies evenly spread over frequency range of $f = 9.95$–10.05 GHz. Both here and in Figures 2.26 and 2.27 below, the thin line is for illumination and reception at vertical polarization, and the bold line is for illumination and reception at horizontal one.

It is worth mentioning that the larger part of computation time in numerical RCS evaluation by the methods proposed here is spent on calculating the field scattered from smooth surface parts. In this regard, the necessity of frequency averaging (in order to get reliable RCS estimates) leads to further increase in computation burden. One of the factors that make RCS the fast oscillating function versus frequency and illumination aspect is the corresponding dependence on these parameters of phase differences between echoes from different parts of the object surface. To decrease the influence of this factor, we propose below to use the sum of separate object parts' RCSs as a reliable RCS estimate of the RCS of object of interest. Since such sum does not account for phase differences of fields scattered from different object's parts, then such RCS estimate is hereinafter called the "noncoherent" RCS. In its turn, the common sense coherent RCS (accounting for phase differences) is called hereinafter the "instantaneous" RCS.

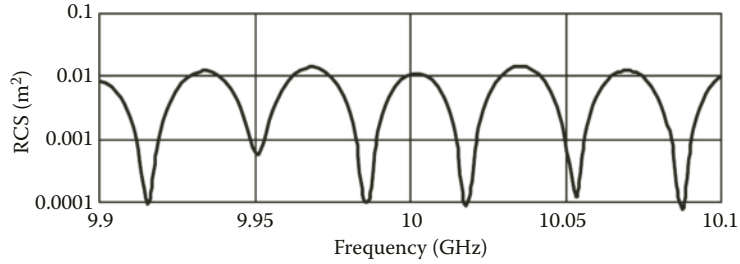

FIGURE 2.24 RCS of cruise missile model versus frequency ($\varphi = 0°$, $\theta = 20°$).

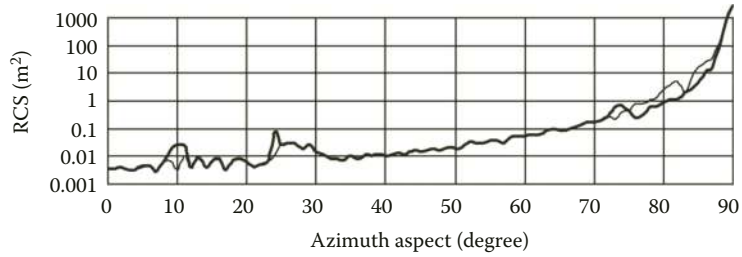

FIGURE 2.25 Frequency averaged RCS of cruise missile model versus azimuth aspect given its illumination in the plane of wings.

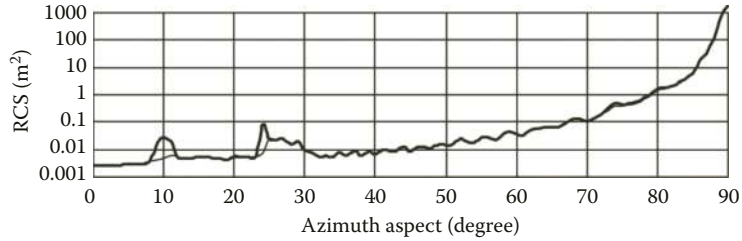

FIGURE 2.26 Noncoherent RCS of cruise missile model versus azimuth aspect given its illumination in the plane of wings.

Particularly, the surface of cruise missile model (Figure 2.22) is split into 11 smooth and 15 edge scattering parts (elements). For instance, the missile body is split into six elements, three of them form the upper surface part (nose, fuselage, and tail) and other three complete the lower part of the body. Separate smooth parts are also the surfaces of wings and empennage except for some vicinity of sharp edges.

Figure 2.26 shows noncoherent RCS of cruise missile model versus azimuth aspect given its illumination in plane of wings.

The noncoherent RCS versus azimuth aspect is practically the same as the frequency averaged instantaneous one shown in Figure 2.25. We can state that values of noncoherent RCS are good and quite reliable RCS estimates given certain frequency and aspect ranges. Besides, the values of noncoherent RCS are obtained by computation at single frequency that lightens computation burden and saves time.

Figure 2.27 shows the noncoherent RCS versus azimuth aspect (for monostatic radar) and versus bistatic angle (for bistatic radar). Figure 2.27a shows the RCS versus azimuth aspect given elevation angle –20° (target illumination from below), and Figure 2.27b shows similar dependence given elevation angle +20° (target illumination from above). In case of illumination from below, the mean RCS value is lower than in case of illumination from above. The peaks of dependencies are close by amplitude, which is determined by scattering of radar wave at local edge scatterers. The RCS outside these peaks is determined by wave scattering at smooth part of the object surface. Since the lower part of the missile model body is of smaller curvature than that of upper part, then the echo signal is weaker given the target illumination from below than that given its illumination from above. Figure 2.27c shows the RCS versus elevation angle given azimuth aspect of 0°.

Figure 2.27d shows the RCS of the model versus bistatic angle given elevation angle of illumination and reception equal to 0° and azimuth angle of illumination also equal to 0° (radar illumination is along the object's axis and signal reception is in plane of wings).

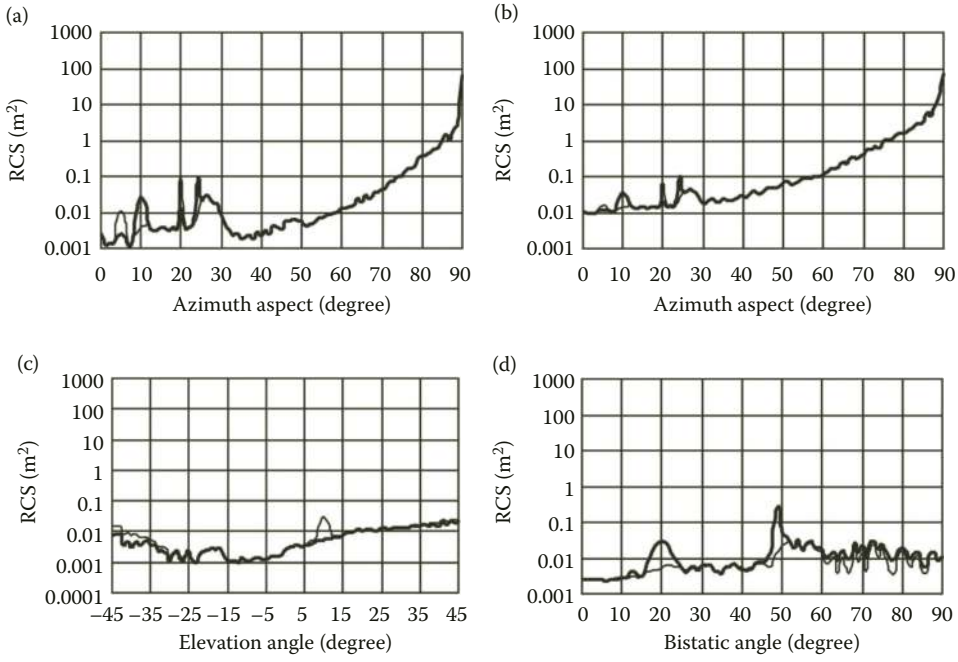

FIGURE 2.27 Noncoherent RCS dependencies for different aspects and bistatic angles.

The latter plot practically coincides with the one shown in Figure 2.26 except that it is stretched along the argument axis by the factor of two. For instance, in Figure 2.26 the main peaks of the plot that are determined by scattering at local edge parts appear at azimuth aspects of 10° and 24°. Similar peaks in Figure 2.27d appear at aspects of 20° and 48°, respectively. Given target illumination at azimuth aspect of 0°, such values of bistatic angle correspond to specular reflection from the edges, which provide sharp RCS increase at azimuth aspects of 10° and 24° given monostatic radar configuration. The latter means that given target illumination along its axis and bistatic radar configuration the RCS peaks appear at bistatic angles that are twice as great as azimuth aspect angles given monostatic radar configuration.

Figure 2.28 presents the noncoherent RCS of the model versus azimuth aspect of its illumination given horizontal polarization of transmit and receive wave. RCS of perfectly conducting model is shown by bold line; the thin line is for the model with nonperfectly reflecting surface. Application of RAM to the smooth parts of the model surface provides significant (by one order of magnitude) decrease in RCS level.

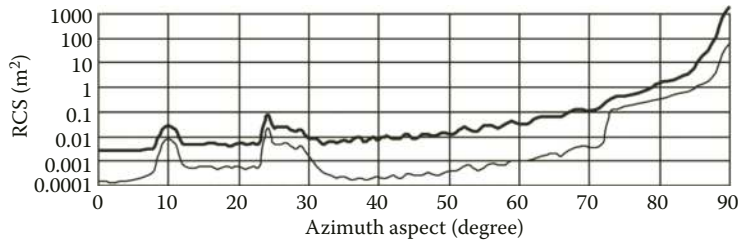

FIGURE 2.28 RCS versus azimuth aspect for the model with perfectly conducting surface and the model covered with RAM.

Application of RAM to the edge parts of the model surface provides decrease in RCS by factor of 2–3 in corresponding angular sectors.

Figure 2.29 shows noncoherent RCS for different aspect, elevation, and bistatic angles given absent and present RAM coating at the model surface. Azimuth aspect of illumination and bistatic angles are the same as for Figure 2.27. Model illumination and signal reception were at horizontal polarization. The bold line is for the model with perfectly conducting surface; the thin line is for the model provided with RAM coating.

Analysis of plots presented in Figure 2.29 shows that application of RAM to the smooth parts of the model surface in monostatic radar leads to the RCS decrease approximately by factor of 10. In case of bistatic radar (Figure 2.29d), application of RAM is less effective in reducing RCS given bistatic angles greater than 50°. Application of toroidal RAM coatings to the edge parts of the model surface reduces their reflections by factors of 1.4–5.

Computation results presented above show that the methods proposed here provide RCS evaluation of standalone objects that have surface irregularities and RAM coatings in cases of monostatic and bistatic radar configuration.

Ref. [42] described the computer software RECOTA by Boeing Aerospace that was designed for computing RCS of complex radar objects. Verification of the aforementioned software has been carried out using experimental RCS dependencies of cruise missile on the aspect of illumination. Cruise missile model presented in Figure 2.30 had perfectly conducting surface. By the data available in the reference and by using our technique (described in Section 2.1), we designed similar model of the missile surface that is presented in Figure 2.31. The surface of the model was represented by parts of 12 ellipsoids and 15 straight edges.

Figures 2.32 and 2.33 show RCS computation results obtained using our method presented in this chapter (black line) and those measured by Boeing Aerospace for the same model (gray line). The results have been obtained for the signal carrier frequency of 12 GHz.

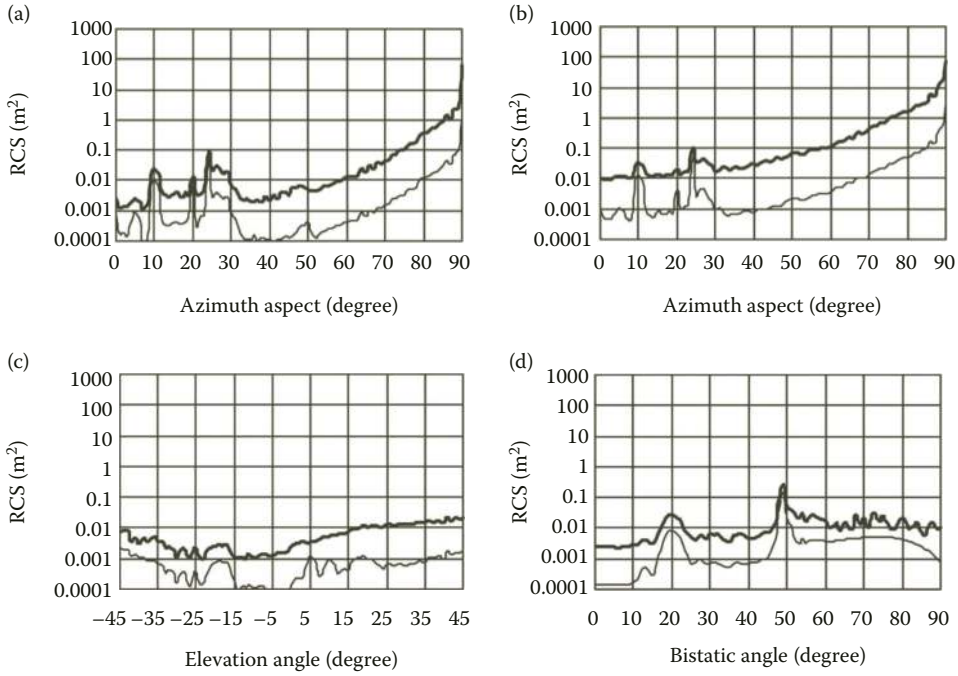

FIGURE 2.29 Noncoherent RCS dependencies for different aspects of its illumination and different bistatic angles for perfectly conducting model and that provided with RAM coating.

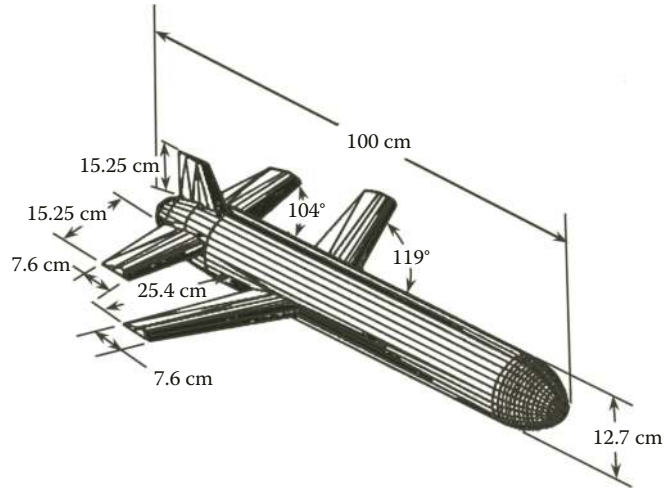

FIGURE 2.30 Model of the Boeing Aerospace cruise missile.

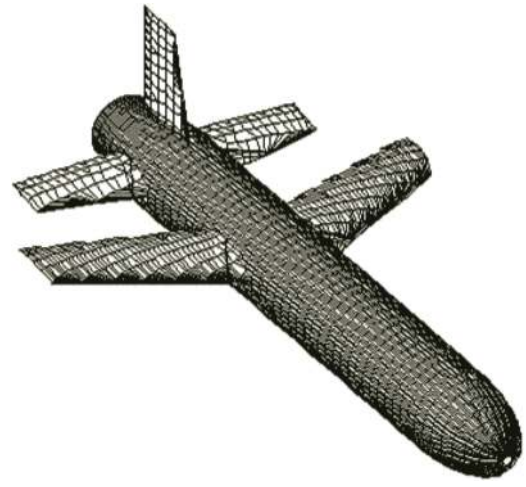

FIGURE 2.31 Model of the cruise missile used in computer simulation.

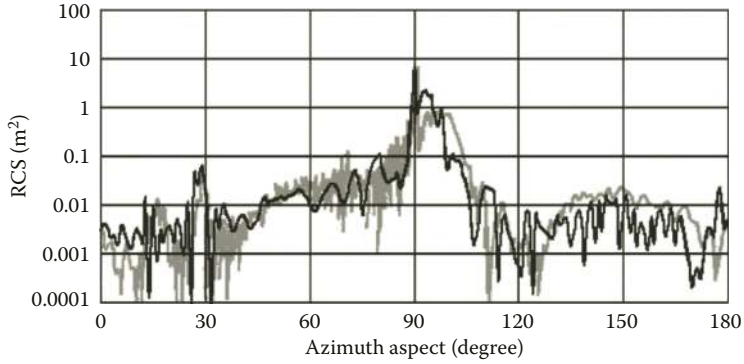

FIGURE 2.32 Computed (black line) and measured (gray line) RCS of cruise missile model versus azimuth aspect given its illumination in plane of wings at vertical polarization.

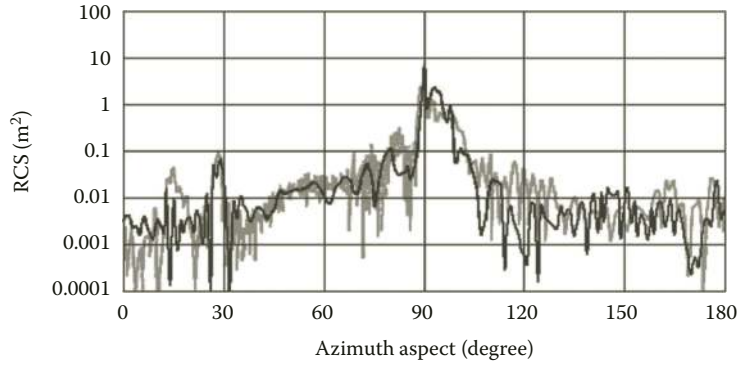

FIGURE 2.33 Computed (black line) and measured (gray line) RCS of cruise missile model versus azimuth aspect given its illumination at the angle –10.5° with respect to the plane of wings (from the lower half-sphere) at horizontal polarization.

Comparison of dependencies presented above shows good coincidence between the results of computer simulation and physical modeling. Some variations that take place (for instance, for azimuth aspects greater than 100°) can be explained by incomplete correspondence between the missile's dummy and its computer model especially in the region of the missile's tail group and rear end of fuselage. The same reasons were pointed out in Ref. [42] as causing the difference in results of experiment and computation by means of RECOTA software.

It is worth mentioning that computation results of the missile scattering characteristics by our method coincide quite well with those obtained by RECOTA software. This is another indirect proof of the proposed method adequacy to real physical processes taking place in radar scattering of electromagnetic waves by the complex-shaped objects.

2.2.7 RCS Reduction of the Complex-Shaped Object by Means of Optimal Distribution of Limited RAM Supply over Its Surface

Significant contributions into RCS of complex-shaped object are brought from regions of strong scattering at smooth convex parts of the object surface [33,34]. It is these parts of the object surface that are covered with RAM for the sake of radar camouflage. However, these RAM coatings are of considerable weight and cost. In this regard, there appears the problem of the most efficient RAM distribution over the object's surface in order to reduce its RCS in certain aspect sectors of illumination and reception given limitations on the volume of RAM that can be applied.

In this section, we develop the method for distributing RAM coating over the complex object's surface that provides RCS reduction in the preset sector of illumination and reception directions given limitations applied to the object's surface percentage that can be covered with RAM. Quasi-optimal RAM distribution method proposed here is based on a whole-numbered linear programming problem. We also present some results of RAM distribution optimization for the simplified aircraft model, as well as evaluate the decrease in its RCS in various sectors of its illumination and reception of echoes.

The object design peculiarities and technology of RAM application suggest that surface to be split into regions, each of which being either RAM-coated or perfectly conducting. In this case, the object's RCS (noncoherent) can be approximately expressed as a sum of partial RCS of these regions:

$$\sigma(\theta) = \sum_{i=1}^{N} \sigma_i(\theta), \tag{2.83}$$

where N is the number of parts the surface is split into, and θ is the aspect angle of the object illumination or echo signal reception, which is argument of RCS function. Since our ultimate goal is to receive the RCS values that were averaged over some sectors of aspect angles, then such RCS approximation expressed by Equation 2.83 is acceptable for our computations. So, here we use the method described in Section 2.2.1 for computing the partial RCSs of separate object parts.

Let us introduce the mean RCS of the whole object and mean partial RCS of the ith surface part, both corresponding to the angle sector of $\theta_1 \le \theta \le \theta_2$, as follows:

$$\bar{\sigma} = \frac{1}{\theta_2 - \theta_1} \int_{\theta_1}^{\theta_2} \sigma(\theta)\, d\theta, \tag{2.84}$$

$$\bar{\sigma}_i = \frac{1}{\theta_2 - \theta_1} \int_{\theta_1}^{\theta_2} \sigma_i(\theta)\, d\theta. \tag{2.85}$$

Having averaged expression (2.83) in the sector of angles as specified above, we obtain

$$\bar{\sigma} = \sum_{i=1}^{N} \bar{\sigma}_i. \tag{2.86}$$

It is this expression (2.86), which is the sum of local area (partial) RCSs of the object averaged in certain aspect sector of illumination and reception, that becomes subject to minimization we are about to carry out. Let us introduce some notations for the partial RCS of ith part of the complex object's surface: $\bar{\sigma}_{i1}$ is the mean partial RCS of ith surface part given that this part is perfectly conducting for this specific angle sector; $\bar{\sigma}_{i2}$ is the mean partial RCS of the same surface part given that its surface is provided with RAM coating. Now, we can represent the RCS of complex object fully covered with RAM as

$$\bar{\sigma}_2 = \sum_{i=1}^{N} \bar{\sigma}_{i2}. \tag{2.87}$$

Subtracting Equation 2.87 from Equation 2.86, we obtain

$$\bar{\sigma} - \bar{\sigma}_2 = \sum_{i=1}^{N} (\bar{\sigma}_i - \bar{\sigma}_{i2}) = \sum_{i=1}^{N} \kappa_i (\bar{\sigma}_{i1} - \bar{\sigma}_{i2}) = \sum_{i=1}^{N} \kappa_i \Delta\sigma_i. \tag{2.88}$$

Here, κ_i is the whole numbered coefficient, which equals to zero if the corresponding ith surface part is covered with RAM, and, otherwise, equals to unit if the ith surface part is perfectly conducting.

Let S_0 denote the maximum possible value of the object's surface area that can bear RAM coating, and S denote the total surface area of the object ($S_0 < S$), so that the local parts adding up to make the whole surface

$$S = \sum_{i=1}^{N} S_i. \tag{2.89}$$

We can express the limitation onto the maximum area of RAM coating using $\kappa_i (i = 1,\ldots,N)$:

$$\sum_{i=1}^{N} (1 - \kappa_i) S_i \leq S_0 \tag{2.90}$$

or in another form

$$\sum_{i=1}^{N} \kappa_i S_i \geq S - S_0. \tag{2.91}$$

Thus, the problem of quasi-optimal distribution of RAM coating over the object's surface has been reduced to the problem of whole numbered linear programming, i.e. the problem of finding binary set of coefficients κ_i that minimize expression (2.88) and satisfy the limitation (2.91). This problem can be solved by any of standard methods. For instance, it can be the additive algorithm or the method of branches and boundaries [61].

As an illustration of this method applicability, we used a simplified aircraft model (Figure 2.34) that consisted of only four three-axial ellipsoids. Ellipsoid axes were as follows: fuselage: $a = 1.25$ m, $b = 1.25$ m, $c = 9$ m; wings: $a = 0.5$ m, $b = 11$ m, $c = 2$ m; horizontal stabilizers: $a = 0.3$ m, $b = 3$ m, $c = 1$ m; vertical stabilizer: $a = 3$ m, $b = 0.3$ m, $c = 1$ m. Centers of ellipsoids that model fuselage and wings are aligned and shifted by distance of 7.6 m with respect to the centers of ellipsoids that model stabilizers.

Illumination signal frequency was assumed to be 10 GHz for the aircraft model RCS computation. We also assumed the RAM coating to have thickness of 1.3 mm, its relative permittivity and permeability being $\varepsilon_1' = 20 + j0.1$ and $\mu_1' = 1.35 + j0.8$, respectively. Material with such properties provides the 15 dB reduction in the RCS of conducting plate given normal wave incidence and the carrier frequency specified above.

To estimate the partially coated aircraft model RCS, we have split its surface into 140 parts, each having area from 0.3 to 4.5 m^2. Next, we computed the values of mean partial RCS of every surface part given it being covered and not covered with RAM for various aspect sectors of object illumination and echo signal reception.

Figure 2.35 shows mean RCS of the aircraft model versus area of optimally distributed RAM coating in the azimuth aspect sector from –10° through +10° with respect to the aircraft axis and the elevation angle sector from 0° through –8° with respect to the wing plane (monostatic radar, illumination from below).

Figure 2.36 shows similar dependence of mean RCS for bistatic radar configuration given direct nose-on illumination and echo signal reception at bistatic angles varying by azimuth aspect from –10° through +10°; elevation aspect from 0° through –8°. The mean RCS in bistatic radar decreases faster than that in monostatic radar case.

The latter is evidently due to the smaller distances the local scattering centers move along the object's surface and, consequently due to the slightly different optimal distribution of RAM coating

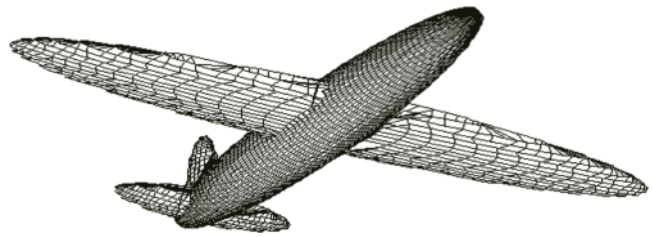

FIGURE 2.34 The aircraft model.

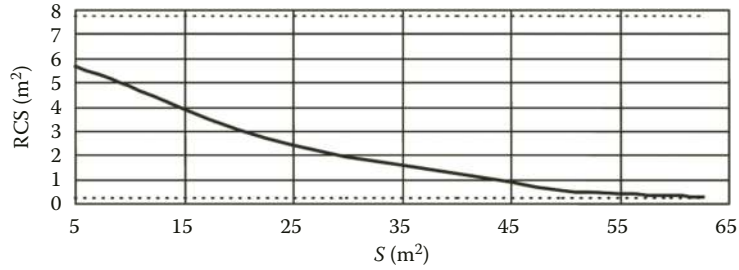

FIGURE 2.35 Mean RCS versus area of optimally distributed RAM coating in monostatic radar.

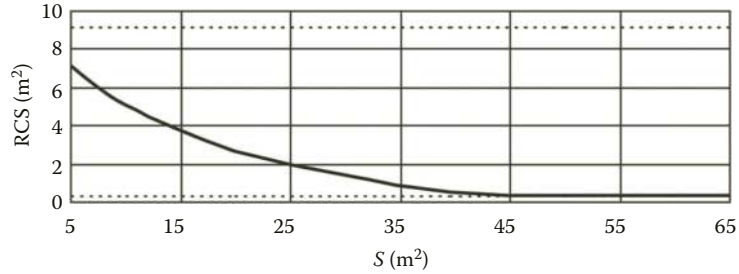

FIGURE 2.36 Mean RCS versus area of optimally distributed RAM coating in bistatic radar.

over the model's surface. Quite acceptable values of reduced RCS can be achieved while only 20–25% of the model surface is covered with RAM.

Results similar to those presented above but obtained given a wider solid angle sectors taken for averaging are given in Figures 2.37 and 2.38 for monostatic and bistatic radar, respectively.

In the latter case, the RCS was averaged over the sector of azimuth aspects from –20° through 20°, and over the sector of elevation aspects from 0° through –20°. It is worth mentioning that application of RAM coating over 50–60 m^2 of the object's surface given its optimal distribution provides almost the same reduction in the RCS as for the fully covered aircraft model.

As an example of quasi-optimal RAM coating distribution over the aircraft model's surface, we consider the two variants differing only by the aspect sectors taken for RCS averaging.

Figure 2.39 shows optimal placement of RAM-coating given monostatic radar and RCS averaging in azimuth aspects over the sector from –5° through +5°, and averaging in elevation aspects over the sector from –3° through +3°. The aircraft view, as seen from above, is presented in Figure 2.39a, and its view, as seen from below, is presented in Figure 2.39b. Placement of RAM coating is highlighted by gray and framed out.

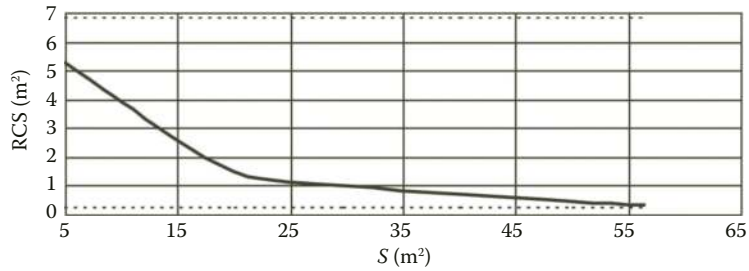

FIGURE 2.37 Mean RCS versus area of optimally distributed RAM coating in monostatic radar obtained given a wider solid angle of averaging.

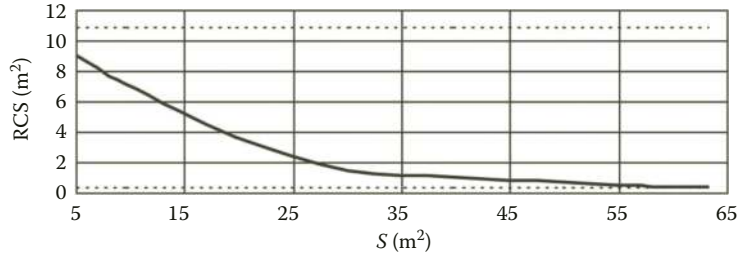

FIGURE 2.38 Mean RCS versus area of optimally distributed RAM coating in bistatic radar obtained given a wider solid angle of averaging.

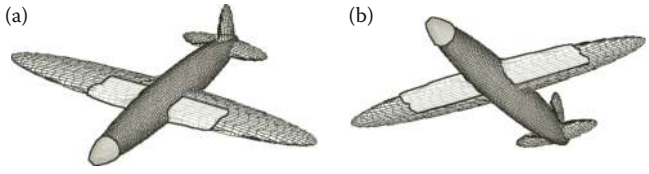

FIGURE 2.39 Optimal placement of RAM coating given monostatic radar and RCS averaging in azimuth aspects over the sector from –5° through +5°, and in elevation aspects over the sector from –3° through +3°.

Area of the RAM coating is 40 m^2. Mean RCS of aircraft model with such RAM distribution as observed nose-on is 0.68 m^2, the mean RCS of the fully covered model being 0.26 m^2 and the mean RCS of perfectly conducting model being 8.11 m^2.

Figure 2.40 shows optimal placement of RAM coating given monostatic radar and RCS averaging in azimuth aspects over the sector from –20° through +20°, and averaging in elevation aspects over the sector from 0° through –20°.

Area of the RAM coating is also 40 m^2. Mean RCS of the aircraft model given such solid angle of averaging and optimal RAM distribution is 0.74 m^2, mean RCS of fully covered model being 0.23 m^2, and mean RCS of perfectly conducting model being 6.81 m^2. Comparison of the two figures reveals significant difference between the variants of optimal distribution of limited volume of RAM given different angle sectors of aircraft observation by radar.

This method for optimizing the RAM-coating distribution over the surface of complex-shaped objects is quite simple and can be easily programmed. Using this method, we obtained approximate estimate of the level, which the RCS can be reduced to in specific aspect sectors of the object observation given optimal distribution of RAM over the part of object's surface. We came to a conclusion that in a wide aspect sector of the object observation one can significantly reduce its RCS applying RAM coating to only 20–25% of the object's surface.

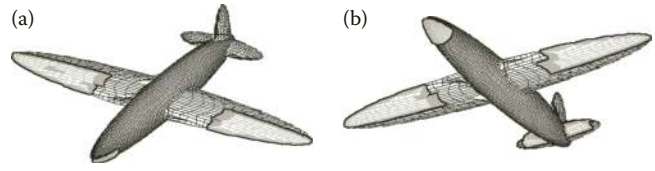

FIGURE 2.40 Optimal placement of RAM coating given monostatic radar and RCS averaging in azimuth aspects over the sector from –20° through +20°, and in elevation aspects over the sector from 0° through –20°.

2.2.8 Reduction of the Radar Scattering Level from a Local Edge Scatterer by Optimizing Its Shape

In this section, we develop the method for reducing the level of radar scattering from local edge scatterers. Method is based on the scattering characteristics computation of the object's surface fractures presented in Section 2.2.4 and on the analysis of the model fracture (edge) RCS dependence on its shape.

Practically every radar object (both ground and airborne) has surface fractures (sharp edges). Presence of such fractures can lead to an increase in the object's RCS. In this regard, it is necessary, first, to account for contribution from local edge scatterers into total field scattered by the object; and, second, to take all possible measures for decreasing the scattering level from edges.

In our computations here, we use the method for evaluating the contribution from local edge scatterers provided with RAM coating into total field scattered from the object [34,55]. The method is based on solution of the simulative problem of arbitrary incidence of plane electromagnetic wave onto perfectly conducting wedge with cylindrically shaped radar absorbent on its rib [46].

To illustrate the method, let us consider the straight sharp edge 0.6 m long (Figure 2.41). External angle of the wedge representing this edge equals to 360° (the wedge is flat). Wave incidence is in plane of wedge's faces, azimuth angle of 0° corresponding to normal incidence of wave onto the edge. Azimuth angles of –90° and 90° correspond to the wedge illumination along the straight edge. Incident wave polarization vector $\vec{p}$ is parallel to the wedge's faces. Illumination signal wavelength is 3 cm. Figure 2.42 shows the RCS of straight edge versus azimuth aspect angle of its radar observation in monostatic radar configuration.

The highest peak of RCS dependence corresponds to normal incidence of illuminating wave onto the edge (0.08 m^2). The major lobe width by the half power level is about one-and-a-half degrees. Despite the relatively narrow angle sector, in which this edge can contribute significantly into total scattered field, the problem of reducing the maximum RCS level of the edge given arbitrary aspect of its radar observation or given certain sector of aspects (for instance, RCS reduction at zero azimuth aspect) can arise.

As an alternative to the straight edge, we consider the following variants: single saw tooth-shaped edge (Figure 2.43a), triple saw tooth-shaped edge (Figure 2.43b), the edge shaped as a circular segment (Figure 2.43c), the edge shaped as triple circular segment (Figure 2.43d). In every case

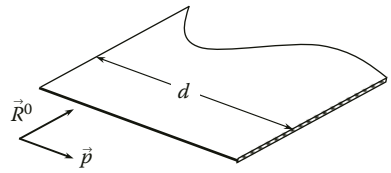

FIGURE 2.41 Straight edge.

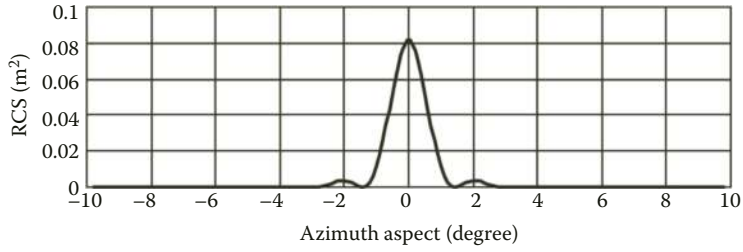

FIGURE 2.42 Straight edge RCS versus azimuth aspect.

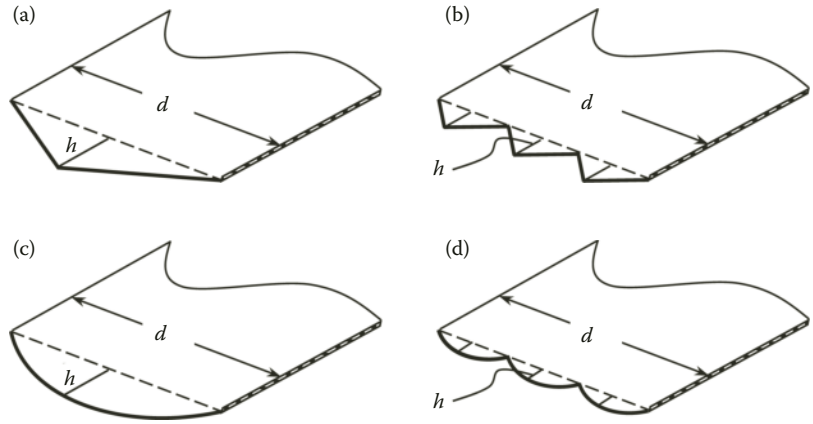

FIGURE 2.43 Variants of shaping the local edge scatterer.

to be considered, the distance between the edge ends d is constant. As a variable parameter in every of four examples given below, we set the height of saw tooth (or circular segment) h.

Figure 2.44 shows the RCS of edge shaped as single saw tooth (Figure 2.43a) versus azimuth aspect. Thin line is for the tooth height $h = 0.05$ m, the bold line is for tooth height $h = 0.10$ m. Maxima of scattering correspond to the directions of normal wave incidence onto the edge segments.

As it follows from the plots, replacement of straight edge with the saw tooth-shaped one leads to fourfold decrease in its maximum RCS and to shift of the maximum scattering direction to the side aspects. The "payment" for this decrease in appearance of two maximum scattering directions instead of one as well as the major lobe spread up to 4°. The amplitude and spread of the scattering lobes keep their values despite the change of the saw tooth height h since they are determined by edge segment length.

Figure 2.45 shows the RCS of edge shaped as triple saw tooth (Figure 2.43b) versus azimuth aspect. This is the edge shaping type that is used for decreasing the radar scattering level from edges of the B-2 bomber air intakes [48]. The thin line is for the tooth height $h = 0.02$ m, and the bold line is for the tooth height $h = 0.05$ m. As in case of single saw tooth-shaped edge, scattering maxima correspond to normal wave incidence onto partial edge segments. The RCS maxima themselves are lower than in previous case. Difference in the major lobe amplitudes in Figure 2.45 is due to the constructive interference of echoes from partial edge segments. The spread of RCS lobes now is about 10°, which is due to further decrease in straight segment length.

While evaluating the contribution from rectilinear and curved (elliptical) fractures into total field scattered by the complex-shaped object [34], we figured out that curved surface fractures contribute less by RCS absolute value but in the wider angular sectors.

Figure 2.46 shows the RCS of edge shaped as single circular segment (Figure 2.43c) versus azimuth aspect. The gray line in Figure 2.46a is for the segment height of 0.02 m, the thin line is for

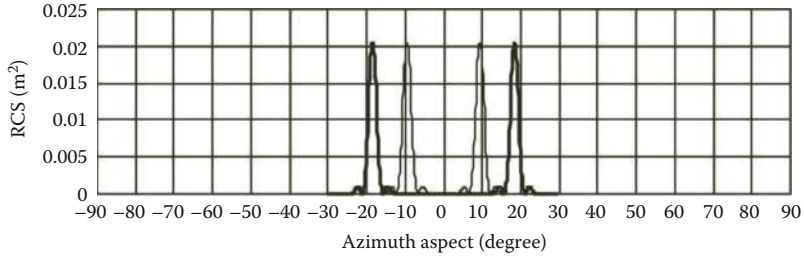

FIGURE 2.44 RCS of edge shaped as single saw tooth versus azimuth aspect.

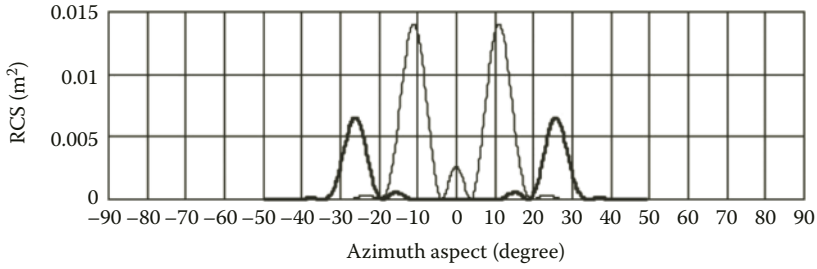

FIGURE 2.45 RCS of edge shaped as triple saw tooth versus azimuth aspect.

the segment height of 0.05 m, and the black bold line is for the segment height $h = 0.07$ m. The black bold line in Figure 2.46b is for the RCS dependence given the circular segment height of 0.09 m, the thin line is for the segment height of 0.10 m, and the gray line is for the segment height of 0.15 m.

As it seen from the dependencies shown above, the use of segment with $h = 0.02$ m height already leads to eightfold reduction in the edge's RCS as compared to that of straight edge, but it occurs at the expense of the major lobe spread increase up to 12°. Further increase of the segment height leads to further widening of the angular sector, in which the edge's RCS exceeds the value of 0.001 m^2.

Analysis of plots in Figure 2.46 shows that the most acceptable segment height is $h = 0.07$ m. The angular sector width, in which the edge's RCS exceeds the level of 0.001 m^2, is about 50°. However, in this case the RCS value oscillates around 0.002 m^2 level almost everywhere except in the two regions of local maxima (reaching 0.0035 m^2). It is worth mentioning that the segment height must be chosen with regard to design features of the object bearing the local edge scatterer of interest. Besides, the use of rounded edges with the segment height greater than 5 cm is also acceptable from the RCS reduction viewpoint since its RCS at any aspect of radar observation does not get greater than 0.005 m^2.

Figure 2.47 shows the RCS of edge shaped as triple circular segment (Figure 2.43d) versus azimuth aspect of observation. The thin line in Figure 2.47 is for the segment's height of 1 cm, the black bold line is for segment's height of 2 cm, and the gray line is for the segment's height of 5 cm. All the three dependencies are of oscillating nature, which is due to interference of partial echoes from separate segments. The RCS maxima for most of the dependencies do exceed the level of 0.01 m^2, which is higher than those for edge shaped as single circular segment. The spread of lobes

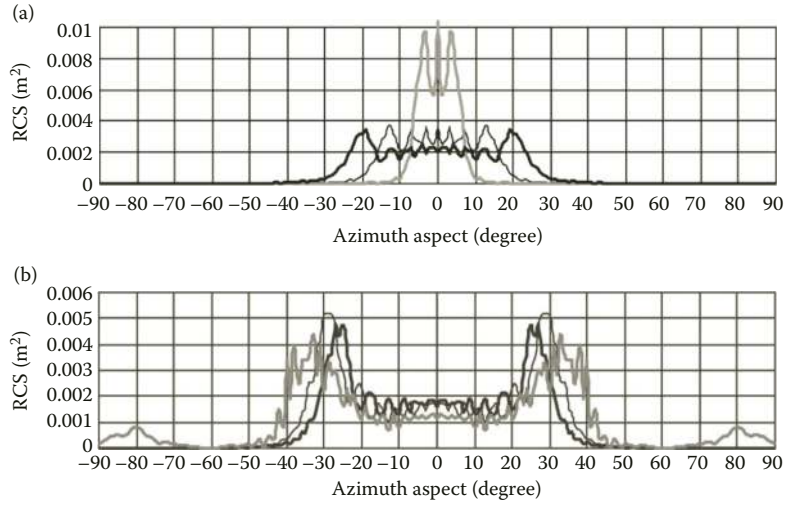

FIGURE 2.46 RCS of edge shaped as single circular segment.

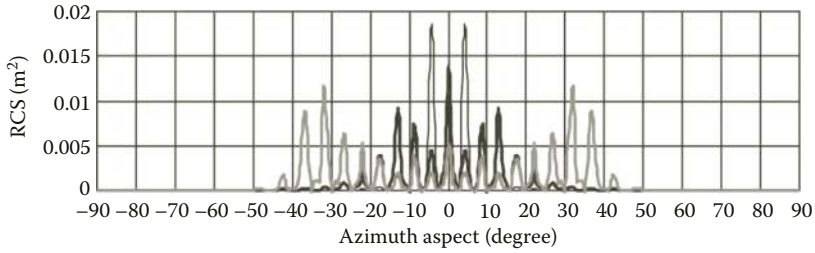

FIGURE 2.47 RCS of the edge shaped as triple circular segment versus azimuth aspect.

does not exceed the value of 2°, and given the sector of observation aspects from −40° through 40° the RCS dependence has 17 peaks, most of which go higher than 0.005 m^2. Besides, all the maxima of RCS dependence given the segment's height of 2 cm are concentrated within azimuth aspects from −15° through +15° and their absolute value does not exceed 0.01 m^2.

If the edge consists of three circular segments, each one of them having the local scattering center ("specular point") at almost any illumination aspect, then we can state that values of RCS maxima would also change significantly given even small variations in the illumination signal wavelength. In this regard, the edge shaping as multiple circular segments leads to its RCS reduction in a narrow frequency range of illumination signal.

Shaping of the local edge scatterer provides significant decrease in its maximum RCS level. Shape selection for the edge is determined by the requirements to its maximum RCS and to the angular dependence of its RCS.

2.3 METHOD FOR COMPUTING SCATTERING CHARACTERISTICS OF GROUND COMPLEX-SHAPED OBJECTS

Vitaly A. Vasilets and Oleg I. Sukharevsky

The method proposed here is basically based on the scattering characteristic computation method developed above in Section 2.1 for standalone objects, but it additionally provides taking into account the underlying surface with given electromagnetic properties. Due to the presence of the "air–ground" interface, there are two mutually overlapping illuminated regions, the first being created by the direct incident wave, and the second being created by the wave scattered from the ground surface. Integral representations obtained below allow us to single out the four basic wave propagation paths in the system formed due to the object's standing on the ground (Figure 2.48): "transmitter–object–receiver," "transmitter–object–ground–receiver," "transmitter–ground–object–ground–receiver," and "transmitter–ground–object–receiver." The method is also applicable for the ground objects provided with RAM coating and for the objects with surface fractures.

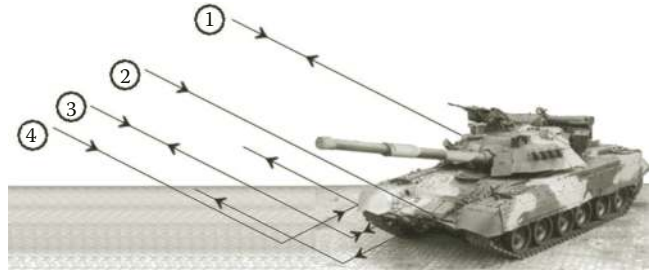

FIGURE 2.48 Basic paths of electromagnetic wave propagation for the case of ground object illumination.

2.3.1 Plane Electromagnetic Wave Scattering at Perfectly Conducting Object Placed in the Vicinity of Homogeneous Half-Space

We present here the approximate method for computing characteristics of plane wave backscattering from electrically large object with perfectly conducting surface that also has small curvatures, the object itself being in the interface vicinity of homogeneous half-space (possibly having complex parameters).

An importance of such problem formulation is conditioned particularly by the necessity of getting *a priori* information on backscattering characteristics of ground objects for the sake of their detection and identification by radar.

The method is based on integral field representations that follow from the Lorentz reciprocity theorem when electromagnetic interaction is accounted for between perfectly conducting scatterer and the interface of homogeneous half-space.

Computation of scattering from the object placed above the underlying surface must account for their mutual interaction, that is, one must consider the "perfectly conducting object—half-space with the ground properties" system (Figure 2.49) and account for the intrasystem interactions.

In order to account for the underlying surface influence on the scattering, one has to consider four basic paths of electromagnetic wave propagation. Multiple reflections of backscattered wave can be neglected, in first approximation, as the second-order effects.

Let $\vec{\mathcal{E}}(\vec{x}|\vec{x}_0, \vec{p})$, $\vec{\mathcal{H}}(\vec{x}|\vec{x}_0, \vec{p})$ be the field excited by the point dipole placed at point x_0, the field being characterized by the vector-moment $\vec{p}$ in the presence of half-space V^1. The field $\vec{\mathcal{E}}(\vec{x}|\vec{x}_0, \vec{p})$, $\vec{\mathcal{H}}(\vec{x}|\vec{x}_0, \vec{p})$ satisfies the Maxwell equation system:

$$\left.\begin{aligned} \operatorname{rot}\vec{\mathcal{E}} &= j\omega\mu_0\vec{\mathcal{H}} \\ \operatorname{rot}\vec{\mathcal{H}} &= -j\omega\varepsilon\vec{\mathcal{E}} - j\omega\vec{p}\delta(\vec{x}-\vec{x}_0) \end{aligned}\right\}, \tag{2.92}$$

where $\varepsilon = \begin{cases} \varepsilon_0, & x_0 \in V^0, \\ \varepsilon_1, & x_0 \in V^1. \end{cases}$

It should be noted that if the main part of illumination signal spectrum is situated above the 50 MHz mark, then dispersive properties of the propagation medium with parameters of the ground can be neglected [62].

Equation system (2.92) is complemented with boundary conditions at the propagation media interface D:

$$\vec{\mathcal{E}}^{+T} = \vec{\mathcal{E}}^{-T}; \quad \vec{\mathcal{H}}^{+T} = \vec{\mathcal{H}}^{-T}. \tag{2.93}$$

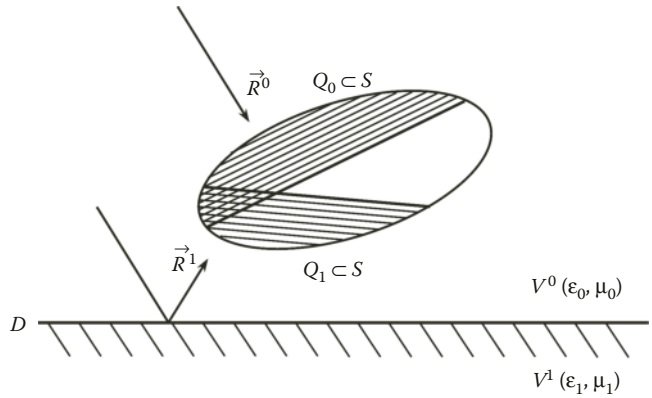

FIGURE 2.49 The "object–ground" system.

Let us consider field $\vec{E}(\vec{x}), \vec{H}(\vec{x})$ excited by the definite volume current density $\vec{J}$ in V^0 given presence of half-space V^1 and perfectly conducting object S in it. Given all these conditions, the Maxwell equations take the following form:

$$\left.\begin{aligned} \operatorname{rot}\vec{E} &= j\omega\mu_0\vec{H} \\ \operatorname{rot}\vec{H} &= -j\omega\varepsilon\vec{E} + \vec{J} \end{aligned}\right\}. \tag{2.94}$$

Let us note that the region V^0 is bounded by $D \bigcup S$ (Figure 2.49). Boundary conditions at the interface D, which are as follows:

$$\vec{E}^{+T} = \vec{E}^{-T}, \quad \vec{H}^{+T} = \vec{H}^{-T}, \tag{2.95}$$

are complemented with requirement to the tangential component of electric field intensity to be equal to zero at the surface S, that is

$$\vec{E}^T\Big|_S = 0. \tag{2.96}$$

Now, we are ready to apply the Lorentz reciprocity theorem to the fields $\vec{E}(\vec{x}), \vec{H}(\vec{x})$, and $\vec{\mathcal{E}}(\vec{x}|\vec{x}_0, \vec{p}), \vec{\mathcal{H}}(\vec{x}|\vec{x}_0, \vec{p})$ in the region V^0 given that $x_0 \in V^0$

$$\int_D (\vec{E}^{-T}\cdot\vec{\mathcal{H}}^{-\perp} - \vec{\mathcal{E}}^{-T}\cdot\vec{\mathrm{H}}^{-\perp})\mathrm{d}S - \int_S \vec{\mathcal{E}}^{-T}\cdot\vec{H}^{-\perp}\mathrm{d}S = -\int_{V^0} (j\omega\delta(\vec{x}-\vec{x}_0)\vec{p}\cdot\vec{E} + \vec{J}\cdot\vec{\mathcal{E}})\mathrm{d}V. \tag{2.97}$$

Now, using the superposition principle and filtering property of δ-function, we get the following:

$$j\omega\vec{p}(\vec{E}(\vec{x}_0) - \vec{\mathcal{E}}(\vec{x}_0)) = \int_S \vec{\mathcal{E}}^T\cdot\vec{H}^{\perp}(\vec{x})\mathrm{d}S - \int_D (\vec{E}^{-T}\cdot\vec{\mathcal{H}}^{-\perp} - \vec{\mathcal{E}}^{-T}\cdot\vec{H}^{-\perp})\mathrm{d}S, \tag{2.98}$$

where $\vec{\mathcal{E}}(\vec{x}_0)$ is the field excited in half-space V^0 by the predetermined distribution of extraneous currents $\vec{J}$ given that scatterer S is absent.

Having applied the Lorentz reciprocity theorem to the same fields in the region V^1, we obtain

$$\int_D (\vec{E}^{+T}\cdot\vec{\mathcal{H}}^{+\perp} - \vec{\mathcal{E}}^{+T}\cdot\vec{H}^{+\perp})\mathrm{d}S = 0. \tag{2.99}$$

Here, $\vec{A}^T = \vec{A} - \vec{n}(\vec{A}\cdot\vec{n})$, $\vec{B}^{\perp} = (\vec{n}\times\vec{B})$, and $\vec{n}$ is the unit-vector of the normal to the corresponding boundary.

Summing expressions (2.98) and (2.99) term by term and accounting for the boundary conditions (2.93), (2.95), and (2.96), we can obtain the following integral representation:

$$j\omega\vec{p}\cdot(\vec{E}(\vec{x}_0) - \vec{\mathcal{E}}(\vec{x}_0)) = \int_S \vec{\mathcal{E}}(\vec{x}|\vec{x}_0, \vec{p})\cdot\vec{H}^{\perp}(x)\mathrm{d}S. \tag{2.100}$$

Let the vector $\vec{x}_0$ be directed toward the illumination source, $-\vec{R}^0$, and let it have the length r:

$$\vec{x}_0 = -r\vec{R}^0. \tag{2.101}$$

Assuming that $r \to \infty$, we can represent Equation 2.100 in the following form:

$$j\omega \vec{p} \cdot (\vec{E}(\vec{R}^0) - \vec{\mathcal{E}}(\vec{R}^0)) = \int_S \vec{\mathcal{E}}^T(x|\vec{R}^0, \vec{p}) \cdot \vec{H}^{\perp}(x)\,\mathrm{d}S, \tag{2.102}$$

where $\vec{\mathcal{E}}^T(x|\vec{R}^0, \vec{p})$ is the field excited by plane wave

$$\vec{\mathcal{E}}_0(x|\vec{R}^0, \vec{p}) = k_0^2 \omega \sqrt{\frac{\mu_0}{\varepsilon_0}}\, \vec{p}^0 \exp(j\, k_0(\vec{R}^0 \cdot \vec{x}))\Omega(k_0 r), \tag{2.103}$$

$$\Omega(k_0 r) = \frac{1}{4\pi}\frac{\exp(jk_0 r)}{k_0 r}, \quad \vec{p}^0 = \vec{p} - \vec{R}^0(\vec{p} \cdot \vec{R}^0),$$

that propagates in the direction $\vec{R}^0$ given that only half-space V^1 is present (scatterer S being absent); $\vec{E}(\vec{R}^0), \vec{\mathcal{E}}(\vec{R}^0)$ are the backscattering diagrams of the system under consideration given that scatterer S is present and absent, respectively.

Expression for the incident wave (2.103) has been obtained as a result of proceeding to the limit in the form of vector function:

$$\vec{\mathcal{E}}\left(\vec{x}|\vec{x}_0, \vec{p}\right) = \frac{1}{\varepsilon_0}\left[\vec{\nabla}(\vec{p} \cdot \vec{\nabla} g) + k_0^2 \vec{p} g\right], \quad g(\vec{x}, \vec{x}_0) = \frac{\exp(j\, k_0 |\vec{x} - \vec{x}_0|)}{4\pi|\vec{x} - \vec{x}_0|},$$

which expresses the field of electrical dipole placed in free space and localized to the point $x_0 \in V^0$ given that x_0 goes away infinitely. Here, we use asymptotic representation of function $g(\vec{x}, \vec{x}_0)$ given that $r \to \infty$:

$$g(\vec{x}, \vec{x}_0) \sim k_0 \Omega(k_0 r) \exp(j\, k_0(\vec{R}^0 \cdot \vec{x})).$$

In general case, plane wave (2.103) is incident obliquely onto the interface D between the two media. In this case, the field scattered in the direction $-\vec{R}^0$ can be assumed to be equal to zero. So, the field above surface D given absent scatterer S can be expressed as follows:

$$\vec{\mathcal{E}}(\vec{x}|\vec{R}^0, \vec{p}) = k_0^2 \omega \sqrt{\frac{\mu_0}{\varepsilon_0}}\left[\vec{p}^0 \exp(j\, k_0(\vec{R}^0 \cdot \vec{x})) + \vec{p}^1 \exp(j\, k_0(\vec{R}^1 \cdot \vec{x}))\right]\Omega(k_0 r), \tag{2.104}$$

where $\vec{R}^1 = \vec{R}^0 - 2\vec{n}(\vec{R}^0 \cdot \vec{n})$ is the propagation direction of wave reflected from the plane of surface D, and $\vec{p}^1$ is the vector coefficient of reflection from underlying surface, this coefficient being computed using Equations 2.12 and 2.13 according to method presented in Ref. [29].

Finally, we consider that the scatterer's surface S is illuminated by, first, direct plane wave propagating in direction $\vec{R}^0$ and, second, the wave reflected from the plane D.

While doing so, we need also to account for phase differences of the illumination wave that occur due to reflection from the interface D. To illustrate this, we assume, in some coordinate system $Ox_1x_2x_2$, the point M at the object's surface to be determined by the radius-vector $\vec{x}$ and let the point A be the point of wave reflection at the plane D, from which reflected ray arrives to point M at S (Figure 2.50).

The plane D is determined by the equality

$$(\vec{x} \cdot \vec{n}) + h = 0, \tag{2.105}$$

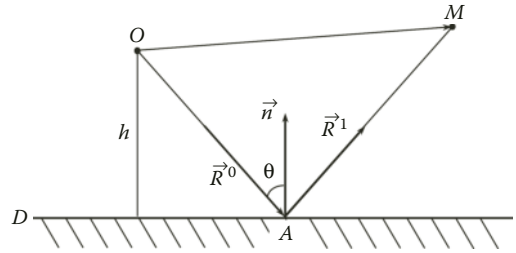

FIGURE 2.50 To the issue of incident wave reflection from underlying surface.

where h is the distance from plane D to the coordinate system origin along the unit-vector of normal $\vec{n}$ to the plane D, and $\vec{x}$ is the radius vector of a point at the plane.

Let us introduce the following notation $\vec{a} = \vec{OA} = \vec{x} - \rho\vec{R}^1$, $\vec{\xi} = \vec{AM} = \vec{x} - \vec{a} = \rho\vec{R}^1$, where the value ρ is determined from condition of point A belonging to plane D:

$$\rho = \frac{(\vec{x}\cdot\vec{n}) + h}{(\vec{R}^1\cdot\vec{n})}. \tag{2.106}$$

Now, the incident wave (2.103) can be presented as

$$\begin{aligned}\vec{E}_0(\vec{x}|\vec{R}^0,\vec{p}) &= k_0^2\omega\sqrt{\frac{\mu_0}{\varepsilon_0}}\vec{p}^0\exp(jk_0(\vec{R}^0\cdot(\vec{a}+\vec{\xi})))\Omega(k_0r)\\ &= k_0^2\omega\sqrt{\frac{\mu_0}{\varepsilon_0}}\Omega(k_0r)\vec{p}^0\exp(jk_0(\vec{R}^0\cdot\vec{a}))\exp(jk_0(\vec{R}^0\cdot\vec{\xi})) = \hat{\vec{p}}^0\exp(jk_0(\vec{R}^0\cdot\vec{\xi})),\end{aligned}$$

and the wave reflected from the plane D accordingly takes the form

$$\begin{aligned}\vec{E}(\vec{x}|\vec{R}^1,\vec{p}^1) &= \hat{\vec{p}}^1\exp(jk_0(\vec{R}^1\cdot\vec{\xi})) = k_0^2\omega\sqrt{\frac{\mu_0}{\varepsilon_0}}\Omega(k_0r)\vec{p}^1\exp(jk_0(\vec{R}^0\cdot\vec{a}))\exp(jk_0(\vec{R}^1\cdot\vec{\xi}))\\ &= k_0^2\omega\sqrt{\frac{\mu_0}{\varepsilon_0}}\Omega(k_0r)\vec{p}^1\exp(jk_0((\vec{R}^0-\vec{R}^1)\cdot\vec{a}+\vec{R}^1\cdot\vec{x})).\end{aligned}$$

So, the resulted field at point $\vec{x}$ of the object's surface S that accounts for phase differences between direct wave and wave reflected from plane D can be written as

$$\vec{E}(\vec{x}|\vec{R}^0,\vec{p}) = k_0^2\omega\sqrt{\frac{\mu_0}{\varepsilon_0}}\Omega(k_0r)\Big[\vec{p}^0\exp(jk_0(\vec{R}^0\cdot\vec{x})) + \vec{p}^1\exp(jk_0((\vec{R}^0-\vec{R}^1)\cdot\vec{a}+\vec{R}^1\cdot\vec{x}))\Big]. \tag{2.107}$$

Then, having accounted for Equation 2.107, from expression (2.102), we get

$$\begin{aligned}\vec{p}\cdot\vec{E}(\vec{R}^0) = -j\Omega(k_0r)k_0^2\sqrt{\frac{\mu_0}{\varepsilon_0}}\int_S[&\vec{p}^0\exp(jk_0(\vec{R}^0\cdot\vec{x}))\\ &+\vec{p}^1\exp(jk_0((\vec{R}^0-\vec{R}^1)\cdot\vec{a}+\vec{R}^1\cdot\vec{x}))]\cdot\vec{H}^{\perp}(\vec{x})\,dS.\end{aligned} \tag{2.108}$$

Let us note that $\vec{H}^{\perp}(\vec{x})$ is the current density over surface S excited by the plane wave propagating along $\vec{R}^0$ given that boundary D of half-space V^1 is present. Presence of half-space V^1 in the system under consideration leads to the appearance of additional wave incident on the object surface S that is the direct wave reflection from surface D and that propagates in the direction $\vec{R}^1$. Therefore, there are two mutually overlapping (in general) illuminated regions Q_0 and Q_1 that appear at the object's surface (Figure 2.49). In the physical optics approximation, the surface current density over illuminated smooth part of S can be presented as

$$\vec{H}^{\perp}(\vec{x}) = \begin{cases} 2\vec{n}_S \times \vec{H}_1^0, & \vec{x} \in Q_0, \\ 2\vec{n}_S \times \vec{H}_2^0, & \vec{x} \in Q_1, \end{cases} \tag{2.109}$$

where

$$\begin{aligned} \vec{H}_1^0 &= (\vec{R}^0 \times \vec{p}^0)\sqrt{\frac{\varepsilon_0}{\mu_0}}\exp(jk_0(\vec{R}^0 \cdot \vec{x})), \\ \vec{H}_2^0 &= (\vec{R}^1 \times \vec{p}^1)\sqrt{\frac{\varepsilon_0}{\mu_0}}\exp(jk_0(\vec{R}^0 - \vec{R}^1) \cdot \vec{a})\exp(jk_0(\vec{R}^1 \cdot \vec{x})). \end{aligned} \tag{2.110}$$

So, the right-hand part of Equation 2.108 can be represented as a sum of four integrals of the $\Gamma = \int\limits_{Q} f(\vec{x})\exp(jk_0\Theta(\vec{x}))\mathrm{d}S$ kind:

$$\begin{aligned} \vec{p} \cdot \vec{E}(\vec{R}^0) = -jk_0 \frac{\exp(jk_0 r)}{2\pi r}\sqrt{\frac{\mu_0}{\varepsilon_0}} \Bigg\{ & \int\limits_{Q_0} \vec{p}^0 \exp(jk_0(\vec{R}^0 \cdot \vec{x})) \cdot (\vec{n}_S \times (\vec{R}^0 \times \vec{p}^0))\sqrt{\frac{\varepsilon_0}{\mu_0}}\exp(jk_0(\vec{R}^0 \cdot \vec{x}))\mathrm{d}S \\ & + \int\limits_{Q_0} \vec{p}^1 \exp(jk_0((\vec{R}^0 - \vec{R}^1) \cdot \vec{a} + \vec{R}^1 \cdot \vec{x})) \cdot (\vec{n}_S \times (\vec{R}^0 \times \vec{p}^0))\sqrt{\frac{\varepsilon_0}{\mu_0}}\exp(jk_0(\vec{R}^0 \cdot \vec{x}))\mathrm{d}S \\ & + \int\limits_{Q_1} \vec{p}^0 \exp(jk_0(\vec{R}^0 \cdot \vec{x})) \cdot (\vec{n}_S \times (\vec{R}^1 \times \vec{p}^1))\sqrt{\frac{\varepsilon_0}{\mu_0}}\exp(jk_0((\vec{R}^0 - \vec{R}^1) \cdot \vec{a} + \vec{R}^1 \cdot \vec{x}))\mathrm{d}S \\ & + \int\limits_{Q_1} \vec{p}^1 \exp(jk_0((\vec{R}^0 - \vec{R}^1) \cdot \vec{a} + \vec{R}^1 \cdot \vec{x})) \cdot (\vec{n}_S \times (\vec{R}^1 \times \vec{p}^1)) \\ & \times \sqrt{\frac{\varepsilon_0}{\mu_0}}\exp(jk_0((\vec{R}^0 - \vec{R}^1) \cdot \vec{a} + \vec{R}^1 \cdot \vec{x}))\mathrm{d}S \Bigg\}. \end{aligned} \tag{2.111}$$

Here, the two first integrals are to be integrated over illuminated region Q_0, and the other two integrals are to be integrated over illuminated region Q_1.

The functions corresponding to $f(\vec{x})$ and $\Theta(\vec{x})$ in every integral are slow oscillating. In their turn, the functions in the integrand of Equation 2.111 are fast oscillating and they necessitate application of cubature formulas described in Section 2.2.2.

In a similar manner, we can obtain the expression for computing the field scattered from local edge scatterers that accounts for underlying surface. However, in this case we need the bistatic solution of the problem of wave scattering at local edge scatterer [31].

In Section 2.3.3, we shall also present the method for evaluating contributions from local edge scatterers provided with RAM coating into the RCS of ground object with nonperfectly reflecting surface.

Using expressions obtained for the fields scattered from smooth parts of the surface and from local edge scatterers, we can evaluate total field scattered from the object placed close to the underlying surface.

2.3.2 Scattering Characteristics of Perfectly Conducting Model of a Ground Object

To prove the applicability of method developed above, we simulated the process of plane electromagnetic wave scattering from the model of tank (Figure 2.51) standing on the ground.

The model's length was 8 m, its width was 3 m, and its height was 2 m. We assumed the underlying surface to consist of brown loam of equivalent dry density of 1.2 g/cm^3. The dry soil properties were as follows (moisture content was 1%): $\varepsilon' = 3 + j0.38$, $\mu' = 1 + j0$; and the moist soil properties were as follows (moisture content was 20%): $\varepsilon' = 17 + j0.9$, $\mu' = 1 + j0$.

As the elevation angle, we consider the angle between the normal to ground and the incidence direction vector. So, in case of the object illumination parallel to the ground this elevation angle is 0°. Azimuth aspect is counted off the head-on direction.

RCS computation for the model was carried out in the azimuth aspect sector from 0° through 90°. The elevation angle was 30°. Illumination signal frequency was assumed equal to 10 GHz ($\lambda = 0.03$ m).

Figure 2.52 shows instantaneous RCS of perfectly conducting tank model standing on dry soil versus azimuth aspect. RCS dependence at horizontal polarization is shown with bold line, and the thin line is for the RCS dependence at vertical polarization. Figure 2.53 shows similar dependencies for the tank standing on moist soil.

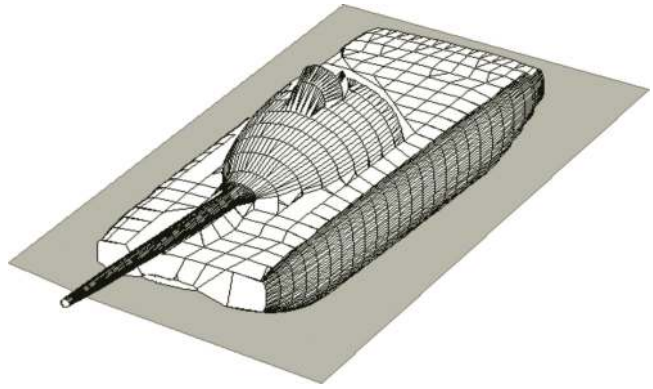

FIGURE 2.51 The model of a tank.

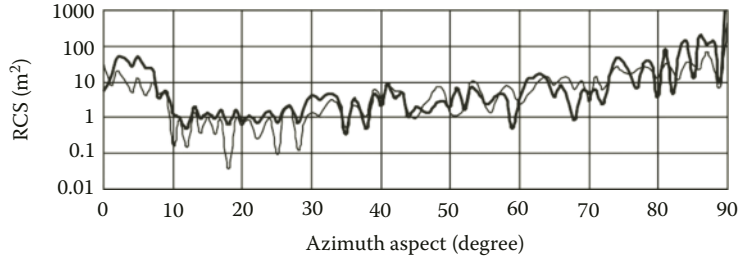

FIGURE 2.52 Instantaneous RCS of the tank model standing on dry soil versus azimuth aspect.

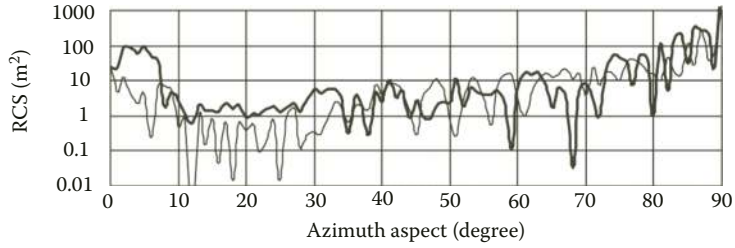

FIGURE 2.53 Instantaneous RCS of the tank model standing on moist soil versus azimuth aspect.

Maximum RCS values take place at head-on and side-on model illumination regardless of incident wave polarization and soil type. The RCS at vertical polarization is lower than that at horizontal polarization through almost all the aspects. This can be explained by the smaller contribution from underlying surface given vertical polarization of illumination signal. At some aspects, the vertical polarization RCS goes higher than that at horizontal polarization. The latter is due to the stronger scattering from vertical edges of the model surface than that from the horizontal ones. In case of wet soil, the model RCS is higher than that in case of dry soil; the difference is especially observable at horizontal polarization of illumination signal.

In the high-frequency range being considered, the RCS of an object, like scattered field itself, is the fast oscillating function of frequency.

When objects get sounded by real radar signals, their RCS values become somewhat averaged over the frequency ranges corresponding to the signal bandwidths. As it is shown in Figure 2.24, reliable estimates of RCS can only be obtained given their averaging in the frequency range at least 5 MHz wide. Figure 2.54 shows the plot of tank model RCS versus azimuth aspect given that it stands on dry soil, which correspond to those shown in Figure 2.52. The RCS values were averaged in the frequency range of $f = 9.95–10.05$ GHz. To achieve this, we took 50 RCS values at fixed frequencies evenly spaced over this range. Figure 2.55 shows the averaged RCS of the tank model standing on moist soil versus azimuth aspect, these dependencies corresponding to those shown in Figure 2.53. The bold line is for the RCS at horizontal polarization, and the thin line is for the RCS at vertical polarization.

The plots of Figures 2.54 and 2.55 are smoother than those in Figures 2.52 and 2.53. This is due to RCS averaging in frequency and due to corresponding decrease in the influence of coherent summation of contributions from different parts of the model's surface.

To save the computation time when computing reliable RCS estimates, we computed the corresponding values of noncoherent RCS for the same model. Figure 2.56 shows the noncoherent RCS of the tank model standing on dry soil versus azimuth aspect. Figure 2.57 shows the same dependencies for the model standing on moist soil.

The latter dependencies of noncoherent RCS are even more smoothed out than those averaged in frequencies (Figures 2.54 and 2.55). Therefore, these noncoherent RCSs values are good and quite

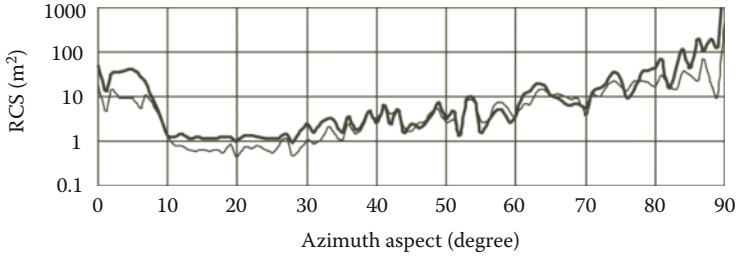

FIGURE 2.54 Averaged RCS of the tank model standing on dry soil versus azimuth aspect.

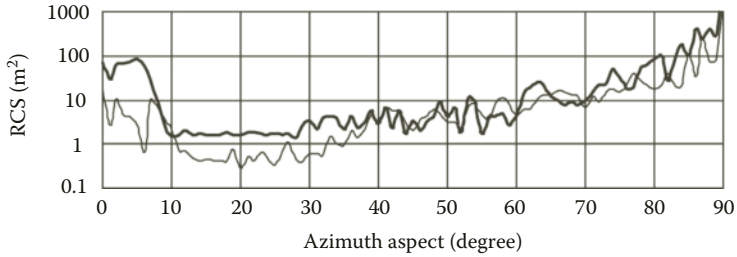

FIGURE 2.55 Averaged RCS of the tank model standing on moist soil versus azimuth aspect.

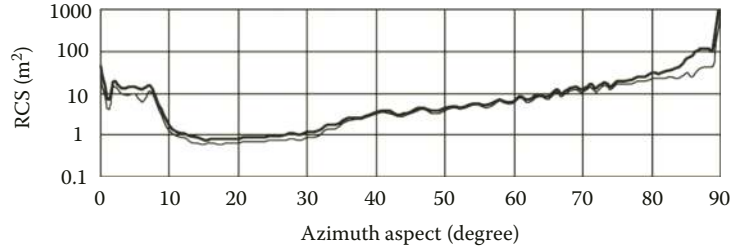

FIGURE 2.56 Noncoherent RCS of the tank model standing on dry soil versus azimuth aspect.

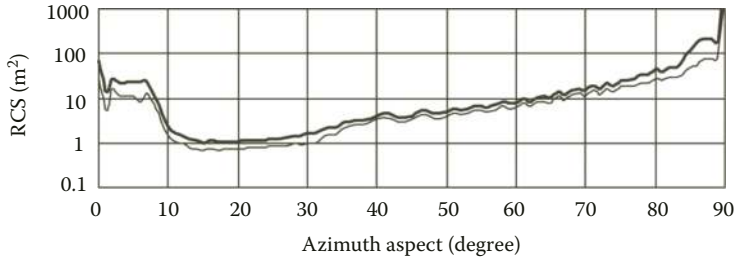

FIGURE 2.57 Noncoherent RCS of the tank model standing on moist soil versus azimuth aspect.

reliable estimates of the object RCS given certain sector of aspects and certain range of illumination frequencies. It is worth noting that noncoherent RCS value is obtained by scattering computation at single frequency, which lightens the computation burden considerably.

Figures 2.58 through 2.60 show these dependencies of noncoherent RCS of the tank model given different elevation angle of its illumination.

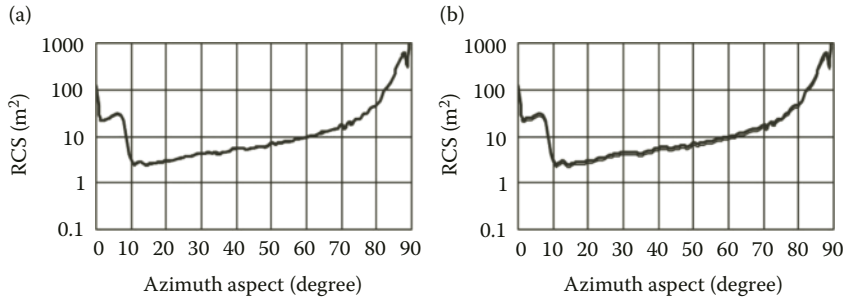

FIGURE 2.58 Noncoherent RCS of the tank model versus azimuth aspect given 0° elevation angle, the model was standing on: (a) dry soil; (b) moist soil.

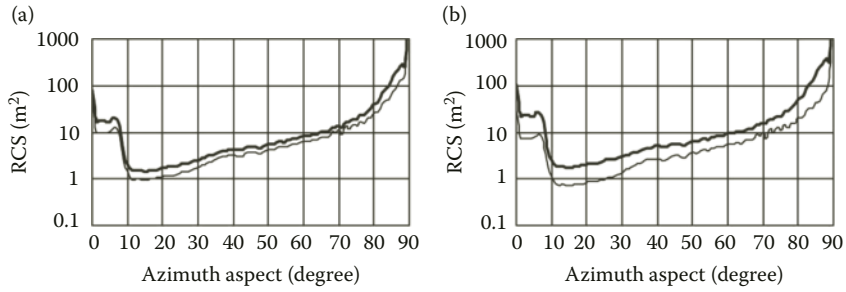

FIGURE 2.59 Noncoherent RCS of the tank model versus azimuth aspect given 10° elevation angle, the model was standing on: (a) dry soil; (b) moist soil.

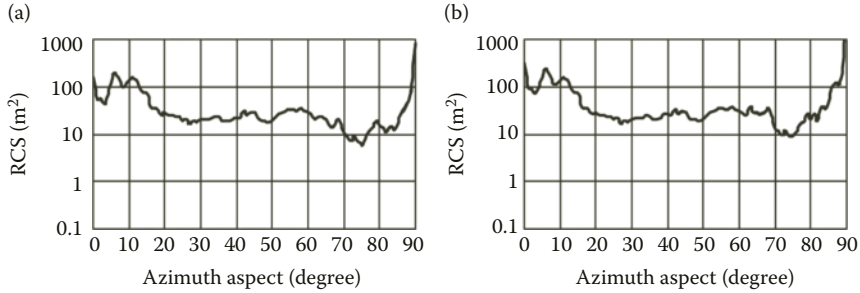

FIGURE 2.60 Noncoherent RCS of the tank model versus azimuth aspect given 75° elevation angle, the model was standing on: (a) dry soil; (b) moist soil.

RCS dependencies presented above show that when the model is illuminated along the ground surface, then there is no difference in RCS values at vertical and horizontal polarization. The latter is due to the fact that given illumination directions close to those being tangent to the ground, ground reflection coefficient approaches unit at any polarization of incident wave and along any propagation path considered of incident wave. The surface fractures, in their turn, are either obscured or they do not backscatter. Given object sounding at elevation angles close to 90°, the RCS values for the two polarizations are close to each other again since the wave propagated along the "radar–object–radar" path contributes most to the scattered field and ground reflections are almost absent. The largest difference between the RCS at two polarizations takes place given elevation angles of 10° and 30° (Figures 2.56, 2.57, and 2.59) when the difference in reflection coefficients at the two polarization is significant. This is why the RCS of tank model standing on moist soil is higher than that of standing on dry soil given these elevation angles of 10° and 30°. When the elevation angles are approaching 0° or 90°, the influence of the soil type is much smaller.

2.3.3 Method for Computing RCS of Ground Object with Nonperfectly Reflecting Surface

The method developed here is based on integral representations of fields derived from the Lorentz reciprocity theorem while taking into account electromagnetic interactions between the scatterer and the interface between free space and homogeneous half-space. Besides this, the method accounts for the presents of discontinuities (sharp edges and radar absorbents) at the surface of the object of interest.

Let us consider the plane monochromatic wave (2.1) incidence onto nonperfectly reflecting ground object. Using the Lorentz reciprocity theorem [11], we can express the field scattered by the object with surface S as

$$\vec{p}\cdot\vec{E}(x_0)=\frac{1}{j\omega}\int_S[\vec{H}^{\perp}(x)\cdot\vec{\mathcal{E}}(x|x_0,\vec{p})+\vec{E}^{\perp}(x)\cdot\vec{\mathcal{H}}(x|x_0,\vec{p})]\mathrm{d}S_x, \tag{2.112}$$

where $\vec{\mathcal{E}},\vec{\mathcal{H}}(x|x_0,\vec{p})$ is the field of electrical dipole placed at point x_0, the dipole having the vector-moment $\vec{p}$ given the presence of interface D of half-space V^1 (Figure 2.49), and $(\vec{E}^{\perp},\vec{H}^{\perp})$ are, as before, the 90° rotated tangential components of resulted total field at the object's surface S. Particularly, if the object's boundary discontinuity is due to the presence of uniform radar absorbent layer backed by perfectly conducting object's surface, then the field $(\vec{E},\vec{H})$ can be found by using solution to the simulative problem presented in Section 2.1. Let us note that for the case of backscattering $\vec{x}_0=-r\cdot\vec{R}^0$. If we put now $r\to\infty$, then the dipole field can be asymptotically expressed as

$$\begin{aligned}\vec{\mathcal{E}}(\vec{x}|\vec{x}_0,\vec{p})&\sim\Omega(k_0r)\vec{\mathcal{E}}(\vec{x}|\vec{R}^0,\vec{p}),\\ \vec{\mathcal{H}}(\vec{x}|\vec{x}_0,\vec{p})&\sim\Omega(k_0r)\vec{\mathcal{H}}(\vec{x}|\vec{R}^0,\vec{p}),\end{aligned} \tag{2.113}$$

where

$$\Omega(k_0r)=\frac{e^{jk_0r}}{4\pi k_0r}.$$

The field $\vec{\mathcal{E}}(\vec{x}|\vec{R}_0,\vec{p})$, $\vec{\mathcal{H}}(\vec{x}|\vec{R}_0,\vec{p})$ is excited by plane wave

$$\begin{aligned}\vec{\mathcal{E}}_0(\vec{x}|\vec{R}^0,\vec{p})&=k_0{}^2\omega\sqrt{\frac{\mu_0}{\varepsilon_0}}\vec{p}^{\,\mathrm{T}}\exp(jk_0(\vec{R}^0\cdot\vec{x})),\\ \vec{\mathcal{H}}_0(\vec{x}|\vec{R}^0,\vec{p})&=-k_0{}^2\omega\vec{p}^{\,\perp}\exp(jk_0(\vec{R}^0\cdot\vec{x})),\end{aligned} \tag{2.114}$$

where $\vec{p}^{\,\perp}=\vec{R}^0\times\vec{p}$, $\vec{p}^{\,\mathrm{T}}=\vec{p}-\vec{R}^0(\vec{R}^0\cdot\vec{p})$.

Consequently, the field over interface D given that scatterer S is absent can be expressed as

$$\vec{\mathcal{E}}(\vec{x}|\vec{R}^0,\vec{p})=k_0^2\omega\sqrt{\frac{\mu_0}{\varepsilon_0}}\Big[\vec{p}^{\,0}\exp(jk_0(\vec{R}^0\cdot\vec{x}))+\vec{p}^{\,1}\exp(jk_0(\vec{R}^1\cdot\vec{x}))\Big], \tag{2.115}$$

$$\vec{\mathcal{H}}(\vec{x}|\vec{R}^0,\vec{p})=-k_0^2\omega\Big[\vec{p}^{\,0\perp}\exp(jk_0(\vec{R}^0\cdot\vec{x}))+\vec{p}^{\,1\perp}\exp(jk_0(\vec{R}^1\cdot\vec{x}))\Big], \tag{2.116}$$

where $\vec{p}^{\,0\perp}=\vec{R}^0\times\vec{p}^{\,0}$, $\vec{p}^{\,1\perp}=\vec{R}^1\times\vec{p}^{\,1}$, $\vec{p}^{\,0}=\vec{p}^{\,T}$, and $\vec{p}^{\,1}$ is the vector calculated by expressions (2.12) and (2.13).

So, like it was in Section 2.3.1, we consider that the object's surface S is illuminated, first, by direct plane wave propagating in direction $\bar{R}^0$ and, second, by the wave reflected from the plane D, the latter propagating in direction $\bar{R}^1$ (Figure 2.49).

Phase differences that appear due to wave reflection from the interface D are accounted for in the same manner as for the perfectly conducting object. For instance, the electrical field component of resulted incident field at point $\vec{x}$ of the object's surface S that accounts for phase differences due to primary wave reflection from plane D can be written as

$$\vec{\mathcal{E}}(\vec{x}|\vec{R}^0,\vec{p})=k_0^2\omega\sqrt{\frac{\mu_0}{\varepsilon_0}}\Omega(k_0r)\Big[\vec{p}^{\,0}\exp(jk_0(\vec{R}^0\cdot\vec{x}))+\vec{p}^{\,1}\exp(jk_0((\vec{R}^0-\vec{R}^1)\cdot\vec{c}+\vec{R}^1\cdot\vec{x}))\Big], \tag{2.117}$$

where $\vec{c} = \vec{x} - \dfrac{(\vec{x}\cdot\vec{n})+h}{(\vec{R}^1\cdot\vec{n})}\vec{R}^1$; $\vec{n}$ is the normal to the plane D; and h is the distance from the center of coordinate system tied to object down to the surface D (Figure 2.50). In the same manner, we can write expression for $\vec{\mathcal{H}}(\vec{x}|\vec{R}^0,\vec{p})$.

Now, accounting for the fields $\vec{E}(\vec{x}|\vec{R}^0,\vec{p})$, $\vec{\mathcal{H}}(\vec{x}|\vec{R}^0,\vec{p})$ from the expression (2.112), we can obtain expression for total field scattered in direction $-\vec{R}^0$ (above the surface D) given that object S is present:

$$\vec{p}\cdot\vec{E}(\vec{R}^0) = -jk_0\Omega(k_0 r)\int_S\left[\sqrt{\frac{\mu_0}{\varepsilon_0}}\left[\vec{p}^0\exp(jk_0(\vec{R}^0\cdot\vec{x})) + \vec{p}^1\exp(jk_0((\vec{R}^0-\vec{R}^1)\cdot\vec{c}+\vec{R}^1\cdot\vec{x}))\right]\cdot\vec{H}^{\perp}(\vec{x})\right.$$
$$\left.+\left[\vec{p}^{0\perp}\exp(jk_0(\vec{R}^0\cdot\vec{x})) + \vec{p}^{1\perp}\exp(jk_0((\vec{R}^0-\vec{R}^1)\cdot\vec{c}+\vec{R}^1\cdot\vec{x}))\right]\cdot\vec{E}^{\perp}(\vec{x})\right]\mathrm{d}S. \tag{2.118}$$

We note here that $\vec{H}^{\perp}(\vec{x})$ is the equivalent current density of electric current over surface S of nonperfectly reflecting object. This surface current density $\vec{H}^{\perp}(\vec{x})$ is excited by plane wave propagating in direction $\vec{R}^0$ given that the interface D of the half-space V^1 is present (Figure 2.49). In the physical optics approximation, the value of $\vec{H}^{\perp}(\vec{x})$ for smooth parts of the surface S can be expressed as

$$\vec{H}^{\perp}(\vec{x}) = \begin{cases}\vec{n}_S\times\vec{H}_1, & \vec{x}\in Q_0,\\ \vec{n}_S\times\vec{H}_2, & \vec{x}\in Q_1,\end{cases} \tag{2.119}$$

where

$$\vec{H}_1 = (\vec{R}^0\times\vec{p}^0)\sqrt{\frac{\varepsilon_0}{\mu_0}}\exp(jk_0(\vec{R}^0\cdot\vec{x})) + (\vec{R}^{01}\times\vec{p}^{01})\sqrt{\frac{\varepsilon_0}{\mu_0}}\exp(jk_0(\vec{R}^{01}\cdot\vec{x})),$$
$$\vec{H}_2 = (\vec{R}^1\times\vec{p}^1)\sqrt{\frac{\varepsilon_0}{\mu_0}}\exp(jk_0(\vec{R}^0-\vec{R}^1)\cdot\vec{c})\exp(jk_0(\vec{R}^1\cdot\vec{x}))$$
$$+(\vec{R}^{11}\times\vec{p}^{11})\sqrt{\frac{\varepsilon_0}{\mu_0}}\exp(jk_0(\vec{R}^0-\vec{R}^1)\cdot\vec{c})\exp(jk_0(\vec{R}^{11}\cdot\vec{x})). \tag{2.120}$$

Here, $\vec{n}_S$ is the normal to the object's surface S; $\vec{R}^{01} = \vec{R}^0 - 2\vec{n}_S(\vec{R}^0\cdot\vec{n}_S)$, $\vec{R}^{11} = \vec{R}^1 - 2\vec{n}_S(\vec{R}^1\cdot\vec{n}_S)$; and $\vec{p}^{01}$, $\vec{p}^{11}$ are the complex vector coefficients of reflection from nonperfectly reflecting object's surface given its illumination in directions $\vec{R}^0$ и $\vec{R}^1$, respectively. Vectors $\vec{p}^{01}$ and $\vec{p}^{11}$ can be computed using the method described in Section 2.1.1.

In expression (2.112), the value of $\vec{E}^{\perp}(\vec{x})$ describes an equivalent density of magnetic current over surface S. In the physical optics approximation, the value of $\vec{E}^{\perp}(\vec{x})$ can be written as

$$\vec{E}^{\perp}(\vec{x}) = \begin{cases}\vec{n}_S\times\vec{E}_1, & \vec{x}\in Q_0,\\ \vec{n}_S\times\vec{E}_2, & \vec{x}\in Q_1,\end{cases} \tag{2.121}$$

where

$$\vec{E}_1 = \vec{p}^0\exp(jk_0(\vec{R}^0\cdot\vec{x})) + \vec{p}^{01}\exp(jk_0(\vec{R}^{01}\cdot\vec{x})),$$
$$\vec{E}_2 = \vec{p}^1\exp(jk_0(\vec{R}^0-\vec{R}^1)\cdot\vec{c})\exp(jk_0(\vec{R}^1\cdot\vec{x})) + \vec{p}^{11}\exp(jk_0(\vec{R}^0-\vec{R}^1)\cdot\vec{c})\exp(jk_0(\vec{R}^{11}\cdot\vec{x})). \tag{2.122}$$

Taking into account Equations 2.119 through 2.122, expression (2.118) can be presented as

$$\vec{p}\cdot\vec{E}(\vec{R}^0) = -jk_0\frac{\exp(jk_0r)}{2\pi r}\left\{\int\limits_{Q_0}\left[\vec{p}^0\cdot(\vec{n}_S\times\vec{H}_1)+(\vec{R}^0\times\vec{p}^0)\cdot(\vec{n}_S\times\vec{E}_1)\right]\exp(jk_0(\vec{R}^0\cdot\vec{x}))\,dS\right.$$
$$+\int\limits_{Q_0}\left[\vec{p}^1\cdot(\vec{n}_S\times\vec{H}_1)+(\vec{R}^1\times\vec{p}^1)\cdot(\vec{n}_S\times\vec{E}_1)\right]\exp(jk_0((\vec{R}^0-\vec{R}^1)\cdot\vec{c}+\vec{R}^1\cdot\vec{x}))\,dS$$
$$+\int\limits_{Q_1}\left[\vec{p}^0\cdot(\vec{n}_S\times\vec{H}_2)+(\vec{R}^0\times\vec{p}^0)\cdot(\vec{n}_S\times\vec{E}_2)\right]\exp(jk_0(\vec{R}^0\cdot\vec{x}))\,dS$$
$$\left.+\int\limits_{Q_1}\left[\vec{p}^1\cdot(\vec{n}_S\times\vec{H}_2)+(\vec{R}^1\times\vec{p}^1)\cdot(\vec{n}_S\times\vec{E}_2)\right]\exp(jk_0((\vec{R}^0-\vec{R}^1).\vec{c}+\vec{R}^1\cdot\vec{x}))\,dS\right\}. \tag{2.123}$$

The first two integrals are over illuminated region Q_0, the other two integrals are over illuminated region Q_1. Integrands in Equation 2.123 are fast oscillating functions, which necessitates the cubature formulas to be applied as described in Section 2.2.

Having applied the cubature formula (Section 2.2.2) to the integrals in Equation 2.123, we can compute the field scattered from smooth part of the object's surface.

For the field scattered from local edge scatterers of ground object, we use the same expression (2.112). The expression for resulted total field at point $\vec{X}$ of the surface S enveloping the object that accounts for phase differences due to reflection of primary wave from the interface plane D can be written in the same manner as in Equation 2.117:

$$\vec{\mathcal{E}}(\vec{X}|\vec{R}^0,\vec{p}) = k_0^2\omega\sqrt{\frac{\mu_0}{\varepsilon_0}}\Omega(k_0r)\left[\vec{p}^0\exp(jk_0(\vec{R}^0\cdot\vec{X}))+\vec{p}^1\exp(jk_0((\vec{R}^0-\vec{R}^1)\cdot\vec{C}+\vec{R}^1\cdot\vec{X}))\right], \tag{2.124}$$

$$\vec{\mathcal{H}}(\vec{X}|\vec{R}^0,\vec{p}) = k_0^2\omega\Omega(k_0r)\left[\vec{p}^{0\perp}\exp(jk_0(\vec{R}^0\cdot\vec{X}))+p^{1\perp}\exp(jk_0((\vec{R}^0-\vec{R}^1)\cdot\vec{C}+\vec{R}^1\cdot\vec{X}))\right], \tag{2.125}$$

where $\Omega(k_0r)=\dfrac{\exp(jk_0r)}{4\pi k_0r}$, $\vec{C}=\vec{X}-\dfrac{(\vec{X}\cdot\vec{n})+h}{(\vec{R}^1\cdot\vec{n})}\vec{R}^1$, $\vec{p}^{0\perp}=\vec{R}^0\times\vec{p}^0$, $\vec{p}^{1\perp}=\vec{R}^1\times\vec{p}^1$; $\vec{n}$ is the normal to the plane D; and h is the distance from the coordinate system tied to object down to the plane D (Figure 2.50).

Now, the field scattered from local edge scatterers of ground object in the backward direction $-\vec{R}^0$ can be expressed as

$$\vec{p}\cdot\vec{E}(\vec{R}^0) = -jk_0\frac{\exp(jk_0r)}{2\pi r}(F_0+F_1), \tag{2.126}$$

$$F_0 = \int\limits_{W_0}\left[\sqrt{\frac{\mu_0}{\varepsilon_0}}\vec{H}^{a\perp}(\vec{x})\cdot\left[\vec{p}^0\exp(jk_0(\vec{R}^0\cdot\vec{X}))+\vec{p}^1\exp(jk_0((\vec{R}^0-\vec{R}^1)\cdot\vec{C}+\vec{R}^1\cdot\vec{X}))\right]\right.$$
$$\left.+\vec{E}^{a\perp}(\vec{x})\cdot\left[\vec{p}^{0\perp}\exp(jk_0(\vec{R}^0\cdot\vec{X}))+\vec{p}^{1\perp}\exp(jk_0((\vec{R}^0-\vec{R}^1)\cdot\vec{C}+\vec{R}^1\cdot\vec{X}))\right]\right]dS, \tag{2.127}$$

$$F_1 = \int_{W_1} \left[\sqrt{\frac{\mu_0}{\varepsilon_0}} \vec{H}^{b\perp}(\vec{x}) \cdot \left[\vec{p}^{\,0} \exp(jk_0(\vec{R}^0 \cdot \vec{X})) + \vec{p}^{\,1} \exp(jk_0((\vec{R}^0 - \vec{R}^1) \cdot \vec{C} + \vec{R}^1 \cdot \vec{X})) \right] \right.$$
$$\left. + \vec{E}^{b\perp}(\vec{x}) \cdot \left[\vec{p}^{\,0\perp} \exp(jk_0(\vec{R}^0 \cdot \vec{X})) + \vec{p}^{\,1\perp} \exp(jk_0((\vec{R}^0 - \vec{R}^1) \cdot \vec{C} + \vec{R}^1 \cdot \vec{X})) \right] \right] dS. \quad (2.128)$$

Here, W_0 is the whole set of toroidal surfaces enveloping the edges that are illuminated by wave propagating in direction $\vec{R}^0$ (Figure 2.61); W_1 is the whole set of toroidal surfaces enveloping the edges illuminated by wave reflected from the interface plane D; $\vec{E}^{a\perp} = (\vec{n}_0 \times \vec{E}^a)$ and $\vec{H}^{a\perp} = (\vec{n}_0 \times \vec{H}^a)$ are the surface densities of equivalent magnetic and electric currents over the surface W_0 ($\vec{n}_0$ is the normal to the surface W_0) given its illumination in direction $\vec{R}^0$; $\vec{E}^{b\perp} = (\vec{n}_1 \times \vec{E}^b)$ and $\vec{H}^{b\perp} = (\vec{n}_1 \times \vec{H}^b)$ are the surface densities of equivalent magnetic and electric currents over the surface W_1 ($\vec{n}_1$ is the normal to the surface W_1) given its illumination in direction $\vec{R}^1$.

Let us consider the integral F_0 over surface W_0. To do so, we need to express coordinates of the points $\vec{X}$ at the surface W_0 as follows:

$$\vec{X} = \vec{x}(\upsilon) + \vec{\tau}, \quad (2.129)$$

where $\vec{x}(\upsilon)$ is the radius-vector of a point at the surface fracture Y given its edge line's parameter equal to υ, and $\vec{\tau}$ is the vector orthogonal to the edge at this point that has constant length z_0, and which direction is determined by vector $\theta(0 \le \theta \le \phi\pi)$ (Figure 2.15).

It is convenient to split the phase correcting vector coefficient $\vec{C}$ in two parts:

$$\vec{C} = \vec{c}_0(\vec{x}(\upsilon)) + \vec{c}_1(\vec{\tau}), \quad (2.130)$$

where $\vec{c}_0(\vec{x}(\upsilon)) = \vec{x}(\upsilon) - \dfrac{(\vec{x}(\upsilon) \cdot \vec{n}) + h}{(\vec{R}^1 \cdot \vec{n})} \vec{R}^1$; $\vec{c}_1(\vec{\tau}) = \vec{\tau} - \dfrac{(\vec{\tau} \cdot \vec{n})}{(\vec{R}^1 \cdot \vec{n})} \vec{R}^1$.

Then, the $\vec{E}^a$ and $\vec{H}^a$ can be represented as follows:

$$\begin{pmatrix} \vec{E}^a \\ \vec{H}^a \end{pmatrix} = \begin{pmatrix} \tilde{\vec{E}}^a \\ \tilde{\vec{H}}^a \end{pmatrix} \exp(jk_0(\vec{R}^0 \cdot \vec{x}(\upsilon))), \quad (2.131)$$

where $\tilde{\vec{E}}^a$, $\tilde{\vec{H}}^a$ are the intensity vectors of the field excited at W_0 by plane wave

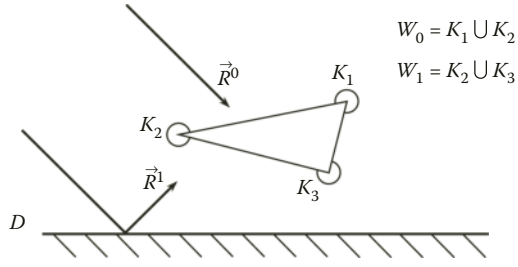

FIGURE 2.61 To the determination of surfaces W_0 and W_1.

$$\tilde{\tilde{E}}^{0a}(\vec{\tau}) = \vec{p}^{\,0}\exp(jk_0(\vec{R}^0\cdot\vec{\tau})),$$

$$\tilde{\tilde{H}}^{0a}(\vec{\tau}) = \sqrt{\frac{\varepsilon_0}{\mu_0}}(\vec{R}^0\times\vec{p}^{\,0})\exp(jk_0(\vec{R}^0\cdot\vec{\tau})).$$

Taking into account all that we stated above, the integral F_0 over surface W_0 can be written as

$$\begin{aligned}F_0 = {} & \sqrt{\frac{\mu_0}{\varepsilon_0}}\int\limits_{W_0}\left[\tilde{\tilde{H}}^{a\perp}(\vec{\tau})\cdot\vec{p}^{\,0} + \sqrt{\frac{\varepsilon_0}{\mu_0}}\tilde{\tilde{E}}^{a\perp}(\vec{\tau})\cdot(\vec{R}^0\times\vec{p}^{\,0})\right]\exp(jk_0(\vec{R}^0\cdot\vec{X}))\exp(jk_0(\vec{R}^0\cdot\vec{x}(\upsilon)))\,\mathrm{d}S\\ & + \sqrt{\frac{\mu_0}{\varepsilon_0}}\int\limits_{W_0}\left[\tilde{\tilde{H}}^{a\perp}(\vec{\tau})\cdot\vec{p}^{\,1} + \sqrt{\frac{\varepsilon_0}{\mu_0}}\tilde{\tilde{E}}^{a\perp}(\vec{\tau})\cdot(\vec{R}^1\times\vec{p}^{\,1})\right]\exp(jk_0((\vec{R}^0-\vec{R}^1)\cdot\vec{C}+\vec{R}^1\cdot\vec{X}))\\ & \times\exp(jk_0(\vec{R}^0\cdot\vec{x}(\upsilon)))\,\mathrm{d}S.\end{aligned} \tag{2.132}$$

Having replaced the surface integral by the double one, we write integral F_0 in the following form:

$$\begin{aligned}F_0 = {} & \sqrt{\frac{\mu_0}{\varepsilon_0}}\vec{p}^{\,0}\cdot\int\limits_{Y_0}\exp(jk_0\,2(\vec{R}^0\cdot\vec{x}(\upsilon)))\,\vec{D}_{00}\,\mathrm{d}\upsilon\\ & + \sqrt{\frac{\mu_0}{\varepsilon_0}}\vec{p}^{\,1}\cdot\int\limits_{Y_0}\exp(jk_0((\vec{R}^0-\vec{R}^1)\cdot\vec{c}_0(\vec{x}(\upsilon))+(\vec{R}^0+\vec{R}^1)\cdot\vec{x}(\upsilon)))\,\vec{D}_{01}\,\mathrm{d}\upsilon,\end{aligned} \tag{2.133}$$

$$\begin{aligned}\vec{D}_{00} &= \int\limits_{W_0'}\exp(jk_0(\vec{R}^0\cdot\vec{\tau}))\,\vec{B}_{00}\,\mathrm{d}z,\\ \vec{B}_{00} &= \tilde{\tilde{H}}^{a\perp}(\vec{\tau}) + \sqrt{\frac{\varepsilon_0}{\mu_0}}(\tilde{\tilde{E}}^{a\perp}(\vec{\tau})\times\vec{R}^0),\\ \vec{D}_{01} &= \int\limits_{W_0'}\exp(jk_0((\vec{R}^0-\vec{R}^1)\cdot\vec{c}_1(\vec{\tau})+\vec{R}^1\cdot\vec{\tau}))\vec{B}_{01}\,\mathrm{d}z,\end{aligned} \tag{2.134}$$

$\mathrm{d}z = z_0\,\mathrm{d}\theta$ being the element of the arc W_0' length;

$$\vec{B}_{01} = \tilde{\tilde{H}}^{a\perp}(\vec{\tau}) + \sqrt{\frac{\varepsilon_0}{\mu_0}}(\tilde{\tilde{E}}^{a\perp}(\vec{\tau})\times\vec{R}^1). \tag{2.135}$$

Here, Y_0 is the whole set of edge lines that are enveloped by the surface W_0, and W_0' is the crossing line between surface W_0 and the plane perpendicular to the edge.

We can see that the first summand in expression for integral F_0 is the same as the corresponding expression for the field scattered from the local edge scatterer of standalone object.

Let us consider the integral F_1 over surface W_1. The field $(\vec{E}^b, \vec{H}^b)$ can be represented in the following form:

$$\begin{pmatrix} \vec{E}^b \\ \vec{H}^b \end{pmatrix} = \begin{pmatrix} \tilde{\vec{E}}^b \\ \tilde{\vec{H}}^b \end{pmatrix} \exp(jk_0[(\vec{R}^0 - \vec{R}^1) \cdot \vec{c}_0(\vec{x}(\upsilon)) + (\vec{R}^1 \cdot \vec{x}(\upsilon))]), \tag{2.136}$$

where $\tilde{\vec{E}}^b$, $\tilde{\vec{H}}^b$ are the intensity vectors of the field excited at W_1 by plane wave

$$\tilde{\vec{E}}^{0b}(\vec{\tau}) = \vec{p}^1 \exp[jk_0((\vec{R}^0 - \vec{R}^1) \cdot \vec{c}_1(\vec{\tau}) + (\vec{R}^1 \cdot \vec{\tau}))],$$

$$\tilde{\vec{H}}^{0b}(\vec{\tau}) = \sqrt{\frac{\varepsilon_0}{\mu_0}}(\vec{R}^1 \times \vec{p}^1)\exp[jk_0((\vec{R}^0 - \vec{R}^1) \cdot \vec{c}_1(\vec{\tau}) + (\vec{R}^1 \cdot \vec{\tau}))].$$

Taking into account Equation 2.136, we can write expression (2.128) for the integral F_1 as follows:

$$\begin{aligned} F_1 = & \sqrt{\frac{\mu_0}{\varepsilon_0}} \int_{W_1} \left[\tilde{\vec{H}}^{b\perp} \cdot \vec{p}^0 + \sqrt{\frac{\varepsilon_0}{\mu_0}} \tilde{\vec{E}}^{b\perp} \cdot (\vec{R}^0 \times \vec{p}^0) \right] \exp(jk_0(\vec{R}^0 \cdot \vec{X})) \\ & \times \exp(jk_0((\vec{R}^0 - \vec{R}^1) \cdot \vec{c}_0(\vec{x}(\upsilon)) + \vec{R}^1 \cdot \vec{x}(\upsilon)))\,\mathrm{d}S \\ & + \sqrt{\frac{\mu_0}{\varepsilon_0}} \int_{W_1} \left[\tilde{\vec{H}}^{b\perp} \cdot \vec{p}^1 + \sqrt{\frac{\varepsilon_0}{\mu_0}} \tilde{\vec{E}}^{b\perp} \cdot (\vec{R}^1 \times \vec{p}^1) \right] \exp(jk_0((\vec{R}^0 - \vec{R}^1) \cdot \vec{C} + \vec{R}^1 \cdot \vec{X})) \\ & \times \exp(jk_0((\vec{R}^0 - \vec{R}^1) \cdot \vec{c}_0(\vec{x}(\upsilon)) + \vec{R}^1 \cdot \vec{x}(\upsilon)))\,\mathrm{d}S. \end{aligned} \tag{2.137}$$

Having replaced the integral over surface by double integral, we can rewrite expression for F_1 as follows:

$$\begin{aligned} F_1 = & \sqrt{\frac{\mu_0}{\varepsilon_0}} \vec{p}^0 \cdot \int_{Y_1} \exp(jk_0((\vec{R}^0 - \vec{R}^1) \cdot \vec{c}_0(\vec{x}(\upsilon)) + (\vec{R}^0 + \vec{R}^1) \cdot \vec{x}(\upsilon)))\vec{D}_{10}\,\mathrm{d}\upsilon \\ & + \sqrt{\frac{\mu_0}{\varepsilon_0}} \vec{p}^1 \cdot \int_{Y_1} \exp(jk_0 2((\vec{R}^0 - \vec{R}^1) \cdot \vec{c}_0(\vec{x}(\upsilon)) + \vec{R}^1 \cdot \vec{x}(\upsilon)))\vec{D}_{11}\,\mathrm{d}\upsilon, \end{aligned} \tag{2.138}$$

$$\vec{D}_{10} = \int_{W_1'} \exp(jk_0(\vec{R}^0 \cdot \vec{\tau}))\vec{B}_{10}\,\mathrm{d}z, \quad \vec{B}_{10} = \tilde{\vec{H}}^{b\perp}(\vec{\tau}) + \sqrt{\frac{\varepsilon_0}{\mu_0}}(\tilde{\vec{E}}^{b\perp} \times \vec{R}^0), \tag{2.139}$$

$$\begin{aligned} \vec{D}_{11} &= \int_{W_1'} \exp(jk_0((\vec{R}^0 - \vec{R}^1) \cdot \vec{c}_1(\vec{\tau}) + \vec{R}^1 \cdot \vec{\tau}))\vec{B}_{11}\,\mathrm{d}z, \\ \vec{B}_{11} &= \tilde{\vec{H}}^{b\perp}(\vec{\tau}) + \sqrt{\frac{\varepsilon_0}{\mu_0}}(\tilde{\vec{E}}^{b\perp} \times \vec{R}^1), \end{aligned} \tag{2.140}$$

where Y_1 is the whole set of fracture lines that are enveloped by the surface W_1, and W_1' is the crossing line between the surface W_1 and the plane perpendicular to the fracture line.

Now, the problem is reduced to finding four vector coefficients: $\vec{D}_{00}$, $\vec{D}_{01}$, $\vec{D}_{10}$, $\vec{D}_{11}$, which can be solved in the same manner as it was done in Section 2.2.4 by numerical integration procedure for the vector coefficient $\vec{D}$.

As it follows from Equations 2.133 and 2.138, computation of scattering from local edge scatterers of ground object can be interpreted by terms of the four path wave propagation picture as it was done for the case of electromagnetic wave scattering from the smooth part of the object's surface. By adding together components scattered from smooth surface part and local edge scatterers of the object, one can estimate the field scattered from the object standing on the underlying surface.

2.3.4 Scattering Characteristics of Nonperfectly Reflecting Model of a Ground Object

Applicability of the method developed here was verified by computer simulation of plane electromagnetic wave scattering from nonperfectly reflecting model of a tank (Figure 2.51), which was provided with RAM coating and put on the ground.

The model length was 8 m, its width was 3 m, and its height was 2 m. In simulation we assumed RAM with the following properties: relative permittivity and permeability were $\varepsilon' = 20 + j0.1$ and $\mu' = 1.35 + j0.8$, respectively, coating thickness over smooth parts of the surface was 1.3 mm, radius of radar-absorbing toroid at the fracture ribs was 1 mm. As underlying surface, we took the soil with properties of brown loam. Relative permittivity and permeability of dry soil (given moisture content of 1%) were $\varepsilon' = 3 + j0.38$ and $\mu' = 1 + j0$, respectively; the moist soil (given moisture content of 20%) had the following relative permittivity and permeability: $\varepsilon' = 17 + j0.9$, $\mu' = 1 + j0$.

RCS computation was provided for the azimuth aspects from 0° through 90° with increment of 1°. Illumination signal wavelength was assumed to be 10 GHz ($\lambda = 0.03$ m). RCS estimations presented in Figures 2.62 through 2.65 were provided for the elevation angle of 30°.

Figure 2.62 shows instantaneous RCS of the tank model standing on dry soil versus azimuth aspect of its radar observation. RCS at horizontal polarization is shown with bold black curve, and

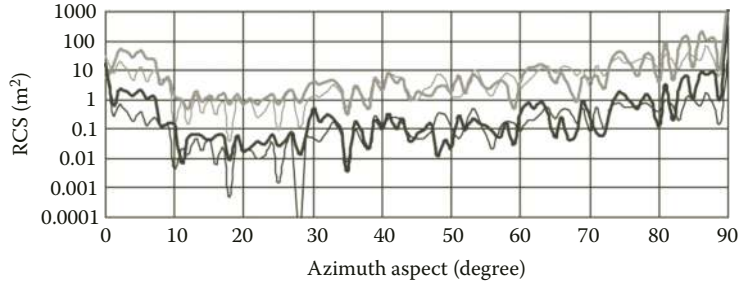

FIGURE 2.62 Instantaneous RCS of the RAM-coated tank model standing on dry soil.

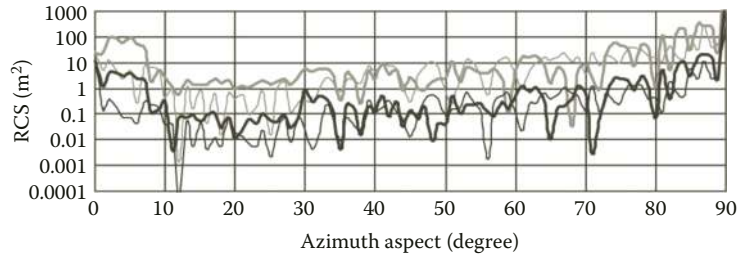

FIGURE 2.63 Instantaneous RCS of the RAM-coated tank model standing on moist soil.

the RCS at vertical one is shown with thin black curve. Figure 2.63 shows similar RCS dependencies for the tank model standing on moist soil. Gray curves at these plots show corresponding RCS dependencies for the perfectly conducting model.

All basic qualitative relationships of RCS for the tank model provided with RAM coating were practically the same as for the perfectly conducting model at both polarizations of illumination signal (Section 2.3.2).

In order to save computation time when obtaining reliable RCS estimates, we computed also the noncoherent RCS values. Figure 2.64 shows such noncoherent RCS of the tank model standing on dry soil versus azimuth aspect of its observation. Figure 2.65 shows similar dependencies of noncoherent RCS of the tank model standing on moist soil. RCS of the RAM-coated model is shown with black curves; the gray curves are for the perfectly conducting model. Bold lines are for the RCS at horizontal polarization, and the thin lines are for RCS at vertical polarization.

RCS of the RAM-coated model is, in average, 10-fold less than that of the perfectly conducting model. RCS values at vertical polarization are lower than those at horizontal polarization, which is even more evident for the case of moist soil (Figure 2.65).

The noncoherent dependencies of RCS presented above are smoother compared to instantaneous RCS dependencies, and they provide reliable estimate for the RCS given specific frequency range and sector of observation aspects.

Figures 2.66 through 2.68 show dependencies of noncoherent RCS of the tank model given various elevation angles of its illumination. Dependencies presented above show that behavior of noncoherent RCS of perfectly conducting model correlate strongly with RCS behavior of the RAM-coated model. The dependencies are almost the same for all the azimuths and elevation angles except that the RCS of RAM-coated model is about 10-fold lower compared to RCS of perfectly conducting model given the use of this specific RAM coating.

The level of RCS reduction goes as high as 16 dB. Variations in the RCS levels given different kinds of underlying surface become more evident as the elevation angle increases. Main qualitative RCS relationships for the ground model, which has perfectly conducting and nonperfectly reflecting surface, practically coincide with each other. Particularly, given target illumination along the ground surface, there is almost no difference between the RCS at vertical and horizontal polarization. These

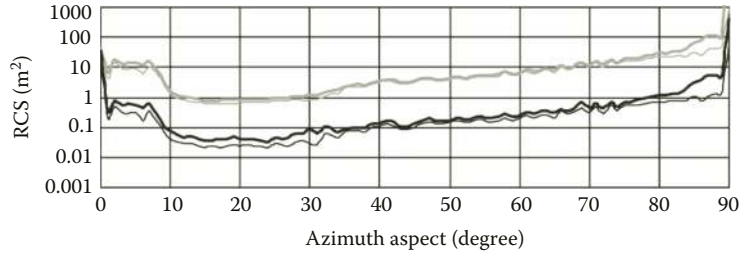

FIGURE 2.64 Noncoherent RCS of the tank model standing on dry soil.

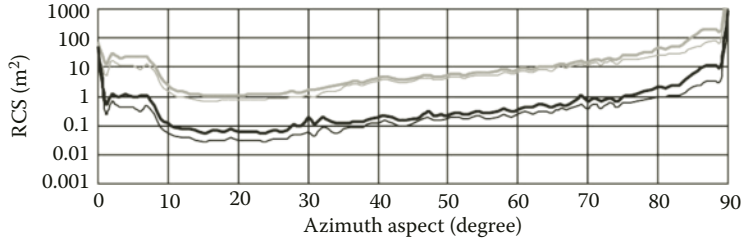

FIGURE 2.65 Noncoherent RCS of the tank model standing on moist soil.

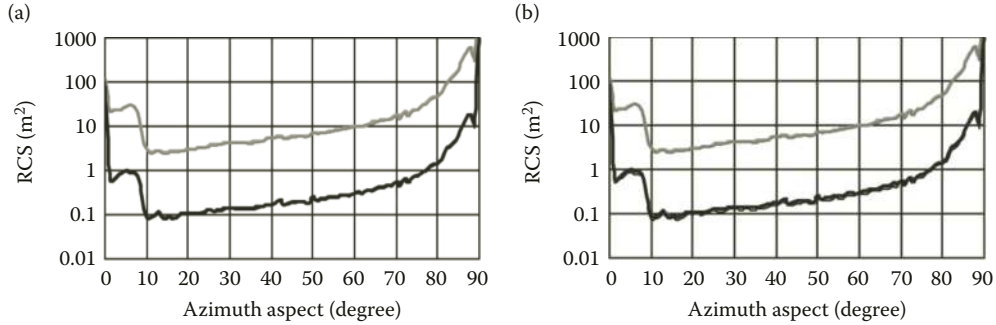

FIGURE 2.66 Noncoherent RCS of the tank model versus azimuth aspect at elevation angle of 0° (a – dry soil, b – moist soil).

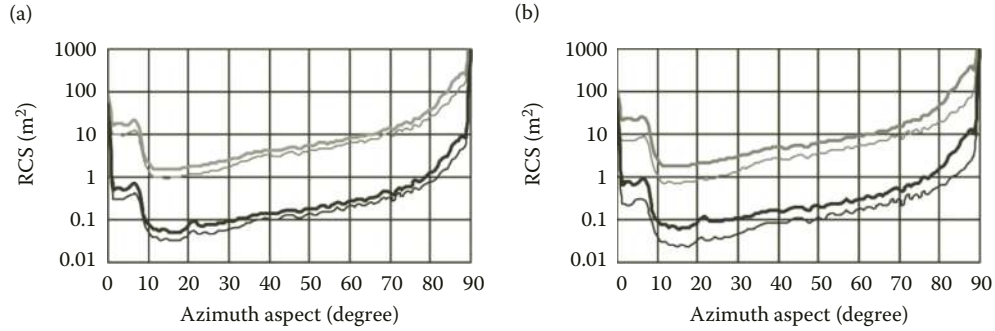

FIGURE 2.67 Noncoherent RCS of the tank model versus azimuth aspect at elevation angle of 10° (a – dry soil, b – moist soil).

RCS values are practically the same since, for the illumination directions approaching those being tangent to the ground surface, the reflection coefficient approaches unit given any signal polarization.

When the tank model is illuminated at elevation angles approaching 90°, then the values of its RCS at horizontal and vertical polarization are close to each other since the direct wave propagating without reflecting from the ground contributes mostly into total scattered field. As it was the case for the perfectly conducting model, the maximum difference between the RCS values at vertical and horizontal polarizations is observed at elevation angles of 10° and 30°. At these elevation angles of the model illumination, the ground reflection coefficients at the two polarizations differ from each other, and the waves propagating via ground reflection contribute significantly to total field

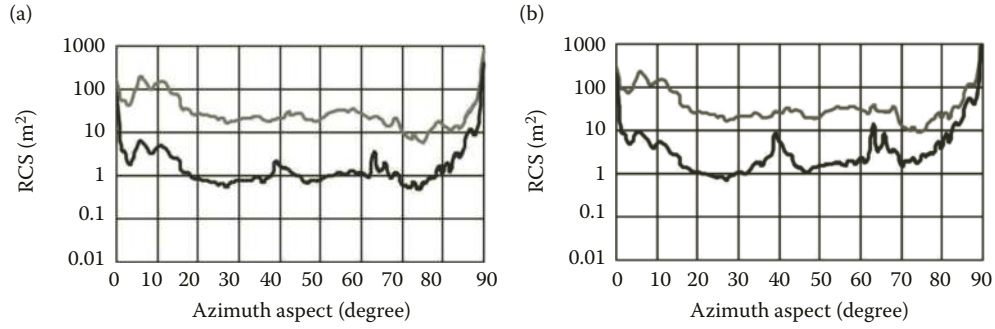

FIGURE 2.68 Noncoherent RCS of the tank model versus azimuth aspect at elevation angle of 75° (a – dry soil, b – moist soil).

scattered from the object. As it was the case for the perfectly conducting model, for the elevation angles of 10° and 30° the RCS of the RAM-coated tank model standing on moist soil is higher than that of standing on dry soil. At the elevation angles approaching 0° and 90°, the influence of the soil type on the RCS level decreases significantly.

2.4 SCATTERING CHARACTERISTICS OF REFLECTOR ANTENNA SYSTEMS

Sergey V. Nechitaylo and Oleg I. Sukharevsky

In last few decades, the detection capabilities of radar means have increased considerably with respect to both airborne and ground (marine) targets. Therefore, special attention is paid now to the measures as to decreasing the radar visibility (RV) of weapon systems.

Many studies were dedicated to solving this problem [63–69]. We have shown earlier that by applying RAM coating and shaping the surface of weapon systems in a specific way, one can achieve significant reduction in its RV. In this case, the antenna systems (AS) of weapons may become one of its unmasking elements. The latter is due to the fact that based on basic functional assignment of the antenna (transmission and reception of radio waves) its surface cannot be nonreflecting.

So, considering the importance of antenna systems one needs to be capable of evaluating their scattering characteristics. In this section, we consider the way for computing scattering characteristics of reflector antennas including those under radio transparent radomes as well as the way for reducing their RV at specific aspects of their observation by means of applying RAM coating to some of the antenna elements.

Reflector antennas (RA) are used widely in different specimens of military equipment and armament. The latter is due to their high performance achieved given simple design and low cost. In this regard, the armament designers are interested in the methods for reducing radar visibility of such antennas by means of applying RAM coating to some of their elements.

Onboard forward-looking antennas installed onboard modern combat aircraft significantly increase their RCS, especially when observed nose-on. Development of general RCS computation method introduced below includes quantitative evaluation of contribution from such antennas into the field scattered from the whole airborne object. In this section, we also consider the method for computing scattering characteristics of reflector antenna systems placed under dielectric radomes (Figure 2.69).

The field scattered in the backward direction from the antenna is presented in the form of a sum, first summand of which corresponds to the scattering from the radome only (given that antenna itself is absent) and the second integral summand corresponds to the contribution from the antenna into the field scattered by the "antenna–radome" system. The latter summand includes all the intrasystem interactions. While doing this, we assumed that current density over antenna reflector is induced by the primary wave propagated directly through the radome wall, and by the secondary wave reflected once from the inner surface of the radome wall.

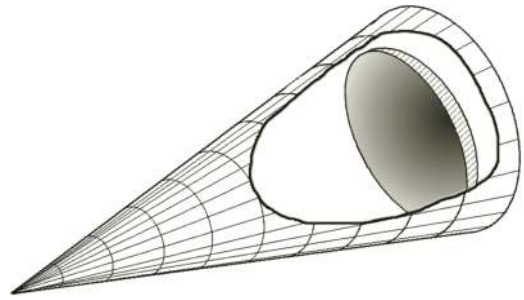

FIGURE 2.69 Model of reflector antenna system under the cone radome.

The use of asymptotic methods of short wave diffraction allows us to provide computations for the radomes with small surface curvature. The ogive-shaped radomes used in practice, which take the middle position between the radomes with conically and spherically shaped tips, do not satisfy the latter condition. Besides, the use of asymptotical ray and current methods is complicated by the necessity of accounting for multiple wave reflections inside the radome. In this case, one should use the method of integral equations [70–76]. However, these issues are beyond the scope of this book.

2.4.1 Computation of Scattering Characteristics of Electrically Large Antennas and the Measures for Reducing Their Radar Visibility

Reduction in radar visibility of antenna by giving it specific shape is unacceptable since the form of reflector is determined by the necessity of providing the antenna with specific directivity pattern. In this regard, application of RAM coating to the antenna surface fractures comes to the foreground. The main surface fracture present in any reflector antenna is the rim of its reflector. Therefore, in this section, we consider computational expressions providing scattering characteristics of the antennas, reflector's rim of which is covered with RAM.

Let us consider a reflector antenna in free space. We assume that antenna dimensions are greater than illumination signal wavelength (this condition holds for the pencil beam antennas). We also assume the antenna reflector to be an infinitely thin screen D shaped as paraboloid of revolution, the rim of which being provided with toroidal RAM coating. Properties of the coating are characterized by ε_A, μ_A, and its cross section in the plane orthogonal to the rim is a circle with radius ρ (Figure 2.70).

We assume that plane monochromatic wave (2.1) is incident onto the antenna reflector.

Here, as in the rest of the book, we consider that time dependence of the field has the form of $\exp(-j\omega t)$.

2.4.1.1 Basic Mathematical Expressions for Computing Electromagnetic Field Scattered from Electrically Large Reflector Antenna with RAM Coating at Its Rim

To solve the problem formulated above, we use the integral representation of scattered field of the Stratton–Chu type [29] (which, in its turn, can be obtained using the Lorentz reciprocity theorem [11,77]):

$$\vec{H}^{scat}(\vec{x}_0) = \int_S \left[-(\vec{H}^{\perp} \times \vec{\nabla} g) + j\omega\varepsilon_0 g \vec{E}^{\perp} - \frac{1}{j\omega\mu_0}(\vec{E}^{\perp} \cdot \vec{\nabla})\vec{\nabla} g \right] ds, \tag{2.141}$$

where $\vec{x}_0$ is the radius-vector of observation point, S is any closed surface enveloping the screen D (Figure 2.70), $\vec{E}^{\perp} = \vec{n} \times \vec{E}$, $\vec{H}^{\perp} = \vec{n} \times \vec{H}$ are the tangential components of total field at the surface S,

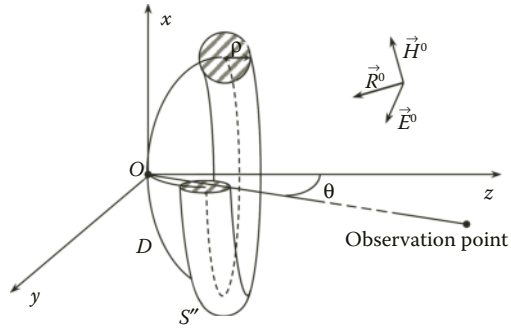

FIGURE 2.70 Reflector antenna geometry.

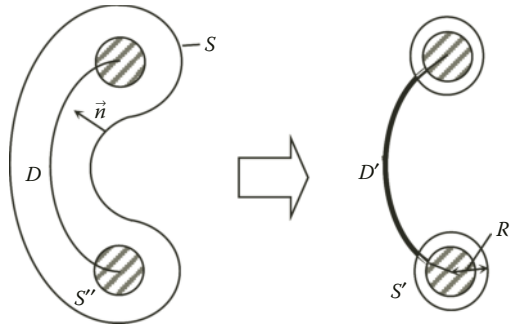

FIGURE 2.71 Cross section of the screen by plane xOz.

$\vec{n}$ is the inner, with respect to S, normal, $g = \exp(jk_0 r)/4\pi r$, $r = |\vec{x}_0 - \vec{x}|$, and $\vec{x}$ is the radius vector of a point at the surface S.

We now assume the surface S to be tending to D (Figure 2.71) everywhere except the rim vicinity. In the vicinity of the rim, we assume the surface S to be tending to toroidal surface S' that envelopes the absorbent surface S''.

As a result, we get the following expression for the scattered field:

$$\vec{H}^{scat}(\vec{x}_0) = \int_{S'} \left[-(\vec{H}^{\perp} \times \vec{\nabla} g) + j\omega\varepsilon_0 g \vec{E}^{\perp} - \frac{1}{j\omega\mu_0} (\vec{E}^{\perp} \cdot \vec{\nabla}) \vec{\nabla} g \right] \mathrm{d}s - \int_{D'} \vec{K} \times \vec{\nabla} g \, \mathrm{d}s, \tag{2.142}$$

where D' is such part of surface D that excludes the rim vicinity bounded by surface S' (in Figure 2.71 this surface D' is highlighted with bold line). The variable $\vec{K}$, which enters expression (2.142), is the jump in surface current density induced at D':

$$\vec{K} = (\vec{H}^{\perp})^{+} - (\vec{H}^{\perp})^{-}, \tag{2.143}$$

where $(\vec{H}^{\perp})^{+}$ and $(\vec{H}^{\perp})^{-}$ are the surface densities of electric current over illuminated and obscured sides of the screen, respectively.

Let us find expressions for computing field scattered by the screen in the far-field zone. To do this, we use asymptotic of the functions g and $\vec{\nabla} g$ given $r \to \infty$ [77]:

$$g \underset{r\to\infty}{\sim} \frac{\exp\left(jk_0 |\vec{x}_0|\right) \exp\left[-jk_0 (\vec{r}^{\,0} \cdot \vec{x})\right]}{4\pi |\vec{x}_0|}, \tag{2.144}$$

$$\vec{\nabla} g \underset{r\to\infty}{\sim} -jk_0 \frac{\exp\left(jk_0 |\vec{x}_0|\right) \exp[-jk_0 (\vec{r}^{\,0} \cdot \vec{x})]}{4\pi |\vec{x}_0|} \vec{r}^{\,0}, \tag{2.145}$$

where $\vec{r}^{\,0}$ is the unit-vector directed to the observation point.

Taking into account expressions (2.144) and (2.145), we get the following:

$$\vec{H}^{scat}(\vec{r}^{\,0}) \approx jk_0 \frac{\exp\left(jk_0 |\vec{x}_0|\right)}{4\pi |\vec{x}_0|} (\vec{I}_{S'} + \vec{I}_{D'}) \times \vec{r}^{\,0}, \tag{2.146}$$

where

$$\vec{I}_{S'} = \int_{S'} \left[\vec{H}^{\perp} - \sqrt{\frac{\varepsilon_0}{\mu_0}} (\vec{E}^{\perp} \times \vec{r}^{\,0}) \right] \exp[-jk_0(\vec{r}^{\,0} \cdot \vec{x})] \mathrm{d}s, \tag{2.147}$$

$$\vec{I}_{D'} = \sqrt{\frac{\varepsilon_0}{\mu_0}} \int_{D'} \vec{K} \exp[-jk_0(\vec{r}^{\,0} \cdot \vec{x})] \, \mathrm{d}s. \tag{2.148}$$

Since geometrical dimensions of surface D' are large compared to signal wavelength, and the surface itself does not include the vicinity of the reflector rim where the irregular component of surface current density plays significant role, then contribution of the surface D' into scattered field is computed in approximation of physical optics. Particularly,

$$(\vec{H}^{\perp})^{+} = 2(\vec{n} \times \vec{H}^{0}), \quad (\vec{H}^{\perp})^{-} = 0. \tag{2.149}$$

Once expression (2.149) is used, then Equation 2.148 takes the form

$$\vec{I}_{D'} = 2\sqrt{\frac{\varepsilon_0}{\mu_0}} \int_{D'_+} \vec{n} \times (\vec{R}^0 \times \vec{p}^{\,0}) \exp[jk_0(\vec{R}^0 - \vec{r}^{\,0}) \cdot \vec{x}] \mathrm{d}s, \tag{2.150}$$

where D'_+ is the illuminated part of surface D'.

Since the integrand in Equation 2.150 has fast oscillating exponential multiplier, then this integral should be computed using cubature formula (2.15) obtained above in Section 2.2.2 for the integral of the form: $M = \int_{S'_1} f(\vec{x}) \exp(jk_0 \Omega(\vec{x})) \mathrm{d}s$, in which the amplitude and phase function of integrand have the following form: $f(\vec{x}) = \vec{n}(\vec{x}) \times (\vec{R}^0 \times \vec{p}^{\,0})$ and $\Omega(\vec{x}) = jk_0(\vec{R}^0 - \vec{r}^{\,0}) \cdot \vec{x}$, respectively. It is worth noting that the use of cubature formula requires the surface D'_+ to be triangulated, that is, replaced by a set of flat triangles $\{\Delta_j\}$. Within every triangle, the amplitude and phase functions are linearly interpolated. Then, the integral M is represented by a sum of integrals over all the triangles Δ_j.

In Ref. [51], the estimate of the cubature formula (2.15) residual was found. It can be used either as accuracy estimate for the integral (2.14) or as an indicator of required number of triangles, which the surface D'_+ to be split into in order to provide the needed calculation accuracy.

Contribution from the vicinity of reflector rim into total scattered field is determined by expression (2.147). Let us represent radius-vector of a point at surface S' in expression (2.147) in the form of the sum (see Figure 2.72):

$$\vec{x} = \vec{X}(l) + \vec{\xi}(\varphi), \tag{2.151}$$

where $\vec{X}(l)$ is the radius-vector of a point at the rim that has the arc coordinate l, and $\vec{\xi}(\varphi)$ is the vector orthogonal to the rim at point l that has the length $R \geq \rho$ and orientation of which is determined by angle $\varphi (0 \leq \varphi \leq 2\pi)$. Angle φ is counted off the half-plane that is tangent to the reflector rim at point l.

Based on Equation 2.151, the values $\vec{H}^{\perp}$ and $\vec{E}^{\perp}$ at point with radius-vector $\vec{x}$ at the surface S' can be expressed as follows:

$$\begin{aligned} \vec{H}^{\perp} &= \vec{\tilde{H}}^{\perp}(\vec{\xi}) \exp(jk_0(\vec{R}^0 \cdot \vec{X}(l))), \\ \vec{E}^{\perp} &= \vec{\tilde{E}}^{\perp}(\vec{\xi}) \exp(jk_0(\vec{R}^0 \cdot \vec{X}(l))), \end{aligned} \tag{2.152}$$

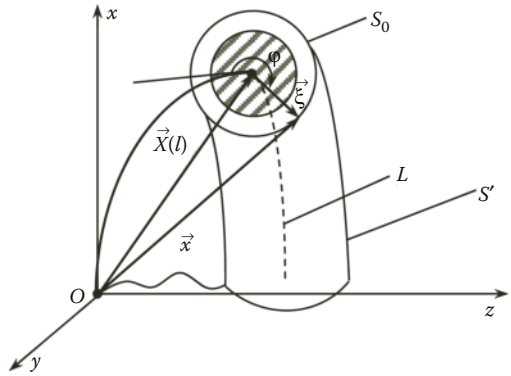

FIGURE 2.72 To explanation of the integration over surface S'.

where $\vec{\tilde{H}}^{\perp}(\vec{\xi})$ and $\vec{\tilde{E}}^{\perp}(\vec{\xi})$ are the surface densities of electric and magnetic currents, respectively, at points of surface S' that are excited by incident wave:

$$\begin{aligned}\vec{\tilde{E}}^{0}(\vec{\xi}) &= \vec{p}^{\,0}\exp(jk_0(\vec{R}^{0}\cdot\vec{\xi})),\\ \vec{\tilde{H}}^{0}(\vec{\xi}) &= \sqrt{\varepsilon_0/\mu_0}\,(\vec{R}^{0}\times\vec{p}^{\,0})\exp(jk_0(\vec{R}^{0}\cdot\vec{\xi})).\end{aligned} \tag{2.153}$$

So, the surface integral entering the expression (2.147) can be represented as a double one like it was done in Ref. [31]. External integral is along the rim line L:

$$\vec{I}_{S'}(\vec{r}^{\,0}) = \int_L \exp[jk_0((\vec{R}^{0}-\vec{r}^{\,0})\cdot\vec{X}(l))]\;\vec{M}(l,\vec{r}^{\,0})\,\mathrm{d}l, \tag{2.154}$$

where $\mathrm{d}l$ is the arc element of L. Internal integral, in its turn, is along the line S_0, which is the crossing line between the integration surface S' and the plane orthogonal to the reflector rim at point l. In our case, this S_0 is the circumference of radius R (Figure 2.72). Expression for $\vec{M}(l,\vec{r}^{\,0})$ takes the form:

$$\vec{M}(l,\vec{r}^{\,0}) = \int_{S_0}\exp[-jk_0(\vec{r}^{\,0}\cdot\vec{\xi})]\left(\vec{\tilde{H}}^{\perp}(\vec{\xi}) - \sqrt{\frac{\varepsilon_0}{\mu_0}}(\vec{\tilde{E}}^{\perp}(\vec{\xi})\times\vec{r}^{\,0})\right)\mathrm{d}q, \tag{2.155}$$

where $\mathrm{d}q = R\mathrm{d}\varphi$ is the arc element of circumference S_0. In our computations, we assumed the radius R to be equal to half the wavelength of incident field. Such choice of R is conditioned by the fact that, as is shown in Ref. [29], at the distances larger than half the wavelength from the wedge's edge the values of total field at the wedge's faces are close to those computed in approximation of physical optics.

Integral (2.154) can be evaluated by the stationary phase method [25]. The equation for finding stationary phase points l_0 at the rim L has the following form:

$$h'(l_0) = (\vec{R}^{0}-\vec{r}^{\,0})\cdot\vec{X}'(l_0) = 0. \tag{2.156}$$

However, for the circular edge, which is the reflector's rim in our model, there is a situation when it is impossible to apply the stationary phase method. This situation corresponds to the axial

illumination of reflector in case of monostatic radar, where the whole rim becomes "specular" region. The value of integral $I_{S'}(r^0)$ can be obtained by numerical integration (in our computations, results of which will be presented below, we used the five-point Gaussian integration formula [78]).

Once the stationary phase points have been found, they need to be checked for "visibility" from both the transmitter and receiver directions. We provided such check using the ray tracing method described in Ref. [47]. The essence of the method can be explained by example of checking the stationary point with coordinates (x_0, y_0, z_0) for its visibility from the direction set by R^0. The check is provided by solving simultaneous equations:

$$\begin{cases} x = x_0 + R_x^0 t, \\ y = y_0 + R_y^0 t, \\ z = z_0 + R_z^0 t, \\ x^2 + y^2 - 4fz = 0, \end{cases} \tag{2.157}$$

where R_x^0, R_y^0, R_z^0 are the projections of vector R^0 onto axes x, y, and z, respectively, and f is the focal distance of the antenna reflector.

In simultaneous Equations 2.157, the first three expressions describe parametrically the straight line passing through point (x_0, y_0, z_0) in the direction R^0, the fourth equation describes the reflector geometry. Having solved simultaneous Equations 2.157 with respect to t, we obtain the second-order equation with roots t_1, t_2. One of the roots always equals to 0. If the nonzero root is negative, it means that ray being considered crosses the antenna reflector at some point that obscures point (x_0, y_0, z_0). In the same manner, we check the point for its visibility from the receiving direction. If this stationary point is not visible from at least one of these directions, its contribution into scattered field is not accounted for. In case of monostatic radar, only one check is necessary. Having provided such check for every stationary phase point and having applied the stationary phase point method itself, we obtain the following expression:

$$I_{S'}(r^0) \sim \sum_{l_0^{vis}} \exp\left[jk_0(R^0 - r^0) \cdot x(l_0) + \operatorname{sgn}[(R^0 - r^0) \cdot n_L(l_0)] j \frac{\pi}{4} \right] \cdot M(l_0, r^0) \sqrt{\frac{2\pi}{k_0 æ(l_0) \left| (R^0 - r^0) \cdot n_L(l_0) \right|}}, \tag{2.158}$$

where $n_L(l_0)$ is the unit-vector of major normal to L at point l_0, the symbol l_0^{vis} means that summation is done over all "visible" stationary phase points at the rim, and $æ(l_0)$ is the curvature of curve L at point l_0.

When the integral (2.154) is to be computed using expression (2.158), one need to know the value of function $M(l, r^0)$ at point l_0. Due to the fact that integrand in Equation 2.155 is smooth enough, the $M(l_0, r^0)$ can be evaluated using one-dimensional numerical integration. In our computation, we used the five-point composite Gauss formula [78]. For this purpose, we needed to find the values for $\vec{\tilde{H}}^{\perp}(\vec{\xi})$ and $\vec{\tilde{E}}^{\perp}(\vec{\xi})$ along the line S_0. Taking into account the large electric dimensions of the reflector and small curvature of its rim, we can assume the values of $\vec{\tilde{H}}^{\perp}(\vec{\xi})$ and $\vec{\tilde{E}}^{\perp}(\vec{\xi})$, like it was explained in Section 2.2.4, to be equal approximately to those values that would have been excited at the surface of absorbent cylinder if the latter had been covering the edge of perfectly conducting half-plane that was tangent to the reflector surface at point l_0.

As in Section 2.2.4, we computed the values of $\vec{\tilde{H}}^{\perp}(\vec{\xi})$ and $\vec{\tilde{E}}^{\perp}(\vec{\xi})$ using solution to the simulative problem of oblique incidence of plane electromagnetic wave onto perfectly conducting wedge

provided with RAM coating at its edge [46], the only difference being in the value of external angle of the wedge, which became equal to 2π. In this case, the wedge itself turned into a half-plane (Figure 2.73).

Like it was in Section 2.2.4, we represent the $\tilde{E}_3$ and $\tilde{H}_3$ as $\tilde{E}_3 = u(x_1', x_2') \exp(jk_0 x_3' R_3^0)$, $\tilde{H}_3 = v(x_1', x_2') \exp(jk_0 x_3' R_3^0)$, and introduce the vector $w = \begin{pmatrix} u(x_1', x_2') \\ v(x_1', x_2') \end{pmatrix}$. In our case, the value of w outside the absorbent cylinder can be decomposed into series (2.78), but with respect to the Bessel functions of half-integer index. The latter is so because we took the parameter ϕ determining the angular aperture of the wedge to be equal to two. So, the series is as follows:

$$w = \sum_{m=0}^{\infty} \left[A_m J_{\frac{m}{2}}(\eta_0 r) + C_m H_{\frac{m}{2}}^{(1)}(\eta_0 r) \right] f_m(\varphi), \tag{2.159}$$

where $J_{\frac{m}{2}}(\eta_0 r)$ is the Bessel function, $H_{\frac{m}{2}}^{(1)}(\eta_0 r)$ is the Hankel function, $\eta_0 = k_0 \sqrt{1 - (R_3^0)^2}$, and $f_m(\varphi) = \begin{pmatrix} \sin(\varphi m/2) \\ \cos(\varphi m/2) \end{pmatrix}$.

Expressions for the matrix (2×2) coefficients A_m, and C_m were received in Ref. [46].

Having known the values of $u(x_1', x_2')$ and $v(x_1', x_2')$, we can use the Maxwell equations to find all other components of the sought field.

Finally, using expression (2.159) for computing $M(l, r^0)$ by formula (2.155) and taking into account that $\vec{\tilde{H}}^{\perp}(\vec{\xi}) = \vec{n} \times \vec{\tilde{H}}(\vec{\xi})$ and $\vec{\tilde{E}}^{\perp}(\vec{\xi}) = \vec{n} \times \vec{\tilde{E}}(\vec{\xi})$, we find the resulted contribution from all visible parts of the reflector rim into resulted scattered field.

In order to prove the applicability of the method described above, we compared the computational results to the results of real scattering of plane wave at the antenna reflector in anechoic chamber.

As antenna reflector, we took the paraboloid of revolution with aperture of 0.3 m and focal distance of 0.137 m. Computation was carried out for the wavelength of $\lambda = 0.032$ m.

The results of computation and experiment are shown in Figure 2.74.

The figure shows RCS of paraboloid of revolution versus observation angle θ that is counted off the reflector's axis of revolution in plane yOz (refer to Figure 2.70). Polarization vector of incident field was oriented along the axis Ox (hereinafter, we refer to such vector orientation as vertical polarization, and we refer to the case of polarization vector being perpendicular to axis Ox as horizontal one). The bold line is for experimental RCS values, and the thin line is for computed RCS values.

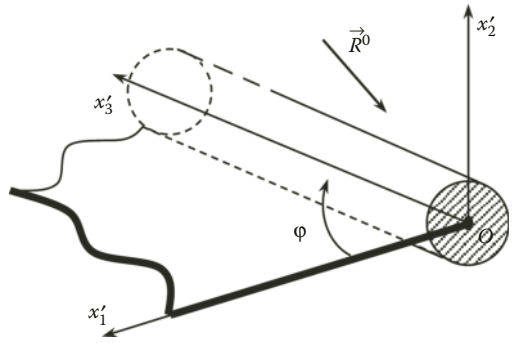

FIGURE 2.73 The half-plane with radar absorbent cylinder at its edge.

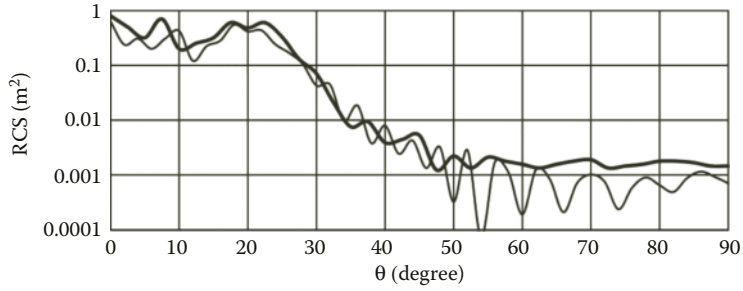

FIGURE 2.74 Backscattering diagram of paraboloid of revolution.

As seen from the plot, the results of computation agree quite well with the experiment. Small deviation of the two curves is due to, first, some misalignment of vertical plane containing the axis of paraboloid with the direction toward the receiving antenna that took place in measurements and, second, value of the observation aspect θ increment was equal to 2.5°, because of which some ravines of the dependence could have been missed.

2.4.1.2 Study of the Possibility to Reduce RCS of Reflector Antennas by Means of Applying Radar Absorbent Coating to the Reflector Rim

Reflector antennas are installed on a wide range of airborne objects (forward-looking radar antenna of aircraft, radar seeker antennas of different purpose missiles). Therefore, in this section we present computation results for backscattering diagrams of parabolic reflector antennas of different geometrical dimensions in case of application of different thickness RAM coating to their reflectors' rims.

In Section 2.4.1.1, we gave the expression for RCS of finite paraboloid of revolution in conditions of its axial illumination, monostatic radar configuration, and physical optics approximation:

$$\sigma = 2\pi q^2(1 - \cos(2k_0 d)), \tag{2.160}$$

where q is the parameter of parabolic reflector equal to double focal distance of paraboloid, and d is the paraboloid depth.

It is seen from Equation 2.160 that RCS is oscillating function versus frequency (or wave number k) of incident field. Therefore, small frequency deviation can lead to considerable change in the RCS value. So, this instantaneous RCS must be averaged over some frequency range in order to obtain reliable RCS estimate. It is advisable to match the frequency range used for averaging the antenna RCS of airborne objects to the signal bandwidth of surveillance (warning) radar.

One of the basic means for detecting airborne objects today is the Airborne Warning and Control System (AWACS) aircraft. The radar of AWACS aircraft operates in S-band (from 7.5 cm through 15 cm). So, we set the frequency range for averaging RCS of antennas considered below to be lying inside the S-band, namely it shall be from 8.5 cm through 9.5 cm. It is worth mentioning that with this operating frequency band in mind, the onboard antennas considered below can indeed be regarded as passive scatterers, since the operating wavelengths of AWACS radar are, in average, two to three times as large as operating wavelengths of the most of these antennas.

Geometric parameters of parabolic reflectors, for which we computed scattering characteristics, are presented in Table 2.1.

Computation results for backscattering diagrams of the three AS under consideration are presented in Figures 2.75 through 2.77. Figure 2.75 corresponds to AS #1, Figure 2.76 corresponds to AS #2, and Figure 2.77 corresponds to AS #3. In all of these three figures, the plots marked as (a) correspond to antenna illumination at vertical polarization and the plots marked as (b) correspond

TABLE 2.1
Geometric Parameters of Parabolic Reflectors of Onboard Antennas

Antenna Number	Reflector Diameter (m)	Reflector Focal Distance (m)
AS #1	0.63	0.233
AS #2	0.33	0.15
AS #3	0.365	0.166

to horizontal polarization. Thin lines are for backscattering diagrams of perfectly conducting reflector, the bold lines are for the reflector, whose rim is provided with toroidal RAM coating of 0.016 m radius, and the dashed lines are for the reflector, whose rim is provided with toroidal RAM coating of 0.008 m radius.

Properties of absorbent were assumed to be as follows: $\varepsilon' = 1 + j10$, $\mu' = 1 + j10$. These properties correspond to the so-called Zommerfeld-type absorbent. Such absorbents are described in [18,79]. Electromagnetic field inside such absorbent fades very quickly as the wave propagates inside the material, since the imaginary parts of ε' and μ', which condition the losses, are great. When the incident field hits the absorbent's surface at right angle, the absorbent material's impedance matches that of free space, that is, $Z = \sqrt{\mu_a/\varepsilon_a} = \sqrt{\mu_0/\varepsilon_0} = Z_0$ (Z_0 is the impedance of free space; Z is impedance the surface; ε_a, μ_a are the absolute permittivity and permeability of RAM).

In order to analyze the backscattering diagrams in Figures 2.75 through 2.77, it is convenient to split the whole sector of antenna observation aspects θ into three subsectors (Figure 2.70). The first subsector would include the aspects θ close to axial illumination of antenna system. In this subsector, we observe either peak or ravine of backscattering diagram. In Figure 2.75, this subsector includes aspect angles $0 \le \theta \le 5°$; in Figure 2.76, it includes aspects $0 \le \theta \le 7°$; and in Figure 2.77,

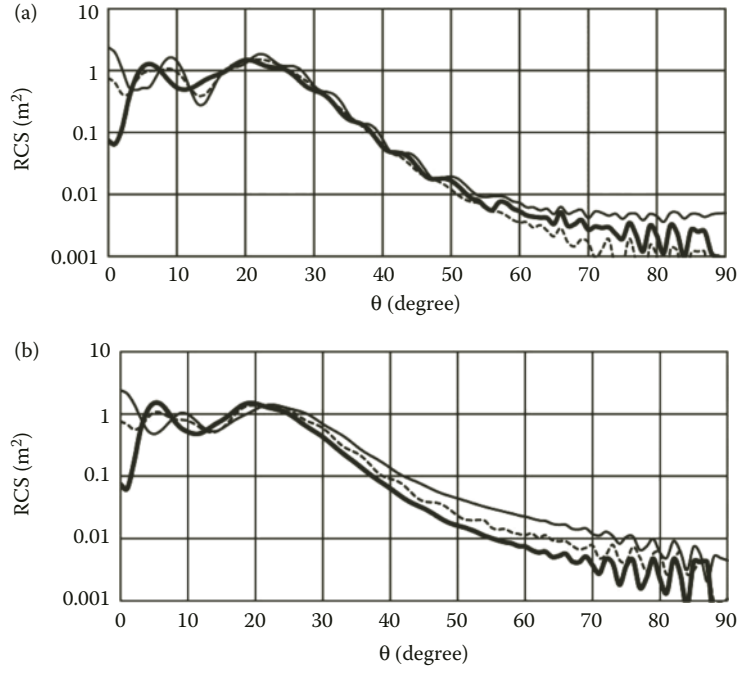

FIGURE 2.75 Backscattering diagrams of antenna system #1 (a – vertical polarization, b – horizontal polarization).

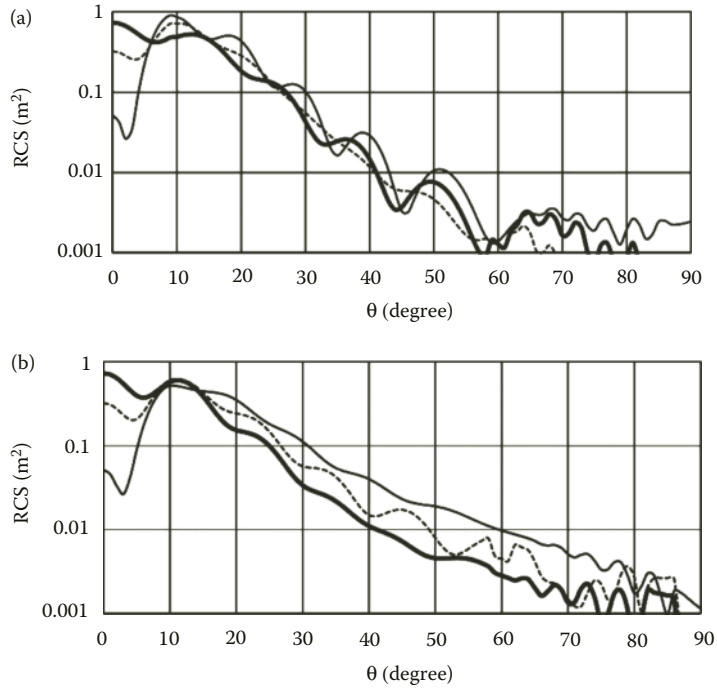

FIGURE 2.76 Backscattering diagrams of antenna system #2 (a – vertical polarization, b – horizontal polarization).

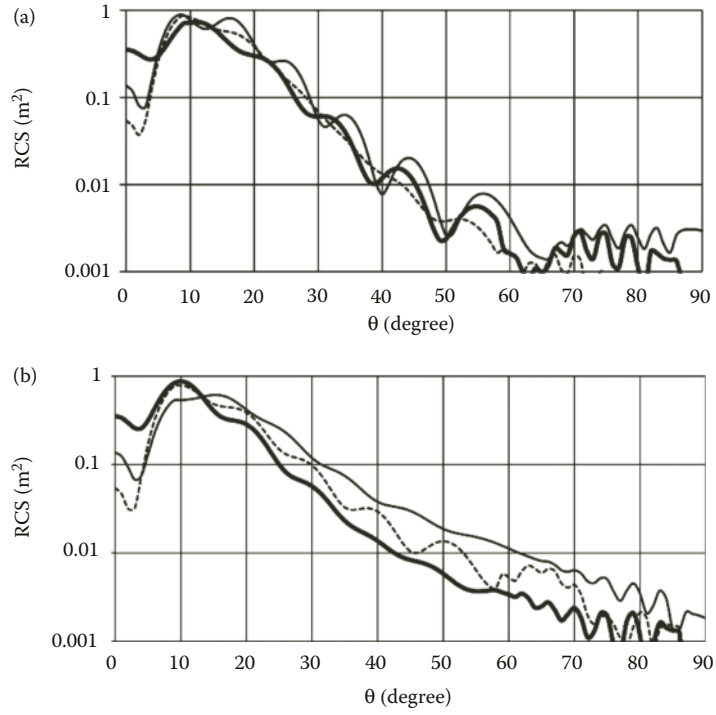

FIGURE 2.77 Backscattering diagrams of antenna system #3 (a – vertical polarization, b – horizontal polarization).

it includes aspects $0 \le \theta \le 8°$. If antenna system is observed at aspect angles lying in this subsector, then application of RAM coating to the antenna reflector rim can decrease its RCS (Figure 2.75), but such RAM application can increase the antenna system RCS as well (Figure 2.76).

Such RCS increase can be explained by the fact that given axial illumination of finite paraboloid of revolution by a monostatic radar, its RCS is the oscillating function versus wavelength of incident field. Such property of this function can already be seen from Equation 2.160, which does not account for irregular current component (due to the reflector's rim). Figure 2.78 shows the RCS of paraboloid versus wavelength of incident field computed using expression (2.160). Here, bold solid line corresponds to RCS dependence of AS #1, thin solid line corresponds to the RCS dependence of AS #2, and thin dashed line corresponds to the RCS dependence of AS #3. Analysis of Figure 2.78 shows that given the signal wavelength lies between 0.085 m and 0.095 m the values of RCS for AS #1 approach their maxima.

Our computations show that fields scattered by the smooth surface part and edge local scatterers interfere constructively for antenna system #1 given this wavelength band, which explains the maximum in its RCS. Application of RAM coating to the antenna reflector's rim leads to the antenna RCS decrease in the first subsector of observation aspects θ.

In case of AS #2, we observe destructive interference of the fields scattered by the smooth surface part and edge local scatterers of antenna reflector, which results in minimal antenna RCS for the aspect angle of $\theta = 0$. In this situation, application of RAM to the reflector's rim decreases the contribution into resulted scattered field from the edge local scatterers, but the resulted field scattered from paraboloid in direction of $\theta = 0$ goes up (Figure 2.76).

RCS of AS #3 (dashed line in Figure 2.78) does not reach its minimum in this first angle subsector and in the wavelength band under consideration. Therefore, application of toroidal RAM coating with radius 0.008 m leads to decrease in RCS level (Figure 2.77) and increase in the RAM-coating radius up to 0.016 m, on the contrary, leads to increase in RCS level (bold line in Figure 2.77).

Analysis of Figure 2.78 shows that in the first subsector of aspects θ we should expect the reduction in antenna RCS due to RAM coating at the reflector's rim within those wavelength bands, in which the antenna RCS approaches its maximum (Figure 2.78). For instance, results of backscattering diagram computation for AS #2 given the averaging over the wavelength band from 0.055 m through 0.065 m presented in Figure 2.79 (the lines designation being the same as in Figure 2.76) show the efficiency of RAM-coating application to the antenna reflector's rim.

The second subsector of aspect angles θ would include observation aspects, at which the specular reflection region appears at smooth part of reflector's surface that contributes mostly into the field scattered backward. For the AS #1, this subsector includes aspect angles $5° < \theta \le 28°$; for AS #2, it includes the aspects $7° < \theta \le 18°$; and for AS #3, it includes the aspects $8° < \theta \le 17°$. It can be seen

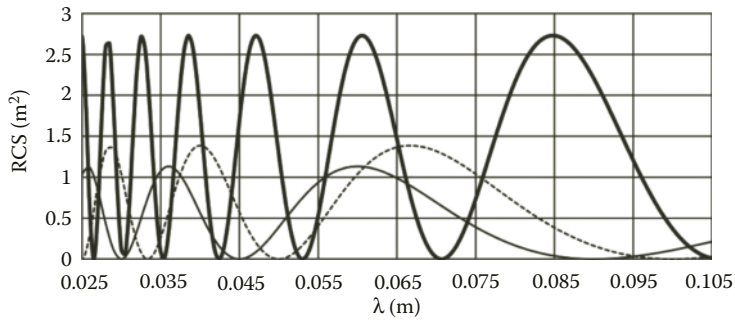

FIGURE 2.78 RCS of antenna systems versus incident field wavelength given axial illumination of their reflectors computed in physical optics approximation (bold solid line – AS #1, thin solid line – AS #2, thin dashed line – AS #3).

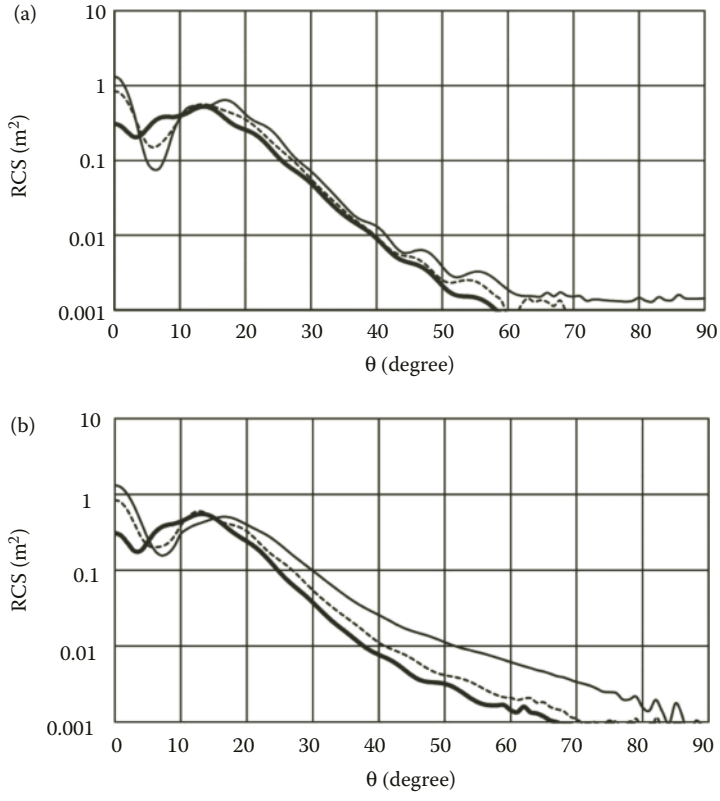

FIGURE 2.79 Backscattering diagrams of antenna system #2 given averaging in the wavelength band of incident wave from 0.055 m through 0.065 m (a – vertical polarization, b – horizontal polarization).

from Figures 2.75 through 2.77 that application of RAM coating to reflector's rim in this case does not have any significant influence on reduction in the backscattered field level.

In the third subsector of observation aspects, this specular reflection region at smooth part of the reflector's surface is absent, so the edge local scatterers (reflector's rim) contribute significantly into backscattered field. For the case of AS #1, this third subsector of observation aspects includes the angles $28° < \theta \le 90°$; for AS #2, it includes aspects $18° < \theta \le 90°$; and for AS #3, it includes the aspects $17° < \theta \le 90°$. Therefore, in this third subsector of antenna observation aspects θ, application of toroidal RAM coating to the reflector's rim again leads to significant reduction in the antenna RCS.

Computation results presented above indicate that for every specific reflector antenna, one should evaluate the properties and parameters of RAM coating at its rim while bearing specific sector of aspect angles in mind.

2.4.2 Radar Scattering of Three-Dimensional Model of Onboard Reflector Antenna under the Cone Radome

Here, we seek for engineering expressions to compute backscattering characteristics of radar equipment situated in the nose part of air vehicle. In this regard, we consider the three-dimensional model of reflector antenna system placed under the conical radome (Figure 2.80), which is illuminated from outside by plane electromagnetic wave (2.1) (given $p^0 = p$).

Application of the Lorentz reciprocity theorem to the sought total field (E, H) and to auxiliary field $(\hat{E}, \hat{H}(x|x_0, p))$, the latter corresponding to that of electric dipole placed at point x_0 that has

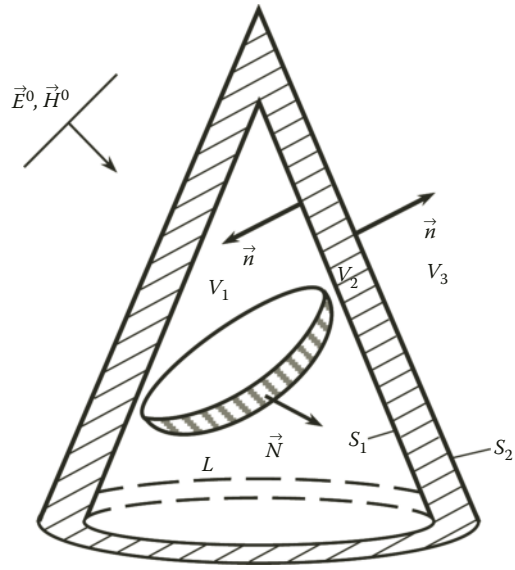

FIGURE 2.80 The "antenna–radome" system.

the vector-moment p given that only radome is present, allows us to obtain integral representation of the field we seek

$$j\omega p \cdot E(x_0) = j\omega p \cdot E^{scat.}_{radome}(x_0) + \int_L (K(x) \cdot \hat{E}^T(x|x_0, p))\mathrm{d}S, \tag{2.161}$$

where $E^{scat.}_{radome}(x_0)$ is the field scattered by the radome only, $K(x)$ is the surface current density over the antenna reflector's surface. Integral summand of expression (2.161) represents the response of antenna reflector onto incident wave that takes into account electromagnetic wave interaction with the radome. Having placed $x_0 = -rR^0$ and having further assumed that $r \to \infty$, we receive expression for resulted field scattered from the "antenna–radome" system in the far-field zone:

$$p \cdot E(R^0) \sim p \cdot E^{scat.}_{radome}(R^0) - jk_0 \frac{e^{jk_0 r}}{4\pi r}\sqrt{\frac{\mu_0}{\varepsilon_0}}\int_L (\hat{E}(x) \cdot K(x))\mathrm{d}S. \tag{2.162}$$

Here, $\hat{E}(x)$ is the field excited by primary incident plane wave (2.1) in points over the reflector's surface L given that only radome is present. We are going to compute this field by method of geometrical optics.

Under approximation assumed above, we represent $(\hat{E}(x), \hat{H}(x))$ as a sum of field that passes to reflector directly through the illuminated part of radome (propagation path 1 in Figure 2.81) and the field that passes to reflector via single reflection from the inner wall of radome (propagation path 2 in Figure 2.81).

The field corresponding to propagation path 1 in Figure 2.81 can be presented as

$$\vec{\hat{E}}_1(\vec{x}) = [\tau_\perp p_\perp \vec{e}_\perp + \tau_\parallel p_\parallel (\vec{R}^0 \times \vec{e}_\perp)] \exp(jk_0(\vec{R}^0 \cdot \vec{x})), \tag{2.163}$$

$$\vec{\hat{H}}_1(\vec{x}) = \sqrt{\frac{\varepsilon_0}{\mu_0}}[\tau_\perp p_\perp (\vec{R}^0 \times \vec{e}_\perp) - \tau_\parallel p_\parallel \vec{e}_\perp] \exp(jk_0(\vec{R}^0 \cdot \vec{x})), \tag{2.164}$$

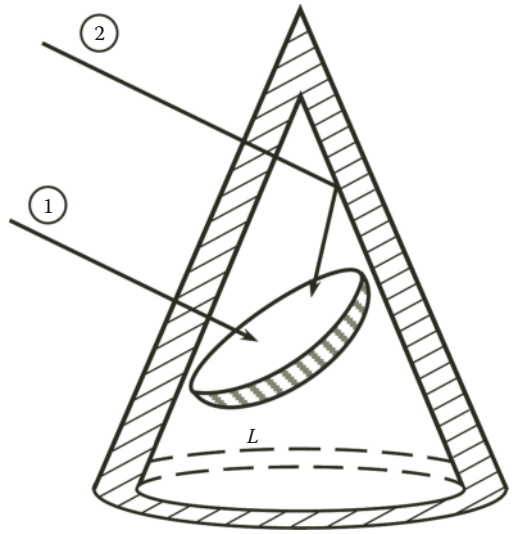

FIGURE 2.81 Propagation paths of incident wave.

where $e_{\perp} = \dfrac{R^0 \times n}{\left|R^0 \times n\right|}$, $\vec{e}_{\parallel} = (\vec{R}^0 \times \vec{e}_{\perp})$, $p_{\perp} = (p \cdot e_{\perp})$, $p_{\parallel} = (\vec{p} \cdot \vec{e}_{\parallel})$, and n is the vector of the normal to the radome surface.

Complex-valued coefficients $\tau_{\perp}, \tau_{\parallel}$ describe propagation of plane electromagnetic wave through flat uniform layer with the properties of radome at two mutually orthogonal polarizations. As parallel polarization marked by sign $\parallel$, we consider the situation where electric field intensity vector of incident wave belongs to the plane passing through vector R^0 and normal n at every particular point of the radome surface. Accordingly, the perpendicular polarization, marked by sign $\perp$, corresponds to situation where electric field intensity vector is orthogonal to the plane specified above. General expression for the propagation coefficient can be presented as follows:

$$\tau = \left(\left(\cos \kappa\delta + \frac{j}{c}\sin \kappa\delta\right) + \left(\cos \kappa\delta - \frac{j}{c}\sin \kappa\delta\right)\rho\right) \exp(-jk_0\delta\cos\theta), \tag{2.165}$$

where ρ is the complex-valued coefficient of reflection from plain uniform layer of material that has the properties of radome. This coefficient can be expressed as

$$\rho = \frac{j(c^2 - 1)\sin \kappa\delta}{2c\cos \kappa\delta - j(c^2 + 1)\sin \kappa\delta}. \tag{2.166}$$

Here, $c = \dfrac{\sqrt{\varepsilon' - \sin^2\theta}}{\beta\cos\theta}$, $\kappa = k_0\sqrt{\varepsilon' - \sin^2\theta}$, $\cos\theta = |(R^0 \cdot n)|$, $\sin^2\theta = 1 - (R^0 \cdot n)^2$, ε' is relative permittivity of the radome material, and δ is the radome thickness.

$$\beta = \begin{cases} 1 & \text{in case } \perp \text{ polarization,} \\ \varepsilon' & \text{in case } \parallel \text{ polarization.} \end{cases}$$

In case of polarization $\perp$, we have $\rho = \rho_{\perp}$, $\tau = \tau_{\perp}$; and in case of polarization $\parallel$, we have $\rho = \rho_{\parallel}$, $\tau = \tau_{\parallel}$.

If the ray passing through radome at some point x_0 does not hit the reflector, then it must pass through radome once again at some point x_1. If we find, in this case, the values for $\tau_\perp, \tau_\parallel$, $\rho_\perp, \rho_\parallel$, $e_\perp, e_\parallel$, at point x_0, then we can compute the intensity vector of electric field that has propagated through radome at point x_0 and that is incident onto its inner surface at point x_1

$$p_1 \exp(jk_0(R^0 \cdot x_1)), \quad p_1 = \tau_\perp p_\perp e_\perp + \tau_\parallel p_\parallel e_\parallel. \tag{2.167}$$

Vector p_1, wave incidence direction R_0, and the normal $n(x_1)$ to inner surface of radome S_1 at point x_1 can be used for finding $\tau_{1\perp}$, $\tau_{1\parallel}$, $\rho_{1\perp}$, $\rho_{1\parallel}$, $e_{1\perp}$, $e_{1\parallel}$ by means of formulas (2.165) and (2.166). The field that has reflected from inner surface of radome at point x_1 and that is incident onto antenna's reflector (path 2 in Figure 2.81) can be represented as follows:

$$\vec{\hat{E}}_2(\vec{x}) = [\rho_{1\perp} p_{1\perp} \vec{e}_{1\perp} + \rho_{1\parallel} p_{1\parallel} (\vec{R}^1 \times \vec{e}_{1\perp})] \exp(jk_0[(\vec{R}^0 \cdot \vec{x}_1) + (\vec{R}^1 \cdot \vec{x})]), \tag{2.168}$$

$$\vec{\hat{H}}_2(\vec{x}) = \sqrt{\frac{\varepsilon_0}{\mu_0}} [-\rho_{1\parallel} p_{1\parallel} \vec{e}_{1\perp} + \rho_{1\perp} p_{1\perp} (\vec{R}^1 \times \vec{e}_{1\perp})] \exp(jk_0[(\vec{R}^0 \cdot \vec{x}_1) + (\vec{R}^1 \cdot \vec{x})]), \tag{2.169}$$

where $R^1 = R^0 - 2n(x_1)(R^0 \cdot n(x_1))$.

It should be noted that once plane electromagnetic wave bounces off the inner surface of radome, then caustic surface may form. Computation of such caustic surface that appears in case of oblique incidence of plane wave onto the radome cone has been carried out in Refs. [80,81]. The ray passing through such caustic surface changes its phase by $\pi/2$ [82,83], which has to be taken into account for the wave hitting the antenna after reflection from the radome inner surface.

Surface current density $K(x)$ over antenna reflector in expression (2.162) is computed in the form of sum of currents excited on the reflector's surface by "direct" and "reflected" waves (path 1 and path 2 in Figure 2.81). In the physical optics approximation, current surface density can be expressed as

$$K(x) = 2(N \times \hat{H}), \tag{2.170}$$

where N is the vector of normal to the reflector's surface at point x, and $\hat{H}$ can be computed as a sum of magnetic field intensities for the first and second paths of incident wave propagation according to expressions (2.164) and (2.169), respectively.

The field $p \cdot E^{scat}_{radome}(R^0)$ scattered by radome can be computed using Kirchhoff's approximation

$$p \cdot E^{scat}_{radome}(R^0) \approx -jk_0 \frac{e^{jk_0 r}}{4\pi r} \iint\limits_{S_{illum.}} \Big[(p \cdot (n \times H'(x))) \sqrt{\frac{\mu_0}{\varepsilon_0}} + E'(x) \cdot (n \times (p \times R^0)) \Big] \exp(jk_0(R^0 \cdot x)) \, dS. \tag{2.171}$$

Here, (E', H') is the field at (or close to) illuminated surface of radome, which in Kirchhoff's approximation can be expressed as

$$\vec{E}'(\vec{x}) \approx \left[\rho_\perp(\vec{x}) p_\perp(\vec{x}) \frac{(\vec{R}^1 \times \vec{n})}{|\vec{R}^1 \times \vec{n}|} + \rho_\parallel(\vec{x}) p_\parallel(\vec{x}) \frac{\vec{R}^1 \times (\vec{R}^1 \times \vec{n})}{|\vec{R}^1 \times (\vec{R}^1 \times \vec{n})|} \right] \exp(jk_0(\vec{R}^1 \cdot \vec{x})), \tag{2.172}$$

$$H'(x) = \frac{1}{j\omega\mu_0}\nabla \times E'(x), \tag{2.173}$$

where $R^1 = R^0 - 2n(R^0 \cdot n)$, and $n = n(x)$ is the normal to the outer radome surface S_2. For dielectric radome of conical shape, representation (2.171) can be simplified and reduced to single integral by angular coordinate α tied to the illuminated part of radome:

$$p \cdot E^{scat.}_{radome}(R^0) \approx -jk_0 \frac{e^{jk_0 r}}{4\pi r} \frac{\sin\theta}{\cos^2\theta} \int_{\alpha_0}^{\alpha_1} \Psi(\alpha)\,d\alpha, \tag{2.174}$$

where

$$\Psi(\alpha) = F(\alpha)\left[\frac{h\exp(j2k_0 h\varphi(\alpha))}{2jk_0\varphi(\alpha)} + \frac{\exp(j2k_0 h\varphi(\alpha)) - 1}{4k_0^2\varphi^2(\alpha)}\right],$$

$$F(\alpha) = (\rho_\perp(\alpha)p_\perp^2(\alpha) - \rho_\parallel(\alpha)p_\parallel^2(\alpha))(R^0 \cdot n(\alpha)),$$

$$\varphi(\alpha) = \mathrm{tg}\,\theta(R_1^0\cos\alpha + R_2^0\sin\alpha) + R_3^0,$$

$$\alpha_0 = \mathrm{arcctg}\frac{\eta}{\sqrt{1-\eta^2}}, \quad \alpha_1 = 2\pi - \alpha_0, \quad \eta = \frac{\mathrm{tg}\theta}{\mathrm{tg}\gamma},$$

h is the radome height, θ is half-angle of the cone, γ is the angle between the cone axis and the vector R^0, $n(\alpha)$ is the vector of normal to outer surface of radome S_2.

For numerical computation, we take the antenna model with the following characteristics (Figure 2.82): the tip of radome cone is placed at the coordinate system origin, its axis coinciding with the

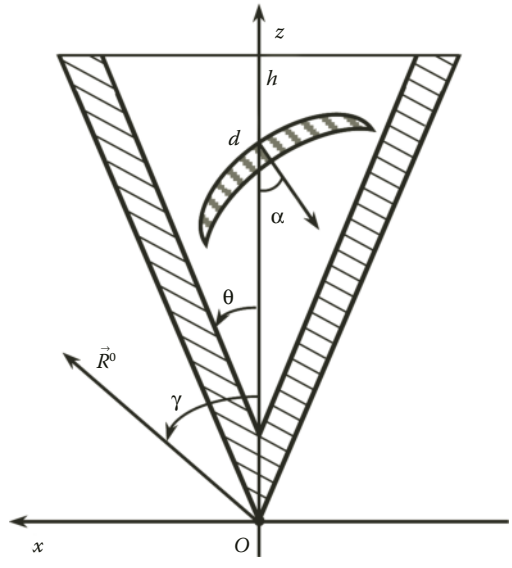

FIGURE 2.82 To the description of computer model of reflector antenna.

axis Oz. The rest of the parameters are as follows: radome height $h = 1$ m, half-angle of the cone (the angle between the cone's axis and generatrix) $\theta = 20°$, relative permittivity of the radome material $\varepsilon' = 7 + j0$, distance between the cone tip and the center of parabolic reflector $d = 0.75$ m, reflector's radius $a = 0.25$ m. Antenna can turn under the radome around axis Oy. Unit-vector of the wave incidence direction R^0 belongs to the plane Oxz ($R^0 = \{\sin\gamma, 0, \cos\gamma\}$).

In the process of our computer simulation, we considered three kinds of reflector antennas: the first one has almost flat reflector (focal parameter $q = 10$ m, reflector depth is about 3 mm), the second one has focal parameter $q = 1$ m with reflector depth of 3 cm, and the third one is the so-called "deep" reflector antenna (focal parameter $q = 25$ cm, reflector depth is 12 cm).

Figure 2.83 shows RCS of antenna with focal parameter $q = 1$ m versus its illumination angle γ given that radome is absent. Illumination signal wavelength was $\lambda = 3$ cm. Antenna reflector position was shifted by angle $\alpha = 45°$ in plane Oxz. Figure 2.84 shows RCS of the same antenna versus its illumination angle γ given that 5.6 mm thick radome is present (the radome wall thickness was matched to the incidence angle of 20°). Polarization vector of incident wave was perpendicular to plane Oxz (u-polarization). Thin black line shows contribution into antenna RCS from the field that was directly incident onto the antenna reflector (path 1 in Figure 2.81). The dashed gray line shows contribution into antenna RCS from the field that was incident onto the antenna reflector after bouncing off the inner wall of radome (path 2 in Figure 2.81). Bold black line shows the resulted RCS of antenna reflector that takes into account its electrodynamic interaction with radome.

Figure 2.85 shows RCS of the "antenna–radome" system. Thin black line shows resulted RCS of antenna reflector that takes into account its electromagnetic interaction with radome. Gray dashed line shows contribution into the "antenna–radome" system RCS from radome itself, resulted RCS of the system being shown by solid bold line. Analysis of Figures 2.84 and 2.85 and their comparison to the RCS dependence of antenna reflector without any radome shows that matched radome does not influence, in general, the antenna reflector RCS in quite wide angular sector. However, at some illumination angles, the presence of radome changes the resulted value of reflector RCS considerably. For instance, given reflector illumination at the angle of 45° (antenna reflector was illuminated along its axis), the influence of radome leads to sevenfold reduction in the RCS of whole system. The influence of field that was incident on the reflector after reflection from the inner radome wall led to considerable change in the reflector RCS given angles of its illumination greater than 60°. Reflections from the radome provide significant contributions into the system RCS given small values of illumination angles γ as well as given illumination angle $\gamma = 70°$, which corresponds to the wave incidence perpendicularly to the radome cone generatrix.

Dependencies similar to those shown in Figures 2.84 and 2.85, but for the situation where polarization vector of incident wave belongs to plane Oxz (v-polarization), are presented in Figures 2.86 and 2.87, respectively.

Given v-polarization of incident wave, the influence of radome onto the RCS of whole system decreases. The latter is due to decrease in field reflection from the inner wall of radome, decrease

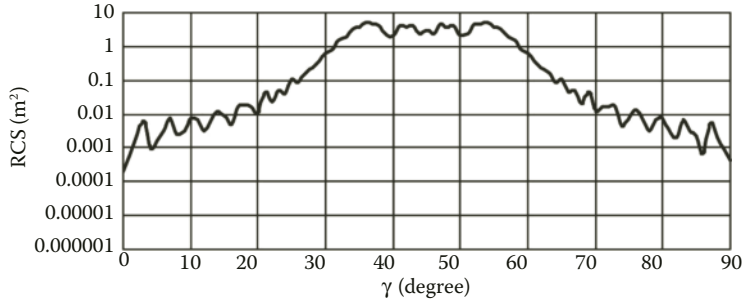

FIGURE 2.83 RCS of antenna reflector given that radome is absent.

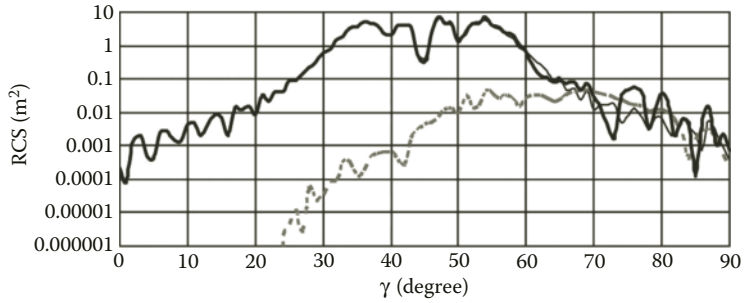

FIGURE 2.84 RCS of antenna reflector given that radome is present (*u*-polarization case).

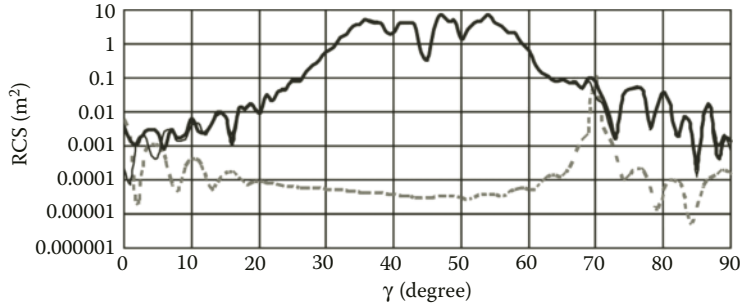

FIGURE 2.85 RCS of the "antenna–radome" system (*u*-polarization case).

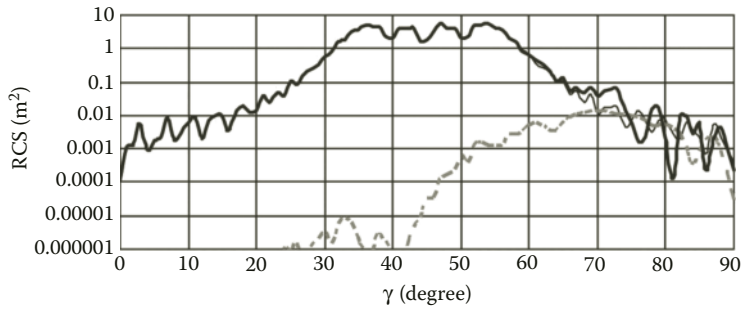

FIGURE 2.86 RCS of antenna given that radome is present (*v*-polarization case).

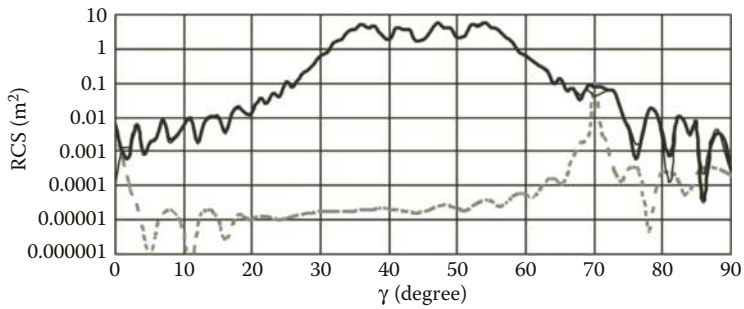

FIGURE 2.87 RCS of the "antenna–radome" system (*v*-polarization case).

in scattering from the radome itself, and the behavior of the whole "antenna–radome" system, which, given the *v*-polarization, comes closer to that of antenna without any radome compared to the case of *u*-polarization. For instance, given the *v*-polarization of wave and its incidence at $\gamma = 45°$, RCS of the system is almost the same as that of antenna without any radome for this aspect of illumination.

To evaluate the influence of radome on the whole system RCS given axial illumination of antenna reflector, we consider here the dependence of RCS on the antenna reflector depth (Figure 2.88). Reflector depth δ changes from 3 cm (illumination signal wavelength) through 10.5 cm (3.5 times the wavelength), which corresponds to change in focal parameter from $q = 1$ m to $q = 0.3$ m. Gray solid line shows RCS dependence on the antenna reflector depth given that radome is absent. Black solid line corresponds to the RCS dependence of antenna under radome given *v*-polarization of incident wave, and the dashed line corresponds to RCS dependence of antenna under radome given *u*-polarization.

RCS dependencies of antenna under radome are shifted to the right with respect to those of standalone antenna without any radome. Particularly, the dependence given *u*-polarization is shifted even more than others. Axial illumination of parabolic reflector leads to formation of Fresnel zones at its surface similar to those formed at the surface of convex objects (sphere for example). Its RCS is determined in this case by summation of fields scattered from the first and the last Fresnel zones at reflector's surface. The change in reflector's depth leads to periodic appearance or disappearance of Fresnel zones at the reflector's rim. Consequently, this periodicity of RCS variations is related to the wavelength of illumination signal. As it is seen from dependencies of Figure 2.88, the presence of radome influences considerably the formation of Fresnel zones. Given *u*-polarization, particularly, this influence gets even stronger.

Analysis of RCS computation results for the system with flat reflector ($q = 10$ m) shows the same tendencies as for the antenna with $q = 1$ m, that is, significant contribution into RCS of scattering from radome as well as from wave bouncing off the radome's inner wall given some aspect angles of illumination. RCS dependence in this case has sharp peak at illumination aspect of 45°, which is due to geometrical optics reflection from almost flat round screen the antenna reflector degenerates into. RCS of the system with "deep" antenna reflector ($q = 0.25$ m) is of oscillating (from 1 m to 10 m^2) nature in the whole sector of aspects (from 0° to 90°). Besides, presence of wave bounced off the inner wall of radome does not have any significant influence on the RCS of antenna.

Accounting for electromagnetic interactions between antenna and its radome provides much more accurate prediction of the "antenna–radome" system RCS and, as a result, it increases the accuracy of RCS prediction for the whole object bearing antenna under a radome. Angular and other dependencies of RCS are of oscillating nature and they change in wide range. Therefore, one should provide averaging of RCS values in corresponding sectors of aspect angles in order to receive reliable estimates of RCS for airborne objects with antennas under the radomes.

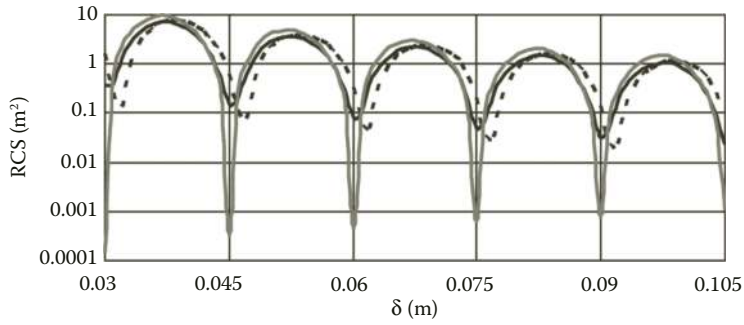

FIGURE 2.88 Antenna RCS versus its reflector depth.

2.5 APPROXIMATION OF SMOOTHED IMPULSE RESPONSE FOR OBJECTS ILLUMINATED BY SIGNALS OCCUPYING CERTAIN FREQUENCY BANDS

Vitaly A. Vasilets and Oleg I. Sukharevsky

In many up-to-date radar tasks, one comes across the need to obtain impulse responses (high-range resolution profiles of various objects [84]). Such high-range resolution profiles (HRRPs) provide us with scattering data regarding separate local regions of intense scattering at the object's surface. HRRP can be used for solving the radar recognition problems for various objects. In Chapter 3, we shall present HRRP examples for complex aerial and ground objects.

It is convenient to use impulse response (IR) approximation of an object in order to obtain the object's HRRP, which is the object's scattering response onto impulse plane wave.

As a smoothed approximation of impulse plane wave

$$\begin{aligned} \mathcal{E}^0(t,x\,|\,R^0) &= p\delta(t-R^0\cdot x),\\ \mathcal{H}^0(t,x\,|\,R^0) &= \sqrt{\frac{\varepsilon_0}{\mu_0}}(R^0\times p)\delta(t-R^0\cdot x), \end{aligned} \tag{2.175}$$

considered as primary incident field for obtaining the IR, we chose the short Gaussian video pulse:

$$\begin{aligned} \tilde{\vec{\mathcal{E}}}^0(\vec{R}^0,t) &= \vec{p}Q(t-\vec{R}^0\cdot\vec{x}),\\ \tilde{\vec{\mathcal{H}}}^0(\vec{R}^0,t) &= \sqrt{\frac{\varepsilon_0}{\mu_0}}(\vec{R}^0\times\vec{p})Q(t-\vec{R}^0\cdot\vec{x}),\\ Q(t) &= \frac{1}{\sqrt{\pi}\,\tau_p}\exp(-t^2/\tau_p^2)\,(\tau_p\ll 1). \end{aligned} \tag{2.176}$$

If we use the following representation:

$$e^{-\frac{(t-R^0\cdot x)^2}{\tau_p{}^2}} = \int_{-\infty}^{\infty} e^{-\frac{(t-z)^2}{\tau_p{}^2}}\,\delta(z-R^0\cdot x)\,\mathrm{d}z,$$

then, due to the problem linearity and superposition principle (we could also use the theorem of the convolution's Fourier transform), the object's response on the incident field (2.176) can be presented as the Fourier transform

$$\mathcal{H}(r^0,t) = \frac{1}{2\pi}\int_{-\infty}^{\infty} H(r^0,k)\,S(k)e^{-jkt}\,\mathrm{d}k, \tag{2.177}$$

where $S(k)=e^{-\beta k^2}, (\beta=\tau_p^2/4\ll 1)$ is the spectrum density of function $Q(t)$, and $H(r^0,k)$ is the frequency response of scattering object given its radar observation from the direction set by unit-vector r^0.

However, IR of the object is used practically for obtaining the object's scattering response on a signal specified by spectrum density occupying certain frequency range $[k_1,k_2]$.

So, we can use the following function as a smoothed approximation for object's impulse response:

$$\mathcal{H}(r^0,t) = \frac{1}{2\pi}\int_{k_1}^{k_2} H(r^0,k)e^{-jkt}\,\mathrm{d}k, \tag{2.178}$$

(since $\beta\ll 1$ and $S(k)$ is close to unit within frequency band bounded by $[k_1,k_2]$).

The function $\mathcal{H}(r^0, t)$ is computed by fast Fourier transform (FFT) algorithm. Besides, in all computation examples in this book, we set the frequency increment of ≈ 10 MHz, which provides correct estimation of variations in $\mathcal{H}(r^0, t)$ for all the cases considered in the book.

In the following, we use the amplitude–frequency response (AFR) of the object, which is frequency f ($f = ck/2\pi$, c is the speed of light) dependence of normalized value of projection of magnetic field intensity at reception point onto unit-vector of receiving (transmitting) antenna p

$$F(k) = 2\pi R(p \cdot H(r^0, k)), \tag{2.179}$$

where R is the distance from the object to observation point. We shall present also the quadrature components of AFR.

Consequently, we consider the following value as smoothed IR:

$$A(t) = \frac{1}{2\pi} \int_{k_1}^{k_2} F(k) e^{-jkt} \, dk. \tag{2.180}$$

As a matter of fact, the dependence $|A(t)|$ is the HRRP of the object given its illumination with the signal with rectangular amplitude spectrum.

Computation results. As examples of objects for computing their smoothed IR, we consider here the following: two cylinders and the cone–sphere. Their view is presented in Figure 2.89.

Both perfectly conducting objects and those having RAM coating at their fractures and smooth parts of surface are considered below. RAM coating assumed here had the following properties: $\varepsilon' = 20 + j0.1$, $\mu' = 1.35 + j0.8$, coating thickness at smooth parts of surface was 0.0013 m, radius of toroidal RAM coating for the fractures was 0.01 m. Horizontal polarization for all the objects corresponded to the vector of electric field intensity belonging to the plane passing through the object's axis and containing the wave vector of incident wave. Vertical polarization corresponded to the electric field intensity vector orthogonal to that plane.

Figures 2.90 through 2.96 show scattering computation results for the first cylinder (Figure 2.89a), radius of which (0.66 m) is considerably greater than its length (0.28 m).

Figure 2.90 shows amplitudes of the scattered field quadrature components versus frequency of illumination signal changing from 0.75 MHz through 1.25 GHz, the observation aspect being 45° with respect to the cylinder axis and illumination signal polarization being horizontal. Surface of the cylinder was perfectly conducting.

Absolute value of smoothed impulse response of perfectly conducting cylinder for its observation aspect of 45° with respect to cylinder's axis is shown in Figure 2.91, illumination signal occupying the range from 0.75 GHz through 1.25 GHz. Bold line corresponds to the cylinder response at horizontal polarization and the thin line corresponds to its response at vertical one. It is worth

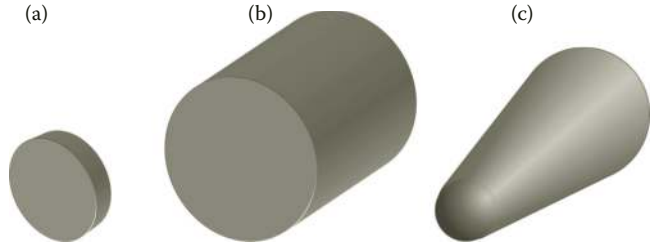

FIGURE 2.89 Example of the objects: (a) cylinder with radius 0.66m and length 0.28m; (b) cylinder with radius 1.66m and length 3.28m; (c) truncated cone caped with the half-sphere (sphere radius is 0.16m, cone height is 1.8m, bases radii are 0.16m and 0.35m).

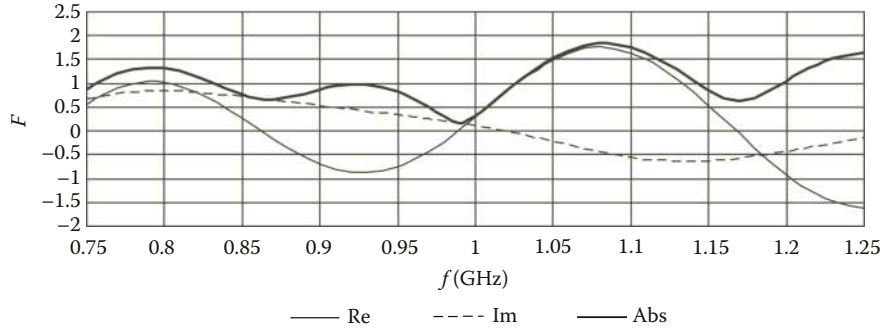

FIGURE 2.90 Amplitude–frequency response of the object model given its observation aspect of 45° and illumination frequency ranging from 0.75 MHz through 1.25 GHz.

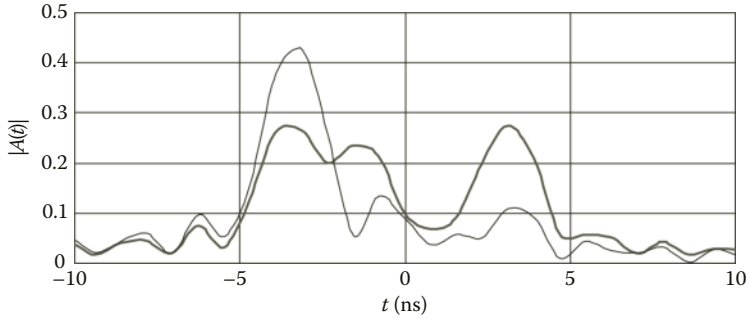

FIGURE 2.91 Absolute value of the smoothed impulse response of the object model given its observation at the aspect of 45° and illumination signal spectrum occupying the range from 0.75 GHz through 1.25 GHz.

mentioning that these two responses differ from each other significantly by the peak amplitudes. The latter is due to scattering differences at the edge local scatterers of the cylinder.

Figure 2.92 shows the same dependencies as in Figure 2.90, but for illumination signal frequency ranging from 9.35 GHz through 10.65 GHz.

Absolute values of the smoothed impulse responses given its observation aspect of 10° (with respect to cylinder's axis) and illumination spectrum occupying the range from 9.35 GHz through

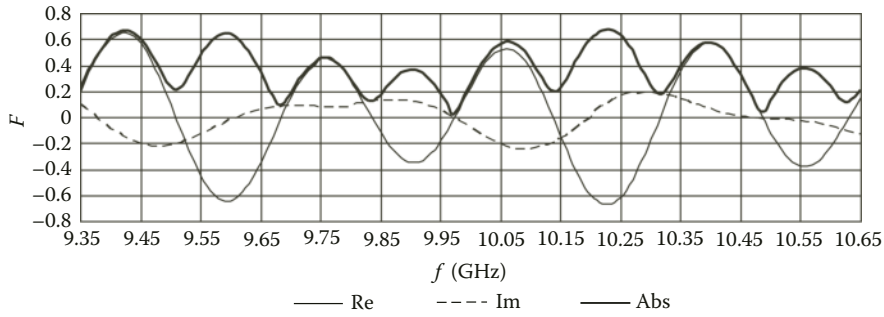

FIGURE 2.92 Amplitude–frequency response of the object given its observation aspect of 45° and illumination frequency ranging from 9.35 GHz through 10.65 GHz.

10.65 GHz are shown in Figures 2.93 and 2.94 for horizontal and vertical polarizations, respectively. Bold lines in these figures correspond to the response of perfectly conducting cylinder, the thin lines correspond to the response of cylinder provided with RAM coatings as described above. The responses (HRRPs) of Figures 2.93 and 2.94 have two major peaks. The first peaks in these figures correspond to the return from the first edge local scatterer at the front base of cylinder, and the second peaks correspond to superpositions of returns from second edge local scatterer at the cylinder's front basis and the visible part of edge scatterer at rear cylinder's base. The peak amplitude is lowered due to application of RAM coating at both polarizations, but, practically, it mostly happens for the first peak. The amplitude of second peak is somewhat lowered only at horizontal polarization. It is worth mentioning that given the use of RAM with such properties, the amplitude of peaks can even go up (sometimes significantly) when the cylinder is observed at broadside aspects. The latter is due to the fact that scattering from the toroidal RAM coating itself exceeds that from the clear edge local scatterer. Besides, one must bear in mind that this RAM coating is quite narrowband, that is, it is designed for the illumination signal wavelength of 3 cm, and the actual signal bandwidth for the smoothed IR is 1.3 GHz.

Typical results illustrating this phenomenon are presented in Figures 2.95 and 2.96. These figures show the same dependencies as in Figures 2.93 and 2.94, but for the aspect angle of 45°.

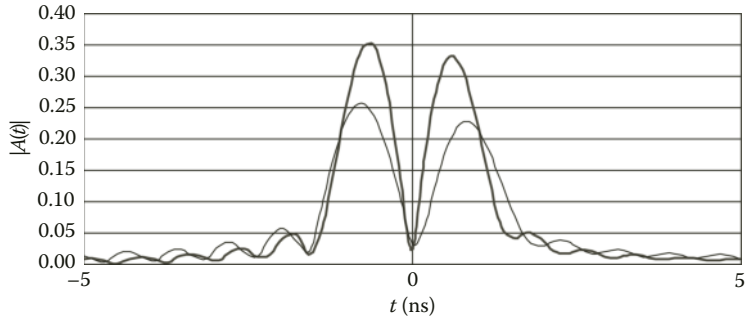

FIGURE 2.93 Absolute value of the smoothed IR of the object model given its observation at the aspect of 10° and the horizontally polarized illumination signal's spectrum occupying the range from 9.35 GHz through 10.65 GHz.

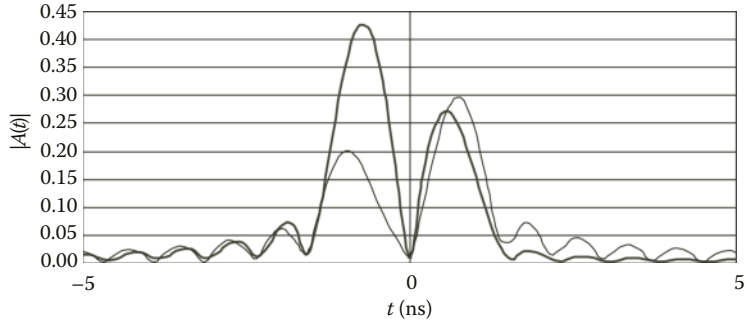

FIGURE 2.94 Absolute value of the smoothed IR of the object model given its observation at the aspect of 10° and the vertically polarized illumination signal's spectrum occupying the range from 9.35 GHz through 10.65 GHz.

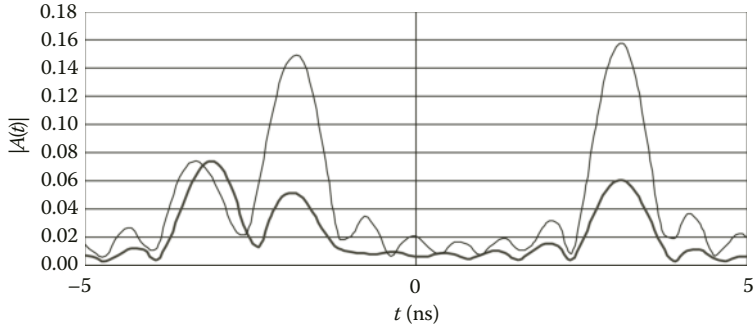

FIGURE 2.95 Absolute value of the smoothed IR of the object model given its observation at the aspect of 45° and the horizontally polarized illumination signal's spectrum occupying the range from 9.35 GHz through 10.65 GHz.

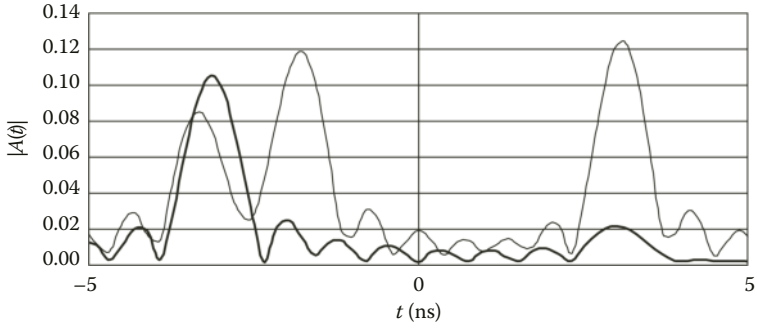

FIGURE 2.96 Absolute value of the smoothed IR of the object model given its observation at the aspect of 45° and the vertically polarized illumination signal's spectrum occupying the range from 9.35 GHz through 10.65 GHz.

The first ($t \approx -3$ ns) and third ($t \approx 3$ ns) peaks of these responses correspond to echoes from edge local scatterers at front base of the cylinder and the second peak ($t \approx -2$ ns) of these responses corresponds to echo from the visible part of edge scatterer at rear cylinder's base.

Figures 2.97 through 2.100 show the smoothed IR of the cylinder presented in Figure 2.89b. This cylinder has the base with 1.66 m radius and its length is 3.28 m. Parameters of simulation are the same as for Figures 2.93 through 2.96.

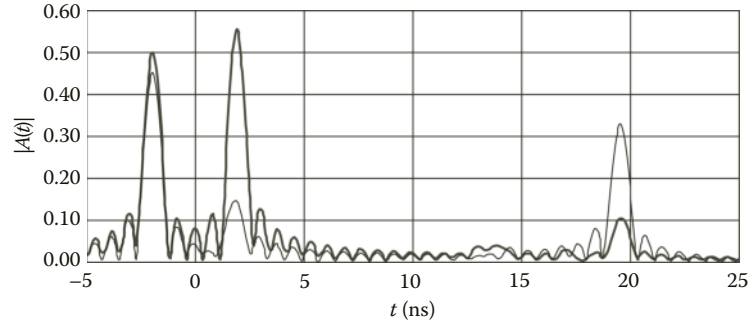

FIGURE 2.97 Absolute value of the smoothed IR of the object model given its observation at the aspect of 10° and the horizontally polarized illumination signal's spectrum occupying the range from 9.35 GHz through 10.65 GHz.

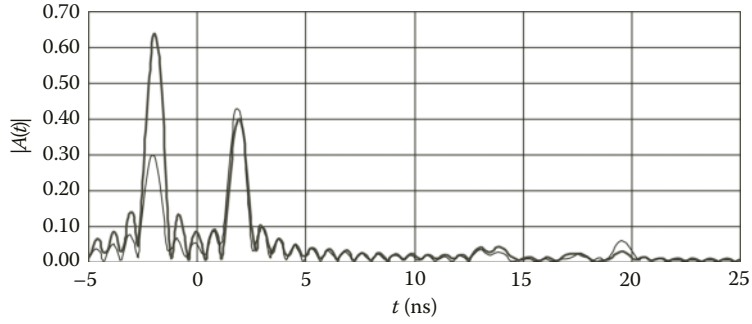

FIGURE 2.98 Absolute value of the smoothed IR of the object model given its observation at the aspect of 10° and the vertically polarized illumination signal's spectrum occupying the range from 9.35 GHz through 10.65 GHz.

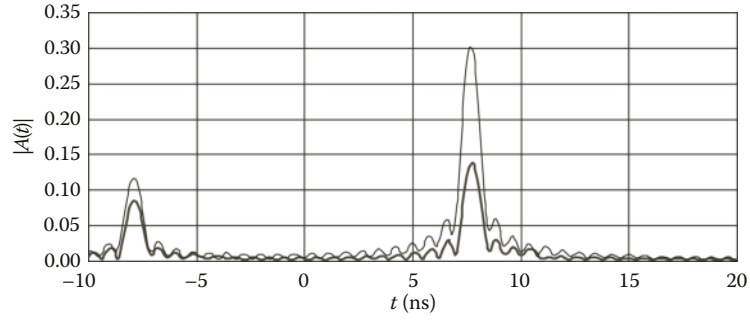

FIGURE 2.99 Absolute value of the smoothed IR of the object model given its observation at the aspect of 45° and the horizontally polarized illumination signal's spectrum occupying the range from 9.35 GHz through 10.65 GHz.

It should be noted that unlike the previous object observed at the aspect of 10° (Figures 2.97 and 2.98) the echoes from all the three visible local edge scatterers are evidently separate from one another. Besides, given the object illumination at vertical polarization (Figure 2.98), the amplitude of echo from the edge at rear cylinder's base ($t \approx 19.5$ ns) is very small. Application of RAM coating to the edges provides considerable decrease in the amplitude of second peak ($t \approx 2$ ns) and

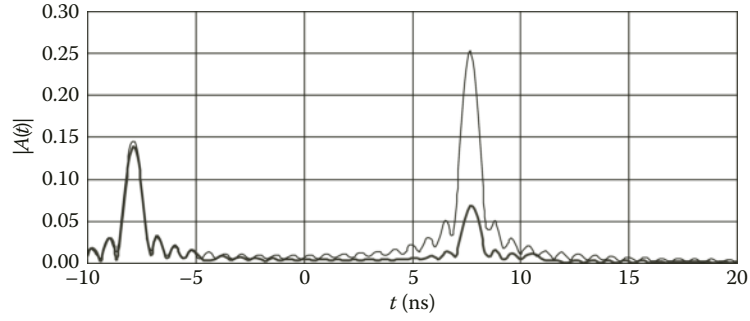

FIGURE 2.100 Absolute value of the smoothed IR of the object model given its observation at the aspect of 45° and the vertically polarized illumination signal's spectrum occupying the range from 9.35 GHz through 10.65 GHz.

significant increase in the amplitude of third peak ($t \approx 19.5$ ns) given the cylinder illumination at horizontal polarization. In case of vertical polarization, the amplitude of first peak of the cylinder's smoothed IR ($t \approx -2$ ns) gets considerably lower.

Results obtained for the observation angle of 45° (Figures 2.99 and 2.100) show that the second peak of smoothed IR ($t \approx 8$ ns) is formed by superposition of echoes from the second local edge scatterer at front cylinder's base and the visible part of the edge at its rear base. Application of RAM coating to the cylinder bases' rims leads to significant increase of second peak ($t \approx 8$ ns) of the smoothed IR for both polarizations.

The object shown in Figure 2.89c is the truncated cone caped with the half-sphere. Sphere radius is 0.16 m, the cone height being 1.8 m and its bases having radii of 0.16 m and 0.35 m.

The smoothed IR of the object observed at the aspect angle of 45° given illumination signal occupying the range from 0.75 GHz through 1.25 GHz is shown in Figure 2.101. The bold line shows the object response at horizontal polarization and the thin line is for vertical one. The main difference between the responses at different polarizations is observed in the echo from the visible part of local edge scatterer (the second highest peak, $t \approx 7$ ns, at the plot). The first highest peak ($t \approx -1$ ns) is due to scattering from the half-sphere, so the echoes at both polarizations are the same.

The absolute value of smoothed IR of the object model given its observation at the aspect of 45° and the illumination signal's spectrum occupying the range from 9.35 GHz through 10.65 GHz is shown in Figure 2.102, illumination signal polarization being horizontal. Bold line represents the response of perfectly conducting cone–sphere object, and the thin line is for the response from the same object provided with RAM coating (as described above). The first highest peak ($t \approx -1$ ns) is

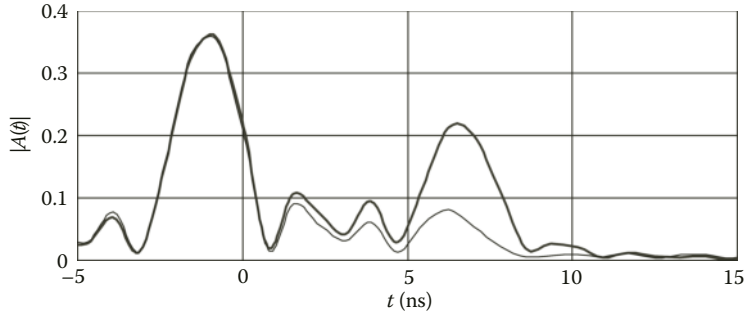

FIGURE 2.101 Absolute value of the smoothed IR of the object model given its observation at the aspect of 45° and the illumination signal's spectrum occupying the range from 0.75 GHz through 1.25 GHz.

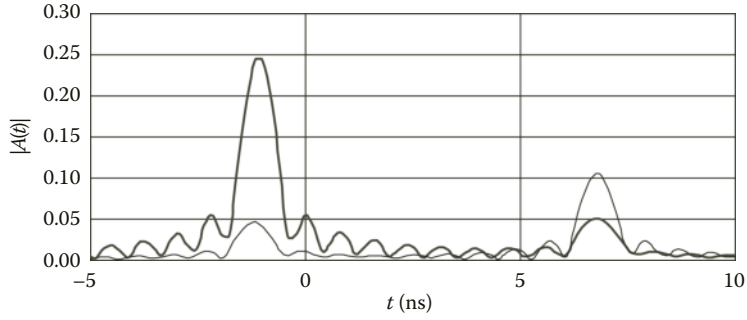

FIGURE 2.102 Absolute value of the smoothed IR of the object model given its observation at the aspect of 45° and the horizontally polarized illumination signal's spectrum occupying the range from 9.35 GHz through 10.65 GHz.

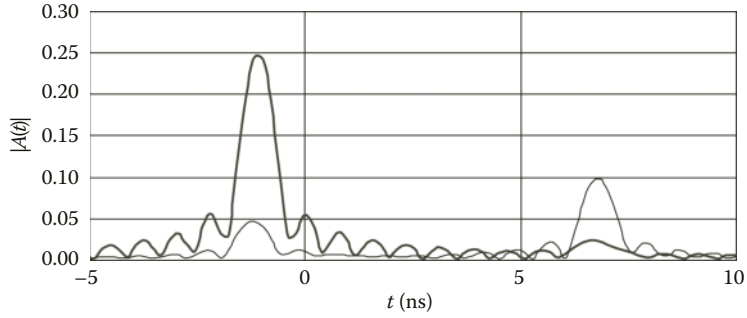

FIGURE 2.103 Absolute value of the smoothed IR of the object model given its observation at the aspect of 45° and the vertically polarized illumination signal's spectrum occupying the range from 9.35 GHz through 10.65 GHz.

due to scattering from the front half-sphere. It goes down given that RAM coating is applied to its surface. The peak around $t \approx 6.4$ ns delay time is due to scattering from the rear local edge scatterer, and it goes up if the RAM coating is applied.

The same computational results for the case of vertical polarization of illumination signal are shown in Figure 2.103.

So, the method developed in this section allows us to evaluate the HRRPs (the smoothed IRs for certain frequency ranges) of both perfectly conducting objects and objects provided with RAM coating. As it turned out, application of RAM does not always lead to suppressing echoes the HRRPs consist of. However, the RAM-coating presence does always change the form of HRRP.

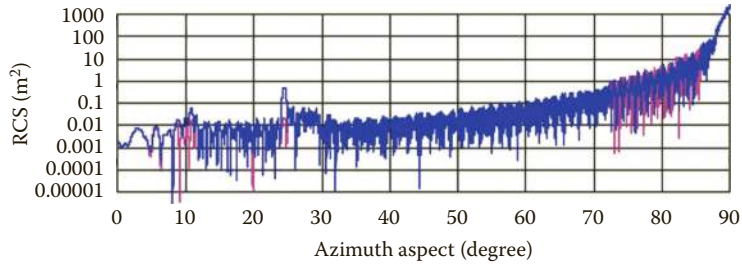

FIGURE 2.23 RCS of the cruise missile model versus azimuth aspect given its illumination in the plane of wings.

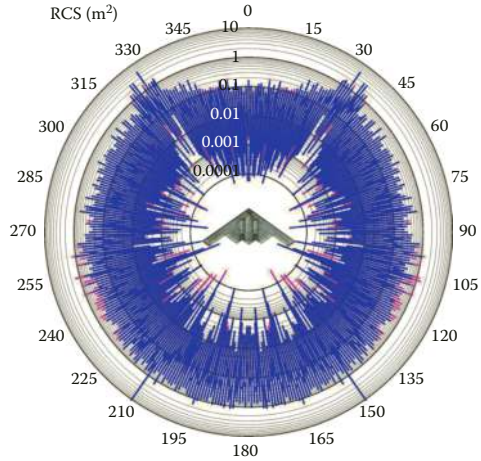

FIGURE 3.4 Circular diagrams of instantaneous RCS given radar observation of B-2 aircraft model at carrier frequency of 10 GHz (3 cm wavelength).

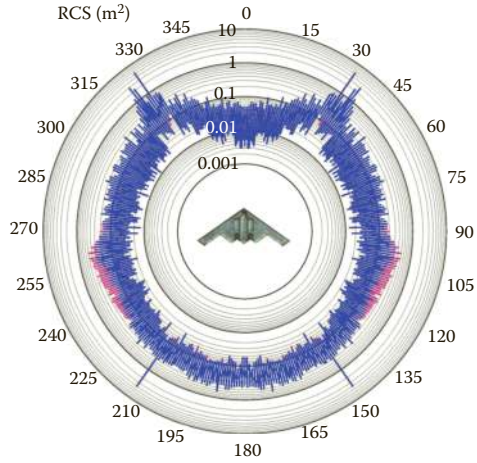

FIGURE 3.9 Circular diagrams of noncoherent RCS given radar observation of B-2 aircraft model at carrier frequency of 10 GHz (3 cm wavelength).

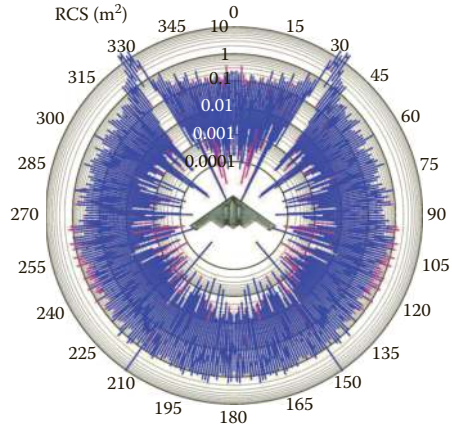

FIGURE 3.10 Circular diagrams of instantaneous RCS given radar observation of B-2 aircraft model at carrier frequency of 3 GHz (10 cm wavelength).

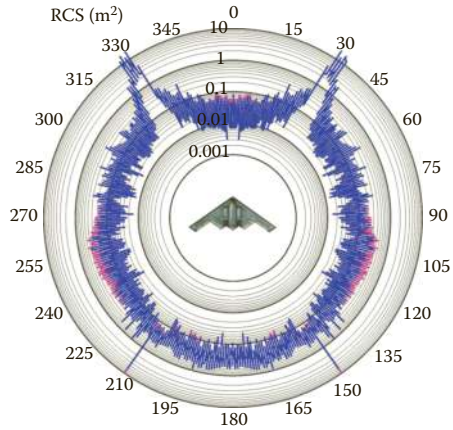

FIGURE 3.15 Circular diagrams of noncoherent RCS of B-2 aircraft model given its radar observation at carrier frequency of 3 GHz (10 cm wavelength).

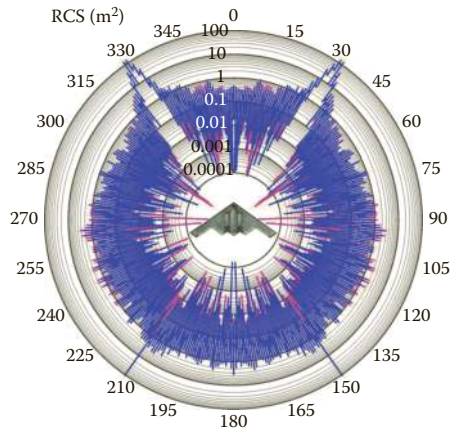

FIGURE 3.16 Circular diagrams of instantaneous RCS given radar observation of B-2 aircraft model at carrier frequency of 1 GHz (30 cm wavelength).

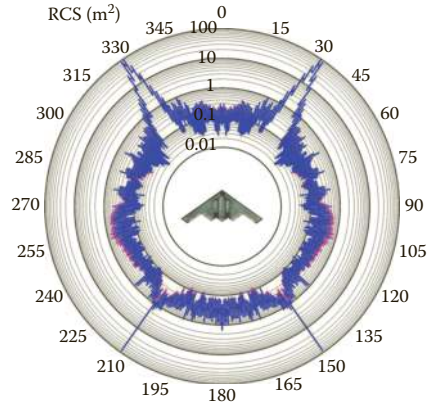

FIGURE 3.21 Circular diagrams of noncoherent RCS of B-2 aircraft model given its radar observation at carrier frequency of 1 GHz (30 cm wavelength).

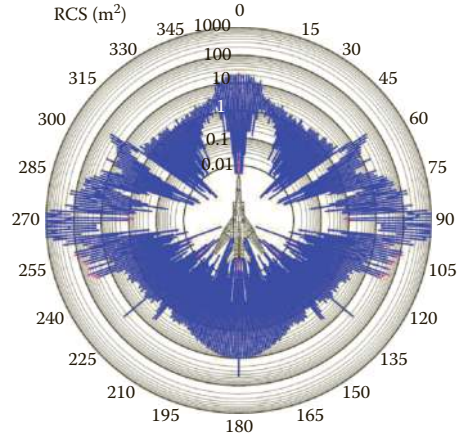

FIGURE 3.33 Circular diagrams of instantaneous RCS given radar observation of Tu-22M3 aircraft model at carrier frequency of 10 GHz (3 cm wavelength).

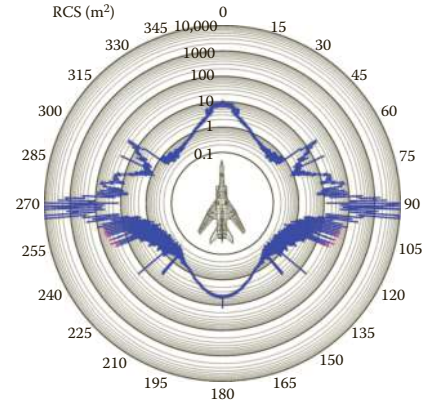

FIGURE 3.38 Circular diagrams of noncoherent RCS given radar observation of Tu-22M3 aircraft model at carrier frequency of 10 GHz (3 cm wavelength).

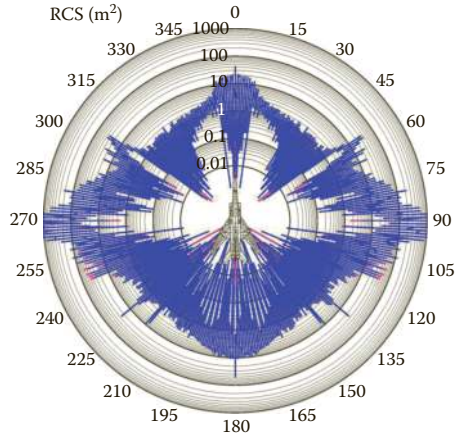

FIGURE 3.39 Circular diagrams of instantaneous RCS given radar observation of Tu-22M3 aircraft model at carrier frequency of 3 GHz (10 cm wavelength).

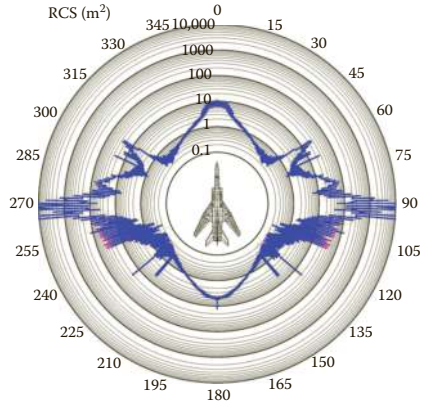

FIGURE 3.44 Circular diagrams of noncoherent RCS of Tu-22M3 aircraft model given its radar observation at carrier frequency of 3 GHz (10 cm wavelength).

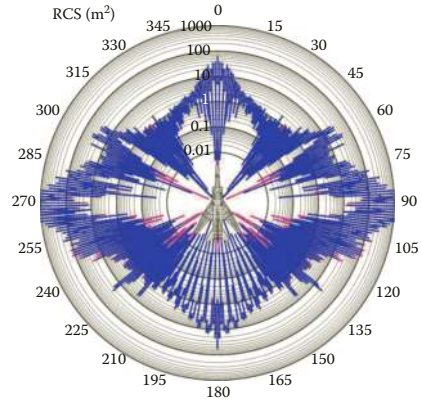

FIGURE 3.45 Circular diagrams of instantaneous RCS given radar observation of Tu-22M3 aircraft model at carrier frequency of 1 GHz (30 cm wavelength).

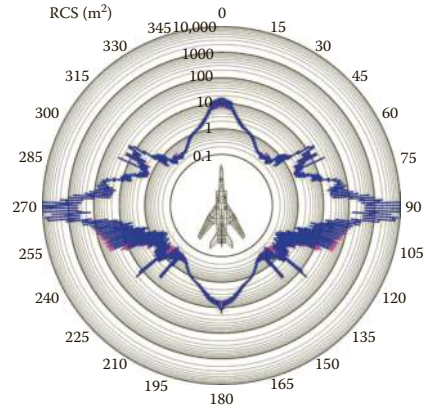

FIGURE 3.50 Circular diagrams of noncoherent RCS of Tu-22M3 aircraft model given its radar observation at carrier frequency of 1 GHz (30 cm wavelength).

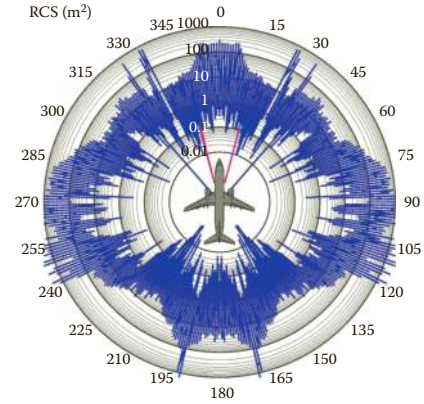

FIGURE 3.62 Circular diagrams of instantaneous RCS given radar observation of Boeing-737-400 aircraft model at carrier frequency of 10 GHz (3 cm wavelength).

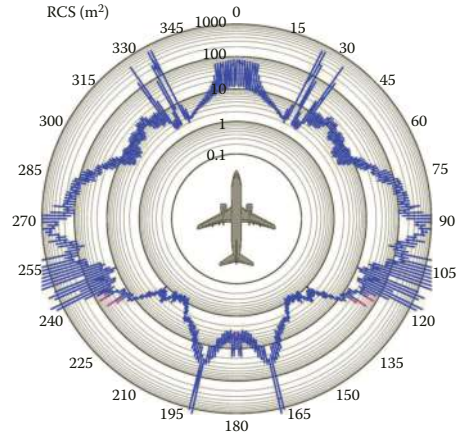

FIGURE 3.67 Circular diagrams of noncoherent RCS given radar observation of Boeing-737-400 aircraft model at carrier frequency of 10 GHz (3 cm wavelength).

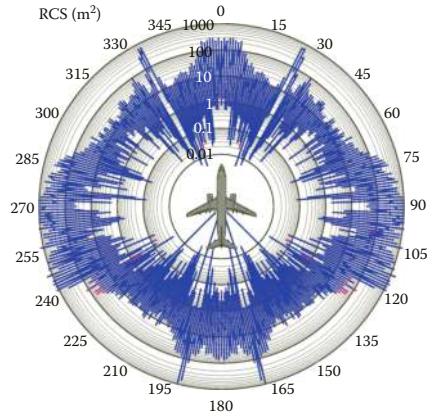

FIGURE 3.68 Circular diagrams of instantaneous RCS given radar observation of Boeing-737-400 aircraft model at carrier frequency of 3 GHz (10 cm wavelength).

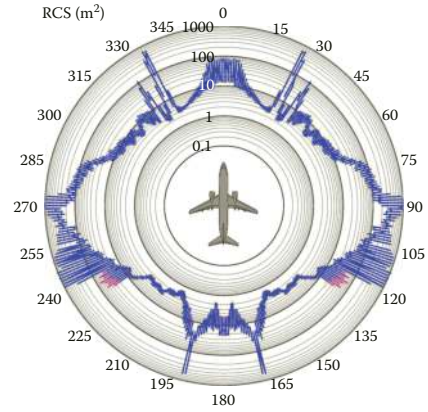

FIGURE 3.73 Circular diagrams of noncoherent RCS of Boeing-737-400 aircraft model given its radar observation at carrier frequency of 3 GHz (10 cm wavelength).

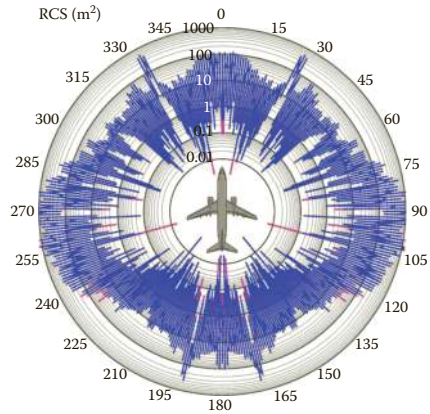

FIGURE 3.74 Circular diagrams of instantaneous RCS given radar observation of Boeing-737-400 aircraft model at carrier frequency of 1 GHz (30 cm wavelength).

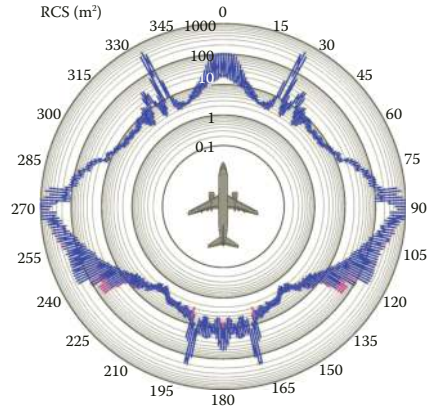

FIGURE 3.79 Circular diagrams of noncoherent RCS of Boeing-737-400 aircraft model given its radar observation at carrier frequency of 1 GHz (30 cm wavelength).

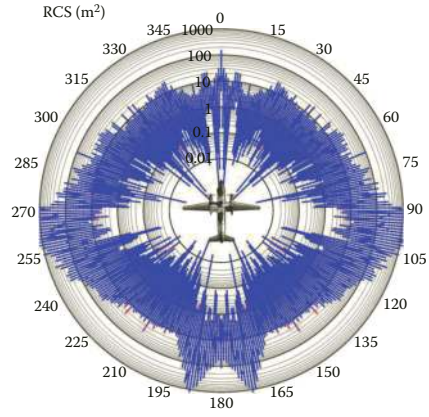

FIGURE 3.91 Circular diagrams of instantaneous RCS given radar observation of An-26 aircraft model at carrier frequency of 10 GHz (3 cm wavelength).

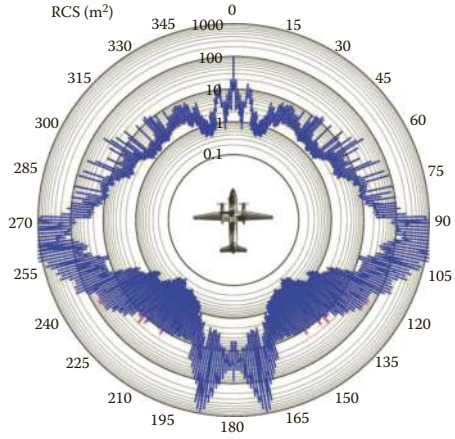

FIGURE 3.96 Circular diagrams of noncoherent RCS given radar observation of An-26 aircraft model at carrier frequency of 10 GHz (3 cm wavelength).

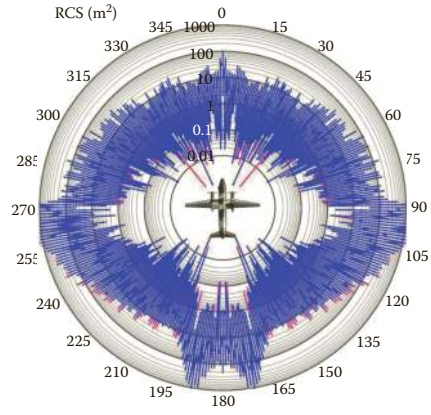

FIGURE 3.97 Circular diagrams of instantaneous RCS given radar observation of An-26 aircraft model at carrier frequency of 3 GHz (10 cm wavelength).

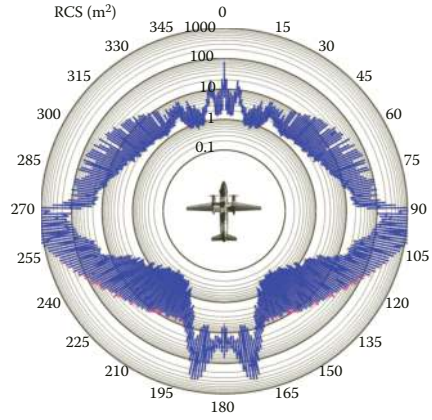

FIGURE 3.102 Circular diagrams of noncoherent RCS of An-26 aircraft model given its radar observation at carrier frequency of 3 GHz (10 cm wavelength).

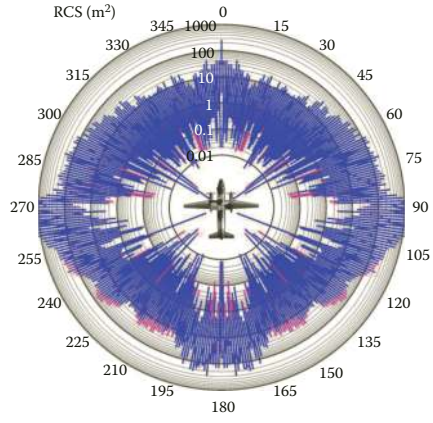

FIGURE 3.103 Circular diagrams of instantaneous RCS given radar observation of An-26 aircraft model at carrier frequency of 1 GHz (30 cm wavelength).

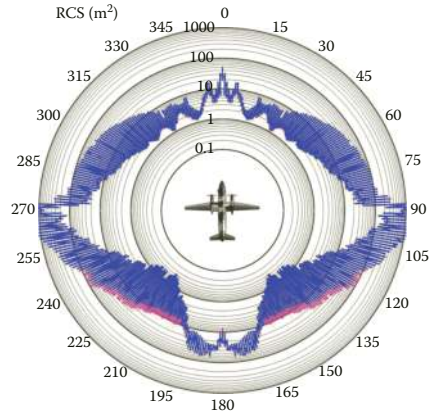

FIGURE 3.108 Circular diagrams of noncoherent RCS of An-26 aircraft model given its radar observation at carrier frequency of 1 GHz (30 cm wavelength).

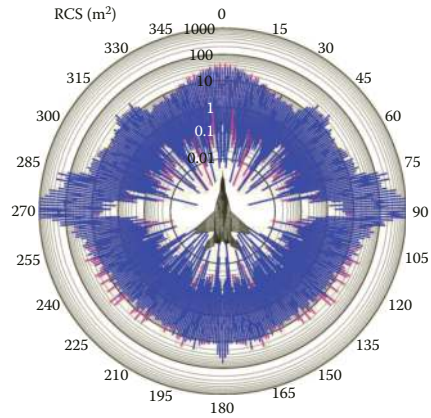

FIGURE 3.122 Circular diagrams of instantaneous RCS given radar observation of MiG-29 aircraft model at carrier frequency of 10 GHz (3 cm wavelength).

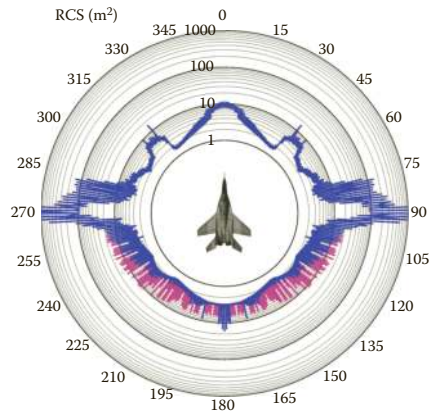

FIGURE 3.127 Circular diagrams of noncoherent RCS given radar observation of MiG-29 aircraft model at carrier frequency of 10 GHz (3 cm wavelength).

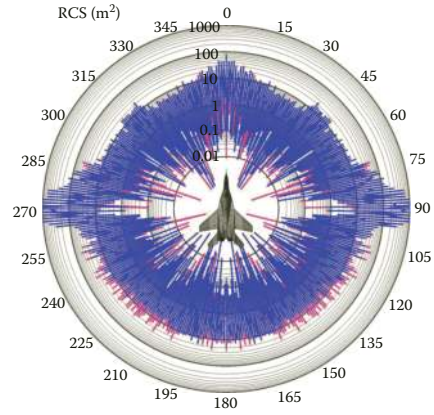

FIGURE 3.128 Circular diagrams of instantaneous RCS given radar observation of MiG-29 aircraft model at carrier frequency of 3 GHz (10 cm wavelength).

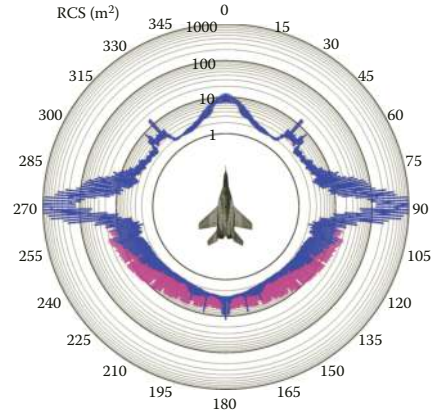

FIGURE 3.133 Circular diagrams of noncoherent RCS of MiG-29 aircraft model given its radar observation at carrier frequency of 3 GHz (10 cm wavelength).

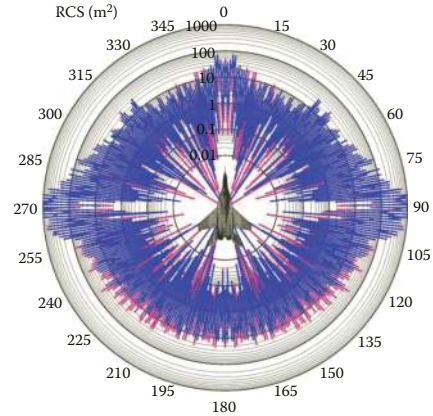

FIGURE 3.134 Circular diagrams of instantaneous RCS given radar observation of MiG-29 aircraft model at carrier frequency of 1 GHz (30 cm wavelength).

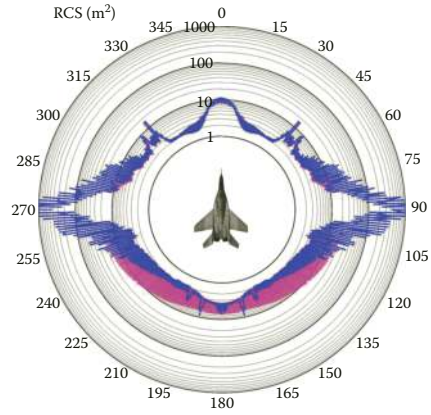

FIGURE 3.139 Circular diagrams of noncoherent RCS of MiG-29 aircraft model given its radar observation at carrier frequency of 1 GHz (30 cm wavelength).

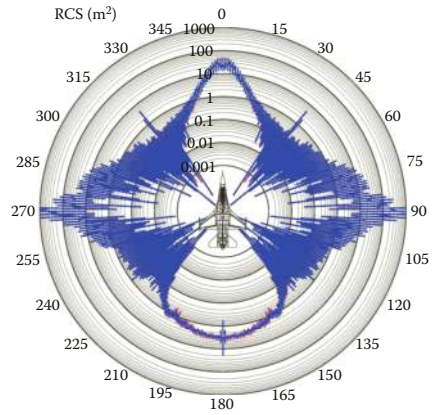

FIGURE 3.151 Circular diagrams of instantaneous RCS given radar observation of F-16 aircraft model at carrier frequency of 10 GHz (3 cm wavelength).

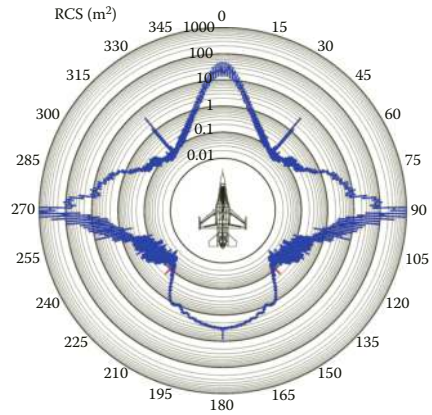

FIGURE 3.156 Circular diagrams of noncoherent RCS given radar observation of F-16 aircraft model at carrier frequency of 10 GHz (3 cm wavelength).

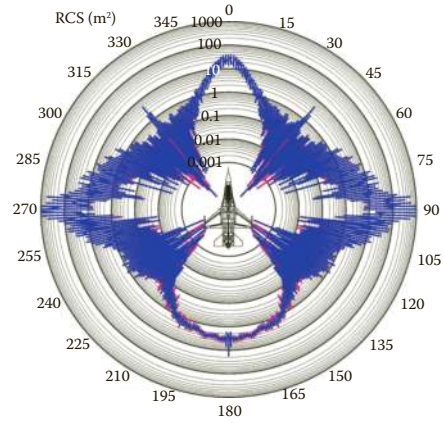

FIGURE 3.157 Circular diagrams of instantaneous RCS given radar observation of F-16 aircraft model at carrier frequency of 3 GHz (10 cm wavelength).

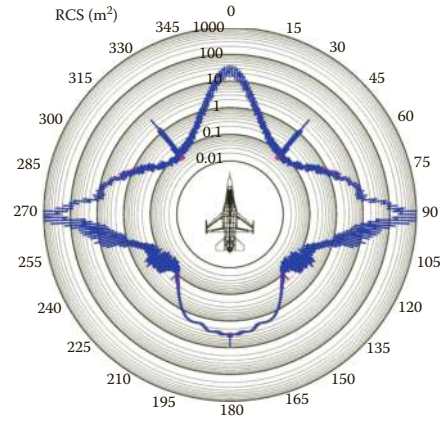

FIGURE 3.162 Circular diagrams of noncoherent RCS of F-16 aircraft model given its radar observation at carrier frequency of 3 GHz (10 cm wavelength).

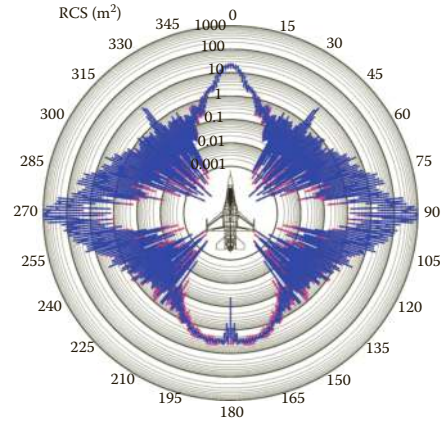

FIGURE 3.163 Circular diagrams of instantaneous RCS given radar observation of F-16 aircraft model at carrier frequency of 1 GHz (30 cm wavelength).

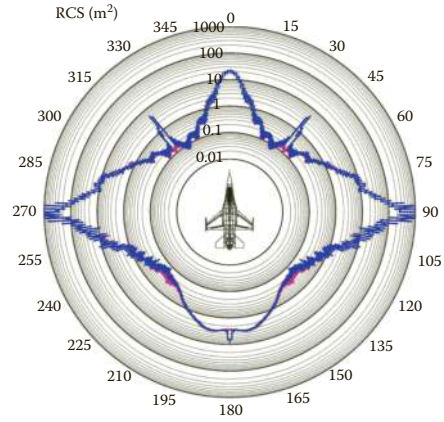

FIGURE 3.168 Circular diagrams of noncoherent RCS of F-16 aircraft model given its radar observation at carrier frequency of 1 GHz (30 cm wavelength).

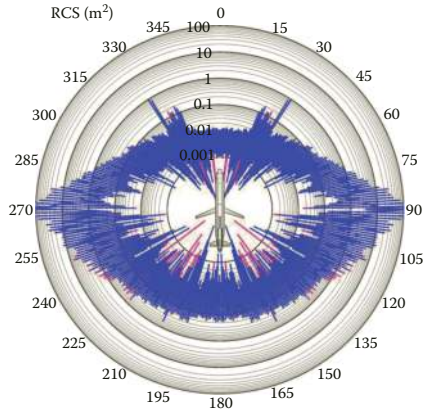

FIGURE 3.179 Circular diagrams of instantaneous RCS given radar observation of AGM-86 ALCM model at carrier frequency of 10 GHz (3 cm wavelength).

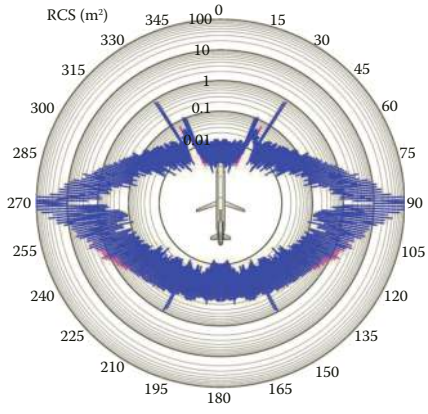

FIGURE 3.184 Circular diagrams of noncoherent RCS given radar observation of AGM-86 ALCM model at carrier frequency of 10 GHz (3 cm wavelength).

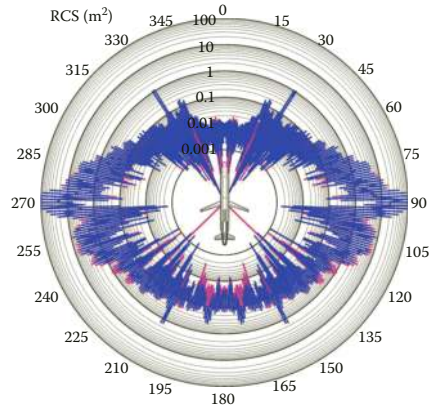

FIGURE 3.185 Circular diagrams of instantaneous RCS given radar observation of AGM-86 ALCM model at carrier frequency of 3 GHz (10 cm wavelength).

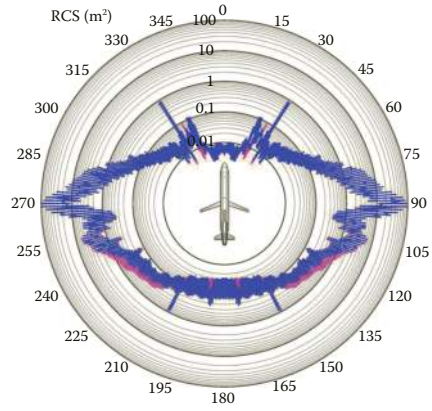

FIGURE 3.190 Circular diagrams of noncoherent RCS of AGM-86 ALCM model given its radar observation at carrier frequency of 3 GHz (10 cm wavelength).

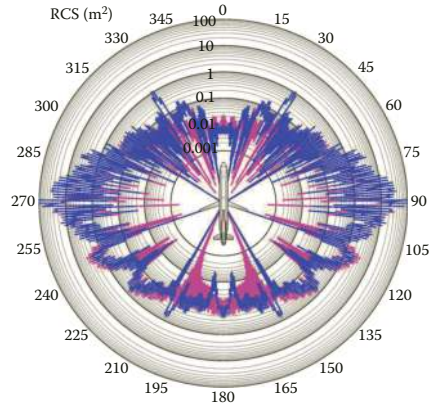

FIGURE 3.191 Circular diagrams of instantaneous RCS given radar observation of AGM-86 ALCM model at carrier frequency of 1 GHz (30 cm wavelength).

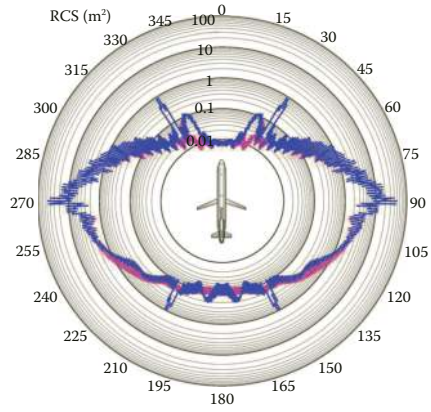

FIGURE 3.196 Circular diagrams of noncoherent RCS of AGM-86 ALCM model given its radar observation at carrier frequency of 1 GHz (30 cm wavelength).

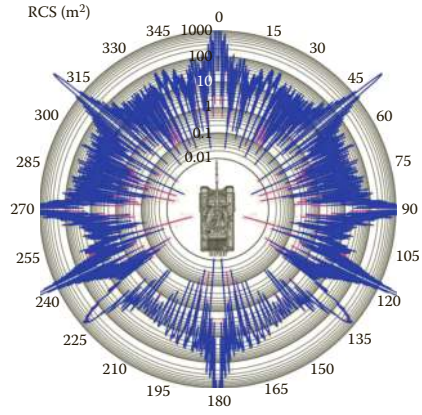

FIGURE 3.210 Circular diagrams of instantaneous RCS given radar observation of T-90 tank model (ε = 1°, underlying surface – dry soil).

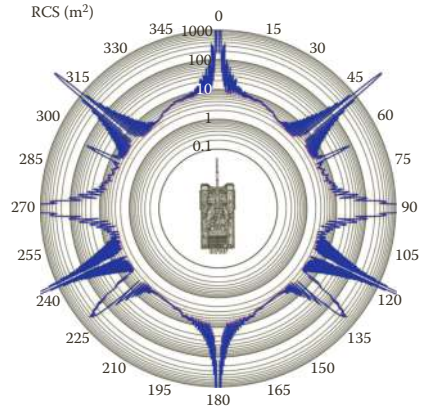

FIGURE 3.215 Circular diagrams of noncoherent RCS given radar observation of T-90 tank model (ε = 1°, underlying surface – dry soil).

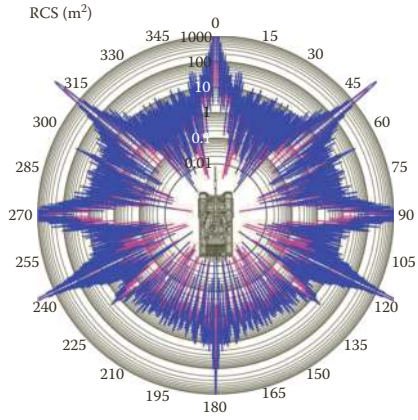

FIGURE 3.216 Circular diagrams of instantaneous RCS given radar observation of T-90 tank model (ε = 10°, underlying surface – dry soil).

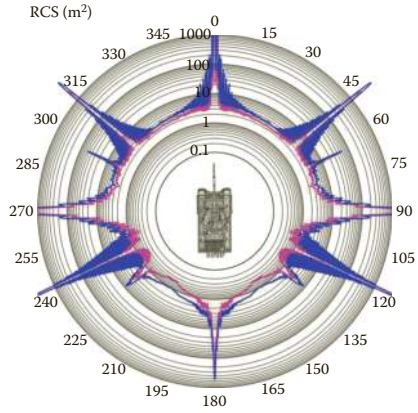

FIGURE 3.221 Circular diagrams of noncoherent RCS of T-90 tank model (ε = 10°, underlying surface – dry soil).

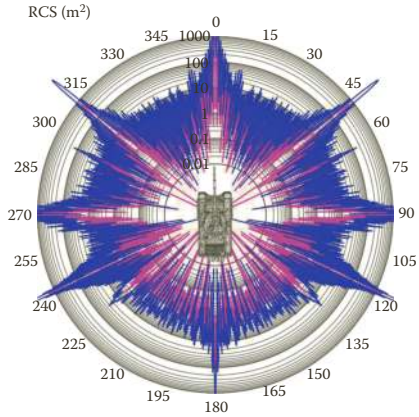

FIGURE 3.222 Circular diagrams of instantaneous RCS of T-90 tank model (ε = 10°, underlying surface – moist soil).

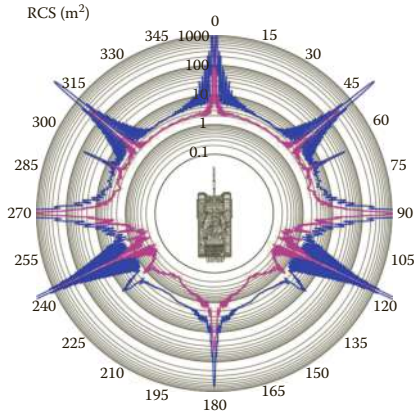

FIGURE 3.227 Circular diagrams of noncoherent RCS of T-90 tank model (ε = 10°, underlying surface – moist soil).

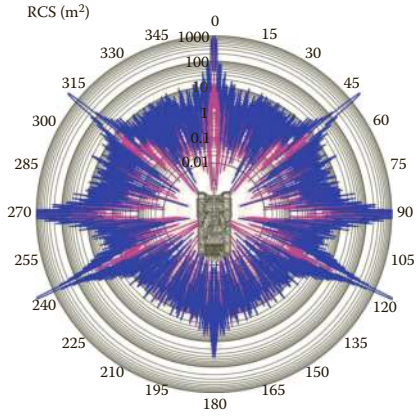

FIGURE 3.228 Circular diagrams of instanteneous RCS of T-90 tank model (ε = 30°, underlying surface – dry soil).

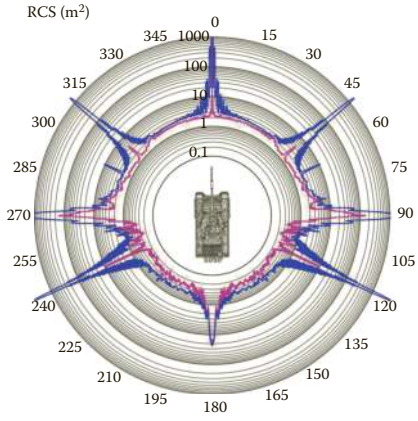

FIGURE 3.233 Circular diagrams of noncoherent RCS of T-90 tank model (ε = 30°, underlying surface – dry soil).

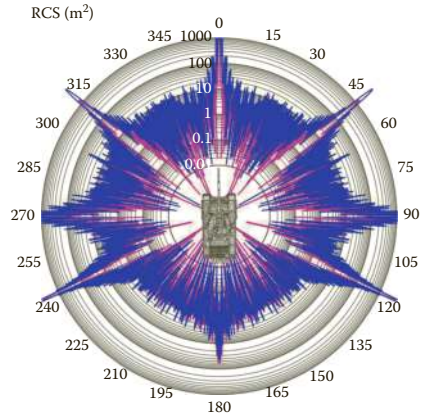

FIGURE 3.234 Circular diagrams of instanteneous RCS of T-90 tank model (ε = 30°, underlying surface – moist soil).

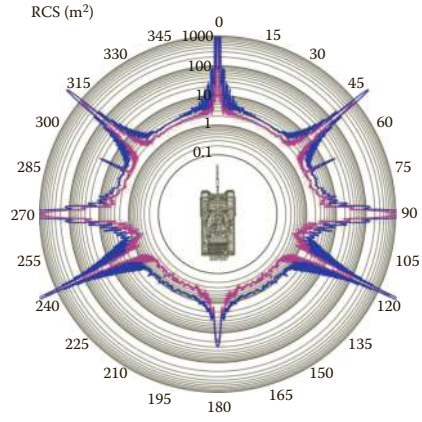

FIGURE 3.239 Circular diagrams of noncoherent RCS of T-90 tank model (ε = 30°, underlying surface – moist soil).

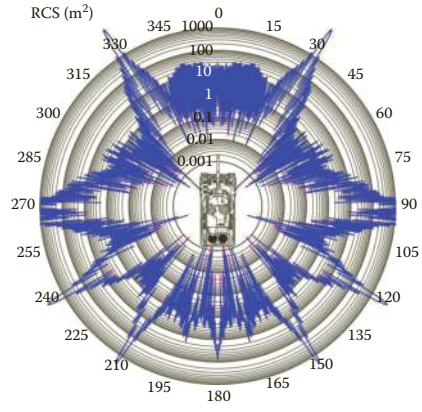

FIGURE 3.262 Circular diagrams of instantaneous RCS given radar observation of Leopard-2 tank model (ε = 1°, underlying surface – dry soil).

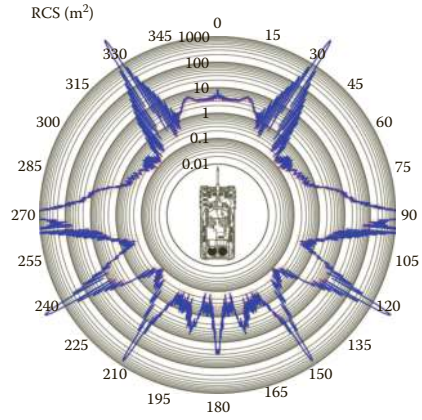

FIGURE 3.267 Circular diagrams of noncoherent RCS given radar observation of Leopard-2 tank model (ε = 1°, underlying surface – dry soil).

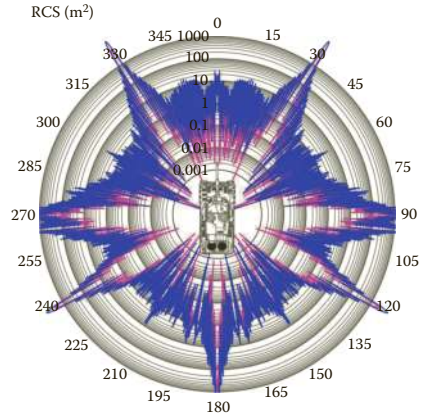

FIGURE 3.268 Circular diagrams of instantaneous RCS given radar observation of Leopard-2 tank model (ε = 10°, underlying surface – dry soil).

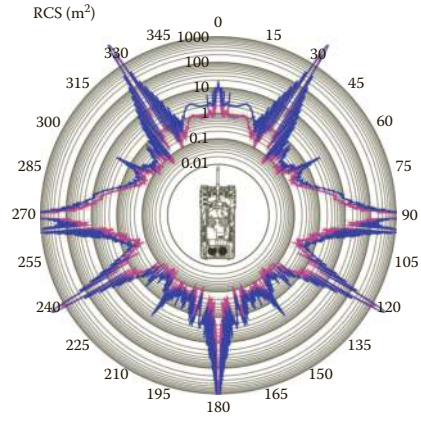

FIGURE 3.273 Circular diagrams of noncoherent RCS of Leopard-2 tank model (ε = 10°, underlying surface – dry soil).

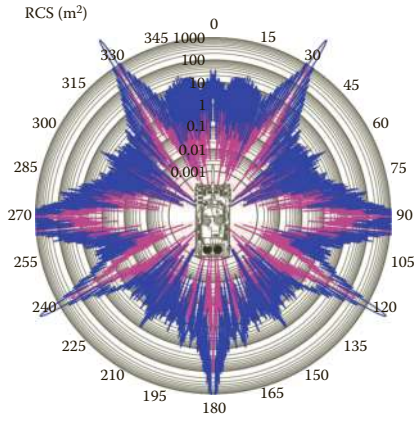

FIGURE 3.274 Circular diagrams of instanteneous RCS of Leopard-2 tank model (ε = 10°, underlying surface – moist soil).

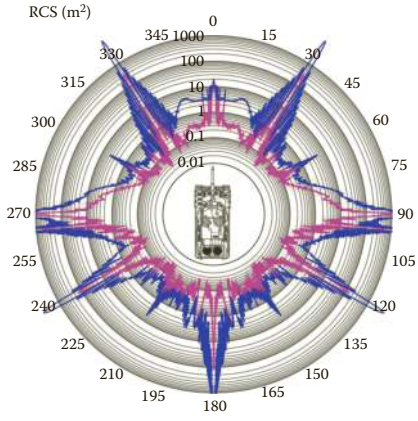

FIGURE 3.279 Circular diagrams of noncoherent RCS of Leopard-2 tank model (ε = 10°, underlying surface – moist soil).

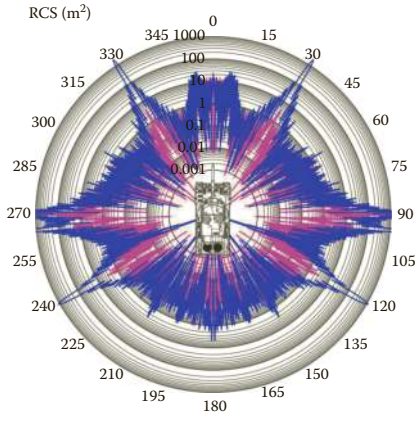

FIGURE 3.280 Circular diagrams of instanteneous RCS of Leopard-2 tank model (ε = 30°, underlying surface – dry soil).

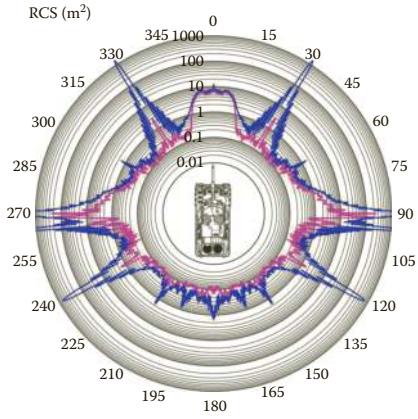

FIGURE 3.285 Circular diagrams of noncoherent RCS of Leopard-2 tank model (ε = 30°, underlying surface – dry soil).

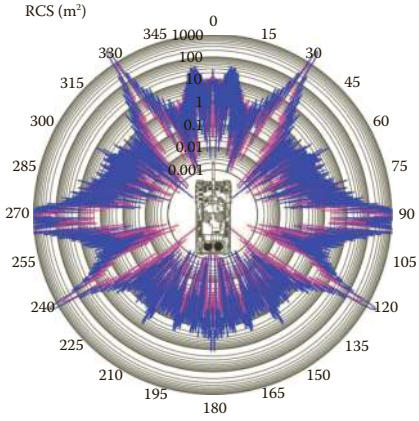

FIGURE 3.286 Circular diagrams of instanteneous RCS of Leopard-2 tank model (ε = 30°, underlying surface – moist soil).

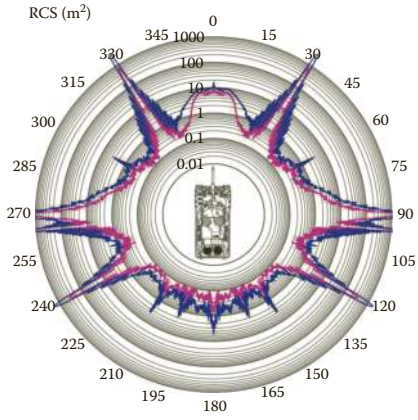

FIGURE 3.291 Circular diagrams of noncoherent RCS of Leopard-2 tank model (ε = 30°, underlying surface – moist soil).

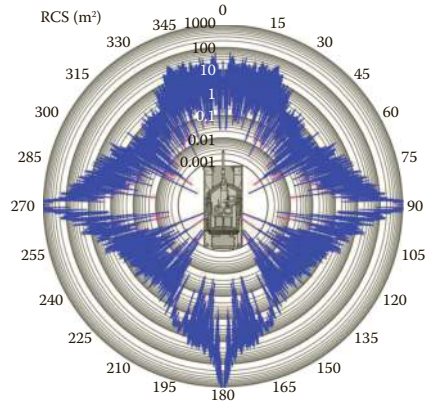

FIGURE 3.311 Circular diagrams of instantaneous RCS given radar observation of M1A1 Abrams tank model (ε = 1°, underlying surface – dry soil).

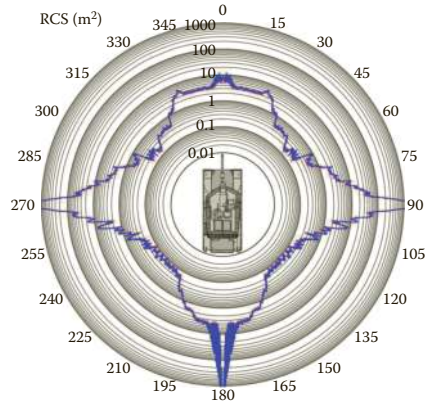

FIGURE 3.316 Circular diagrams of noncoherent RCS given radar observation of M1A1 Abrams tank model (ε = 1°, underlying surface – dry soil).

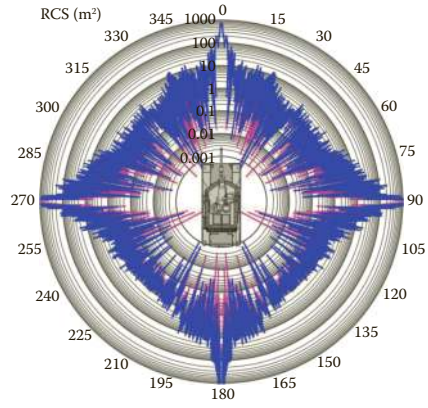

FIGURE 3.317 Circular diagrams of instantaneous RCS given radar observation of M1A1 Abrams tank model (ε = 10°, underlying surface – dry soil).

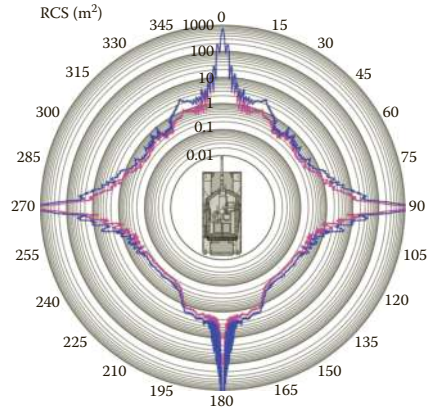

FIGURE 3.322 Circular diagrams of noncoherent RCS of M1A1 Abrams tank model (ε = 10°, underlying surface – dry soil).

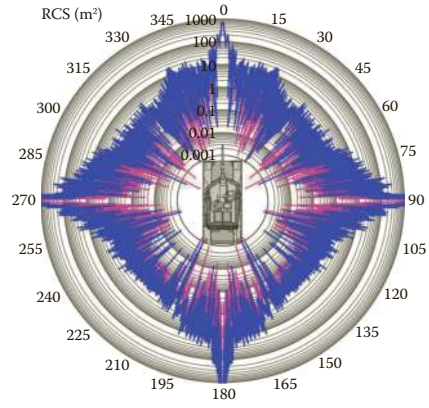

FIGURE 3.323 Circular diagrams of instantaneous RCS of M1A1 Abrams tank model (ε = 10°, underlying surface – moist soil).

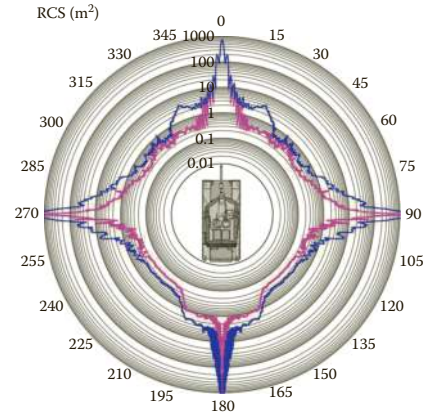

FIGURE 3.328 Circular diagrams of noncoherent RCS of M1A1 Abrams tank model (ε = 10°, underlying surface – moist soil).

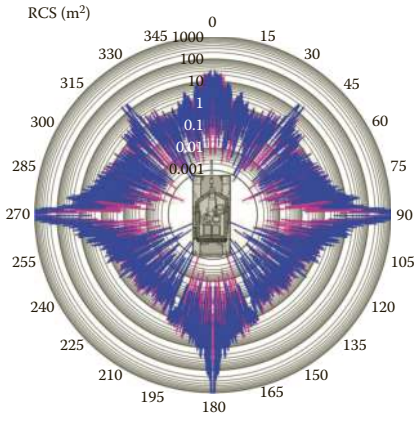

FIGURE 3.329 Circular diagrams of instantaneous RCS of M1A1 Abrams tank model (ε = 30°, underlying surface – dry soil).

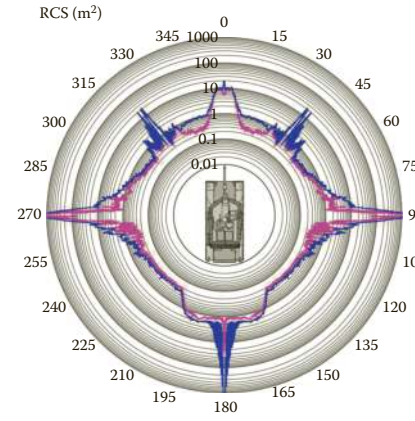

FIGURE 3.334 Circular diagrams of noncoherent RCS of M1A1 Abrams tank model (ε = 30°, underlying surface – dry soil).

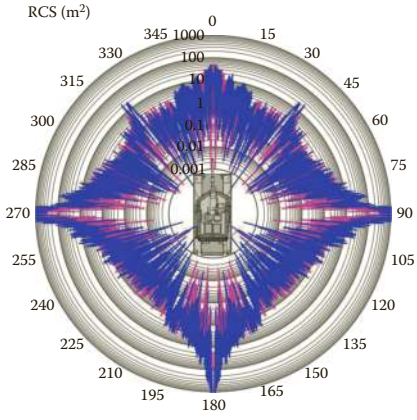

FIGURE 3.335 Circular diagrams of instantaneous RCS of M1A1 Abrams tank model (ε = 30°, underlying surface – moist soil).

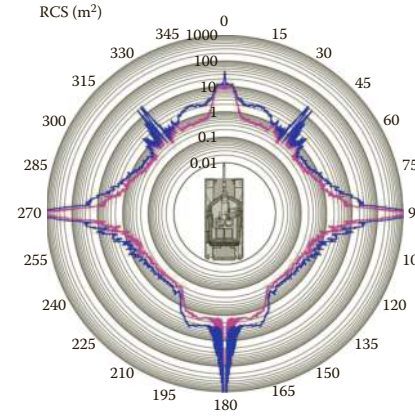

FIGURE 3.340 Circular diagrams of noncoherent RCS of M1A1 Abrams tank model (ε = 30°, underlying surface – moist soil).

3 Scattering Characteristics of Some Airborne and Ground Objects

Vitaly A. Vasilets, Sergey V. Nechitaylo, Oleg I. Sukharevsky, and Valery M. Orlenko

CONTENTS

This chapter is intended for reference and it basically concludes theoretical studies presented in the first two chapters. It contains results of the radar scattering characteristic computer simulation for a number of airborne and ground objects that were obtained using methods developed in the previous chapters.

We present the following radar scattering characteristics: circular diagrams of instantaneous RCS, as wells as mean and median RCS values in specific angular sectors of the object illumination. Such scattering characteristics were computed for a number of airborne objects (B-2, Tu-22M3 strategic bombers, Boeing-737 passenger aircraft, An-26 transport aircraft; MiG-29, F-16 fighter jets, and AGM-86 cruise missile given their radar observation at elevation angles close to the plane of wings) as well as ground objects (Russian main battle tank—T-90, German tank—Leopard-2, and American tank—M1A1 Abrams given their radar observation at different elevation angles).

Besides, we present circular diagrams of the so-called "noncoherent" RCS. As in Chapter 2, we consider the noncoherent RCS to be computed as a sum of RCSs of all parts of ellipsoids and edges constituting the object surface model.

Since the radar target aspect can be regarded as random value, its RCS at any given moment can be regarded as random value too. Probability distribution of such random value can be evaluated by diagrams of instantaneous RCS obtained as a result of computation or experiment. Along with RCS σ, its square root $\sqrt{\sigma}$ is often used in radar theory, the latter being proportional to the radar echo amplitude. Therefore, this chapter features the distribution histograms of radar echo amplitude multiplier $\sqrt{\sigma}$ given the object observation at the most common aspect angles. From a number of possible probability distributions (normal, Rayleigh, lognormal, Weibull, β-distribution, Γ-distribution), we chose the ones that fit best empirical probability distributions according to Kolmogorov–Smirnoff criterion (while doing this we also determined the parameters of theoretical probability distributions).

Commonly adopted in radar technique of evaluating range of target detection with probability equal to 0.5 requires that median RCS value be available. Therefore, for every radar target considered in this chapter we provide median RCS values for specific sectors of the radar observation azimuth aspects. As median RCS, we consider such nonrandom RCS value, which corresponds to condition that probabilities of random RCS being below and above this median in specific angular sector of the object observation are equal to 0.5.

All the characteristics mentioned above are presented for monostatic radar configuration.

3.1 SCATTERING CHARACTERISTICS OF AIRBORNE OBJECTS

Scattering computation results for airborne objects were obtained at the following illumination frequencies: 10 GHz (radar signal wavelength is about 3 cm), 3 GHz (wavelength is 10 cm), and 1 GHz (wavelength is about 30 cm). Other parameters of illumination were as follows: azimuth aspect increment was 0.02°, azimuth aspect β (Figure 3.1) being counted off from the nose-on aspect (0° corresponds to the nose-on radar observation, 180° corresponds to the tail-on observation). Considering the fact that aircraft aspect in elevation plane may vary during flight, we chose this elevation angle aspect to be random value distributed uniformly in the range $-3° \pm 4°$ with respect to the wing plane (elevation angle aspect of –3° corresponds to the radar observation from the lower hemisphere [Figure 3.1]). Computation results were obtained for monostatic radar configuration and two mutually orthogonal polarizations of illumination signal: horizontal—electrical field intensity vector of incident wave p_{h}^0 lying in the plane of wings; and vertical—electrical field intensity vector of incident wave p_{v}^0 being orthogonal to vector p_{h}^0 and belonging to the plane that is perpendicular to the wing plane and passes through the incidence direction vector. Hereinafter, blue curves correspond to horizontal polarization of incident wave and red curves correspond to its vertical polarization.

Computation of mean RCS may result in very large values when the air vehicle is observed at side-on aspects due to scattering from idealized (almost flat) surface in directions close to normal. Such anomalously great values can distort the corresponding histograms of mean RCS. Therefore, to obtain

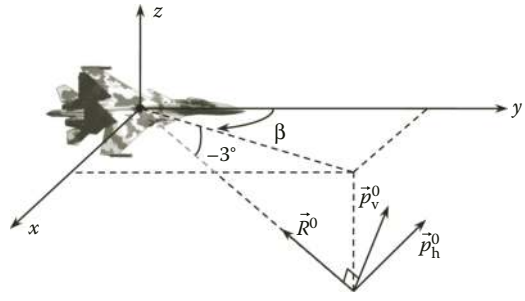

FIGURE 3.1 Geometry of airborne object illumination.

mean RCS values close to real ones, we discarded 0.2% of the largest instantaneous RCS values in the azimuth aspect averaging sector from 45° through 135°; in the azimuth aspect averaging sector from 80° through 100°, we discarded, in the same manner, 1% of the largest instantaneous RCS values.

Distribution histograms of the echo signal's amplitude multiplier (square root from RCS) are given for the azimuth aspect sector of object illumination from –20° through +20° (nose-on aspects of airborne radar objects) and horizontal polarization of incident electromagnetic wave.

Along with histograms, we also present theoretical probability densities for the radar echo amplitude multiplier (selected from the ones mentioned above), which fit best the empirical probability distributions by the Kolmogorov–Smirnov criterion. Black lines in figures containing histograms correspond to probability densities (specified in the side notes) multiplied by the area of corresponding histograms.

It is worth mentioning that in some cases, despite the fact that theoretical curves fit empirical distributions quite well by Kolmogorov–Smirnov criterion, these curves of theoretical probability distributions can deviate considerably from the histogram envelopes. In this situation, the end user may try to find other theoretical probability distributions that better fit the histograms presented below or use the histograms themselves.

Also, there are examples of high-range resolution profiles (HRRPs) computed for the airborne objects given various central frequencies and various widths of illumination signal spectrum.

3.1.1 Scattering Characteristics of B-2 Strategic Bomber Aircraft

The contract for creation of "stealth" bomber aircraft under the code name ATB was given to Northrop company in 1981 [48]. Along with Northrop, other companies also contributed to the program: Boeing (radio electronics), Ling-TeamCo Wout (new materials and structures), and General Electric (engines). The first flight of aircraft officially designated as B-2 Spirit in 1987 was in 1989. In 1993, the first B-2 aircraft was put into service in the US Air Force. Today only 15 of 21 aircrafts are in service; the other four being used as trainers, and one being made into a flying laboratory for testing perspective precision weapons. On February 23, 2008, B-2 Spirit of Kansas, 89-0127 crashed on the runway shortly after takeoff from Andersen Air Force Base in Guam. Total cost of all B-2s produced (not accounting for the infrastructure build for their testing and maintenance) was US$46.4 billion. Today, the work for upgrading the aircraft is being carried out; they plan to complete by 2014.

B-2 aircraft is designed according to the "flying wing" scheme and it does not have vertical stabilizers (Figure 3.2). Conventional rudders were replaced by the so-called split brake-rudders and

FIGURE 3.2 External view of B-2 bomber.

differential thrust. The split brake-rudders are pairs of flaps at the trailing edge of wings that are simultaneously deflected up and down. The planform of B-2 is generated by 12 straight lines that enable concentration of all intensive radar signatures in few basic narrow angular sectors. Aircraft design features the use of the so-called "four leaf" scattering layout: parallel sections of leading and trailing edges and of hatch covers, landing gear bay and engine compartment covers, as well as air intake cowlings lead to the formation of four X-shaped sectors of major backscattering on circular backscattering diagram (two sectors in front hemisphere and other two in rear hemisphere). When observed nose-on or side-on, the aircraft is practically devoid of straight edges and flat surfaces. The inside of the leading edge of the wing is filled with spiky radar absorbent honeycomb structure.

The aircraft airframe is basically made of titanium and aluminum alloys with wide use of carbon–graphite composites [49]. The basic load-bearing element of the aircraft hull is the single longeron titanium torsion box situated in the central front part of the body and adjacent intermediate sections. Carbon–graphite wing consoles with no taper are attached to this central torsion box.

According to available data on the B-2 aircraft structure, we designed the model of its surface (Figure 3.3) suitable for computing the aircraft radar scattering; parameters of the model being presented in the Table 3.1 below. We also considered the B-2 aircraft model with suppositional distribution of RAM over its surface. Let us note that since the actual properties of RAM coating have not been known to us, we assumed the model to be covered with RAM having unchanging relative permittivity and permeability: $\varepsilon' = 1 + j5$, $\mu' = 1 + j5$. The latter values correspond to the radar absorbent of Sommefeld's type, and they correspond to some forms of existing ferromagnetic RAM coatings [85,86]. Leading wing's edge (shown in black in Figure 3.3) is the front boundary of the airframe region that is made of long metallic tubes filled with radar absorbent. In the aircraft surface model, we accounted for this circumstance in the following way. Tangential components of field E and H at points of the wing surface marked black in Figure 3.3 were assumed to be equal to those at the interface of half space consisting of the tube filling material ($\varepsilon' = 1 + j5$, $\mu' = 1 + j5$) and being tangential to the corresponding point of the wing. In case of the model with nonperfectly reflecting surface, the depth of RAM coating was assumed to be variable. It varied from 3 mm for the frontal airframe part to 2.5 mm for its rear part and to 2 mm for the rest of model's surface. Besides, the surface of the cockpit canopy and the upper wing's wedge behind the engines' nozzles were assumed to be perfectly conducting in the model.

Figures 3.4 through 3.21 show diagrams of mean and median RCS given the B-2 aircraft model illumination at vertical and horizontal polarization, the latter having been averaged over different angular sectors, as well as circular diagrams of instantaneous and noncoherent RCS for the frequency ranges of our interest.

Figures 3.22 through 3.24 show the amplitude distributions of echo signals for the frequency ranges of interest given horizontal polarization of illumination wave.

Table 3.2 summarizes the parameters of empirical probability distributions that mostly fit the simulation data for square root of RCS.

FIGURE 3.3 Model of the B-2 bomber surface.

TABLE 3.1
Geometrical Characteristics of B-2 Strategic Bomber Aircraft

Airframe Characteristics (Figure 3.2)		Aircraft Surface Model Characteristics (Figure 3.3)	
Aircraft length	20.9 m	Number of parts of ellipsoids in the model	26
Aircraft height	5.45 m	Number of straight wedge parts in the model	22
Wing span	52.4 m		
Wing's area	464.5 m^2		

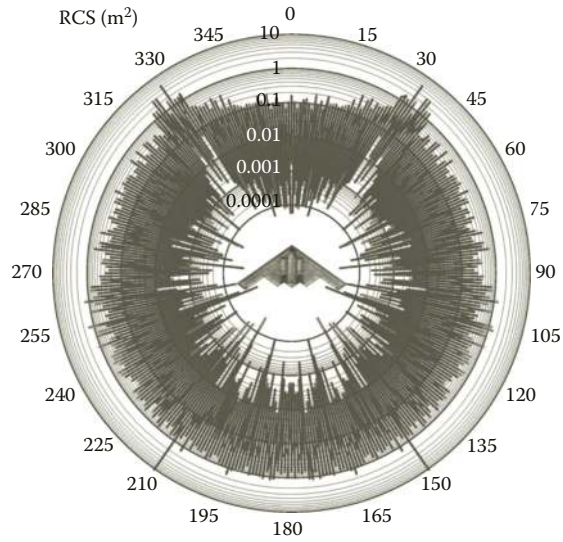

FIGURE 3.4 (**See color insert.**) Circular diagrams of instantaneous RCS given radar observation of B-2 aircraft model at carrier frequency of 10 GHz (3 cm wavelength).

In Section 3.1.2, there are examples of HRRPs computed for the aircraft given various central frequencies of signal spectrum and its widths.

Table 3.2 contains expressions and parameters of probability distributions that fit best empirical distributions of the RCS square root given various carrier frequencies and polarizations of illumination signal.

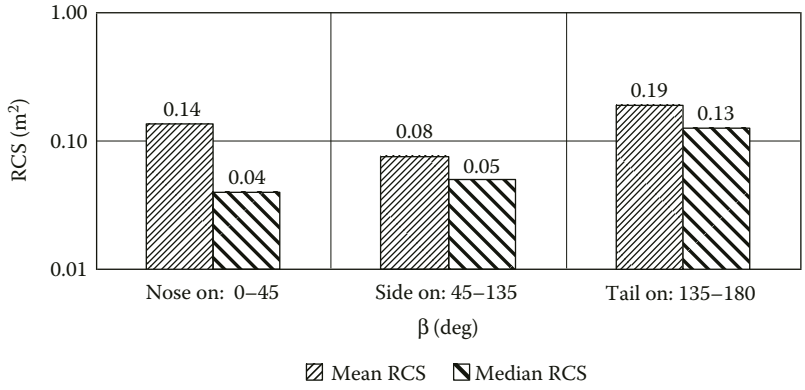

FIGURE 3.5 Diagrams of mean and median RCS of the B-2 aircraft model in three sectors of azimuth aspect given its radar observation at horizontal polarization and carrier frequency of 10 GHz (3 cm wavelength).

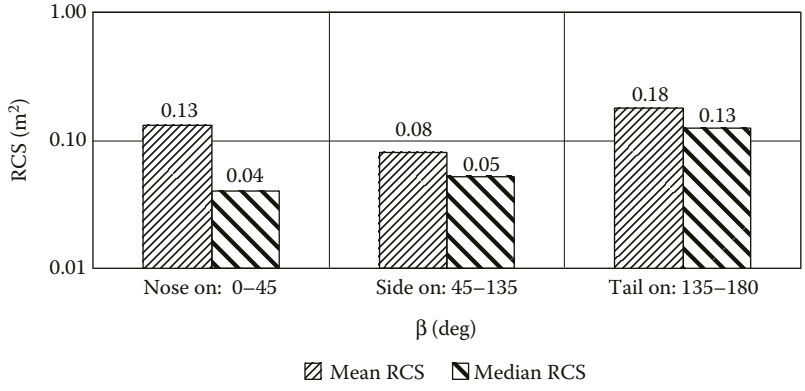

FIGURE 3.6 Diagrams of mean and median RCS of the B-2 aircraft model in three sectors of azimuth aspect given its radar observation at vertical polarization and carrier frequency of 10 GHz (3 cm wavelength).

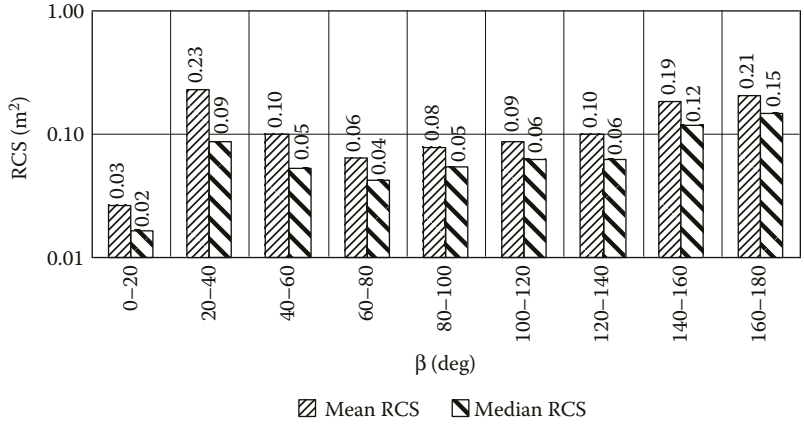

FIGURE 3.7 Diagrams of mean and median RCS of the B-2 aircraft model in 20-degree sectors of azimuth aspect given its radar observation at horizontal polarization and carrier frequency of 10 GHz (3 cm wavelength).

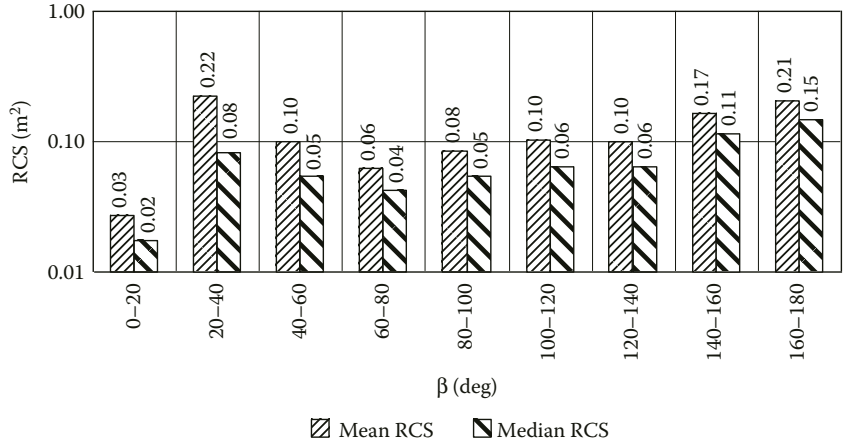

FIGURE 3.8 Diagrams of mean and median RCS of the B-2 aircraft model in 20-degree sectors of azimuth aspect given its radar observation at vertical polarization and carrier frequency of 10 GHz (3 cm wavelength).

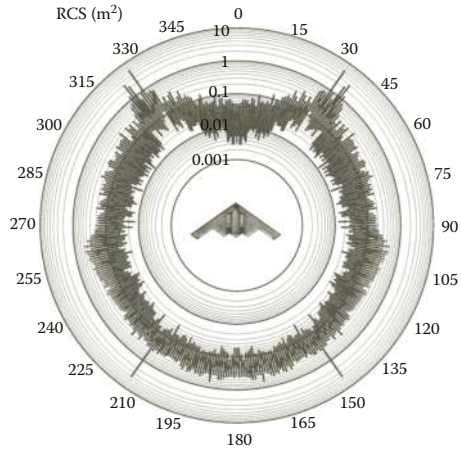

FIGURE 3.9 (**See color insert.**) Circular diagrams of noncoherent RCS given radar observation of B-2 aircraft model at carrier frequency of 10 GHz (3 cm wavelength).

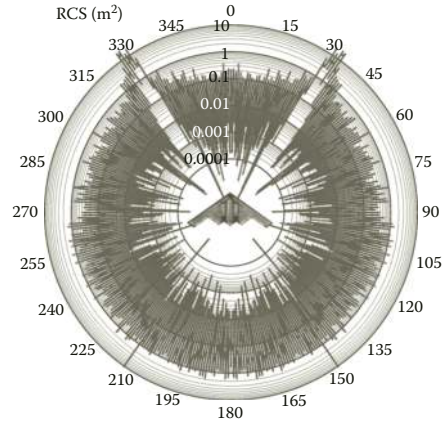

FIGURE 3.10 (**See color insert.**) Circular diagrams of instantaneous RCS given radar observation of B-2 aircraft model at carrier frequency of 3 GHz (10 cm wavelength).

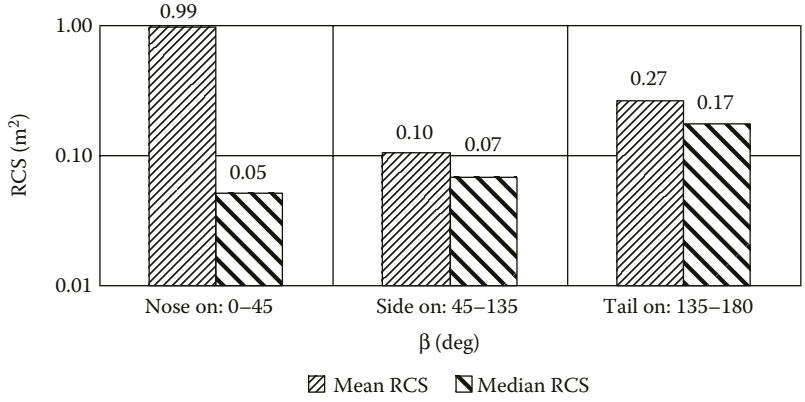

FIGURE 3.11 Diagrams of mean and median RCS of the B-2 aircraft model in three sectors of azimuth aspect given its radar observation at horizontal polarization and carrier frequency of 3 GHz (10 cm wavelength).

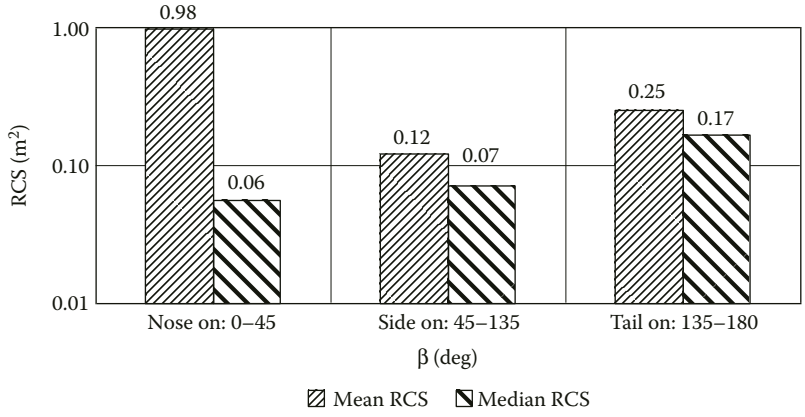

FIGURE 3.12 Diagrams of mean and median RCS of the B-2 aircraft model in three sectors of azimuth aspect given its radar observation at vertical polarization and carrier frequency of 3 GHz (10 cm wavelength).

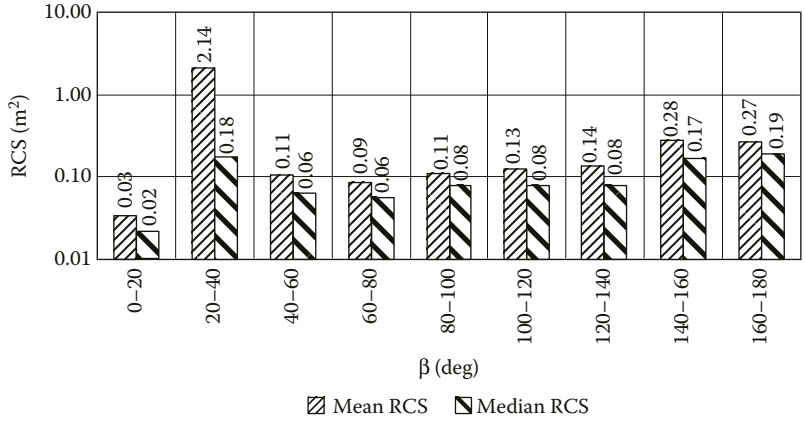

FIGURE 3.13 Diagrams of mean and median RCS of the B-2 aircraft model in 20-degree sectors of azimuth aspect given its radar observation at horizontal polarization and carrier frequency of 3 GHz (10 cm wavelength).

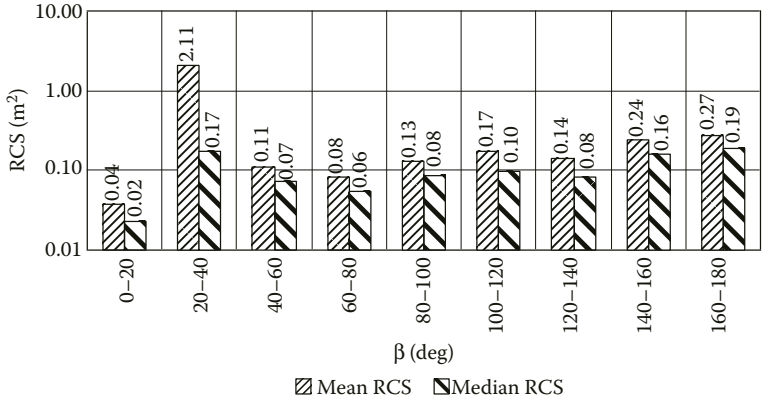

FIGURE 3.14 Diagrams of mean and median RCS of the B-2 aircraft model in 20-degree sectors of azimuth aspect given its radar observation at vertical polarization and carrier frequency of 3 GHz (10 cm wavelength).

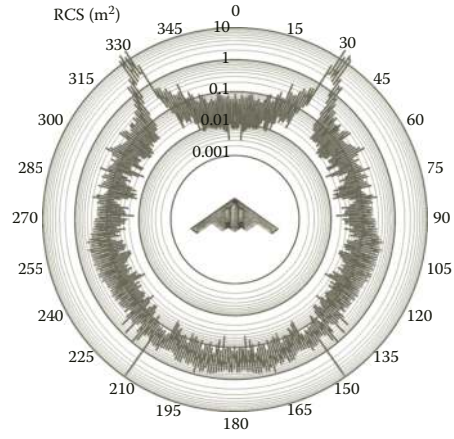

FIGURE 3.15 (**See color insert.**) Circular diagrams of noncoherent RCS of B-2 aircraft model given its radar observation at carrier frequency of 3 GHz (10 cm wavelength).

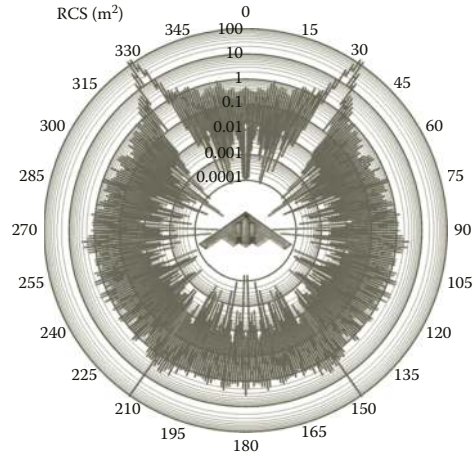

FIGURE 3.16 (**See color insert.**) Circular diagrams of instantaneous RCS given radar observation of the B-2 aircraft model at carrier frequency of 1 GHz (30 cm wavelength).

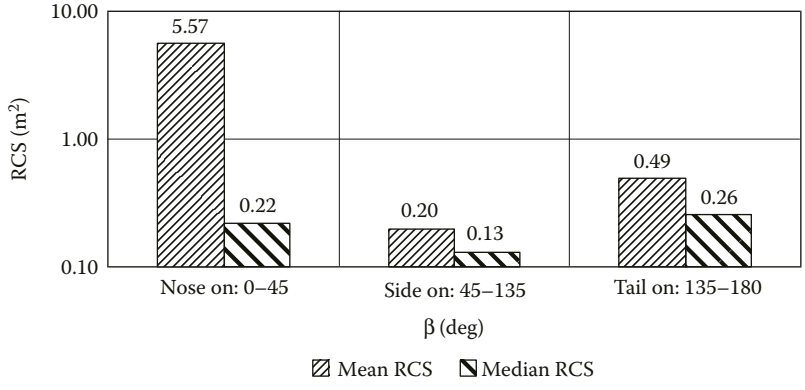

FIGURE 3.17 Diagrams of mean and median RCS of the B-2 aircraft model in three sectors of azimuth aspect given its radar observation at horizontal polarization and carrier frequency of 1 GHz (30 cm wavelength).

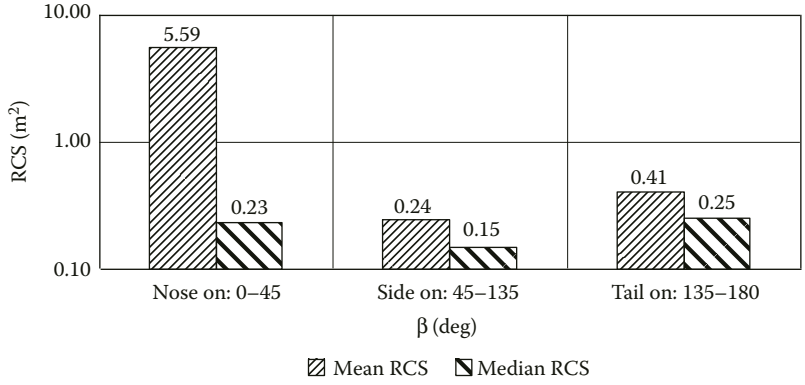

FIGURE 3.18 Diagrams of mean and median RCS of the B-2 aircraft model in three sectors of azimuth aspect given its radar observation at vertical polarization and carrier frequency of 1 GHz (30 cm wavelength).

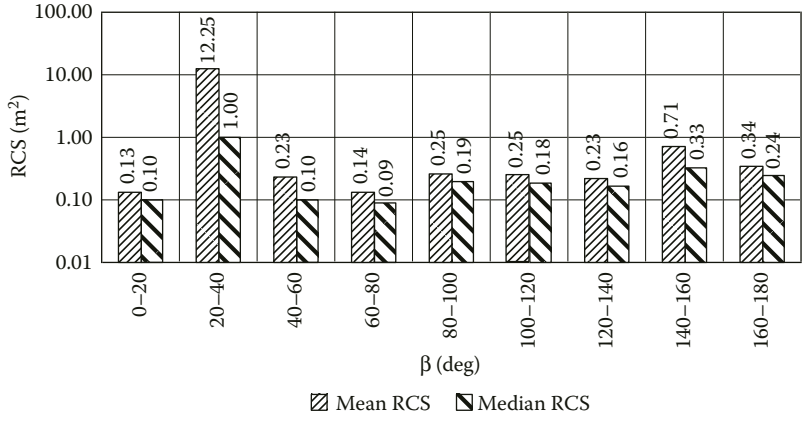

FIGURE 3.19 Diagrams of mean and median RCS of the B-2 aircraft model in 20-degree sectors of azimuth aspect given its radar observation at horizontal polarization and carrier frequency of 1 GHz (30 cm wavelength).

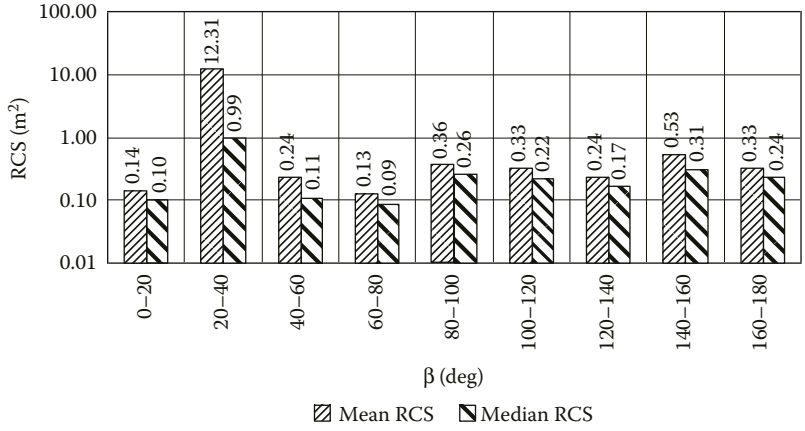

FIGURE 3.20 Diagrams of mean and median RCS of the B-2 aircraft model in 20-degree sectors of azimuth aspect given its radar observation at vertical polarization and carrier frequency of 1 GHz (30 cm wavelength).

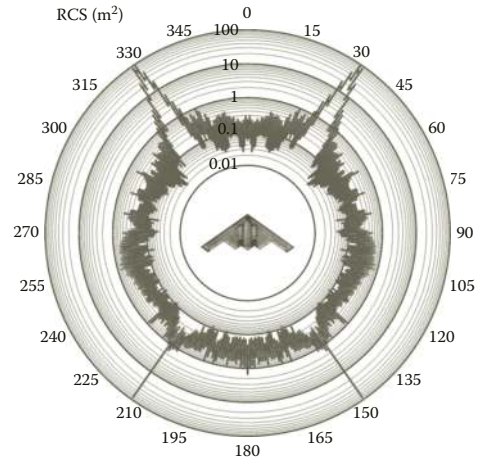

FIGURE 3.21 (**See color insert.**) Circular diagrams of noncoherent RCS of B-2 aircraft model given its radar observation at carrier frequency of 1 GHz (30 cm wavelength).

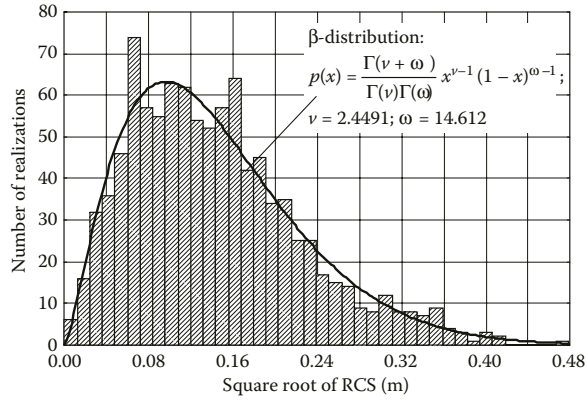

FIGURE 3.22 Amplitude distribution of echo signal from B-2 aircraft model at carrier frequency of 10 GHz given its horizontal polarization.

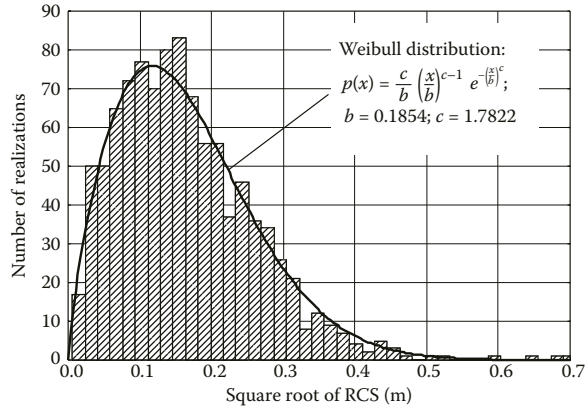

FIGURE 3.23 Amplitude distribution of echo signal from B-2 aircraft model at carrier frequency of 3 GHz given its horizontal polarization.

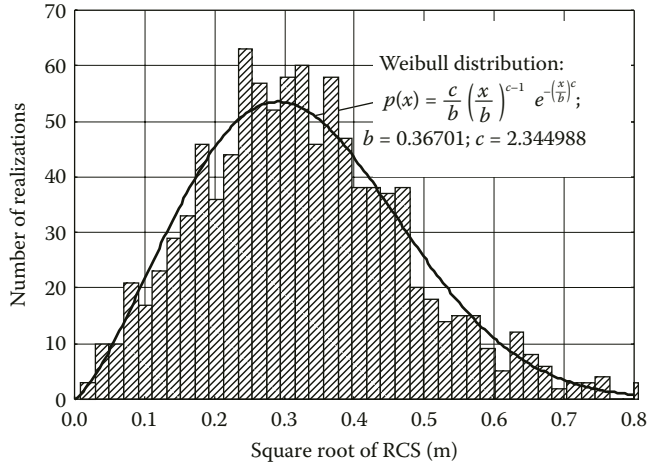

FIGURE 3.24 Amplitude distribution of echo signal from B-2 aircraft model at carrier frequency of 1 GHz given its horizontal polarization.

TABLE 3.2
Parameters of Probability Distributions for the Echo Signal Amplitudes for B-2 aircraft

Wavelength	Polarization	Distribution Kind	Distribution Parameters
3 cm	Horizontal	β-distribution: $p(x) = \frac{\Gamma(\nu+\omega)}{\Gamma(\nu)\Gamma(\omega)} x^{\nu-1}(1-x)^{\omega-1}$, where $\Gamma(\nu)$ is the gamma-function	$\nu = 2.4491$ $\omega = 14.612$
3 cm	Vertical	β-distribution	$\nu = 2.39636$ $\omega = 13.48536$
10 cm	Horizontal	Weibull distribution: $p(x) = \frac{c}{b}\left(\frac{x}{b}\right)^{c-1} e^{-\left(\frac{x}{b}\right)^c}$	$b = 0.1854$ $c = 1.7822$
10 cm	Vertical	β-distribution	$\nu = 2.37642$ $\omega = 10.81251$
30 cm	Horizontal	Weibull distribution	$b = 0.36701$ $c = 2.344988$
30 cm	Vertical	Weibull distribution	$b = 0.37423$ $c = 2.306958$

3.1.2 Impulse Responses of B-2 Strategic Bomber Aircraft

As an example, we consider HRRPs of the B-2 aircraft observed at the elevation angle of –3° (illumination from below) and azimuth aspect of 35° (perpendicularly to the wing's leading edge).

Figures 3.25 and 3.26 show HRRPs of B-2 aircraft given its illumination with signals at carrier frequency of 10 GHz (3 cm wavelength) for the cases of horizontal and vertical polarizations, respectively. Solid line corresponds to HRRP obtained using signal with rectangular amplitude spectrum of 1 GHz bandwidth. Dashed line corresponds to HRRP obtained using signal with rectangular spectrum of 250 MHz bandwidth.

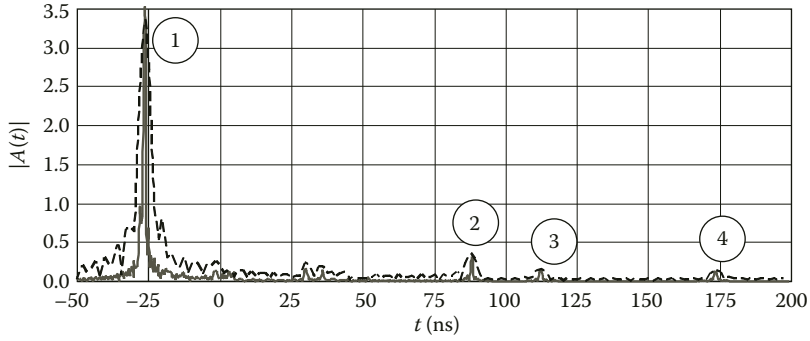

FIGURE 3.25 HRRPs of B-2 aircraft given its illumination by signal with center spectrum frequency of 10 GHz (3 cm wavelength), horizontal polarization.

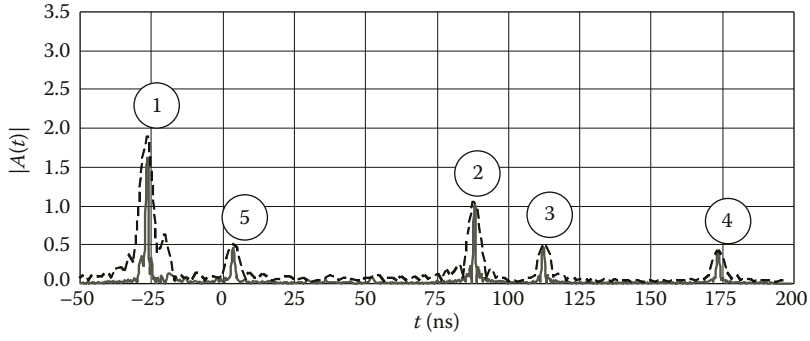

FIGURE 3.26 HRRPs of B-2 aircraft given its illumination by signals with center spectrum frequency of 10 GHz (3 cm wavelength), vertical polarization.

Peaks #1 correspond to scattering from the leading edge of aircraft's wing. The amplitude of echo from the wing's leading edge is higher for the case of horizontal polarization. Peaks #2 correspond to scattering from trailing edge of aircraft's body. Peaks #3 correspond to scattering from the trailing edge of the further wing's rear extension. Peaks #4 correspond to scattering from straight wing's tip of the further wing. It is worth mentioning that amplitudes of peaks #2, #3, and #4 are higher in case of vertical polarization of illumination signal. The later is due to scattering peculiarities of edge local scatterers given their illumination along the face of scattering wedge and toward its edge. Peaks #5 in Figure 3.26 correspond to scattering from air intake situated at the upper surface of the nearer wing. It should be noted that air intake does not provide any echo at horizontal polarization. This can be probably explained by destructive interference of partial echoes from horizontally oriented parts of "saw-tooth"-shaped upper edge of the air intake.

Figures 3.27 and 3.28 show HRRPs of B-2 aircraft given its illumination by signals with spectra centered at 3 GHz (10 cm wavelength) for the cases of horizontal and vertical polarization, respectively. Bold solid line corresponds to HRRP obtained using signal with rectangular spectrum of 1 GHz bandwidth. Thin dashed line corresponds to HRRP obtained using signal with rectangular spectrum of 250 MHz bandwidth.

HRRPs shown in Figures 3.27 and 3.28 contain the following peaks marked with numbers.

Peaks #1 are due to scattering from the leading edge of the aircraft's wing. Amplitude of the response from wing's leading edge is higher for the case of horizontal polarization. Peaks #2 are due to scattering from the air intake. Peaks #3 are due to scattering from the trailing edge of the nearer wing's rear extension. Peaks #4 are due to scattering from trailing edge of aircraft's body. Peaks

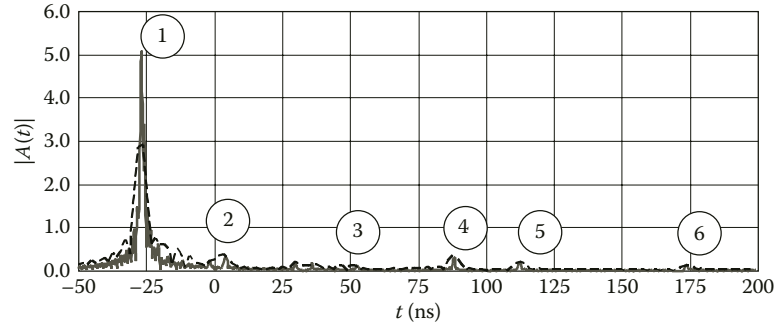

FIGURE 3.27 HRRPs of B-2 aircraft given its illumination by signals with center spectrum frequency of 3 GHz (10 cm wavelength), horizontal polarization.

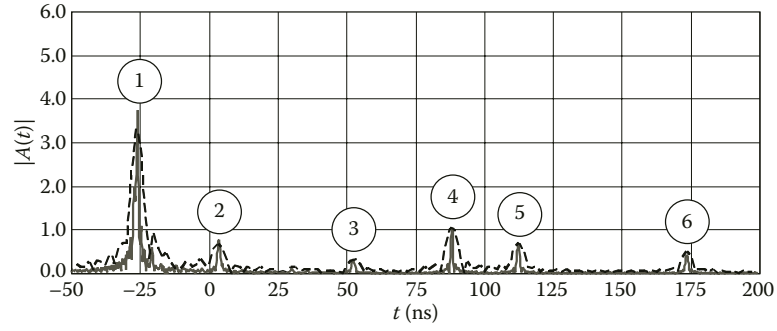

FIGURE 3.28 HRRPs of B-2 aircraft given its illumination by signals with center spectrum frequency of 3 GHz (10 cm wavelength), vertical polarization.

#5 are due to scattering from trailing edge of the further wing's rear extension. Peaks #6 are due to scattering from the straight edge tip of the further aircraft wing. Amplitude of peaks #3, #4, #5, and #6 is higher in case of vertical polarization.

Figures 3.29 and 3.30 show corresponding HRRPs of B-2 aircraft given its illumination by signals with spectra centered at 1 GHz (30 cm wavelength) for the cases of horizontal and vertical polarization, respectively. Bold solid line corresponds to HRRP obtained using signal with rectangular spectrum of 1 GHz bandwidth. Thin dashed line corresponds to HRRP obtained using signal with rectangular spectrum of 250 MHz bandwidth.

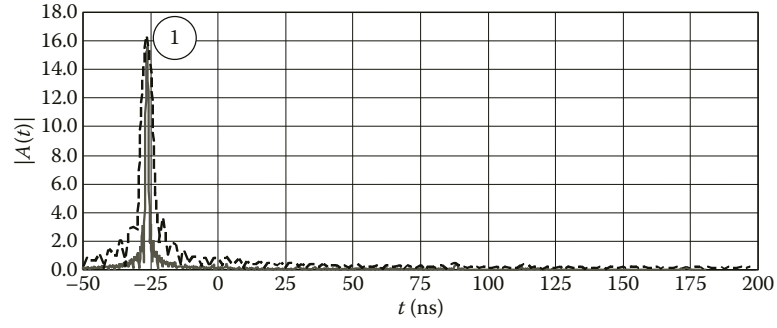

FIGURE 3.29 HRRPs of B-2 aircraft given its illumination by signals with center spectrum frequency of 1 GHz (30 cm wavelength), horizontal polarization.

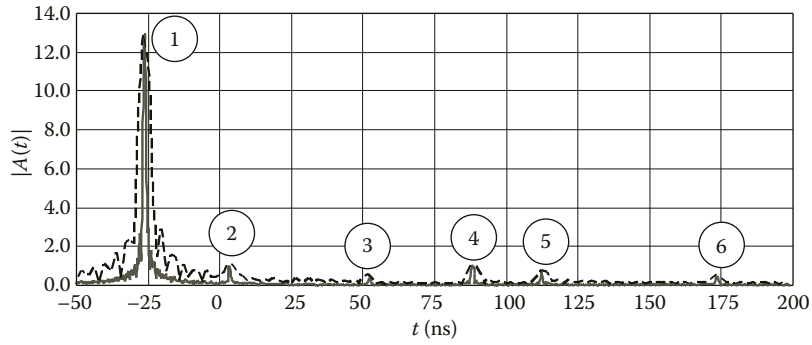

FIGURE 3.30 HRRPs of B-2 aircraft given its illumination by signals with center spectrum frequency of 1 GHz (30 cm wavelength), vertical polarization.

Peaks #1 are due to scattering from the wing's leading edge. Besides, peak #1 is the only one that can be singled out in HRRP given horizontal polarization of illumination signal (Figure 3.29). Peaks #2 in Figure 3.30 are due to the scattering from air intake. Peaks #3 in Figure 3.30 are due to scattering from trailing edge of the nearer wing's rear extension. Peaks #4 in Figure 3.30 are due to scattering from trailing edge of the aircraft body. Peaks #5 in Figure 3.30 are due to scattering from trailing edge of the further wing's rear extension. Peaks #6 in Figure 3.30 are due to scattering from the straight edge tip of the further aircraft wing.

It is worth mentioning that despite radar absorbent materials present in the wing's construction, its illumination in the direction perpendicular to leading wings' edge results in considerable (several units of relative amplitude) increase of the echo amplitude due to significant extent of the leading edge. For the rest of the aspect angles of the aircraft illumination, maximum amplitude of such echoes, according to our computation results, is of the order of tenth and hundredth fraction of relative amplitude unit.

3.1.3 Scattering Characteristics of Tu-22M3 Long-Range Bomber Aircraft

The first prototype of Tu-22M3 long-range bomber aircraft was developed as a result of deep upgrade of the Tu-22M bomber aircraft. In 1978, the aircraft had been put in for mass production. However, new armaments installed on it required additional time for testing and refinement, and hence the final version of Tu-22M3 had officially entered service only in March 1989 [87].

The Tu-22M3 was designed according to standard aerodynamic scheme and had the variable sweep wing, it also featured an all-moving horizontal stabilizer and single fin vertical stabilizer (Figure 3.31). The airframe was basically made of aluminum alloys. The wing consisted of a fixed wing part and consoles that swept back and forth (the consoles at Tu-22M3 could be set to the sweep angle values of 20°, 30°, and 65°, at the earlier prototypes the sweep back angle had been limited to 60°). Theoretical studies and flight tests revealed the following advantages of heavy strike aircraft having such wing design: aerodynamic quality as averaged over flight significantly increased due to its increase on a subsonic flight speed given moderate wing sweep that provided an increase in flight range; the aircraft obtained an improved capability of landing and taking-off with the minimum sweep angle; with the wing swept back, the aircraft became optimized for the flight at high supersonic speeds, at maximum angle of wing sweep the aircraft could accelerate faster and, as a result, the time of passing through the transonic region decreased; the vertical G-force in the ground vicinity was lower, which provided aircraft with supersonic penetration speeds at extremely low level. In the zone of wing-turning mechanism, there were wing fences preventing air overflow to the consoles. The variable wing sweep aircraft design led to new approach to the placement and use of aerodynamic controls: ailerons were removed from the wing; the spoilers and differentially deflecting

FIGURE 3.31 Tu-22M3 long-range bomber aircraft.

stabilizers were installed instead; take-off and landing characteristics were farther improved by leading edge flaps running along the whole wingspan length.

For the scattering characteristics computation, we used the perfectly conducting model of the aircraft surface (Figure 3.32). Parameters of computer model are summarized in Table 3.3.

Figures 3.33 through 3.50 show diagrams of mean and median RCS given the Tu-22M3 aircraft model illumination at vertical and horizontal polarization, the latter having been averaged over different angular sectors, as well as circular diagrams of instantaneous and noncoherent RCS for the frequency ranges of our interest.

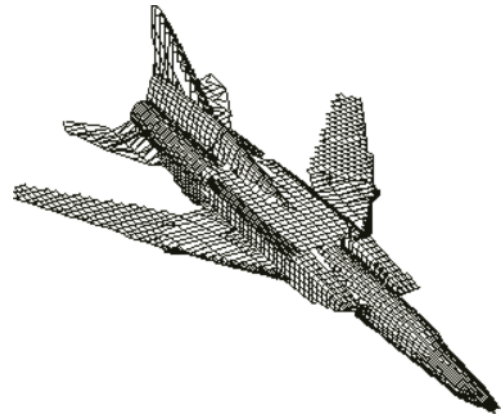

FIGURE 3.32 Surface model of the Tu-22M3 aircraft.

TABLE 3.3
Geometrical Characteristics of Tu-22M3 Long-Range Bomber Aircraft

Airframe Characteristics (Figure 3.31)	
Aircraft length	41.46 m
Aircraft height	11.05 m
Wing span:	
Maximum (20°)	34.28 m
Minimum (65°)	23.3 m
Wing's area:	
Maximum (20°)	183.57 m^2
Minimum (65°)	175.8 m^2

Aircraft Surface Model Characteristics (Figure 3.32)	
Number of parts of ellipsoids in the model	50
Number of straight wedge parts in the model	25
Sweep back angle of the turning consoles	65°

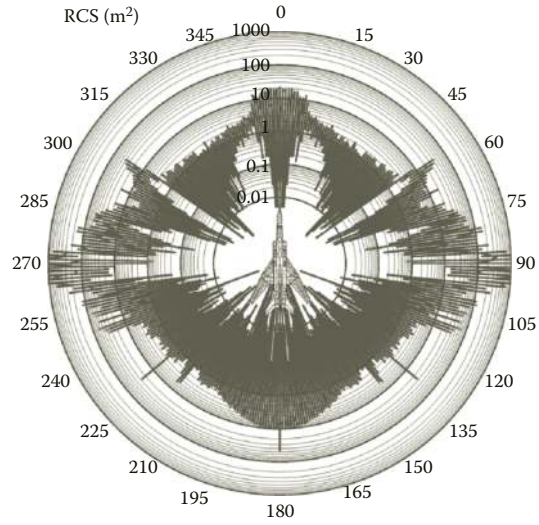

FIGURE 3.33 (**See color insert.**) Circular diagrams of instantaneous RCS given radar observation of Tu-22M3 aircraft model at carrier frequency of 10 GHz (3 cm wavelength).

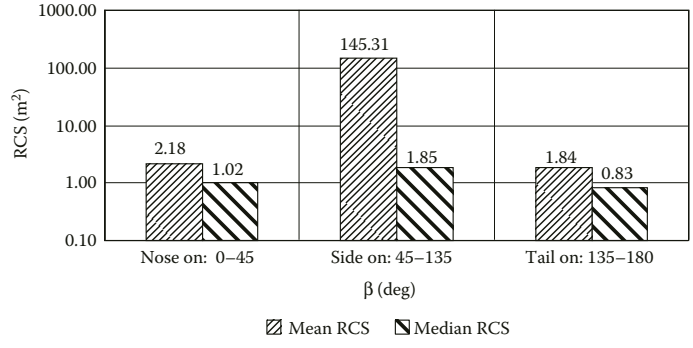

FIGURE 3.34 Diagrams of mean and median RCS of the Tu-22M3 aircraft model in three sectors of azimuth aspect given its radar observation at horizontal polarization and carrier frequency of 10 GHz (3 cm wavelength).

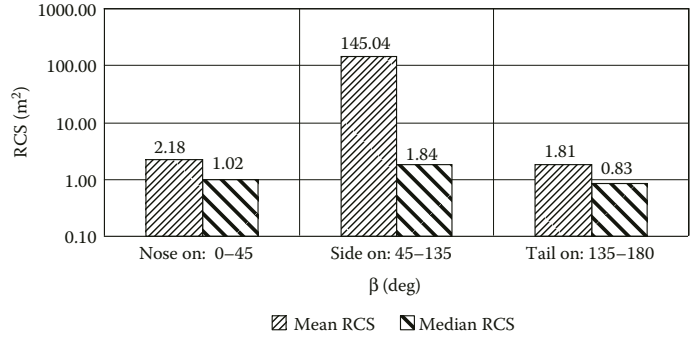

FIGURE 3.35 Diagrams of mean and median RCS of the Tu-22M3 aircraft model in three sectors of azimuth aspect given its radar observation at vertical polarization and carrier frequency of 10 GHz (3 cm wavelength).

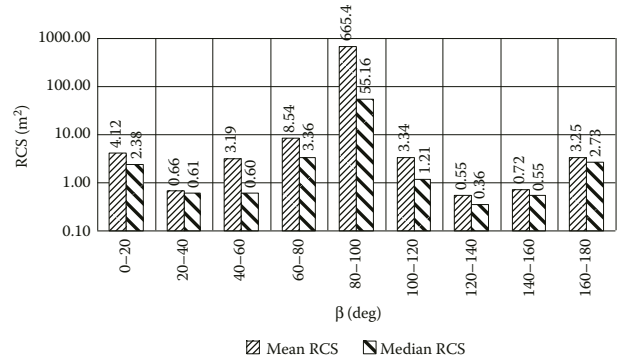

FIGURE 3.36 Diagrams of mean and median RCS of the Tu-22M3 aircraft model in 20-degree sectors of azimuth aspect given its radar observation at horizontal polarization and carrier frequency of 10 GHz (3 cm wavelength).

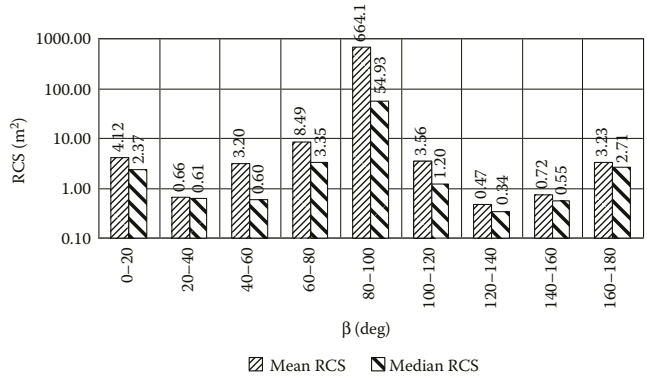

FIGURE 3.37 Diagrams of mean and median RCS of the Tu-22M3 aircraft model in 20-degree sectors of azimuth aspect given its radar observation at vertical polarization and carrier frequency of 10 GHz (3 cm wavelength).

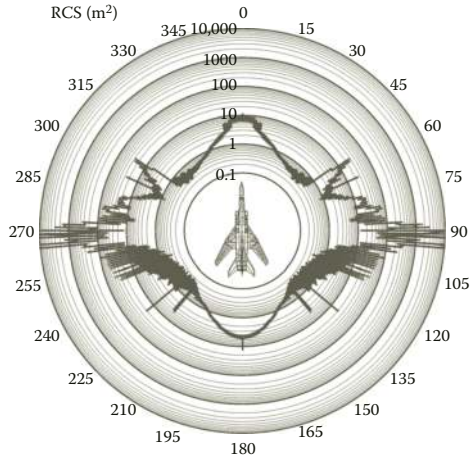

FIGURE 3.38 (**See color insert.**) Circular diagrams of noncoherent RCS given radar observation of Tu-22M3 aircraft model at carrier frequency of 10 GHz (3 cm wavelength).

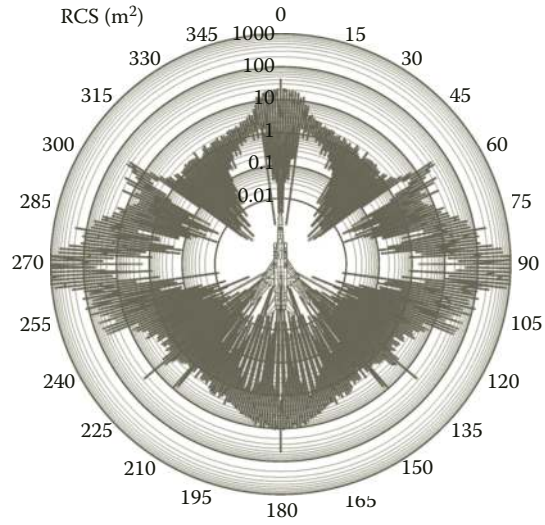

FIGURE 3.39 (**See color insert.**) Circular diagrams of instantaneous RCS given radar observation of Tu-22M3 aircraft model at carrier frequency of 3 GHz (10 cm wavelength).

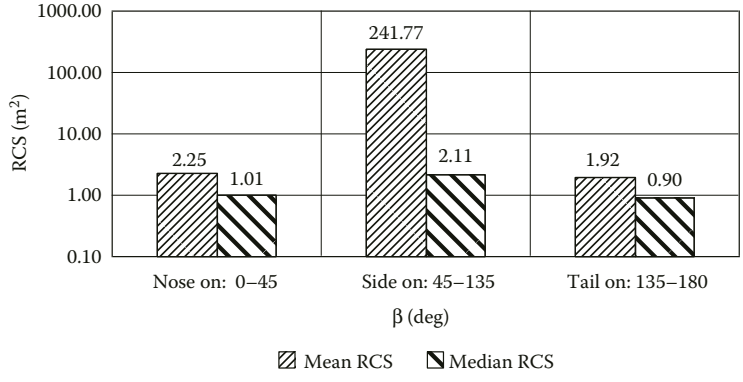

FIGURE 3.40 Diagrams of mean and median RCS of the Tu-22M3 aircraft model in three sectors of azimuth aspect given its radar observation at horizontal polarization and carrier frequency of 3 GHz (10 cm wavelength).

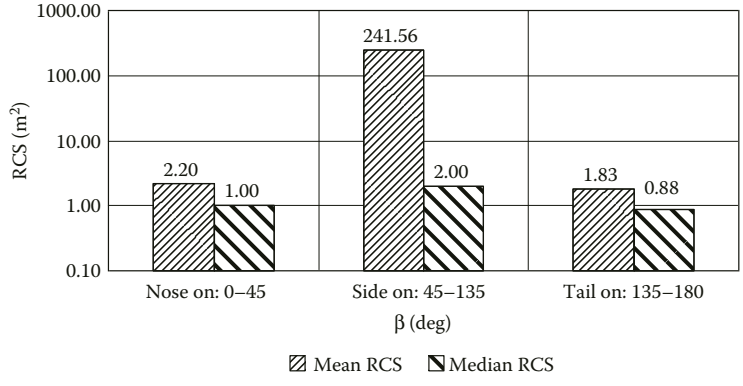

FIGURE 3.41 Diagrams of mean and median RCS of the Tu-22M3 aircraft model in three sectors of azimuth aspect given its radar observation at vertical polarization and carrier frequency of 3 GHz (10 cm wavelength).

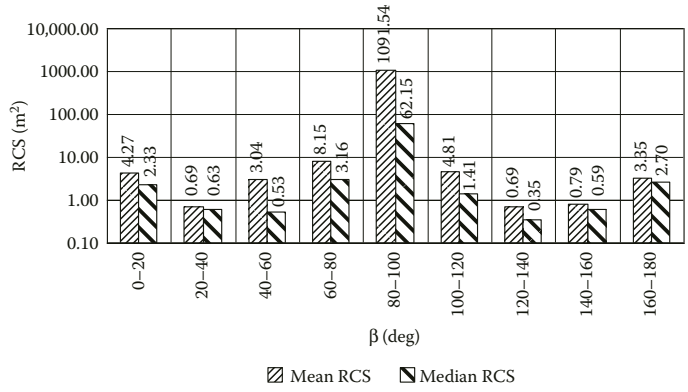

FIGURE 3.42 Diagrams of mean and median RCS of the Tu-22M3 aircraft model in 20-degree sectors of azimuth aspect given its radar observation at horizontal polarization and carrier frequency of 3 GHz (10 cm wavelength).

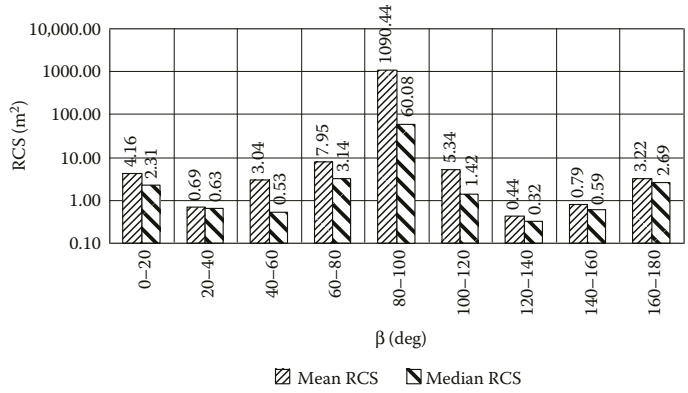

FIGURE 3.43 Diagrams of mean and median RCS of the Tu-22M3 aircraft model in 20-degree sectors of azimuth aspect given its radar observation at vertical polarization and carrier frequency of 3 GHz (10 cm wavelength).

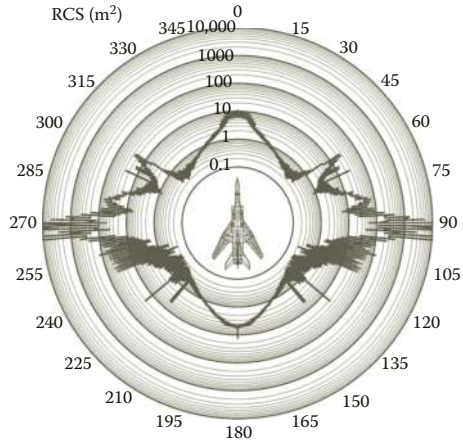

FIGURE 3.44 (**See color insert.**) Circular diagrams of noncoherent RCS of Tu-22M3 aircraft model given its radar observation at carrier frequency of 3 GHz (10 cm wavelength).

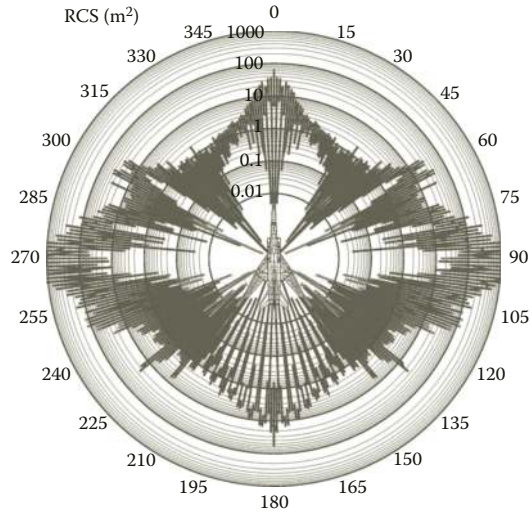

FIGURE 3.45 (**See color insert.**) Circular diagrams of instantaneous RCS given radar observation of Tu-22M3 aircraft model at carrier frequency of 1 GHz (30 cm wavelength).

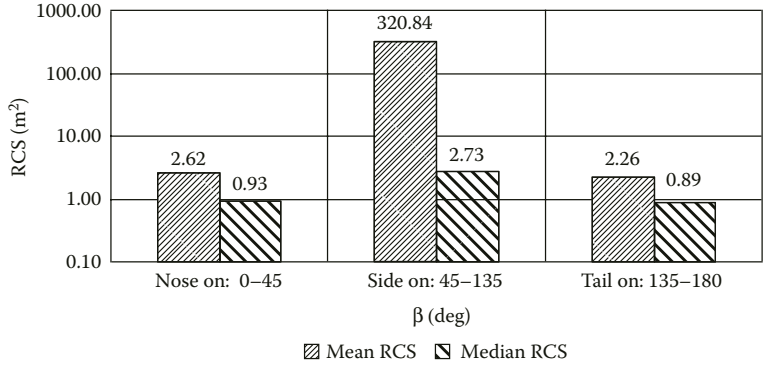

FIGURE 3.46 Diagrams of mean and median RCS of Tu-22M3 aircraft model in three sectors of azimuth aspect given its radar observation at horizontal polarization and carrier frequency of 1 GHz (30 cm wavelength).

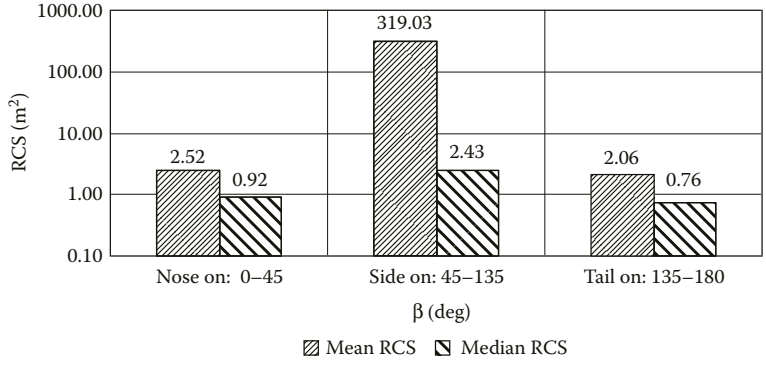

FIGURE 3.47 Diagrams of mean and median RCS of Tu-22M3 aircraft model in three sectors of azimuth aspect given its radar observation at vertical polarization and carrier frequency of 1 GHz (30 cm wavelength).

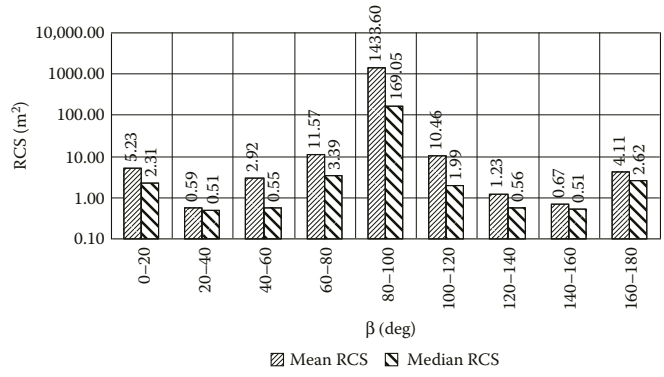

FIGURE 3.48 Diagrams of mean and median RCS of Tu-22M3 aircraft model in 20-degree sectors of azimuth aspect given its radar observation at horizontal polarization and carrier frequency of 1 GHz (30 cm wavelength).

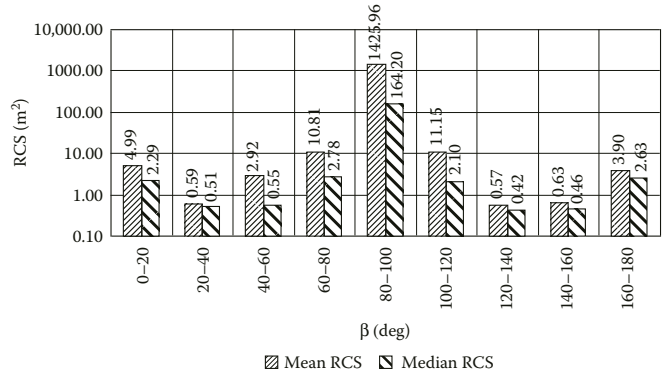

FIGURE 3.49 Diagrams of mean and median RCS of Tu-22M3 aircraft model in 20-degree sectors of azimuth aspect given its radar observation at vertical polarization and carrier frequency of 1 GHz (30 cm wavelength).

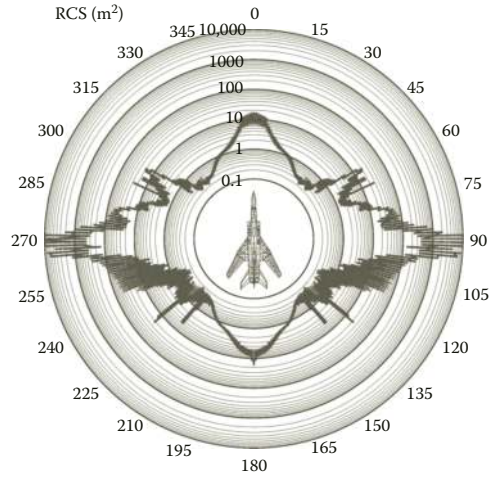

FIGURE 3.50 (**See color insert.**) Circular diagrams of noncoherent RCS of Tu-22M3 aircraft model given its radar observation at carrier frequency of 1 GHz (30 cm wavelength).

Figures 3.51 through 3.53 show the amplitude distributions of echo signals for the frequency ranges of interest given horizontal polarization of illumination wave.

Table 3.4 summarizes the parameters of empirical probability distributions that mostly fit the simulation data for square root of RCS.

In Section 3.1.4, there are examples of HRRPs computed for the aircraft given various central frequencies of signal spectrum and its widths.

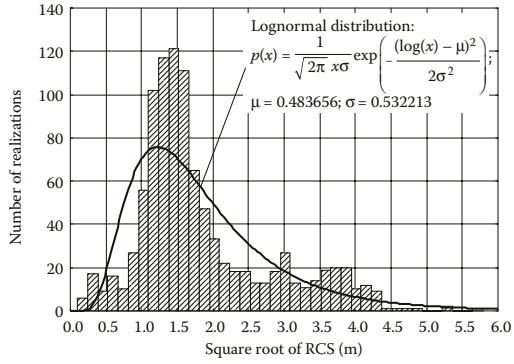

FIGURE 3.51 Amplitude distribution of echo signal of Tu-22M3 aircraft model at carrier frequency of 10 GHz given its horizontal polarization.

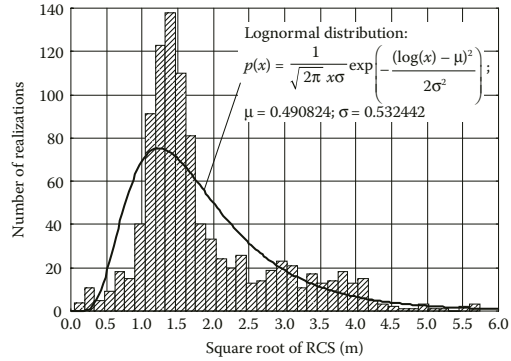

FIGURE 3.52 Amplitude distribution of echo signal of Tu-22M3 aircraft model at carrier frequency of 3 GHz given its horizontal polarization.

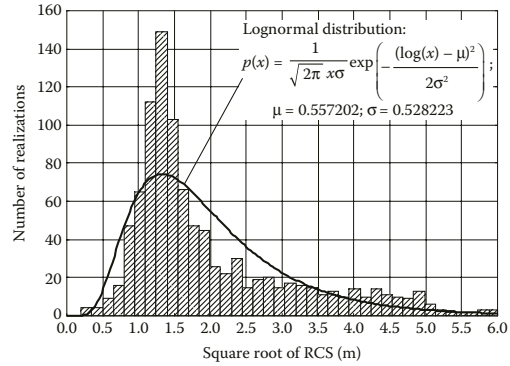

FIGURE 3.53 Amplitude distribution of echo signal of Tu-22M3 aircraft model at carrier frequency of 1 GHz given its horizontal polarization.

TABLE 3.4
Parameters of Probability Distributions for the Echo Signal Amplitudes for Tu-22M3 Aircraft Model

Wavelength	Polarization	Distribution Kind	Distribution Parameters
3 cm	Horizontal	Lognormal distribution: $p(x) = \frac{1}{\sqrt{2\pi}\, x\sigma}\exp\left(-\frac{(\log(x)-\mu)^2}{2\sigma^2}\right)$,	$\mu = 0.483656$ $\sigma = 0.532213$
3 cm	Vertical	Lognormal distribution	$\mu = 0.478054$ $\sigma = 0.537757$
10 cm	Horizontal	Lognormal distribution	$\mu = 0.490824$ $\sigma = 0.532442$
10 cm	Vertical	Lognormal distribution	$\mu = 0.477216$ $\sigma = 0.550485$
30 cm	Horizontal	Lognormal distribution	$\mu = 0.557202$ $\sigma = 0.528223$
30 cm	Vertical	Lognormal distribution	$\mu = 0.517806$ $\sigma = 0.556563$

3.1.4 Impulse Responses of Tu-22M3 Long-Range Bomber Aircraft

As an example, we consider HRRPs of the Tu-22M3 aircraft observed at the elevation angle of –3° (illumination from below) and azimuth aspect of 65° (perpendicularly to the wing's leading edge given its maximum sweep back—supersonic flight).

Figures 3.54 and 3.55 show HRRPs of Tu-22M3 aircraft given its illumination with signal at central frequency of 10 GHz (3 cm wavelength) for the cases of horizontal and vertical polarization, respectively. Bold solid line corresponds to HRRP obtained using signal with rectangular amplitude spectrum of 1 GHz bandwidth. Thin dashed line corresponds to HRRP obtained using signal with rectangular spectrum of 250 MHz bandwidth.

Peaks #1 are due to scattering from the nose part of aircraft body. Peaks #2 are due to scattering from wing's leading edge. Peak amplitude of the echo from wing's leading edge is significantly higher for the case of horizontal polarization. Peaks #3 are due to scattering from the aircraft's empennage. Peaks #4 in Figure 3.55 are due to scattering from the air intake. It is worth noting that in Figure 3.54 the peak that is due to scattering from air intake is barely seen since it is hidden behind the intense echo from the wing's leading edge.

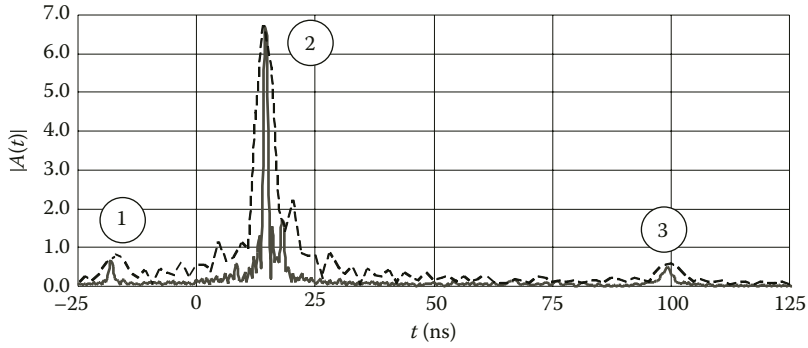

FIGURE 3.54 HRRPs of Tu-22M3 aircraft given its illumination by signal with center spectrum frequency of 10 GHz (3 cm wavelength), horizontal polarization.

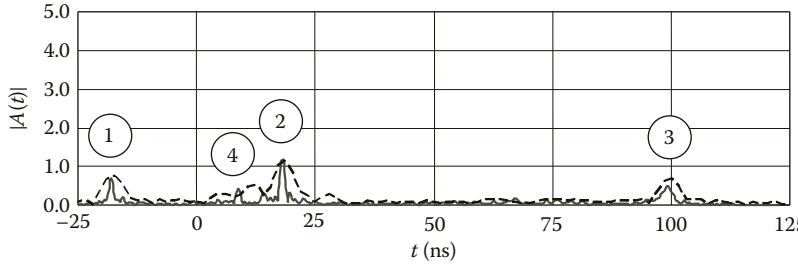

FIGURE 3.55 HRRPs of Tu-22M3 aircraft given its illumination by signals with center spectrum frequency of 10 GHz (3 cm wavelength), vertical polarization.

Figures 3.56 and 3.57 show HRRPs of Tu-22M3 aircraft given its illumination by signals with spectra centered at 3 GHz (10 cm wavelength) for the cases of horizontal and vertical polarization, respectively. Solid bold line corresponds to HRRP obtained using signal with rectangular spectrum of 1 GHz bandwidth. Thin dashed line corresponds to HRRP obtained using signal with rectangular spectrum of 250 MHz bandwidth.

HRRPs shown in Figures 3.56 and 3.57 contain the following peaks marked with numbers. The view of these HRRPs is similar to those shown above for the case of illumination signals with spectra centered at 10 GHz frequency (3 cm wavelength).

Peaks #1 are due to scattering from the nose part of aircraft body. Peaks #2 are due to scattering from wing's leading edge. Peaks #3 are due to scattering from the aircraft's empennage.

Figures 3.58 and 3.59 show HRRPs of Tu-22M3 aircraft given its illumination by signals with spectra centered at 1 GHz (30 cm wavelength) for the cases of horizontal and vertical polarization, respectively. Solid bold line corresponds to HRRP obtained using signal with rectangular spectrum

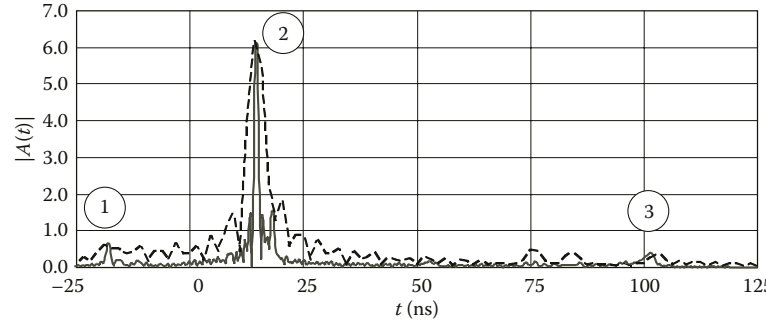

FIGURE 3.56 HRRPs of Tu-22M3 aircraft given its illumination by signals with center spectrum frequency of 3 GHz (10 cm wavelength), horizontal polarization.

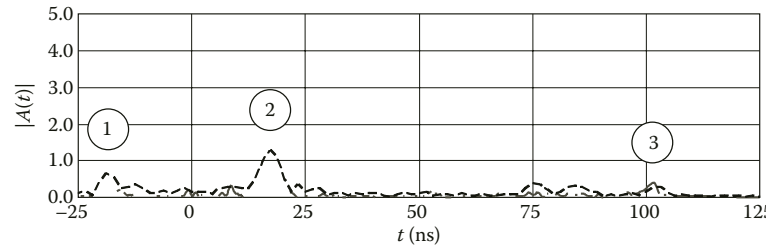

FIGURE 3.57 HRRPs of Tu-22M3 aircraft given its illumination by signals with center spectrum frequency of 3 GHz (10 cm wavelength), vertical polarization.

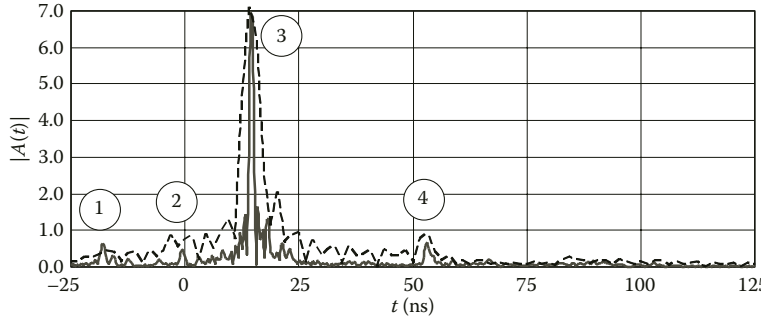

FIGURE 3.58 HRRPs of Tu-22M3 aircraft given its illumination by signals with center spectrum frequency of 1 GHz (30 cm wavelength), horizontal polarization.

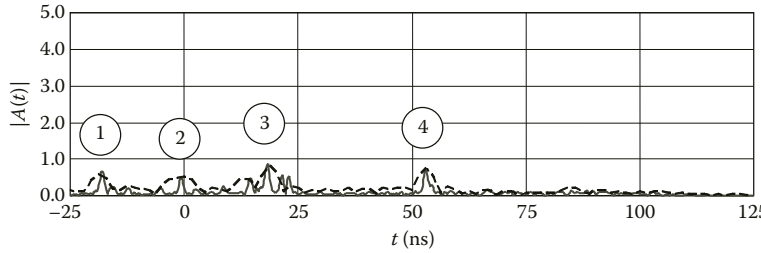

FIGURE 3.59 HRRPs of Tu-22M3 aircraft given its illumination by signals with center spectrum frequency of 1 GHz (30 cm wavelength), vertical polarization.

of 1 GHz bandwidth. Thin dashed line corresponds to HRRP obtained using signal with rectangular spectrum of 250 MHz bandwidth.

Peaks #1 are due to scattering from the nose part of aircraft's body. Peaks #2 are due to scattering from the pilot's cabin. Peaks #3 are due to scattering from the wing's leading edge. Peaks #4 are due to scattering from the wing-to-body joint.

3.1.5 Scattering Characteristics of Boeing 737-400 Medium-Range Airliner

The development of Boeing 737 airplane began in February 1965 [88, 89]. Right from the beginning, Boeing developed two variants: 737-100 with capacity of 100–103 seats, and 737-200 with capacity of 115 seats. The first prototype of 737-100 started the flight test program on April 9, 1967, and the first Boeing 737-200 performed its maiden flight on August 8, 1967. Certification of the 737-100 model was completed in December 1967; however it was not very popular, and only 50 airplanes were shipped to the customers. More attention was paid to the 737-200 model, which had also been certified in December 1967.

As a result of further upgrade, the Boeing 737-200 Advanced variant was developed that served as basis for the development of a large family of very different airplanes. Maiden flight of this airplane modification was performed on April 15, 1971, and the first lot was shipped to the customer by the end of May. Originally, the take-off weight of the 737-200 Advanced was 54.2 tons, which was soon increased, first to 56.47, and then to 58.1 tons. Convertible variant of Boeing 737-200C Advanced also featured the 2.14×3.4 m freight door right behind the cockpit.

Up-to-date modifications of Boeing 737 medium-range airliner are based on the Boeing 737-200 Advanced variant. First flight of the Boeing 737-300 prototype was performed in 1984. Boeing 737-300 differs from the 737-200 model by elongated 2.64 m body, by somewhat larger wingspan that provided more lift, better performance at low speed, improved short-field capability, and fuel economy

at cruise speed. Boeing 737-300 has become the basis for the creation of a wide family of short- and medium-range airliners (737-400, -500, -600, -700, and -800). In April 2001, the certification procedure was completed for the new modification—737-900 with capacity increased up to 190 passengers.

Currently, Boeing 737 is the most mass produced civil aircraft. Besides, by the year 2001 the number of Boeing 737 airplanes of different modification that have been sold achieved the level of 4300.

For our scattering computation, we chose the Boeing 737-400 variant (Figure 3.60). Basic geometrical characteristics of the plane and computer model of its surface are given in the Table 3.5 below (Figure 3.61).

Figures 3.62 through 3.79 show diagrams of mean and median RCS given the Boeing 737-400 aircraft model illumination at vertical and horizontal polarization, the latter having been averaged over different angular sectors, as well as circular diagrams of instantaneous and noncoherent RCS for the frequency ranges of our interest.

FIGURE 3.60 Boeing 737-400 airliner.

TABLE 3.5
Geometrical Characteristics of Boeing 737-400 Medium-Range Airliner

Airframe Characteristics (Figure 3.60)		Aircraft Surface Model Characteristics (Figure 3.61)	
Aircraft length	36.04 m	Number of parts of ellipsoids in the model	58
Aircraft height	11.13 m	Number of straight wedge parts in the model	25
Wing span	28.88 m		
Wing's area	105.4 m^2		

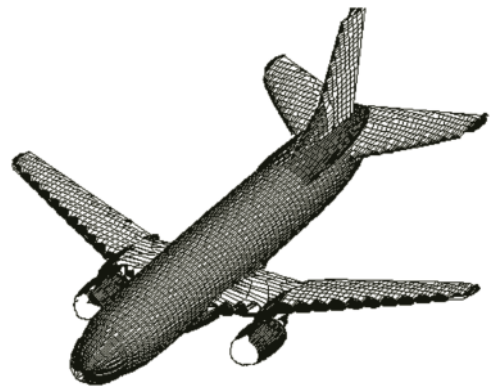

FIGURE 3.61 Computer model of the Boeing 737-400 surface.

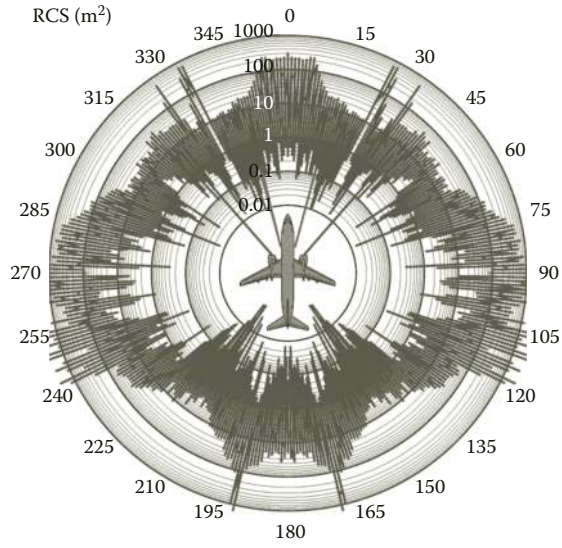

FIGURE 3.62 (**See color insert.**) Circular diagrams of instantaneous RCS given radar observation of Boeing 737-400 aircraft model at carrier frequency of 10 GHz (3 cm wavelength).

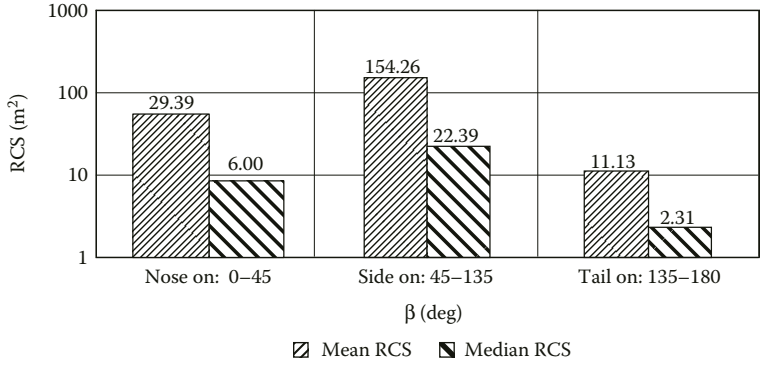

FIGURE 3.63 Diagrams of mean and median RCS of Boeing 737-400 aircraft model in three sectors of azimuth aspect given its radar observation at horizontal polarization and carrier frequency of 10 GHz (3 cm wavelength).

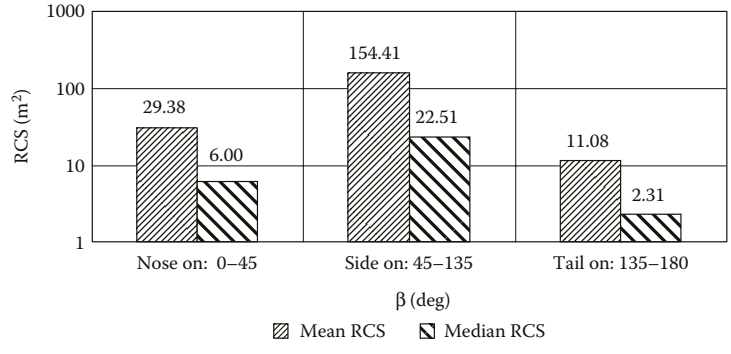

FIGURE 3.64 Diagrams of mean and median RCS of Boeing 737-400 aircraft model in three sectors of azimuth aspect given its radar observation at vertical polarization and carrier frequency of 10 GHz (3 cm wavelength)

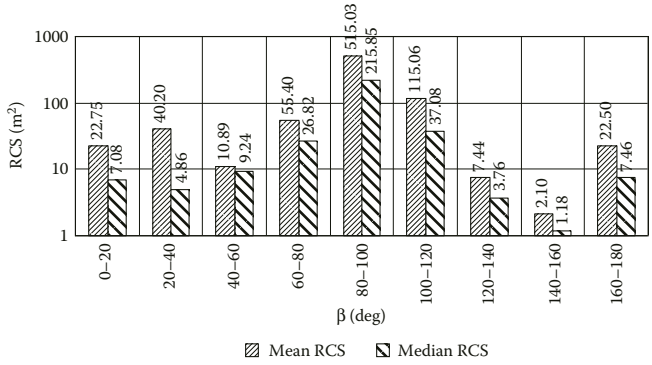

FIGURE 3.65 Diagrams of mean and median RCS of Boeing 737-400 aircraft model in 20-degree sectors of azimuth aspect given its radar observation at horizontal polarization and carrier frequency of 10 GHz (3 cm wavelength).

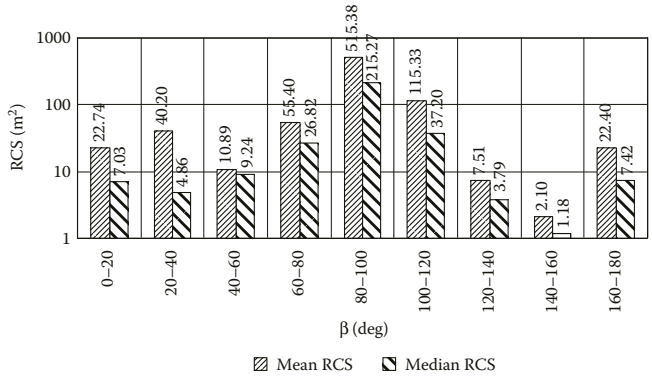

FIGURE 3.66 Diagrams of mean and median RCS of Boeing 737-400 aircraft model in 20-degree sectors of azimuth aspect given its radar observation at vertical polarization and carrier frequency of 10 GHz (3 cm wavelength).

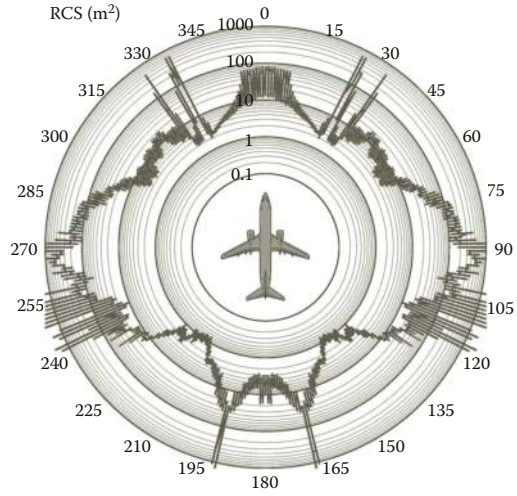

FIGURE 3.67 (**See color insert.**) Circular diagrams of noncoherent RCS given radar observation of Boeing 737-400 aircraft model at carrier frequency of 10 GHz (3 cm wavelength).

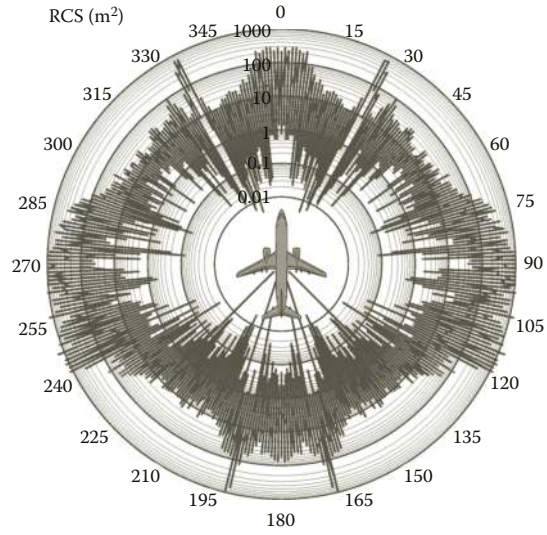

FIGURE 3.68 (**See color insert.**) Circular diagrams of instantaneous RCS given radar observation of Boeing 737-400 aircraft model at carrier frequency of 3 GHz (10 cm wavelength).

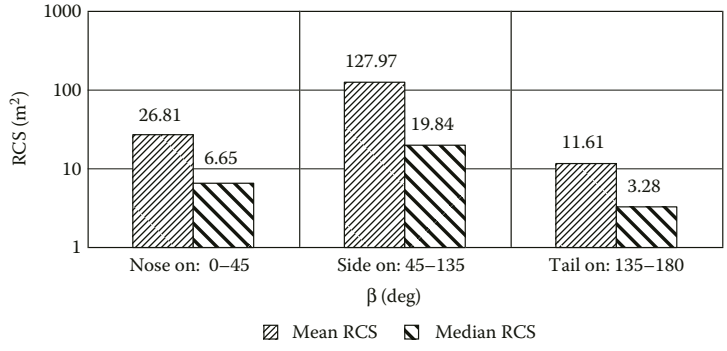

FIGURE 3.69 Diagrams of mean and median RCS of Boeing 737-400 aircraft model in three sectors of azimuth aspect given its radar observation at horizontal polarization and carrier frequency of 3 GHz (10 cm wavelength).

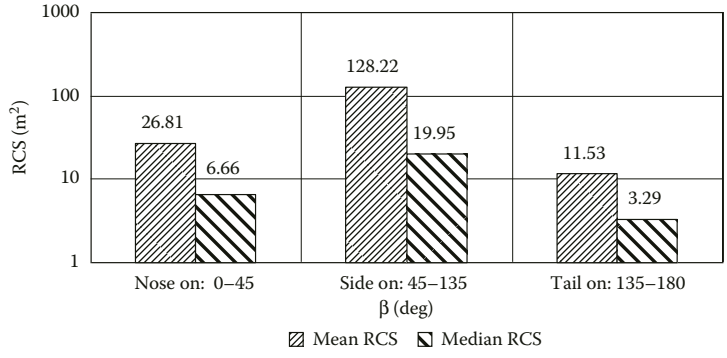

FIGURE 3.70 Diagrams of mean and median RCS of Boeing 737-400 aircraft model in three sectors of azimuth aspect given its radar observation at vertical polarization and carrier frequency of 3 GHz (10 cm wavelength).

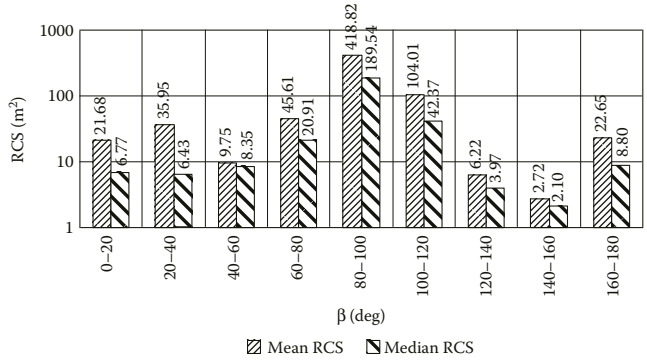

FIGURE 3.71 Diagrams of mean and median RCS of Boeing 737-400 aircraft model in 20-degree sectors of azimuth aspect given its radar observation at horizontal polarization and carrier frequency of 3 GHz (10 cm wavelength).

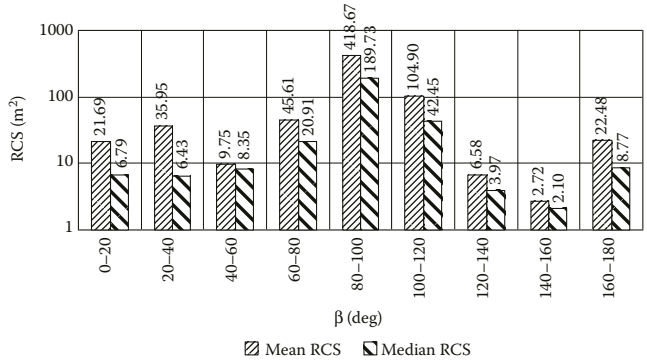

FIGURE 3.72 Diagrams of mean and median RCS of Boeing 737-400 aircraft model in 20-degree sectors of azimuth aspect given its radar observation at vertical polarization and carrier frequency of 3 GHz (10 cm wavelength).

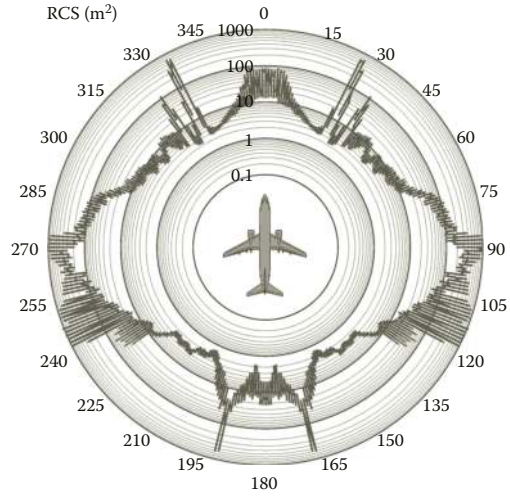

FIGURE 3.73 (**See color insert.**) Circular diagrams of noncoherent RCS of Boeing 737-400 aircraft model given its radar observation at carrier frequency of 3 GHz (10 cm wavelength).

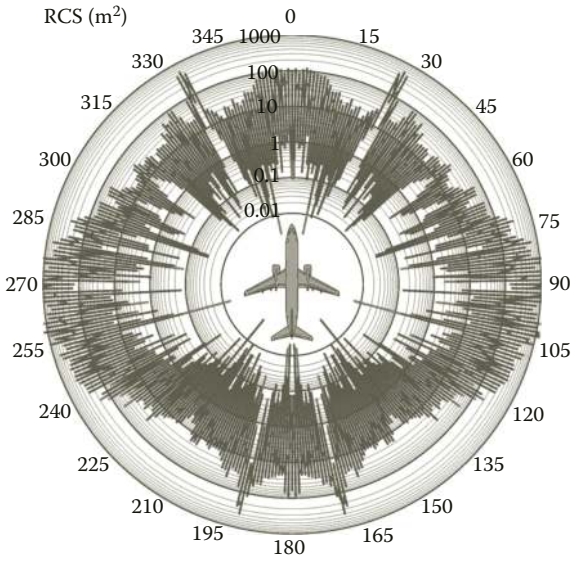

FIGURE 3.74 (**See color insert.**) Circular diagrams of instantaneous RCS given radar observation of Boeing 737-400 aircraft model at carrier frequency of 1 GHz (30 cm wavelength).

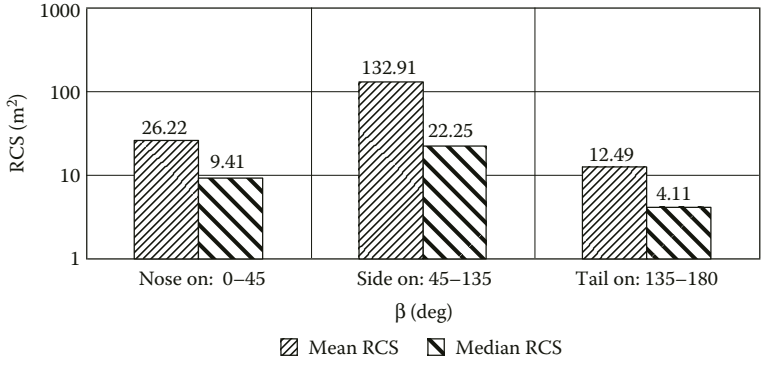

FIGURE 3.75 Diagrams of mean and median RCS of Boeing 737-400 aircraft model in three sectors of azimuth aspect given its radar observation at horizontal polarization and carrier frequency of 1 GHz (30 cm wavelength).

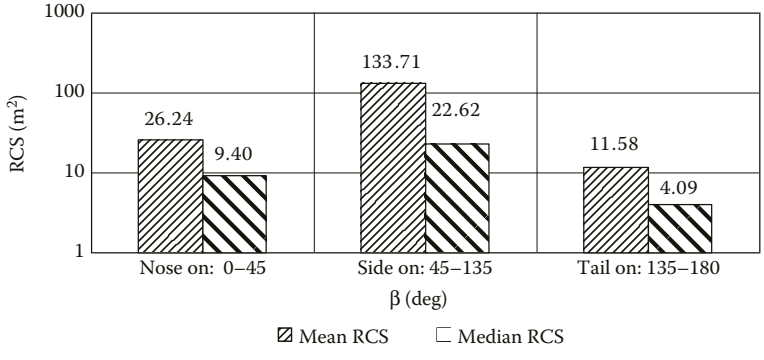

FIGURE 3.76 Diagrams of mean and median RCS of Boeing 737-400 aircraft model in three sectors of azimuth aspect given its radar observation at vertical polarization and carrier frequency of 1 GHz (30 cm wavelength).

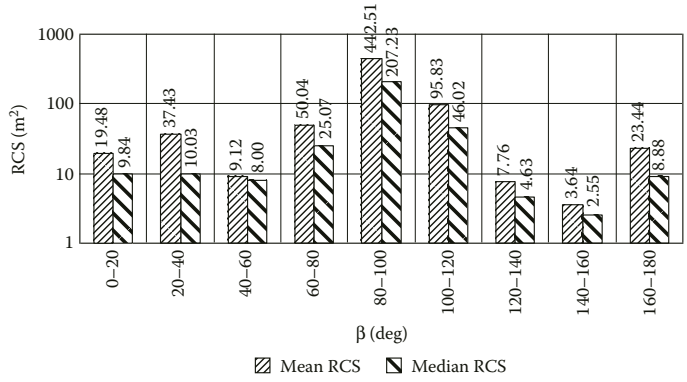

FIGURE 3.77 Diagrams of mean and median RCS of Boeing 737-400 aircraft model in 20-degree sectors of azimuth aspect given its radar observation at horizontal polarization and carrier frequency of 1 GHz (30 cm wavelength).

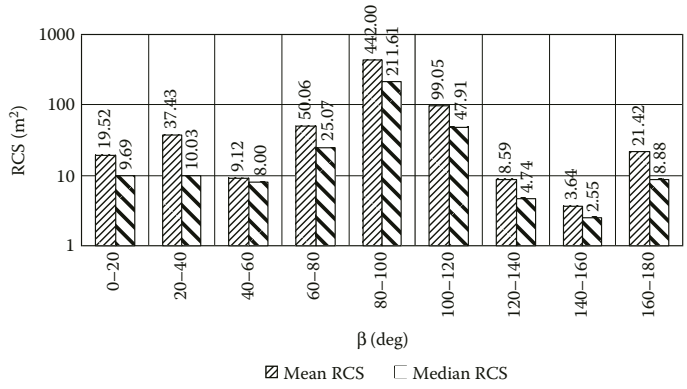

FIGURE 3.78 Diagrams of mean and median RCS of Boeing 737-400 aircraft model in 20-degree sectors of azimuth aspect given its radar observation at vertical polarization and carrier frequency of 1 GHz (30 cm wavelength).

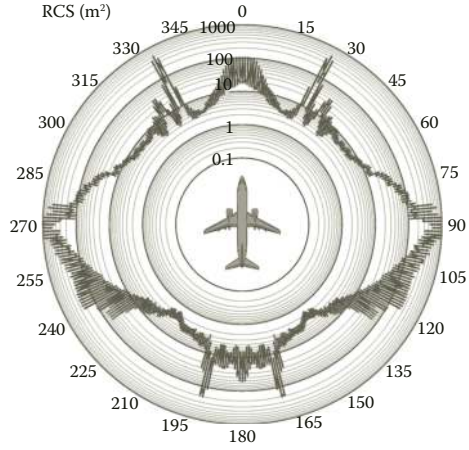

FIGURE 3.79 (**See color insert.**) Circular diagrams of noncoherent RCS of Boeing 737-400 aircraft model given its radar observation at carrier frequency of 1 GHz (30 cm wavelength).

Figures 3.80 through 3.82 show the amplitude distributions of echo signals for the frequency ranges of interest given horizontal polarization of illumination wave.

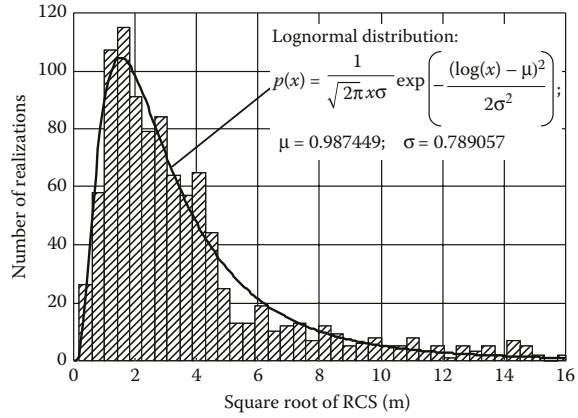

FIGURE 3.80 Amplitude distribution of echo signal of Boeing 737-400 aircraft model at carrier frequency of 10 GHz given its horizontal polarization.

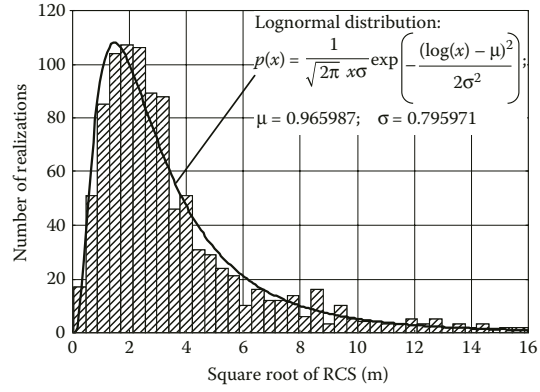

FIGURE 3.81 Amplitude distribution of echo signal of Boeing 737-400 aircraft mode at carrier frequency of 3 GHz given its horizontal polarization.

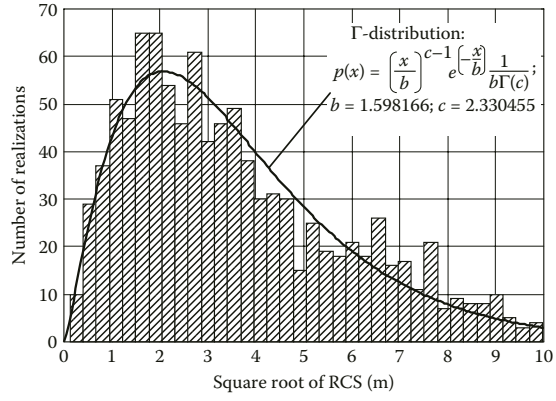

FIGURE 3.82 Amplitude distribution of echo signal of Boeing 737-400 aircraft model at carrier frequency of 1 GHz given its horizontal polarization.

TABLE 3.6
Parameters of Probability Distributions for the Echo Signal Amplitudes for Boeing 737-400 Aircraft Model

Wavelength	Polarization	Distribution Kind	Distribution Parameters
3 cm	Horizontal	Lognormal distribution: $p(x) = \frac{1}{\sqrt{2\pi}x\sigma}\exp\left(-\frac{(\log(x)-\mu)^2}{2\sigma^2}\right)$	$\mu = 0.987449$ $\sigma = 0.789057$
3 cm	Vertical	Lognormal distribution	$\mu = 0.984423$ $\sigma = 0.800425$
10 cm	Horizontal	Lognormal distribution	$\mu = 0.965987$ $\sigma = 0.795971$
10 cm	Vertical	Lognormal distribution	$\mu = 0.965978$ $\sigma = 0.796419$
30 cm	Horizontal	Γ-Distribution: $p(x) = \left(\frac{x}{b}\right)^{c-1} e^{\left(-\frac{x}{b}\right)} \frac{1}{b\Gamma(c)}$ where $\Gamma(c)$ is the gamma-function	$b = 1.598166$ $c = 2.330455$
30 cm	Vertical	Γ-Distribution	$b = 1.592673$ $c = 2.340167$

Table 3.6 summarizes the parameters of empirical probability distributions that fit mostly the simulation data for square root of RCS.

In Section 3.1.6, there are examples of HRRPs computed for the aircraft given various central frequencies of signal spectrum and its widths.

3.1.6 Impulse Responses of Boeing 737-400 Medium-Range Airliner

As an example, we consider HRRPs of Boeing 737-400 aircraft observed at the elevation angle of −8° (illumination from below) and azimuth aspect of 17.2° (perpendicularly to the wing's trailing edge).

Figures 3.83 and 3.84 show HRRPs of Boeing 737-400 aircraft given its illumination with signal at central frequency of 10 GHz (3 cm wavelength) for the cases of horizontal and vertical polarization, respectively. Bold solid line corresponds to HRRP obtained using signal with rectangular amplitude spectrum of 1 GHz bandwidth. Thin dashed line corresponds to HRRP obtained using signal with rectangular spectrum of 250 MHz bandwidth.

Peaks #1 are due to scattering from the nose part of aircraft body. Peaks #2 are due to scattering from the engine nacelle at the nearer wing. Peaks #3 are due to scattering from the engine air intake at the nearer wing. Peaks #4 are due to scattering from the engine nacelle at the farther wing. Peaks #5 are due to scattering from the engine air intake at the farther wing. Peaks #6 are due to scattering from the trailing edge of the nearer wing as well as from the nacelle-to-wing joint. Amplitude of the echo from trailing edge is significantly higher in case of vertical polarization. Peaks #7 are due to scattering from the wing-to-body joint. Peaks #8 are due to scattering from the joint of engine nacelle to the farther wing. Small peaks at the lag time t between 75 and 100 ns are due to scattering from the empennage of the airplane.

Figures 3.85 and 3.86 show HRRPs of Boeing 737-400 aircraft given its illumination by signals with spectra centered at 3 GHz (10 cm wavelength) for the cases of horizontal and vertical polarization, respectively. Solid bold line corresponds to HRRP obtained using signal with rectangular spectrum of 1 GHz bandwidth. Thin dashed line corresponds to HRRP obtained using signal with rectangular spectrum of 250 MHz bandwidth.

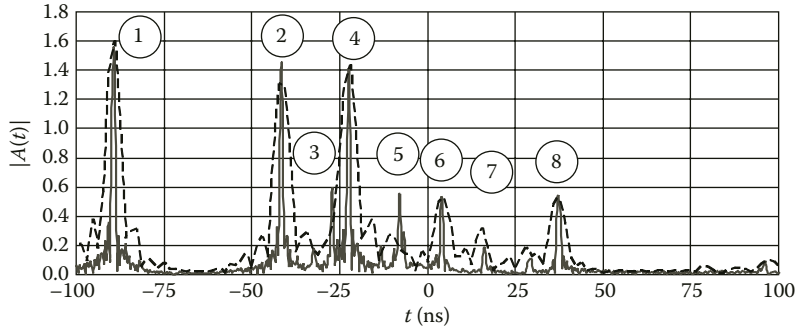

FIGURE 3.83 HRRPs of Boeing 737-400 aircraft given its illumination by signal with center spectrum frequency of 10 GHz (3 cm wavelength), horizontal polarization.

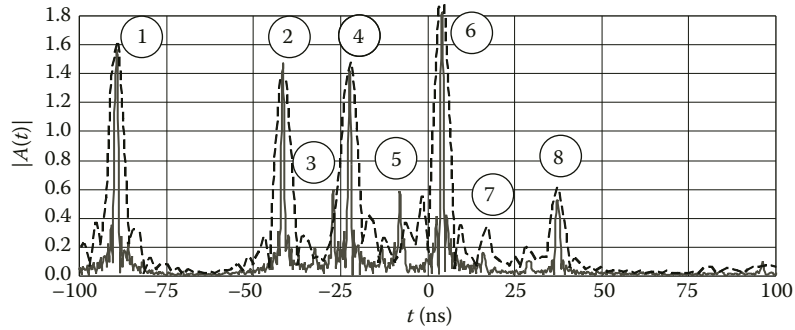

FIGURE 3.84 HRRPs of Boeing 737-400 aircraft given its illumination by signals with center spectrum frequency of 10 GHz (3 cm wavelength), vertical polarization.

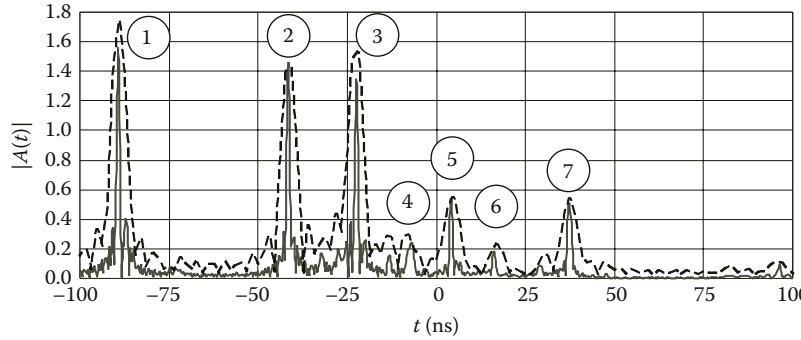

FIGURE 3.85 HRRPs of Boeing 737-400 aircraft given its illumination by signals with center spectrum frequency of 3 GHz (10 cm wavelength), horizontal polarization.

HRRPs shown in Figures 3.85 and 3.86 contain the following peaks marked with numbers. Peaks #1 are due to scattering from the nose part of aircraft body. Peaks #2 are due to scattering from the engine nacelle at the nearer wing. Peaks #3 are due to scattering from the engine nacelle at the farther wing. Peaks #4 and 6 are due to scattering from the wing-to-body joint. Peaks #5 are due to scattering from trailing edge of the nearer wing as well as from the nacelle-to-wing joint. Peaks #7 are due to scattering from the joint of engine nacelle to the farther wing.

Figures 3.87 and 3.88 show HRRPs of Boeing 737-400 aircraft given its illumination by signals with spectra centered at 1 GHz (30 cm wavelength) for the cases of horizontal and vertical

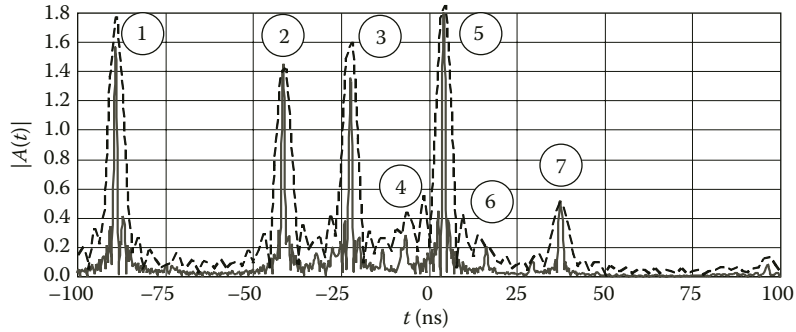

FIGURE 3.86 HRRPs of Boeing 737-400 aircraft given its illumination by signals with center spectrum frequency of 3 GHz (10 cm wavelength), vertical polarization.

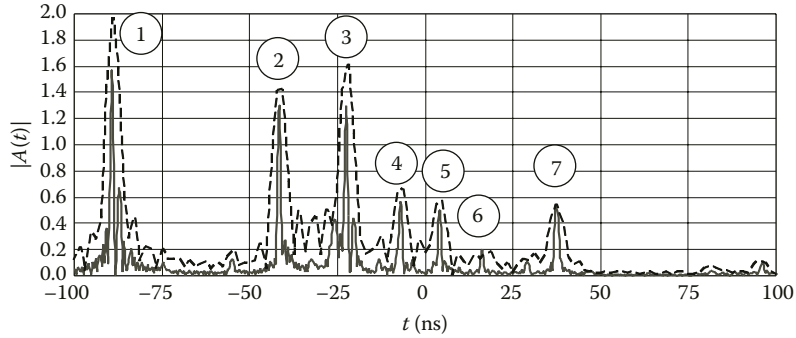

FIGURE 3.87 HRRPs of Boeing 737-400 aircraft given its illumination by signals with center spectrum frequency of 1 GHz (30 cm wavelength), horizontal polarization.

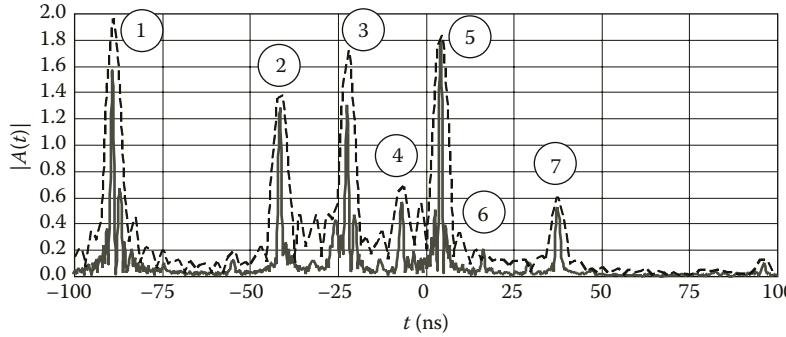

FIGURE 3.88 HRRPs of Boeing 737-400 aircraft given its illumination by signals with center spectrum frequency of 1 GHz (30 cm wavelength), vertical polarization.

polarization, respectively. Solid bold line corresponds to HRRP obtained using signal with rectangular spectrum of 1 GHz bandwidth. Thin dashed line corresponds to HRRP obtained using signal with rectangular spectrum of 250 MHz bandwidth.

The view of these HRRPs is similar to those obtained for illumination signals with spectra centered at frequency of 3 GHz (10 cm wavelength).

Peaks #1 are due to scattering from the nose part of aircraft body. Peaks #2 are due to scattering from the engine nacelle at the nearer wing. Peaks #3 are due to scattering from the engine nacelle at the farther wing. Peaks #4 and #6 are due to scattering from the wing-to-body joint. Peaks #5 are

due to scattering from the trailing edge of the nearer wing as well as from the nacelle-to-wing joint. Peaks #7 are due to scattering from the joint of engine nacelle to the farther wing. Small peaks at the end of HRRP are due to scattering from the empennage of the airplane.

3.1.7 Scattering Characteristics of An-26 Multipurpose Transport Aircraft

An-26 multipurpose transport aircraft is the military version of An-24 passenger airplane. It is designed for tactical airlifting or airdropping personnel, military goods in standard packs including fuel and lubricants in barrels and canisters, as well as for transporting injured or sick people. An-26 is designed as a cantilever monoplane with high-set wing (Figure 3.89) equipped with extension flaps of large span—double slit outside of engine nacelle and single slit at the wing root [90, 91].

Rear part of fuselage has large cargo door that is closed by original cargo ramp. Empennage is traditional, however, it has additional fin under the fuselage. Fuselage itself is of semimonocoque type. Hydraulically operated landing gear consists of three legs each having two wheels. Power plant contains two Ivchenko AI-24VT turbo-prop engines equipped with variable-pitch propellers, as well as RU19A-300 auxiliary turbojet engine mounted into the right engine nacelle. The aircraft has many modifications operated both in Armed Forces and national economy. Among them, there are electronic warfare variants, airborne command posts, medivacs, firefighting aircraft, and so on. Computer model of An-26 aircraft is shown in Figure 3.90. Parameters of the model are shown in Table 3.7.

FIGURE 3.89 An-26 multipurpose transport aircraft.

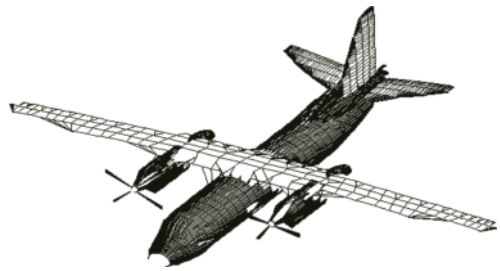

FIGURE 3.90 Computer model of the An-26 surface.

TABLE 3.7
Geometrical Characteristics of An-26 Multipurpose Transport Aircraft

Airframe Characteristics (Figure 3.89)		Aircraft Surface Model Characteristics (Figure 3.90)	
Aircraft length	23.8 m	Number of parts of ellipsoids in the model	40
Aircraft height	8.58 m	Number of straight wedge parts in the model	25
Wing span	29.2 m		
Wing's area	74.98 m^2		

Figures 3.91 through 3.108 show diagrams of mean and median RCS given the An-26 aircraft model illumination at vertical and horizontal polarization, the latter having been averaged over different angular sectors, as well as circular diagrams of instantaneous and noncoherent RCS for the frequency ranges of our interest.

Figures 3.109 through 3.111 show the amplitude distributions of echo signals for the frequency ranges of interest given horizontal polarization of illumination wave.

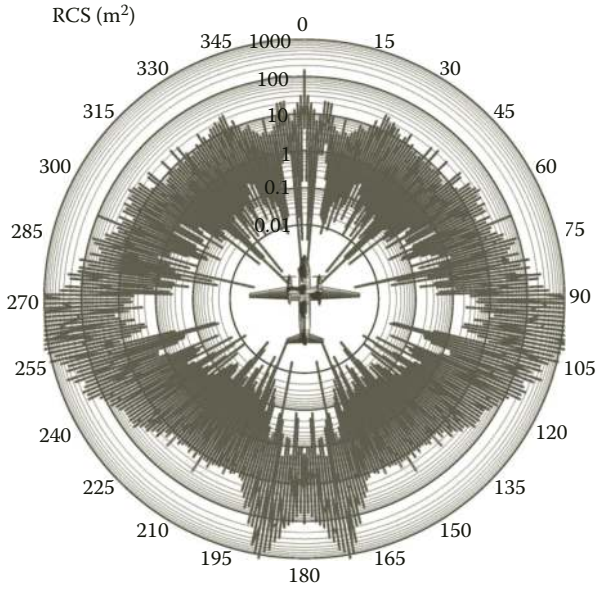

FIGURE 3.91 (**See color insert.**) Circular diagrams of instantaneous RCS given radar observation of An-26 aircraft model at carrier frequency of 10 GHz (3 cm wavelength).

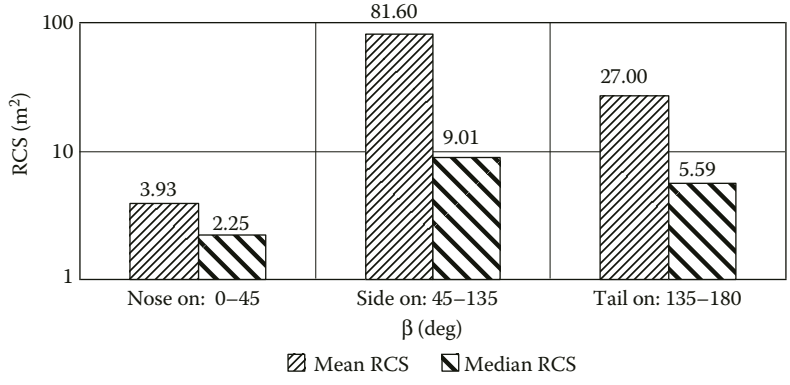

FIGURE 3.92 Diagrams of mean and median RCS of An-26 aircraft model in three sectors of azimuth aspect given its radar observation at horizontal polarization and carrier frequency of 10 GHz (3 cm wavelength).

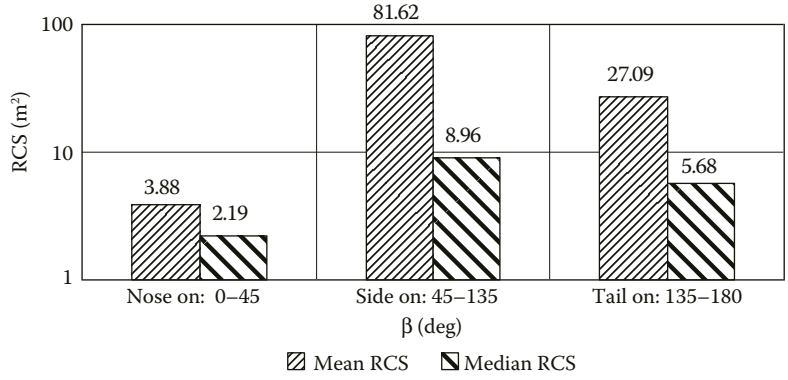

FIGURE 3.93 Diagrams of mean and median RCS of An-26 aircraft model in three sectors of azimuth aspect given its radar observation at vertical polarization and carrier frequency of 10 GHz (3 cm wavelength).

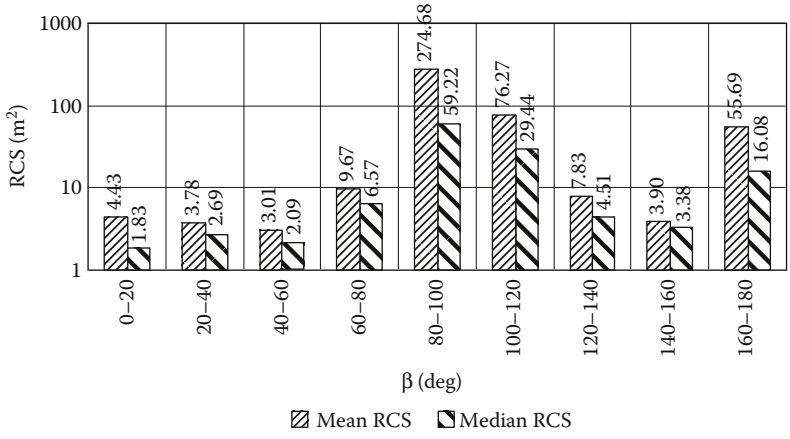

FIGURE 3.94 Diagrams of mean and median RCS of An-26 aircraft model in 20-degree sectors of azimuth aspect given its radar observation at horizontal polarization and carrier frequency of 10 GHz (3 cm wavelength).

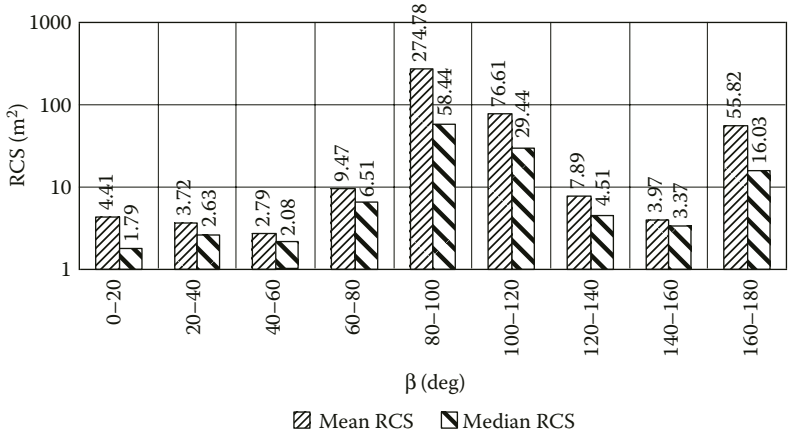

FIGURE 3.95 Diagrams of mean and median RCS of An-26 aircraft model in 20-degree sectors of azimuth aspect given its radar observation at vertical polarization and carrier frequency of 10 GHz (3 cm wavelength).

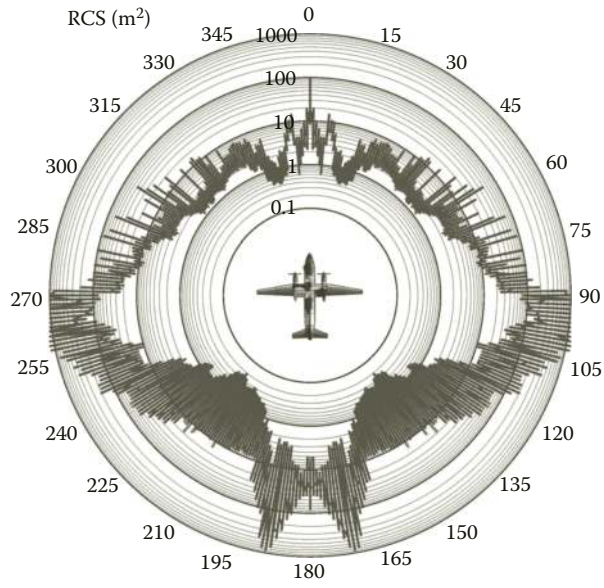

FIGURE 3.96 (**See color insert.**) Circular diagrams of noncoherent RCS given radar observation of An-26 aircraft model at carrier frequency of 10 GHz (3 cm wavelength).

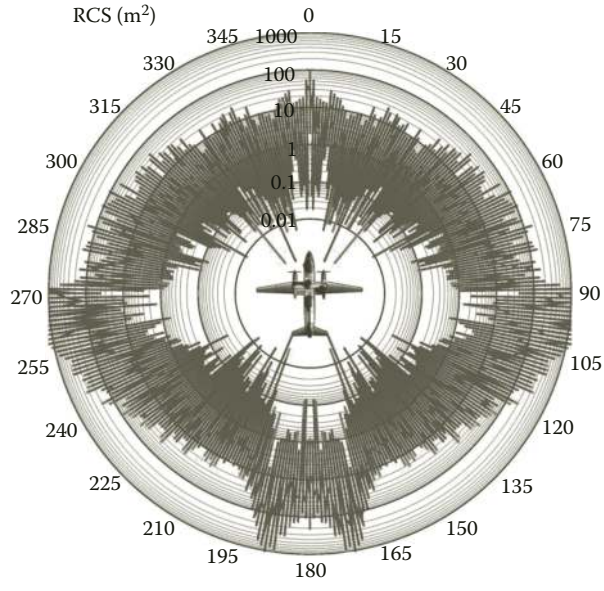

FIGURE 3.97 (**See color insert.**) Circular diagrams of instantaneous RCS given radar observation of An-26 aircraft model at carrier frequency of 3 GHz (10 cm wavelength).

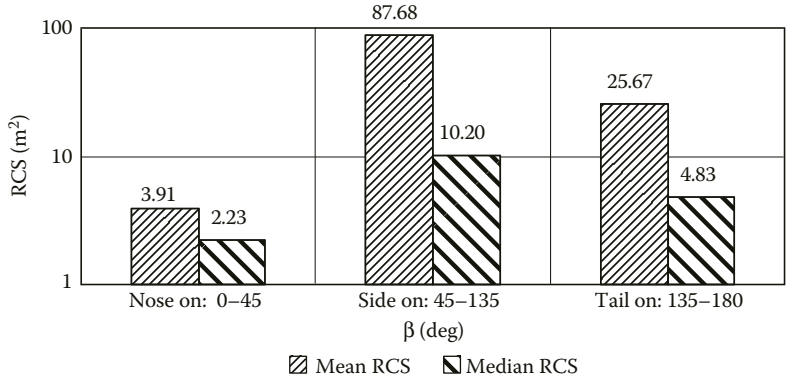

FIGURE 3.98 Diagrams of mean and median RCS of An-26 aircraft model in three sectors of azimuth aspect given its radar observation at horizontal polarization and carrier frequency of 3 GHz (10 cm wavelength).

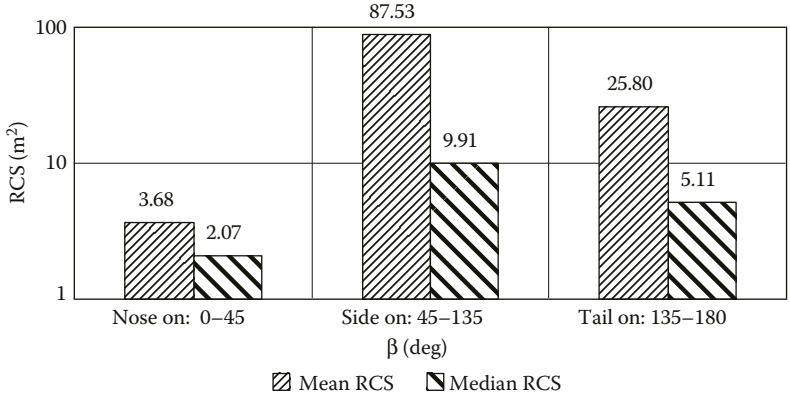

FIGURE 3.99 Diagrams of mean and median RCS of An-26 aircraft model in three sectors of azimuth aspect given its radar observation at vertical polarization and carrier frequency of 3 GHz (10 cm wavelength).

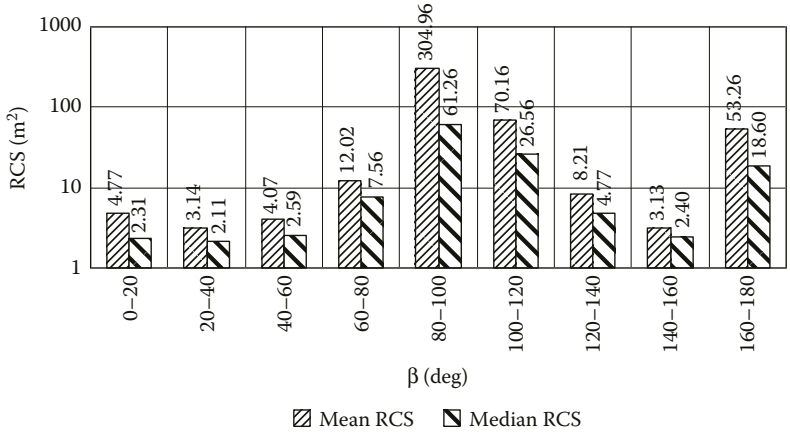

FIGURE 3.100 Diagrams of mean and median RCS of An-26 aircraft model in 20-degree sectors of azimuth aspect given its radar observation at horizontal polarization and carrier frequency of 3 GHz (10 cm wavelength).

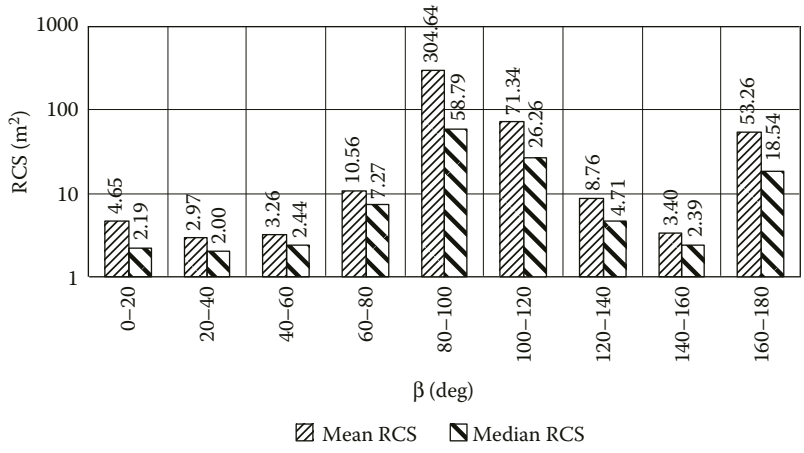

FIGURE 3.101 Diagrams of mean and median RCS of An-26 aircraft model in 20-degree sectors of azimuth aspect given its radar observation at vertical polarization and carrier frequency of 3 GHz (10 cm wavelength).

Table 3.8 summarizes the parameters of empirical probability distributions that fit mostly the simulation data for square root of RCS.

In Section 3.1.8, there are examples of HRRPs computed for the aircraft given various central frequencies of signal spectrum and its widths.

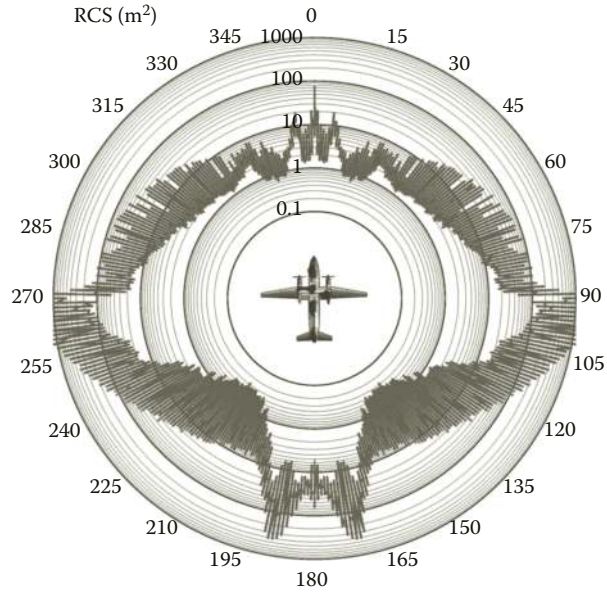

FIGURE 3.102 (**See color insert.**) Circular diagrams of noncoherent RCS of An-26 aircraft model given its radar observation at carrier frequency of 3 GHz (10 cm wavelength).

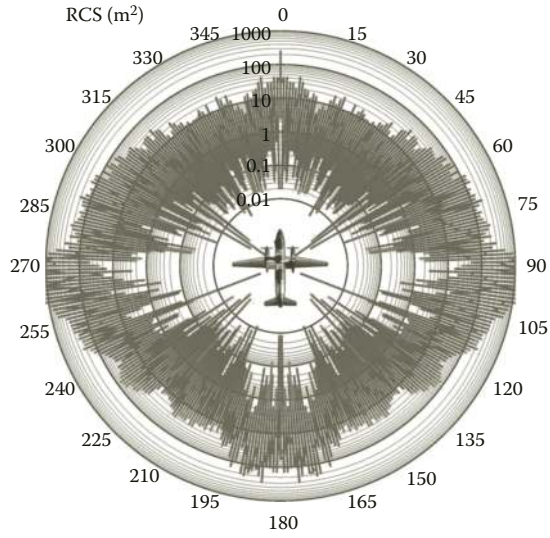

FIGURE 3.103 (**See color insert.**) Circular diagrams of instantaneous RCS given radar observation of An-26 aircraft model at carrier frequency of 1 GHz (30 cm wavelength).

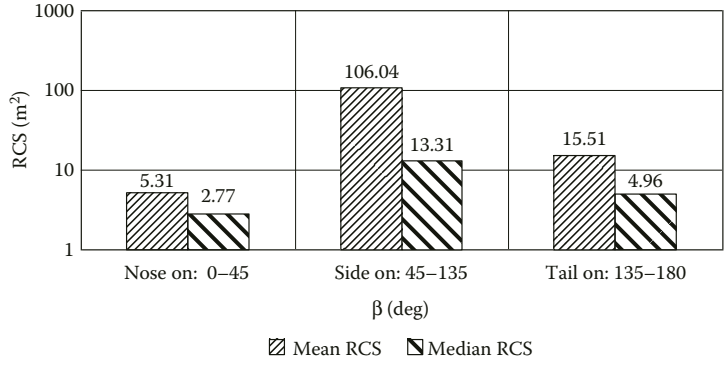

FIGURE 3.104 Diagrams of mean and median RCS of An-26 aircraft model in three sectors of azimuth aspect given its radar observation at horizontal polarization and carrier frequency of 1 GHz (30 cm wavelength).

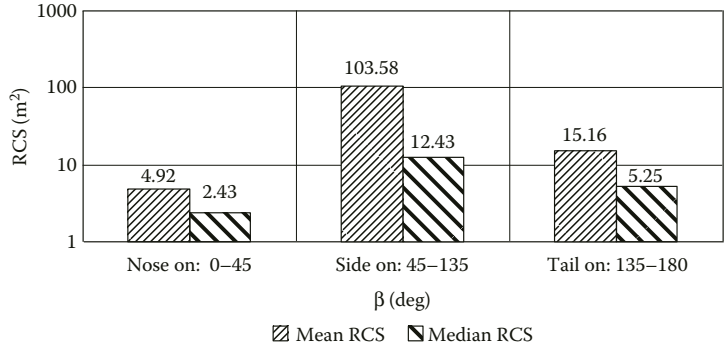

FIGURE 3.105 Diagrams of mean and median RCS of An-26 aircraft model in three sectors of azimuth aspect given its radar observation at vertical polarization and carrier frequency of 1 GHz (30 cm wavelength).

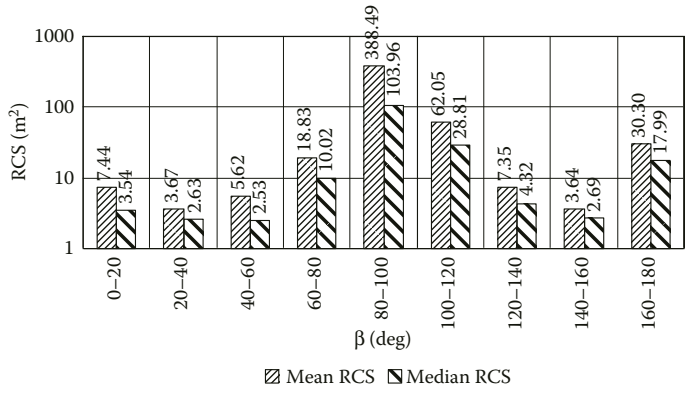

FIGURE 3.106 Diagrams of mean and median RCS of An-26 aircraft model in 20-degree sectors of azimuth aspect given its radar observation at horizontal polarization and carrier frequency of 1 GHz (30 cm wavelength).

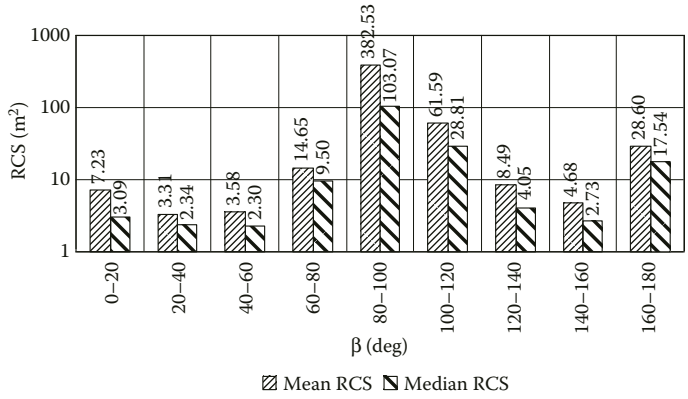

FIGURE 3.107 Diagrams of mean and median RCS of An-26 aircraft model in 20-degree sectors of azimuth aspect given its radar observation at vertical polarization and carrier frequency of 1 GHz (30 cm wavelength).

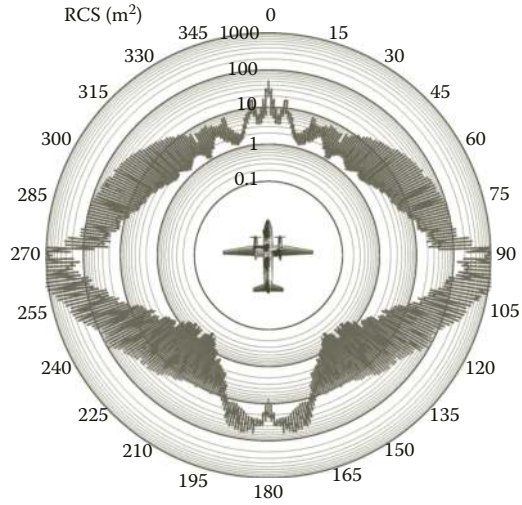

FIGURE 3.108 (**See color insert.**) Circular diagrams of noncoherent RCS of An-26 aircraft model given its radar observation at carrier frequency of 1 GHz (30 cm wavelength).

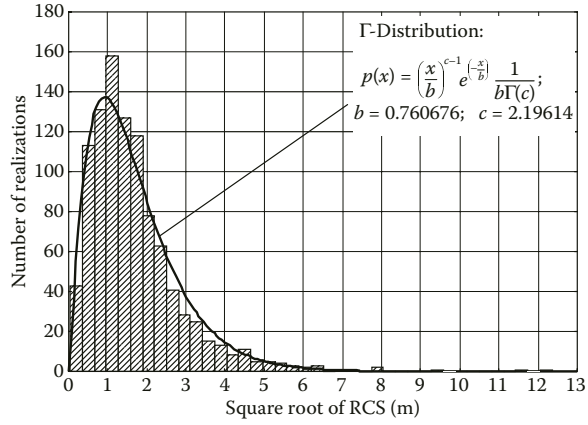

FIGURE 3.109 Amplitude distribution of echo signal of An-26 aircraft model at carrier frequency of 10 GHz given its horizontal polarization.

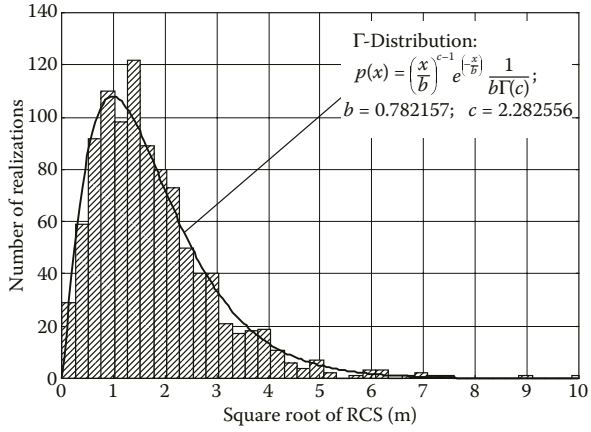

FIGURE 3.110 Amplitude distribution of echo signal of An-26 aircraft model at carrier frequency of 3 GHz given its horizontal polarization.

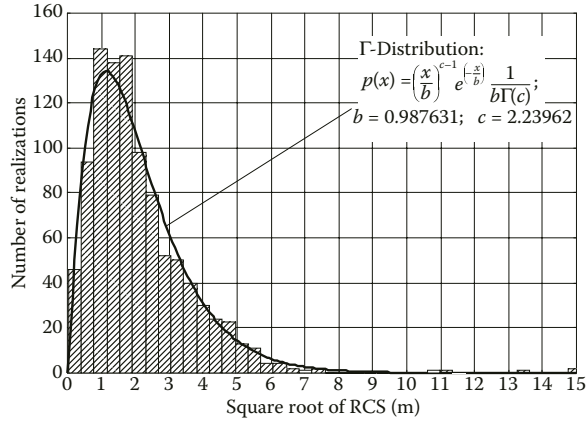

FIGURE 3.111 Amplitude distribution of echo signal of An-26 aircraft model at carrier frequency of 1 GHz given its horizontal polarization.

TABLE 3.8
Parameters of Probability Distributions for the Echo Signal Amplitudes of An-26 Aircraft Model

Wavelength	Polarization	Distribution Kind	Distribution Parameters
3 cm	Horizontal	Γ-Distribution: $p(x) = \left(\frac{x}{b}\right)^{c-1} e^{\left(-\frac{x}{b}\right)} \frac{1}{b\Gamma(c)}$ where Γ (*c*) is the Gamma-function	*b* = 0.760616 *c* = 2.19614
3 cm	Vertical	Γ-Distribution	*b* = 0.761035 *c* = 2.18595
10 cm	Horizontal	Γ-Distribution	*b* = 0.782157 *c* = 2.282556
10 cm	Vertical	Γ-Distribution	*b* = 0.777077 *c* = 2.260024
30 cm	Horizontal	Γ-Distribution	*b* = 0.987631 *c* = 2.23962
30 cm	Vertical	Γ-Distribution	*b* = 1.012708 *c* = 2.13088

3.1.8 Impulse Responses of An-26 Multipurpose Transport Aircraft

As an example, we consider HRRPs of An-26 aircraft observed at the elevation angle of –1° (illumination from below) and azimuth aspect of 18.7° (perpendicularly to the leading edge of horizontal stabilizer).

Figures 3.112 and 3.113 show HRRPs of An-26 aircraft given its illumination with signal at central frequency of 10 GHz (3 cm wavelength) for the cases of horizontal and vertical polarization, respectively. Bold solid line corresponds to HRRP obtained using signal with rectangular amplitude spectrum of 1 GHz bandwidth. Thin dashed line corresponds to HRRP obtained using signal with rectangular spectrum of 250 MHz bandwidth.

Peaks #1 are due to scattering from the nose part of aircraft body. Peaks #2 are due to scattering from the engine at the nearer wing. Peaks #3 are due to scattering from the engine at the farther wing. Peaks #4 in Figure 3.112 are due to scattering from the leading edge of aircraft's horizontal stabilizer. In Figure 3.113 (HRRP of An-26 aircraft given vertical polarization of illumination signal), the corresponding peak is absent.

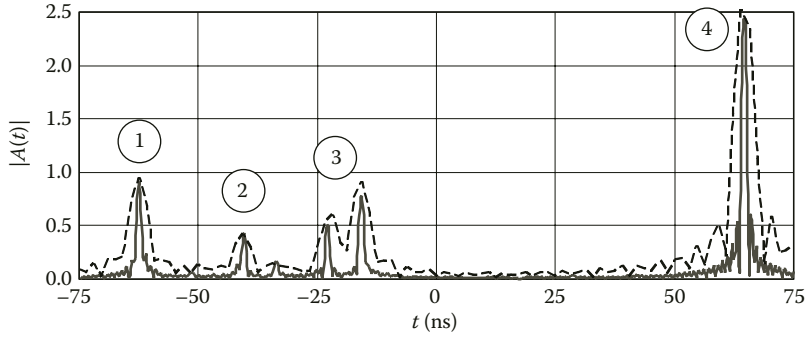

FIGURE 3.112 HRRPs of An-26 aircraft given its illumination by signal with center spectrum frequency of 10 GHz (3 cm wavelength), horizontal polarization.

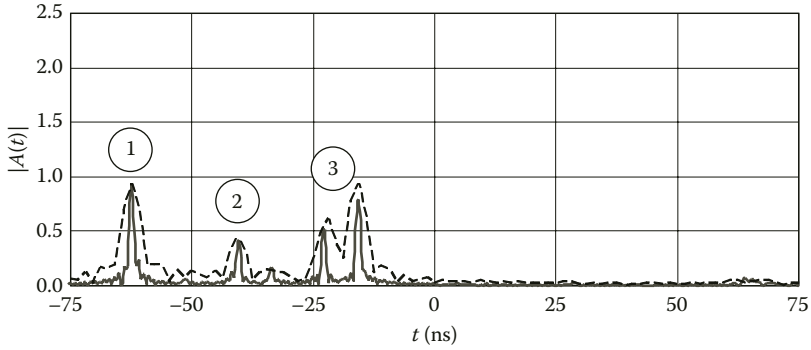

FIGURE 3.113 HRRPs of An-26 aircraft given its illumination by signals with center spectrum frequency of 10 GHz (3 cm wavelength), vertical polarization.

Figures 3.114 and 3.115 show HRRPs of An-26 aircraft given its illumination by signals with spectra centered at 3 GHz (10 cm wavelength) for the cases of horizontal and vertical polarization, respectively. Solid bold line corresponds to HRRP obtained using signal with rectangular spectrum of 1 GHz bandwidth. Thin dashed line corresponds to HRRP obtained using signal with rectangular spectrum of 250 MHz bandwidth.

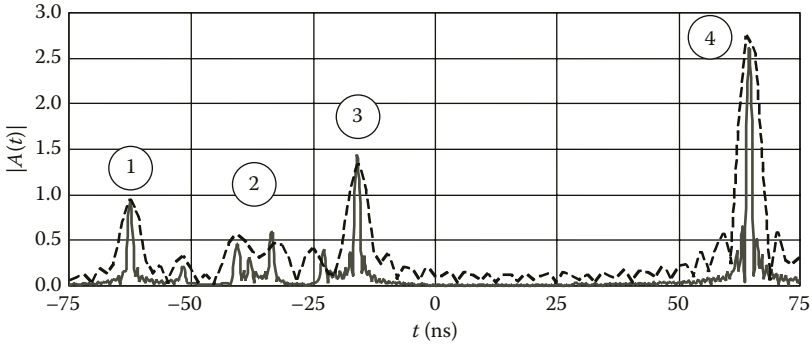

FIGURE 3.114 HRRPs of An-26 aircraft given its illumination by signals with center spectrum frequency of 3 GHz (10 cm wavelength), horizontal polarization.

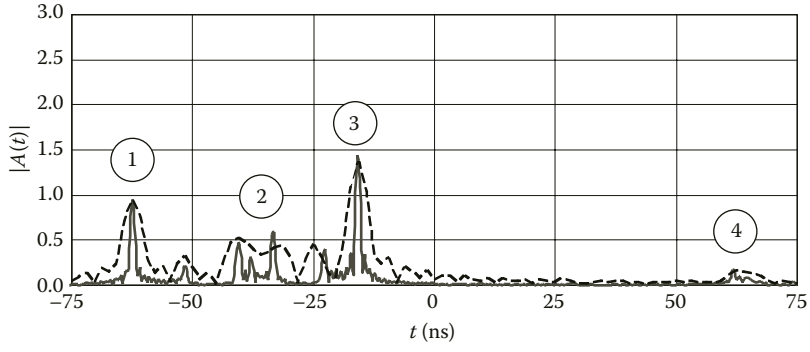

FIGURE 3.115 HRRPs of An-26 aircraft given its illumination by signals with center spectrum frequency of 3 GHz (10 cm wavelength), vertical polarization.

HRRPs shown in Figures 3.114 and 3.115 contain the following peaks marked with numbers. Peaks #1 are due to scattering from the nose part of the aircraft body. Peaks #2 are due to scattering from the engine at the nearer wing. Peaks #3 are due to scattering from the engine at the farther wing. Peaks #4 are due to scattering from the leading edge of aircraft's horizontal stabilizer. Amplitude of the echo from leading edge of horizontal stabilizer is significantly higher for the case of horizontal polarization.

Figures 3.116 and 3.117 show HRRPs of An-26 aircraft given its illumination by signals with spectra centered at 1 GHz (30 cm wavelength) for the cases of horizontal and vertical polarization, respectively. Solid bold line corresponds to HRRP obtained using signal with rectangular spectrum of 1 GHz bandwidth. Thin dashed line corresponds to HRRP obtained using signal with rectangular spectrum of 250 MHz bandwidth.

Peaks #1 are due to scattering from the nose part of the aircraft body. Peaks #2 are due to scattering from the pilot's cockpit. HRRPs computed given different carrier frequencies have these peaks missing or their amplitudes are very low. Peaks #3 are due to scattering from engine at the nearer wing. Peaks #4 are due to scattering from engine at the farther wing. It is worth mentioning that in the latter HRRPs the echoes from individual propeller blades can be singled out. Peaks #5 are due to scattering from the leading edge of aircraft's horizontal stabilizer. Besides, the echo from leading edge of horizontal stabilizer given vertical polarization of illumination signal (Figure 3.117) is well observable and it has amplitude comparable to the echoes from the aircraft's engines.

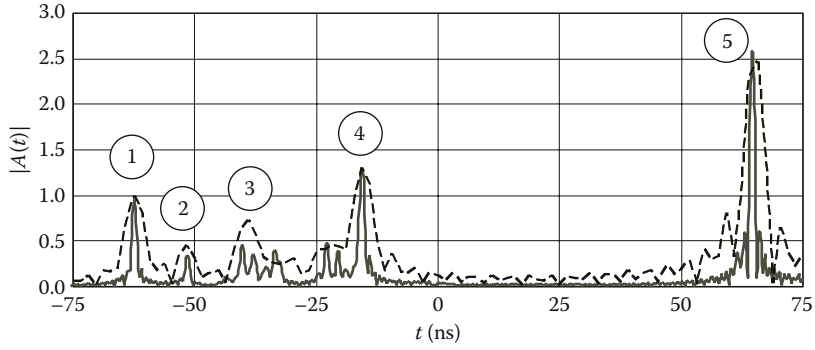

FIGURE 3.116 HRRPs of An-26 aircraft given its illumination by signals with center spectrum frequency of 1 GHz (30 cm wavelength), horizontal polarization.

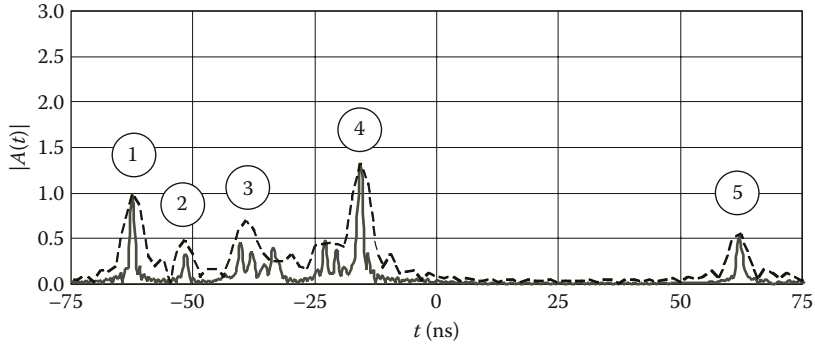

FIGURE 3.117 HRRPs of An-26 aircraft given its illumination by signals with center spectrum frequency of 1 GHz (30 cm wavelength), vertical polarization.

3.1.9 Scattering Characteristics of MiG-29 Front-Line Fighter

MiG-29 fighter is the one seat twin engine all-weather aircraft of the front-line. The aircraft was designed as mean for gaining the air superiority in the tactical battlefield zone and its main goal is to fight the enemy aviation, to cover the troops and logistics objects against air strikes, and to counter the enemy air reconnaissance day and night both in visual and instrument meteorological conditions [92, 93]. High thrust-to-weight ratio, good aerodynamics provide for aircraft high performance including fast acceleration, high climb rate, instantaneous and sustained high g-turns.

The aircraft is designed as integral monoplane featuring the swept wing blended with the leading edge root extensions, and two vertical fins (Figure 3.118). The load-bearing body is of semimonocoque design and it consists of three main sections: front, engine, and rear; it contributes about 40% of the whole lift. The RD-33 engines are installed in separate nacelles placed in the rear fuselage section. The aircraft is mainly made of aluminum, but it includes also titan, steel, and composites based on carbon and honeycombs [93].

The N-091EA onboard radar fits into the nose fuselage section and is covered with ogive radome. The radar units are placed into the compartment right behind the antenna followed by airtight pilot's cockpit. The cockpit features the bubble-type canopy. The canopy is of two sections, the fixed windscreen and the segment that opens up and back. The canopy frame is made of magnesium alloy. Canopy glass is made of three layers that envelop the wires of electrical anti-icing system.

Wedge-type intakes with variable ramp are in the front sections of engine nacelles. Being optimized for flight at transonic and supersonic speeds, they form the four pressure jumps.

The three slit louvers on the upper side of the leading edge root extensions (right behind the upper auxiliary air intakes) alter the auxiliary air flow to the engines. The upper auxiliary intakes have five slits that open during engine start, taxiing, take-off, and landing. When auxiliary air intakes are open, then main intakes are closed preventing ingestion of ground debris into turbofan engines. The main air intakes open once the aircraft gains speed of 200 km/h during take-off and close once the aircraft slows down to 200 km/h during landing.

Central fuselage section (behind the cockpit) houses main fuel tanks. The engines are slightly turned in vertical plane and they are mounted at the angle of 4° with respect to the aircraft longitudinal axis. Rear fuselage section bears the empennage, afterburners, airbrakes, and a drogue-chute container. MiG-29 aircraft has two vertical fins with rudders, the fins being inclined outwards by angle of 6° with respect to the vertical.

Parameters of the model are summarized in Table 3.9.

Computer model of the aircraft surface used for the scattering computation is presented in Figure 3.119. It is worth mentioning that once the MiG-29 fighter is illuminated from the front hemisphere it has the two sources of scattering that can neither be modeled by smooth parts nor by edge scatterers. Such sources of scattering are the antenna under the nose radome and the air intakes. Since these two

FIGURE 3.118 MiG-29 front-line fighter jet.

TABLE 3.9
Geometrical Characteristics of MiG-29 Front-Line Fighter

Airframe Characteristics (Figure 3.118)		Aircraft Surface Model Characteristics (Figure 3.119)	
Aircraft length	17.32 m	Number of parts of ellipsoids in the model	29
Aircraft height	4.73 m	Number of straight wedge parts in the model	42
Wing span	11.36 m		
Wing's area	38.06 m^2		

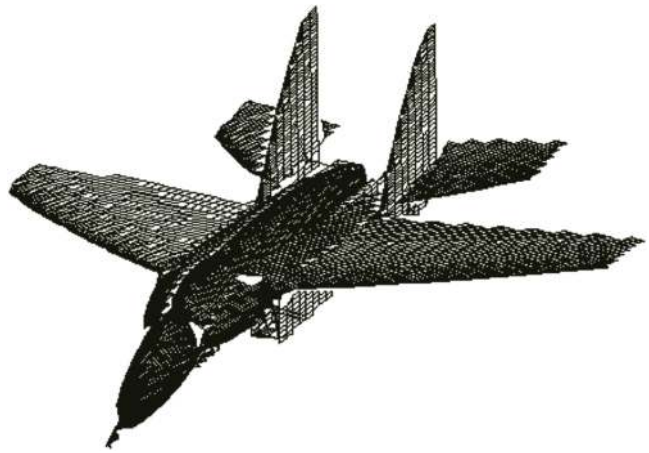

FIGURE 3.119 Computer model of MiG-29 surface.

types of scatterers can contribute significantly to total scattered field, we need to account for such elements in our computer model in order to receive adequate scattering characteristics for the whole plane.

Antenna system under the radio transparent radome is an integral part of Doppler radar N-091EA "Ruby" (included into radar aiming system RLPK-29E) onboard of MiG-29 fighter plane. The radar provides simultaneous tracks of up to 10 air targets, allowing to choose the most dangerous object, and generates data necessary to launch single R-27R missile equipped with semiactive radar seeker.

Antenna system is designed as the reverse Cassegrain architecture [94]. The front concave reflector (Figure 3.120a) has been inclined downwards by 9° with respect to antenna axis and it contains a system of vertical parallel conductors mounted into its surface. This allows signals of only single polarization to pass through the reflector. The main antenna reflector (Figure 3.120b) is shaped as a part of paraboloid of revolution that has the diameter of 71 cm and depth of 1 cm. Besides, at the distance equal to quarter of the radar-operating wavelength from metallic reflector inside the dielectric

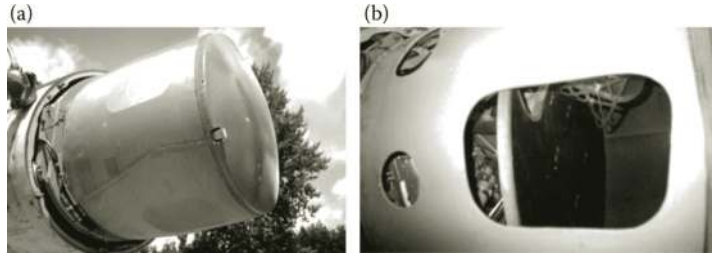

FIGURE 3.120 Antenna system of N-091EA "Ruby" radar.

medium there are half-wave conductors, whose orientation is shifted by 45° with respect to those of the front reflectors. So, when the transmitted signal first hits the front reflector, it bounces back to the main reflector. Once reflected from it, transmitted signal changes its polarization to cross one and passes unobstructed through the front reflector. Signal reception is done in reverse order. Such antenna design saves space, however as a result of trade-off the antenna system becomes quite narrowband. The angles of scan of ±65° in azimuth and +56° through –36° in elevation are provided by rotation of the whole antenna module along circular rails mounted to the front fuselage section as well as by turn of main reflector in vertical plane by ±20°.

Antenna radome (Figure 3.121) is made of glass cloth and it has the following properties: length is 1.91 m, diameter at the basis is 0.9 m, wall thickness is 9 mm, and permittivity is $\varepsilon \approx 3$. The radome axis has been inclined downwards by 9° with respect to the fuselage axis.

Proceeding from the antenna design of N-091EA radar, we can assume that given radar scattering computation at its operating frequency (10 GHz) the signal, whose polarization coincides with orientation of conductors at the front reflector (vertical polarization given zero degree angle of antenna module rotation with respect to its axis), bounces off front antenna reflector only. In its turn, the horizontally polarized signal gets fully consumed by the equivalent load of radar receiver. Given the illumination frequencies outside the radar operating frequency range, we can assume that horizontally polarized illumination wave passes without any loss through the front reflector and scatters at the main antenna reflector without getting consumed by the equivalent antenna load, yet the vertically polarized illumination wave bounces off the front reflector totally.

Contribution from the nose radome into scattering characteristics of antenna system was accounted for under the assumption that radome was cone shaped. Scattering computation has been conducted using solution to the simulative problem of wave scattering at three-dimensional model of onboard reflector antenna under the radome presented in Section 2.4.2.

Accounting for scattering contribution from the air intakes of MiG-29 fighter plane. In works by Kisel' and Fedorenko [95,96], the following approach has been offered to account for scattering from air intakes of aircraft. Air intake gets split into two parts: the waveguide one (from inlet to the fan) and the load of this waveguide (the fan itself). In its turn, the waveguide part is farther split into several sections, the number of which depends on the total length of the airflow channel. Electromagnetic fields in the waveguide part are computed by elaborated iterative physical optics method based on integral field representations. Computation of scattering at the fan is conducted based on integral equation method. As shown in [97], this method can be used for computing scattering characteristics of air intakes that have various configurations, its accuracy being proved by results of physical simulation.

So, the scattering contribution from air intakes of MiG-29 aircraft has been accounted for in our computer model by way of replacing actual intakes by equivalent scatterers shaped as parts of second-order surfaces but having the same RCS as the actual air intakes over wide range of illumination aspects. Besides, we used here the data on RCS of standard air intakes from [97] as a reference.

Figures 3.122 through 3.139 show diagrams of mean and median RCS given the MiG-29 aircraft model illumination at vertical and horizontal polarization, the latter having been averaged over

FIGURE 3.121 The nose radome of MiG-29.

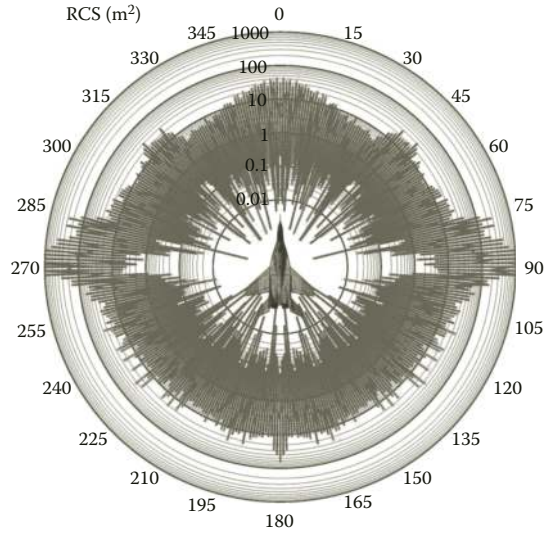

FIGURE 3.122 (**See color insert.**) Circular diagrams of instantaneous RCS given radar observation of MiG-29 aircraft model at carrier frequency of 10 GHz (3 cm wavelength).

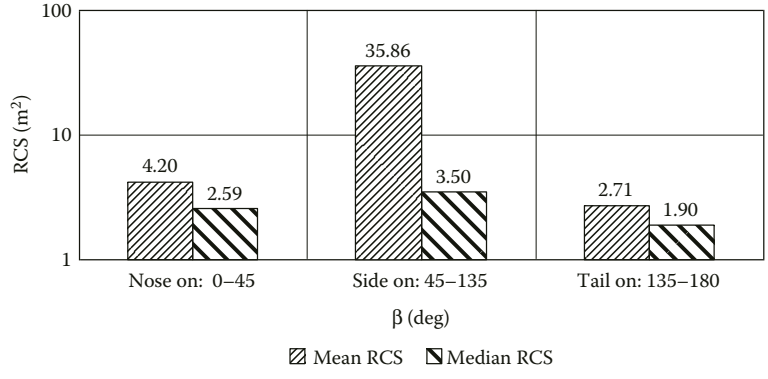

FIGURE 3.123 Diagrams of mean and median RCS of MiG-29 aircraft model in three sectors of azimuth aspect given its radar observation at horizontal polarization and carrier frequency of 10 GHz (3 cm wavelength).

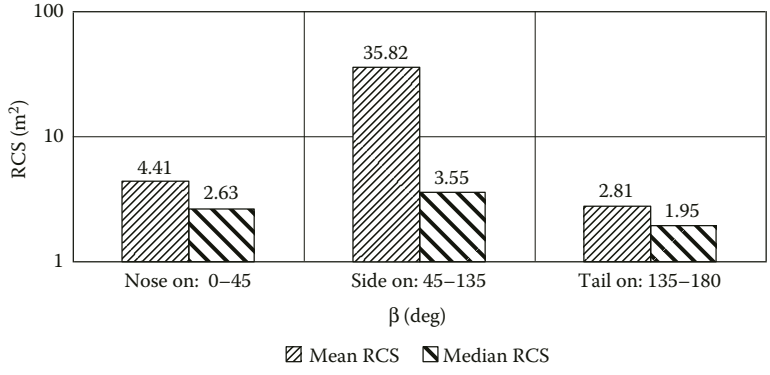

FIGURE 3.124 Diagrams of mean and median RCS of MiG-29 aircraft model in three sectors of azimuth aspect given its radar observation at vertical polarization and carrier frequency of 10 GHz (3 cm wavelength).

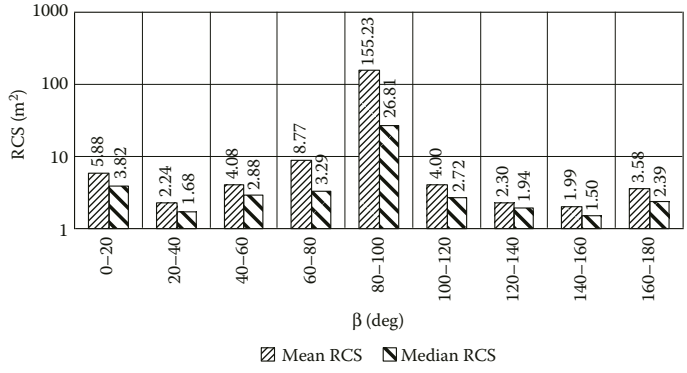

FIGURE 3.125 Diagrams of mean and median RCS of MiG-29 aircraft model in 20-degree sectors of azimuth aspect given its radar observation at horizontal polarization and carrier frequency of 10 GHz (3 cm wavelength).

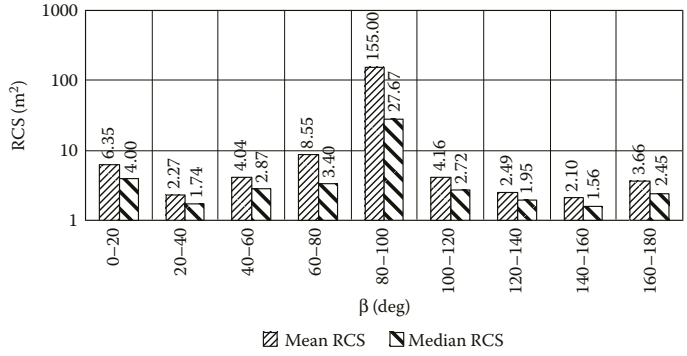

FIGURE 3.126 Diagrams of mean and median RCS of MiG-29 aircraft model in 20-degree sectors of azimuth aspect given its radar observation at vertical polarization and carrier frequency of 10 GHz (3 cm wavelength).

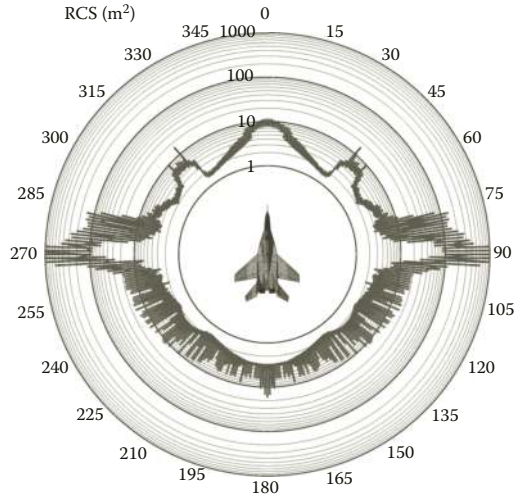

FIGURE 3.127 (**See color insert.**) Circular diagrams of noncoherent RCS given radar observation of MiG-29 aircraft model at carrier frequency of 10 GHz (3 cm wavelength).

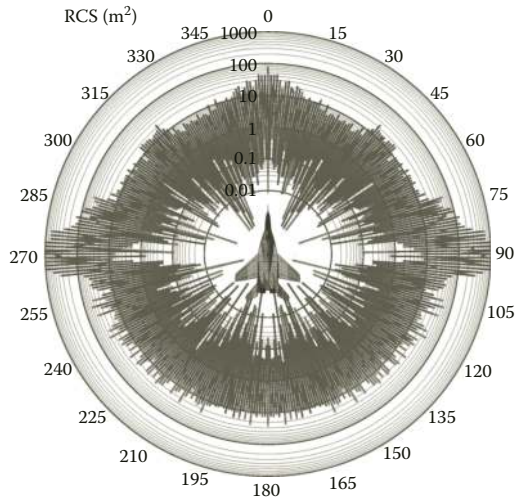

FIGURE 3.128 (**See color insert.**) Circular diagrams of instantaneous RCS given radar observation of MiG-29 aircraft model at carrier frequency of 3 GHz (10 cm wavelength).

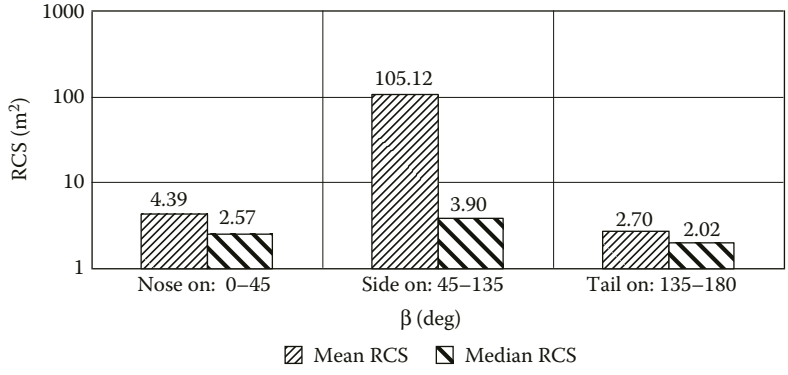

FIGURE 3.129 Diagrams of mean and median RCS of MiG-29 aircraft model in three sectors of azimuth aspect given its radar observation at horizontal polarization and carrier frequency of 3 GHz (10 cm wavelength).

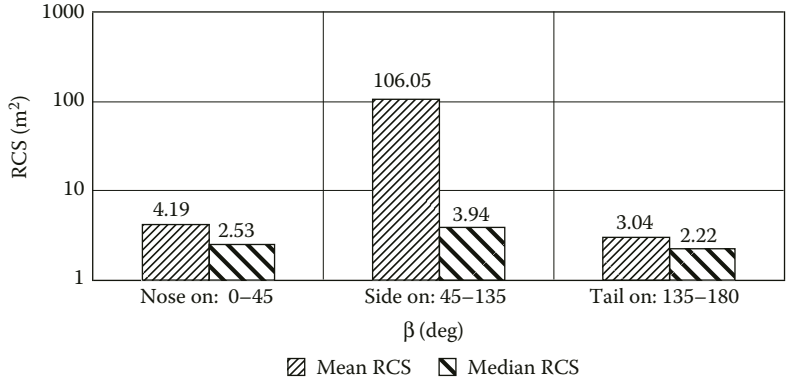

FIGURE 3.130 Diagrams of mean and median RCS of MiG-29 aircraft model in three sectors of azimuth aspect given its radar observation at vertical polarization and carrier frequency of 3 GHz (10 cm wavelength).

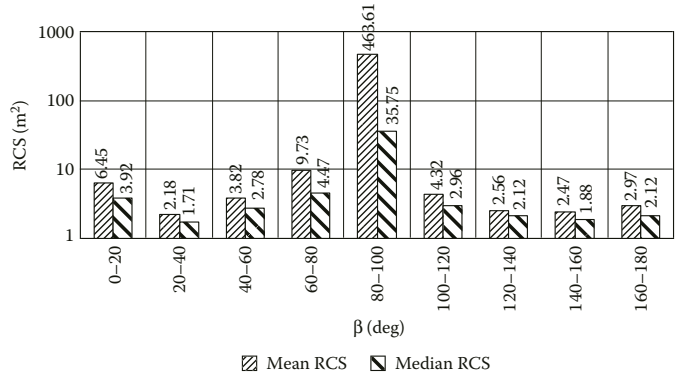

FIGURE 3.131 Diagrams of mean and median RCS of MiG-29 aircraft model in 20-degree sectors of azimuth aspect given its radar observation at horizontal polarization and carrier frequency of 3 GHz (10 cm wavelength).

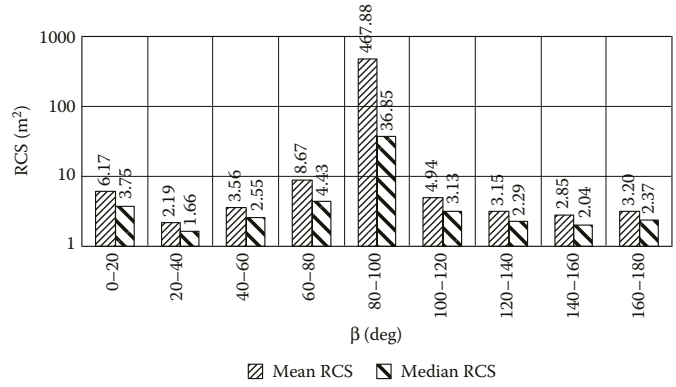

FIGURE 3.132 Diagrams of mean and median RCS of MiG-29 aircraft model in 20-degree sectors of azimuth aspect given its radar observation at vertical polarization and carrier frequency of 3 GHz (10 cm wavelength).

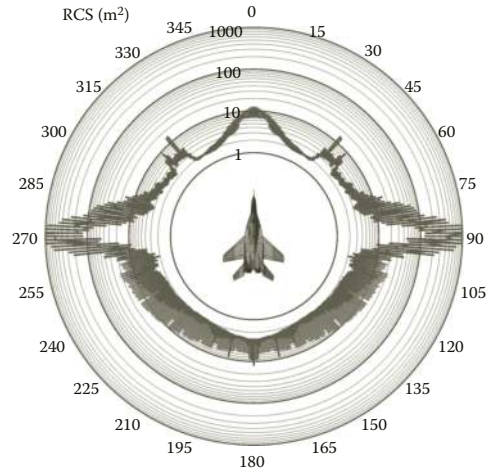

FIGURE 3.133 (**See color insert.**) Circular diagrams of noncoherent RCS of MiG-29 aircraft model given its radar observation at carrier frequency of 3 GHz (10 cm wavelength).

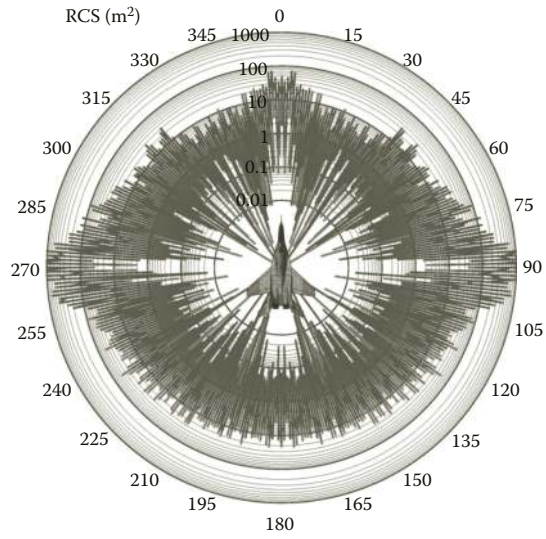

FIGURE 3.134 (**See color insert.**) Circular diagrams of instantaneous RCS given radar observation of MiG-29 aircraft model at carrier frequency of 1 GHz (30 cm wavelength).

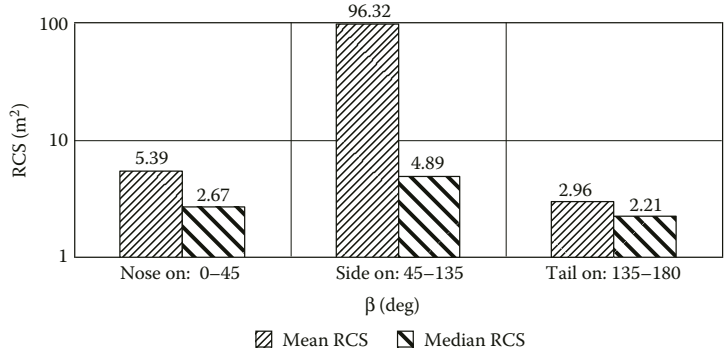

FIGURE 3.135 Diagrams of mean and median RCS of MiG-29 aircraft model in three sectors of azimuth aspect given its radar observation at horizontal polarization and carrier frequency of 1 GHz (30 cm wavelength).

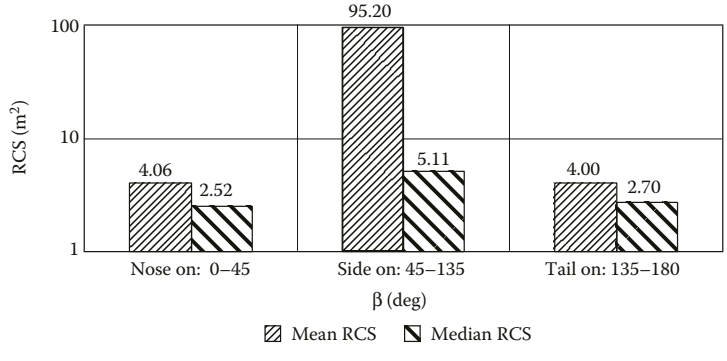

FIGURE 3.136 Diagrams of mean and median RCS of MiG-29 aircraft model in three sectors of azimuth aspect given its radar observation at vertical polarization and carrier frequency of 1 GHz (30 cm wavelength).

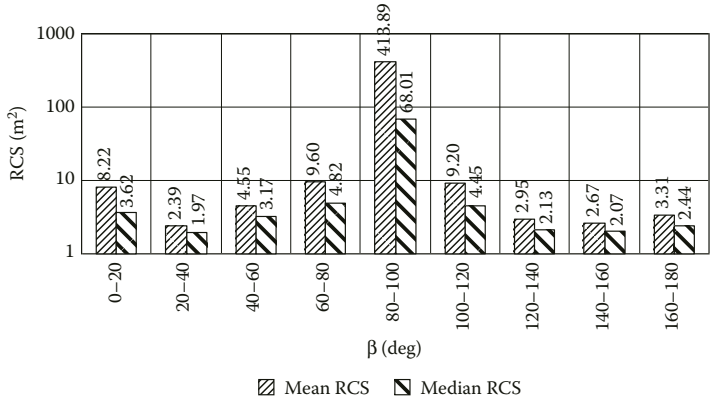

FIGURE 3.137 Diagrams of mean and median RCS of MiG-29 aircraft model in 20-degree sectors of azimuth aspect given its radar observation at horizontal polarization and carrier frequency of 1 GHz (30 cm wavelength).

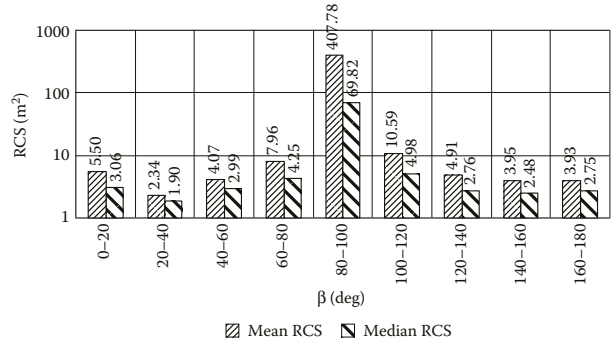

FIGURE 3.138 Diagrams of mean and median RCS of MiG-29 aircraft model in 20-degree sectors of azimuth aspect given its radar observation at vertical polarization and carrier frequency of 1 GHz (30 cm wavelength).

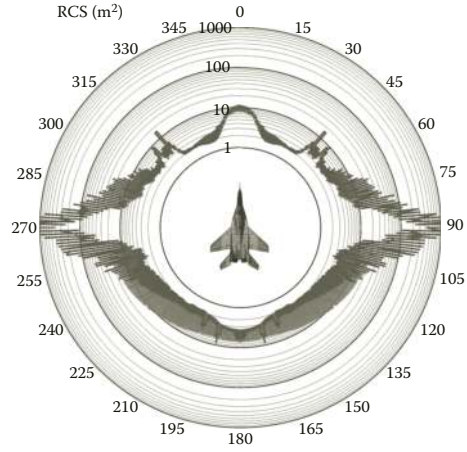

FIGURE 3.139 (**See color insert.**) Circular diagrams of noncoherent RCS of MiG-29 aircraft model given its radar observation at carrier frequency of 1 GHz (30 cm wavelength).

different angular sectors, as well as circular diagrams of instantaneous and noncoherent RCS for the frequency ranges of our interest.

Figures 3.140 through 3.142 show the amplitude distributions of echo signals for the frequency ranges of interest given horizontal polarization of illumination wave.

Table 3.10 summarizes the parameters of empirical probability distributions that fit mostly the simulation data for square root of RCS.

In Section 3.1.10, there are examples of HRRPs computed for the aircraft given various central frequencies of signal spectrum and its widths.

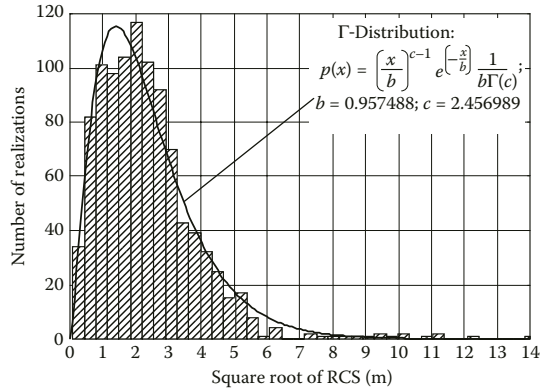

FIGURE 3.140 Amplitude distribution of echo signal of MiG-29 aircraft model at carrier frequency of 10 GHz given its horizontal polarization.

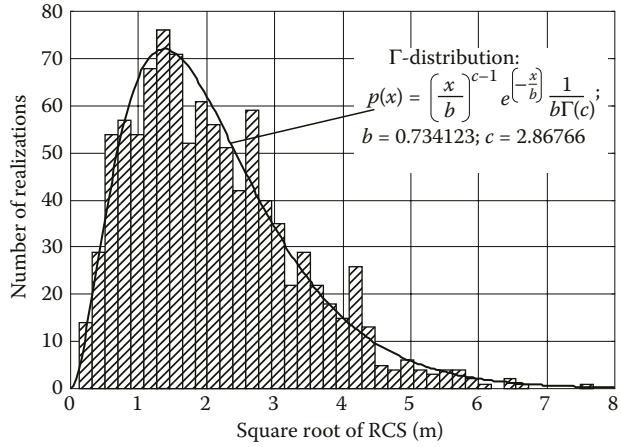

FIGURE 3.141 Amplitude distribution of echo signal of MiG-29 aircraft model at carrier frequency of 3 GHz given its horizontal polarization.

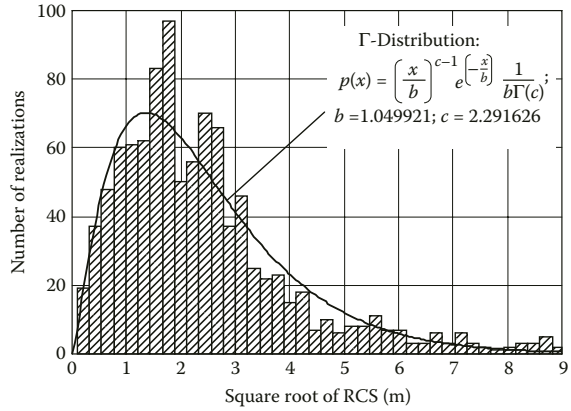

FIGURE 3.142 Amplitude distribution of echo signal of MiG-29 aircraft model at carrier frequency of 1 GHz given its horizontal polarization.

TABLE 3.10
Parameters of Probability Distributions for the Echo Signal Amplitudes of MiG-29 Aircraft Model

Wavelength	Polarization	Distribution Kind	Distribution Parameters
3 cm	Horizontal	Γ-Distribution: $p(x) = \left(\frac{x}{b}\right)^{c-1} e^{\left(-\frac{x}{b}\right)} \frac{1}{b\Gamma(c)}$ where $\Gamma(c)$ is gamma-function	$b = 0.957488$ $c = 2.456989$
3 cm	Vertical	Weibull distribution: $p(x) = \frac{c}{b}\left(\frac{x}{b}\right)^{c-1} e^{-\left(\frac{x}{b}\right)^{c}}$	$b = 2.580824$ $c = 1.891905$
10 cm	Horizontal	Γ-Distribution	$b = 0.734123$ $c = 2.86766$
10 cm	Vertical	Weibull distribution	$b = 2.339237$ $c = 1.816584$
30 cm	Horizontal	Γ-Distribution	$b = 1.049921$ $c = 2.291626$
30 cm	Vertical	Γ-Distribution	$b = 0.899074$ $c = 2.517632$

3.1.10 Impulse Responses of MiG-29 Front-Line Fighter

As an example, we consider HRRPs of MiG-29 aircraft observed at the elevation angle of –3° (illumination from below) and azimuth aspect of 10°.

It should be noted that given radar observation of MiG-29 aircraft from its rear hemisphere the HRRPs obtained at two different polarization of illumination signal can differ quite frequently even though they correspond to the same observation aspect. The reason for that would be different scattering properties of local edge scatterers given different polarizations of illumination signal. At the plots shown below, these differences in HRRPs at the two polarizations are caused also by scattering properties of onboard antenna system at MiG-29 aircraft, design of which together with polarization peculiarities was mentioned in the previous section.

Figures 3.143 and 3.144 show HRRPs of MiG-29 aircraft given its illumination with signal at central frequency of 10 GHz (3 cm wavelength) for the cases of horizontal and vertical polarization, respectively. Bold solid line corresponds to HRRP obtained using signal with rectangular amplitude spectrum of 1 GHz bandwidth. Thin dashed line corresponds to HRRP obtained using signal with rectangular spectrum of 250 MHz bandwidth.

Peaks #1 are due to scattering from the aircraft's air intakes. Peaks #2 in Figure 3.144 are due to scattering from the front (auxiliary) reflector of onboard radar antenna. It is worth mentioning that antenna system does not give any echo at horizontal polarization of illumination signal. The latter is due to polarization and frequency properties of the antenna system as well as due to its assumed orientation with respect to basic polarization directions.

Figures 3.145 and 3.146 show HRRPs of MiG-29 aircraft given its illumination by signals with spectra centered at 3 GHz (10 cm wavelength) for the cases of horizontal and vertical polarization, respectively. Solid bold line corresponds to HRRP obtained using signal with rectangular spectrum of 1 GHz bandwidth. Thin dashed line corresponds to HRRP obtained using signal with rectangular spectrum of 250 MHz bandwidth.

HRRPs shown in Figures 3.145 and 3.146 contain the following peaks marked with numbers.

Peaks #1 are due to scattering from the aircraft's air intakes. Peaks #2 in Figure 3.145 are due to scattering from the main antenna reflector (wavelength of 10 cm is beyond the operating frequency range of the radar). Peaks #2 in Figure 3.146 are due to scattering from the front (auxiliary) reflector of onboard antenna system.

The two reflectors of antenna system have different dimensions and polarization properties as well as are spaced apart, so these facts account for different amplitudes and lags of echoes at different polarization.

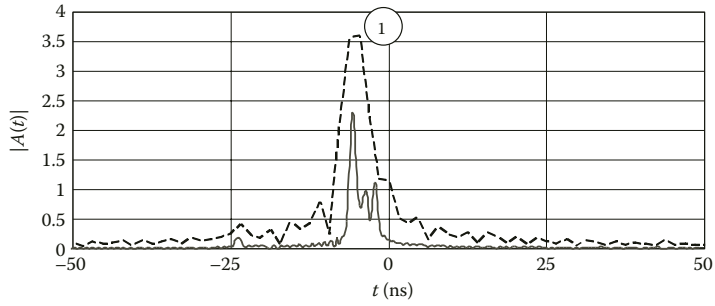

FIGURE 3.143 HRRPs of MiG-29 aircraft given its illumination by signal with center spectrum frequency of 10 GHz (3 cm wavelength), horizontal polarization.

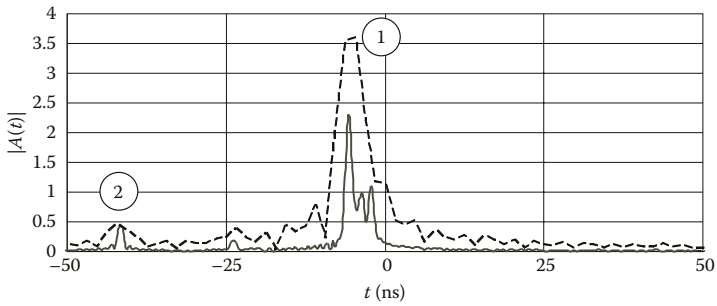

FIGURE 3.144 HRRPs of MiG-29 aircraft given its illumination by signals with center spectrum frequency of 10 GHz (3 cm wavelength), vertical polarization.

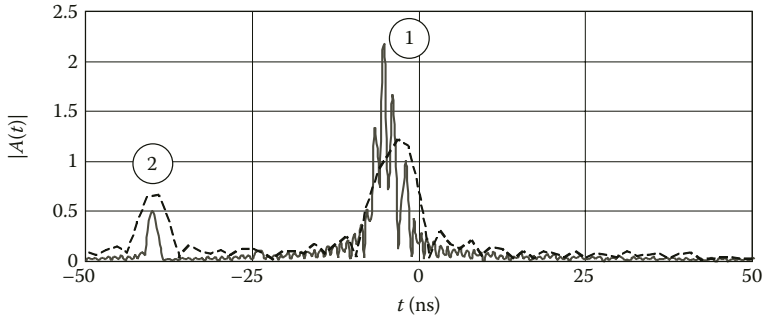

FIGURE 3.145 HRRPs of MiG-29 aircraft given its illumination by signals with center spectrum frequency of 3 GHz (10 cm wavelength), horizontal polarization.

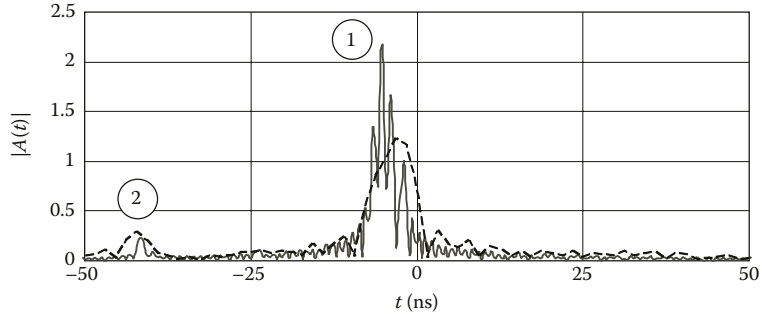

FIGURE 3.146 HRRPs of MiG-29 aircraft given its illumination by signals with center spectrum frequency of 3 GHz (10 cm wavelength), vertical polarization.

Figures 3.147 and 3.148 show HRRPs of MiG-29 aircraft given its illumination by signals with spectra centered at 1 GHz (30 cm wavelength) for the cases of horizontal and vertical polarization, respectively. Solid bold line corresponds to HRRP obtained using signal with rectangular spectrum of 1 GHz bandwidth. Thin dashed line corresponds to HRRP obtained using signal with rectangular spectrum of 250 MHz bandwidth.

Peaks #1 are due to scattering from the aircraft's air intakes. Peaks #2 in Figure 3.147, like those in Figure 3.145, are due to scattering from the main reflector of onboard antenna (wavelength of 30 cm is beyond the operating frequency range of the radar). Peaks #2 in Figure 3.148, like those in Figure 3.146, are due to scattering from the front (auxiliary) reflector of onboard antenna system.

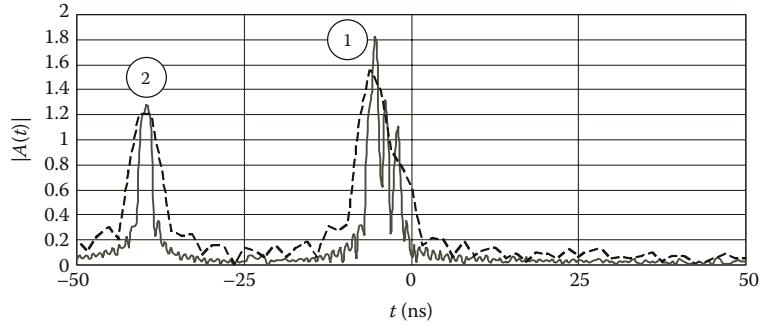

FIGURE 3.147 HRRPs of MiG-29 aircraft given its illumination by signals with center spectrum frequency of 1 GHz (30 cm wavelength), horizontal polarization.

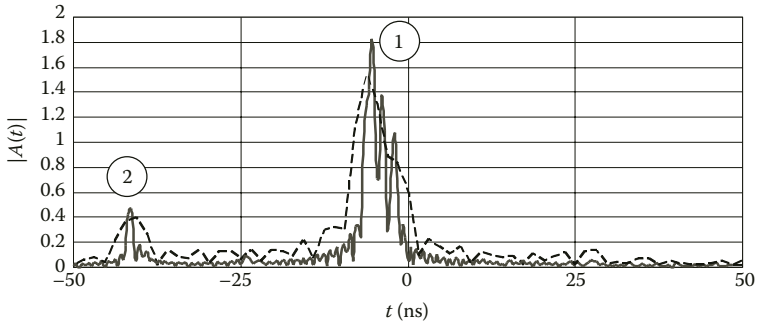

FIGURE 3.148 HRRPs of MiG-29 aircraft given its illumination by signals with center spectrum frequency of 1 GHz (30 cm wavelength), vertical polarization.

We should note that amplitude difference between the peaks corresponding to different polarizations at this wavelength is higher (three times).

3.1.11 Scattering Characteristics of F-16 Multirole Fighter

The F-16 Fighting Falcon fighter originally developed by General Dynamics (now Lockheed Martin) is the high-performance multirole aircraft. It is operated by the Air Forces of more than 22 countries around the world. F-16 is a very nimble aircraft. It can perform the g-turns with up to 9-g force. Pilot's frameless bubble canopy provides for all-round visibility [98].

The prototype of F-16 "Falcon" family, experimental YF-16, has performed its maiden flight on February 2, 1974, and in March 2000 the 4000-th fighter of this type was produced. Despite its significant age, F-16 is kept to be dynamically upgraded and it is still among the world best fighters. Originally developed as cost-effective air superiority day fighter (a little bit delayed American response to the MiG-21 aircraft), it evolved into the all-weather multirole aviation complex with air strike capabilities. Thanks to its capabilities and versatility, the F-16 platform had been put through a number of upgrades and modifications: F-16A—single-seat multirole day fighter; F-16B—two-seat combat and training version of F-16A; F-16C—single-seat improved multirole fighter; F-16D—two-seat combat and training version of F-16C; F-16ADF—antiaircraft defense fighter designed for US National guard; RF-16C (F-16R)—reconnaissance version fitted with ATARS container system. Evidently, even after the fifth-generation fighter enters the world's aviation market the F-16 aircraft will find its customers.

In the second half of 1980s, the F-16C/D aircraft has been fitted with the means for reducing their radar visibility (the canopy has been metalized from the inside, RAM coatings have been placed in the air intake zone). These measures alone (by some sources) provided for 40% reduction of frontal RCS.

In our RCS computations, we used the perfectly conducting model of the aircraft surface (Figure 3.150). Parameters of computer model are summarized in Table 3.11.

Figures 3.151 through 3.168 show diagrams of mean and median RCS given the F-16 aircraft model illumination at vertical and horizontal polarization, the latter having been averaged over

TABLE 3.11
Geometrical Characteristics of F-16 Multirole Fighter

Airframe Characteristics (Figure 3.149)		Aircraft Surface Model Characteristics (Figure 3.150)	
Aircraft length	15.03 m	Number of parts of ellipsoids in the model	42
Aircraft height	5.09 m	Number of straight wedge parts in the model	20
Wing span	9.45 m		
Wing's area	27.87 m^2		

FIGURE 3.149 F-16 multirole fighter.

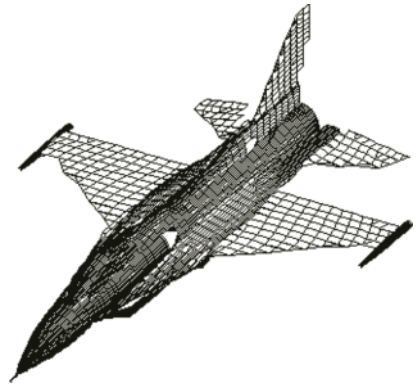

FIGURE 3.150 Computer model of F-16 surface.

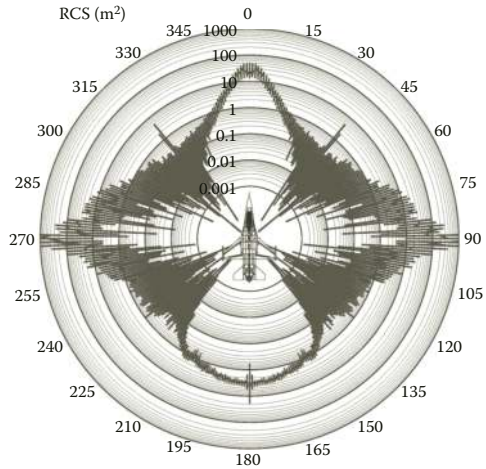

FIGURE 3.151 (**See color insert.**) Circular diagrams of instantaneous RCS given radar observation of F-16 aircraft model at carrier frequency of 10 GHz (3 cm wavelength).

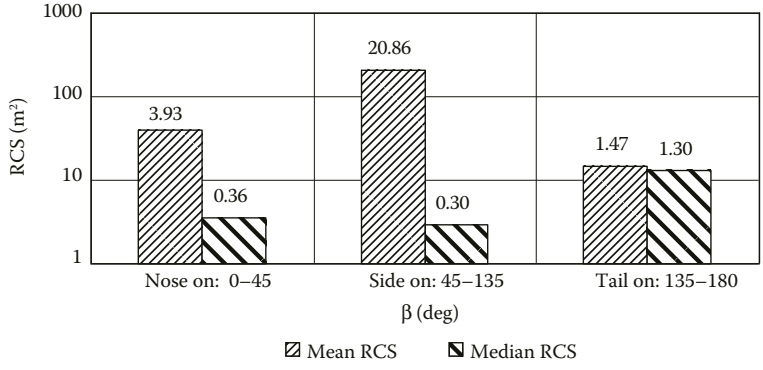

FIGURE 3.152 Diagrams of mean and median RCS of F-16 aircraft model in three sectors of azimuth aspect given its radar observation at horizontal polarization and carrier frequency of 10 GHz (3 cm wavelength).

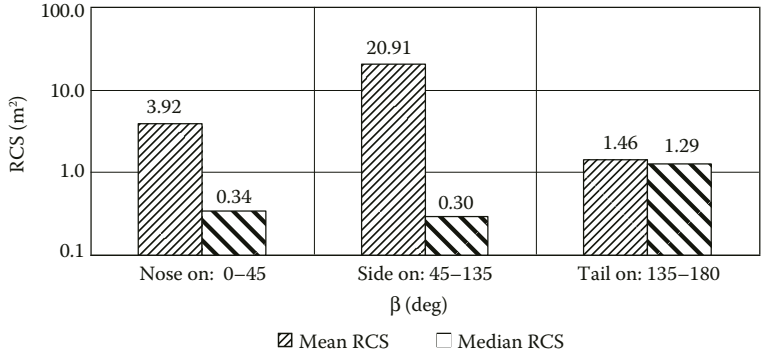

FIGURE 3.153 Diagrams of mean and median RCS of F-16 aircraft model in three sectors of azimuth aspect given its radar observation at vertical polarization and carrier frequency of 10 GHz (3 cm wavelength).

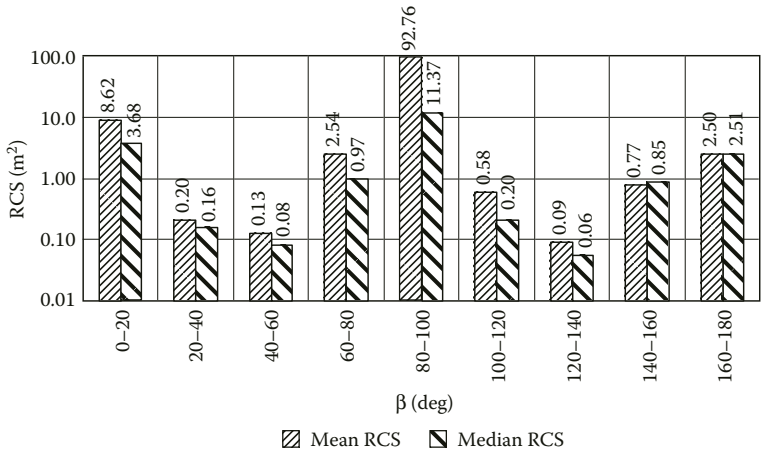

FIGURE 3.154 Diagrams of mean and median RCS of F-16 aircraft model in 20-degree sectors of azimuth aspect given its radar observation at horizontal polarization and carrier frequency of 10 GHz (3 cm wavelength).

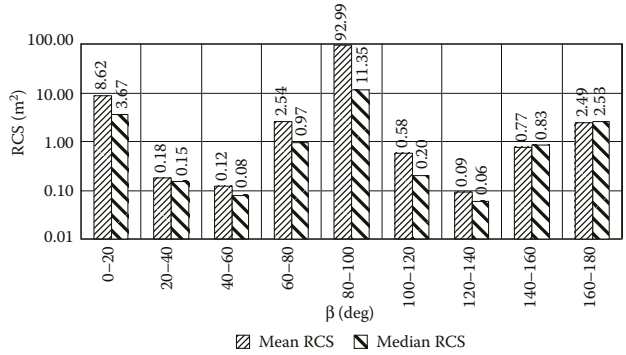

FIGURE 3.155 Diagrams of mean and median RCS of F-16 aircraft model in 20-degree sectors of azimuth aspect given its radar observation at vertical polarization and carrier frequency of 10 GHz (3 cm wavelength).

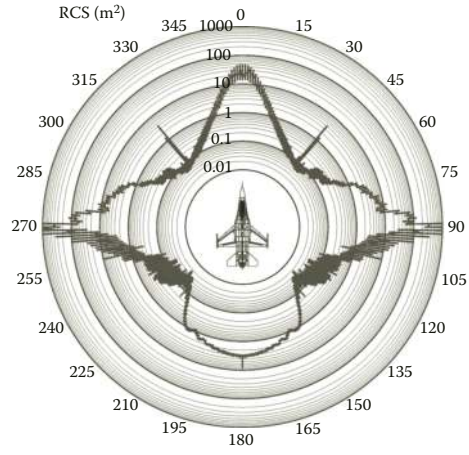

FIGURE 3.156 (**See color insert.**) Circular diagrams of noncoherent RCS given radar observation of F-16 aircraft model at carrier frequency of 10 GHz (3 cm wavelength).

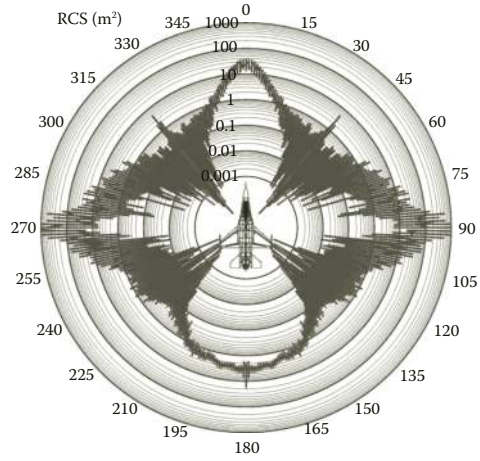

FIGURE 3.157 (**See color insert.**) Circular diagrams of instantaneous RCS given radar observation of F-16 aircraft model at carrier frequency of 3 GHz (10 cm wavelength).

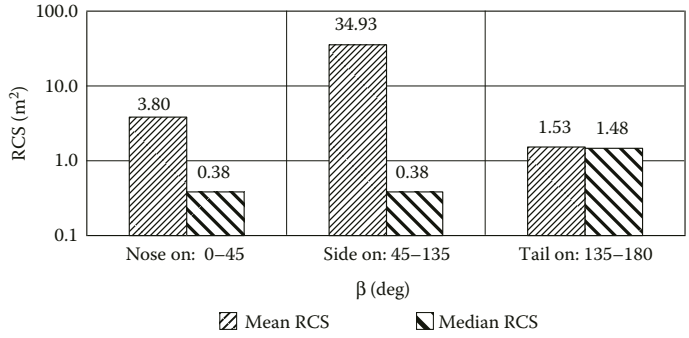

FIGURE 3.158 Diagrams of mean and median RCS of F-16 aircraft model in three sectors of azimuth aspect given its radar observation at horizontal polarization and carrier frequency of 3 GHz (10 cm wavelength).

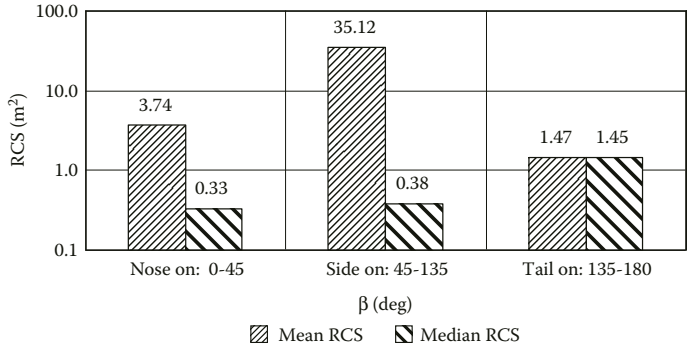

FIGURE 3.159 Diagrams of mean and median RCS of F-16 aircraft model in three sectors of azimuth aspect given its radar observation at vertical polarization and carrier frequency of 3 GHz (10 cm wavelength).

different angular sectors, as well as circular diagrams of instantaneous and noncoherent RCS for the frequency ranges of our interest.

Figures 3.169 through 3.171 show the amplitude distributions of echo signals for the frequency ranges of interest given horizontal polarization of illumination wave.

Table 3.12 summarizes the parameters of empirical probability distributions that fit mostly the simulation data for square root of RCS.

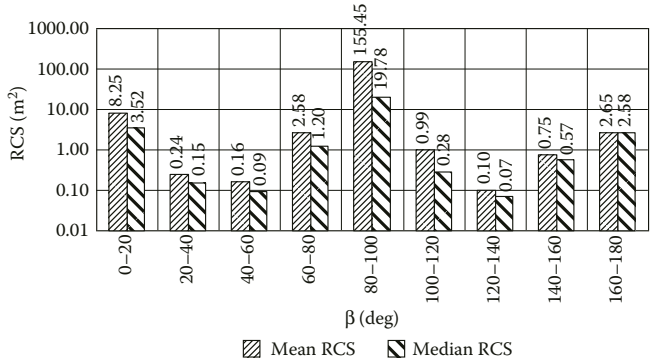

FIGURE 3.160 Diagrams of mean and median RCS of F-16 aircraft model in 20-degree sectors of azimuth aspect given its radar observation at horizontal polarization and carrier frequency of 3 GHz (10 cm wavelength).

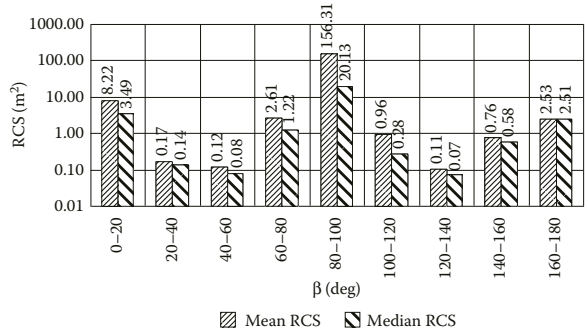

FIGURE 3.161 Diagrams of mean and median RCS of F-16 aircraft model in 20-degree sectors of azimuth aspect given its radar observation at vertical polarization and carrier frequency of 3 GHz (10 cm wavelength).

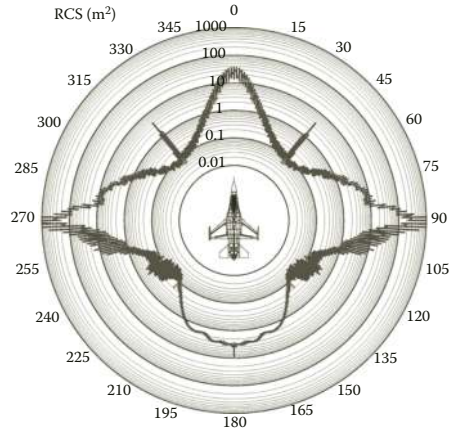

FIGURE 3.162 (**See color insert.**) Circular diagrams of noncoherent RCS of F-16 aircraft model given its radar observation at carrier frequency of 3 GHz (10 cm wavelength).

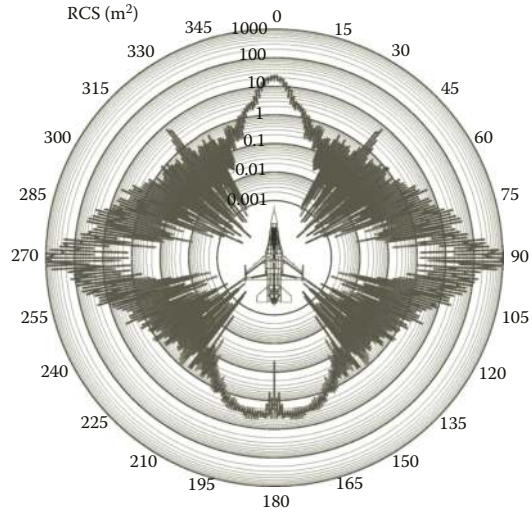

FIGURE 3.163 (**See color insert.**) Circular diagrams of instantaneous RCS given radar observation of F-16 aircraft model at carrier frequency of 1 GHz (30 cm wavelength).

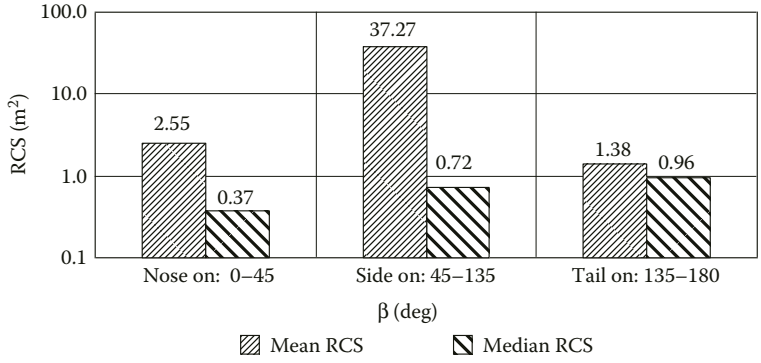

FIGURE 3.164 Diagrams of mean and median RCS of F-16 aircraft model in three sectors of azimuth aspect given its radar observation at horizontal polarization and carrier frequency of 1 GHz (30 cm wavelength).

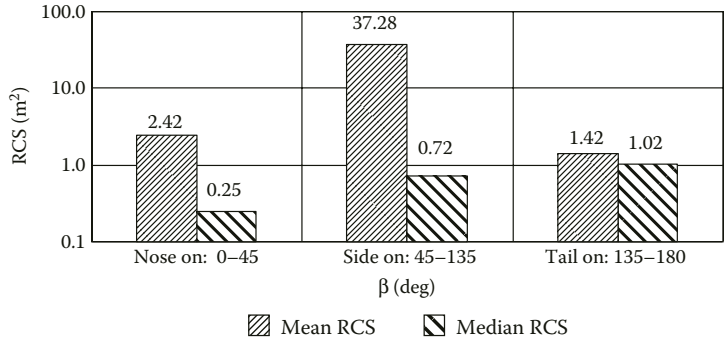

FIGURE 3.165 Diagrams of mean and median RCS of F-16 aircraft model in three sectors of azimuth aspect given its radar observation at vertical polarization and carrier frequency of 1 GHz (30 cm wavelength).

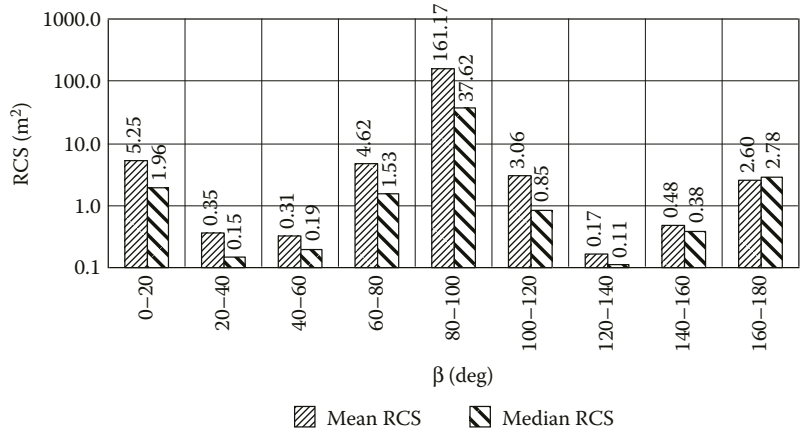

FIGURE 3.166 Diagrams of mean and median RCS of F-16 aircraft model in 20-degree sectors of azimuth aspect given its radar observation at horizontal polarization and carrier frequency of 1 GHz (30 cm wavelength).

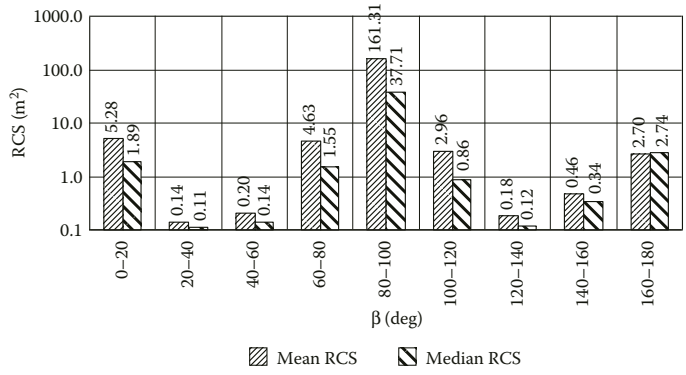

FIGURE 3.167 Diagrams of mean and median RCS of F-16 aircraft model in 20-degree sectors of azimuth aspect given its radar observation at vertical polarization and carrier frequency of 1 GHz (30 cm wavelength).

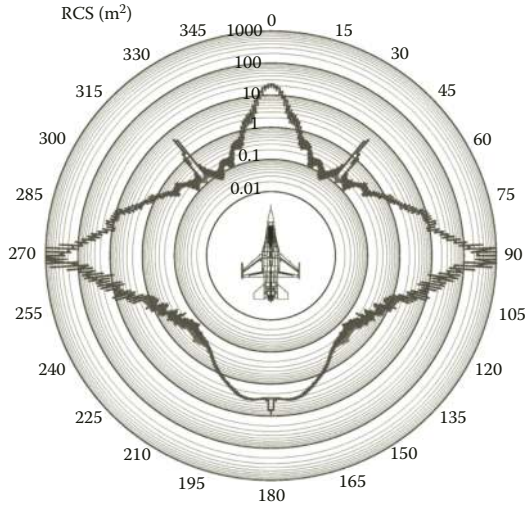

FIGURE 3.168 (**See color insert.**) Circular diagrams of noncoherent RCS of F-16 aircraft model given its radar observation at carrier frequency of 1 GHz (30 cm wavelength).

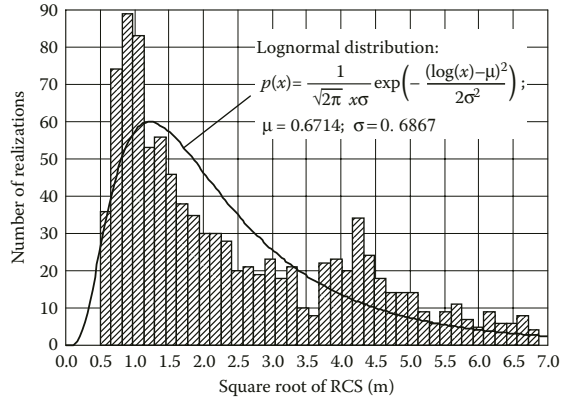

FIGURE 3.169 Amplitude distribution of echo signal of F-16 aircraft model at carrier frequency of 10 GHz given its horizontal polarization.

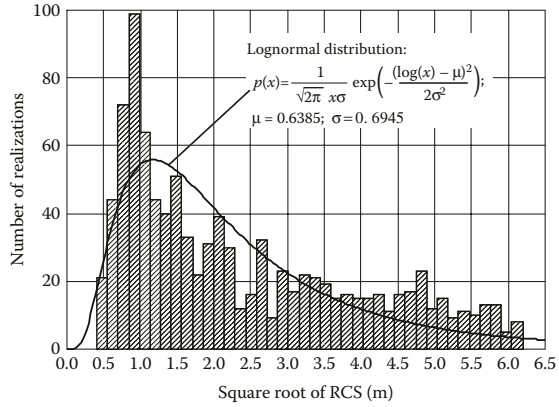

FIGURE 3.170 Amplitude distribution of echo signal of F-16 aircraft model at carrier frequency of 3 GHz given its horizontal polarization.

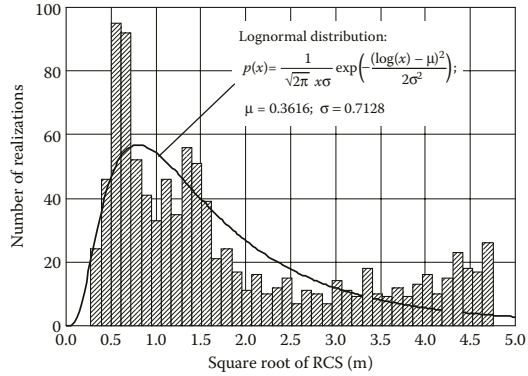

FIGURE 3.171 Amplitude distribution of echo signal of F-16 aircraft model at carrier frequency of 1 GHz given its horizontal polarization.

TABLE 3.12
Parameters of Probability Distributions for the Echo Signal Amplitudes of F-16 Aircraft Model

Wavelength	Polarization	Distribution Kind	Distribution Parameters
3 cm	Horizontal	Lognormal distribution: $p(x)=\frac{1}{\sqrt{2\pi}\,x\sigma}\exp\left(-\frac{(\log(x)-\mu)^2}{2\sigma^2}\right)$	μ = 0.6714 σ = 0.6867
3 cm	Vertical	Lognormal distribution	μ = 0.6706 σ = 0.6875
10 cm	Horizontal	Lognormal distribution	μ = 0.6385 σ = 0.6945
10 cm	Vertical	Lognormal distribution	μ = 0.6381 σ = 0.6945
30 cm	Horizontal	Lognormal distribution	μ = 0.3616 σ = 0.7128
30 cm	Vertical	Lognormal distribution	μ = 0.3503 σ = 0.725

In Section 3.1.12, there are examples of HRRPs computed for the aircraft given various central frequencies of signal spectrum and its widths.

3.1.12 Impulse Responses of F-16 Multirole Fighter

As an example, we consider HRRPs of F-16 aircraft observed at the elevation angle of –3° (illumination from below) and azimuth aspect of 40°.

Figure 3.172 shows HRRPs of F-16 aircraft given its illumination with signal at central frequency of 10 GHz (3 cm wavelength). Since there is practically no difference in HRRPs obtained for horizontal and vertical polarization, we present here only the corresponding impulse responses for the case of horizontal polarization of illumination signal. Bold solid line corresponds to HRRP obtained using signal with rectangular amplitude spectrum of 1 GHz bandwidth. Thin dashed line corresponds to HRRP obtained using signal with rectangular spectrum of 250 MHz bandwidth.

Peaks of HRRPs in Figure 3.172 are numbered from 1 through 4.

Peaks #1 are due to scattering from the Pitot tube, which is placed at the front of radar antenna radome. Peaks #2 are due to scattering from the aircraft air intake. Peaks #3 are due to scattering from horizontal stabilizer. Peaks #4 are due to scattering from vertical rudder.

Figures 3.173 and 3.174 show HRRPs of F-16 aircraft given its illumination by signals with spectra centered at 3 GHz (10 cm wavelength) for the cases of horizontal and vertical polarization, respectively. Solid bold line corresponds to HRRP obtained using signal with rectangular spectrum of 1 GHz bandwidth. Thin dashed line corresponds to HRRP obtained using signal with rectangular spectrum of 250 MHz bandwidth.

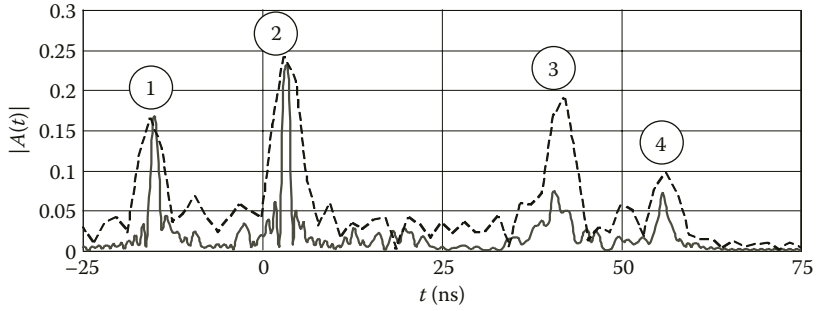

FIGURE 3.172 HRRPs of F-16 aircraft given its illumination by signals with center spectrum frequency of 10 GHz (3 cm wavelength).

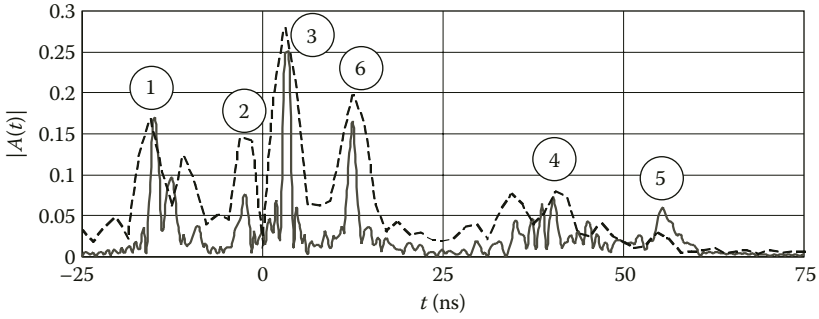

FIGURE 3.173 HRRPs of F-16 aircraft given its illumination by signal with center spectrum frequency of 10 GHz (3 cm wavelength), horizontal polarization.

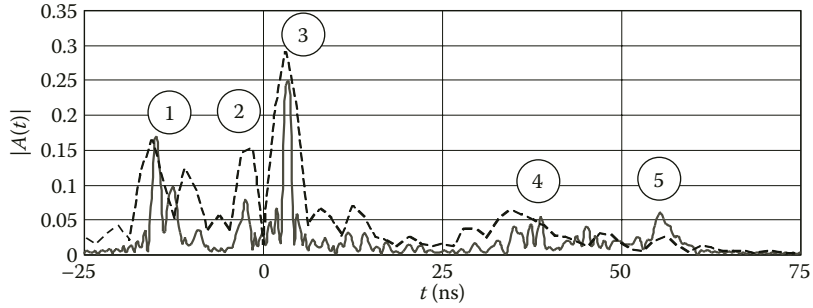

FIGURE 3.174 HRRPs of F-16 aircraft given its illumination by signals with center spectrum frequency of 10 GHz (3 cm wavelength), vertical polarization.

The peaks of HRRPs in Figures 3.173 and 3.174 are numbered. The peaks #1 are due to scattering from the Pitot tube, which is placed at the front of radar antenna radome. Peaks #2 are due to scattering from the pilot's cockpit. Peaks #3 are due to scattering from the aircraft air intake. Peaks #4 are due to scattering from the horizontal stabilizer. Peaks #5 are due to scattering from vertical rudder. The peak amplitude of echo from the wing's leading edge is significantly lower in case of vertical polarization as compared to that for the case of horizontal one. The latter is due to different polarization properties of scattering from the edge. Therefore, in Figure 3.174 the peak due to scattering from the wing's leading edge is not marked out. In Figure 3.173 (horizontal polarization), the peaks #6 correspond to the echo from the leading edge of wing. It is worth mentioning that peaks #4 in these two figures differ in amplitude too.

Figures 3.175 and 3.176 show HRRPs of F-16 aircraft given its illumination by signals with spectra centered at 1 GHz (30 cm wavelength) for the cases of horizontal and vertical polarization, respectively. Solid bold line corresponds to HRRP obtained using signal with rectangular spectrum of 1 GHz bandwidth. Thin dashed line corresponds to HRRP obtained using signal with rectangular spectrum of 250 MHz bandwidth.

The amplitudes of HRRP peaks in Figures 3.175 and 3.176 are so different that in HRRP obtained for the case of horizontal polarization (Figure 3.175) only two major peaks can be singled out. Peaks #1 are due to scattering from the wing's leading edge. Peaks #2 are due to scattering from the leading edge of horizontal stabilizer. Amplitudes of these two peaks dominate those of other peaks. HRRP obtained for the case of vertical polarization (Figure 3.176) contains more peaks of the lower amplitude. Peaks #1 are due to scattering from the Pitot tube, which is placed at the front of radar antenna radome. Peaks #2 are due to scattering from the

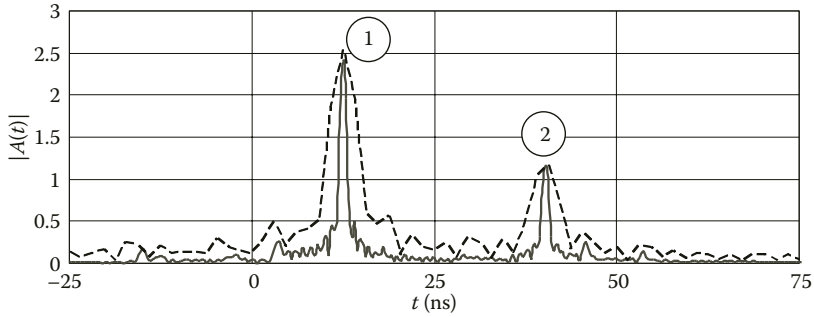

FIGURE 3.175 HRRPs of F-16 aircraft given its illumination by signals with center spectrum frequency of 1 GHz (30 cm wavelength), horizontal polarization.

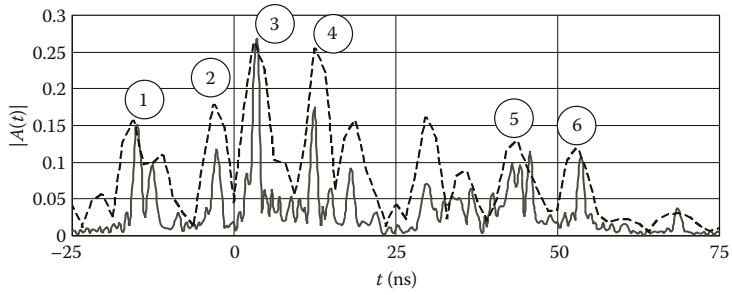

FIGURE 3.176 HRRPs of F-16 aircraft given its illumination by signals with center spectrum frequency of 1 GHz (30 cm wavelength), vertical polarization.

pilot's cockpit. Peaks #3 are due to scattering from the aircraft air intake. Peaks #4 are due to scattering from the wing's leading edge. The latter peak amplitude is ten times lower than that of corresponding peak #1 in Figure 3.175. Peaks #5 are due to scattering from horizontal stabilizer. Peak #6 is due to scattering from the vertical rudder.

3.1.13 Scattering Characteristics of AGM-86 ALCM

The AGM-86 air launch cruise missile (ALCM) (Figure 3.177) is the main long-range weapon system of B-52H bomber aircraft. With their nuclear warheads having been replaced by conventional ones, the AGM-86 is kept in the armament inventory in foreseeable future as a very effective weapon [99].

The first launch of AGM-86B has been performed in 1979, and in August 1981 the missiles were put into the inventory of B-52G/H bomber aircraft. The AGM-86B cruise missile has single F107-WR-100 or -101 turbojet engine and it is able to carry the W-80-1 variable power thermonuclear warhead. Prior to launch the wings and empennage are stowed in the fuselage, they are deployed in 2 s after the launch.

A total of 1715 specimens of AGM-86B cruise missile were produced by 1986 at the Boeing factories, and then the production was stopped. In 1986, the Boeing Company started to refit part of the AGM-86B missiles to the standard named AGM-86C. The basic change consisted in replacing thermonuclear warhead by the 900 kg high-explosive fragmentation one. AGM-86C missiles have also been equipped with GPS navigation receiver and digital scene matching area correlator (DSMAC) that significantly improved its accuracy (mean circular deviation reduced to 10 m).

In November 2001, the flight tests of AGM-86D Block II cruise missile were carried out that was equipped with the new 540 kg advanced unitary penetrator (AUP) warhead, which was designed to destroy heavily fortified targets or those placed deep in the ground.

FIGURE 3.177 AGM-86 cruise missile.

In our scattering computation, we used the perfectly conducting surface model of the missile shown in Figure 3.178. Parameters of computer model are summarized in Table 3.13.

Figures 3.179 through 3.196 show diagrams of mean and median RCS given the AGM-86 model illumination at vertical and horizontal polarization, the latter having been averaged over different

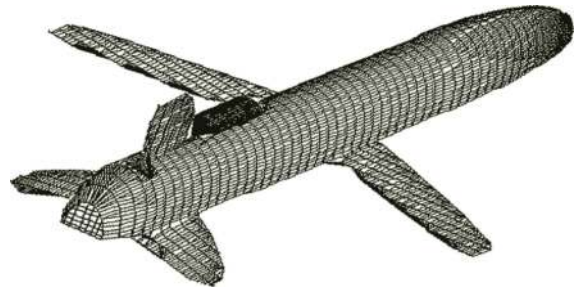

FIGURE 3.178 Computer model of AGM-86 surface.

TABLE 3.13
Geometrical Characteristics of AGM-86 ALCM

Airframe Characteristics (Figure 3.177)		Aircraft Surface Model Characteristics (Figure 3.178)	
Missile length	6.32 m	Number of parts of ellipsoids in the model	12
Diameter	0.62 m	Number of straight wedge parts in the model	15
Wing span	3.66 m		

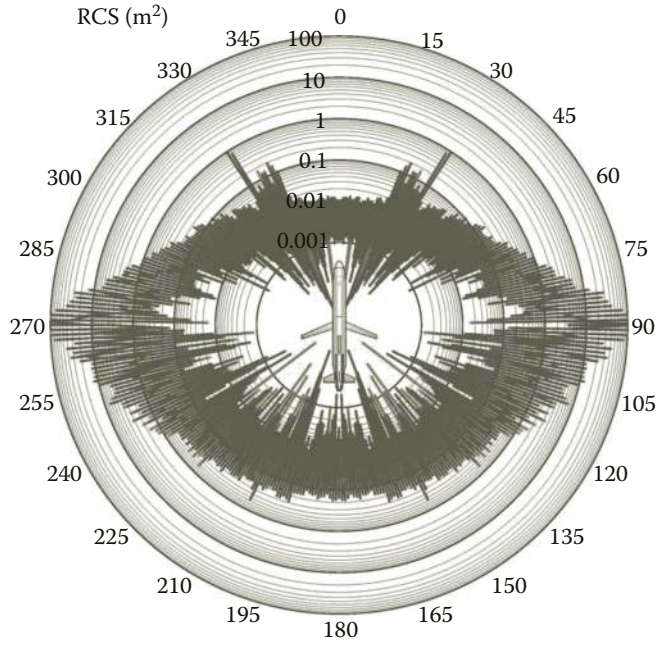

FIGURE 3.179 (**See color insert.**) Circular diagrams of instantaneous RCS given radar observation of AGM-86 ALCM model at carrier frequency of 10 GHz (3 cm wavelength).

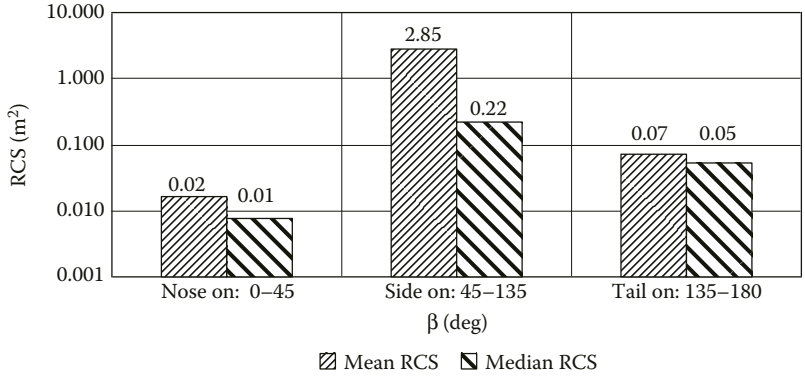

FIGURE 3.180 Diagrams of mean and median RCS of AGM-86 ALCM model in three sectors of azimuth aspect given its radar observation at horizontal polarization and carrier frequency of 10 GHz (3 cm wavelength).

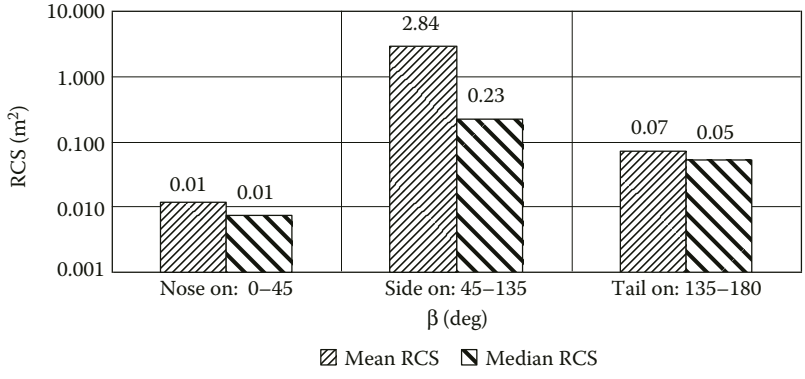

FIGURE 3.181 Diagrams of mean and median RCS of AGM-86 ALCM model in three sectors of azimuth aspect given its radar observation at vertical polarization and carrier frequency of 10 GHz (3 cm wavelength).

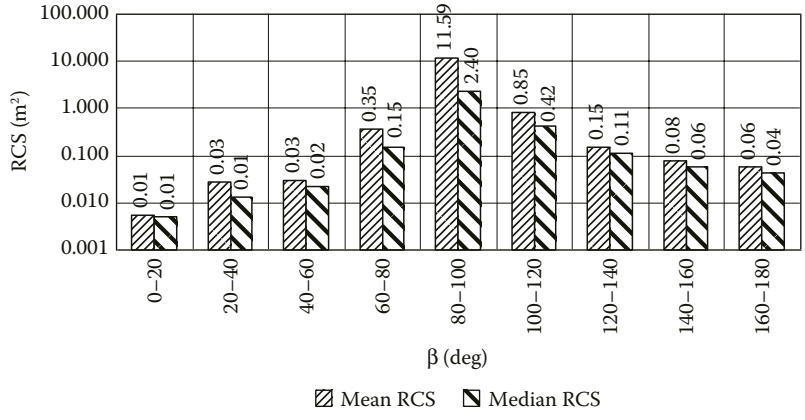

FIGURE 3.182 Diagrams of mean and median RCS of AGM-86 ALCM model in 20-degree sectors of azimuth aspect given its radar observation at horizontal polarization and carrier frequency of 10 GHz (3 cm wavelength).

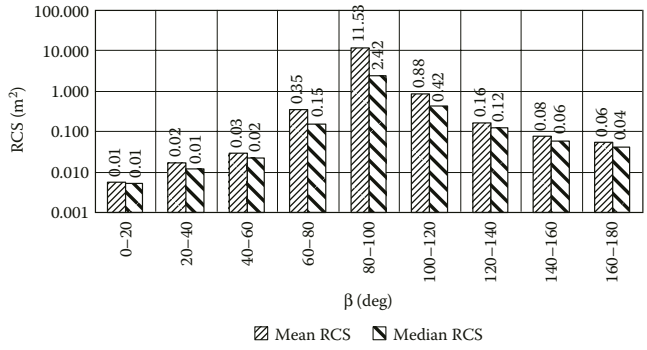

FIGURE 3.183 Diagrams of mean and median RCS of AGM-86 ALCM model in 20-degree sectors of azimuth aspect given its radar observation at vertical polarization and carrier frequency of 10 GHz (3 cm wavelength).

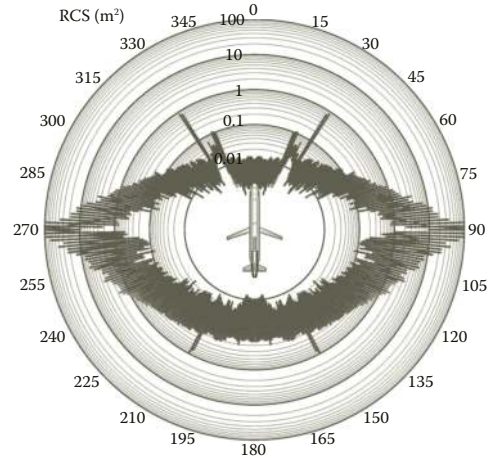

FIGURE 3.184 (**See color insert.**) Circular diagrams of noncoherent RCS given radar observation of AGM-86 ALCM model at carrier frequency of 10 GHz (3 cm wavelength).

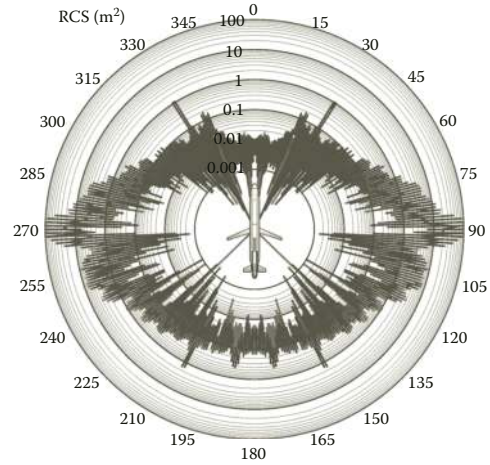

FIGURE 3.185 (**See color insert.**) Circular diagrams of instantaneous RCS given radar observation of AGM-86 ALCM model at carrier frequency of 3 GHz (10 cm wavelength).

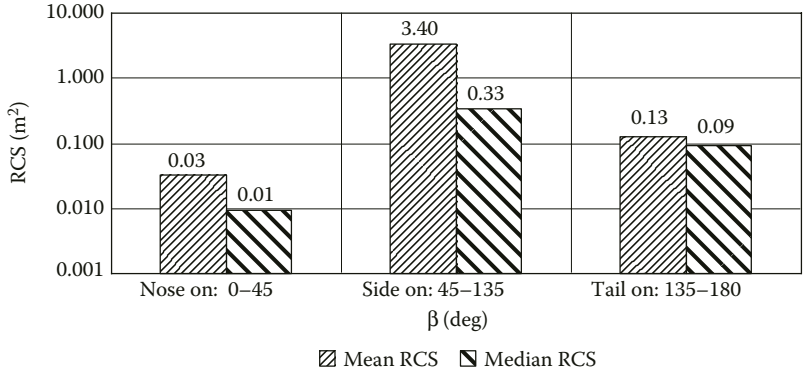

FIGURE 3.186 Diagrams of mean and median RCS of AGM-86 ALCM model in three sectors of azimuth aspect given its radar observation at horizontal polarization and carrier frequency of 3 GHz (10 cm wavelength).

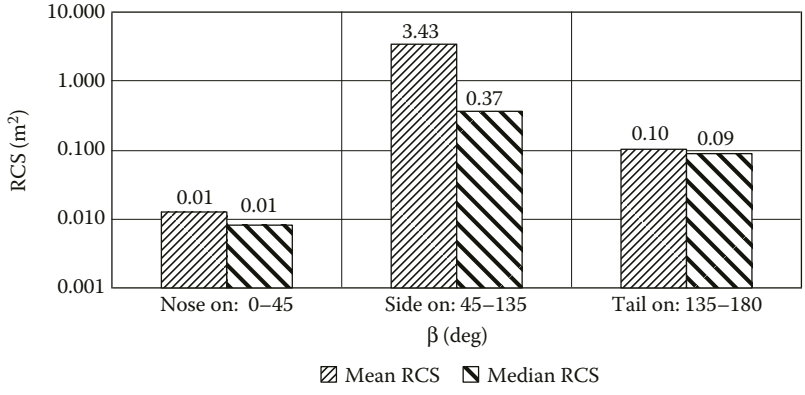

FIGURE 3.187 Diagrams of mean and median RCS of AGM-86 ALCM model in three sectors of azimuth aspect given its radar observation at vertical polarization and carrier frequency of 3 GHz (10 cm wavelength).

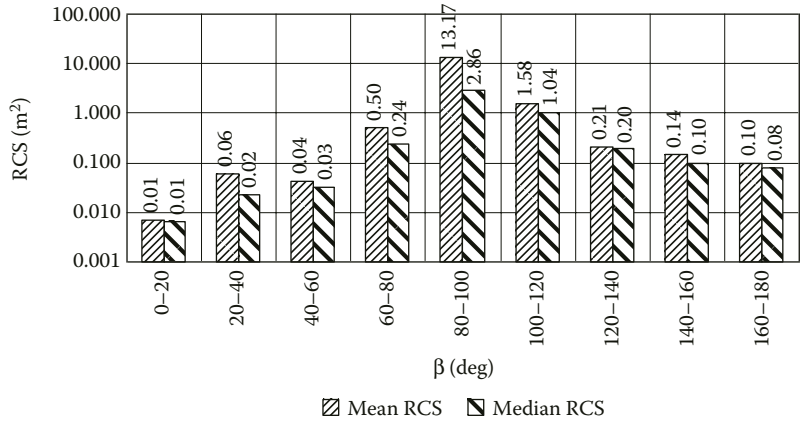

FIGURE 3.188 Diagrams of mean and median RCS of AGM-86 ALCM model in 20-degree sectors of azimuth aspect given its radar observation at horizontal polarization and carrier frequency of 3 GHz (10 cm wavelength).

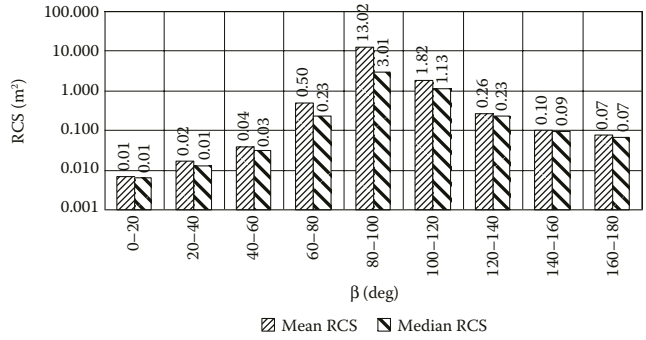

FIGURE 3.189 Diagrams of mean and median RCS of AGM-86 ALCM model in 20-degree sectors of azimuth aspect given its radar observation at vertical polarization and carrier frequency of 3 GHz (10 cm wavelength).

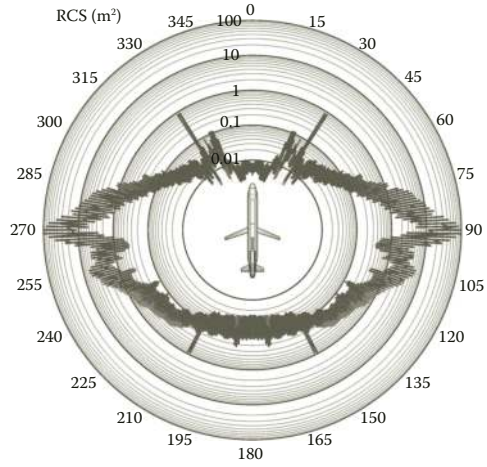

FIGURE 3.190 (**See color insert.**) Circular diagrams of noncoherent RCS of AGM-86 ALCM model given its radar observation at carrier frequency of 3 GHz (10 cm wavelength).

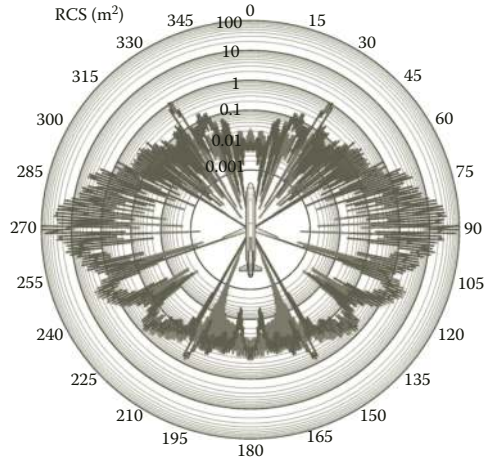

FIGURE 3.191 (**See color insert.**) Circular diagrams of instantaneous RCS given radar observation of AGM-86 ALCM model at carrier frequency of 1 GHz (30 cm wavelength).

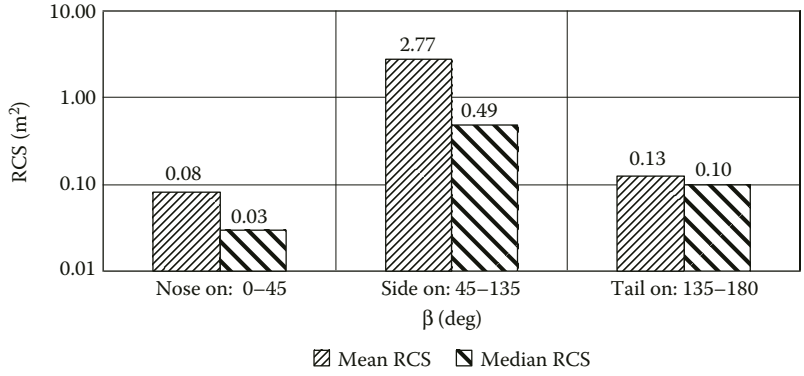

FIGURE 3.192 Diagrams of mean and median RCS of AGM-86 ALCM model in three sectors of azimuth aspect given its radar observation at horizontal polarization and carrier frequency of 1 GHz (30 cm wavelength).

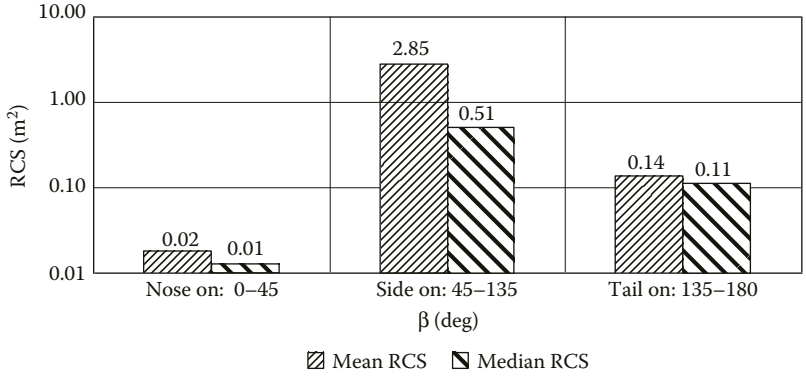

FIGURE 3.193 Diagrams of mean and median RCS of AGM-86 ALCM model in three sectors of azimuth aspect given its radar observation at vertical polarization and carrier frequency of 1 GHz (30 cm wavelength).

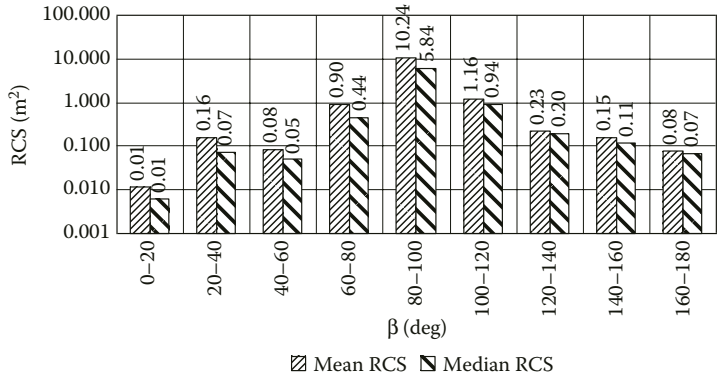

FIGURE 3.194 Diagrams of mean and median RCS of AGM-86 ALCM model in 20-degree sectors of azimuth aspect given its radar observation at horizontal polarization and carrier frequency of 1 GHz (30 cm wavelength).

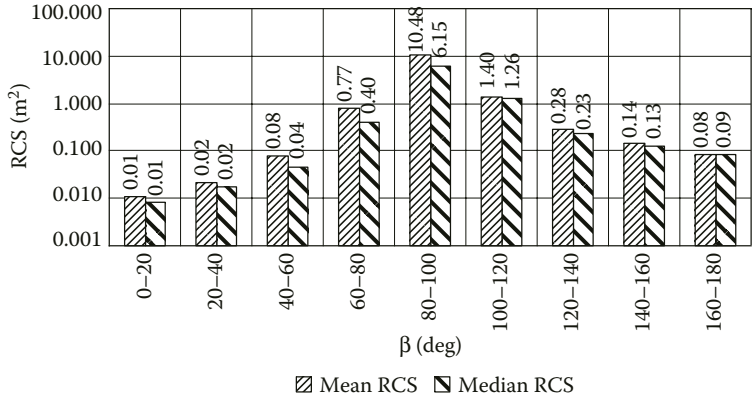

FIGURE 3.195 Diagrams of mean and median RCS of AGM-86 ALCM model in 20-degree sectors of azimuth aspect given its radar observation at vertical polarization and carrier frequency of 1 GHz (30 cm wavelength).

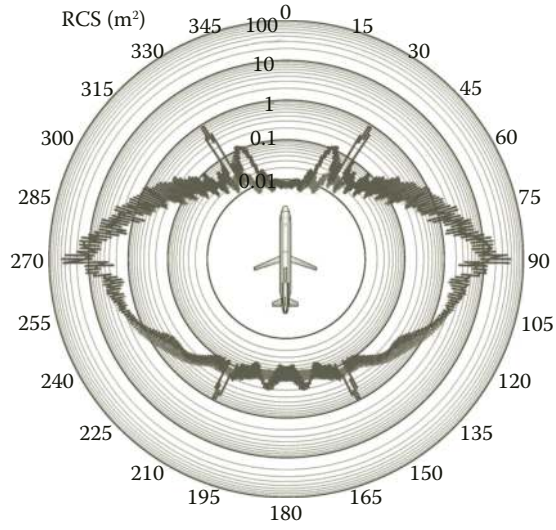

FIGURE 3.196 (**See color insert.**) Circular diagrams of noncoherent RCS of AGM-86 ALCM model given its radar observation at carrier frequency of 1 GHz (30 cm wavelength).

angular sectors, as well as circular diagrams of instantaneous and noncoherent RCS for the frequency ranges of our interest.

Figures 3.197 through 3.199 show the amplitude distributions of echo signals for the frequency ranges of interest given horizontal polarization of illumination wave.

Table 3.14 summarizes the parameters of empirical probability distributions that fit mostly the simulation data for square root of RCS.

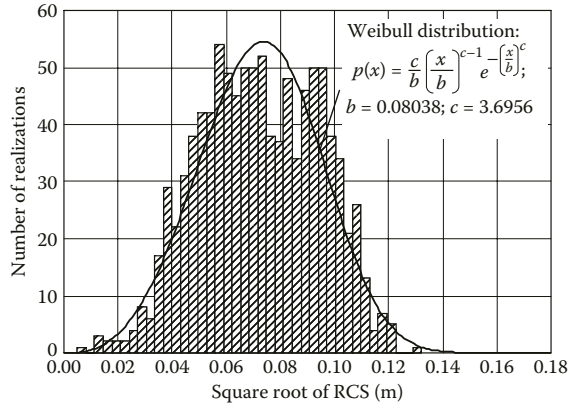

FIGURE 3.197 Amplitude distribution of echo signal of AGM-86 ALCM model at carrier frequency of 10 GHz given its horizontal polarization.

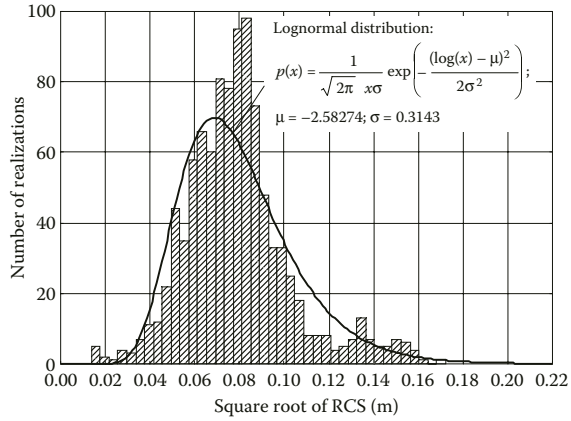

FIGURE 3.198 Amplitude distribution of echo signal of AGM-86 ALCM model at carrier frequency of 3 GHz given its horizontal polarization.

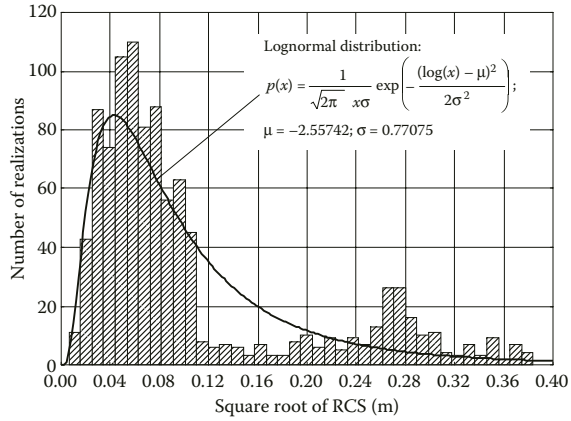

FIGURE 3.199 Amplitude distribution of echo signal of AGM-86 ALCM model at carrier frequency of 1 GHz given its horizontal polarization.

TABLE 3.14
Parameters of Probability Distributions for the Echo Signal Amplitudes of AGM-86 ALCM Model

Wavelength	Polarization	Distribution Kind	Distribution Parameters
3 cm	Horizontal	Weibull distribution: $p(x) = \frac{c}{b}\left(\frac{x}{b}\right)^{c-1} e^{-\left(\frac{x}{b}\right)^{c}}$	$b = 0.08038$ $c = 3.6956$
3 cm	Vertical	Weibull distribution:	$b = 0.08035$ $c = 3.6566$
10 cm	Horizontal	Lognormal distribution: $p(x) = \frac{1}{\sqrt{2\pi}\, x\sigma}\exp\left(-\frac{(\log(x)-\mu)^2}{2\sigma^2}\right)$	$\mu = -2.58274$ $\sigma = 0.3143$
10 cm	Vertical	β-distribution: $p(x) = \frac{\Gamma(\nu+\omega)}{\Gamma(\nu)\Gamma(\omega)} x^{\nu-1}(1-x)^{\omega-1}$, where $\Gamma(\nu)$ is the Gamma function	$\nu = 12.21349$ $\omega = 145.0882$
30 cm	Horizontal	Lognormal distribution	$\mu = -2.55742$ $\sigma = 0.77075$
30 cm	Vertical	Normal distribution: $p(x) = \frac{1}{\sigma\sqrt{2\pi}}\exp\left(-\frac{(x-\mu)^2}{2\sigma^2}\right)$	$\mu = 0.09308$ $\sigma = 0.03406$

In Section 3.1.14, there are examples of HRRPs computed for the missile given various central frequencies of signal spectrum and its widths.

3.1.14 Impulse Responses of AGM-86 ALCM

As an example, we consider HRRPs of the AGM-86 ALCM observed at the elevation angle of –3° (illumination from below) and azimuth aspect of 23° (illumination perpendicularly to the leading edge of horizontal empennage).

Figures 3.200 and 3.201 show HRRPs of AGM-86 ALCM given its illumination with signals at carrier frequency of 10 GHz (3 cm wavelength) for the cases of horizontal and vertical polarizations, respectively. Solid line corresponds to HRRP obtained using signal with rectangular

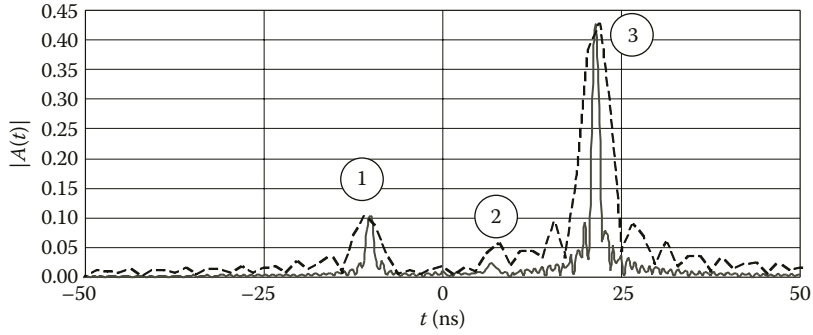

FIGURE 3.200 HRRPs of AGM-86 ALCM given its illumination by signal with center spectrum frequency of 10 GHz (3 cm wavelength), horizontal polarization.

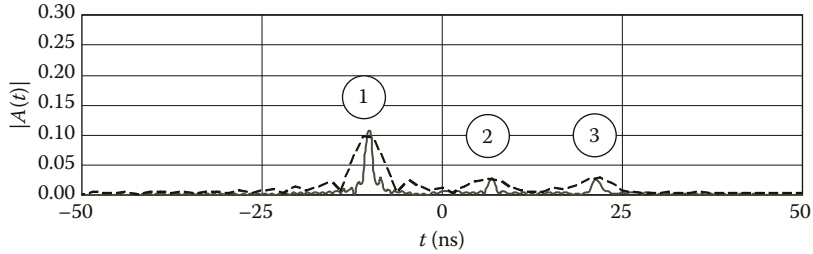

FIGURE 3.201 HRRPs of AGM-86 ALCM given its illumination by signals with center spectrum frequency of 10 GHz (3 cm wavelength), vertical polarization.

amplitude spectrum of 1 GHz bandwidth. Dashed line corresponds to HRRP obtained using signal with rectangular spectrum of 250 MHz bandwidth.

Peaks #1 are due to scattering from the nose part of fuselage. Peaks #2 are due to scattering from the wing. Peaks #3 are due to scattering from the leading edge of horizontal empennage. The echo amplitude for the leading edge of horizontal empennage is significantly higher for the case of horizontal polarization.

Figures 3.202 and 3.203 show HRRPs of AGM-86 ALCM given its illumination by signals with spectra centered at 3 GHz (10 cm wavelength) for the cases of horizontal and vertical polarization, respectively. Bold solid line corresponds to HRRP obtained using signal with rectangular spectrum of 1 GHz bandwidth. Thin dashed line corresponds to HRRP obtained using signal with rectangular spectrum of 250 MHz bandwidth.

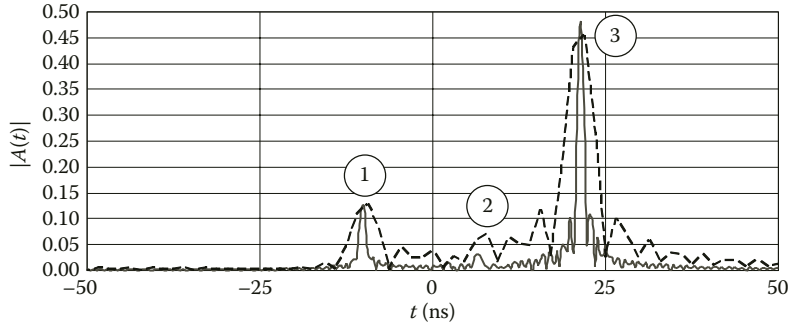

FIGURE 3.202 HRRPs of AGM-86 ALCM given its illumination by signals with center spectrum frequency of 3 GHz (10 cm wavelength), horizontal polarization.

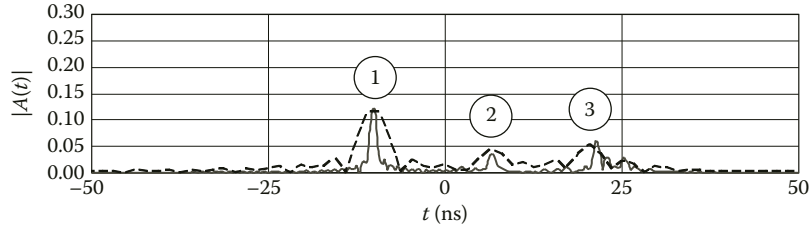

FIGURE 3.203 HRRPs of AGM-86 ALCM given its illumination by signals with center spectrum frequency of 3 GHz (10 cm wavelength), vertical polarization.

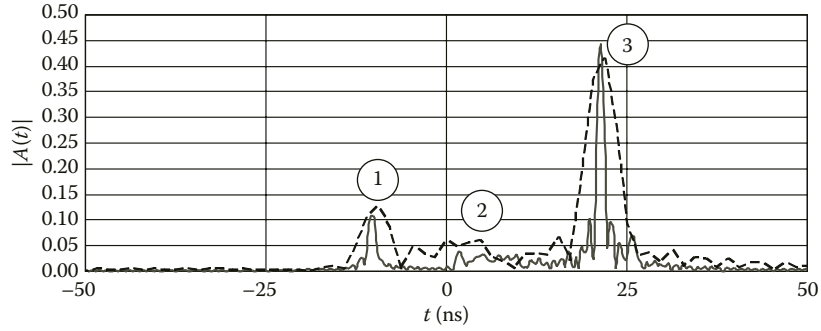

FIGURE 3.204 HRRPs of AGM-86 ALCM given its illumination by signals with center spectrum frequency of 1 GHz (30 cm wavelength), horizontal polarization.

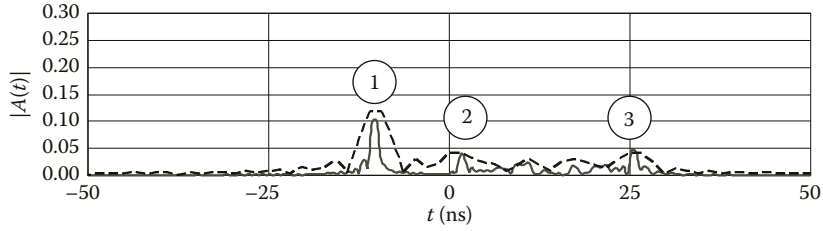

FIGURE 3.205 HRRPs of AGM-86 ALCM given its illumination by signals with center spectrum frequency of 1 GHz (30 cm wavelength), vertical polarization.

HRRPs shown in Figures 3.202 and 3.203 contain the following peaks marked with numbers. The view of these HRRPs is similar to those obtained for the illumination signals with spectra centered at 10 GHz (3 cm wavelength).

Peaks #1 are due to scattering from the nose part of fuselage. Peaks #2 are due to scattering from the wing. Peaks #3 are due to scattering from the leading edge of missile's horizontal empennage.

Figures 3.204 and 3.205 show HRRPs of AGM-86 ALCM given its illumination by signals with spectra centered at 1 GHz (30 cm wavelength) for the cases of horizontal and vertical polarization, respectively. Bold solid line corresponds to HRRP obtained using signal with rectangular spectrum of 1 GHz bandwidth. Thin dashed line corresponds to HRRP obtained using signal with rectangular spectrum of 250 MHz bandwidth.

Peaks #1 are due scattering from the nose part of fuselage. Peaks #2 are due to scattering from the wing. Peaks #3 are due to scattering from the leading edge of missile's horizontal empennage.

3.2 SCATTERING CHARACTERISTICS OF GROUND OBJECTS

When computing scattering characteristics of ground objects, we assumed the following elevation angles ε of their radar illumination (Figure 3.206): 1° (illumination by the ground-based radar systems); 10° and 30° (illumination by the airborne radar systems). Increment in azimuth aspect was set to 0.02°, the azimuth aspect angle β itself being counted off counterclockwise from the head-on direction (0° corresponds to the head-on illumination, 180° corresponds to the stern-on illumination). Scattering computation results are presented for the illumination frequency of 10 GHz (3 cm wavelength).

Computation results are given for the case of monostatic radar given two orthogonal polarizations of illumination signal: the horizontal one, for which the vector of electrical field intensity of illumination wave p_{h}^0 is parallel to the underlying surface; and the vertical one, for which the vector of electrical field intensity of illumination wave p_{v}^0 is orthogonal to p_{h}^0 and belongs to the plane that

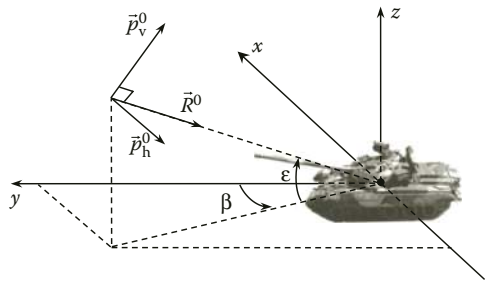

FIGURE 3.206 Geometry of the ground object illumination.

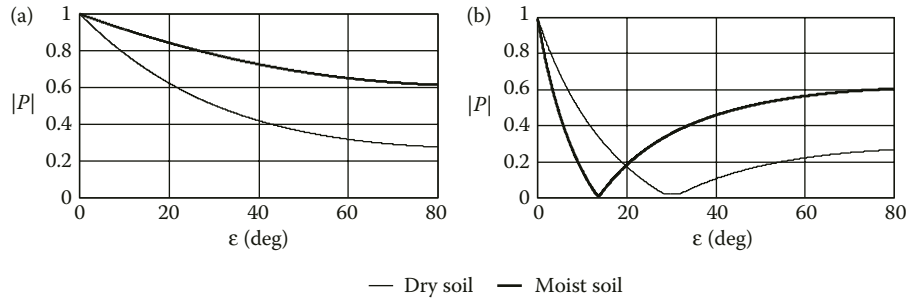

FIGURE 3.207 Modulus of reflection coefficient for the dry and moist soil given horizontal (a) and vertical (b) polarization of illumination wave.

is perpendicular to the underlying surface plane and that includes at the same time the propagation direction vector of plane incident wave. Below, all the curves corresponding to horizontal polarization are blue and those corresponding to vertical polarization are red.

We present the computation results obtained in assumption of two types of underlying surface that possess the most common values of relative permittivity. These two types are the following: dry soil ($\varepsilon' = 3 + j0.4$); moist soil (relative moist content being 20%) $\varepsilon' = 17 + j0.9$. Relative permeability was equal to unity for the both soil types. When the illumination elevation angle $\varepsilon = 1°$, the modules of reflection coefficients $|P|$ are close to one another and they approach the unit irrespectively of underlying surface characteristics (Figure 3.207). Therefore, in this case only scattering diagrams corresponding to dry soil are presented. The difference in scattering diagrams given the different types of soil becomes more prominent when the elevation angle of the object illumination increases.

The histograms of echo signal amplitude distribution (distribution of the square root from RCS) are shown for the two values of elevation angles: $\varepsilon = 1°$ and $\varepsilon = 30°$ given averaging in the two main sectors of azimuth aspects: from –10° through 10 and from 10° through 30°. Such diagrams were obtained by the scattering data computed given azimuth aspect angle increment of 0.02°. As in case of airborne objects, we compared the echo signal amplitude histograms to a number of empirical probability distributions and found those that fitted our computation data the most.

There are also examples of HRRPs computed for the tank models given various illumination signal spectrum widths.

3.2.1 Scattering Characteristics of T-90 Main Battle Tank

The Russian T-90 tank is the latest modification of the T-72 machine, it entered service in 1993 [100]. T-90 tank keeps up with Soviet tradition of tank construction—the classical layout, in which its major weapons are housed in the turret, power plant and transmission are in the aft section, and

the crew is accommodated separately: tank commander and gunner occupying the fighting compartment, and the driver occupying the driving compartment. The exterior of the T-90 tank (Figure 3.208) is practically the same as of T-72B one. The T-72 tank, in its turn, has been developed by the "Uralvagonzavod" design bureau as an upgrade of T-64A tank designed and produced by the Malyshev plant in Kharkiv [101].

In our computations, we used the perfectly conducting computer model of the tank surface shown in Figure 3.209. Parameters of computer mode are summarized in Table 3.15.

Figures 3.210 through 3.239 show diagrams of mean and median RCS and circular diagrams of instantaneous and noncoherent RCS obtained for the T-90 tank model. The results are given for vertical and horizontal polarization, two types of underling surface and three elevation angles.

Figures 3.240 through 3.247 show the amplitude distributions of echo signals for two azimuth aspect angle sectors and two elevation angles.

Tables 3.16 and 3.17 summarize the parameters of distributions that fit mostly the simulation data for square root of RCS.

In Section 3.2.2, there are examples of HRRPs computed for the tank model given various illumination signal spectrum widths.

FIGURE 3.208 T-90 main battle tank.

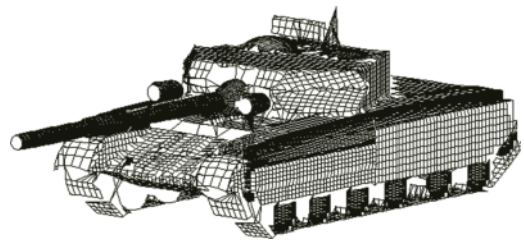

FIGURE 3.209 Computer model of T-90 surface.

TABLE 3.15
Geometrical Characteristics of T-90 Main Battle Tank

Hull Characteristics (Figure 3.208)		**Tank Surface Model Characteristics (Figure 3.209)**	
Tank length (gun included)	9.53 m	Number of parts of ellipsoids in the model	89
Width	3.46 m	Number of straight wedge parts in the model	34
Height	2.23 m		
Combat weight	46.5 tonne		

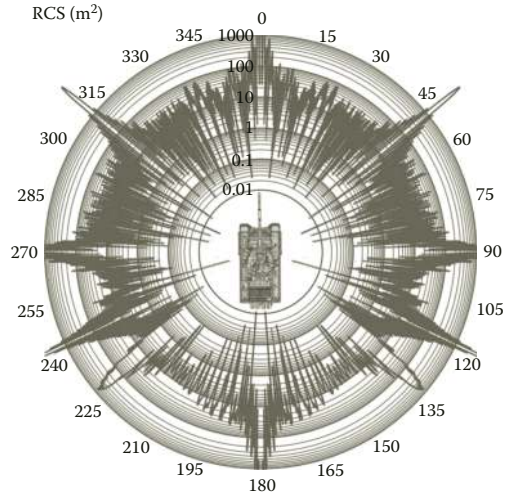

FIGURE 3.210 (**See color insert.**) Circular diagrams of instantaneous RCS given radar observation of T-90 tank model (ε = 1°, underlying surface – dry soil).

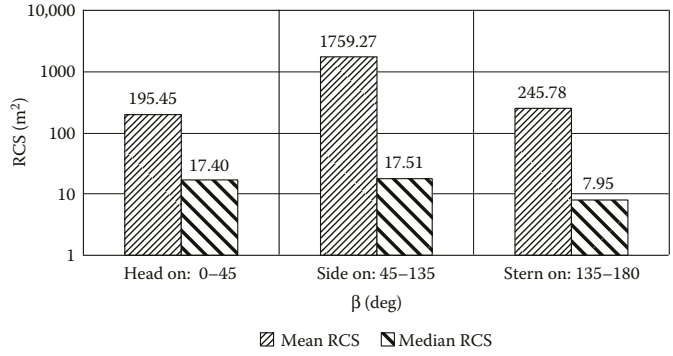

FIGURE 3.211 Diagrams of mean and median RCS of the T-90 tank model in three sectors of azimuth aspect given its radar observation at horizontal polarization (ε = 1°, underlying surface – dry soil).

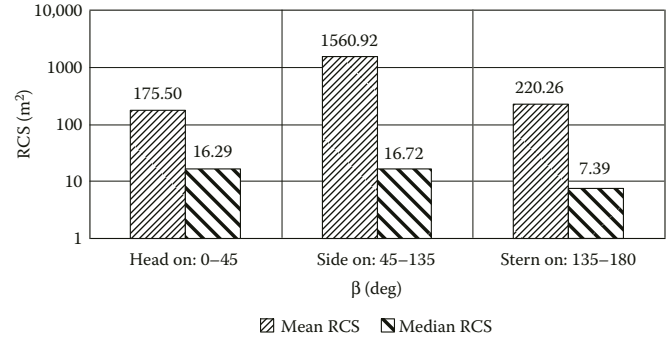

FIGURE 3.212 Diagrams of mean and median RCS of the T-90 tank model in three sectors of azimuth aspect given its radar observation at vertical polarization (ε = 1°, underlying surface – dry soil).

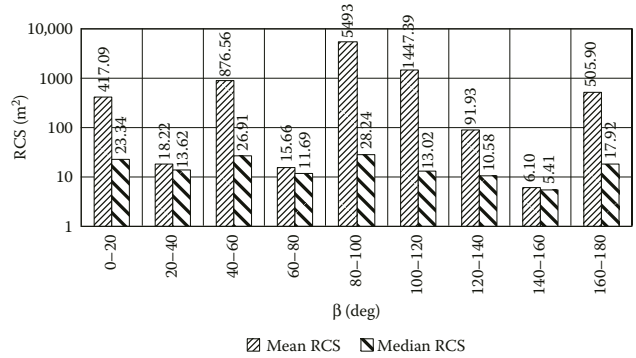

FIGURE 3.213 Diagrams of mean and median RCS of the T-90 tank model in 20-degree sectors of azimuth aspect given its radar observation at horizontal polarization (ε = 1°, underlying surface – dry soil).

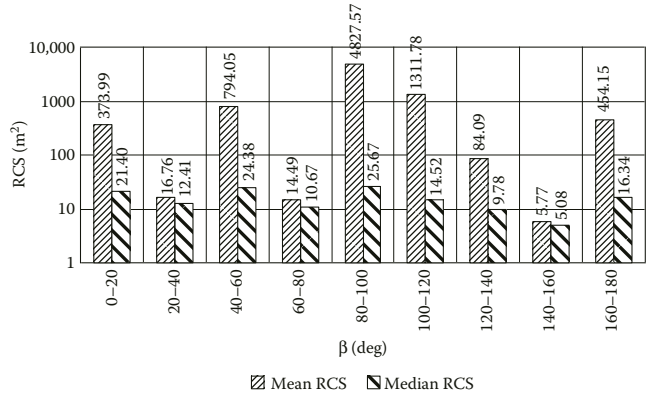

FIGURE 3.214 Diagrams of mean and median RCS of the T-90 tank model in 20-degree sectors of azimuth aspect given its radar observation at vertical polarization (ε = 1°, underlying surface – dry soil).

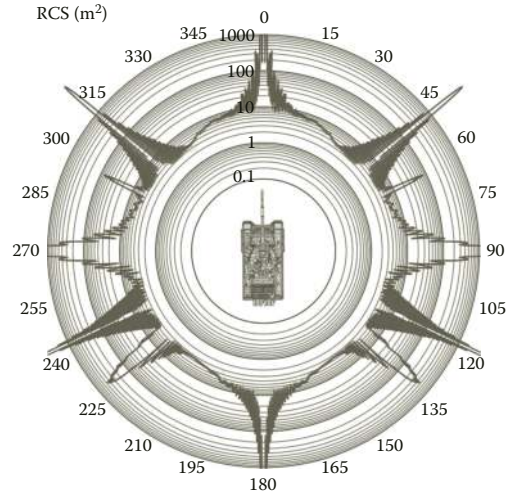

FIGURE 3.215 (**See color insert.**) Circular diagrams of noncoherent RCS given radar observation of T-90 tank model (ε = 1°, underlying surface – dry soil).

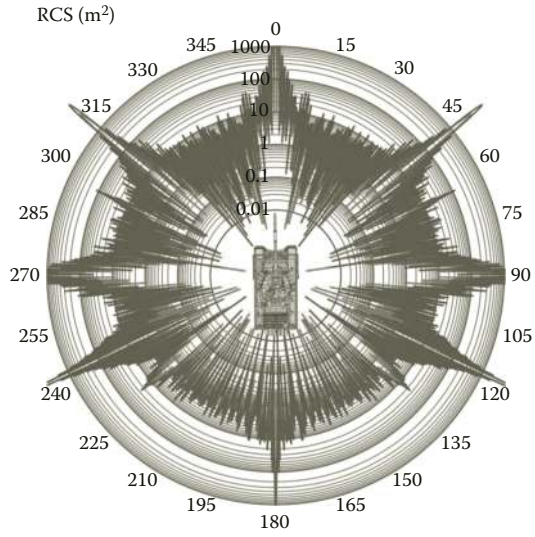

FIGURE 3.216 (**See color insert.**) Circular diagrams of instantaneous RCS given radar observation of T-90 tank model (ε = 10°, underlying surface – dry soil).

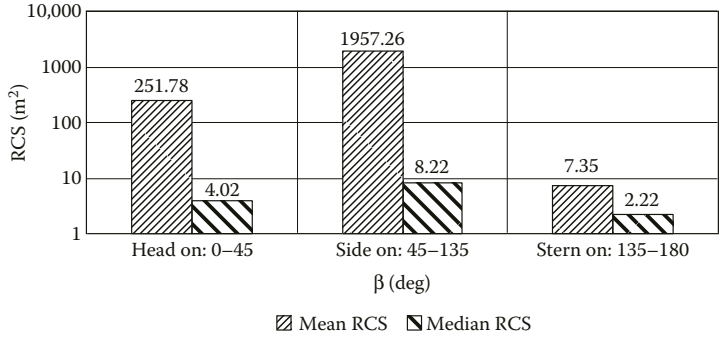

FIGURE 3.217 Diagrams of mean and median RCS of the T-90 tank model in three sectors of azimuth aspect given its radar observation at horizontal polarization (ε = 10°, underlying surface – dry soil).

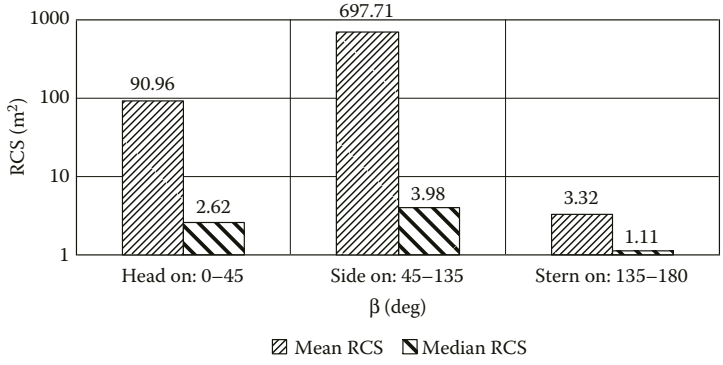

FIGURE 3.218 Diagrams of mean and median RCS of the T-90 tank model in three sectors of azimuth aspect given its radar observation at vertical polarization (ε = 10°, underlying surface – dry soil).

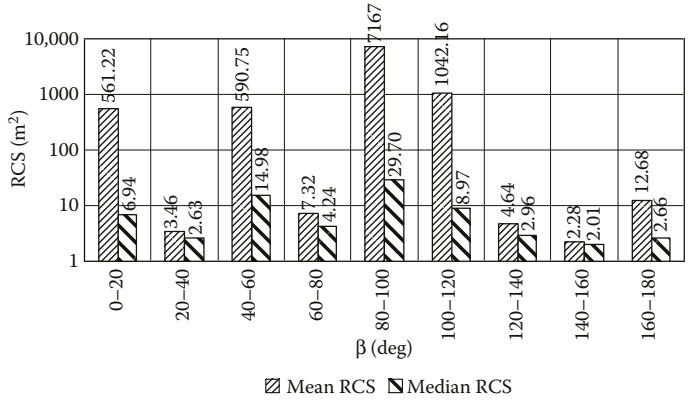

FIGURE 3.219 Diagrams of mean and median RCS of the T-90 tank model in 20-degree sectors of azimuth aspect given its radar observation at horizontal polarization (ε = 10°, underlying surface – dry soil).

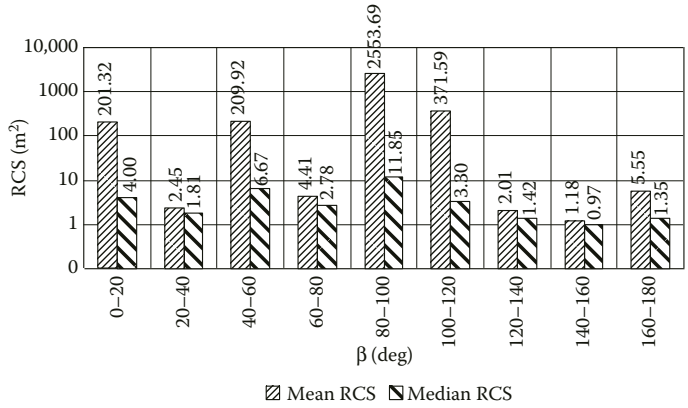

FIGURE 3.220 Diagrams of mean and median RCS of the T-90 tank model in 20-degree sectors of azimuth aspect given its radar observation at vertical polarization (ε = 10°, underlying surface – dry soil).

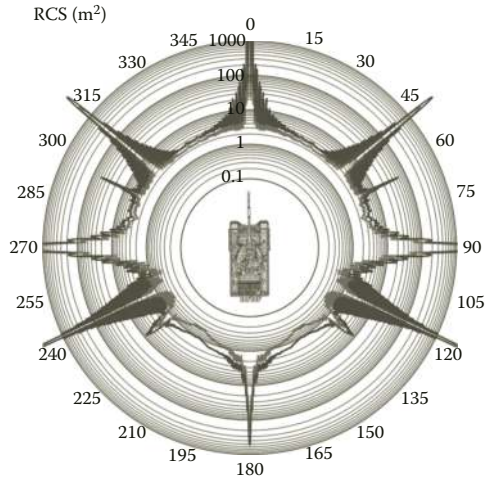

FIGURE 3.221 (**See color insert.**) Circular diagrams of noncoherent RCS of T-90 tank model (ε = 10°, underlying surface – dry soil).

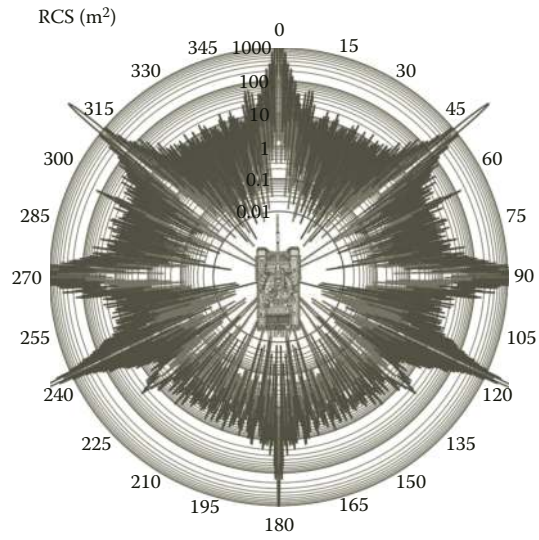

FIGURE 3.222 (**See color insert.**) Circular diagrams of instantaneous RCS of T-90 tank model (ε = 10°, underlying surface – moist soil).

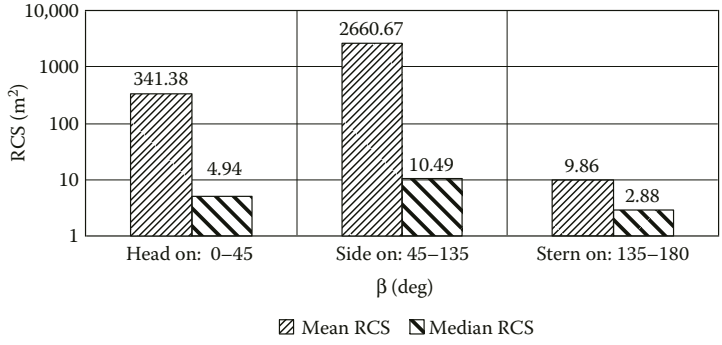

FIGURE 3.223 Diagrams of mean and median RCS of the T-90 tank model in three sectors of azimuth aspect given its radar observation at horizontal polarization (ε = 10°, underlying surface – moist soil).

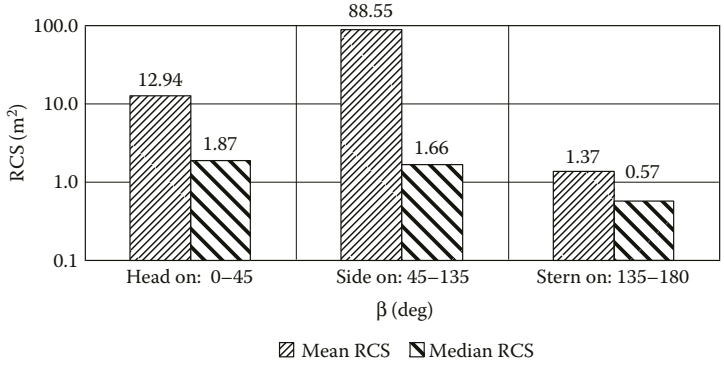

FIGURE 3.224 Diagrams of mean and median RCS of the T-90 tank model in three sectors of azimuth aspect given its radar observation at vertical polarization (ε = 10°, underlying surface – moist soil).

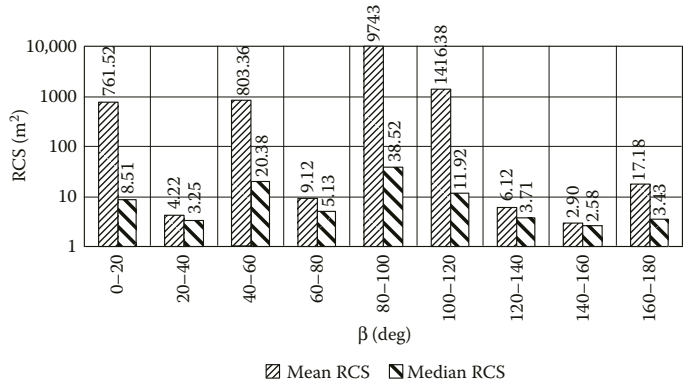

FIGURE 3.225 Diagrams of mean and median RCS of the T-90 tank model in 20-degree sectors of azimuth aspect given its radar observation at horizontal polarization (ε = 10°, underlying surface – moist soil).

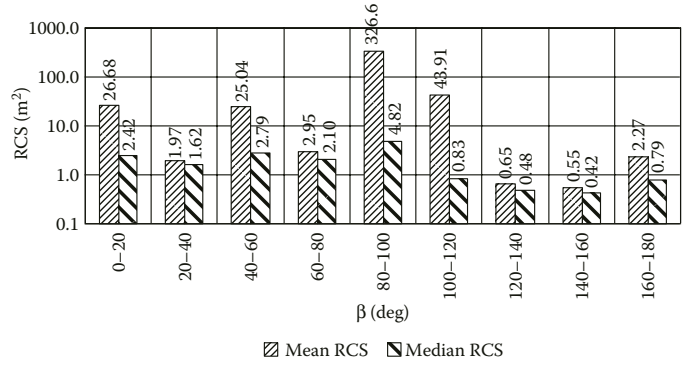

FIGURE 3.226 Diagrams of mean and median RCS of the T-90 tank model in 20-degree sectors of azimuth aspect given its radar observation at vertical polarization (ε = 10°, underlying surface – moist soil).

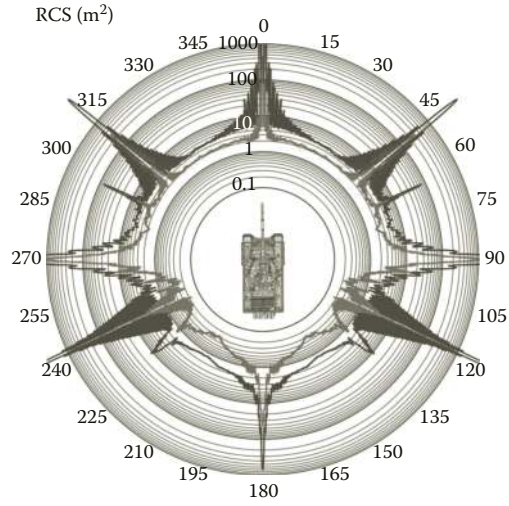

FIGURE 3.227 (**See color insert.**) Circular diagrams of noncoherent RCS of T-90 tank model (ε = 10°, underlying surface – moist soil).

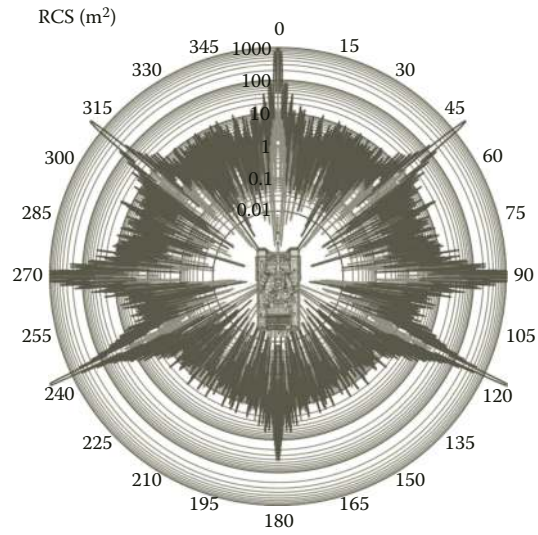

FIGURE 3.228 (**See color insert.**) Circular diagrams of instanteneous RCS of T-90 tank model (ε = 30°, underlying surface – dry soil).

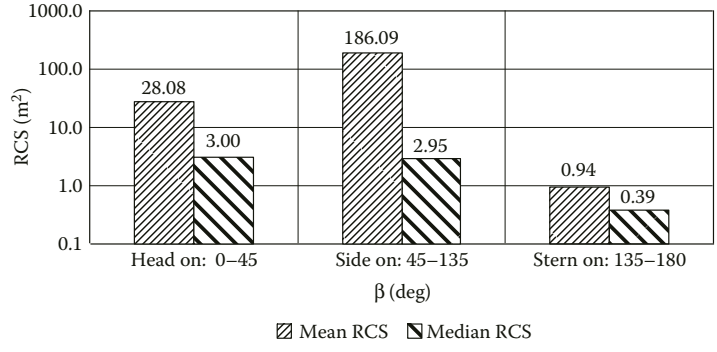

FIGURE 3.229 Diagrams of mean and median RCS of the T-90 tank model in three sectors of azimuth aspect given its radar observation at horizontal polarization (ε = 30°, underlying surface – dry soil).

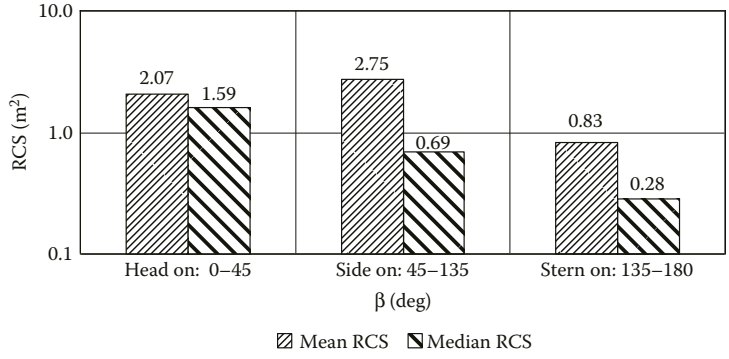

FIGURE 3.230 Diagrams of mean and median RCS of the T-90 tank model in three sectors of azimuth aspect given its radar observation at vertical polarization (ε = 30°, underlying surface – dry soil).

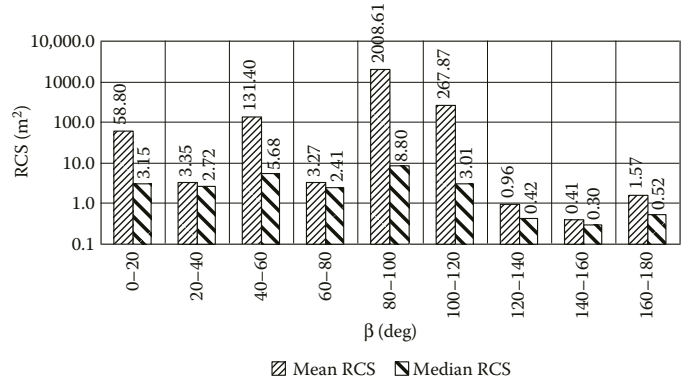

FIGURE 3.231 Diagrams of mean and median RCS of the T-90 tank model in 20-degree sectors of azimuth aspect given its radar observation at horizontal polarization (ε = 30°, underlying surface – dry soil).

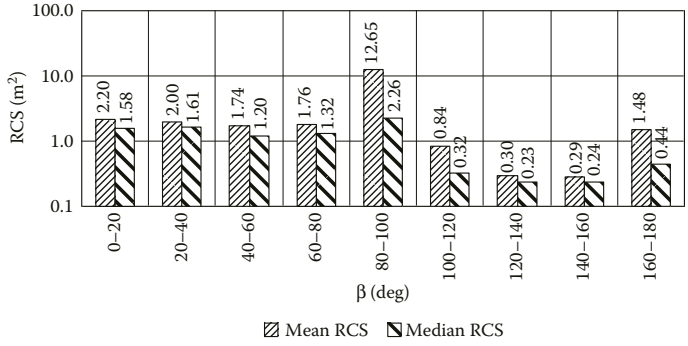

FIGURE 3.232 Diagrams of mean and median RCS of the T-90 tank model in 20-degree sectors of azimuth aspect given its radar observation at vertical polarization (ε = 30°, underlying surface – dry soil).

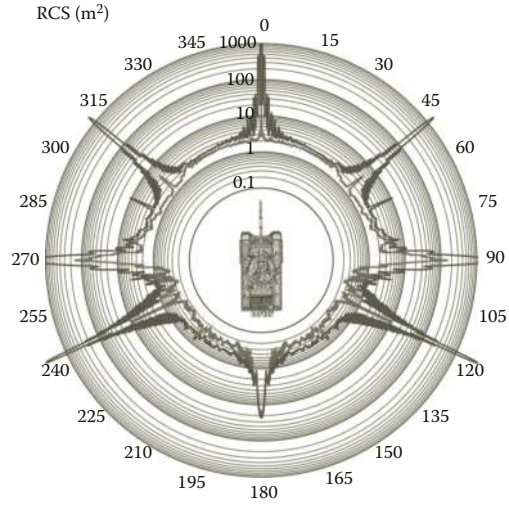

FIGURE 3.233 (**See color insert.**) Circular diagrams of noncoherent RCS of T-90 tank model (ε = 30°, underlying surface – dry soil).

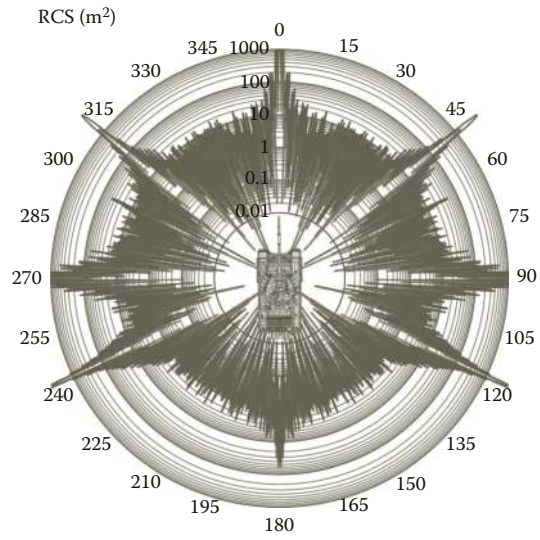

FIGURE 3.234 (**See color insert.**) Circular diagrams of instanteneous RCS of T-90 tank model (ε = 30°, underlying surface – moist soil).

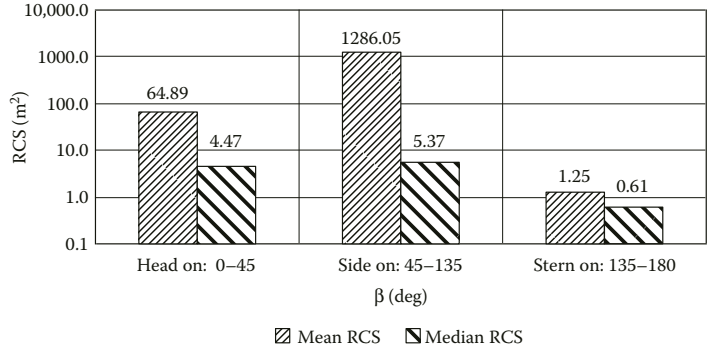

FIGURE 3.235 Diagrams of mean and median RCS of the T-90 tank model in three sectors of azimuth aspect given its radar observation at horizontal polarization (ε = 30°, underlying surface – moist soil).

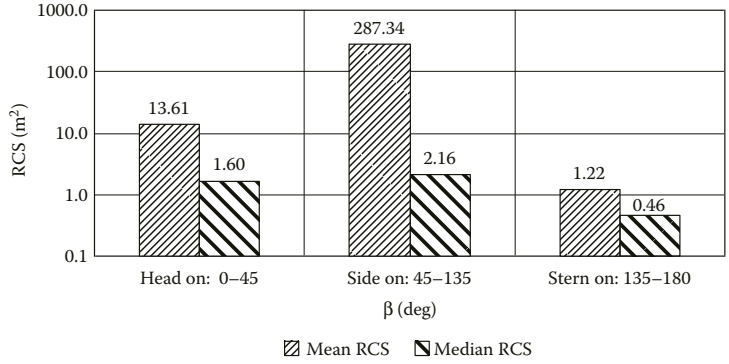

FIGURE 3.236 Diagrams of mean and median RCS of the T-90 tank model in three sectors of azimuth aspect given its radar observation at vertical polarization (ε = 30°, underlying surface – moist soil).

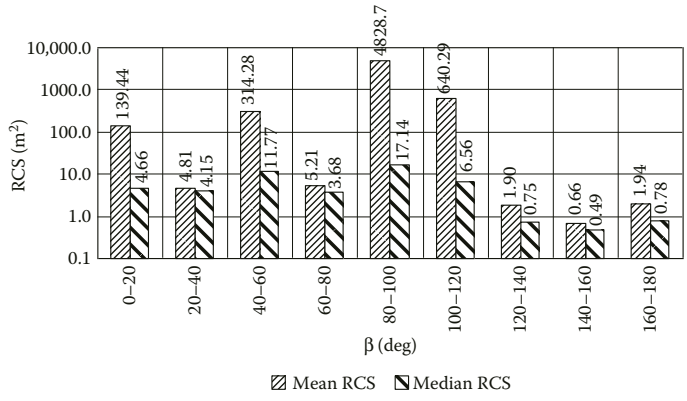

FIGURE 3.237 Diagrams of mean and median RCS of the T-90 tank model in 20-degree sectors of azimuth aspect given its radar observation at horizontal polarization (ε = 30°, underlying surface – moist soil).

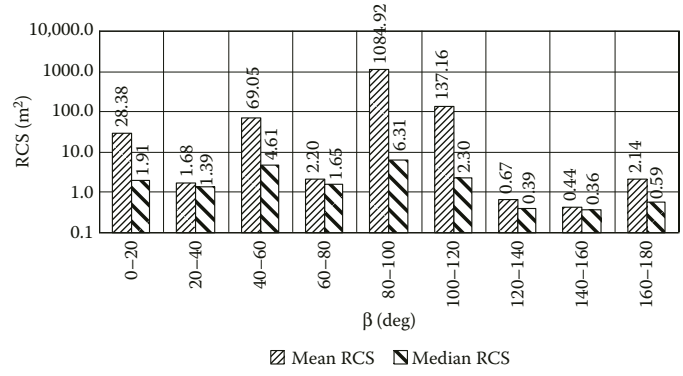

FIGURE 3.238 Diagrams of mean and median RCS of the T-90 tank model in 20-degree sectors of azimuth aspect given its radar observation at vertical polarization (ε = 30°, underlying surface – moist soil).

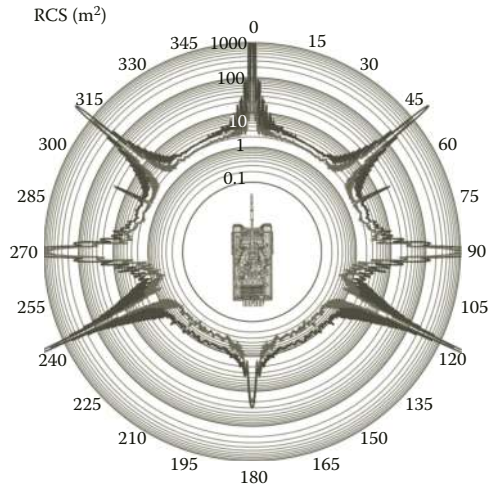

FIGURE 3.239 (**See color insert.**) Circular diagrams of noncoherent RCS of T-90 tank model (ε = 30°, underlying surface – moist soil).

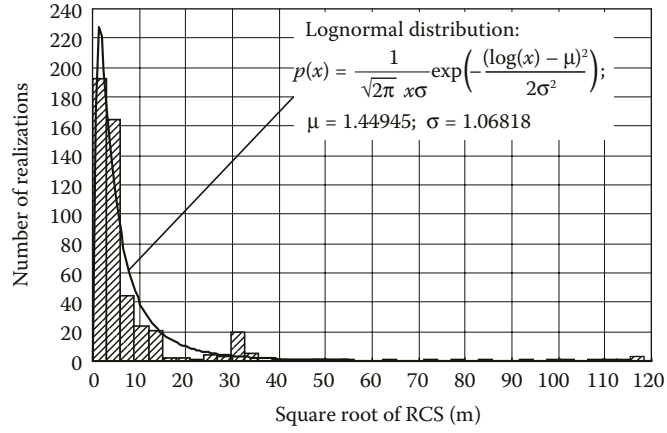

FIGURE 3.240 Amplitude distribution of echo signal given radar observation of T-90 tank model in the azimuth aspect sector from –10° through +10°, horizontal polarization (ε = 1°, underlying surface – dry soil).

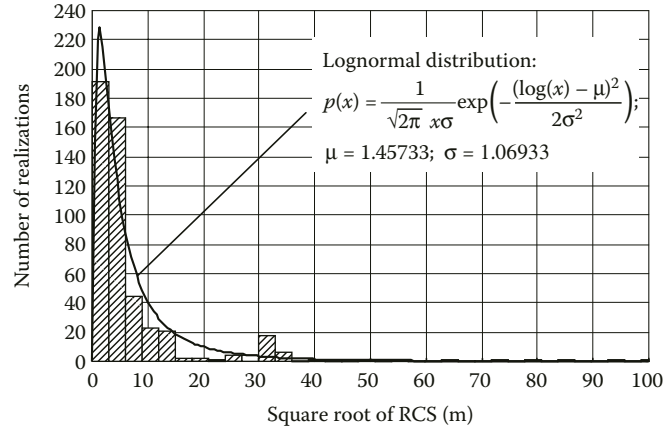

FIGURE 3.241 Amplitude distribution of echo signal given radar observation of T-90 tank model in the azimuth aspect sector from –10° through +10°, horizontal polarization (ε = 1°, underlying surface – moist soil).

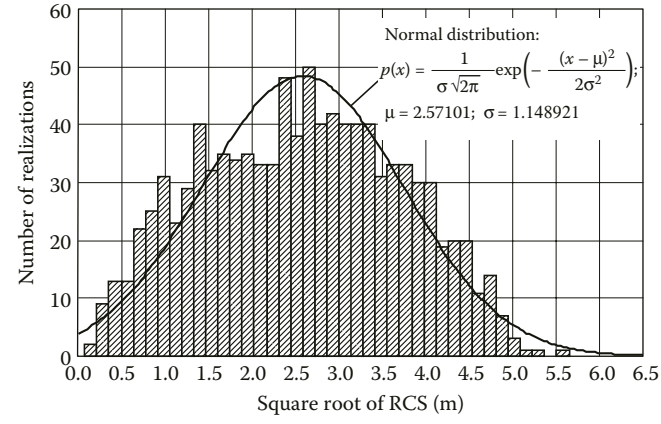

FIGURE 3.242 Amplitude distribution of echo signal given radar observation of T-90 tank model in the azimuth aspect sector from 10° through 30°, horizontal polarization (ε = 1°, underlying surface – dry soil).

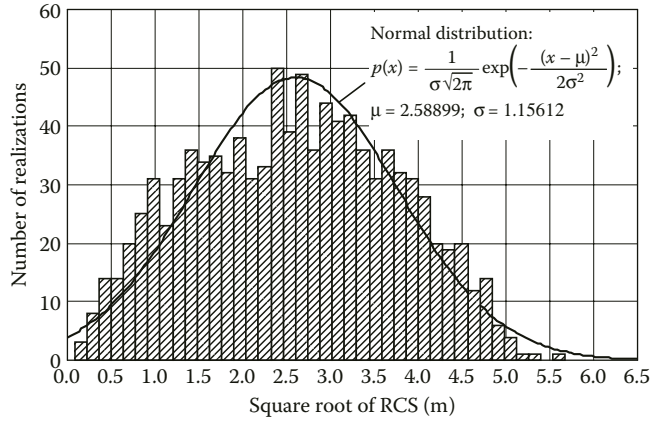

FIGURE 3.243 Amplitude distribution of echo signal given radar observation of T-90 tank model in the azimuth aspect sector from 10° through 30°, horizontal polarization (ε = 1°, underlying surface – moist soil).

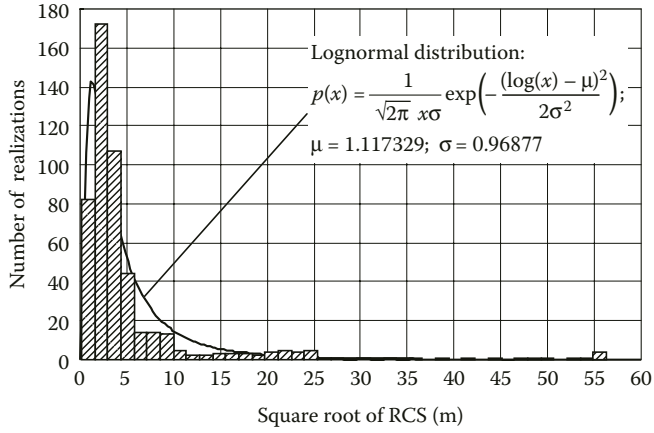

FIGURE 3.244 Amplitude distribution of echo signal given radar observation of T-90 tank model in the azimuth aspect sector from –10° through +10°, horizontal polarization (ε = 30°, underlying surface – dry soil).

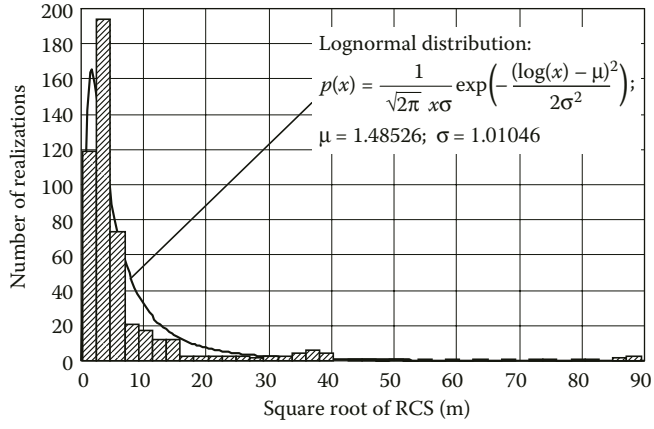

FIGURE 3.245 Amplitude distribution of echo signal given radar observation of T-90 tank model in the azimuth aspect sector from –10° through +10°, horizontal polarization (ε = 30°, underlying surface – moist soil).

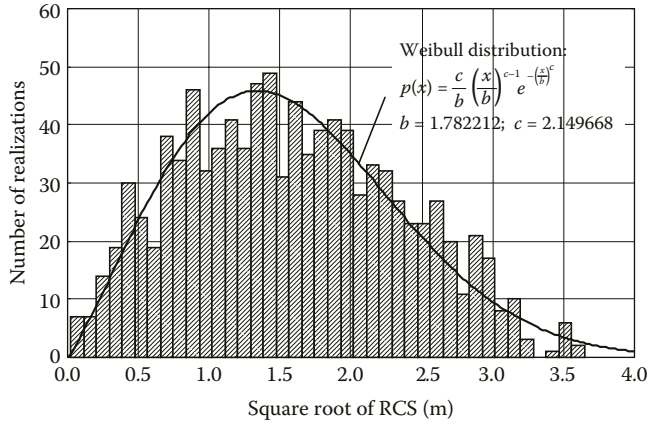

FIGURE 3.246 Amplitude distribution of echo signal given radar observation of T-90 tank model in the azimuth aspect sector from 10° through 30°, horizontal polarization (ε = 30°, underlying surface – dry soil).

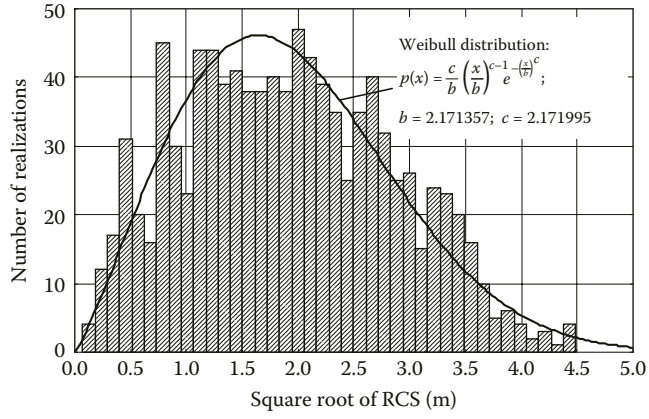

FIGURE 3.247 Amplitude distribution of echo signal given radar observation of T-90 tank model in the azimuth aspect sector from 10° through 30°, horizontal polarization (ε = 30°, underlying surface – moist soil).

TABLE 3.16
Parameters of Probability Distributions for the Echo Signal Amplitudes of T-90 Tank Model Given Elevation Angle of Illumination Equal to 1°

Azimuth Aspect Range	Soil Type	Polarization	Distribution Kind	Distribution Parameters
−10° ⋯ +10°	Dry soil	Horizontal	Lognormal distribution: $p(x) = \frac{1}{\sqrt{2\pi}x\sigma}\exp\left(-\frac{(\log(x)-\mu)^2}{2\sigma^2}\right)$	μ = 1.44945 σ =1.06818
		Vertical	Lognormal distribution	μ = 1.40716 σ = 1.09705

(*continued*)

TABLE 3.16 (continued)
Parameters of Probability Distributions for the Echo Signal Amplitudes of T-90 Tank Model Given Elevation Angle of Illumination Equal to 1°

Azimuth Aspect Range	Soil Type	Polarization	Distribution Kind	Distribution Parameters
	Moist soil	Horizontal	Lognormal distribution	$\mu = 1.45733$ $\sigma = 1.06933$
		Vertical	Lognormal distribution	$\mu = 1.36692$ $\sigma = 1.09704$
10° ⋯ 30°	Dry soil	Horizontal	Normal distribution: $p(x) = \frac{1}{\sigma\sqrt{2\pi}}\exp\left(-\frac{(x-\mu)^2}{2\sigma^2}\right)$	$\mu = 2.57101$ $\sigma = 1.148921$
		Vertical	Weibull distribution: $p(x) = \frac{c}{b}\left(\frac{x}{b}\right)^{c-1} e^{-\left(\frac{x}{b}\right)^c}$	$b = 2.75873$ $c = 2.32431$
	Moist soil	Horizontal	Normal distribution	$\mu = 2.58899$ $\sigma = 1.15612$
		Vertical	Weibull distribution	$b = 2.671515$ $c = 2.320417$

TABLE 3.17
Parameters of Probability Distributions for the Echo Signal Amplitudes of T-90 Tank Model Given Elevation Angle of Illumination Equal to 30°

Azimuth Aspect Range	Soil Type	Polarization	Distribution Kind	Distribution Parameters
−10° ⋯ +10°	Dry soil	Horizontal	Lognormal distribution: $p(x) = \frac{1}{\sqrt{2\pi}x\sigma}\exp\left(-\frac{(\log(x)-\mu)^2}{2\sigma^2}\right)$	$\mu = 1.117329$ $\sigma = 0.96877$
		Vertical	Normal distribution: $p(x) = \frac{1}{\sigma\sqrt{2\pi}}\exp\left(-\frac{(x-\mu)^2}{2\sigma^2}\right)$	$\mu = 1.588124$ $\sigma = 0.732297$
	Moist soil	Horizontal	Lognormal distribution	$\mu = 1.48526$ $\sigma = 1.01046$
		Vertical	lognormal distribution	$\mu = 0.71735$ $\sigma = 1.04842$
10° ⋯ 30°	Dry soil	Horizontal	Weibull distribution: $p(x) = \frac{c}{b}\left(\frac{x}{b}\right)^{c-1} e^{-\left(\frac{x}{b}\right)^c}$	$b = 1.782212$ $c = 2.149668$
		Vertical	Weibull distribution	$b = 1.381546$ $c = 2.163581$
	Moist soil	Horizontal	Weibull distribution	$b = 2.171357$ $c = 2.171995$
		Vertical	Rayleigh distribution: $p(x) = \frac{x}{b^2}\exp\left(-\frac{x^2}{2b^2}\right)$	$b = 0.927724$

3.2.2 Impulse Responses of T-90 Main Battle Tank

As an example, we consider HRRP of the T-90 main battle tank observed at the azimuth aspect of 15° and carrier frequency of 10 GHz (3 cm wavelength).

Bold solid lines in all figures below correspond to HRRPs obtained using signal with rectangular amplitude spectrum of 1 GHz bandwidth. Thin dashed lines correspond to HRRP obtained using signal with rectangular spectrum of 250 MHz bandwidth. Both wideband signals are centered at the same carrier frequency.

Figures 3.248 and 3.249 show HRRPs of T-90 tank standing on the dry soil given its illumination at the grazing elevation angle of 1° for the cases of horizontal and vertical polarization of illumination wave, respectively.

Figures 3.250 and 3.251 show HRRPs of T-90 tank standing on the moist soil given its illumination at grazing elevation angle of 1° for the cases of horizontal and vertical polarization of illumination wave, respectively.

Peaks #1 are due to scattering from the right track cover. Peaks #2 are due to scattering from the left track cover. Peaks #3 correspond to the earliest time of wave incidence upon the tank's turret. Peaks #4 correspond to the latest time of wave incidence upon the tank turret's front panel. Peaks #5 are due to scattering from the machine-gun superstructure.

It should be noted that edge local scatterers of the turret surface contribute somewhat into the amplitude of peaks #3 and #4. So, there is some difference in the amplitudes of peaks #3 and #4 given horizontal and vertical polarization of incident wave, respectively. Such difference in the

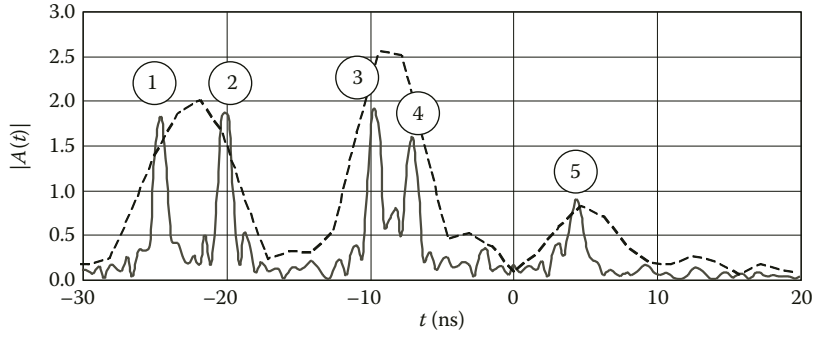

FIGURE 3.248 HRRP of T-90 tank model standing on dry soil given its radar observation at elevation of 1°, horizontal polarization.

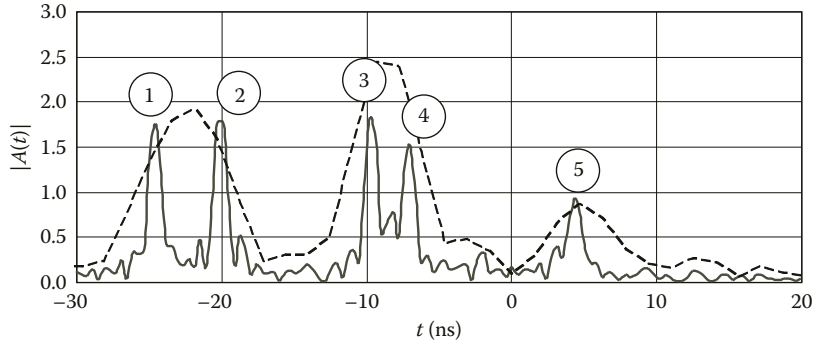

FIGURE 3.249 HRRP of T-90 tank model standing on dry soil given its radar observation at elevation of 1°, vertical polarization.

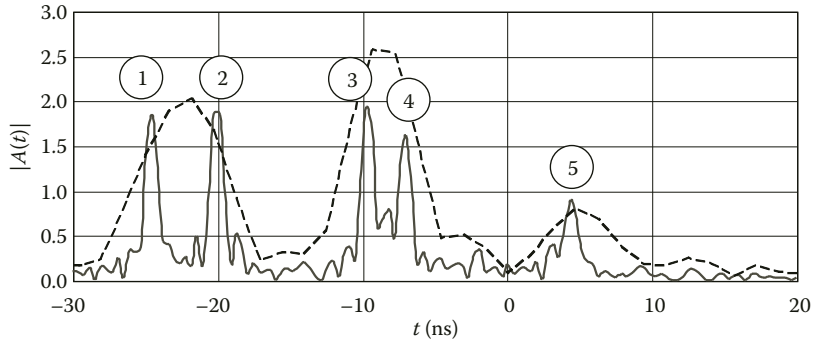

FIGURE 3.250 HRRP of T-90 tank model standing on moist soil given its radar observation at elevation of 1°, horizontal polarization.

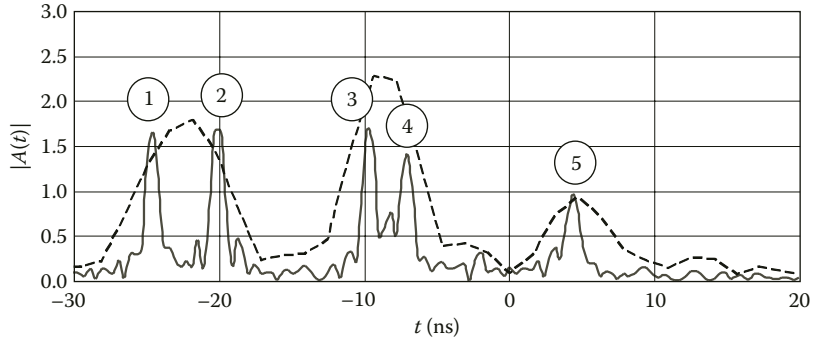

FIGURE 3.251 HRRP of T-90 tank model standing on moist soil given its radar observation at elevation of 1°, vertical polarization.

amplitudes of peaks #3 and #4 cannot be accounted by influence of underlying surface since, given radar observation of the tank model at grazing elevation of 1°, the surface reflection coefficients approach unit irrespectively of polarization and soil type.

Figures 3.252 and 3.253 show HRRPs of T-90 tank standing on the dry soil given its illumination at the elevation angle of 10° for the cases of horizontal and vertical polarization of illumination wave, respectively.

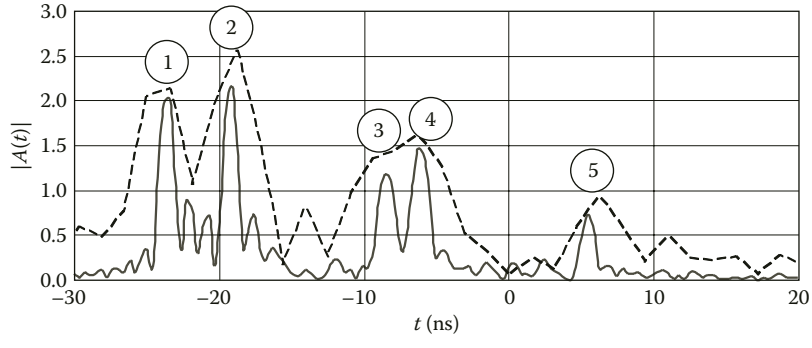

FIGURE 3.252 HRRP of T-90 tank model standing on dry soil given its radar observation at elevation of 10°, horizontal polarization.

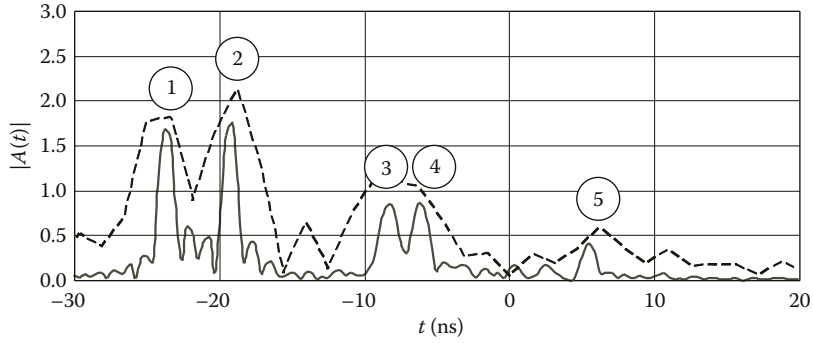

FIGURE 3.253 HRRP of T-90 tank model standing on dry soil given its radar observation at elevation of 10°, vertical polarization.

Figures 3.254 and 3.255 show HRRPs of T-90 tank standing on the moist soil given its illumination at the elevation angle of 10° for the cases of horizontal and vertical polarization of illumination wave, respectively.

The peaks of HRRPs in Figures 3.252 through 3.255 are numbered. Peaks #1 are due to scattering from the right track cover. Peaks #2 are due to scattering from the left track cover. Peaks #3 and #4 are due to scattering from the turret's front panel, the influence of underlying surface being accounted for. Peaks #5 are due to scattering from the turret's machine-gun superstructure, the influence of underlying surface being also accounted for.

Amplitude of HRRP peaks at horizontal polarization (Figures 3.252 and 3.254) is larger for the case of moist soil. This is conditioned by the greater reflection coefficient of moist soil at horizontal polarization given 10° angle of wave incidence (elevation angle). At the same time, the amplitudes of HRRP peaks at vertical polarization (Figures 3.253 and 3.255) are greater for the case of dry soil. This is conditioned by the fact that, given moist soil, the incidence (elevation) angle of 10° is close to the Bruster angle and the reflection coefficient at vertical polarization approaches zero.

Some of the peaks (#3, #4, and #5) correspond to the echoes that could be obtained only if the influence of underlying surface had been accounted for. Such peaks are of negligible amplitude or absent altogether in HRRPs obtained given vertical polarization of incident wave, where the ground reflection coefficient is significantly less than unit.

Figures 3.256 and 3.257 show HRRPs of T-90 tank standing on the dry soil given its illumination at the elevation angle of 30° for the cases of horizontal and vertical polarization of illumination wave, respectively.

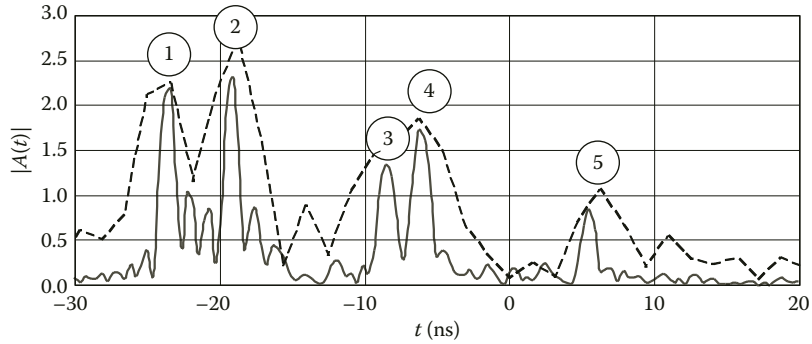

FIGURE 3.254 HRRP of T-90 tank model standing on moist soil given its radar observation at elevation of 10°, horizontal polarization.

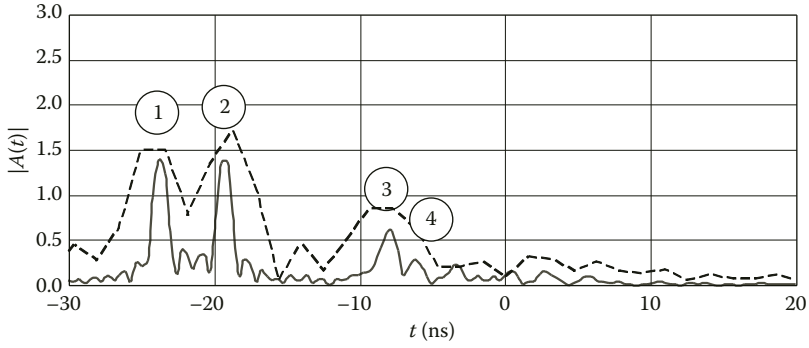

FIGURE 3.255 HRRP of T-90 tank model standing on moist soil given its radar observation at elevation of 10°, vertical polarization.

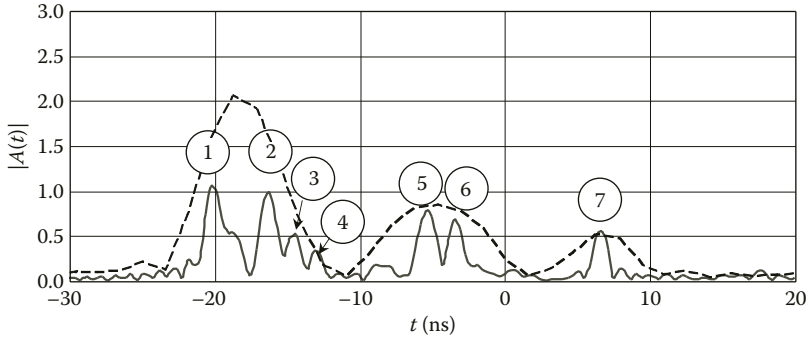

FIGURE 3.256 HRRP of T-90 tank model standing on dry soil given its radar observation at elevation of 30°, horizontal polarization.

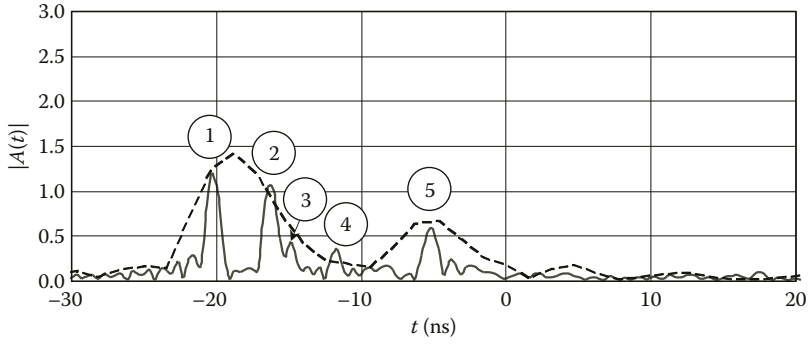

FIGURE 3.257 HRRP of T-90 tank model standing on dry soil given its radar observation at elevation of 30°, vertical polarization.

Figures 3.258 and 3.259 show HRRPs of T-90 tank standing on the moist soil given its illumination at the elevation angle of 30° for the cases of horizontal and vertical polarization of illumination wave, respectively.

The peaks of HRRPs in Figures 3.256 through 3.259 are numbered. Peaks #1 are due to scattering from the right track cover. Peaks #2 are due to scattering from the left track cover. Peaks #3 are due to scattering from left track (ground scattering is accounted for). Peaks #4 are due to

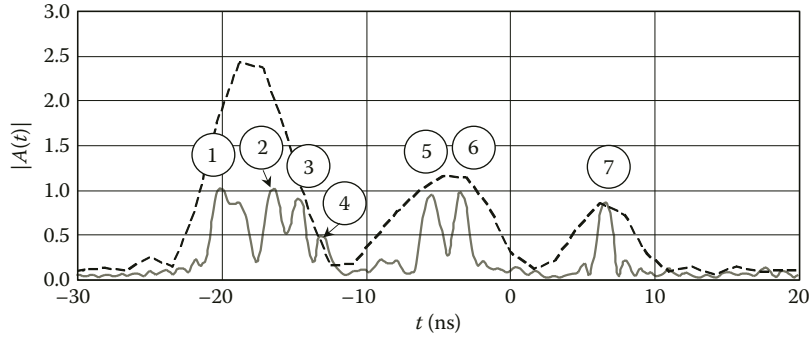

FIGURE 3.258 HRRP of T-90 tank model standing on moist soil given its radar observation at elevation of 30°, horizontal polarization.

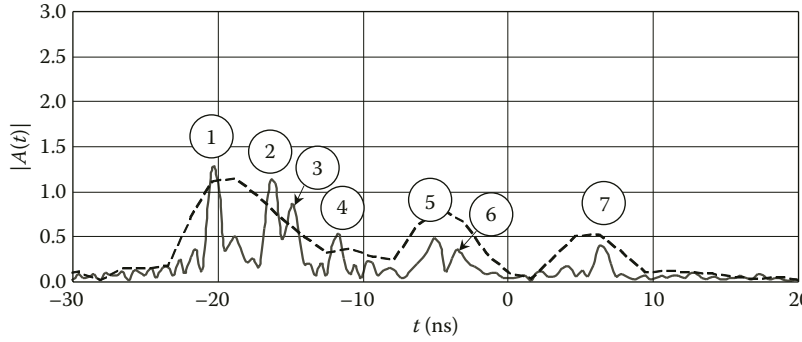

FIGURE 3.259 HRRP of T-90 tank model standing on moist soil given its radar observation at elevation of 30°, vertical polarization.

scattering from the side panel of tank's track skirt (ground scattering is accounted for). Peaks #5 are due scattering from the hatch on top of turret. Peaks #6 are due to scattering from the front panel of turret, ground influence being accounted for. Peaks #7 are due scattering from the machine-gun superstructure of the turret, ground influence being also accounted for. It should be noted that some of the peaks (#3, #6, and #7) correspond to the echoes that could be obtained only if the influence of underlying surface had been accounted for. Such peaks are of negligible amplitude or absent altogether in some HRRPs (Figure 3.257). The time shift of peaks #4 is also observable at the HRRP obtained given vertical polarization of incident wave (Figures 3.257 and 3.259). This apparently is due to the fact that, given horizontal polarization, the main scattering contribution is provided by the smooth part of side panel of tank's track skirt, whereas given vertical polarization the main contribution into these echoes is due to vertically oriented local edge scatterers of the same side panel.

Amplitude of peaks, both given horizontal (Figures 3.256 and 3.258) and vertical (Figures 3.257 and 3.259) polarization of incident wave, is greater for the case of moist soil. The latter is due to the greater reflection coefficients of moist soil for both horizontal and vertical polarizations given wave incidence angle (elevation) of 30°.

3.2.3 Scattering Characteristics of Leopard-2 Main Battle Tank

The Leopard-2 is apparently one of the most successful projects for developing the latter generation of battle tanks. Total number of specimens produced by now exceeds 3200. The Leopard-2 tanks are in service of the armies of Austria, Denmark, Germany, the Netherlands, Switzerland, Swiss, Finland, and so on. In March 2003, the contract had been put forward for furnishing 170 specimens

of Leopard-2 tanks of 2A6EX modification to the armed forces of Greece. In March 2006, the government of Chile made a contract for furnishing the 118 specimens of Leopard-2 tanks of 2A4 modification that had been decommissioned from the German army [102].

The tank has classical layout (Figure 3.260). Driver's compartment hatch is in the hull's forepart and it is slightly shifted to the right. It gets partially closed by the turret when the gun points straight forward. Despite the large inclination of the glacis armor (81°), the driver is still in sitting position while driving. The inside volume of driver's compartment is 2.4 m^3.

Tank commander and the gunner take their positions to the right of the gun; the loader takes his position to the left of it. The height of the fighting compartment from the turning floor up to ceiling inside the turret is 1650 mm, which is the lower margin providing the normal operating conditions for the loader in standing position. The inside volume of the fighting compartment is 10.1 m^3.

The engine and transmission compartment with the diesel engine placed along the tank's axis occupies the volume of 6.9 m^3 in the aft hull's section. It is separated by the fire-proofed bulkhead from the fighting compartment.

Considerable volume of the machine's inside space (19.4 m^3) conditioned its heavy weight (55.2 t) and overall width of 3700 mm. The latter, in its turn, necessitated the use of removable side armor screens to make it possible to ship the tank by railway.

The main tank's weapon is its 120 mm smoothbore gun by "Reinmetal." The gun barrel is equipped with thermal sleeve and bore evacuator made of glass-reinforced plastic.

Forehead of the hull and turret is protected by the multilayered combined spaced armor. The hull and turret are made up by welding. The turret's front armor plates have special hatches for mounting and dismounting the packs of combined armor barriers. The side armor is enforced by the removable anti-hollow-charge armor screens that consist of multiple layers and that are 110 mm thick in their frontal area. The front plates of turret's armor are vertical.

In our computations, we used the perfectly conducting computer model of the tank surface (Figure 3.261) that consisted of 57 smooth surface parts and 24 local edge scatterers. Parameters of the model are summarized in Table 3.18.

Figures 3.262 through 3.291 show diagrams of mean and median RCS and circular diagrams of instantaneous and noncoherent RCS obtained for the Leopard-2 tank model. The results are given for vertical and horizontal polarization, two types of underling surface and three elevation angles.

Figures 3.292 through 3.299 show the amplitude distributions of echo signals for two azimuth aspect sectors and two elevation angles.

Tables 3.19 and 3.20 summarize the parameters of distributions that fit mostly the simulation data for square root of RCS.

In Section 3.2.4, there are examples of HRRPs computed for the tank model given various illumination signal spectrum widths.

FIGURE 3.260 Leopard-2A4 basic combat tank.

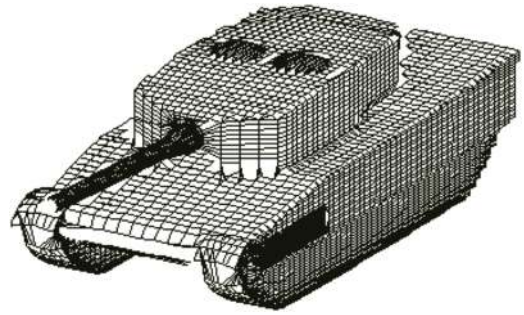

FIGURE 3.261 Computer model of Leopard-2 surface.

TABLE 3.18
Geometrical Characteristics of Leopard-2 Main Battle Tank

Hull Characteristics (Figure 3.260)		**Tank Surface Model Characteristics (Figure 3.261)**	
Tank length (gun included)	9.67 m	Number of parts of ellipsoids in the model	57
Width	3.70 m	Number of straight wedge parts in the model	24
Height	2.48 m		
Combat weight	55.15 t		

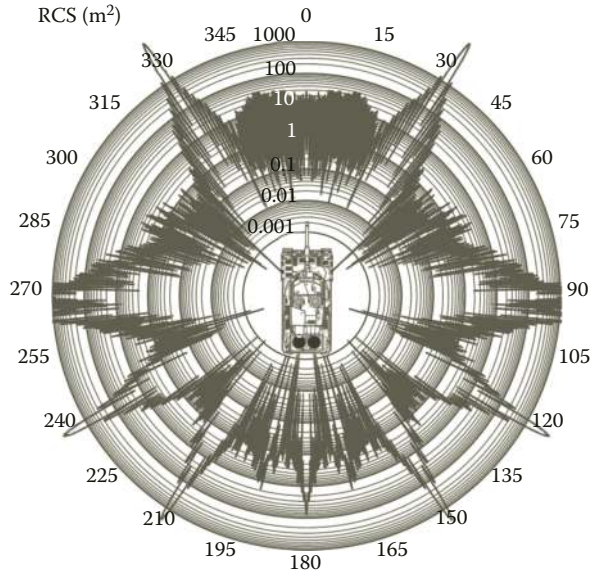

FIGURE 3.262 (**See color insert.**) Circular diagrams of instantaneous RCS given radar observation of Leopard-2 tank model (ε = 1°, underlying surface – dry soil).

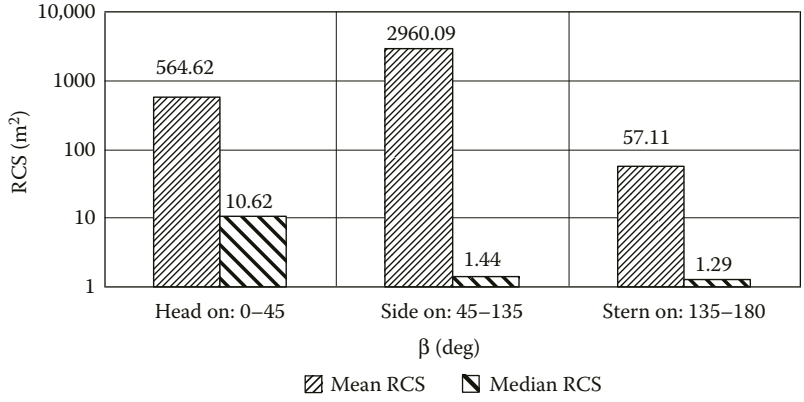

FIGURE 3.263 Diagrams of mean and median RCS of the Leopard-2 tank model in three sectors of azimuth aspect given its radar observation at horizontal polarization (ε = 1°, underlying surface – dry soil).

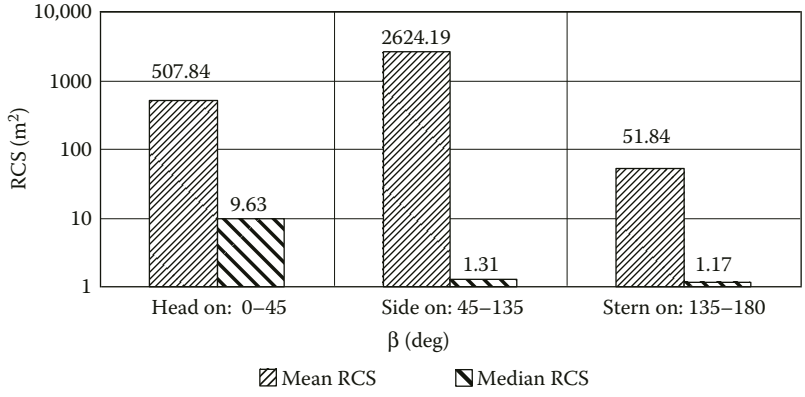

FIGURE 3.264 Diagrams of mean and median RCS of the Leopard-2 tank model in three sectors of azimuth aspect given its radar observation at vertical polarization (ε = 1°, underlying surface – dry soil).

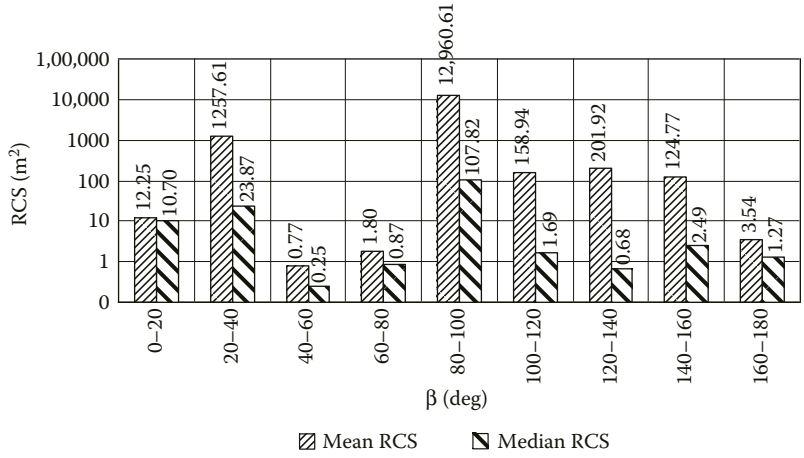

FIGURE 3.265 Diagrams of mean and median RCS of the Leopard-2 tank model in 20-degree sectors of azimuth aspect given its radar observation at horizontal polarization (ε = 1°, underlying surface – dry soil).

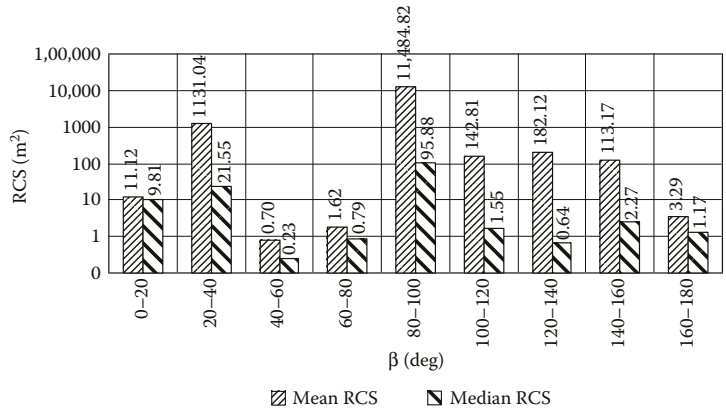

FIGURE 3.266 Diagrams of mean and median RCS of the Leopard-2 tank model in 20-degree sectors of azimuth aspect given its radar observation at vertical polarization (ε = 1°, underlying surface – dry soil).

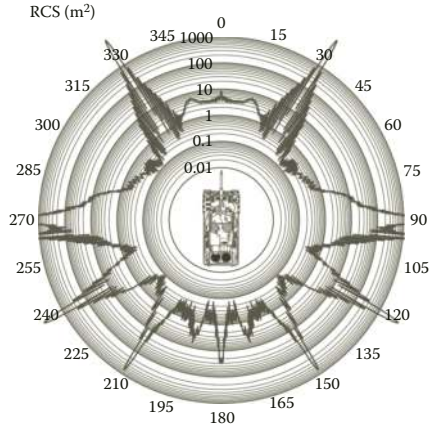

FIGURE 3.267 (**See color insert.**) Circular diagrams of noncoherent RCS given radar observation of Leopard-2 tank model (ε = 1°, underlying surface – dry soil).

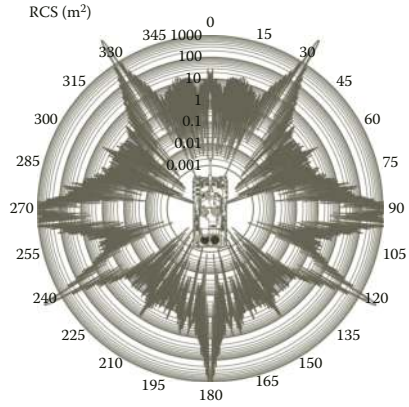

FIGURE 3.268 (**See color insert.**) Circular diagrams of instantaneous RCS given radar observation of Leopard-2 tank model (ε = 10°, underlying surface – dry soil).

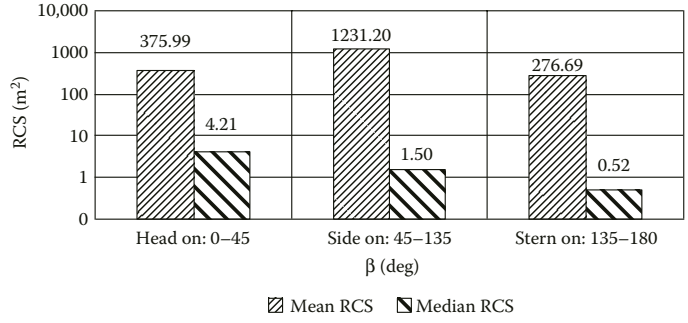

FIGURE 3.269 Diagrams of mean and median RCS of the Leopard-2 tank model in three sectors of azimuth aspect given its radar observation at horizontal polarization (ε = 10°, underlying surface – dry soil).

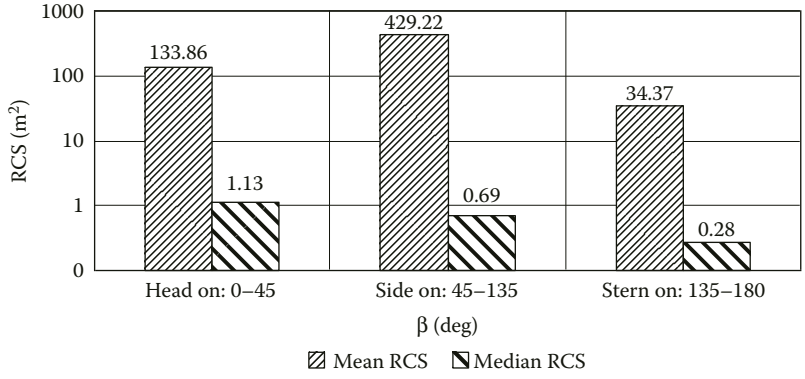

FIGURE 3.270 Diagrams of mean and median RCS of the Leopard-2 tank model in three sectors of azimuth aspect given its radar observation at vertical polarization (ε = 10°, underlying surface – dry soil).

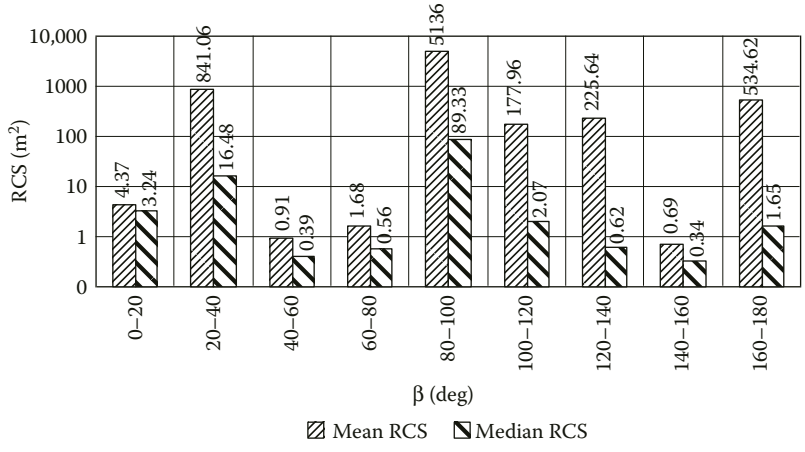

FIGURE 3.271 Diagrams of mean and median RCS of the Leopard-2 tank model in 20-degree sectors of azimuth aspect given its radar observation at horizontal polarization (ε = 10°, underlying surface – dry soil).

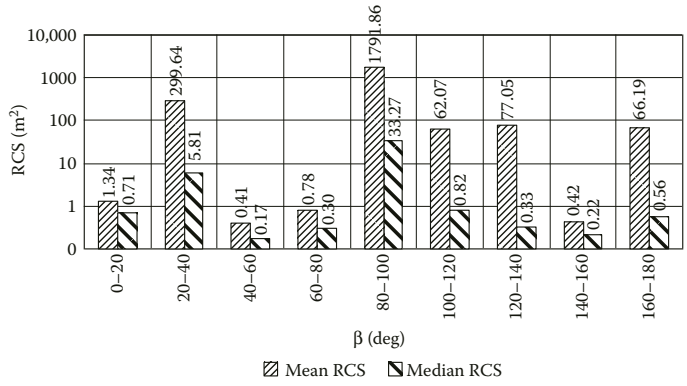

FIGURE 3.272 Diagrams of mean and median RCS of the Leopard-2 tank model in 20-degree sectors of azimuth aspect given its radar observation at vertical polarization (ε = 10°, underlying surface – dry soil).

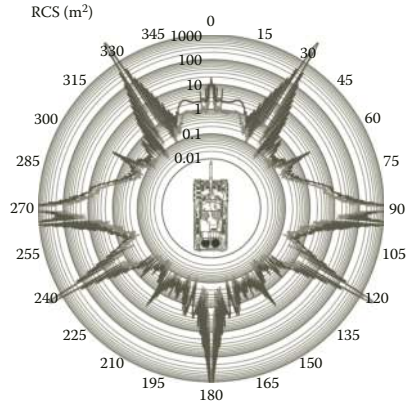

FIGURE 3.273 (**See color insert.**) Circular diagrams of noncoherent RCS of Leopard-2 tank model (ε = 10°, underlying surface – dry soil).

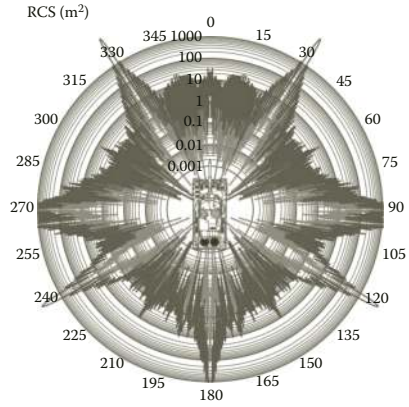

FIGURE 3.274 (**See color insert.**) Circular diagrams of instanteneous RCS of Leopard-2 tank model (ε = 10°, underlying surface – moist soil).

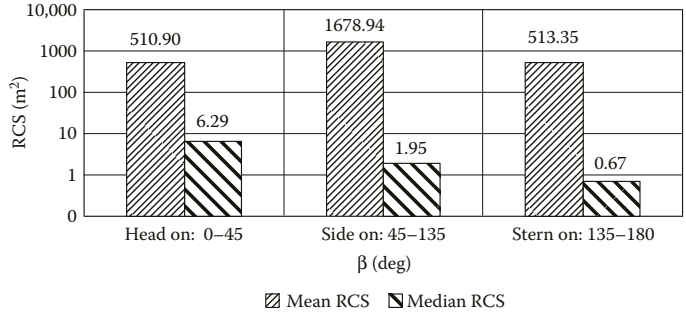

FIGURE 3.275 Diagrams of mean and median RCS of the Leopard-2 tank model in three sectors of azimuth aspect given its radar observation at horizontal polarization (ε = 10°, underlying surface – moist soil).

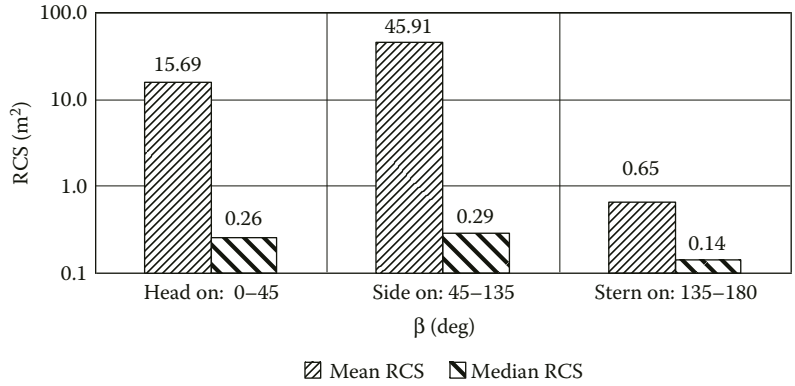

FIGURE 3.276 Diagrams of mean and median RCS of the Leopard-2 tank model in three sectors of azimuth aspect given its radar observation at vertical polarization (ε = 10°, underlying surface – moist soil).

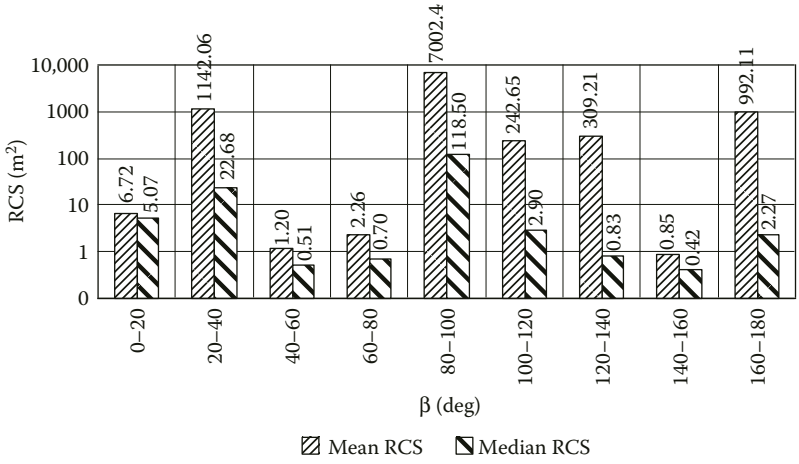

FIGURE 3.277 Diagrams of mean and median RCS of the Leopard-2 tank model in 20-degree sectors of azimuth aspect given its radar observation at horizontal polarization (ε = 10°, underlying surface – moist soil).

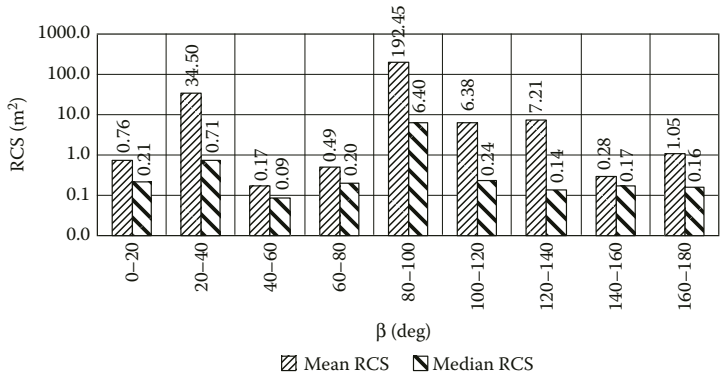

FIGURE 3.278 Diagrams of mean and median RCS of the Leopard-2 tank model in 20-degree sectors of azimuth aspect given its radar observation at vertical polarization (ε = 10°, underlying surface – moist soil).

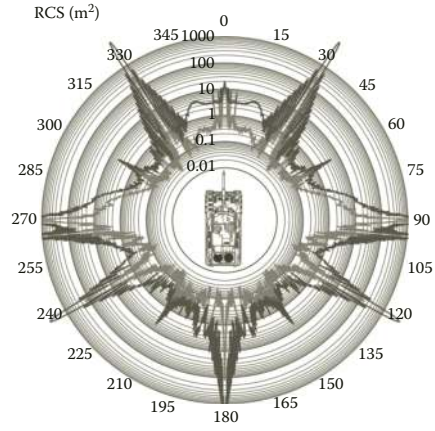

FIGURE 3.279 (**See color insert.**) Circular diagrams of noncoherent RCS of Leopard-2 tank model (ε = 10°, underlying surface – moist soil).

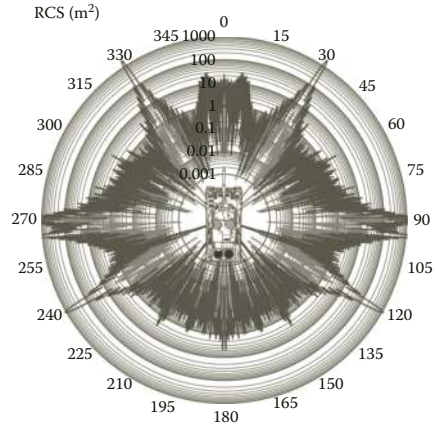

FIGURE 3.280 (**See color insert.**) Circular diagrams of instanteneous RCS of Leopard-2 tank model (ε = 30°, underlying surface – dry soil).

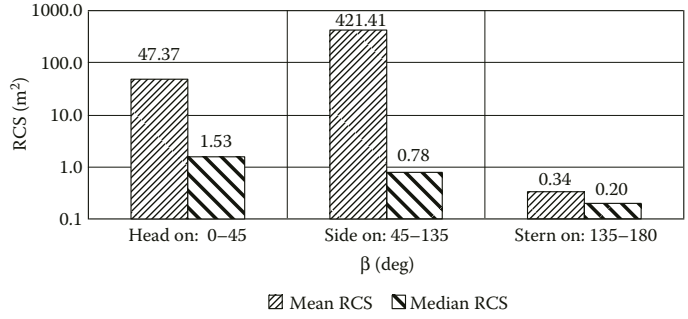

FIGURE 3.281 Diagrams of mean and median RCS of the Leopard-2 tank model in three sectors of azimuth aspect given its radar observation at horizontal polarization (ε = 30°, underlying surface – dry soil).

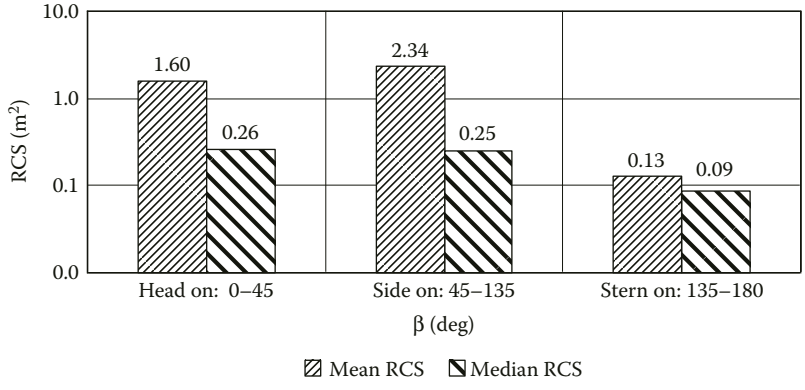

FIGURE 3.282 Diagrams of mean and median RCS of the Leopard-2 tank model in three sectors of azimuth aspect given its radar observation at vertical polarization (ε = 30°, underlying surface – dry soil).

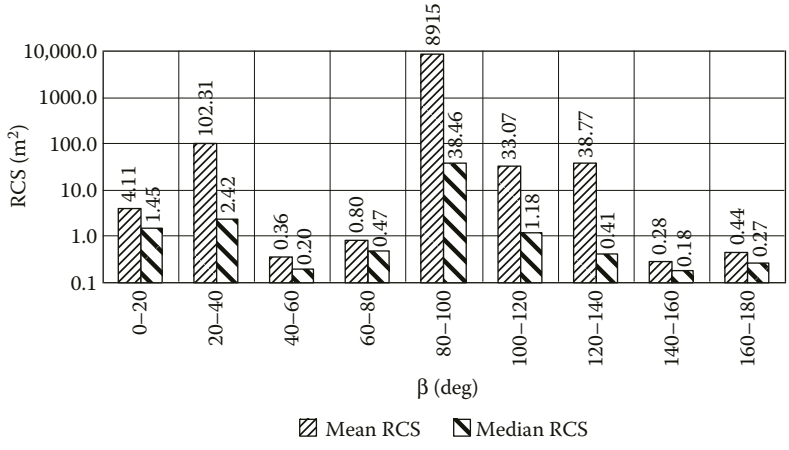

FIGURE 3.283 Diagrams of mean and median RCS of the Leopard-2 tank model in 20-degree sectors of azimuth aspect given its radar observation at horizontal polarization (ε = 30°, underlying surface – dry soil).

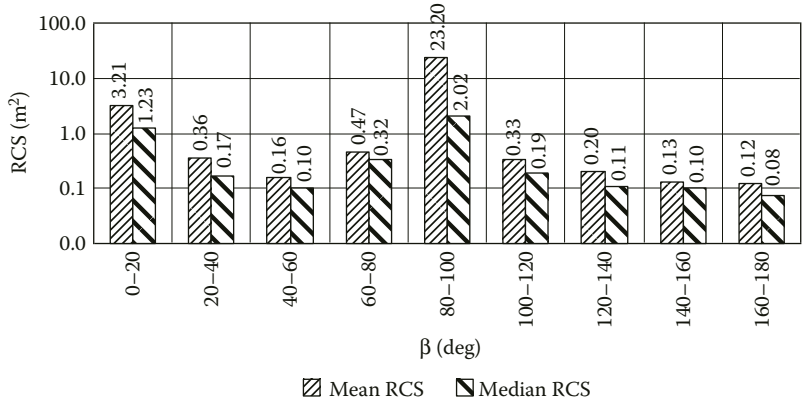

FIGURE 3.284 Diagrams of mean and median RCS of the Leopard-2 tank model in 20-degree sectors of azimuth aspect given its radar observation at vertical polarization (ε = 30°, underlying surface – dry soil).

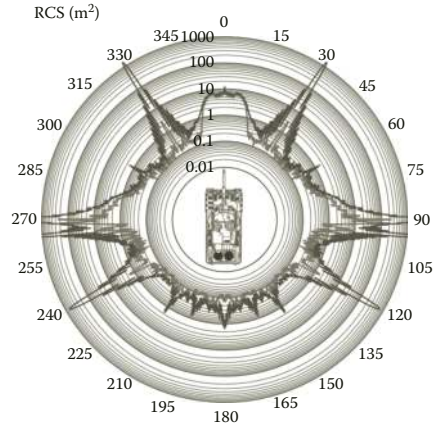

FIGURE 3.285 (**See color insert.**) Circular diagrams of noncoherent RCS of Leopard-2 tank model (ε = 30°, underlying surface – dry soil).

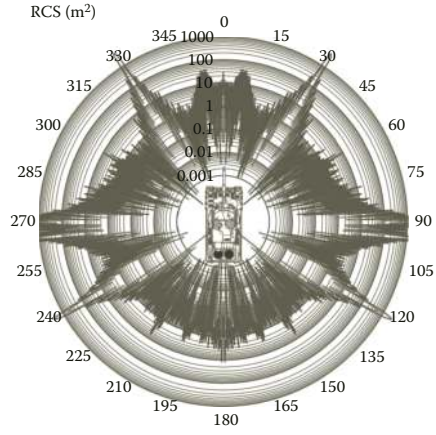

FIGURE 3.286 (**See color insert.**) Circular diagrams of instanteneous RCS of Leopard-2 tank model (ε = 30°, underlying surface – moist soil).

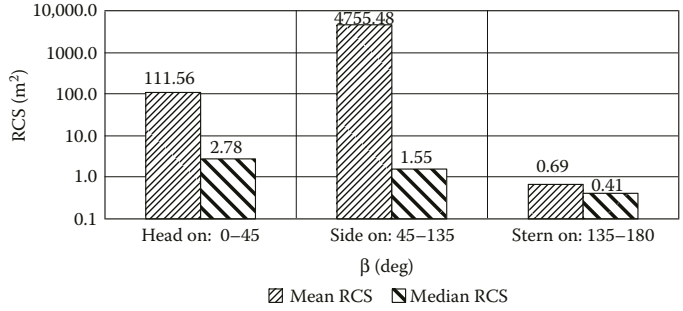

FIGURE 3.287 Diagrams of mean and median RCS of the Leopard-2 tank model in three sectors of azimuth aspect given its radar observation at horizontal polarization (ε = 30°, underlying surface – moist soil).

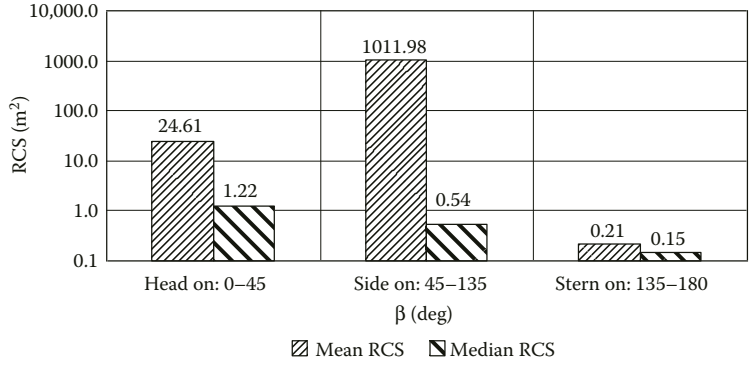

FIGURE 3.288 Diagrams of mean and median RCS of the Leopard-2 tank model in three sectors of azimuth aspect given its radar observation at vertical polarization (ε = 30°, underlying surface – moist soil).

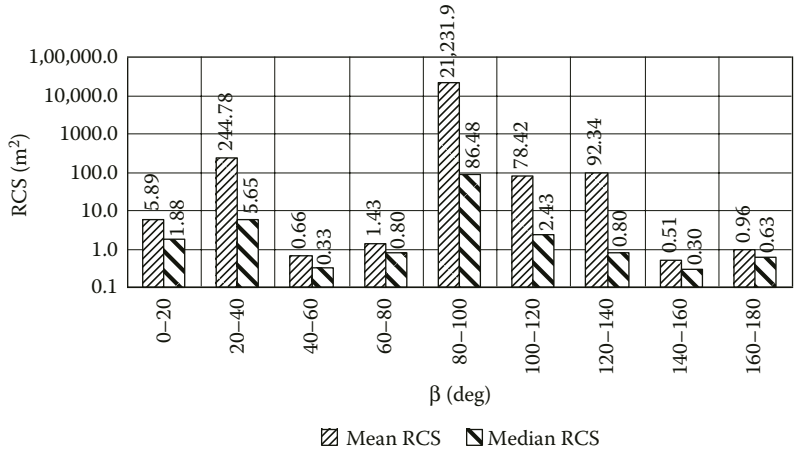

FIGURE 3.289 Diagrams of mean and median RCS of the Leopard-2 tank model in 20-degree sectors of azimuth aspect given its radar observation at horizontal polarization (ε = 30°, underlying surface – moist soil).

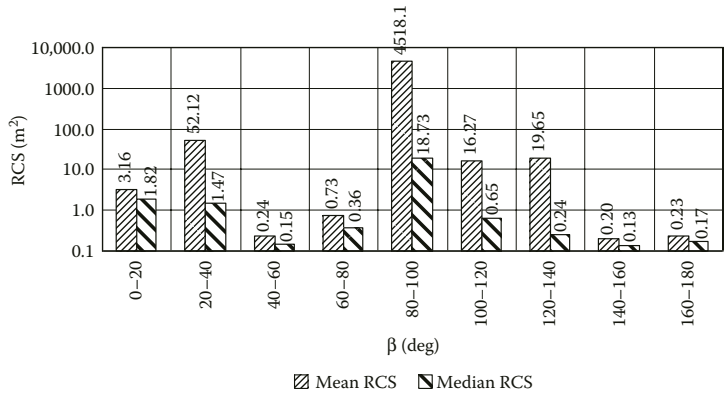

FIGURE 3.290 Diagrams of mean and median RCS of the Leopard-2 tank model in 20-degree sectors of azimuth aspect given its radar observation at vertical polarization (ε = 30°, underlying surface – moist soil).

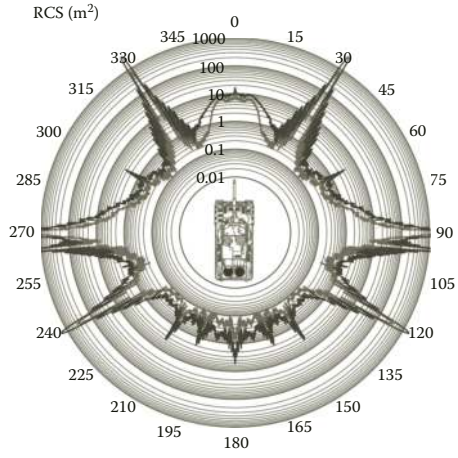

FIGURE 3.291 (**See color insert.**) Circular diagrams of noncoherent RCS of Leopard-2 tank model (ε = 30°, underlying surface – moist soil).

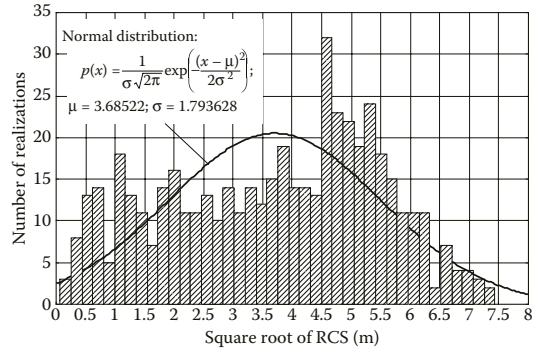

FIGURE 3.292 Amplitude distribution of echo signal given radar observation of Leopard-2 tank model in the azimuth aspect sector from –10° through +10°, horizontal polarization (ε = 1°, underlying surface – dry soil).

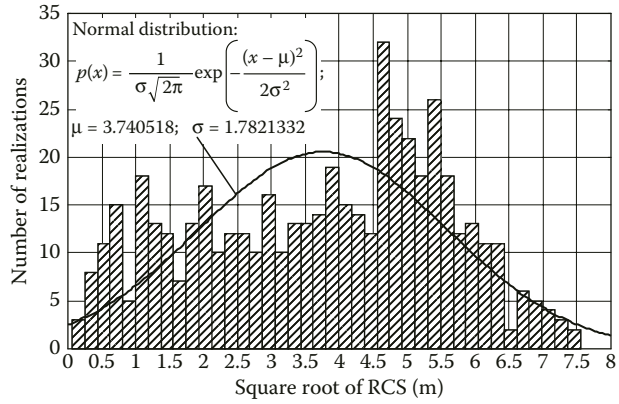

FIGURE 3.293 Amplitude distribution of echo signal given radar observation of Leopard-2 tank model in the azimuth aspect sector from –10° through +10°, horizontal polarization (ε = 1°, underlying surface – moist soil).

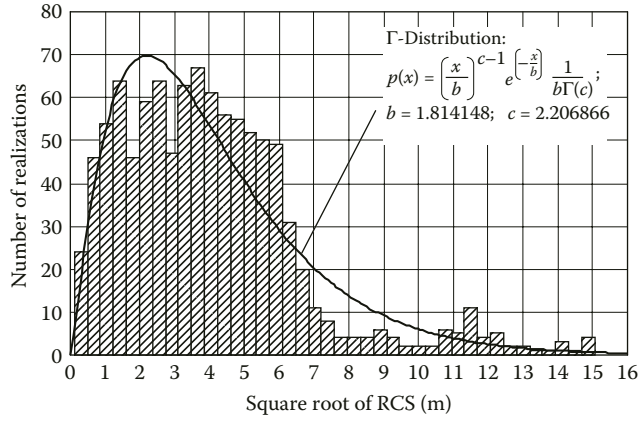

FIGURE 3.294 Amplitude distribution of echo signal given radar observation of Leopard-2 tank model in the azimuth aspect sector from 10° through 30°, horizontal polarization (ε = 1°, underlying surface – dry soil).

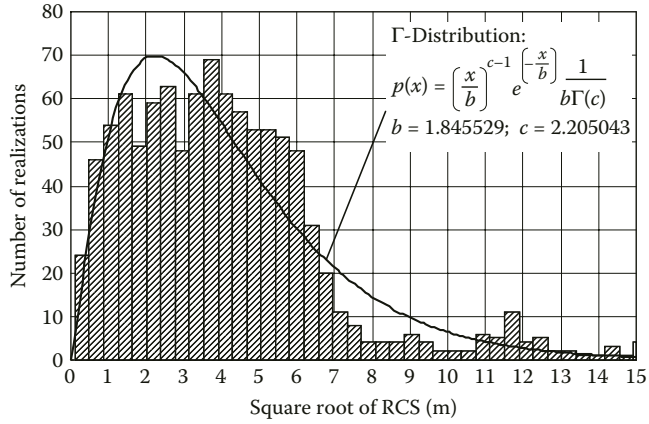

FIGURE 3.295 Amplitude distribution of echo signal given radar observation of Leopard-2 tank model in the azimuth aspect sector from 10° through 30°, horizontal polarization (ε = 1°, underlying surface – moist soil).

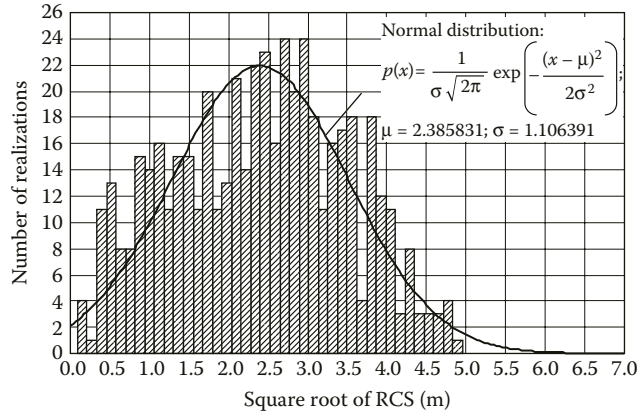

FIGURE 3.296 Amplitude distribution of echo signal given radar observation of Leopard-2 tank model in the azimuth aspect sector from –10° through +10°, horizontal polarization (ε = 30°, underlying surface – dry soil).

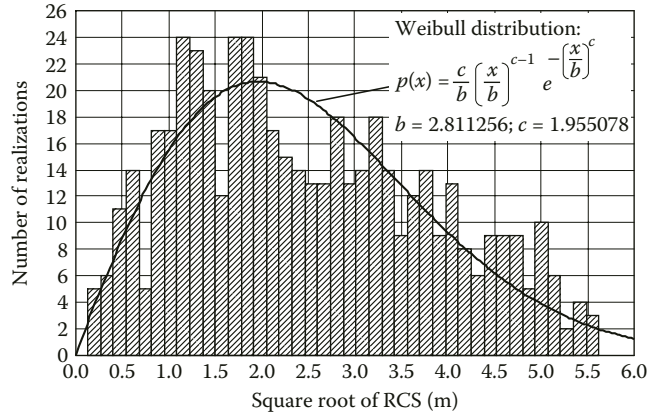

FIGURE 3.297 Amplitude distribution of echo signal given radar observation of Leopard-2 tank model in the azimuth aspect sector from –10° through +10°, horizontal polarization (ε = 30°, underlying surface – moist soil).

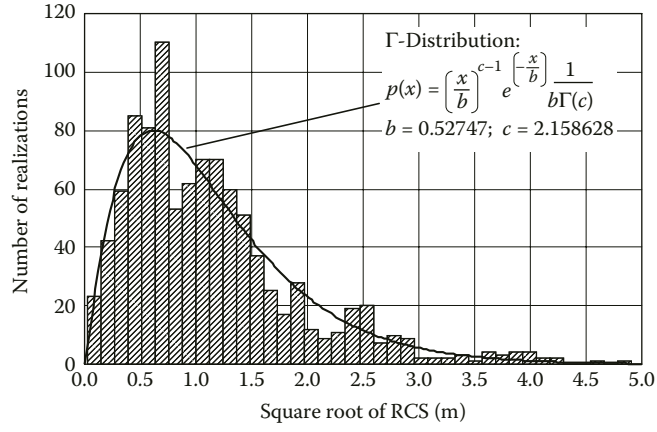

FIGURE 3.298 Amplitude distribution of echo signal given radar observation of Leopard-2 tank model in the azimuth aspect sector from 10° through 30°, horizontal polarization (ε = 30°, underlying surface – dry soil).

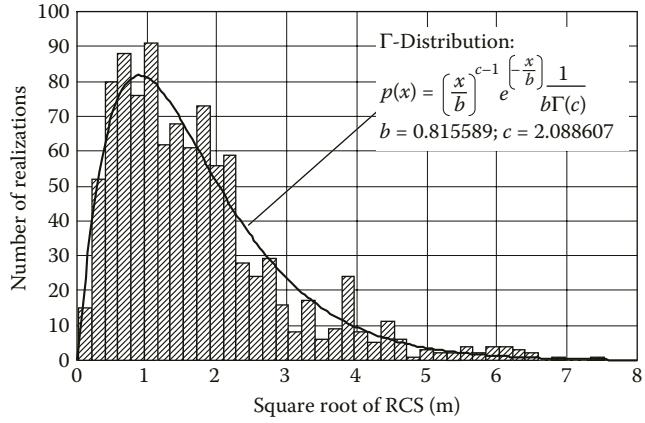

FIGURE 3.299 Amplitude distribution of echo signal given radar observation of Leonard-2 tank model in the azimuth aspect sector from 10° through 30°, horizontal polarization (ε = 30°, underlying surface – moist soil).

TABLE 3.19
Parameters of Probability Distributions for the Echo Signal Amplitudes of Leopard-2 Tank Model Given Elevation Angle of Illumination Equal to 1°

Azimuth Aspect Range	Soil Type	Polarization	Distribution Kind	Distribution Parameters
−10° ⋯ +10°	Dry soil	Horizontal	Normal distribution: $p(x) = \frac{1}{\sigma\sqrt{2\pi}} \exp\left(-\frac{(x-\mu)^2}{2\sigma^2}\right)$	μ = 3.68522 σ = 1.793628
		Vertical	Normal distribution	μ = 3.518374 σ = 1.710021
	Moist soil	Horizontal	Normal distribution	μ = 3.740518 σ = 1.821332
		Vertical	Normal distribution	μ = 3.28975 σ = 1.595294
10° ⋯ 30°	Dry soil	Horizontal	Γ-distribution: $p(x) = \left(\frac{x}{b}\right)^{c-1} e^{\left(-\frac{x}{b}\right)} \frac{1}{b\Gamma(c)}$, where Γ(c) is the gamma-function	b = 1.814148 c = 2.206866
		Vertical	Γ-distribution	b = 1.7225911 c = 2.21231
	Moist soil	Horizontal	Γ-distribution	b = 1.845529 c = 2.205043
		Vertical	Γ-distribution	b = 1.594283 c = 2.220279

TABLE 3.20
Parameters of Probability Distributions for the Echo Signal Amplitudes of Leopard-2 Tank Model Given Elevation Angle of Illumination Equal to 30°

Azimuth Aspect Range	Soil Type	Polarization	Distribution Kind	Distribution Parameters
–10° ⋯ +10°	Dry soil	Horizontal	Normal distribution: $p(x) = \frac{1}{\sigma\sqrt{2\pi}}\exp\left(-\frac{(x-\mu)^2}{2\sigma^2}\right)$	$\mu = 2.385831$ $\sigma = 1.106391$
		Vertical	Normal distribution	$\mu = 2.171519$ $\sigma = 0.98248$
	Moist soil	Horizontal	Weibull distribution: $p(x) = \frac{c}{b}\left(\frac{x}{b}\right)^{c-1} e^{-\left(\frac{x}{b}\right)^c}$	$b = 2.811256$ $c = 1.955078$
		Vertical	Normal distribution	$\mu = 1.89439$ $\sigma = 0.838508$
10° ⋯ 30°	Dry soil	Horizontal	Γ-distribution: $p(x) = \left(\frac{x}{b}\right)^{c-1} e^{\left(-\frac{x}{b}\right)} \frac{1}{b\Gamma(c)}$, where $\Gamma(c)$ is Gamma-function	$b = 0.52747$ $c = 2.158628$
		Vertical	Lognormal distribution: $p(x) = \frac{1}{\sqrt{2\pi}x\sigma}\exp\left(-\frac{(\log(x)-\mu)^2}{2\sigma^2}\right)$	$\mu = -1.04413$ $\sigma = 0.709801$
	Moist soil	Horizontal	Γ-distribution	$b = 0.815589$ $c = 2.088607$
		Vertical	Γ-distribution	$b = 0.42271$ $c = 2.362732$

3.2.4 Impulse Responses of Leopard-2 Main Battle Tank

As an example, we consider HRRPs of the Leopard-2 main battle tank observed at the azimuth aspect of 15° and carrier frequency of 10 GHz (3 cm wavelength).

Bold solid lines in Figures 3.300 through 3.308 below correspond to HRRPs obtained using signal with rectangular amplitude spectrum of 1 GHz bandwidth. Thin dashed lines correspond to HRRP obtained using signal with rectangular spectrum of 250 MHz bandwidth. Both wideband signals are centered at the same carrier frequency.

Figure 3.300 shows HRRPs of Leopard-2 tank model illuminated at grazing elevation angle of 1° (illumination almost along the ground). Unlike the T-90 tank model, the surface fractures do not contribute significantly into total echo from Leopard-2 tank model given this elevation. So, the difference between this tank model's HRRPs obtained given horizontal and vertical polarization of illuminating wave as well as given dry and moist soil as underlying surface is almost absent. Therefore, we present only impulse responses of the Leopard-2 tank model standing on dry soil given its illumination at horizontal polarization.

Peaks #1 are due to scattering from the right track cover. Peaks #2 are due to scattering from the side surface of right track skirt. Peaks #3 are due to scattering from the left track cover. Peaks #4 are due to scattering from the main gun mantlet. Peaks #5 are due to scattering from side surfaces of the turret and the right track cover. Peaks #6 are due to scattering from the turret's rear edge. Peaks #7 are due to scattering from the tank's stern.

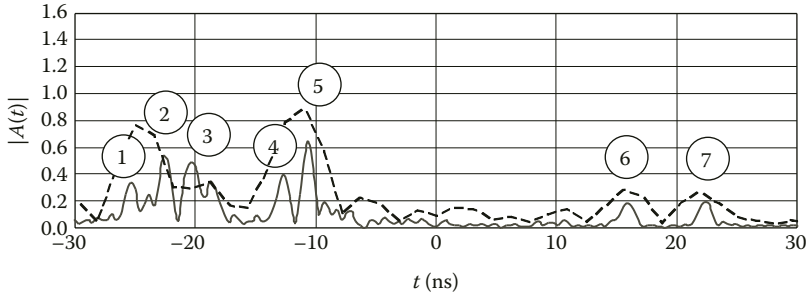

FIGURE 3.300 HRRPs of Leopard-2 tank model standing on dry soil given its radar observation at elevation of 1°, horizontal polarization.

Figures 3.301 and 3.302 show HRRPs of Leopard-2 tank model standing on dry soil (as underlying surface) given its illumination at the elevation angle of 10° by the waves with horizontal and vertical polarizations, respectively.

Figures 3.303 and 3.304 show HRRPs of Leopard-2 tank model standing on moist soil (as underlying surface) given its illumination at the elevation angle of 10° by the waves with horizontal and vertical polarizations, respectively.

Some peaks in Figures 3.301 through 3.304 are numbered. Peaks #1 are due to scattering from the right track cover. Peaks #2 are due to scattering from the left track cover. Peaks #3 are due to scattering from the side surface of right track skirt. Peaks #4 are due to scattering from the turret's rear edge. Peaks #5 are due scattering from the tank's stern.

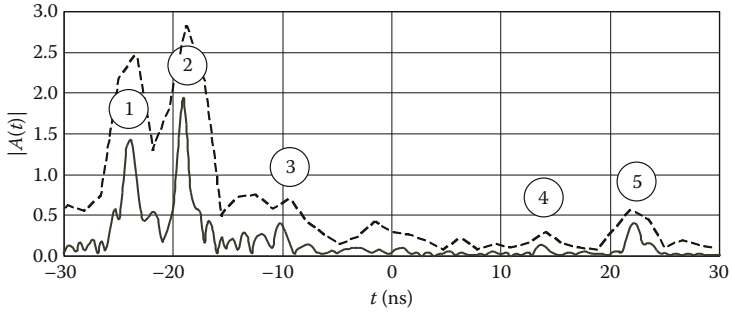

FIGURE 3.301 HRRPs of Leopard-2 tank model standing on dry soil given its radar observation at elevation of 10°, horizontal polarization.

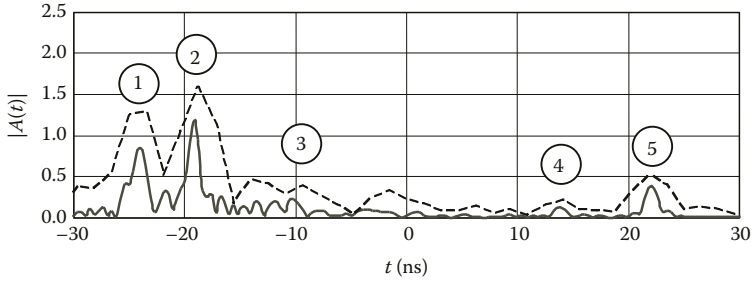

FIGURE 3.302 HRRPs of Leopard-2 tank model standing on dry soil given its radar observation at elevation of 10°, vertical polarization.

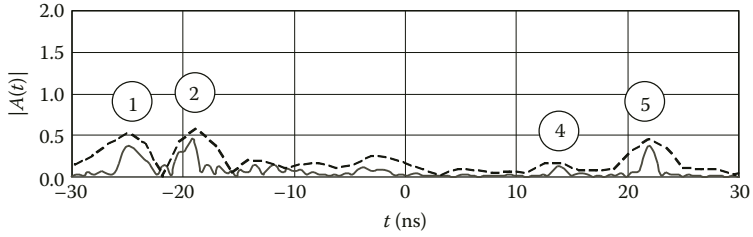

FIGURE 3.303 HRRPs of Leopard-2 tank model standing on moist soil given its radar observation at elevation of 10°, horizontal polarization.

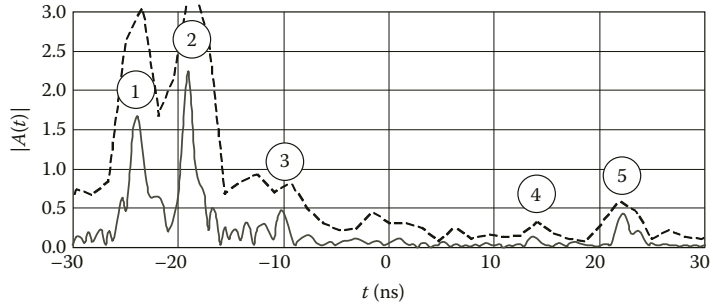

FIGURE 3.304 HRRPs of Leopard-2 tank model standing on moist soil given its radar observation at elevation of 10°, vertical polarization.

It is worth mentioning that the peaks are the superpositions of echoes propagated along different paths and shifted by different time delays thereof. Therefore, some peaks (for instance peaks #5) start to split. The amplitudes of peaks obtained at horizontal polarization (Figures 3.301 and 3.303) are greater in case of tank standing on moist soil. The latter is conditioned by the greater reflection coefficient of moist soil given illumination elevation angle of 10° at horizontal polarization. At the same time, given vertical polarization of illumination wave (Figures 3.302 and 3.304), the peak amplitudes are greater for the case of dry soil. The latter is due to the fact that elevation angle of illumination equal to 10° is close to the Bruster angle in case of moist soil, which leads to the surface reflection coefficient at vertical polarization approaching zero.

Amplitudes of most of HRRP peaks are greater in case of horizontal polarization than of those in case of vertical one given any soil type. The latter indicates the fact that electromagnetic energy bounced off the underlying surface significantly influences the HRRP formation.

Figures 3.305 and 3.306 show the HRRPs of Leopard-2 tank model standing on dry soil (as underlying surface) given its illumination at the elevation angle of 30° by the waves with horizontal and vertical polarizations respectively.

Figures 3.307 and 3.308 show the HRRPs of Leopard-2 tank model standing on moist soil (as underlying surface) given its illumination at the elevation angle of 30° by the waves with horizontal and vertical polarizations, respectively.

Some HRRP peaks in Figures 3.305 through 3.308 are numbered. Peaks #1 are due to scattering from the right track cover. Peaks #2 are due to scattering from the left track cover and from the right tank's track (surface reflection is accounted for). Peaks #3 are due to scattering from the right tank's track (surface reflection is accounted for). Peaks #4 and #5 are due to scattering from the left tank's track (surface reflection is accounted for). Peaks #6 are due to scattering from the hatch on turret's top. Peaks #7 are due to scattering from the tank's stern, surface scattering being accounted for. It should be noted that some peaks are due to echoes that could be received only via mediation of underlying surface. So, such peaks (for instance peaks # 3, #4, #5, and #7) can have

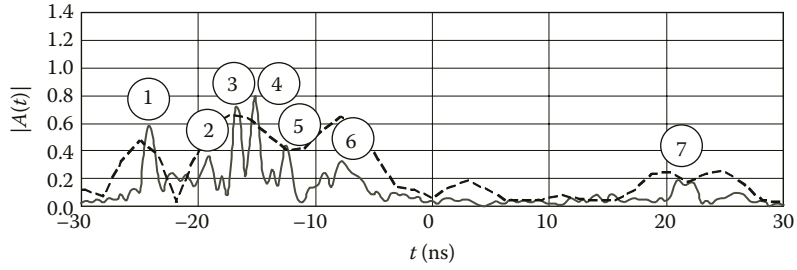

FIGURE 3.305 HRRPs of Leopard-2 tank model standing on dry soil given its radar observation at elevation of 30°, horizontal polarization.

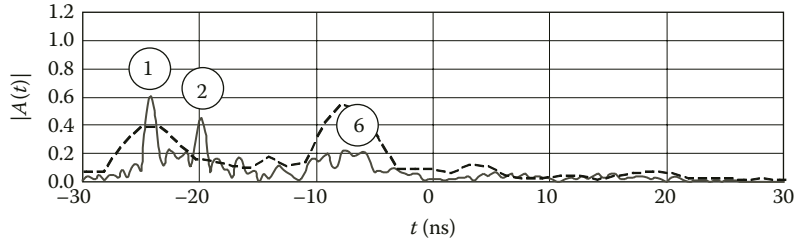

FIGURE 3.306 HRRPs of Leopard-2 tank model standing on dry soil given its radar observation at elevation of 30°, vertical polarization.

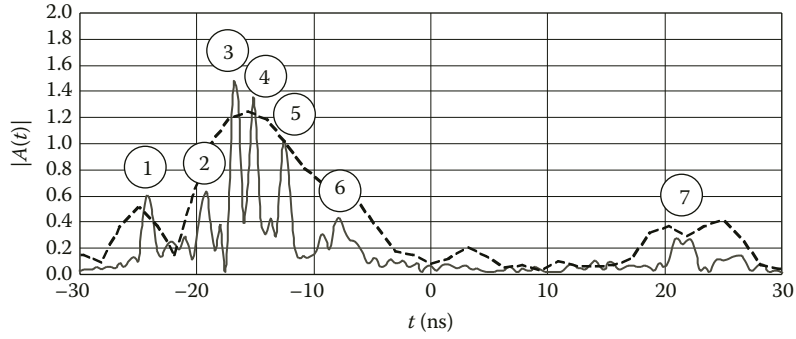

FIGURE 3.307 HRRPs of Leopard-2 tank model standing on moist soil given its radar observation at elevation of 30°, horizontal polarization.

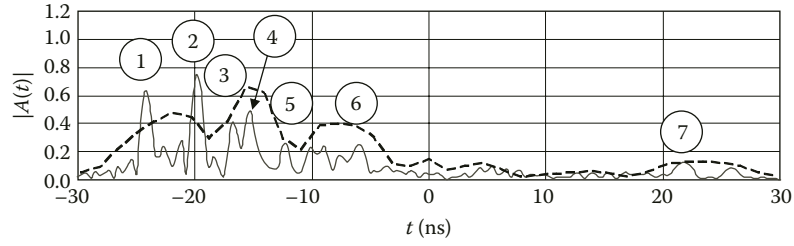

FIGURE 3.308 HRRPs of Leopard-2 tank model standing on moist soil given its radar observation at elevation of 30°, vertical polarization.

negligible amplitudes or can be absent altogether (Figure 3.306). Amplitudes of peaks given horizontal (Figures 3.305 and 3.307) and vertical (Figures 3.306 and 3.308) polarization of illumination wave are greater for the case of moist soil. This is due to the greater surface reflection coefficients of moist soil for both polarizations given illumination elevation angle of 30°.

3.2.5 Scattering Characteristics of M1A1 Abrams Main Battle Tank

Although the first specimens of series produced M1 Abrams tanks were made in 1980 at the government-owned Lima Army Tank Plant, the series production itself had not started until September 1981. Production of the baseline variant of M1 was stopped in January 1985, when a total of 2374 tanks of this modification had been produced [103].

The front hull part houses the driver's compartment of 2.5 m^3 volume. Fighting compartment of the 10.4 m^3 volume includes the hull center and circularly rotating turret. The turret houses primary and secondary weapons—the M68E1 stabilized in two planes 105 mm rifled gun with coaxial M240 7.62 mm machine gun. In front of the commander's hatch, there is a 12.7 mm Brauning M2 machine gun, and in front of the loader's hatch there is a MAG-58 machine gun.

The M1 Abrams tank design was aimed at the drastic increase in its protection against variety of weapons as compared to its predecessors (the M60). This aim has been achieved by the complex of design solutions: tank visibility reduction, application of heavy armor of new type, decrease in the heavy armor surface and use of armor cutouts, and designing rational internal layout. The low tank visibility is facilitated by the low tank's silhouette and disruptive pattern paint job that provided better masking capability compared to plain olive drab color scheme of M60 tanks.

The tank's hull and turret are made by welding (Figure 3.309). The hull consists of five large blocks. The turret consists of outer and inner armor shells tied together by stiffening ribs, the space between them being filled with combined armor packs consisting of steel and nonmetallic materials. Transmission is protected with sectional skirt screens (seven sections per side) made of spaced armor with filling. Each section thickness (except the first one) is about 70 mm, their total weight on both sides being 1.5 tons. Thickness of armor plates varies over the whole tank's surface according to statistics of hits by rounds: the glacis plate thickness goes up from 50 mm in its lower part to 125 mm at the turret's barbette; armor thickness around power plant and transmission compartment varies from 25 mm to 32.5 mm, that of turret varies from 25 mm to 125 mm, and that of hull's sides varies from 45 mm to 60 mm. In total, armor accounts for about 56% of the tank mass. The armor itself is based on the British-designed "Chobham" armor.

Computer model of the tank surface used in our scattering computations (Figure 3.310) consisted of 53 parts of ellipsoids and of 22 local edge scatterers. Parameters of computer model are summarized in Table 3.21.

Figures 3.311 through 3.340 show diagrams of mean and median RCS and circular diagrams of instantaneous and noncoherent RCS obtained for the M1A1 Abrams tank model. The results are given for vertical and horizontal polarization, two types of underling surface and three elevation angles.

FIGURE 3.309 M1A1 Abrams main battle tank.

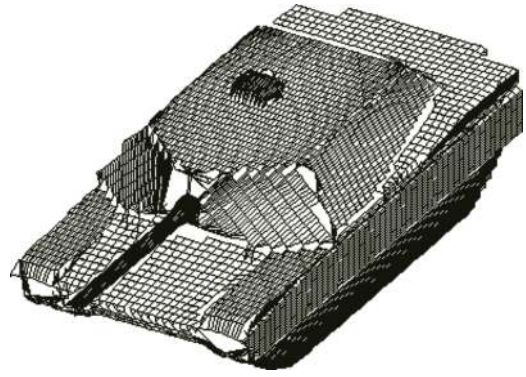

FIGURE 3.310 Computer model of M1A1 Abrams tank surface.

TABLE 3.21
Geometrical Characteristics of M1A1 Main Battle Tank

Hull Characteristics (Figure 3.309)		Tank Surface Model Characteristics (Figure 3.310)	
Tank length (gun included)	9.828 m	Number of parts of ellipsoids in the model	53
Width	3.65 m	Number of straight wedge parts in the model	22
Height	2.438 m		
Combat weight	57.15 t		

Figures 3.341 through 3.348 show the amplitude distributions of echo signals for two azimuth aspect sectors and two elevation angles.

Tables 3.22 and 3.23 summarize the parameters of distributions that fit mostly the simulation data for square root of RCS.

In Section 3.2.6, there are examples of HRRPs computed for the tank model given various illumination signal spectrum widths.

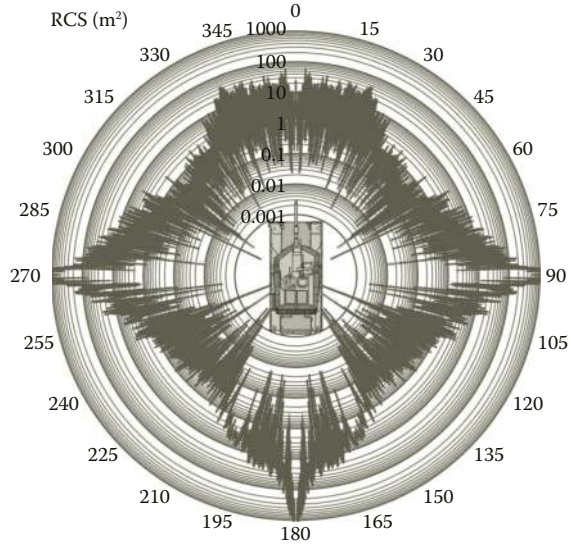

FIGURE 3.311 (**See color insert.**) Circular diagrams of instantaneous RCS given radar observation of M1A1 Abrams tank model (ε = 1°, underlying surface – dry soil).

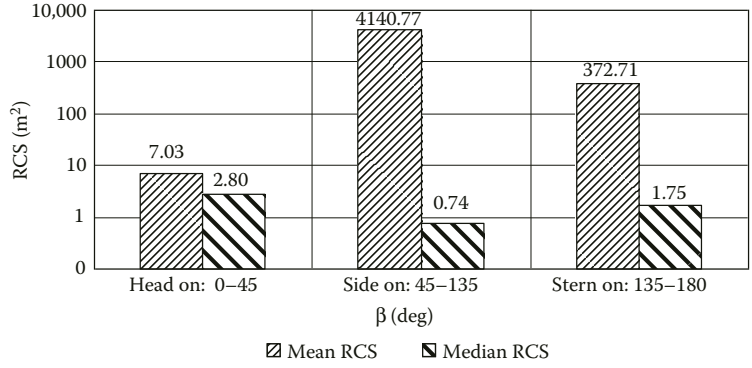

FIGURE 3.312 Diagrams of mean and median RCS of the M1A1 Abrams tank model in three sectors of azimuth aspect given its radar observation at horizontal polarization (ε = 1°, underlying surface – dry soil).

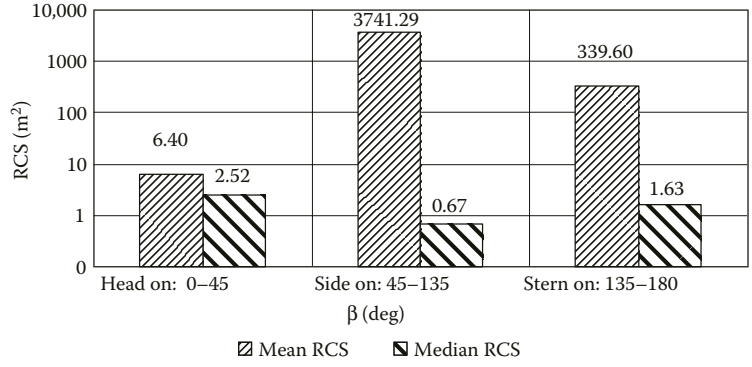

FIGURE 3.313 Diagrams of mean and median RCS of the M1A1 Abrams tank model in three sectors of azimuth aspect given its radar observation at vertical polarization (ε = 1°, underlying surface – dry soil).

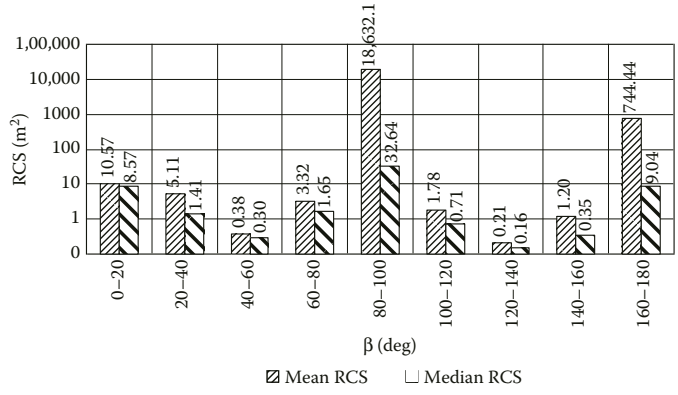

FIGURE 3.314 Diagrams of mean and median RCS of the M1A1 Abrams tank model in 20-degree sectors of azimuth aspect given its radar observation at horizontal polarization (ε = 1°, underlying surface – dry soil).

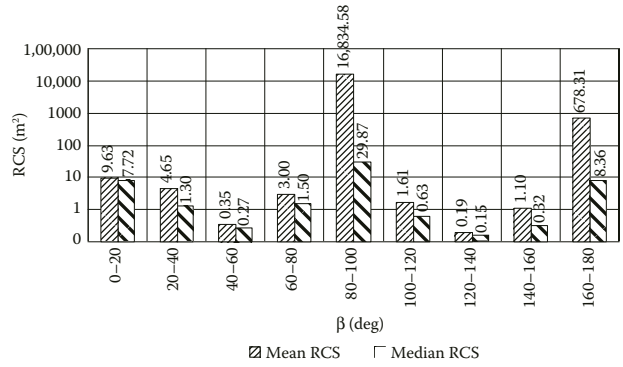

FIGURE 3.315 Diagrams of mean and median RCS of the M1A1 Abrams tank model in 20-degree sectors of azimuth aspect given its radar observation at vertical polarization (ε = 1°, underlying surface – dry soil).

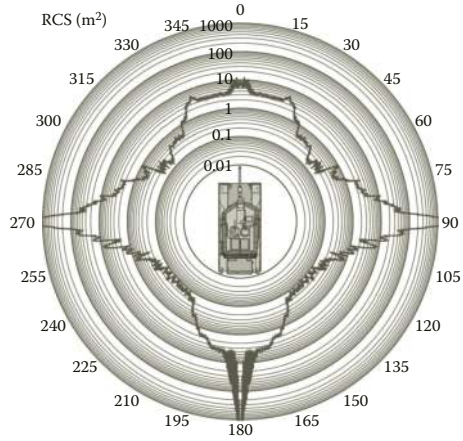

FIGURE 3.316 (**See color insert.**) Circular diagrams of noncoherent RCS given radar observation of M1A1 Abrams tank model (ε = 1°, underlying surface – dry soil).

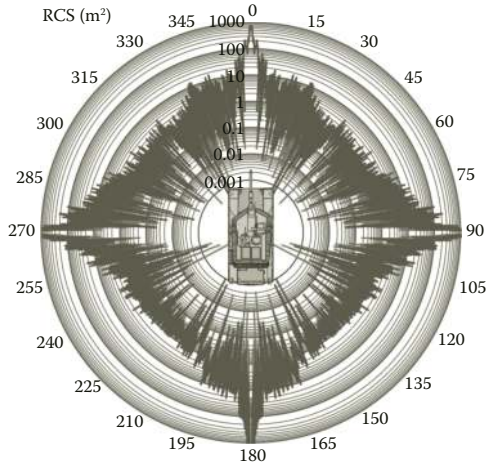

FIGURE 3.317 (**See color insert.**) Circular diagrams of instantaneous RCS given radar observation of M1A1 Abrams tank model (ε = 10°, underlying surface – dry soil).

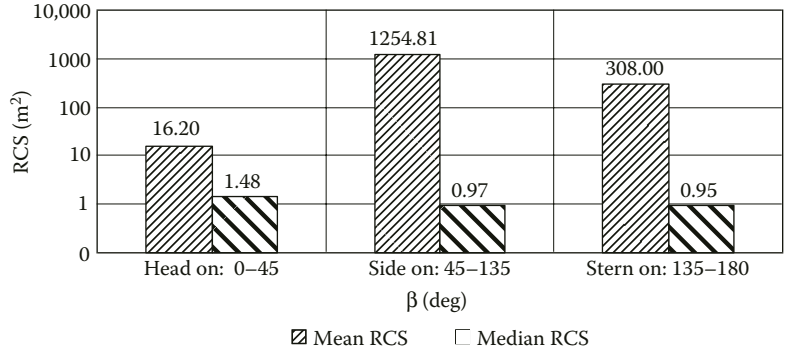

FIGURE 3.318 Diagrams of mean and median RCS of the M1A1 Abrams tank model in three sectors of azimuth aspect given its radar observation at horizontal polarization (ε = 10°, underlying surface – dry soil).

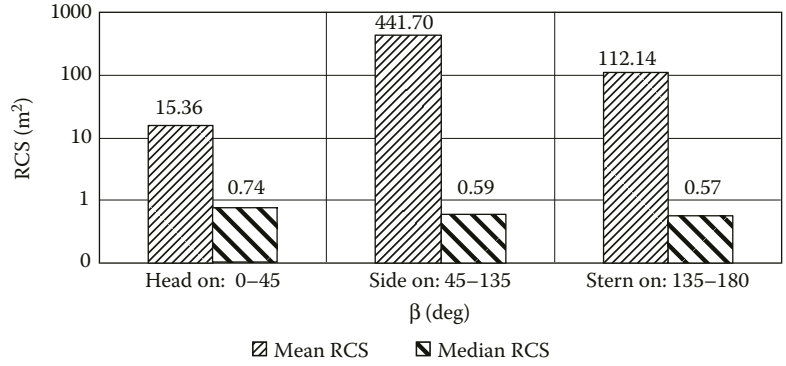

FIGURE 3.319 Diagrams of mean and median RCS of the M1A1 Abrams tank model in three sectors of azimuth aspect given its radar observation at vertical polarization (ε = 10°, underlying surface – dry soil).

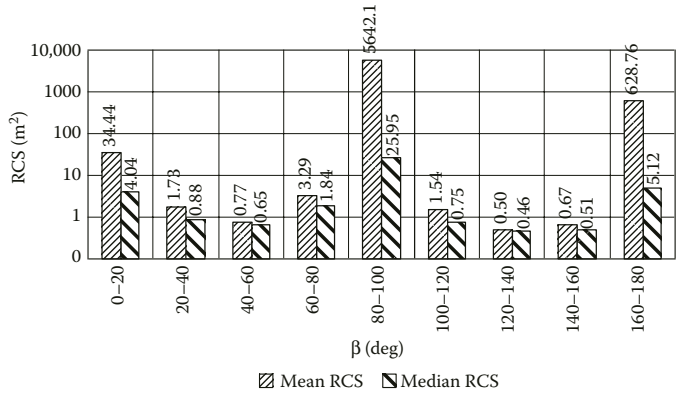

FIGURE 3.320 Diagrams of mean and median RCS of the M1A1 Abrams tank model in 20-degree sectors of azimuth aspect given its radar observation at horizontal polarization (ε = 10°, underlying surface – dry soil).

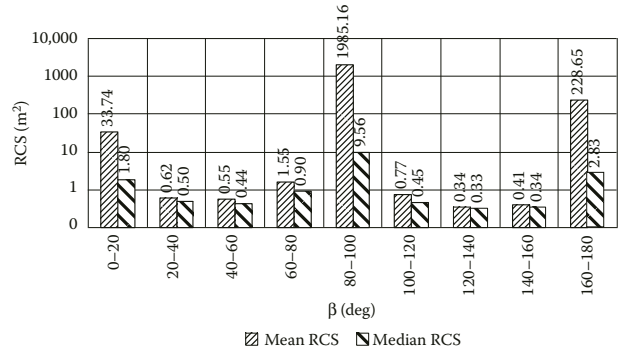

FIGURE 3.321 Diagrams of mean and median RCS of the M1A1 Abrams tank model in 20-degree sectors of azimuth aspect given its radar observation at vertical polarization (ε = 10°, underlying surface – dry soil).

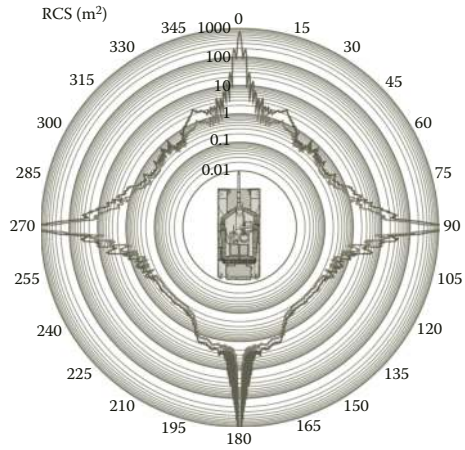

FIGURE 3.322 (**See color insert.**) Circular diagrams of noncoherent RCS of M1A1 Abrams tank model (ε = 10°, underlying surface – dry soil).

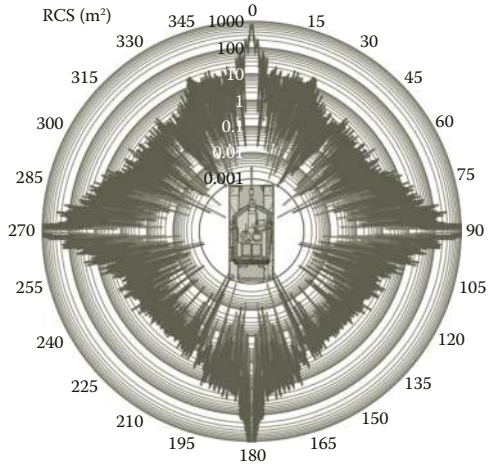

FIGURE 3.323 (**See color insert.**) Circular diagrams of instantaneous RCS of M1A1 Abrams tank model (ε = 10°, underlying surface – moist soil).

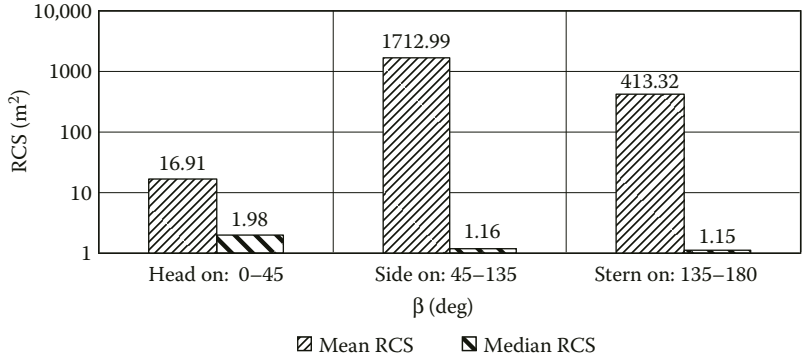

FIGURE 3.324 Diagrams of mean and median RCS of the M1A1 Abrams tank model in three sectors of azimuth aspect given its radar observation at horizontal polarization (ε = 10°, underlying surface – moist soil).

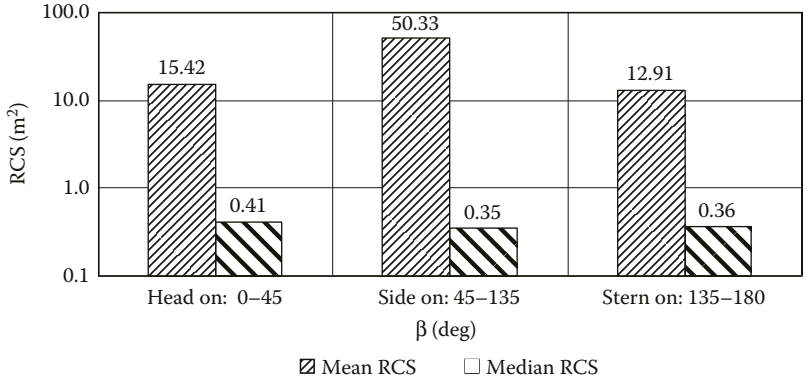

FIGURE 3.325 Diagrams of mean and median RCS of the M1A1 Abrams tank model in three sectors of azimuth aspect given its radar observation at vertical polarization (ε = 10°, underlying surface – moist soil).

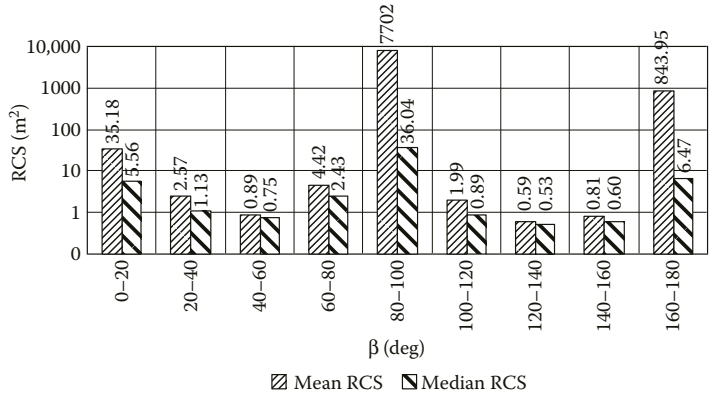

FIGURE 3.326 Diagrams of mean and median RCS of the M1A1 Abrams tank model in 20-degree sectors of azimuth aspect given its radar observation at horizontal polarization (ε = 10°, underlying surface – moist soil).

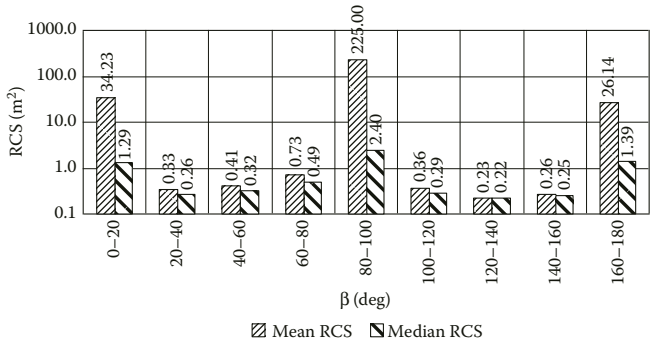

FIGURE 3.327 Diagrams of mean and median RCS of the M1A1 Abrams tank model in 20-degree sectors of azimuth aspect given its radar observation at vertical polarization (ε = 10°, underlying surface – moist soil).

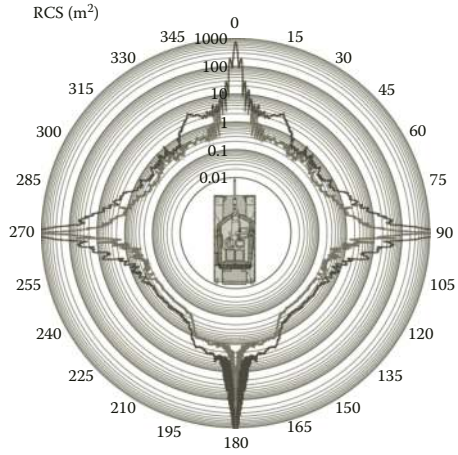

FIGURE 3.328 (**See color insert.**) Circular diagrams of noncoherent RCS of M1A1 Abrams tank model (ε = 10°, underlying surface – moist soil).

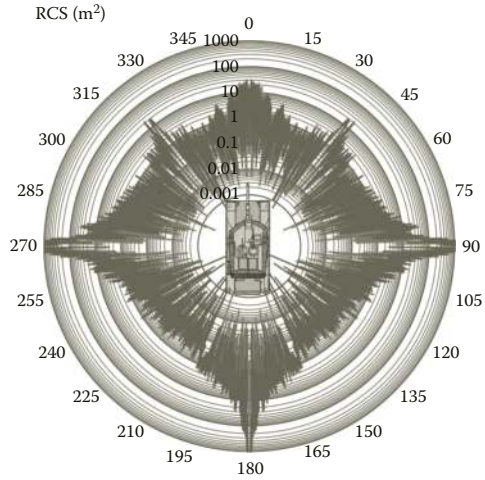

FIGURE 3.329 (**See color insert.**) Circular diagrams of instantaneous RCS of M1A1 Abrams tank model (ε = 30°, underlying surface – dry soil).

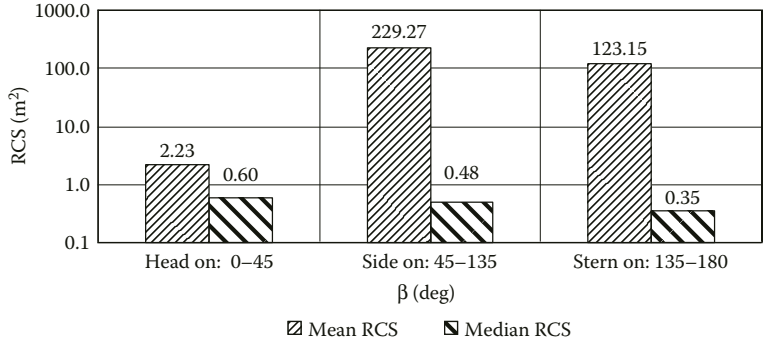

FIGURE 3.330 Diagrams of mean and median RCS of the M1A1 Abrams tank model in three sectors of azimuth aspect given its radar observation at horizontal polarization (ε = 30°, underlying surface – dry soil).

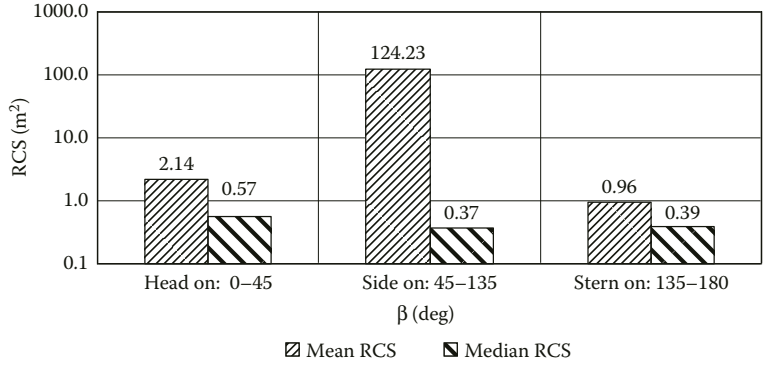

FIGURE 3.331 Diagrams of mean and median RCS of the M1A1 Abrams tank model in three sectors of azimuth aspect given its radar observation at vertical polarization (ε = 30°, underlying surface – dry soil).

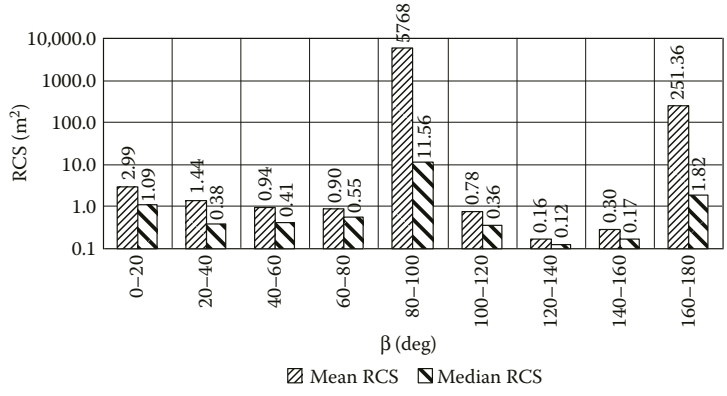

FIGURE 3.332 Diagrams of mean and median RCS of the M1A1 Abrams tank model in 20-degree sectors of azimuth aspect given its radar observation at horizontal polarization (ε = 30°, underlying surface – dry soil).

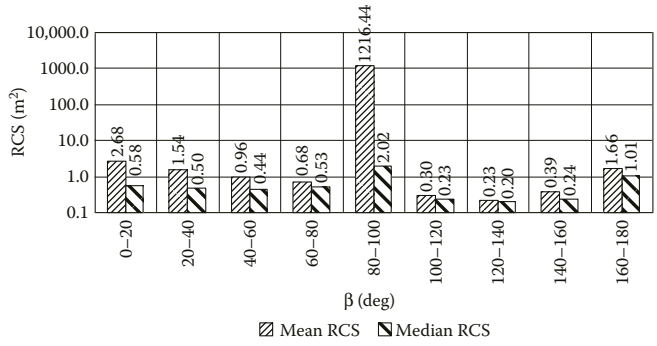

FIGURE 3.333 Diagrams of mean and median RCS of the M1A1 Abrams tank model in 20-degree sectors of azimuth aspect given its radar observation at vertical polarization (ε = 30°, underlying surface – dry soil).

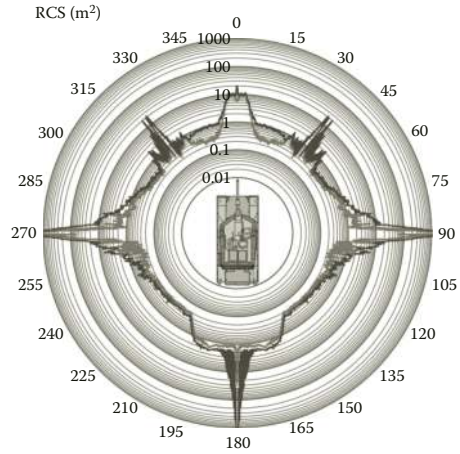

FIGURE 3.334 (**See color insert.**) Circular diagrams of noncoherent RCS of M1A1 Abrams tank model (ε = 30°, underlying surface – dry soil).

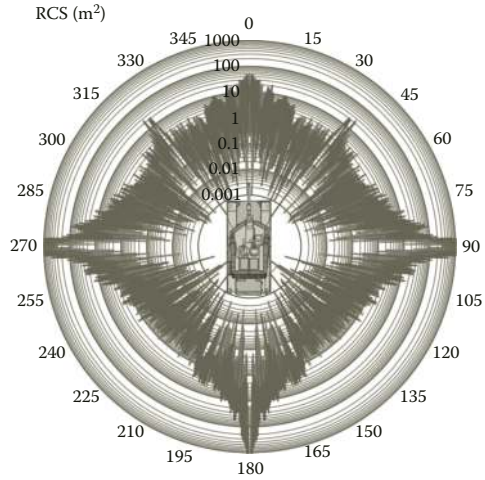

FIGURE 3.335 (**See color insert.**) Circular diagrams of instantaneous RCS of M1A1 Abrams tank model (ε = 30°, underlying surface – moist soil).

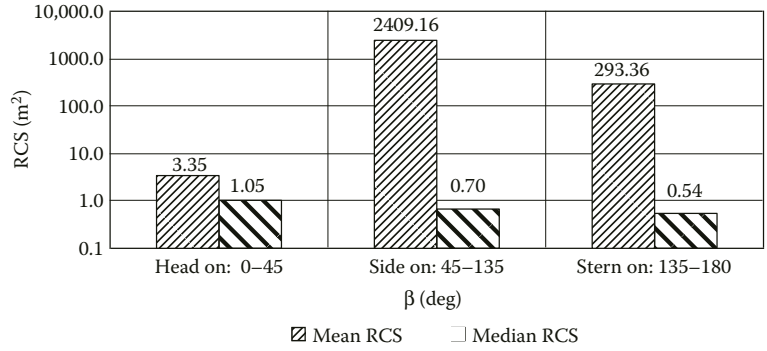

FIGURE 3.336 Diagrams of mean and median RCS of the M1A1 Abrams tank model in three sectors of azimuth aspect given its radar observation at horizontal polarization (ε = 30°, underlying surface – moist soil).

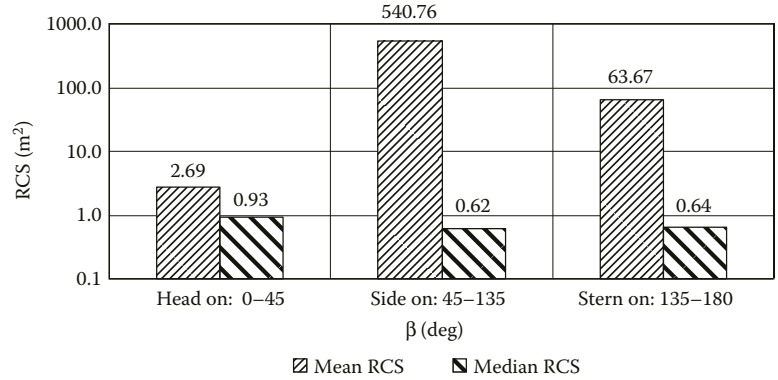

FIGURE 3.337 Diagrams of mean and median RCS of the M1A1 Abrams tank model in three sectors of azimuth aspect given its radar observation at vertical polarization (ε = 30°, underlying surface – moist soil).

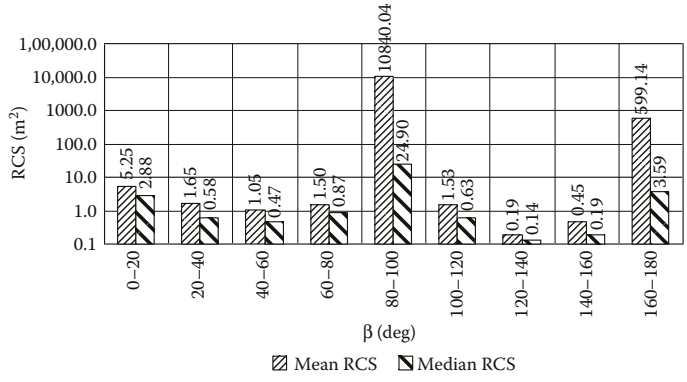

FIGURE 3.338 Diagrams of mean and median RCS of the M1A1 Abrams tank model in 20-degree sectors of azimuth aspect given its radar observation at horizontal polarization (ε = 30°, underlying surface – moist soil).

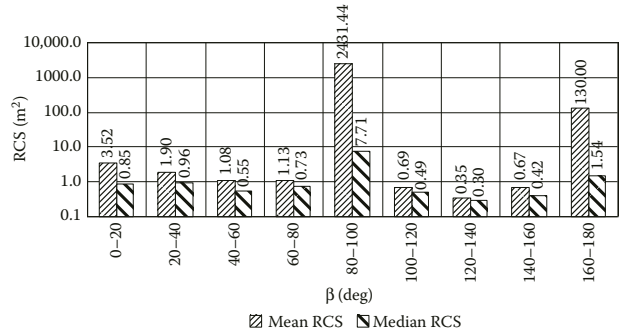

FIGURE 3.339 Diagrams of mean and median RCS of the M1A1 Abrams tank model in 20-degree sectors of azimuth aspect given its radar observation at vertical polarization (ε = 30°, underlying surface – moist soil).

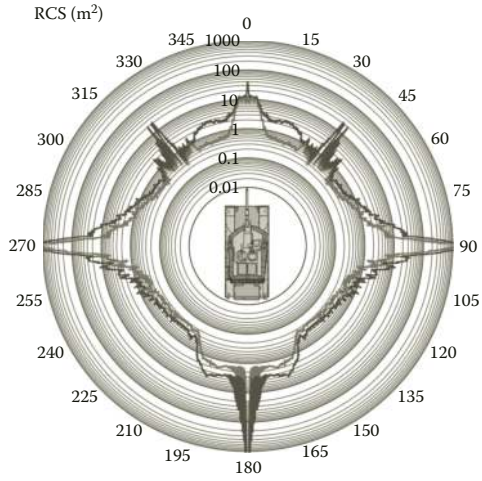

FIGURE 3.340 (**See color insert.**) Circular diagrams of noncoherent RCS of M1A1 Abrams tank model (ε = 30°, underlying surface – moist soil).

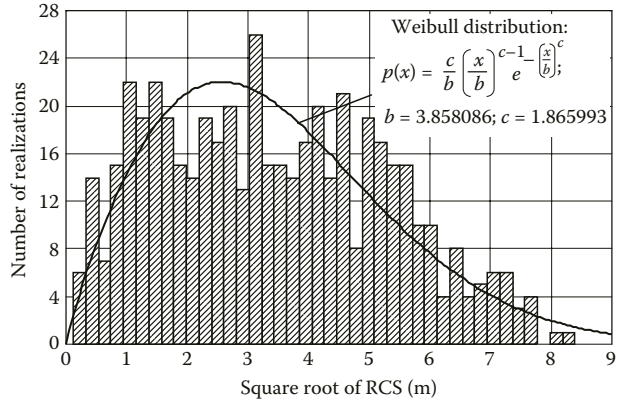

FIGURE 3.341 Amplitude distribution of echo signal given radar observation of M1A1 Abrams tank model in the azimuth aspect sector from –10° through +10°, horizontal polarization (ε = 1°, underlying surface – dry soil).

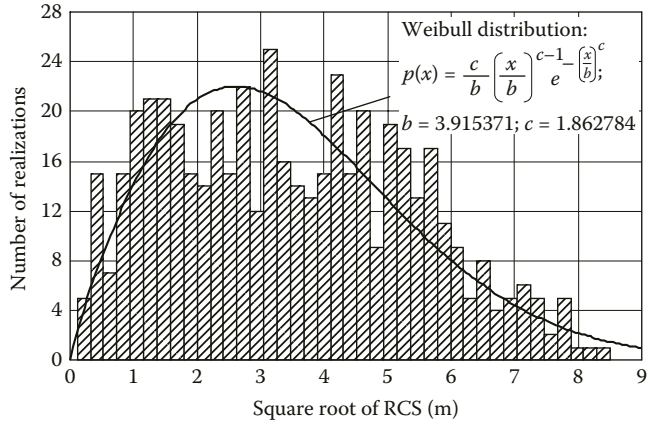

FIGURE 3.342 Amplitude distribution of echo signal given radar observation of M1A1 Abrams tank model in the azimuth aspect sector from –10° through +10°, horizontal polarization (ε = 1°, underlying surface – moist soil).

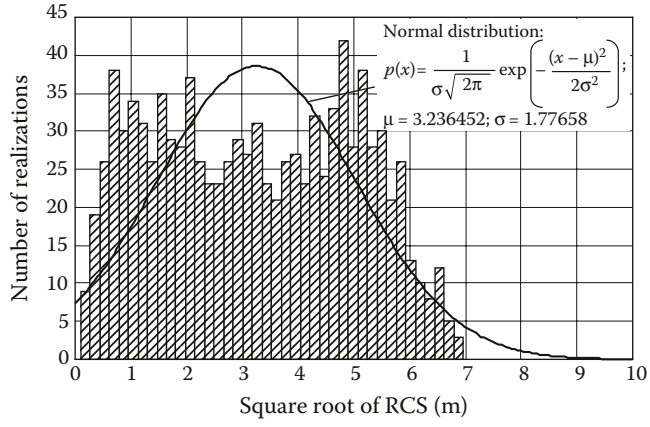

FIGURE 3.343 Amplitude distribution of echo signal given radar observation of M1A1 Abrams tank model in the azimuth aspect sector from 10° through 30°, horizontal polarization (ε = 1°, underlying surface – dry soil).

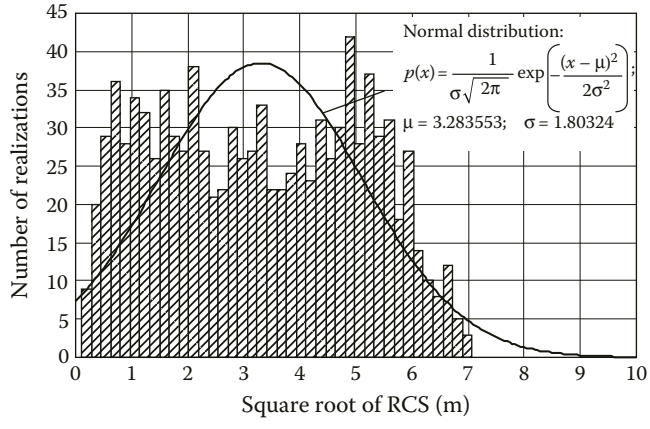

FIGURE 3.344 Amplitude distribution of echo signal given radar observation of M1A1 Abrams tank model in the azimuth aspect sector from 10° through 30°, horizontal polarization (ε = 1°, underlying surface – moist soil).

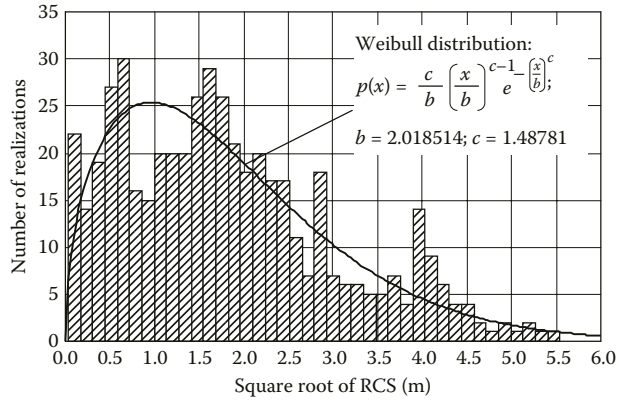

FIGURE 3.345 Amplitude distribution of echo signal given radar observation of M1A1 Abrams tank model in the azimuth aspect sector from –10° through +10°, horizontal polarization (ε = 30°, underlying surface – dry soil).

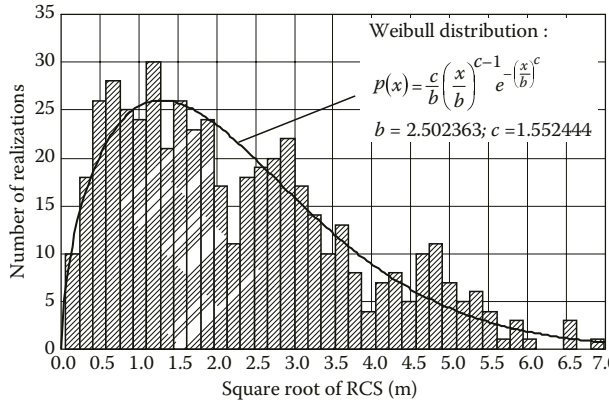

FIGURE 3.346 Amplitude distribution of echo signal given radar observation of M1A1 Abrams tank model in the azimuth aspect sector from –10° through +10°, horizontal polarization (ε = 30°, underlying surface – moist soil).

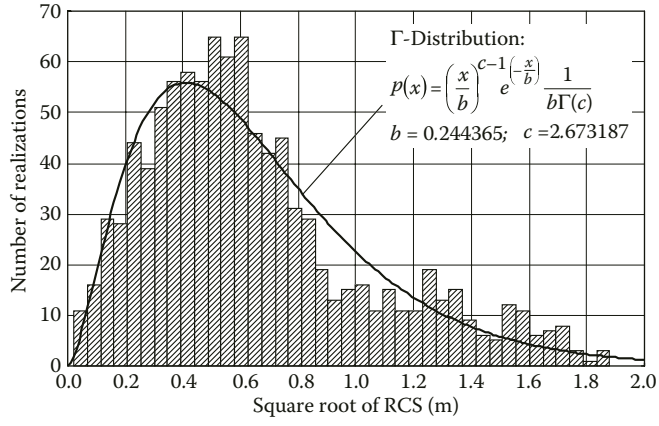

FIGURE 3.347 Amplitude distribution of echo signal given radar observation of M1A1 Abrams tank model in the azimuth aspect sector from 10° through 30°, horizontal polarization (ε = 30°, underlying surface – dry soil).

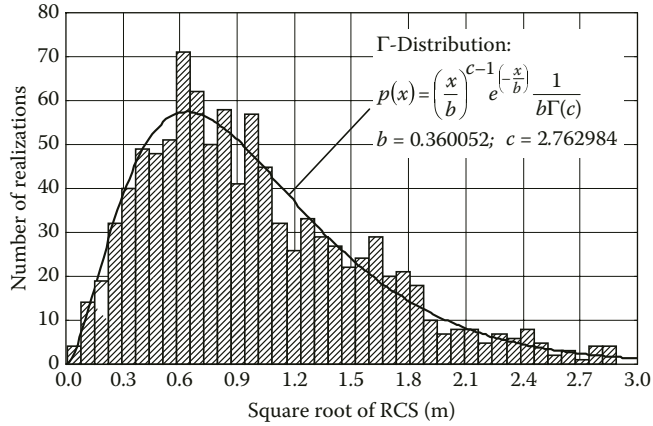

FIGURE 3.348 Amplitude distribution of echo signal given radar observation of M1A1 Abrams tank model in the azimuth aspect sector from 10° through 30°, horizontal polarization (ε = 30°, underlying surface – moist soil).

TABLE 3.22
Parameters of Probability Distributions for the Echo Signal Amplitudes of M1A1 Abrams Tank Model Given Elevation Angle of Illumination Equal to 1°

Azimuth Aspect Range	Soil Type	Polarization	Distribution Kind	Distribution Parameters
			Weibull distribution:	$b = 3.858086$
			$p(x) = \frac{c}{b}\left(\frac{x}{b}\right)^{c-1} e^{-\left(\frac{x}{b}\right)^c}$	$c = 1.865993$
−10° ⋯ +10°	Dry soil	Horizontal		
		Vertical	Weibull distribution	$b = 3.683428$
				$c = 1.873687$
	Moist soil	Horizontal	Weibull distribution	$b = 3.915371$
				$c = 1.862784$
		Vertical	Weibull distribution	$b = 3.444218$
				$c = 1.884252$
10° ⋯ 30°	Dry soil	Horizontal	Normal distribution:	$\mu = 3.236452$
			$p(x) = \frac{1}{\sigma\sqrt{2\pi}} \exp\left(-\frac{(x-\mu)^2}{2\sigma^2}\right)$	$\sigma = 1.77658$
		Vertical	Normal distribution	$\mu = 3.085798$
				$\sigma = 1.69432$
	Moist soil	Horizontal	Normal distribution	$\mu = 3.283558$
				$\sigma = 1.80324$
		Vertical	Normal distribution	$\mu = 2.878823$
				$\sigma = 1.5822$

TABLE 3.23
Parameters of Probability Distributions for the Echo Signal Amplitudes of M1A1 Abrams Tank Model Given Elevation Angle of Illumination Equal to 30°

Azimuth Aspect Range	Soil Type	Polarization	Distribution Kind	Distribution Parameters
−10° ⋯ +10°	Dry soil	Horizontal	Weibull distribution: $p(x) = \frac{c}{b}\left(\frac{x}{b}\right)^{c-1} e^{-\left(\frac{x}{b}\right)^{c}}$	$b = 2.018514$ $c = 1.48781$
		Vertical	Γ-Distribution: $p(x) = \left(\frac{x}{b}\right)^{c-1} e^{\left(-\frac{x}{b}\right)} \frac{1}{b\Gamma(c)}$, where Γ is Gamma-function	$b = 0.988648$ $c = 1.84323$
	Moist soil	Horizontal	Weibull distribution	$b = 2.502363$ $c = 1.552444$
		Vertical	Γ-Distribution	$\mu = 1.133567$ $\sigma = 1.817716$
10° ⋯ 30°	Dry soil	Horizontal	Γ-Distribution	$b = 0.244365$ $c = 2.673187$
		Vertical	Γ-Distribution	$b = 0.200213$ $c = 2.838689$
	Moist soil	Horizontal	Γ-Distribution	$b = 0.360052$ $c = 2.762984$
		Vertical	Γ-Distribution	$b = 0.230819$ $c = 3.47689$

3.2.6 Impulse Responses of M1A1 Abrams Main Battle Tank

As an example, we consider HRRPs of the M1A1 Abrams main battle tank observed at the azimuth aspect of 15° and carrier frequency of 10 GHz (3 cm wavelength).

Bold solid lines in Figures 3.349 through 3.357 below correspond to HRRPs obtained using signal with rectangular amplitude spectrum of 1 GHz bandwidth. Thin dashed lines correspond to HRRPs obtained using signal with rectangular spectrum of 250 MHz bandwidth. Both wideband signals are centered at the same carrier frequency.

Figure 3.349 shows HRRPs of M1A1 Abrams tank model illuminated at grazing elevation angle of 1° (illumination almost along the ground). Unlike the T-90 tank model, the surface fractures do not contribute significantly into total echo from M1A1 Abrams tank model given this elevation. So, the difference between this tank model's HRRPs obtained given horizontal and vertical polarization of illuminating wave, as well as given dry and moist soil as underlying surface, is almost absent. Therefore, we present only impulse responses of the M1A1 Abrams tank model standing on dry soil given its illumination at horizontal polarization.

Peaks #1 are due to scattering from the right track cover. Peaks #2 are due to scattering from the left track cover. Peaks #3 are due to scattering from the gun's mantlet. Peaks #4 are due to scattering from the hatch on top of turret. Peaks #5 are due to scattering from the tank's stern.

Figures 3.350 and 3.351 show HRRPs of M1A1 Abrams tank model standing on dry soil (as underlying surface) given its illumination at the elevation angle of 10° by the waves with horizontal and vertical polarizations respectively.

Figures 3.352 and 3.353 show HRRPs of M1A1 Abrams tank model standing on moist soil (as underlying surface) given its illumination at the elevation angle of 10° by the waves with horizontal and vertical polarizations respectively.

Some peaks in Figures 3.350 through 3.353 are numbered. Peaks #1 are due to scattering from the right track cover. Peaks #2 are due to scattering from the left track cover. Peaks #3 are due to scattering from the turret's mantlet. Peaks #4 are due to scattering from the hatch on top of the turret. It is worth mentioning that the peaks are the superpositions of echoes propagated along different paths and shifted by different time lags thereof. So, some peaks (for instance peaks #3 and #4) start to split. The amplitudes of peaks obtained at horizontal polarization (Figures 3.350 and 3.352) are greater in case of tank standing on moist soil. The latter is conditioned by the greater reflection coefficient of moist soil given illumination elevation angle of 10° at horizontal polarization. At the same time, given vertical polarization of illumination wave (Figures 3.351 and 3.353), the peak amplitudes are greater for the case of dry soil. The latter is due to the fact that elevation angle of illumination equal to 10° is close to the Bruster angle in case of moist soil, which leads to the surface reflection coefficient at vertical polarization approaching zero.

Figures 3.354 and 3.355 show the HRRPs of M1A1 Abrams tank model standing on dry soil (as underlying surface) given its illumination at the elevation angle of 30° by the waves with horizontal and vertical polarizations respectively.

Figures 3.356 and 3.357 show the HRRPs of M1A1 Abrams tank model standing on the moist soil (as underlying surface) given its illumination at the elevation angle of 30° by the waves with horizontal and vertical polarizations respectively.

Some peaks in Figures 3.354 through 3.357 are numbered. Peaks #1 are due to scattering from the right track cover. Peaks #2 are due to scattering from the left track cover. Peaks #3 are due to

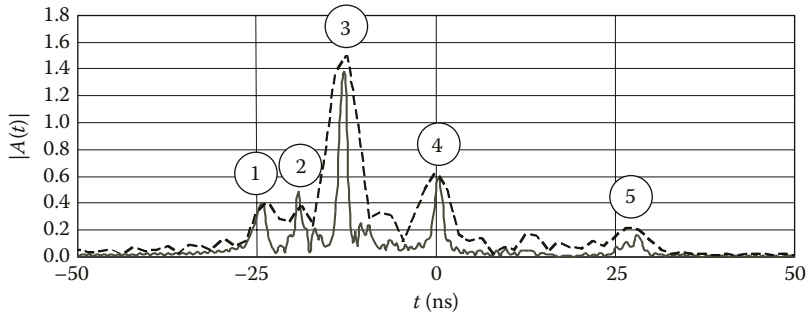

FIGURE 3.349 HRRPs of M1A1 Abrams tank model standing on dry soil given its radar observation at elevation of 1°, horizontal polarization.

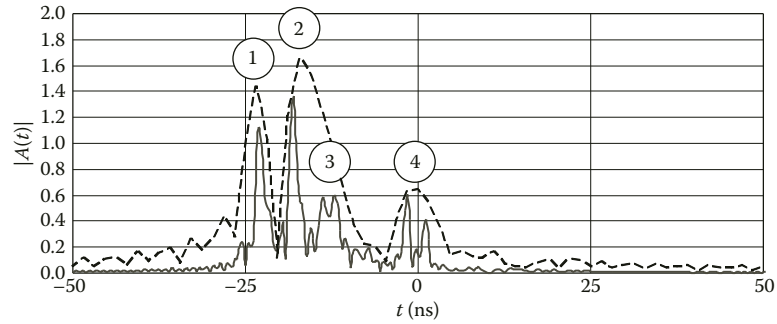

FIGURE 3.350 HRRPs of M1A1 Abrams tank model standing on dry soil given its radar observation at elevation of 10°, horizontal polarization.

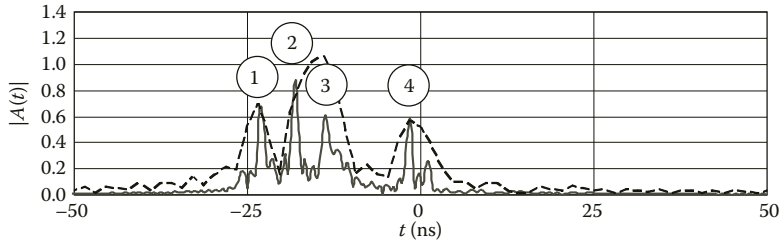

FIGURE 3.351 HRRPs of M1A1 Abrams tank model standing on dry soil given its radar observation at elevation of 10°, vertical polarization.

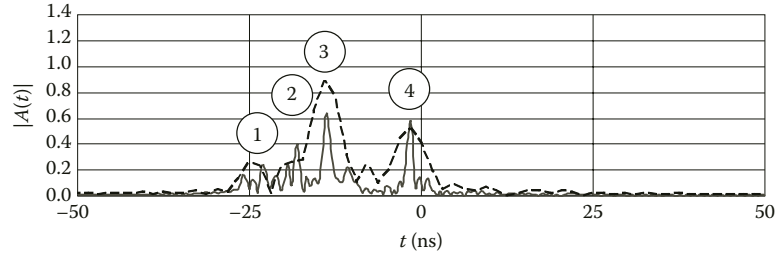

FIGURE 3.352 HRRPs of M1A1 Abrams tank model standing on moist soil given its radar observation at elevation of 10°, horizontal polarization.

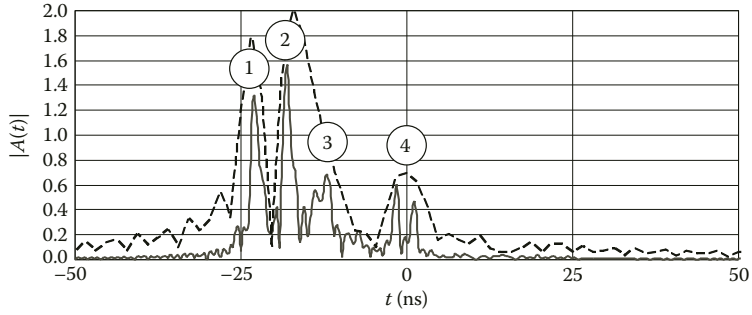

FIGURE 3.353 HRRPs of M1A1 Abrams tank model standing on moist soil given its radar observation at elevation of 10°, vertical polarization.

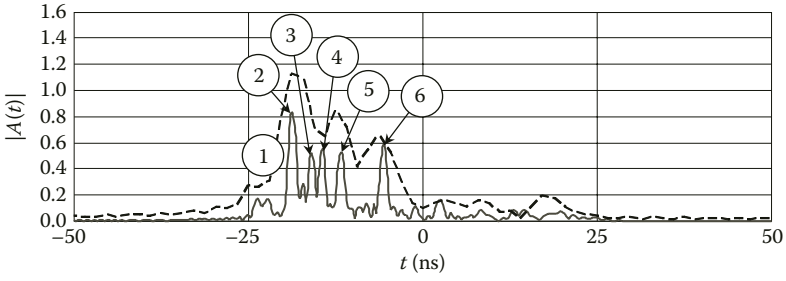

FIGURE 3.354 HRRPs of M1A1 Abrams tank model standing on dry soil given its radar observation at elevation of 30°, horizontal polarization.

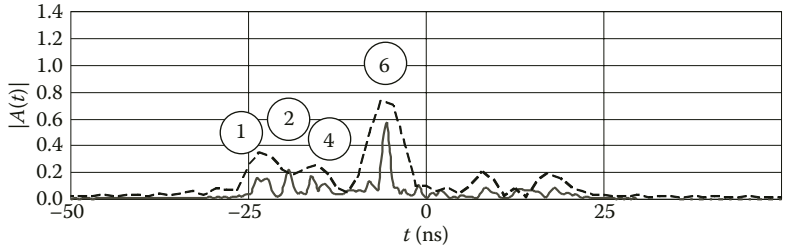

FIGURE 3.355 HRRPs of M1A1 Abrams tank model standing on dry soil given its radar observation at elevation of 30°, vertical polarization.

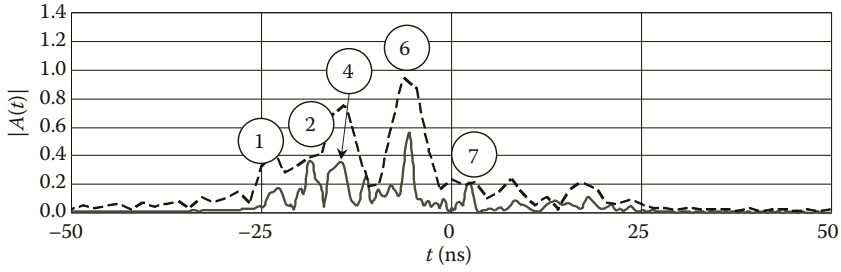

FIGURE 3.356 HRRPs of M1A1 Abrams tank model standing on moist soil given its radar observation at elevation of 30°, horizontal polarization.

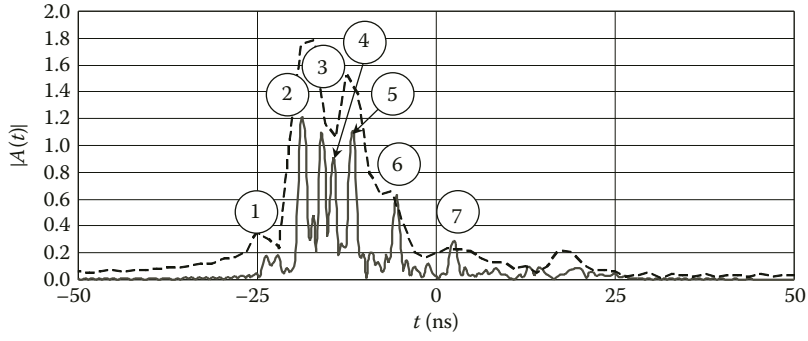

FIGURE 3.357 HRRPs of M1A1 Abrams tank model standing on moist soil given its radar observation at elevation of 30°, vertical polarization.

scattering from the right track (surface scattering is accounted for). Peaks #4 are due to scattering from the turret's mantlet. Peaks #5 are due to scattering from the left track (surface scattering is accounted for). Peaks #6 are due to scattering from the hatch on top of the turret. Peaks #7 are due to scattering from the turret via mediation of underlying surface. It should be noted that some peaks are due to echoes that could be obtained only via mediation of underlying surface. So, such peaks, (for instance peaks #3, #5, and #7) can have negligible amplitude or be absent altogether in some HRRPs (Figures 3.355 and 3.357). Amplitudes of peaks given horizontal (Figures 3.354 and 3.356) and vertical (Figures 3.355 and 3.357) polarization of illumination wave are greater for the case of moist soil. This is due to the greater surface reflection coefficients of moist soil for both polarizations given illumination elevation angle of 30°.

References

1. Lvova, L.A. 2003. Radar visibility of air vehicles, Russian Federal Nuclear Center - the All-Russian Research Institute of Theoretical Physics (*RFYaC–VNIITPh*), Snezhinsk (in Russian).
2. Chernyak, V.S., Zaslavky, L.P., and Osipov, L.V. 1987. Multi-site radar stations and systems, *Zarubezhnaya radiolektronika*, 2, 9–69 (in Russian).
3. Sukharevsky, O.I., Gorelyshev, S.A., and Sazonov, A.Z. 2000. On the strict and approximated computation of radar cross-section (RCS) of three dimensional objects, *Collection of Papers,* Kharkiv Military University, 4(30), 53–63 (in Russian).
4. Nikolsky, V.V. and Nikolskaya, T.I. 1989. *Electrodynamics and Propagation of Radio Waves*, Nauka, Moscow (in Russian).
5. Kenaugh, E.M. and Moffatt, D.L. 1965. Transient and impulse response approximation, *Proceedings of the IEEE*, 53(8), 893–901.
6. Gupta, I.J. and Burnside, W.D. 1987. A physical optics correction for backscattering from curved surfaces, *IEEE Transactions of the AP*, 35(5), 553–561.
7. Ufimtsev, P.Y. 1971. Method of edge waves in the physical theory of diffraction, *Foreign Technology Div Wright-Patterson AFB Ohio*, No. FTD-HC-23-259-71.
8. Ufimtsev, P. 2003. *Theory of Edge Diffraction in Electromagnetics*, Tech Science Press, Encino, California.
9. http://www.feko.info.
10. Sukharevsky, O.I. 1987. Generalized Lorentz lemma and integral representations of some electro dynamical problems, *Soviet Journal of Communications Technology and Electronics*, 32(11), 2255–2262 (in Russian).
11. Silver, S. 1949. *Microwave Antenna Theory and Design*, *MIT Radiation Laboratory Series*, 12, McGraw-Hill, New York.
12. Benenson, L.S. and Pheld, Ya. N. 1993. Some new quadratic lemmas for electro dynamic fields, *Soviet Journal of Communications Technology and Electronics*, 38(7), 1179–1187 (in Russian).
13. Bakhrah, L.D., Benenson, L.S., and Zelkin, E.G. et al. 1997. *Antenna Technology Handbook,* Pheld, Ya. N. and Zelkin, E.G. (eds)*,* 5 Vols., Vol. 1, *IPRZhR*, Moscow (in Russian).
14. Pheld, Ya. N. 1981. On computation of field excited by aperture antenna, *Soviet Journal of Communications Technology and Electronics*, 26(1), 178–179 (in Russian).
15. Sukharevsky, O.I. 1983. Radiation of antenna array under dielectric radome in the presence of perfectly conducting underlying surface *Radiotekhnika,* Kharkiv Institute of Radio electronics, *Kharkiv*, 60, 43–49 (in Russian).
16. Sukharevsky, I.V. and Sukharevsky, O.I. 1985. About the field excited by radiating aperture in the presence of scattering objects, *Waves and Diffraction-85. Short Thesis of Paper for the IX All-Union Symposium on Diffraction and Propagation of Radio Waves*, Tbilisi, 1, 270–273 (in Russian).
17. Sukharevskiy, I.V. and Sukharevsky, O.I. 1986. Calculation of the field excited by a radiating aperture in the presence of an arbitrary system of scatters, *Soviet Journal of Communications Technology and Electronics*, 31(5), 8–13.
18. Zakhariev, L.N. and Lemansky, A.A. 1972. *Wave Scattering by Black Bodies*, Soviet radio, Moscow (in Russian).
19. Kaplun, V.A. 1974. *UHF Antenna Radomes*, Soviet radio, Moscow (in Russian).
20. Vakman, D.E. 1962. *Asymptotic Methods in Linear Radio Techniques*, Soviet radio, Moscow (in Russian).
21. Kontorovich, M.I. and Muraviev, Yu. K. 1952. Derivation of geometrical optics reflection laws on the basis of asymptotic consideration of diffraction problems, *Journal of Technical Physics*, 22(3), 394–409 (in Russian).
22. Sukharevsky, I.V. and Sukharevsky, O.I. 2000. The determination of shortwave asymptotics of scattered fields by the stationary-phase method, *Telecommunications and Radio Engineering*, 54(7), 14–22.
23. Goursat, E. 1959. *A Course in Mathematical Analysis*, Vol. 1, Dover, New York.
24. Fedoryuk, M.V. 1963. The stationary phase method for multidimensional integrals, *USSR Computational Mathematics and Mathematical Physics*, 2(1), 152–157 (in Russian).
25. Fedoryuk, M.V. 1977. *Saddle-Point Method*, Nauka, Moscow (in Russian).

26. Povzner, A.Y. and Sukharevsky, I.V. 1962. On finding the asymptotes to the solutions of short-wate diffraction problems, *USSR Computational Mathematics and Mathematical Physics*, 1(2), 249–276 (in Russian).
27. Honl, H., Maue, A.W., and Westpfahl, K. 1961. *Handbuch der Physik*, Springer-Verlag, Berlin, 25(1), 218–573.
28. Sukharevsky, O.I. and Vasilets, V.A. 1996. Impulse characteristics of smooth objects in bistatic case, *Journal of Electromagnetic Waves and Applications*, 10(12), 1613–1622.
29. Sirenko, Yu. K., Sukharevsky, I.V., Sukharevsky, O.I., and Yashina, N.P. 2000. *Fundamental and Applied Problems of Electromagnetic Wave Scattering*, Krok, Kharkiv (in Russian).
30. Shirman, Y.D., Gorshkov, S.A, Leschenko, S.P., Orlenko, V.M., Sedyshev, S.Y., and Sukharevsky, O.I. 2002. *Computer Simulation of Aerial Target Radar Scattering, Recognition, Detection, and Tracking*, Shirman (ed.), Artech House, London, Boston.
31. Sukharevsky, O.I. and Dobrodnyak, A.F. 1989. Scattering of a finite ideally conducting cylinder where the discontinuity lines have absorption coatings in the bistatic case, *Radiophysics and Quantum Electronics*, 32(12), 1126–1131.
32. Gradshteyn, I.S. and Ryzhik, I.M. 2000. *Table of Integrals, Series and Products*, 5th edition, Academic, New York.
33. Sukharevsky, O.I., Vasiets, V.A., Sazonov, A.Z., and Tkachuk, K.I. 2000. Computation of scattering of electromagnetic wave on perfectly conducting object partially covered with radar absorbent material by means of triangulation formulas. *Radio Physics and Radio Astronomy*, 5(1), 47–54 (in Russian).
34. Sukharevsky, O.I., Vasilets, V.A., Gorelyshev, S.A., Nechitaylo, S.V., and Tkachuk, K.I. 2001. Radar cross-section of the objects with non-perfectly conducting surface that has fractures, *Zarubezhnaya Radioelektronika*, 6, 41–48 (in Russian).
35. Sukharevsky, O.I., Vasilets, V.A., Gorelyshev, S.A., and Shramkov, A. Yu. 1998. Impulse signal scattering at perfectly conducting object situated in the vicinity of interface between two media, *Collection of Papers*, Kharkiv Military University, Kharkiv, 16, 78–85 (in Russian).
36. Sukharevsky, O.I., Gorelyshev, S.A., Vasilets, V.A., and Muzychenko, A.V. 1998. Pulse signal inverse scattering by perfectly conducting object located near uniform half-space, *Radio Physics and Radio Astronomy*, 3(2), 136–145.
37. Sukharevsky, O.I., Vasilets, V.A., Gorelyshev, S.A., and Muzychenko, A.V. 2000. Pulse signal scattering from perfectly conducting complex object located near uniform half-space. *Progress in Electromagnetic Research, PIER 29*, 29, 169–185.
38. Vasilets, V.A. 2001. Method for computing RCS of perfectly conducting ground object, *Collection of Papers*, Kharkiv Military University, Kharkiv, 7(37), 90–92 (in Russian).
39. Sukharevsky, O.I., Vasilets, V.A., Sazonov, A.Z., and Tkachuk, K.I. 2003. Method for computing RCS of ground object with non-perfectly conducting surface, *Interservice Subject Collection of Papers Electromagnetic Wave Scattering*, TGRU, Taganrog, 12, 9–15 (in Russian).
40. Klimov, V.E. and Klishin, V.V. 1983. Axiomatization of the three dimensional object geometry synthesis problem, *Izvestiya Academii Nauk, USSR, Technical Cybernetics*, 4, 57–62 (in Russian).
41. Mittra, R. 1973. *Computer Techniques for Electromagnetics,* 7. Pergamon Press, Oxford and New York.
42. Youssef, N.N. 1989. Radar cross section of complex targets, *Proceedings of the IEEE*, 77(5), 722–734.
43. Varganov, M.E. et al. 1985. *Radar Characteristics of Air Vehicles*, Tuchkov, L.T. (ed.), *Radio i svyaz*, Moscow (in Russian).
44. Shtager, E.A. 1986. Wave scattering at the bodies of complex shape, *Radio i svyaz*, Moscow (in Russian).
45. Shirman, Ya. D., Gorshkov, S.A., Leshchenko, S.P., Bratchenko, G.D., and Orlenko, V.M. 1996. Simulation of radar scattering, detection, recognition, and tracking, *Zarubezhnaya Radioelektronika*, 11, 3–63 (in Russian).
46. Sukharevsky, O.I. and Dobrodnyak, A.F. 1988. Three-dimensional problem of diffraction by an ideally conducting wedge with a radio-absorbing cylinder on the edge, *Radiophysics and Quantum Electronics*, 31(9), 763–769.
47. Rogers, D.F. and Adams, J.A. 1989. *Mathematical Elements for Computer Graphics*, 2nd edition, McGraw-Hill, Inc, New York, NY.
48. Sweetman, B. 1992. *Northrop B-2 Stealth Bomber: The Complete History, Technology, and Operational Development of the Stealth Bomber (Mil-Tech Series)*, Motorbooks Intl., USA.
49. Sweetman, B. and Dorr, R.F. 1997. B-2 Stealth Bomber, *World Air Power Journal*, 31, 50p.
50. Brekhovskikh, L.M. 1980. *Waves in Layered Media*, Academic Press, New York.
51. Sukharevsky, I.V. and Semenyaka, E.N. 1999. *Additional Chapters of Higher Mathematics. Issue 5: Quadrature and Cubature Formulas (Classics and Modern Developments)*, Kharkov Military University, Kharkov (in Russian).

52. Zamyatin, V.I., Bakhvalov, B.N., and Sukharevsky, O.I. 1978. Computer calculation of directivity patterns of curved radiating surfaces, *Journal of Communication Technologies and Electronics*, 23(6), 1289–1293 (in Russian).
53. Fok, V.A. 1945. Diffraction at a convex body, *Journal of Experimental and Theoretical Physics*, 15(12), 693–698 (in Russian).
54. Vasilets, V.A. and Tkachuk, K.I. 2004. Electromagnetic scattering characteristics of aerial and ground radar objects, in: *Proceedings of International Conference on Mathematical Methods in Electromagnetic Theory MMET-2004,* Dniepropetrovsk, 589–591.
55. Sukharevsky, O.I., Vasilets, V.A., and Gorelyshev, S.A. 2001. RCS of the objects with non-perfectly scattering surface that has fractures, in: *Proceedings of the All-Russian Conference Radiation and Scattering of EMW IZEMV-2001*, TGRU, Taganrog, 46–48 (in Russian).
56. Ruck, G.T., Barrick, D.E., Stuart, W.D., and Krichbaum, C.K. 1970. *Radar Cross Section Handbook*, Ruck, G.T. (ed.). Plenum Press, New York.
57. Knott, E.F. 2004. *Radar Cross Section*, Knott, E., Shaeffer, J., Tuley, M. (eds), 2nd edition, SciTech Publishing, Inc. Raleigh, NC 27613.
58. Kouyoumjian, R.G. and Peters, L., Jr. 1965. Range requirements in radar cross-section measurements, *Proceedings of the IEEE*, 53(8), 920–928.
59. Mayzel's, E.N. and Torgovanov, V.A. 1972. *Measurement of the Scattering Characteristics of Radar Targets*, Kolosov, M.A. (ed.), Soviet Radio, Moscow (in Russian).
60. Barton, D.K. and Ward, H. R. 1984. *Handbook of Radar Measurement*. Prentice-Hall, Englewood Cliffs, NJ1969; Artech House, Dedham, MA.
61. Romanovsky, V.O. 1977. *Algorithms and Solutions to the Extremum Problems*, Nauka, Moscow (in Russian).
62. King, R.W. and Smith, G.S. 1981. *Antennas in Matter-Fundamental*, *Theory and Applications*, MIT Press, Cambridge, MA.
63. Anan'in, E.V., Vaksman, R.G., and Patrakov, Yu. M. 1994. Methods for reducing radar visibility, *Zarubezhnaya Radioelektronika*, 4–5, 5–21 (in Russian).
64. Mikhaylov, G.D., Sergeev, V.I., Solomin, E.A., and Voronov, V.A. 1994. Methods and means for reducing radar visibility of antenna systems, *Zarubezhnaya Radioelektronika*, 4–5, 54–59 (in Russian).
65. Masalov, S.A., Ryzhak, A.V., Sukharevsky, O.I., and Shkil, V.M. 1999. Physical grounds of wide-band stealth technologies, *Mozhaysky Higher Engineering and Command School*, St. Petersburg, Russia (in Russian).
66. Ufimtsev, P. 1996. Comments on diffraction principles and limitations of RCS reduction techniques, *Proceedings of the IEEE*, 84(12), 1830–1851.
67. Petrov, B.M. and Semenikhin, A.I. 1994. Controlled impedance coatings and structures, *Zarubezhnaya Radioelektronika*, 6, 9–16 (in Russian).
68. Nebabin, V.G. and Belous, O.I. 1987. Methods and techniques for countering radar recognition, *Zarubezhnaya Radioelektronika*, 2, 38–47 (in Russian).
69. Martynov, N.A. and Mironenko, G.N. 1996. Evaluation of electromagnetic wave scattering characteristics of complex shape bodies, which are partially covered with radar absorbent material, *Radiotekhnika*, 6, 102–105 (in Russian).
70. Kukobko, S.V., Sazonov, A.Z., and Sukharevsky, I.O. 2005. Electro dynamical method for simulating two-dimensional model of the two-reflector antenna system under the nose dielectric radome, *Radiofizika i Radioastronomiya*, 10(2), 157–162 (in Russian).
71. Kukobko, S.V., Sazonov, A.Z., and Sukharevsky, I.O. 2004. Iterative calculation method for two-dimensional model of reflector-type antenna with sharp nose radome, in: *Proceedings of International Conference on Mathematical Methods in Electromagnetic Theory MMET-2004*, Dniepropetrovsk (Ukraine), 409–411.
72. Sukharevsky, O.I., Kukobko, S.V., and Sazonov, A.Z. 2005. Volume integral equation analysis of two-dimensional radome with a sharp nose, *IEEE Transactions on Antennas and Propagation*, 54(4), 1500–1506.
73. Kukobko, S.V., Sazonov, A.Z., and Sukharevsky, I.O. 2005. Mathematical simulation of reflector-type antenna with sharp nose radome scattering (two-dimensional problem), in: *Proceedings of International Conference on Antenna Theory and Techniques ICATT-2005*, Kiev (Ukraine), 180–183.
74. Kozakoff, D.J. 2009. *Analysis of Radome-Enclosed Antennas*, Artech House, Boston, London.
75. Gibson, W.C. 2008. *The Method of Moments in Electromagnetics*, Boca Raton: Chapman & Hall CRC. Taylor & Francis Group.
76. Volakis, J.L. and Sertel, K. 2012. *Integral Equation Methods for Electromagnetics*, Raleigh, NC.

77. Goldshtein, L.D. and Zernov, N.V. 1971. *Electromagnetic Fields and Waves*, Soviet radio, Moscow (in Russian).
78. Booth, A.D. 1957. *Numerical Methods*, Butterworth Scientific Publications, London.
79. Stepanov, Y.G. 1971. Antiradar camouflage. Army Foreign Science and Technology Center, Charlottesville, VA, USA, Report No. FSTC-HT-23-442-70.
80. Sukharevsky, O.I., Vasilets, V.A., Sazonov, A.Z., and Tkachuk, K.I. 2004. Computer simulation of caustic surface appearing due to scattering from the cone's inner surface, *Radiotekhnika: All-Ukrainian Interservice Collection of Papers*, 139, 56–59 (in Russian).
81. Sukharevsky, I.V. and Vashinsky, S.E. 1998. About the stationary phase points and caustic influence on lateral radiation of antenna systems with radomes, in: *Proceedings of International Conference on Mathematical Methods in Electromagnetic Theory MMET-98,* Kharkov (Ukraine), Vol. 2, 537–539.
82. Borovikov, V.A. and Kinber, B. Ye. 1994. Geometrical theory of diffraction, *IEE Electromagnetic Wave Series* 37, Institution of Electrical Engineers, London.
83. Sukharevsky, I.V., Vazhinsky, S.V., and Sukharevsky, I.O. 2010. 3-D radome-enclosed aperture antenna analyses and far-side radiation, *IEEE Transactions on Antennas and Propagation,* 58(9), 2843–2849.
84. Wehner, D.R. 1995. *High Resolution Radar*, 2nd edition, Artech House, Boston, London.
85. Gabrielyan, D.D., Zvezdina, M. Yu., and Sinyavsky, G.P. 2005. Diffraction problems for the surfaces with radar absorbent coatings, *Uspekhi Sovremennoy Radioelektroniki*, 12, 3–15 (in Russian).
86. Alimin, B.F. and Torgovanov, V.A. 1976. Methods for computing the properties of electromagnetic wave absorbers, *Zarubezhnaya Radioelektronika*, 3, 29–57 (in Russian).
87. Lake, J. 2002. *The Great Book of Bombers: The World's Most Important Bombers from World War I to the Present Day,* MBI Publishing Company, St. Paul, Minnesota.
88. Sharpe, M. and Shaw, R. 2001. *Boeing 737–100 and 200*,MBI Publishing Company, Osceola, Wisconsin.
89. Bowers, P.M. 1989. *Boeing Aircraft Since 1916*, Naval Institute Press, Annapolis, Maryland.
90. Gordon, Y. 2010. Dmitriy Komissarov and Sergey Komissarov, *Antonov's Turboprop Twins: An-24, An-26, An-30, An-32*. Red Star Vol. 12, Midland Publishing Ltd., Hinckley.
91. Robert, J. (ed.) 2004. *The Encyclopedia of Aircraft: Over 3,000 Military and Civil Aircraft from the Wright Flyer to the Stealth Bomber*, 1st edition, Thunder Bay Press, San Diego, CA.
92. Eden, P. (ed.) 2004. Mikoyan MiG-29 Fulcrum. *Encyclopedia of Modern Military Aircraft,* Amber Books, London.
93. Spick, M. (ed.) 2000. MiG-29 Fulcrum. The Flanker. *Great Book of Modern Warplanes*, MBI Publishing, St. Paul, Minnesota.
94. Gordon, Y. and Davison, P. 2005. *Mikoyan Gurevich MiG-29 Fulcrum*, Specialty Press, North Branch, Minnesota.
95. Kisel', V.N. and Fedorenko, A.I. 2000. Electromagnetic scattering from cavities with complex objects inside, in: *Proceedings of International Conference on Mathematical Methods in Electromagnetic Theory MMET-2000*, Kharkov (Ukraine), Vol. 2, 447–449.
96. Kisel', V.N. and Fedorenko, A.I. 2002. Electromagnetic modeling of the jet aircraft intake with the interior impeller, in: *Proceedings of the International Conference on Mathematical Methods in Electromagnetic Theory (MMET-2002)*, Kiev, Ukraine, 2, 508–510.
97. Lagarkov, A.N. and Kisel, V.N. 2007. Electromagnetic energy absorption within extensive impedance structures, in: *Proceedings of the International Conference on Materials for Advanced Technologies (ICMAT 2007)* (SUNTEC, Singapore, 2007), Hock, L., Matitsine, S., Beng, G.Y., and Bing, K.L. (eds), World Scientific, Singapore, 3–10.
98. Peacock, L. 1997. On falcon wings: The F-16 story. *The Royal Air Force Benevolent Fund Enterprises*, RAF Fairford, United Kingdom.
99. The New Weapons of the World Encyclopedia. 2007. *An International Encyclopedia from 5000 B.C. to the 21st Century*. St. Martin's Press, New York, NY.
100. Mallika, J. 2006. Issue Brief No. 19: T-90S Bhishma. Institute of Peace and Conflicts Studies. URL accessed July 24.
101. Zaloga, S. and Markov, D. 2000. *Russia's T-80U Main Battle Tank*, Hong Kong, Concord.
102. Frank Lobitz. 2009. Kampfpanzer Leopard 2—Entwicklung und Einsatz in der Bundeswehr (Leopard 2 Main Battle Tank—Development and German Army Service). Tankograd Publishing, Erlangen, Germany.
103. Zaloga, S.J. and Sarson, P. 1993. M1 Abrams Maine Battle Tank 1982–1992. *Osprey Military*, Reed International Books Ltd, New Vanguard.

Index

S

T

W

Z